



UNIVERSITAT POLITÈCNICA
DE CATALUNYA
BARCELONATECH

Biointerfaces based on the combination of synthetic polymers and biomolecules

Anna Puiggalí-Jou

ADVERTIMENT La consulta d'aquesta tesi queda condicionada a l'acceptació de les següents condicions d'ús: La difusió d'aquesta tesi per mitjà del repositori institucional UPCommons (<http://upcommons.upc.edu/tesis>) i el repositori cooperatiu TDX (<http://www.tdx.cat/>) ha estat autoritzada pels titulars dels drets de propietat intel·lectual **únicament per a usos privats** emmarcats en activitats d'investigació i docència. No s'autoritza la seva reproducció amb finalitats de lucre ni la seva difusió i posada a disposició des d'un lloc aliè al servei UPCommons o TDX. No s'autoritza la presentació del seu contingut en una finestra o marc aliè a UPCommons (*framing*). Aquesta reserva de drets afecta tant al resum de presentació de la tesi com als seus continguts. En la utilització o cita de parts de la tesi és obligat indicar el nom de la persona autora.

ADVERTENCIA La consulta de esta tesis queda condicionada a la aceptación de las siguientes condiciones de uso: La difusión de esta tesis por medio del repositorio institucional UPCommons (<http://upcommons.upc.edu/tesis>) y el repositorio cooperativo TDR (<http://www.tdx.cat/?locale-attribute=es>) ha sido autorizada por los titulares de los derechos de propiedad intelectual **únicamente para usos privados enmarcados** en actividades de investigación y docencia. No se autoriza su reproducción con finalidades de lucro ni su difusión y puesta a disposición desde un sitio ajeno al servicio UPCommons No se autoriza la presentación de su contenido en una ventana o marco ajeno a UPCommons (*framing*). Esta reserva de derechos afecta tanto al resumen de presentación de la tesis como a sus contenidos. En la utilización o cita de partes de la tesis es obligado indicar el nombre de la persona autora.

WARNING On having consulted this thesis you're accepting the following use conditions: Spreading this thesis by the institutional repository UPCommons (<http://upcommons.upc.edu/tesis>) and the cooperative repository TDX (<http://www.tdx.cat/?locale-attribute=en>) has been authorized by the titular of the intellectual property rights **only for private uses** placed in investigation and teaching activities. Reproduction with lucrative aims is not authorized neither its spreading nor availability from a site foreign to the UPCommons service. Introducing its content in a window or frame foreign to the UPCommons service is not authorized (*framing*). These rights affect to the presentation summary of the thesis as well as to its contents. In the using or citation of parts of the thesis it's obliged to indicate the name of the author.

BIOINTERFACES BASED ON THE COMBINATION OF SYNTHETIC POLYMERS AND BIOMOLECULES

Presented by Anna Puiggali-Jou

Supervisors: Dr. Luis Javier del Valle and Prof. Carlos Alemán

Tutor: Raimon Jané Campos

Thesis submitted to obtain the degree Doctor of Philosophy in Biomedical
Engineering at Universitat Politècnica de Catalunya

Barcelona, January 2019

Departament d'Enginyeria Química

Grup d'Innovació en Materials i Enginyeria Molecular



UNIVERSITAT POLITÈCNICA
DE CATALUNYA
BARCELONATECH



A Ramon

*Forget your perfect offering.
There is a crack, a crack in everything.
That's how the light gets in.*

(Leonard Cohen)

Abstract

During the last decades, research focused on the preparation of highly selective and smart materials has increased considerably. For instances, it has been possible to achieve intelligent drug nano-carriers, biomolecular sensors, platforms to promote cell growth and differentiation among many other striking applications. Two mentionable factors that helped such development are the incorporation of biological moieties onto this interfaces to gain specificity and the combination of more than one material in order to get a synergistic effect between the different components (i.e. conducting polymers suffer from poor mechanical strength, therefore, its combination with polyesters can reduce their fragility).

This thesis has been devoted to the design and development of high performance polymeric materials for multiple functions related to the biomedical field, such as passive ion transport membranes, drug delivery systems and the addition of selectivity in different surfaces. The work gives special emphasis to the characterization of these platforms, like its surface chemistry, topology, biocompatibility or its mechanical strength. Besides, these systems have been synthesized in a large variety of shapes, from free-standing nanomembranes to polymeric nanoparticles.

The Thesis is divided in three parts:

The first encloses all the studies realized for the generation of hybrid nanoporated membranes in order to achieve controlled ion diffusion. Specifically, an outer membrane protein, Omp2a, was considered for these studies. Primarily, the protein was purified, folded and characterized in an ambient resembling to the one encountered in nature, its mechanical forces and conductivity were analysed. The project was followed by the immobilization of Omp2a into silicon microcantilevers to acquire greater knowledge of its folding and unfolding processes upon thermal stress. Next, artificial polymeric membranes containing nanofeatures were developed with the final purpose to immobilize Omp2a via protein confinement. Then, the conductivity of the membrane with different electrolyte media solutions was tested.

The second part describes the state-of-the-art of drug delivery systems prepared with intrinsically conducting polymers to achieve controlled drug release upon electrical stimuli. Furthermore, two systems based on poly(3,4-ethylenedioxythiophene) (PEDOT) nanoparticles are described. Particularly, curcumin was employed as a model neutral drug and incorporated within the PEDOT nanoparticles. The oxidation state of the PEDOT chains regulated the drug release. Later on, a similar system was generated with polyester microfibers loaded with curcumin and nanoparticles. The driving force for the later drug release was the actuation of the PEDOT nanoparticles.

Lastly, the third part reports the immobilization of a pentapeptide called CREKA and its analog CR(MMe)EKA onto PEDOT and silicon surfaces. The addition of the pentapeptides favoured the

selectivity of those interfaces towards clotted plasma proteins such as fibrin and fibrinogen. PEDOT-peptide material allowed the electrochemical detection of the proteins by an increase in membrane resistance and these interactions were evaluated with microcantilevers by measuring the difference on weight when they were incubated with different protein concentrations.

Overall, the compilation of the studies presented in this Thesis offer a comprehensive view on how modifying and generating hybrid materials is possible to optimize and exploit their capabilities for a wide range of applications.

Acknowledgements

Sí, per fi! Ja era hora. Ara és la meva, ara és el meu moment; el moment de tancar una etapa, de dir ja n'hi ha hagut prou, de posar punt i final a aquest llibre. Quin martiri, semblava que no s'acabaria mai! Però, com sempre, després de la tempesta surt el sol i et pots sentir orgullosa de tot el camí que has recorregut. Els fruits sorgits d'aquest esforç no haurien estat possibles sense l'ajuda i motivació de molta gent. Durant aquest viatge he intentat exprémer el màxim de mi mateixa, aprofitar cada oportunitat per aprendre una tècnica nova, visitar un nou país o conèixer científics de tot arreu; he pogut experimentar la fascinació, l'admiració i una gratitud immensa envers moltes persones.

Surely, it has not been an easy task, more than four years experiencing happiness, disappointment, curiosity, excitement... just for a glimpse of science. But, indeed, the work is done, and there is nothing left to say but thank you to all the people who have collaborated in this project and in my personal growth.

Primer de tot vull donar les gràcies als meus directors, Carlos i Lucho, per donar-me l'oportunitat de realitzar una tesi doctoral; realment, una experiència de vida. Però sobretot, per les hores invertides, ja sigui a l'hora d'escriure (no he conegut ningú tan eficaç com tu, Carlos) o a l'hora de treballar al laboratori (Lucho, qui sap on són totes les coses, com aconseguir-les o tots els trucs). A tots dos, gràcies per la paciència, la perseverança, la bona voluntat i per deixar-me fer i desfer al meu gust.

I am also thankful to our collaborators:

Prof. Eric Perpete and Dr. Catherine Michaux working at the University of Namur. Thanks to them I discovered the hard work required in molecular biology and the enjoyment of Belgium beers! Thanks for making my stay so comfortable and for all the knowledge about transmembrane proteins.

Thanks to Prof. Slawomir Sek working at the University of Warsaw with whom I discovered the AFM world. I have to admit that I saw him giving a talk in Barcelona, and since that moment I decided that I wanted to learn from him. His passion, optimism and kindness make me feel like at home in a very cold city, especially in November!

My special thanks to Prof. Marcelo Calderon working at the Freie University of Berlin for welcoming me in his amazing team. I have never been in such a long group seminar, oh God, how many questions! From him I learned that to grasp the surface is not enough, it is necessary to look a bit further, to not be shy and discuss, argue... because it is only then when you can learn something.

Estic molt agraïda a tots els membres del grup, presents, passats i futurs. A la Mar, la meua primera companya de despatx, per ser la meua motivació per continuar endavant; quantes coses hauré après de tu! A l'Elaine, per les discussions sobre impedància, per l'organització del lab i per estar disposada a escoltar-me. Gràcies Georgina, per estar sempre a punt, amunt i avall, i sense cap

pèl a la llengua. *A Angelica, por su amabilidad y por tener una familia preciosa.* Al Francesc, pels seus coneixements d'electroquímica i d'AFM. Al David i al Guillem, per la vostra saviesa i pensament crític. Al Jordi, amb qui he patit la tesi, compartit l'estada a Bèlgica i viscut tantes anècdotes. Al Guillem, l'amo de la festa; quants riures, sobretot a l'hora de netejar el lab. *A Brenda, por su carisma y paciencia, por ser la mejor compañera de mesa del lab. Also to you Max, to our endless discussions about the importance of Omp2a and SCALA, I really value our friendship. A Neudys, por acoger a los nuevos siempre con una sonrisa. A Mary-Cruz, por transmitir alegría a toneladas. A Sonia, por ser tan dulce.* Al Dídac, per la seva honestetat, i al Jordi, per portar la música a dins. *A Hamidreza, por su bondad. A Ludmila, a quien deseo lo mejor en su doctorado.* A l'Ina, la Silvana, la Cinthia, l'Enric, l'Amir, el Reza, el Hamidreza II... Al Manolo, la Maria Teresa, les Lourdes, la Núria, el Joan i el Jordi. *Also to those who only stayed for a short period like Maryam, Paula, Marcele, Amir or to our students Judith, Paolo, Alberto and Roberto.*

Als tècnics del centre Multiescala, a la Montse per tots els anàlisis d'XPS i per confiar en mi, i al Trifon per ensenyar-me a utilitzar la majoria d'aparells del centre i compartir amb mi una mica del seu temps.

Des de l'inici del grau que compartim les il·lusions i desil·lusions, Laura i Marta; tot i la distància, us sento molt a prop.

Als amics de tota la vida, aquells que seran allà pel que calgui, que tenen la capacitat de fer-te oblidar tots els problemes; en especial, als *graciencs* i a les *nenes maques*.

A tu, Edu; qui sap si un dia acabarem junts, si farem una família, si viurem a Barcelona o perduts pel món; però ara que podem, gaudim de la incertesa del futur.

Als de casa, que aguanten tot el mal humor contingut de les frustracions i decepcions. Els que tot i així t'encoratgen a seguir endavant. Gràcies per insistir en què fes el doctorat. Gràcies per la joia de compartir la vida i sobretot pels sopars i *tuppers!* A la meva mare, pel seu pragmatisme i capacitat de trobar una solució per a tot, i al meu pare, per les converses infinites. Al Jordi, per ser el millor germà que podria demanar. I al Levi, que s'ha passat hores i hores dormint sobre la funda del meu ordinador. Sense oblidar l'Elvira i els avis que ja no hi són: Ramon, Francesca i Jordi.

A tots vosaltres, moltes gràcies.

Table of contents

<u>Abstract</u>	I
<u>Acknowledgments</u>	III
<u>Table of contents</u>	V
<u>List of figures</u>	VIII
<u>List of tables</u>	XIII
<u>List of abbreviations</u>	XVI
<u>List of symbols</u>	XXXI
<u>CHAPTER 1 - Introduction</u>	1
1.1 Motivation of the Thesis research	3
1.2 Biomaterials, evolution and prospective	5
1.3 References.....	9
<u>CHAPTER 2 - Objectives</u>	11
<u>CHAPTER 3 - Biomimetic hybrid membranes</u>	19
SUMMARY	21
3.1 Introduction	23
3.2 Cell membranes: Description and biological relevance.....	24
3.3 Expression of membrane proteins	25
3.4 Incorporation onto polymeric substrates.....	29
3.4.1 Amphiphilic copolymers	29
3.4.2 Nanostructured polymers.....	40
3.5 Conclusions and outlook.....	49
3.6 References.....	50
<u>CHAPTER 4 - Charecterization of Omp2a</u>	59
SUMMARY.....	61
4.1 Introduction	63
4.2 Materials and methods	63
4.3 Properties of Omp2a-Based Supported Lipid Bilayers	65
4.3.1 Methods.....	66
4.3.2 Results and discussion	70
4.3.3 Conclusions.....	95
4.4 Thermomechanical response of Omp2a for biomimetics.....	96

4.4.1 Methods	97
4.4.2 Results and discussion	102
4.4.3 Conclusions	121
4.7 References.....	122

CHAPTER 5 - Incorporation of Omp2a onto nanoporated membranes.....131

SUMMARY	133
5.1 Introduction.....	135
5.2 Materials and methods.....	136
5.3 Nanoperforations in poly(lactic acid) free-standing nanomembranes	137
5.3.1 Methods	138
5.3.2 Results and discussion	141
5.3.3 Conclusions	156
5.4 Confinement of a β -barrel protein in nanoporated free-standing nanomembranes for ion transport.....	158
5.4.1 Methods	160
5.4.2 Results and discussion	163
5.4.3 Conclusions	193
5.5 References.....	194

CHAPTER 6 - Drug delivery systems based on intrinsically conducting polymers...203

SUMMARY	205
6.1 Introduction: drug delivery systems (DDSs)	207
6.2 Intrinsically conducting polymers	209
6.3 Architecture of ICPs for DDSs.....	212
6.4 Drug loading.....	213
6.5 Drug release.....	215
6.5.1 Cyclic voltammetry (CV).....	215
6.5.2 Chronoamperometry and chronopotentiometry	217
6.6 Nanostructure matters	218
6.6.1 Polymer films.....	219
6.6.2 Polymer nanoparticles	227
6.6.3 Polymer nanowires, fibers and nanotubes	231
6.6.4 Polymer nanoporous films and sponges.....	236
6.6.5 Polymer hydrogels.....	241
6.6.6 Polymer composites	244
6.6.7 Hybrid 3D-structures	251
6.7 Conclusions and outlook	252

6.8 References.....	253
<u>CHAPTER 7 - Electrostimulated release</u>	263
SUMMARY.....	265
7.1 Introduction	267
7.2 Materials and methods	269
7.3 Electrostimulated release of neutral drugs from polythiophene nanoparticles: smart regulation of drug-polymer interactions.....	271
7.3.1 Methods.....	271
7.3.2 Results and discussion.....	274
7.3.3 Conclusions.....	289
7.4 Smart drug delivery from electrospun fibers through electro-responsive polymeric nanoparticles	290
7.4.1 Methods.....	292
7.4.2 Results and discussion.....	297
7.4.3 Conclusion	315
7.5 References.....	315
<u>CHAPTER 8 - CREKA</u>	327
SUMMARY.....	329
8.1 Introduction	331
8.2 Fibrin association at hybrid biointerfaces made of clot-binding peptides and polythiophene ..	332
8.2.1 Methods	333
8.2.2 Results and discussion	339
8.2.3 Conclusions.....	358
8.3 Weighing biointeractions between fibrin(ogen) and clot-binding peptides using microcantilever sensors	359
8.3.1 Methods.....	361
8.3.2 Results and discussion	366
8.3.3 Conclusions.....	377
8.3 References.....	378
<u>CHAPTER 9 - Conclusions</u>	387
9.1 General conclusions	389
9.1 Specific conclusions	391
<u>ANNEX</u>	397

List of figures

CHAPTER 1 - Introduction

Figure 1.1 Evolution of biomaterials. From left to right: classical bioinert materials, followed by the appearance of bioactive and biodegradable materials, which led to the preparation of biomaterials able to mimic biological systems and besides be bioactive and biodegradable. Adapted with permission².....6

CHAPTER 2 - Objectives

Figure 2. 1 Scheme representing the Thesis objectives..... 16

CHAPTER 3 - Biomimetic hybrid membranes

Figure 3.1 (a) Membrane topography of the Aq monomer (left) and crystal structure (side view, left; top view, right) with four water molecules (red balls) shown in aqueous pore region. Helices are labelled H1–H8. Reproduced with permission from reference²⁴. (b) Strand-sequencing using ionic current blockage. A typical trace of the ionic current amplitude (left) through an α -HL pore clearly differentiates between an open pore (top right) and one blocked by a strand of DNA (bottom right) but cannot distinguish between the \sim 12 nucleotides that simultaneously block the narrow transmembrane channel domain (red bracket). Reproduced with permission from reference³⁴. (c) Top view of the gA channel as a space-filling model (color code: white, carbon atoms; blue, nitrogen atoms; red, oxygen atoms) using coordinates from PDB 1MAG. Note how the alternating L–D arrangement allows all amino acid side chains to project outward from the channel lumen and the channel lumen is lined by the peptide backbone. (d) Axial and equatorial views of crystallized OmpF, a representative MP. Reproduced with permission from reference⁸³.....28

Figure 3.2 LA-functionalized PB-PEO vesicles spread onto a bare gold surface. Reproduced with permission from reference⁶⁸. (b) PB-PEO-OH and PB-PEO-LA were transferred onto gold substrates by applying consecutively the LB and LS techniques to form a polymer tethered bilayer (left), where the protein was inserted (right).....32

Figure 3.3 (a) Representation of MP insertion when using BB into solid-supported polymer membrane. (b) Conductance measured when a voltage of 40 mV is applied on bare Au, the bilayer, the bilayer with the protein incorporated using Bio-Beads (bilayer+MloK1+BB), the bilayer with the protein (bilayer+MloK1), and the bilayer with the Bio-Beads (bilayer+BB). Reproduced with permission from reference⁷⁰.....33

Figure 3.4 Schematic illustration of pore-spanning membrane on the PCTE: design and synthesis. (a) Incorporation of AqpZ in PMOXA–PDMS–PMOXA (ABA copolymer) vesicles. (b) Surface modification of the PCTE membrane support in a two-step process: (i) coating with a monolayer of

cysteamine through chemisorption; and (ii) the primary amine are converted to acrylate residues via conjugating with acrylic acid. (c) Pressure-assisted vesicle adsorption on the PCTE support. (d) Covalent-conjugation-driven vesicle rupture and pore-spanning membrane formation. Reproduced with permission from reference ²⁵.34

Figure 3.5 Field-emission scanning electron microscopy (a-c) and atomic force microscopy images (d-f) of the gold coated alumina substrate (a and d), the substrate covered with the polymer membrane (b and e), and the substrate covered with the AqpZ-incorporated polymer membrane (c and f). Reproduced with permission from reference ³⁰.35

Figure 3.6 Field-emission scanning electron microscopy of (a) CA, (b) silanized CA, and (c) AqpZ-containing PMOXA–PDMS–PMOXA triblock copolymer. Reproduced with permission from reference ⁷².36

Figure 3.7 Schemes of AqpZ-embedded vesicular membrane at the top: (a) AqpZ reconstitution into the vesicles formed from ABA block copolymer blends. DDM stands for dodecyl- β -D-maltoside, a detergent for protein stabilization; (b) Immobilization of the vesicles onto the substrate by pressure; (c) addition of the self-assembled monolayer of cysteamine; and (d) PDA-His coating on the top of the membrane. (e-h) Field-emission scanning electron microscopy micrographs at the bottom: (e) gold-coated PCTE membrane with a self-assembled monolayer of cysteamine (pore size 50 nm); (f) PCTE membrane with 3-cycle coating of PDA–His on the top of chemisorbed cysteamine (control); and (g) vesicles immobilized on the PCTE membrane with 3-cycle coating of PDA–His on top. The micrograph displayed in (h) corresponds to a zoom of (g). Adapted with permission from reference ³².37

Figure 3.8 (1) Aqpz-polymer vesicles, (2) porous CA membrane substrate, (3) Aqpz vesicles immobilized on the porous membrane, (4) Aqpz-vesicle-imprinted membrane, and (5) cross-section of the Aqpz-vesicle-imprinted membrane. (b-g) Field-emission scanning electron microscopy micrographs displayed the membrane morphologies: (b, c) top surface and cross-section of the porous substrate CA membrane; (d, e) non-vesicle-imprinted membrane; and (f, g) Aqpz-vesicle-imprinted membrane. Adapted with permission from reference ³³. 38

Figure 3.9 (a) GlpF molecular representation (green) together with ribitol, as a model sugar alcohol (red). Side (right) and front (left) views are represented. (b) Schematic representation of a functionalized surface serving as a sugar alcohol biosensor based on immobilized proteopolymersome nanoreactors with selective transport due to the GlpF presence and detection of sugar alcohols due to the encapsulated enzymes. Adapted with permission from reference ⁷⁵.39

Figure 3.10 Procedure scheme for the fabrication of nanoporated membranes, the modification of nanopore size by atomic layer deposition (ALD), the creation of hydrophobic pore surfaces by vapour exposure treatment with hexamethyldisilazane (HMDS), and the immobilization of gA. Adapted with permission from reference ⁷⁹.41

Figure 3.11 Surface morphology of (a) PNMPy–Omp2a, (b) PNMPy and (c) nanoporated PLA membranes: low- and high-magnification SEM micrographs are displayed at the left and the right,

respectively. Adapted with permission from references ⁸³ and ⁸⁵. (d) 3D AFM phase images of the skin surfaces of nanoporated PLA nanomembranes before (left) and after (right) incubation with a 0.5 mg/mL Omp2a solution. Adapted with permission from reference⁸⁵.42

CHAPTER 4 - Characterization of Omp2a

Figure 4.3.1 Scheme of the liposome fabrication.....	66
Figure 4.3.2 Scheme of the lipids chemical composition.	70
Figure 4.3.3 Topographic AFM images with the corresponding vertical profiles and TEM images of SLBs obtained from liposomes composed of: (a) 4:3 POPC:POPE (Mixt-1); (b) 4:3:1 POPC:POPE:POPG (Mixt-2); and (c) 4:3:1:2 POPC:POPE:POPG:CL (Mixt-3) diluted 1/5 in 1x PBS.	72
Figure 4.3.4 Topographic AFM images of SLB obtained from 4:3:1 PC:PE:PG liposomes incubated onto mica overnight and diluted in 1x PBS at (a) 1/5, (b) 1/10 and (c) 1/20 ratios.	74
Figure 4.3.5 Force-distance curve-based AFM for SLB obtained from 4:3:1 PC:PE:PG liposomes incubated onto mica overnight and diluted in 1x PBS at 1/5 ratio.	74
Figure 4.3.6 The protein was inserted on the lipid bilayer using two different methods: (a) Formation of proteoliposomes from preformed liposomes; and (b) Insertion of the Omp2a protein by direct incorporation the Omp2a protein into SLBs.	75
Figure 4.3.7 DLS results expressed in term of (a) intensity vs diameter, (b) ζ values and (c) CD spectra of proteoliposomes prepared from detergent-mediated reconstitution of the protein using 40, 80 and 100 w/w lipid-to-protein ratio, control liposomes (i.e. preformed liposomes), blank liposomes (i.e. preformed liposomes altered by adding the reconstitution detergent medium but without protein) and Omp2a solution. (d) SDS-PAGE gel for the proteoliposomes. TEM micrographs of (e) blank liposomes and (f) proteoliposomes prepared using 80 w/w lipid-to-protein ratio. Histograms showing the diameter distributions are also displayed.	77
Figure 4.3.8 Topographic AFM images (first row) of SLB obtained from (a) POPC:POPE:POPG (4:3:1) liposomes or from proteoliposomes achieved using (b) 40, (c) 80 and (d) 100 w/w lipid-to-protein ratios spread over mica. Data were recorded on buffer solution (150 mM KCl, 10 mM Tris-HCl, pH 7.8). The red lines in AFM images indicate where from the vertical profile shown below (second row) each image has been extracted. Also, insets of each AFM image and profile are shown below (third and fourth rows, respectively).....	79
Figure 4.3.9 (a) Representative topographic AFM images of SLB obtained from POPC:POPE:POPG (4:3:1) proteoliposomes (80 w/w lipid-to-protein ratio) spread over mica. The red lines in the AFM images indicate the region used to extract vertical profile shown next to each image. (b) TEM images of Omp2a stained with uranyl acetate (scale bar: 10 nm). (c) Representative topographic AFM images of SLB obtained from POPC:POPE:POPG (4:3:1) proteoliposomes (80 w/w lipid-to-protein ratio) spread over mica. Particle analyses were performed on $2 \times 2 \mu\text{m}^2$ images. Light blue regions indicate particles below 45 nm (protein oligomers) while dark blue spots	

correspond to particles above 45 nm (protein aggregates). Data were recorded with a buffer solution (150 mM KCl, 10 mM Tris-HCl, pH 7.8). (d) Particle diameter distribution and height distribution of protein oligomers (< 45 nm).80

Figure 4.3.10 Topographic AFM images of: (a) SLB obtained from POPC:POPE:POPG (4:3:1) liposomes, (b) after being incubated with 0.01 %Triton X-100, and (c) further incubated in a refolding solution with 10 µg/mL of Omp2a. Data were recorded on buffer solution (150 mM KCl, 10 mM Tris-HCl, pH 7.8). The red lines in the AFM images (a-c) indicate where from the vertical profiles shown below have been extracted. 82

Figure 4.3.11 Topographic AFM images of: (a) SLB obtained from POPC:POPE:POPG (4:3:1) liposomes, (b) after being incubated with 0.01 %Triton X-100, and (c) further incubated in a refolding solution with 2 µg/mL of Omp2a. Data were recorded with the buffer solution (150 mM KCl, 10 mM Tris-HCl, pH 7.8). The red square shows where the inset has been obtained from. The red line in the AFM image indicates (c) where from the vertical profile shown below has been extracted. Red circles correspond to protein agglomerates..... 83

Figure 4.3.12 FD-based AFM images of POPC:POPE:POPG (4:3:1) proteoliposomes (80 w/w lipid-to-protein ratio) spread onto mica: (a) topography, (b) DMT modulus map, (c) adhesion map and (d) deformation map. Data were recorded with the buffer solution (150 mM KCl, 10 mM Tris-HCl, pH 7.8). The red lines in the AFM images (a-d) indicate where from the vertical profile shown below or next to each image has been extracted. The histograms below the profiles express the percentage of particles below 45 nm in diameter (protein oligomers) vs the difference in the indicated parameter with respect to lipid bilayer values. 87

Figure 4.3.13 FD-based AFM images of PC:PE:PG (4:3:1) liposomes spread over mica: (a) topography, (b) DMT modulus map, (c) adhesion map, and (d) deformation map . Data were recorded on buffer solution (150 mM KCl, 10 mM Tris-HCl, pH 7.8). The red lines in the AFM images (a-c) indicate where the vertical profile shown below or next to each image has been extracted.....88

Figure 4.3.14 Voltammograms of SWV obtained for bare GCE and GCE covered by refolding buffer (GCE+MPD), spread liposomes (GCE+liposomes) and spread proteoliposomes (GCE+proteoliposomes). 90

Figure 4.3.15 (a) Schemes representing the ITO, the lipid bilayer and the lipid bilayer containing Omp2a with the corresponding EEC used for fitting the experimental data from EIS measurements: RS is the electrolyte resistance; QM and RM are the membrane constant phase element and resistance, respectively; and Qdl is the double layer constant phase element for the electrode surface. (b) Nyquist plots of ITO (green stars), lipid bilayer (purple triangles), lipid bilayer with the reconstituted protein at 100 (blue circles), 80 (red diamonds) and 40 w/w (black squares) lipid-to-protein ratio in 0.1 M KCl. Symbols correspond to experimental data, while lines are the fitted curves according to EEC. (c) Average conductance measured for the lipid bilayer and those

containing the protein at different lipid-to-protein ratios. (d) Bode plots of the systems described in (b)..... 93

Figure 4.4.1 FTIR spectra in the region of amide I of (A) BSA, (B) LYS and (C) Omp2a at 30 °C and 100 °C (left and right, respectively). The deconvolution of the amide I absorption band is displayed in all cases.....103

Figure 4.4.2 CD spectra (left) recorded for (a) BSA, (b) LYS and (c) Omp2a proteins at temperatures ranging from 5 °C to 90 °C (heating runs). Measurements for BSA and LYS were performed using a carbonate buffer, whereas a dodecyl sulfate (SDS) – 2-methyl-2,4-pentanediol (MPD) buffer was used for Omp2a (Supporting Information). The variation of amount of secondary structures (in %) against the temperature is also represented (middle). Effective diameter (right) derived from DLS measurements at temperatures ranging from 20 °C to 60 °C (measures for heating and cooling runs are displayed) for (a) BSA, (b) LYS and (c) Omp2a proteins. Two profiles are displayed for BSA since a bimodal distribution was found for all examined temperatures, while a unimodal histogram was observed for both LYS and Omp2a.....104

Figure 4.4.3 CD spectra recorded for BSA, LYS and Omp2a proteins at temperatures ranging from 90 °C to 5 °C (cooling runs). The figure represents the variation of amount of secondary structures (in %) against the temperature. Results obtained for the heating run are displayed in the main text.....105

Figure 4.4.4 (a) 1D scattering patterns of blank (salts from the buffer solution) and Omp2a samples as dry powder at room temperature. (b) 2D scattering patterns of the blank and Omp2a dried samples at room temperature. (c) 1D scattering pattern of Omp2a when a temperature ramp (heating) is applied. (d) Intensity of the peak profile for the blank and the Omp2a samples at $q = 15.6 \text{ nm}^{-1}$ during the temperature ramp.106

Figure 4.4.5 (a) Protein functionalization protocol for silicon substrates. (b) N 1s, C 1s and O 1s high-resolution XPS spectra for non-functionalized (hydroxylated; Si-OH) and protein functionalized (LYS, BSA or Omp2a) silicon substrates. Peaks from deconvolution are also displayed..... 108

Figure 4.4.6 (a) Average contact angle of non-functionalized and functionalized silicon substrates. Greek letters on the columns refer to significant differences when 1 way ANOVA and Tukey's multiple comparison tests are applied: α vs Si-OH ($p < 0.0001$) and β vs BSA ($p < 0.0001$). (b) Topographic AFM images of non-functionalized and functionalized substrates ($500 \times 500 \text{ nm}^2$). (c) Representative cross sectional profiles for AFM images..... 110

Figure 4.4.7 (a) Silicon chips with arrays of eight cantilevers used for nanomechanical measurements (Micromotive GmbH). (b) Scheme displaying the experimental setup used to evaluate the thermal response of LYS, BSA and Omp2a proteins. Nanomechanical resonance response of a silicon cantilever functionalized with (c) LYS, (d) BSA and (e) Omp2a. The shift with respect to the hydroxylated (non-functionalized) cantilever used as reference is displayed.111

Figure 4.4.8 (a) Nanomechanical response, expressed as resonance frequency shift ($|\Delta f|/f$), of functionalized cantilevers (mean values and standard error of the mean calculated with the data of at least 16 different cantilevers). (b) Relative displacement as a function of the temperature of a representative hydroxylated (non-functionalized) cantilever. Thermomechanical response of cantilevers functionalized with (c) LYS, (d) BSA and (e) Omp2a proteins. Right: mean relative displacement as a function of the temperature (blue, red and green dots in C, D and E, respectively) and the corresponding standard error of the mean (thick light-grey lines), both calculated with the data of at least 7 different cantilevers, are displayed at the right. Left: cartoons schematizing the folded \rightarrow unfolded transitions in c and d, and the trimer \rightarrow large aggregate and β -barrel \rightarrow unfolded transitions in E. The four regions described in the text are labelled in e.112

Figure 4.4.9 (a) Surface stress determined for hydroxylated (control) and protein-functionalized cantilevers at 120 °C. Significant differences are encountered on groups marked with the Greek letter α (<0.05) compared to the control group. (b) Variation of the surface stress for hydroxylated (control) and protein-functionalized cantilevers against the temperature.....120

CHAPTER 5 - Incorporation of Omp2a onto nanoporated membranes

Figure 5.3.1 Three dimensional height (left) and phase (right) AFM images of different PLA and PLA-PEG nanomembranes obtained by mixing PLA (10 mg/mL) : PEG (10 mg/mL) chloroform solutions and applying a spin-coater speed of 7000 rpm: (a) PLA (1:0); (b) 50:50 PLA-PEG; (c) 60:40 PLA-PEG; (d) 80:20 PLA-PEG; and (e) 90:10 PLA-PEG. The AFM image windows are $10 \times 10 \mu\text{m}^2$ in all cases..... 142

Figure 5.3.2 (a) Three dimensional height (left) and phase (right) AFM images of PLA supported nanomembrane prepared using a 10 mg/mL polymer solution in chloroform and a spin-coater speed of 7000 rpm. AFM images of PLA (b) the supported nanomembrane and (c) the corresponding FsNM prepared using a 10 mg/mL polymer solution in HFIP and a spin-coater speed of 7000 rpm. The FsNM was obtained after removing the sacrificial layer of the supported nanomembrane. The AFM image windows are $10 \times 10 \mu\text{m}^2$ in all cases. (d) Representative profilometry of supported. The blue, uncoloured and purple regions correspond to the glass support, the PVA sacrificial layer and the PLA membrane, respectively..... 145

Figure 5.3.3 Schematic representation of the procedure used to prepare perforated PLA nanomembranes from PLA-PVA ultra-thin films by the spin-coating technique. (b) 90:10 PLA-PVA nanomembrane supported onto a SiO_2 wafer (blue arrow) and 90:10 PLA FsNM (red arrow) floating on ultrapure water. 146

Figure 5.3.4 Three dimensional height (left) and phase (right) AFM images of PLA-PVA supported nanomembranes prepared using a (a,b) 80:20 and (c,d) 90:10 PVA:PLA mixture in HFIP. Nanoporated PLA FsNMs obtained via selective water etching using the (b) 80:20 and (d) 90:10 PLA-PVA supported nanomembranes: The AFM image windows are $10 \times 10 \mu\text{m}^2$ in all cases.....148

Figure 5.3.5 Three dimensional height (left) and phase (right) AFM images of (a) PLA-PVA supported nanomembranes prepared using a vigorously stirred 90:10 PVA:PLA mixture in HFIP and (b) nanoporferated PLA FsNMs obtained via selected water etching using the supported nanomembranes displayed in (a). In all cases image windows are $10 \times 10 \mu\text{m}^2$ (top) and $10 \times 10 \mu\text{m}^2$ (bottom).....149

Figure 5.3.6 SEM micrographs of nanoporferated (a and b) 90:10 PLA and (c-g) 90:10 PLA(stir) FsNMs prepared using 90:10 PLA:PVA mixtures in HFIP. Details on a-f are described in the text. A folded 90:10 PLA(stir) FsNM showing the presence of nanoporferations at the two sides is displayed in (g). This SEM image reflects that nanoporferations cross the thickness of the nanomembrane..150

Figure 5.3.7 Pore diameter distribution for (a) 80:20 PLA, (b) 90:10 PLA and (b) 90:10 PLA(stir) nanomembranes. (d) AFM depth profiles for the 80:20 PLA, 90:10 PLA and 90:10 PLA(stir) FsNMs. 151

Figure 5.3.8 (a) Contact angle determined of milliQ water, DMF and EG. (b) Surface energy calculated using OWK and EOS models for non-perforated PLA, 90:10 PLA and 90:10 PLA(stir) FsNMs.....153

Figure 5.3.9 (a) Cellular adhesion and (b) cellular proliferation on the surface of nanoporferated 90:10 PLA and PLA (stir) membranes and non-perforated PLA membranes. Vero and MCDK cells were culture during 24 h (adhesion assay) and 7 days (proliferation (c) Optical microscopy (left) and SEM (right) images of Vero cells adhered onto perforated 90:10 PLA and 90:10 PLA(stir) nanomembranes.....155

Figure 5.4.1 (a) SDS-PAGE of Omp2a. Monomers migrate at 39 kDa while trimers show an apparent molecular weight of 115 kDa. (b) CD spectra for the Omp2a protein: as-obtained, after 4 days of incubation and deposited into the nanoporferations of PLA NMs. (c) DLS results showing the volume percentage of particles towards particle diameter for SDS micelles in the buffer solution used to maintain the protein, the same solution after incorporate the Omp2a protein and a PBS solution with Omp2a.164

Figure 5.4.2 TEM micrographs of Omp2a trimeric units (short red line) and higher aggregates (large red line) derived from solutions stained with 2% uranyl acetate. Scale bar of the high resolution micrographs: 10 nm. The effective diameter (D_{eff} , in nm) distribution for both Omp2a trimers and aggregates are also displayed (top and bottom, respectively).....165

Figure 5.4.3 (a) 3D AFM height images coloured with phase skin: PLA-PVA NM obtained using a 99:1 PLA:PVA mixture (left) and nanoporferated PLA NM derived from PLA-PVA via selective water etching; (b) High magnification SEM micrographs, pore diameter distribution, and AFM height images (2×2 and $0.5 \times 0.5 \mu\text{m}^2$) with their corresponding phase images for nanoporferated PLA NM obtained using 99:1 PLA:PVA mixtures.167

Figure 5.4.4 FTIR spectra of: (a) individual PLA and PVA membranes; (b) as prepared membranes obtained by solvent casting 99:10 and 99:1 PLA:PVA mixtures; (c) membranes of (b) after 2 h in milliQ water; and (d) membranes of (b) after one day in milliQ water.....168

Figure 5.4.5 (a) SEM micrograph and (b) 3D AFM height image ($5 \times 5 \mu\text{m}^2$) of non-perforated PLA NMs..... 169

Figure 5.4.6 (a) Average CA and Rq values ($5 \times 5 \mu\text{m}^2$ surface area) determined for ITO substrate, non-perforated PLA NMs, nanoporated PLA before and after Omp2a incubation. Greek letters on the columns refer to significant differences ($p < 0.05$) when the 1 way ANOVA and Tukey's multiple comparisons test are applied: α vs ITO, β vs non-perforated PLA and δ vs nanoporated-PLA. Images of the drops onto nanoporated PLA with (bottom) and without (top) immobilized Omp2a are also displayed. (b) SEM micrographs of perforated PLA NMs after Omp2a immobilization: low and high magnifications at left and right, respectively. Dashed arrows illustrate the presence of big protein aggregates. (c) AFM height and their corresponding phase images (window: $0.5 \times 0.5 \mu\text{m}^2$) of nanoporated PLA after Omp2a incubation. Several representative cross-sectional profiles showing the topography and dimensions of the nanopores (dashed circles) are also displayed. In all samples, incubation was performed considering a 0.5 mg/mL Omp2a solution. 170

Figure 5.4.7 AFM height and their corresponding phase images (window: $5.0 \times 5.0 \mu\text{m}^2$) of nanoporated PLA after Omp2a deposition..... 171

Figure 5.4.8 (a) 3D AFM phase images of the skin surfaces of perforated PLA NMs before (left) and after (right) incubation with a 0.5 mg/mL Omp2a solution. Oval protein aggregates are clearly identified at the surface and inside the nanopores. Diameter (b) and height (c) distributions of the protein aggregates observed in (a). (d) Results from Bradford assays for non-perforated (incubation with a 0.50 mg/mL Omp2a solution) and perforated (incubation with 0.5 , 0.25 and 0.125 mg/mL Omp2a solutions). Grey spheres represent the retention efficiency (in %) while black bars correspond to the mass of protein entrapped per unit of area ($\mu\text{g}/\text{cm}^2$). Error bars indicate the standard deviation and greek letters on the columns refer to significant differences ($p < 0.05$) in protein entrapped per unit of area ($\mu\text{g}/\text{cm}^2$) when the 1way ANOVA and Tukey's multiple comparisons test are applied: α vs non-perforated PLA, β vs nanoporated-PLA incubated with 0.25 mg/mL and δ vs nanoporated-PLA incubated with 0.125 mg/mL172

Figure 5.4.9 Bode (a, b) and Nyquist (c, d) plots of ITO (circle), non-perforated PLA (square), nanoporated PLA (triangle), Omp2a-coated non-perforated PLA (cross) and Omp2a-filled nanoporated PLA (diamond) in NaCl 0.5 M ; (d) corresponds to an amplified area from (c), for better visualization of high frequency zone. Symbols correspond to experimental data, while lines are fitted curves according to EEC. (e) EEC used for fitting the experimental data from EIS measurements: R_s is the electrolyte resistance; Q_M and R_M are the membrane constant phase element and resistance, respectively; Q_{dl} and R_p are the double layer constant phase element and the pore resistance, respectively. The depicted surfaces are (left) ITO and (right) non-perforated PLA, nanoporated-PLA and Omp2a-filled nanoporated PLA NMs (from top to bottom).175

Figure 5.4.10 Nyquist plots of (a) non-perforated, (b) nanoporated and (c) Omp2a-filled nanoporated PLA NMs in NaCl, KCl and CaCl_2 aqueous solutions at 50 , 100 , 500 and 1000 mM concentrations (black, dark blue, red and light blue profile, respectively). Symbols correspond to

experimental data, while lines are the fittings to the corresponding electrical equivalent circuit (EEC) displayed in **Figure 5.4.9e**..... 179

Figure 5.4.11 (a) Comparison of the NM conductance ($G_m = 1/R_m$) values for Na^+ (grey), K^+ (red), and Ca^{2+} (blue) electrolytes at different concentrations. In most of the cases, values are the mean of 3 samples and their standard deviation. Greek letters on the columns refer to significant differences ($p < 0.05$) when the 2way ANOVA and Tukey's multiple comparisons test are applied: α vs non-perforated PLA, β vs nanoporated-PLA and δ vs Omp2a-filled nanoporated PLA. Dependence of the conductivity (σ ; Eq. 4.4.1) as a function of the ion concentration in solution for (b) Omp2a-filled nanoporated and (c) nanoporated PLA NMs. Non-perforated PLA membrane conductivities are below the dotted orange line. In general the values are the mean of three samples and their standard deviation. 180

Figure 5.4.12 Variation of the Omp2a-filled nanoporated membrane resistance (R_m) with the KCl concentration. The values are the mean of three samples and their standard deviation.....181

CHAPTER 6 - Drug delivery systems based on intrinsically conducting polymers

Figure 6.1 Reversible redox activity of poly(3,4-ethylenedioxythiophene) (PEDOT).....210

Figure 6.2 (a) Scale of material's conductivity (a), adapted from.²⁸ (b) Chemical structure of the most employed ICPs (PAni, PPy and PEDOT). 211

Figure 6.3 SEM images of PPy–Dex coated film: (a) as prepared and (b) after 50 CV cycles. Adapted from⁵⁸.216

Figure 6.4 Scheme of different nanostructures. Adapted form ⁸⁹ 219

Figure 6.5 (a) Micrograph of a polyimide neural probe with 4 PEDOT/Dex coated electrode sites. Procedure for probe insertion is shown in (b) with an optical fibre as guiding tool. The final placement of the electrodes can be seen in (c). Both the passive probe (control) and the active probe (functionalized) were fixated to the skull. The connection of the active probe to the recording/stimulation equipment was achieved via a connector placed on the head of the animal (d).⁸³..... 220

Figure 6.6 (a) Chemical synthesis of PPy NPs (top) and chemical structures of fluorescein (bottom left) and daunorubicin (bottom right). (b) SEM image of fluorescein-encapsulated PPy NPs. (c) Photograph showing the solid-gel transition of the injectable conductive hydrogel. (d) SEM image of air-dried hydrogel containing PPy NPs. Adapted from ref¹⁰⁰.....227

Figure 6.7 (a) Schematic illustration of DOX-attached PPy nanowires (DOX/PPy). DOX molecules were chemically conjugated to the biotin dopants of the PPy nanowires through 1-Ethyl-3-(3-dimethylaminopropyl)-carbodiimide/N-hydroxysuccinimide EDC/NHS chemistry. DOX/ PPy nanowire arrays have synergistic effects in cancer therapy by direct application of an electric potential and localized NIR light. (b) SEM images of the fabricated PPy nanowire arrays. Different

polymerization times were employed to achieve PPy nanowires with length of 5 (left), 15 (middle), and 25 μm (right), respectively. Adapted from¹¹⁰..... 232

Figure 6.8 Schematic representation of PPy scaffold fabrication and drug loading (a). SEM micrographs of: (b) PMMA colloidal crystal template onto the stainless substrate; (c) the PPy film obtained by electropolymerization and subsequent PMMA template removal; (d) and (e) cross sectional views of the PPy structures following the electropolymerization of the dense PPy layer. Reproduced with permission from reference¹¹⁸ 236

Figure 6.9 (a) Scheme of reversible changes in pore size (and the drug release rate) between oxidation and reduction states. (b) Drug flux versus time when the pore diameter is 110 nm (oxidation-blue open circles) and when the reduction state (magenta closed circles). A data point was collected every 10 s. (b,c) In situ AFM height images corresponding to the oxidation and the reduction states, respectively.¹¹⁹. 237

Figure 6.10 Photographs of the ICP-containing solution before crosslinking (a) and after crosslinking with OD (b). Graph showing drug release in phosphate buffered saline (PBS) solution under different electric potentials (c). Addapted from¹²⁵..... 242

Figure 6.11 Scheme representing the loading and release process of CNT nanoreservoirs (i). SEM images of the PPy/CNTa film (a, b) and the PPy/CNTb film (c, d). CNTa: outer diameter 110-170 nm; CNTb: outer diameter 20-30 nm (ii). Reproduced with permission from reference¹³⁴..... 244

Figure 6.12 Corrosion driven drug release. Dex release from PEDOT/GO/Dex films deposited onto a magnesium surface in which the drug delivery is powered by the substrate corrosion. Magnesium samples had either long or short exposed area but the same amount of coverage by the PEDOT/GO/Dex coating. Reproduced with permission from reference¹⁴¹..... 246

Figure 6.13 (a) Cross-section of cellulose–PPy composite film; (b) High magnification image of a. (c) Energy dispersive X-ray spectrum of cellulose–PPy composite film. (d) Digital photo of the drug delivery system with the coating of magnesium layer on the one side of the cellulose–PPy composite film. Adapted from¹⁴². 247

Figure 6.14 Schematics of the microelectronic cardiac patch concept. (a). An image of a freestanding, flexible device consisting of 32 gold electrodes dispersed within a porous mesh of SU-8 (b). Scanning electron micrographs (SEMs) of a $50 \times 50 \mu\text{m}^2$ electrode pad designated for recording cellular electrical activities and cell and tissue stimulation (c) and a larger $150 \times 150 \mu\text{m}^2$ electrode pad, on which electroactive polymer is deposited for controlling the release of biomolecules (that is, growth factors and small molecules) (d). Scale bars, $50 \mu\text{m}$. d,e, Atomic force microscopy images of a pristine gold electrode pad (e) and an electrode with a nanoscale layer of titanium nitride deposited to increase surface area (f). Adapted from¹⁴⁶..... 251

CHAPTER 7 - Electrostimulated release

Figure 7.3.1 (a) Schematic representation of the chemical synthesis of PEDOT NPs by emulsion polymerization. (b) Transmission electron microscopy (TEM) micrographs of PEDOT NPs obtained using the procedure displayed in (a). (c) Chemical structure of CUR and PIP.....276

Figure 7.3.2 SEM images of (a) CUR/PEDOT NPs, (b) PIP/PEDOT NPs, (c) PEDOT NPs (Scale bar: 200 nm). Effective diameter histograms derived from SEM measurements and average values are also displayed. (d) AFM images ($1 \times 1 \mu\text{m}^2$) of (top) PEDOT, (middle) CUR/PEDOT and (bottom) PIP/PEDOT NPs. The graphs displayed in panels corresponds to the profile of the selected particles. (e) AFM images of (top) CUR/PEDOT and (bottom) PIP/PEDOT NPs: 3D height images $2 \times 2 \mu\text{m}^2$ (right column), 2D height images (left top) and 2D phase images (left bottom) $250 \times 250 \text{nm}^2$277

Figure 7.3.3 FTIR spectra of (a) PEDOT NPs, CUR and CUR/PEDOT NPs; and (b) PEDOT NPs, PIP and PIP/PEDOT NPs.....278

Figure 7.3.4 Cumulative drug release comparison between drug/PEDOT NPs and free drug (control) dispersed in aqueous solutions and dialysed against PBS+0.5% Tween 20, the previous PBS solution with 10% EtOH, and with 70% EtOH: (a) CUR and (b) PIP.279

Figure 7.3.5 (a) Camera image of the three electrodes set-up for the electrochemical characterization of unloaded PEDOT and drug/PEDOT NPs. The red arrow points out released CUR in experiments with CUR/PEDOT NPs. WE, CE and RE refer to the working electrode, the counter electrode and the reference electrode, respectively. Cyclic voltammograms for (b) unloaded PEDOT NPs, (c) CUR/PEDOT NPs and (d) PIP/PEDOT NPs recorded from -1.5 to 1.0 V at different varying scan rates (10, 20, 40, 60, 80, 100, 200, 300 and 400 mV/s) using PBS $1 \times$ (pH 7.4) as electrolyte medium. Variation of the current density (j_p) at the anodic and cathodic peaks (e) of CUR and at the anodic peak (f) of PIP against the square root of the scan rate.280

Figure 7.3.6 CV of (a) CUR and (b) PIP in PBS $1 \times$ (pH = 7.4). Initial and final potential: -1.5 V; reversal potential: 1.0 V. Scan rates: 10, 20, 40, 60, 80, 100, 200, 300 and 400 mV/s.....282

Figure 7.3.7 Effect of (a,c) voltage with time constant (3 min) and (b,d) of time with voltage constant (-1.25 V) on drug release for drug/PEDOT NPs: (a,c) CUR and (b,d) PIP ($n = 6$). The percentage of released drug is expressed with respect to the total amount of loaded drug.....283

Figure 7.3.8 (a) Cytotoxicity studies of PEDOT NPs and DBSA on PC3 and MCF-7 cells for 24 h. Although they are represented in the same graphic, assays with PEDOT NPs and DBSA were performed independently. (b) Cytotoxicity evaluation of CUR and CUR/PEDOT NPs on PC3 and MCF-7 cells for 24 h. Values are the mean of 3 samples and bars indicate their standard deviation. Greek letters on the columns/points refer to significant differences when the 2-way ANOVA and Tukey's multiple comparisons test are applied: α , δ , β indicate significant differences observed within the specific concentration group with p-values lower than 0.05, 0.001 and 0.0001, respectively.287

Figure 7.3.9 (a) High magnification fluorescent images of PC3 and MCF-7 cells incubated with nothing (control), PEDOT NPs, CUR and CUR/PEDOT NPs for 24 h. Scale bars represent $40 \mu\text{m}$.

(b) Low magnification cell images of PC₃ and MCF-7 incubated with CUR/PEDOT NPs for 24 h. Scale bars represent 100 μm . For each panel, the images from left to right showed cell nuclei stained by Hoechst (blue), CUR fluorescence (green) and overlays of both images. (c) Cell circularity assessed by ImageJ software. β indicates significant differences with a p-value lower than 0.0001 when a t-test is performed.288

Figure 7.4.1 (a) Chemical structures of PEDOT, CUR and PCL. (b) Schematic representation of the chemical process used to prepare PEDOT NPs. (c) Effective diameter (D_{eff}) of PEDOT NPs derived from dynamic light scattering. The graph is expressed in intensity versus diameter. (d) FTIR spectra of PEDOT NPs doped with DBSA. The main absorption peaks from the thiophene, ether, and sulfonate groups correspond to: stretching modes of C=C in the thiophene ring at 1647 and 1557 cm^{-1} , CH₂ stretching modes at 1478, 1396, and 750 cm^{-1} , C–O–C vibrations at 1206 and 1057 cm^{-1} , and the S–O stretch at 667 cm^{-1}297

Figure 7.4.2 (a) SEM micrograph of PEDOT NPs. Inset: effective diameter histogram derived from SEM measurements. (b) Optical micrographs of electrospun MFs (scale bar: 50 μm). (c) Raman and (d) UV-vis spectra of the investigated systems.298

Figure 7.4.3 Low (inset) and high magnification SEM micrographs (left), effective diameter (D_{eff}) histogram derived from SEM measurements (center) and AFM image (right) of (a) PCL, (b) PCL/CUR, (c) PCL/PEDOT and (d) PCL/PEDOT/CUR electrospun MFs. The average value of D_{eff} , the root mean square roughness (R_q) and widow size of the AFM image are also displayed. The presence of small beads in (a) is highlighted with light blue circles, while PEDOT NPs at the surface of the fibers in (c) and (d) is marked with red dashed lines.301

Figure 7.4.4 (a) Representative high magnification topographic (left, top), height (right, top) and colored phase (left, bottom) AFM images of PCL/PEDOT MFs, supporting the presence of individual PEDOT NPs distributed at the surface of PCL fibers. Cross sectional profile of the PEDOT NP (right, bottom) at the region marked in the height image. (b) Cross section SEM images of PCL/PEDOT. Internally located PEDOT NP is illustrated by the red circle. (c) High magnification topographic AFM image of PCL/PEDOT/CUR. Widow size of the AFM images is displayed in (a) and (c). (d) CA (θ) of water for polymer-modified ITO bare and coated with PCL, PCL/CUR, PCL/PEDOT and PCL/PEDOT/CUR fiber mats. Values correspond to the mean while error bars indicate the standard deviations (i.e. no less than fifteen drops were examined).303

Figure 7.4.5 CVs registered within the potential range of -0.80 to $+1$ V at a scan rate of 100 mV/s using a $\text{K}_4[\text{Fe}(\text{CN})_6]$ solution for (a) commercial polymer-modified ITO electrodes and (b) commercial polymer-modified ITO electrodes coated with PCL, PCL/CUR, PCL/PEDOT and PCL/PEDOT/CUR fiber mats. (c) Peak separation (ΔE_p , in V) and (d) formal potential (E_f , in V) for commercial polymer-modified ITO bare and coated with PCL, PCL/CUR, PCL/PEDOT and PCL/PEDOT/CUR fiber mats. In (c) and (d) values correspond to the mean while error bars indicate the standard deviations (i.e. five independent voltammograms were recorded for each system)....305

Figure 7.4.6 MTT evaluation of MCF-7 cultured on 3D MFs scaffolds for (a) 24 hours and (b) 7 days. Values are the mean and bars indicate their standard deviation (i.e. assays were repeated two times independently and with n=4). Greek letter refers to significant differences when one-way ANOVA and multiple comparison test is applied, p-value is lower than 0.05. (c) Confocal microscopy micrographs displaying the morphology of cells adhered (24 hours) and proliferated (7 days) onto 3D MFs matrices. Cells were stained for the nucleus in blue (Hoechst) and F-actin in green (Phalloidin Atto 488). Scale bar = 100 μ m. Different zones magnification remarked in red. In all cases (a-c) aluminum sheets were used as control substrate.....308

Figure 7.4.7 (a) Scheme representing cells seeded on a 3D scaffold. (b) High magnification fluorescence microscopy images of MCF-7 cells incubated on PCL MFs for 24 hours. Cells found on different planes are marked with red arrows. (c) Cell area quantification (d) and cell circularity after 24 hours and 7 days. Values correspond to the mean, while error bars indicate the standard deviations (i.e. no less than 20 values were considered for each case).....309

Figure 7.4.8 (a) CUR release profiles from PCL/CUR and PCL/PEDOT/CUR MFs in PBS-EtOH. The release profile obtained from PCL/PEDOT/CUR MFs prepared with half of loaded drug is displayed to illustrate the dependence with the CUR concentration. Values correspond to the mean while error bars indicate the standard deviations (i.e. assays were repeated four times). (b) Scheme representing the diffusion mechanism followed by PCL/CUR and PCL/PEDOT/CUR to release CUR in absence of electro-stimulation. (c) CUR release from PCL/CUR and PCL/PEDOT/CUR MFs after electro-stimulate by applying 1, 3 and 5 consecutive potential pulses (the voltage and time-length of each pulse consisted of 1.00 V and 60 s, respectively, consecutive pulses being separated by 5 s). The release obtained from PCL/CUR and PCL/PEDOT/CUR MFs prepared reducing the concentration of loaded drug by a half. (d) Scheme representing the electro-actuation mechanism followed by PCL/PEDOT/CUR MFs to release CUR upon electro-stimulation. (e) SEM micrographs of PCL/PEDOT/CUR fibers after electrostimulation. The magnification of the micrographs increases from left to right. Inset at the right micrograph: effective diameter histogram of superficial PEDOT NPs derived from SEM measurements.....311

CHAPTER 8 - CREKA

Figure 8.2.1 Scheme displaying the synthetic strategy used to prepare PEDOT (control) and PEDOT-peptide bilayered films (a and b, respectively). The strategy involved a two-step process: (1) deposition of the internal PEDOT layer onto the AISI steel electrode; and (2) deposition of PEDOT (a) or PEDOT-peptide (b) onto the layer prepared in (1). It is worth noting that a and b only differ in the absence or presence of peptide in the generation medium used for step 2. After this, subsequent surface functionalization with fibrin and application as selective bioactive surface are also displayed. RE, WE and CE refer to the reference electrode, working electrode and counter electrode, respectively.....339

Figure 8.2.2 Topographic (3D) and height (2D) AFM images of (a) PEDOT, (b) PEDOT-CREKA and (c) PEDOT-CR(NMe)EKA.....	340
Figure 8.2.3 High-resolution XPS spectra in the N 1s region for (a) PEDOT, (b) PEDOT-CREKA, and (c) PEDOT-CR(NMe)EKA. Peaks from deconvolution are also displayed.....	342
Figure 8.2.4 Initial control voltammogram (a), voltammogram after five consecutive oxidation-reduction cycles (b) and variation of the LEA (Eq. 8.2.1) against the number of redox cycles (c) in 0.1 M PBS (pH= 7.4) of PEDOT, PEDOT-CREKA and PEDOT-CR(NMe)EKA. Initial and final potentials: -0.40 V; reversal potential: 0.80 V. Scan rate: 50 mV/s.....	343
Figure 8.2.5 (a) THR-catalyzed polymerization of Fg monitored by DLS. Polymerization was initiated by adding THR (0.01 U/mL) to a Fg (0.4 mg/mL) filtered aqueous solution (5 mM CaCl ₂ and 76 mM NaCl). These experimental conditions were taken from reference. ⁴⁶ Polymer formation was measured through the effective diameter (D_{eff} , in nm) as a function of time (in min). CREKA (b) and CR(NMe)EKA (c) were added (0.1 mg/mL) to the same Fg solutions with and without THR to evaluate the influence of the peptide in the polymerization process. In all cases data correspond to the average of at least three independent experiments.	345
Figure 8.2.6 Adsorption of fibrin and BSA onto the surface of PEDOT and PEDOT-peptide films. Four samples were analysed for each group. Bars represent the mean \pm standard deviation.	347
Figure 8.2.7 Low and high resolution SEM images of fibrin particles adsorbed onto (a) PEDOT-CREKA and (b) PEDOT-CR(NMe)EKA. White boxes in (a) and (b) indicate the magnified regions.	348
Figure 8.2.8 Quantitative assessment of the fibrin particles adsorbed onto PEDOT-CREKA and PEDOT-CR(NMe)EKA surfaces. Histogram showing the percentage of (a) the area and (b) the aspect ratio (AR) of the adsorbed fibrin structures after 60 min of the addition of THR and Fg.....	349
Figure 8.2.9 Optical images of eosin stained fibrin adsorbed on (a) steel, (b) PEDOT, (c) PEDOT-CREKA and (d) PEDOT-CR(NMe)EKA.....	350
Figure 8.2.10 Control voltammograms in 0.1 M PBS (pH= 7.4) of fibrin-coated PEDOT, PEDOT-CREKA and PEDOT-CR(NMe)EKA films. Initial and final potentials: -0.40 V; reversal potential: 0.80 V. Scan rate: 50 mV/s.	352
Figure 8.2.11 (a) Bode plots for all stainless steel electrodes coated with PEDOT-peptide without and with fibrin adsorbed at the surface. (b) Electrical equivalent circuits (EEC) for bare steel, steel coated with PEDOT, PEDOT-CREKA and PEDOT-CR(NMe)EKA without and with fibrin adsorbed at the surface (see Table 8.2.3).	353
Figure 8.2.12 Nyquist plots for all stainless steel electrodes coated with (a) PEDOT-CREKA and (b) PEDOT-CR(NMe)EKA without and with fibrin adsorbed at the surface.....	354
Figure 8.2.13 (a) Percentage of MCF-7 cells attached to different surfaces: bare steel, PEDOT, biocomposites, and biocomposites coated with fibrin. In all cases data correspond to the average of	

five independent assays \pm the standard deviation. Asterisk marks (*) and (***) represent significant difference among the samples at $p < 0.05$ and $p < 0.001$, respectively. SEM micrographs of MCF-7 cells onto PEDOT-CR(NMe)EKA films (b) without and (c) with adsorbed fibrin at the surface. (d) Comparison of the percentage of normal (PNT2) and metastatic (PC3) prostate epithelial cells attached to different surfaces. The description of both the surfaces and the marks is identical to that given for (a). SEM micrographs of PC-3 cells onto (e) PEDOT films and (f) PEDOT-CR(NMe)EKA. Scale bar: 20 μm357

Figure 8.3.1 Experimental set-up for the nanomechanical biosensing tests.....366

Figure 8.3.2 Tumor-homing peptides used in this work CREKA and CR(NMe)EKA367

Figure 8.3.3 Functionalization protocol of silicon surfaces with CREKA or CR(NMe)EKA pentapeptides.367

Figure 8.3.4 (a) CA values of water and (b) Rq of the silicon square surface in each different step of the functionalization process. Greek letters are assigned to statistically significant different groups (p -value < 0.05).368

Figure 8.3.5 N 1s high-resolution XPS spectra for each silicon surface throughout the functionalization protocol. Peaks from deconvolution are also displayed.....370

Figure 8.3.6 Topographical characterization (areas of $5 \times 5 \mu\text{m}^2$): (top) 2D AFM height and (middle) phase micrographs of Si-OH (left) and CR(NMe)EKA (right) surfaces. (bottom) Height profile of a horizontal line drawn as depicted in a).372

Figure 8.3.7 Topographical characterization (areas of $5 \times 5 \mu\text{m}^2$): 2D AFM height (top) and phase micrographs (bottom) of Epoxysilane (left), NTA-NH₂ (middle) and CREKA (right) surfaces. Height profile of a horizontal line drawn as depicted.....373

Figure 8.3.8 Protein adhesion assay carried out in PBS. Absorbance values were obtained from ab-HRP activity. Greek letters on the columns refer to significant differences (p -value < 0.05) when the 2-way ANOVA and Tukey's multiple comparisons test are applied: α vs Si-CR(NMe)EKA BSA absorbance, β vs Fb absorbance on TCP.374

Figure 8.3.9 Eigenmode shape response of the 8 cantilevers of a cleaned chip (1st resonance mode).375

Figure 8.3.10 Nanomechanical response: (a) absolute frequency shift of cantilevers after being incubated with 10 $\mu\text{g}/\text{mL}$ of BSA, Fg and Fb; (b) mechanical resonance frequency of a Si cantilever before and after the Fb recognition event (10 $\mu\text{g}/\text{mL}$ in PBS); (c and d) relative resonance-frequency shift vs protein concentration of (c) Fg and (d) Fb in PBS. Mean values and standard deviations are calculated with the data of a minimum of 10 different cantilevers. Lines are a guide for the eye.....376

Figure 8.3.11 Mechanical resonance frequency of a Si cantilever before and after the biorecognition event with (a) Fg and (b) BSA (10 $\mu\text{g}/\text{mL}$ in PBS).377

List of tables

CHAPTER 3 - Biomimetic hybrid membranes

Table 3.1 Summary of the most important characteristics (i.e. preparation method, polymer, protein and activity) of biomimetic membranes made of polymers..... 44

Table 3.2 Summary of the advantages and disadvantages encountered during the preparation and application of the different type of biomimetic membranes made of polymers.....47

CHAPTER 4 - Characterization of Omp2a

Table 4.3.1 R and CPE (a) for each sample, analyzed in KCl 0.1 M solution, obtained from fitting parameter with the EECs displayed in Figure 4.3.15a. The percentage error associated to each circuit element is included in parentheses. 95

Table 4.4.1 Atomic percent composition (O 1s, C 1s, Si 2p and N 1s) obtained by XPS for non-functionalized (hydroxylated) and protein functionalized (i.e. with BSA, LYS or Omp2a covalently immobilized at the surface) silicon substrates..... 109

CHAPTER 5 - Incorporation of Omp2a onto nanoporated membranes

Table 5.3.1 Physical parameters of non-perforated and perforated PLA NMs derived from 90:10 and 99:1 PLA:PVA mixtures: Average diameter of the nanopores (ϕ), root-mean-square roughness (Rq) ($5 \times 5 \mu\text{m}^2$ surface area) and film thickness (L), which also corresponds to the depth of the pores.....143

Table 5.3.2 Thickness (L) and RMS roughness (Rq) of PLA, PLA-PEG and PLA-PVA ultra-thin films prepared in this work. Observed nanofeatures are also indicated. 146

Table 5.3.3 Average diameter (ϕ) and area (A) of the pores, surface coverage by pores (S), RMS roughness (Rq) and thickness (L) of perforated PLA FsNMs derived from 80:20 and 90:10 PLA:PVA mixtures.....151

Table 5.4.1 Physical parameters of non-perforated and perforated PLA NMs derived from 90:10 and 99:1 PLA:PVA mixtures: Average diameter of the nanopores (ϕ), root-mean-square roughness (Rq) ($5 \times 5 \mu\text{m}^2$ surface area) and film thickness (L), which also corresponds to the depth of the pores. 166

Table 5.4.2 Resistances (R) and constant phase elements (CPE) for each sample, analysed in NaCl 0.5 M solution, from fitting parameters obtained with the EEC displayed in **Figure 5.4.9e**. The percentage error associated to each circuit element is included in parentheses.176

Table 5.4.3 Resistances and CPEs for each sample from fitting parameters obtained with the EEC displayed in **Figure 5.4.9e**. For each system impedance parameters are displayed according to the NaCl concentrations of 50, 100, 500 and 1000 mM. The percentage errors associated to each circuit element have been included in parentheses. 182

Table 5.4.4 Resistances and CPEs for each sample from fitting parameters obtained with the EEC displayed in Figure 5.4.9e . For each system impedance parameters are displayed according to the KCl concentrations of 50, 100, 500 and 1000 mM. The percentage errors associated to each circuit element have been included in parentheses.	184
Table 5.4.5 Resistances and CPEs for each sample from fitting parameters obtained with the EEC displayed in Figure 5.4.9e . For each system impedance parameters are displayed according to the CaCl ₂ concentrations of 50, 100, 500 and 1000 mM. The percentage errors associated to each circuit element have been included in parentheses.	186

CHAPTER 6 - Drug delivery systems based on intrinsically conducting polymers

Table 6.1 Summary of some remarkable examples of polymer films reported in literature with the most important characteristics (i.e. preparation method, polymer, drug, dopant and release mechanism) for DDSs made of ICP.	221
Table 6.2 Summary of some remarkable examples of polymer NPs reported in literature with the most important characteristics (i.e. preparation method, polymer, drug, dopant and release mechanism) for DDSs made of ICP.	229
Table 6.3 Summary of some remarkable examples of polymer nanowires, nanofibers and nanotubes reported in literature with the most important characteristics (i.e. preparation method, polymer, drug, dopant and release mechanism) for DDSs made of ICP.	234
Table 6.4 Summary of some remarkable examples of polymer nanoporous films and sponges reported in literature with the most important characteristics (i.e. preparation method, polymer, drug, dopant and release mechanism) for DDSs made of ICP.	239
Table 6.5 Summary of some remarkable examples of polymer hydrogels reported in literature with the most important characteristics (i.e. preparation method, polymer, drug, dopant and release mechanism) for DDSs made of ICP.	243
Table 6.6 Summary of some remarkable examples of polymer composites reported in literature with the most important characteristics (i.e. preparation method, polymer, drug, dopant and release mechanism) for DDSs made of ICP.	248

CHAPTER 7 - Electrostimulated release

Table 7.3.1 Effective diameter (D_{eff}) determined by SEM and DLS, drug loading ratio (DLR) and ζ -potential of unloaded-PEDOT, CUR/PEDOT and PIP/PEDOT NPs.	278
---	-----

CHAPTER 8 - CREKA

Table 8.2.1 Atomic percent composition (C 1s, N 1s, O 1s and S 2p) and S 2p / N 1s ratio obtained by XPS for PEDOT, PEDOT-CREKA and PEDOT-CR(NMe)EKA.....	341
Table 8.2.2 Contact angle (CA) determined for the surfaces examined in this work before and after adsorption of fibrin.....	351
Table 8.2.3 Resistances and constant phase for each sample analysed with EIS technique and after adjusting the parameters using the EEC shown in Figure 8.2.11b	355
Table 8.3.1 Functionalization protocol of silicon surfaces with CREKA or CR(NMe)EKA pentapeptides.	369
Table 8.3.2 Atomic percentage composition and N/C, N/O and N/Si atomic ratio for CR(NMe)EKA-functionalized surfaces before and after sonication in PBS 1x at 37 °C for 1 hour.	370

List of abbreviations

Abbreviation	Meaning
AFM	Atomic force microscopy
ALD	Atomic layer deposition
Aq	Aquaporins
Aq Z	Aquaporin Z
AR	Aspect ratio
ATP	Adenosine triphosphate
BB	Bio-Beads
BC	Bacterial cellulose
b-OG	N-octyl- β -D-gluco-pyranoside
BSA	Bovine serum albumin
CA	Contact angle
CD	Circular dichroism
Cipro	Ciprofloxacin
CL	Cardiolipine
CNTs	Carbon nanotubes
CP	Chronopotentiometry
CPE	Constant phase element
CREKA	Cys-Arg-Glu-Lys-Ala
CSA	Camphorsulfonic acid
CUR	Curcumin
CV	Cyclic voltammetry
DBS	Dodecyl benzene sulfonate
DDM	n-dodecyl- β -D-maltoside
XXVI	

DDM	Dodecyl-b-D-maltoside
DDSs	Drug delivery systems
Dex	Dexamethasone
DLR	Drug loading ratio
DLS	Dynamic light scattering
DMF	N,N-dimethyl formamide
DMT	Derjaguin, Muller, Toporov
DOX	Doxorubicin
EDC	1-[(3-Dimethylamino)propyl]-3-ethylcarbodiimide methiodide
EDX	Energy-dispersive X-ray
EEC	Electrical equivalent circuit
EG	Ethylene glycol
EIS	Electrochemical impedance spectroscopy
EOS	Equation-of-State
EPR	Enhancing permeability and retention
EtOH	Ethanol
EVA	Ethylene vinyl acetate copolymer
FBS	Fetal bovine serum
FD	Force-distance
FDA	Food and Drug Administration
Fg	Fibrinogen
Flu	Fluorescein
FsNMs	Free-standing nanomembranes
FTIR	Fourier-transform infrared
GCE	Glassy carbon electrodes
GlpF	Glycerol facilitator

GO	Graphene oxide
HFIP	1,1,1,3,3,3-Hexafluoroisopropanol
His	Histidine
HMDS	Hexamethyldisilazane
ICPs	Intrinsically conducting polymers
IMAC	Immobilized metal affinity chromatography
ITO	Indium tin oxide
LA	Lipoic acid
LB	Langmuir-Blodgett
LB	Lysogeny broth
LDAO	Lauryldimethylamine-oxide
LEA	Loss of electroactivity
LS	Langmuir-Schaefer
LYS	Lysozyme
MCF-7	Human breast (adenocarcinoma) cell line
MDCK	Madin-Darby Canine Kidney
MES	2-(N-morpholino)ethanesulfonic acid
MFs	Microfibers
MPD	2-Methyl-2,4-pentanediol
MPs	Membrane proteins
MTT	3-(4,5-dimethylthiazol-2-yl) 2,5-diphenyltetrazolium bromide
NGF	Nerve growth factor
NGR	Asn-Gly-Arg
NHS	N-hydroxysuccinimide
NIR	Near infrared light
NMP	N-methylphenphthiazine

NMs	Nanomembranes
NP-40	Nonyl phenoxy polyethoxy ethanol
NPs	Nanoparticles
NT-3	Neurotrophic factor
NTA-NH₂	N ^α ,N ^α -bis(carboxymethyl)-L-lysine hydrate
OMP	Outer membrane protein
OWK	Owen-Wendt-Kaelble
p(HEMA)	Poly(hydroxyethylmethacrylate)
P/S	Penicillin/streptomycin
PAni	Polyaniline
PB-PEO	Poly(butadiene)-b-poly(ethylene oxide)
PBS	Phosphate buffer solution
PC-3	Normal prostate epithelium cell line
PCL	Polycaprolactone
PCTE	Poly(carbonate) tracked-etched
PDA	Polydopamine
PDB	Protein data bank
PEDOT	Poly(3,4-ethylenedioxythiophene)
PEG	Polyethylene glycol
PET	Poly(ethyleneterephthalate)
PIP	Piperine
PLA	Poly(lactic acid)
PLGA	Poly(lactic- <i>co</i> -glycolic) acid
PLLA	Poly(L-lactide)
PMMA	Poly(methyl methacrylate)
PMOXA-PDMS- PMOXA	Poly(2-methyloxazoline)-block-poly(dimethylsiloxane)-block-poly(2-methyloxazoline)

PNMPy	Poly(N-methylpyrrole)
PNT-2	Normal prostate epithelium cell line
POPC	Phosphatidylcholine
POPE	Phosphatidylethanolamine
POPG	Phosphatidylglycerol
PPV/PAAM	Poly(phenylene vinylene)/polyacrylamide
PPy	Polypyrrole
PS	Polystyrene
PSD	Position detector
PSS	Poly(styrenesulfonate)
PVA	Poly(vinyl alcohol)
PVP	Poly(vinylpyrrolidone)
QNM	Quantitative Nanomechanical Mapping®
RE	Retention efficiency
RGD	Arg-Gly-Asp
SA	Salicylic acid
SCALA	Scanning Laser Analyzer
SD	Standard deviation
SDS	Sodium dodecyl sulfate
SDS-PAGE	Sodium dodecyl sulfate-polyacrylamide gel
SEM	Scanning electron microscopy
SLB	Supported lipid bilayers
SSA	Sulfosalicylic acid
STC	Standard calibration
SWV	Square-wave voltammetry
TCP	Tissue culture polystyrene
XXX	

TEM	Transmission electron microscopy
THR	Thrombin
TRIS	2-Amino-2-(hydroxymethyl)-1,3-propanediol
Trp	Tryptophan
Tyr	Tyrosine
Vero	African green monkey kidney, fibroblast cell line
WAXD	Wide angle X-ray diffraction
αHL	α -haemolysin

List of symbols

Symbol	Meaning
A	Area of the electrode
C_{dl}	Pure capacitance
CPE_c	Coating capacitance
CPE_{diff}	Diffusion capacitance
CPE_{dl}	Double layer capacitance
d	Distance between the tip and the sample
D	Distance
D_{eff}	Effective diameter
ΔT	Change of temperature
Δz	Cantilever deflection
E	Young modulus
E^*	Reduced modulus of elasticity of the sample and tip
E_s	Sample modulus of elasticity

E_t	Tip modulus of elasticity
f	Frequency
F_{adh}	Adhesion force
F_{tip}	Force acting on AFM tip
G_m	Conductance
σ	Conductivity
σ_s	Surface stress
IC_{50}	Half-maximal inhibitory concentration
j_p	Current density
k	Spring rigidity
L_m	Thickness of the membrane
L	Length
M	Effective mass
m	Mass of the protein
m_{drug}	Drug mass
$m_{polymer}$	Polymer mass
θ	Contact angle
Q_{dl}	Double layer semiconductor/electrolyte interface
Q_i	Voltammetric charge
Q_M	Membrane CPE
R	Tip radius
R_c	Coating resistance
R_{dif}	Diffusion resistance
R_M	Membrane resistance
R_p	Polarization resistance
R_q	Root mean square roughness

R_s	Electrolyte resistance
s	Membrane conductivity
S	Displacement
SC	Surface coverage by the perforations
T	thickness
vs	Poisson ratio for the material's sample
vt	Poisson ratio for the material's tip
w	Resonance frequency
W	Width
ζ	Zeta-potential
Z_{CPE}	CPE impedance
ΔQ	Difference of voltammetric charge
τ	Polymerization time

CHAPTER 1:

Introduction

1.1. Motivation of the Thesis Research

Human development goes together with the necessity to resolve problems and take advantage of different resources to build up new and useful gadgets. A clear example is when we check our surroundings and find plenty of utensils that make our life easy. When the generation of new tools is inspired by nature, like plane from birds or liposomes from lipid vesicles, it is known as biomimetics. This concept takes advantage of millions of years of evolution which has led to the generation of unique, marvellous and functional natural materials using minimal resources and efforts. Living organisms excel with fascinating elegance the production of all sorts of materials with a quite variety of shapes and organizations.

In other words, biomimetics is an interdisciplinary field that makes use of the knowledge coming from engineers, chemists, physicists and biologists applied on the synthesis of materials, systems or machines with functions that reassemble those encountered in nature. Within this context, chemistry plays a crucial role because of the necessity to generate synthetic analogues of biomacromolecular structures. Of particular scientific and technological interest are biomimetic membranes that are inspired by natural membrane compartments and organelles but avoid their drawbacks, such as membrane instability and limited control over cargo transport across the boundaries. The research to build chemically controlled bioinspired structures is mainly focused on more complex and hybrid systems. For instance, an ambitious target is to create membranes that regulate the ion or molecule exchange between one side and the other. The approach followed to achieve this can be fully synthetic or hybrid when combines macromolecules found in nature with artificial materials.

Biomimetics is a relative recent field of investigation and it has become possible due to the many advances on the different research areas. We have to take into account that, before to start producing biomimetic materials, it is important to study, characterize and understand biological systems. Herein, we want to take profit of biological membranes to prepare hybrid artificial layers able to facilitate ion transport. For that reason, firstly the focus has been deposited on the study of Omp2a structure, size and thermal properties. Secondly, on its function when is embedded on an ambient resembling those

encountered in nature and, finally, on the generation of hybrid membranes containing this protein. Therefore, we can have membranes able to facilitate ion transport with more robustness, specificity and simplicity. Thus, a combination of natural and artificial products will let to obtain outstanding materials with the advantages of each component.

Particularly, **Part A** of this thesis has been focused on describing the biological role of lipid bilayers and specific transmembrane proteins, in more detail Omp2a, and its functional, structural properties when are embed onto a polymeric artificial membrane made of a biodegradable polyester.

On the other hand, when this need is related to clinical diagnosis, treatment and tissue repair and it is in direct contact with the body the employment of biomaterials as a concept arose. Interestingly, B. M. Holzapfel *et al.*¹ defined this concept as:

“A biomaterial is a substance that has been engineered to take a form which, alone or as part of a complex system, is used to direct, by control of interactions with components of living systems, the course of any therapeutic or diagnostic procedure, in human or veterinary medicine.”

However, the name can lead to misinterpretation of its significance. The use of the term “bio” could make us think as materials that are made by living organisms such as chitin, collagen or bone. For that reason, maybe it would have been easier the name biomedical materials instead of biomaterials.² Strictly, as it is defined by the International Union of Pure and Applied Chemistry (IUPAC), a biomaterial is any material exploited in contact with living tissues, organism or microorganism.³ Biomaterials are used in a wide range of applications which include limb replacements, artificial arteries, contact lenses, artificial teeth and drug delivery systems. Surprisingly, this is not a particular new field; it has been studied and employed for many years. In literature there is some controversy regarding which was the first produced biomaterial due to it goes back to the beginning of the civilizations. However, it is thought that one of the first biomaterials used were gold and ivory for replacements of cranial defects and was done by Egyptians and Romans. Later on, celluloid was the first plastic used for cranial defects and polymethyl methacrylate (PMMA) was one of the first polymers

accepted since World War II. Out of curiosity, during Second World War aviators returning from combat were occasionally and tragically injured by plastic shards penetrating in their eyes.⁴ Interestingly, these plastic pieces could remain on pilot's eyes for many years without generating local inflammation. Starting from this material, Harold Ridley studied its use for implants. He was a pioneer in the field of intraocular lenses using PMMA due to its characteristics; rigid, non-foldable and hydrophobic (water content < 1%).⁵

Part B and C will be devoted to the design of drug delivery systems (DDSs) made of conducting and biodegradable polymers and the preparation of peptide modified interfaces for biomedical purposes.

1.2 Biomaterials, evolution and prospective

During the **1st generation** of biomaterials (1960s-1970s) almost all materials used in the body were made of one single material and the most important characteristic was its biological inertness.⁶ The vast majority of implants were made of already existing materials but with a higher level of purity, the effort being deposited on the elimination of toxic by-products and reducing the corrosion levels. There is no cellular adhesion between the bioinert material and its host tissue.

Subsequently, the **2nd generation** of biomaterials (1980s-1990s) began. The research started to be more focus on materials that were better at reassembling the mechanical and chemical properties of the host tissue. The community was no longer interested in bioinert materials but instead on the opposite, bioactive materials able to modulate and trigger a cellular response. For instances, within this period it is possible to find materials able to release active proteins, growth factors or other molecules of interest promoting the desired therapeutic effect. Additionally, a new concept was born: biodegradable and resorbable biomaterials. These materials would be breakdown and replaced by regenerating tissue leading to an ultimately no noticeable difference between the implant and the host tissue.

The **3rd generation** (2000s and onwards) is trying to combine both previously introduced concepts. Biodegradable materials containing biological active cues to trigger

specific responses are being demanded. In the case of tissue engineering, for instance, progenitor cells are being seeded inside the resorbable scaffold prior to be implanted. These scaffolds are degradable and will be ideally replaced by the host tissue. Another resulting approach from this period is the genetic control of cellular response. Some of these materials are also thought to upregulate or down regulate the expression of some specific genes.

Nowadays, there is no clear separation between the employments of the different materials because no longer classic materials alone are being used. More and more biomaterials get a complex and greater structure that uses not only primary interatomic and intermolecular bonds, but also includes different concepts from nanotechnology and the self-assembly phenomena encountered in nature.⁷ However, there is an important issue by over-complicating devices and making them too expensive for the materials market. Thus, the main challenge is to provide materials sophisticated enough to influence cell behaviour maintaining the maximum simplicity.⁸ Evolution of the biomaterials field is represented in **Figure 1.1**. Concretely, it is necessary to find the minimal cues that would make a difference in resolving a clinical problem. This is now a grown and mature field, which is very present in the market area. Therefore, the ambitious approach to replace entire organs has been divided to smaller and more attainable aims, such as focusing just on valves off the heard instead of the entire organ.

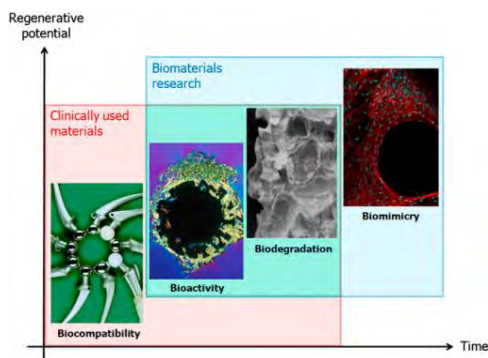


Figure 1.1. Evolution of biomaterials. From left to right: classical bioinert materials, followed by the appearance of bioactive and biodegradable materials, which led to the preparation of biomaterials able to mimic biological systems and besides be bioactive and biodegradable. Adapted with permission².

The demand grows towards materials able to stimulate tissue growth and repair rather to replacement, like living systems do. For example, when a bit more than half of human liver is excised, it has the ability to regrow to its original size.

The biomaterials industry in 2016 was worthy 70.90\$ Billions and with a 16% growth a year it is expected to reach 149.17\$ Bilions by 2021. This huge marked is progressively increasing due to the world-wide governments trying to promote the implantable device market through an increase on funding's and research grants. Not forgetting the booming number of hip and knee replacements, plastic surgeries and the rising number of elders in society (www.marketsandmarkets.com).

Polymers are very convenient for biomedical applications because it's many outstanding properties regarding mechanical strength, easier processability, cheapness and tailorable properties. In this thesis we are just going to focus on two groups of synthetic polymers (biodegradable polyesters and intrinsically conductive polymers); a few characteristics are going to be mentioned. Both present different but interesting qualities.

The main interest in the biomedical field of polyesters is their possibility to be temporary devices, meaning that the material itself is broken down and excreted or reabsorbed without any surgical operation. These are linear aliphatic polyesters, generally hydrophobic, that present tuneable physical and mechanical characteristics which allowed a high development of these materials for biomedical purposes. Examples of different medical applications include inert medical meshes, drug vehicles or physical fixation supports.⁹ For many striking applications such as biosensors, controlled drug delivery systems or tissue electrical stimulation, conducting biomaterials based on graphene, metallic particles, carbon nanotubes or nanowires have been studied. Nevertheless, there are some drawbacks to take into account like non-biodegradability, long-term in vivo toxicity or inhomogeneous distribution of the conducting material. Instead, intrinsically conducting polymers (ICPs) are organic materials with soft nature that provide better mechanical compatibility with host tissues. More importantly ICPs, are not only biocompatible but also bioactive, they can induce a cellular response including promotion of cell adhesion, migration or differentiation by electrical stimulation and/or molecules release.¹⁰ In this thesis the preparation of biomaterials for

drug delivery systems directed to cancer therapy would be discussed as well as the preparation of artificial materials taking advantages of biomolecules to increase its specificity. Besides, an extensive explanation of ICPs and their properties can be found in

Chapter 6.

1.3 References

1. Williams, D. F. On the nature of biomaterials. *Biomaterials*, **2009**, 5897–5909.
2. Holzapfel, B. M.; Reichert, J. C.; Schantz, J.-T.; Gbureck, U.; Rackwitz, L.; Nöth, U.; Jakob, F.; Rudert, M.; Groll, J. and Hutmacher, D.W. How smart do biomaterials need to be? A translational science and clinical point of view. *Adv. Drug Deliv. Rev.* **2012**, 195–218.
3. Vert, M. Doi, Y.; Hellwich, K.-H.; Hess, M.; Hodge, P.; Kubisa, P.; Rinaudo, M. and Schué, F. Terminology for biorelated polymers and applications (IUPAC Recommendations 2012). *Kem. u Ind. Chem. Chem. Eng.* **2014**, 377–410.
4. Burns, J. W. Biology takes centre stage. *Nat. Mater.* **2009**, 441–443.
5. Bellucci, R. An introduction to intraocular lenses: Material, optics, haptics, design and aberration. *Cataract*, **2013**, 38–55.
6. Hench, L. L. and Thompson, I. Twenty-first century challenges for biomaterials. *J. R. Soc. Interface*, **2010**.
7. Boom time for biomaterials. *Nat. Mater.* **2009**, 439.
8. Place, E. S., Evans, N. D. and Stevens, M. M. Complexity in biomaterials for tissue engineering. *Nat. Mater.* **2009**, 457–470.
9. Makadia, H. K. and Siegel, S. J. Biomedical Applications of Biodegradable Polymers. *Polymer (Guildf)*. **2011**, 832–864.
10. Zhao, F., Shi, Y., Pan, L. and Yu, G. Multifunctional Nanostructured Conductive Polymer Gels: Synthesis, Properties, and Applications. *Acc. Chem. Res.* **2017**, 1734–1743.
11. Liu, S.; Wang, J.; Zhang, D.; Zhang, P.; Ou, J.; Liu, B. and Yang, S. Investigation on cell biocompatible behaviors of polyaniline film fabricated via electroless surface polymerization. *Appl. Surf. Sci.* **2010**, 3427–3431.

CHAPTER 2:

Objectives

OBJECTIVES

The results of this Thesis have been organized in three blocks (visualized in a scheme form in **Figure 2.1**) as a function of the objectives set in this section.

The first part is devoted to study biomimetic membranes prepared using the Omp2a outer membrane protein. Although the main aim of this block, which has been entitled “Biomimetic membranes based on Omp2a transmembrane protein”, was to prepare polymer-based artificial free-standing nanomembranes for effective ion separation, fulfilment of a number of specific objectives was necessary for complete understanding and successful achievement of such bioinspired devices. The specific objectives addressed in this block can be summarized as follows:

- 1) Examine the response of Omp2a protein in an artificial configuration closer to the one encountered in nature than to that found in biomimetic polymer-based nanomembranes. For this purpose, the molecular forces and function of the Omp2a protein supported in a lipid bilayer, which consists in planar in vitro assemblies of lipids sitting on a solid support, have been studied using a variety of surface sensitive atomic force microscopy and electrochemical techniques, respectively.
- 2) Investigate the hierarchical organization and response of the Omp2a protein in synthetic environments as a function of the temperature. For this, the thermal transitions of such protein have been identified by combining microcantilever deflection technologies with other techniques, such as FTIR spectroscopy, circular dichroism (CD), dynamic light scattering (DLS), wide angle X-ray diffraction (WAXD), X-ray photoelectron spectroscopy (XPS) and atomic force microscopy (AFM).
- 3) Design and develop an approach to fabricate polymeric free-standing nanomembranes, preferably using biocompatible poly(lactic acid), with a homogeneous distribution of nanopores of controlled diameter crossing the entire ultra-thin film thickness (*i.e.* nanop perforations).
- 4) Immobilize the Omp2a porin into the nanoporation of poly(lactic acid) free-standing nanomembranes to fabricate artificial solid supports for selective ion

transport. Check the benefits associated to the immobilization of Omp2a inside the nanoporations with respect to the immobilization at the surface by comparing the electrochemical impedance response towards different electrolytic media.

The second part of this Thesis is devoted to the utilization of intrinsic conducting polymers as smart drug delivery systems. Two different systems suitable for the controlled release upon electrostimulation have been designed, prepared and characterized. Moreover, the regulated drug release from the smart drug dosage systems developed in this chapter, which has been entitled “Design of intrinsically controlled polymers for drug delivery systems”, is based on very different driving forces. The specific objectives afforded in this block are:

- 5) Develop conducting polymer nanoparticles for the encapsulation and controlled release of hydrophobic drugs. Release of the loaded drug from the nanoparticles is expected to be externally regulated by modulating the drug – polymer interactions through the application of an electric field.
- 6) Prepare a new electrosensitive bioplatform combining a hydrophobic drug, conducting polymer nanoparticles and electrospun polyester fibers. Release of the loaded drug is expected to be regulated by altering the porosity of the polyester fibers using as driving force the isotropic actuation principle of the conducting polymer nanoparticles upon electrostimulation.

Finally, the third and last part, “Surface functionalization with CREKA”, presents a detailed study about the interaction of CREKA (Cys-Arg-Glu-Lys-Ala) and CR(NMe)EKA (Cys-Arg-*N*-methyl-Glu-Lys-Ala), two linear peptide that recognize clotted plasma proteins and selectively home to tumors, with a well-known conducting polymer when prepared as polymer-CREKA and polymer-CR(NMe)EKA biocomposites. Moreover, the biological implications of these interactions have been examined by analysing the fibrinogen thrombin–catalyzed polymerization, the fibrin-adsorption capacity and the attachment of metastatic and normal cells. The specific objectives examined in this block are:

- 7) Prepare and characterize biocomposites based on the combination of an intrinsic conducting polymer and CREKA or CR(NMe)EKA, and analyse how the

replacement of Glu by noncoded *N*-methyl-Glu in the peptide affects the biocomposite-fibrin interactions and the differentiation between normal and tumor cells.

- 8) Explore the biorecognition event between CR(*N*Me)EKA and clotted-plasma proteins (fibrin and fibrinogen) by nanomechanical detection. For this purpose, the development of a suitable experimental protocol for the functionalization of the microcantilevers has been conducted.

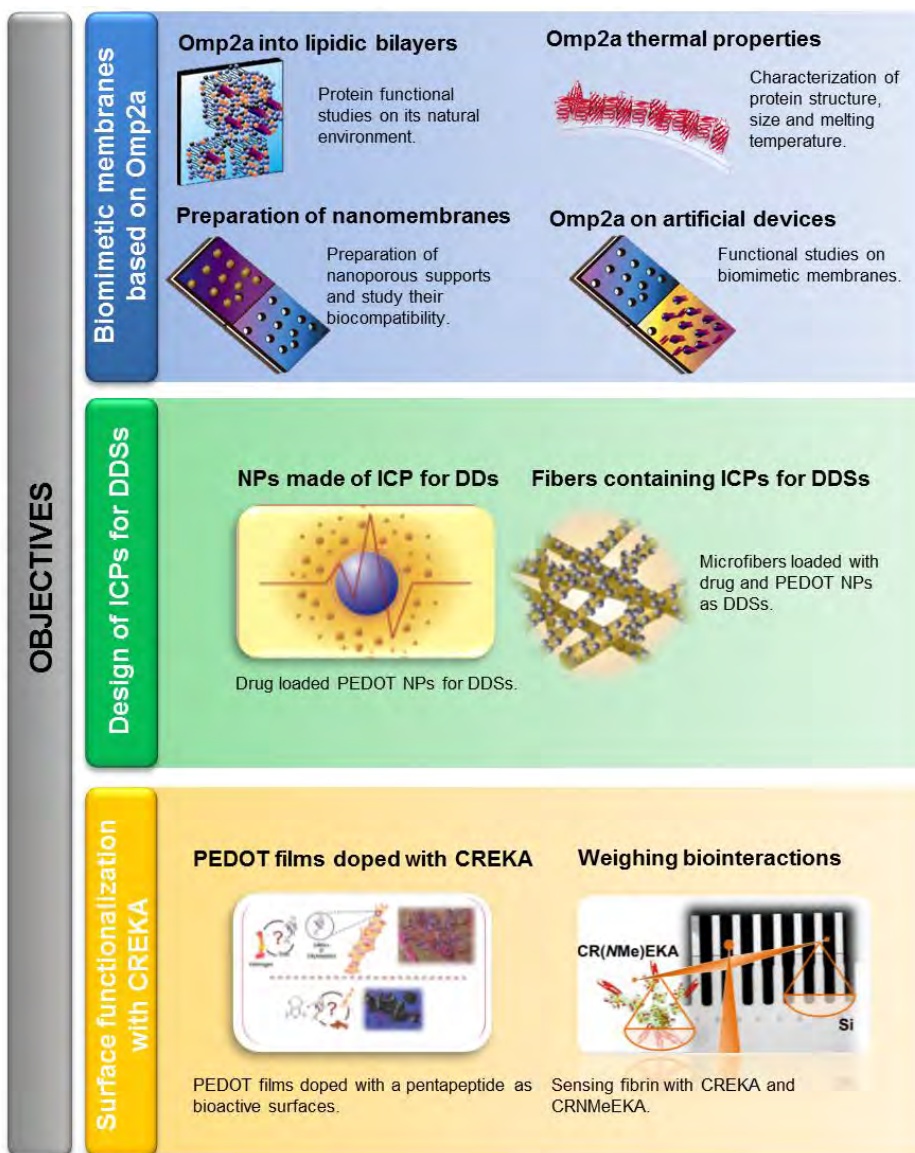


Figure 2. 1 Scheme representing the Thesis objectives.

PART A

Biomimetic membranes based on
Omp2a transmembrane protein

CHAPTER 3:

Biomimetic hybrid membranes

SUMMARY

Molecular sensing, water purification and desalination, drug delivery and DNA sequencing are some striking applications of biomimetic hybrid membranes. These devices take advantage of biomolecules, which have gained excellence on their specificity and efficiency during billions of years, and of artificial materials that load the purified biological molecules and provide technological properties, such as robustness, scalability and suitable nanofeatures to confine the biomolecules. Recent methodological advances allow a more precise control of polymer membranes that support the biomacromolecules, which are expected to improve the design of the next generation of membranes as well as their applicability. In the first section of this chapter we explain the biological relevance of membranes, membrane proteins and the classification used for the latter. Furthermore, the most basic concepts of expression, purification and refolding of recombinant proteins are briefly discussed. After this, we critically analyse the different approaches employed for the production of highly selective hybrid membranes, focusing on novel materials made of self-assembled block copolymers and nanostructured polymers. Finally, a summary of advantages and disadvantages of the different methodologies is presented and the main characteristics of biomimetic hybrid membranes are highlighted.

Publications derived from this work:

Puiggali-Jou, A.; del Valle, L. J.; and Alemán, C. Biomimicking biological membranes incorporating transport proteins onto polymeric supports. Submitted to *Soft Matter*.

3.1 Introduction

An ambitious goal of today's synthetic biology, nanotechnology and bioengineering, is to build constructs analogous to natural systems for tuning and manipulating their complex physical and biological properties. Within this framework, protein-based nanomaterials offer countless potential for biophysical and nanobiomedical applications and serve as new tools for investigating essential biological questions.

Particularly, membrane proteins (MPs) are important key regulators in many biological processes, such as ion transportation, generation of energy and transduction of signals across cell membranes.¹ Besides, MPs constitute about one third of all protein coding genes and are the targets of a huge amount of pharmacological agents.^{2,3} Although knowledge about their structure and function is crucial for the proper interpretation of numerous biologically relevant phenomena, these investigations are often very difficult due to the great complexity of cell membranes. Therefore, there is a continuously growing interest in the development of model systems able to offer suitable platforms to address the above mentioned issues. The most popular models include proteoliposomes, lipid monolayers and solid/supported lipid bilayers. Beyond the use of natural products, it is also possible to incorporate MPs into artificial materials, such as synthetic polymers, which can provide new properties (*e.g.* easiness of handling, robustness and functionalization). Thus, the biological molecules can bring specificity and efficiency, while the robustness and the possibility of tailoring materials to improve the final functionality can be added by the synthetic polymer. As a result, a wide range of applications have been investigated, including, DNA sequencing,⁴ drug delivery,⁵ sensors,⁶ water desalination,^{7,8} and bioelectronics.⁹

Although in the last decade some general reviews on biomimetic membranes have been reported,^{1,10-13} herein a new perspective is offered. More specifically, in this section recent developments and advancements from a processing point of view are discussed. Thus, the classification of the different approaches used to incorporate MPs onto artificial polymeric supports is the primary focus, also giving special emphasis to the analysis of the achieved applications.

3.2 Cell membranes: Description and biological relevance

The structure of biological membranes is mainly driven by the lipid bilayer, even though the majority of its particular functions are played by the proteins embedded in it. The difference on the amount and type of MPs allow its classification. For instance, the protein mass in the myelin membrane, which insulates nerve cell axons, represents less than 25% of the whole membrane. In contrast, 75% is protein in membranes involved in the ATP production, like the internal membranes of mitochondria and chloroplasts. For common plasma membranes, proteins reach approximately 50% of their mass. Regarding to the orientation of MPs in lipid bilayers, biological membranes are not symmetric since the flux of materials needs to follow one particular direction and the recognition events just happen in one side of the membrane.

Lipid bilayers allow facile and rapid diffusion of small non polar molecules such as O₂ (2.3×10^1 cm/s)¹⁴ and CO₂ (3.7×10^{-1} cm/s),¹⁵ and slower diffusion of small polar but not charged molecules like H₂O (3.7×10^{-3} cm/s),¹⁶ urea and glycerol ($\sim 10^{-6}$ cm/s).¹⁷ On the other hand, biological membranes are reluctant to allow the diffusion of charged molecules (ions) no mattering how small they are, because of the charge and their elevated hydration level. For example, the permeability coefficient of Na⁺ and K⁺ is $\sim 10^{-14}$ cm/s.¹⁸

Although lipids constitute a great part of the cell membranes, the high efficiency of the latter for transporting materials across the bilayers is due the presence of MPs. These can be classified into three different groups according to their transport mechanism: channels, pumps and transporters. The first group are pores that allow the passive diffusion across the membrane of ions and molecules depending on the concentration gradient. Their specificity is mainly driven by the size and charge of the solutes. Within this group, gap junctions (cell-cell direct communication), porins, water channels (aquaporins) and ion channels (which are dependent of voltage, ligands or mechanosensitive) are especially relevant. The transport rate of these transmembrane

proteins is high since they do not need any conformational change (10^7 - 10^9 molecules/second).

The second group, which are known as pumps, move ions or electrons against the concentration gradient using chemicals or light as energy power, also described as active transport. These MPs have specific binding sites for ions and molecules and they can also experience conformational changes that allow the transport. Their principal mechanisms include the consumption of energy by adenosine triphosphate (ATP) hydrolysis or by photon absorption in the case of photosynthetic pumps. The transport rate is quite slow compared to the other transport proteins (10^0 - 10^3 molecules/second). Finally, the third and last group involves the transporters. In this case, the ion/molecule transport is energy-independent and, therefore, is called passive. This transport comprises several steps: molecule recognition, translocation from one side to the other of the plasma membrane and the release of the ion/molecule. Hence, the transport rate is also moderate (10^2 - 10^4 molecules/sec). They can be classified as uniporters (just allow the movement of one solute), symporters (two at the same direction) and antiporters (two solutes in opposite directions).

3.3 Expression of membrane proteins

Analysis of the protein structures deposited in the protein data bank (PDB) reveals that, in comparison with soluble proteins, the number of MPs is much lower. This feature reflects that investigations on MPs are not going as fast as those on soluble proteins due to the extra difficulties related to the purification and refolding process.¹⁹ The proteins of interest can oddly be purified from its original membrane because usually their concentration is not enough.²⁰ For that reason, MPs need to be overexpressed, which is performed in different host cells.

Long-established strategies require the transformation (bacteria/yeasts) or transfection (mammalian/insect cells) of cells with a DNA vector that contains the gene of the protein of interest. Subsequently, cultured cells will transcribe and translate the desired proteins. Then, cells are lysed and the over-expressed protein is purified.

Although both prokaryotic and eukaryotic systems can be employed,²¹ the choice of the system is important for a successful recombinant expression. The right choice depends on the type of protein, the needs of post-translational modifications, the effect of toxicity on the host cell, and the desired yield. The main advantage of mammalian systems is that they provide the highest level of protein processing, even though cell culturing is more demanding and expensive. Instead, bacterial cultures are easily scalable and not very demanding or expensive.

There are strategies to overcome the toxicity of the protein overproduction on the host cells. For example, the utilization of strains with higher tolerance, such as the *E. coli* strain C43(DE3). It is worth noting that *E. coli* is one of the most universal system for prokaryotic and eukaryotic MPs due to the broad range of commercially available molecular biology tools and strains.²² Also, it is possible to add fusion partners to improve the expression level of the protein.²³ Moreover, the overproduction can take place in inclusion bodies within the cytoplasm that would result in an easier purification and a lower toxicity but in a greater difficulty to refold the protein afterwards. There are many detergents for protein solubilisation, as for example *n*-dodecyl- β -D-maltoside (DDM), *n*-octyl- β -D-glucopyranoside (b-OG), and lauryldimethylamine-oxide (LDAO). Solubilisation is a demanding step since the correct folding and, consequently, the preservation of the protein function depends on it. Finally, the desired protein needs to be separated from other MPs present in the solution. For this purpose, chromatographic techniques are employed to selectively bind the protein of interest. The most common protocol is based on Immobilized Metal Affinity Chromatography (IMAC) and uses recombinant ion channels containing His-tag at the C- or N- terminal, which complex with transition metals (Zn²⁺, Cu²⁺, Ni²⁺). Consequently, the protein of interest can be efficiently separated and just eluted when a histidine analogue (*e.g.* imidazole) is added to the column.

The proteins that are currently attracting considerable interest due to their functions and easy overproduction are:

- Water channel MPs, known as aquaporins (Aq), are very attractive because of their high water transport rate and selectivity that can be used for water

purification and desalination. The structure of Aq monomers consists in six transmembrane helices and two short helical segments (**Figure 3.1a**), which surround the cytoplasmic and extracellular regions, connected by a narrow aqueous pore.²⁴ When located in the lipid membranes, Aq monomers associate into tetramers, each monomer functioning independently. Nevertheless, a few unsolved questions still remain: is the protein capable to withstand certain conditions (*e.g.* high salinity pressure)? and how can be increased the size of the membranes without any rupturing? In the last five-six years, this field of study has increased considerably.²⁵⁻³³

- α -hemolysin (α -HL), a protein found in the human pathogen *Staphylococcus aureus* bacterium, acts as a toxin and is used since a long time for translocation of single stranded DNA.^{34,35} This porin is very stable and its functionality prevails at temperatures close to 100 °C.³⁶ Because the interior diameter is similar to the diameter of a single nucleic acid strand, the current of ions through the nanopore is partially blocked when the translocation occurs (**Figure 3.1b**). More specifically, as each nucleotide produces a different reduction in the ionic current,³⁷ the incorporation of α -HL to artificial polymer membranes could be employed to detect DNA sequences through this signal.³⁸
- Gramicidin (gA), a hydrophobic pentadecapeptide with a length of 22 Å (**Figure 3.1c**),³⁹⁻⁴¹ organizes in an ion channel that is specific for monovalent cations. This biomolecule has been extensively used as model to study the organization and function of channels-containing membranes.⁴¹
- Outer membrane proteins (OMPs) are typically employed for the fabrication of hybrid biomimetic membranes. The outer membrane is a protecting barrier of gram-negative bacteria. Unlike the MPs located at other systems, the structure of OMPs does not contain α -helices but instead anti-parallel β -barrels (**Figure 3.1d**).⁴² OMPs allow the unspecific passive diffusion of ions and molecules across the membrane. The driving-force is the concentration gradient, whereas the limitation lies on the molecular size since the diffused specie needs to be smaller than the pore.

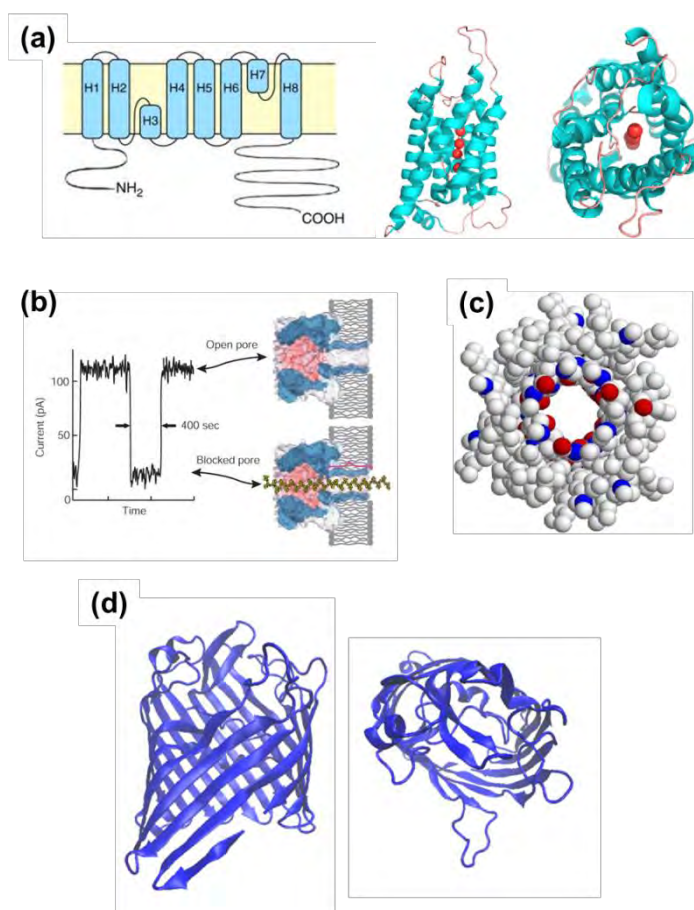


Figure 3.1 (a) Membrane topography of the Aq monomer (left) and crystal structure (side view, left; top view, right) with four water molecules (red balls) shown in aqueous pore region. Helices are labelled H1–H8. Reproduced with permission from reference²⁴. (b) Strand-sequencing using ionic current blockage. A typical trace of the ionic current amplitude (left) through an α -HL pore clearly differentiates between an open pore (top right) and one blocked by a strand of DNA (bottom right) but cannot distinguish between the \sim 12 nucleotides that simultaneously block the narrow transmembrane channel domain (red bracket). Reproduced with permission from reference³⁴. (c) Top view of the gA channel as a space-filling model (color code: white, carbon atoms; blue, nitrogen atoms; red, oxygen atoms) using coordinates from PDB 1MAG. Note how the alternating L–D arrangement allows all amino acid side chains to project outward from the channel lumen and the channel lumen is lined by the peptide backbone. (d) Axial and equatorial views of crystallized OmpF, a representative MP. Reproduced with permission from reference⁸².

3.4 Incorporation onto polymeric substrates

Within the field of biomimetic membranes there is a wide range of strategies and materials studied until now. The modification of artificial membranes with functional molecules within their pores or onto their surfaces, as well as the preparation of artificial channels embedded into block copolymers or lipid bilayers, have already been extensively reviewed by other researchers.¹⁰ Here, we focus on the group that involves the complete incorporation of proteins into hybrid polymeric systems. Thus, our main objective is to illustrate the synthetic processes and the materials used for the development of biomimetic hybrid membranes. **Table 3.1** summarizes the different approaches employed until now that, from the perspective of the employed materials, has been categorized as those based on the utilization of amphiphilic copolymers and nanostructured polymers and **Table 3.2** points out the advantages and disadvantages of each system.

3.4.1 Amphiphilic copolymers

This is the most extensive kind of material employed for manufacturing biomimetic hybrid membranes. Amphiphilic block copolymers can act as artificial building blocks for the generation of membranes capable of incorporating proteins, as do the lipid bilayers. However, the former present other important advantages, such as long-term mechanical stability, tailorable structural parameters and versatile chemical functionality. In dilute aqueous solution, they self-assemble by hydrophobic driving forces, forming different of morphologies, such as spheres, cylinders or lamellas.⁴³ Amphiphilic copolymers are mostly prepared as diblock copolymers with one hydrophobic and one hydrophilic block or as triblock copolymers with two hydrophilic blocks separated by one hydrophobic, the latter being usually named ABA block copolymers. Despite membranes made of amphiphilic copolymers present high mechanical and chemical stability, low water and gas permeability, and customizable properties (*e.g.* a wide range of membrane thickness), they exhibit some drawbacks with regard to lipid membranes: lower

dynamics/fluidity of the bilayer, higher thickness, and lower flexibility. Overall, amphiphilic copolymers hold great potential over lipids as building blocks.^{38,44-48}

A large variety of amphiphilic copolymers have been designed using different monomers and applying diverse synthetic techniques,⁴⁸ such as anionic⁴⁹ and cationic polymerizations,⁵⁰ controlled radical polymerization,^{51,52} ring-opening polymerization,⁵³ and “click” chemistry.^{54,55} Furthermore, advanced individual properties can be added to the building blocks, as for example the regulation of hydrophilicity and hydrophobicity of the blocks, block lengths and length ratios, the functionalization of polymer block,⁵⁶ the addition of stimuli-responsive polymer blocks,^{57,58} and the use of biodegradable polymers.⁵⁹ Two of the most interesting modifications reported in the literature are based on the addition of: (*i*) methacrylate units to stabilize the membrane by cross-linking;⁶⁰ and (*ii*) dyes for imaging.⁶¹

In order to mimic cell membranes, block copolymers can be used without any support (free-standing or self-supported), spread and non-covalently or covalently tethered onto solid supports, spread onto porous solid supports, and bounded as polymer vesicles onto a 2D surface.

Free-standing block copolymers

One of the most straightforward methodologies to study the transport across a membrane is having it as separator of two media and to investigate the exchange of solutes and ions concentrations between them. The experimental set-up required for such studies typically includes free-standing membranes. Although a huge amount of studies have been reported, these are mainly based on free-standing lipid bilayers while only a few of them involve block copolymer. This has been attributed to their lower lateral tension, which could lead to a rapid membrane rupture.⁶² In an early study, artificial and stable giant free-standing monomolecular films of functionalized poly(2-methyloxazoline)-block-poly(dimethylsiloxane)-block-poly(2-methyloxazoline) triblock copolymer, named PMOXA-PDMS-PMOXA, were prepared for the first time.⁴⁶ These copolymer films, which exhibited areas of up to about 1 mm² and thickness of 10 nm, were post-polymerized by UV light using the methacrylate groups found at both chain ends. The reconstitution of a porin in the preformed layer was achieved by adding a

certain amount of the protein to each side of the chamber and, in particular, the incorporation was favoured by applying a potential of 20 mV across the membrane. Despite the high thickness of the polymer membrane compared to lipid ones, the protein was successfully incorporated, leading to an enhancement of the conductance across the layer.⁶³

More recently, Wong *et al.*⁶⁴ used PMOXA–PDMS–PMOXA copolymers to compare the voltage gating ability and threshold voltages of OmpG and alamethicin embedded in lipid bilayers and polymer membranes, which were used to separate two solutions. The molecular properties of the protein (*i.e.* conductance, voltage gating and mobility) were similar for polymer- and lipid-based systems.⁶⁴ Ho *et al.*⁶⁵ studied the effect of the length of PMOXA–PDMS–PMOXA on protein insertion at the air/water interface. Wilhelmy surface pressure measurements (mN/m) revealed greater OmpF insertion for shorter copolymer chains, which was attributed to their enhanced biomimicry of natural lipid-based membranes.⁶⁵

Block copolymers immobilized onto solid supports

Obviously, the use of solid supports for membrane immobilization provides mechanical stability at the air/water interface and even in the dry state monolayers and or free-standing membranes.⁶⁶ The easiest procedure to obtain synthetic solid-supported membranes is the fusion and spreading of polymersomes onto the support (*i.e.* gold or glass surfaces). In order to attain stronger fixation on the solid support, surface-initiated radical polymerization procedures can be also used.⁶⁷

Dorn *et al.*⁶⁸ formed polymersomes with poly(butadiene)-*b*-poly(ethylene oxide), PB-PEO, which were subsequently spread into glass and gold substrates. For the chemical immobilization onto the gold surface, PB-PEO was functionalized with sulfur-containing lipoic acid (LA), which binds properly to the gold surface (**Figure 3.2a**). Covalently bound layers were further incubated with polymyxin B, a peptide able to disrupt lipid membranes.⁶⁹ The, resistance of the membranes without and with the peptide, as determined by electrochemical impedance spectroscopy (EIS), was 4.4 and 1.2 MΩ·cm², respectively, evidencing that the peptide was successfully embedded. Nevertheless, after 7 hours the resistance increased again due to the loss of peptide.⁶⁸

In comparison to the previous example, Zhang *et al.*³⁸ combined two methodologies to obtain a defect-free layer onto a gold substrate. More specifically, Langmuir-Blodgett (LB) and Langmuir-Schaefer (LS) deposition techniques were applied using different terminated polymers: LA functionalized linear PB-PEO (PB-PEO-LA) and hydroxyl-functionalized linear PB-PEO (PB-PEO-OH), respectively (**Figure 3.2b**). Both techniques enabled a strict control of the layer density by regulating the surface pressure of the molecular assembly. Moreover, combination of both methods led to the achievement of large-area, homogeneous, defect-free layers, which were closer to cell membranes. Again, the protein was added after the layer formation and was monitored by measuring the conductance through the PB-PEO layer before and after the addition of α -haemolysin (α HL), at a voltage of 40 mV. A significant increase in conductance was observed after 20 min of the protein addition.

The same two-step methodology was employed by Kowal *et al.*⁷⁰ to generate defect-free layers on solid supports. In this case the PDMS-*b*-PMOXA di-block copolymer with

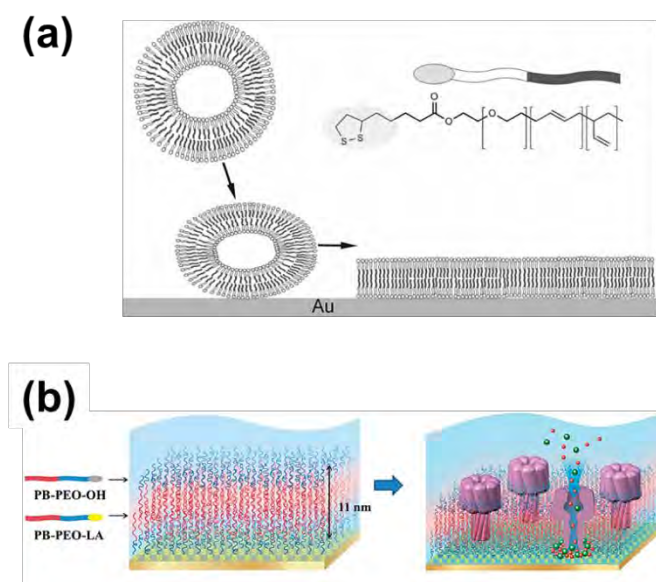


Figure 3.2 LA-functionalized PB-PEO vesicles spread onto a bare gold surface. Reproduced with permission from reference⁶⁸. (b) PB-PEO-OH and PB-PEO-LA were transferred onto gold substrates by applying consecutively the LB and LS techniques to form a polymer tethered bilayer (left), where the protein was inserted (right).

aldehyde ending groups was used to promote the covalent attachment of the polymer membrane through formation of an imine bond with an amino modified gold substrate. More specifically, such authors studied the effectiveness of bio-beads (BB) (*i.e.* non-polar polystyrene adsorbent material) as facilitators of protein incorporation (**Figure 3.3a**). Changes in the conductance of gold substrates were recorded to examine the effects associated with the attachment of the polymer layer and the incorporation of protein and bio-beads. Results showed an increase in the substrate conductance when the protein was incubated with BB, whereas no significant increase was found when the protein was incubated without BB, demonstrating that the latter are necessary to incorporate the protein (**Figure 3.3b**). Thus, bio-beads act as driving force for the insertion of MPs into polymer membranes attached to solid substrates.

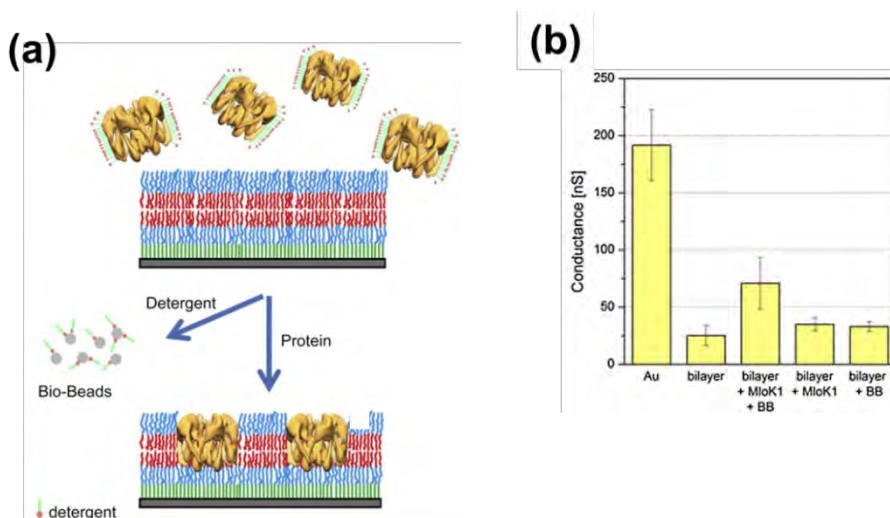


Figure 3.3 (a) Representation of MP insertion when using BB into solid-supported polymer membrane. (b) Conductance measured when a voltage of 40 mV is applied on bare Au, the bilayer, the bilayer with the protein incorporated using Bio-Beads (bilayer+MloK1+BB), the bilayer with the protein (bilayer+MloK1), and the bilayer with the Bio-Beads (bilayer+BB). Reproduced with permission from reference ⁷⁰.

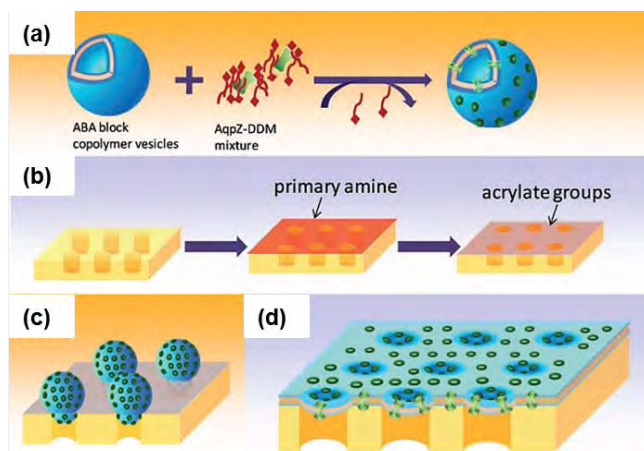


Figure 3.4 Schematic illustration of pore-spanning membrane on the PCTE: design and synthesis. (a) Incorporation of AqpZ in PMOXA–PDMS–PMOXA (ABA copolymer) vesicles. (b) Surface modification of the PCTE membrane support in a two-step process: (i) coating with a monolayer of cysteamine through chemisorption; and (ii) the primary amine are converted to acrylate residues via conjugating with acrylic acid. (c) Pressure-assisted vesicle adsorption on the PCTE support. (d) Covalent-conjugation-driven vesicle rupture and pore-spanning membrane formation. Reproduced with permission from reference ²⁵.

Block copolymers suspended onto porous solid supports

Due to the low stability and difficulty of handling of free-standing copolymer membranes and to the limitations presented by solid supported layers, the field evolved towards copolymer films suspended onto porous solid membranes. In this approach, some zones of the membrane are still free-standing, allowing molecular diffusion without any disturbance.

In a pioneering study, Gonzalez-Pérez *et al.*⁷¹ obtained stable triblock copolymer membranes using scaffolds containing 64 apertures of 300 μm diameter each. The membranes showed high stability, which was evidenced by a long life-time when high polymer concentrations were used (*i.e.* it was stable several days). In order to incorporate ion channels, GA was reconstituted on these membranes and assembled into dimeric channels.

More recently, Wang *et al.*²⁵ presented a new strategy to produce planar pore-spanning biomimetic membranes using proteopolymersomes made of PMOXA–PDMS–PMOXA and Aquaporin Z (AqpZ) (**Figure 3.4a**). Poly(carbonate)

tracked-etched (PCTE) membranes with average pore sizes of 50, 100 or 400 nm were modified with a thin gold layer (60 nm thickness). Then, cysteamine was deposited through chemisorption over the gold surface and the amine residues were transformed into acrylate residues via conjugation of acrylic acid (**Figure 3.4b**). Proteopolymersomes were spanned over the surface (**Figure 3.4c**) and by covalent-conjugation-driven the vesicle rupture occurred (**Figure 3.4d**). Although all the substrates were covered by adapting the pressure to the pore size, membranes with 50 nm pores had much fewer defects compared to the supports with bigger pores.

Duong *et al.*³⁰ spanned polymersomes over porous alumina substrates of different pore diameters, 55 and 100 nm, covered with gold. Substrates with pores of 100 nm resulted uncovered by the membrane film because the spacing was too large, which supported the findings of Wang *et al.*²⁵ However, authors successfully deposited AqpZ-containing proteopolymersomes onto the alumina with pores of 55 nm, preserving the natural functionality of the protein (**Figure 3.5**).

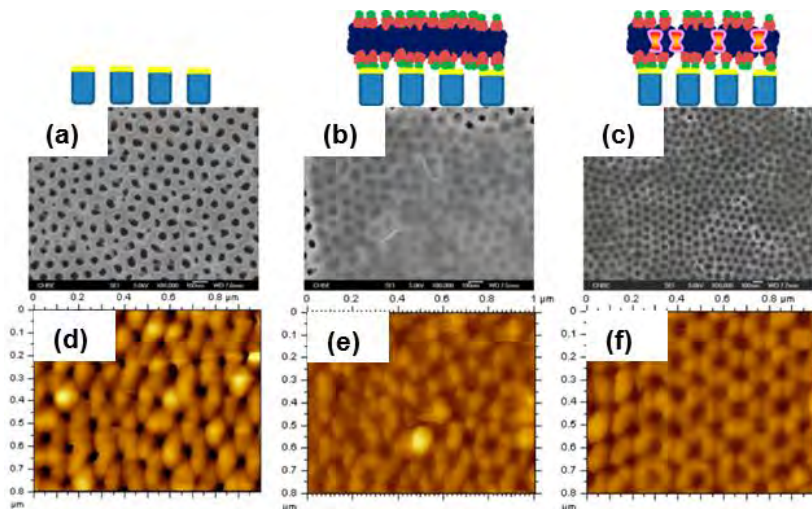


Figure 3.5 Field-emission scanning electron microscopy (a-c) and atomic force microscopy images (d-f) of the gold coated alumina substrate (a and d), the substrate covered with the polymer membrane (b and e), and the substrate covered with the AqpZ-incorporated polymer membrane (c and f). Reproduced with permission from reference ³⁰.

Following this approach but using new materials, planar biomimetic membranes consisting of AqpZ embedded into PMOXA–PDMS–PMOXA layers were fabricated upon a cellulose acetate (CA) substrate functionalized with methacrylate end groups.⁷² Proteopolymersomes were spanned over the CA surface and photocross-linked using UV radiation. The resulting bioinspired device consisted on a selective layer upon the substrate for nano-filtration (**Figure 3.6**). Although this technique presents advantages over the previous ones, it still shows many limitations, such as poor area coverage, membrane defects and difficult scalability to support industrial applications. A similar but at the same time different strategy consists on non-proteopolymersomes disruption but deposition onto porous substrate. Hence, solutes need to cross the whole vesicle and then go through the substrate pore.

Wang *et al.*³² constructed a new design based on a PCTE membrane (pore size 50 nm, porosity 20%) coated with a 50 nm gold layer by vapour deposition. Then, UV cross-linked vesicles were dropped onto the PCTE surface under vacuum. This allowed exerting certain pressure, facilitating the intrusion of the vesicles. The bare gold surface, which was not occupied with protein containing polymersomes, was further functionalized with

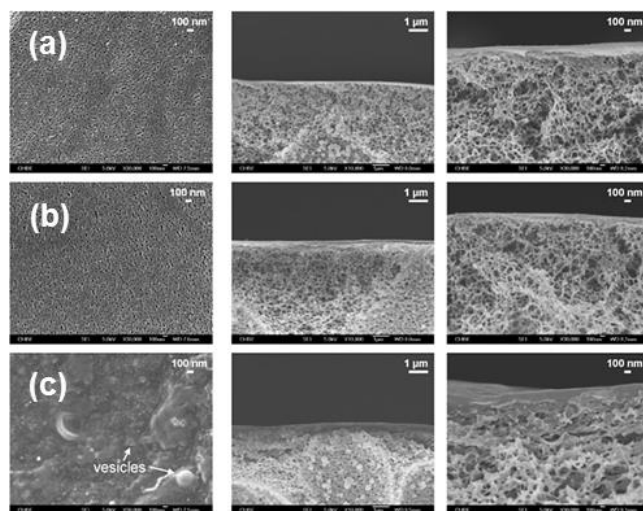


Figure 3.6 Field-emission scanning electron microscopy of (a) CA, (b) silanized CA, and (c) AqpZ-containing PMOXA–PDMS–PMOXA triblock copolymer. Reproduced with permission from reference⁷².

a self-assembled monolayer of cysteamine. Later on, vesicles were immobilized on the membrane through an optimized layer-by-layer polydopamine (PDA)–histidine (His) coating process (**Figure 3.7**).

A similar methodology but using CA with an average pore size of approximately 25 nm as solid support was reported by Xie *et al.*³³ The UV-crosslinked Aqpz-polymer vesicles were covalently immobilized onto the CA membrane through an amidation

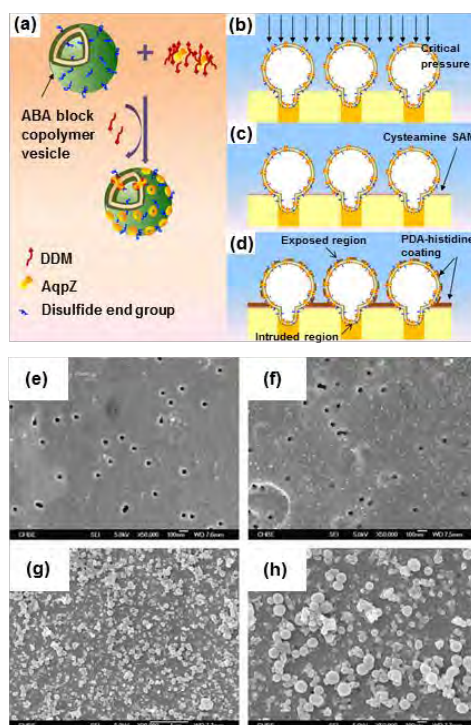


Figure 3.7 Schemes of AqpZ-embedded vesicular membrane at the top: (a) AqpZ reconstitution into the vesicles formed from ABA block copolymer blends. DDM stands for dodecyl-b-D-maltoside, a detergent for protein stabilization; (b) Immobilization of the vesicles onto the substrate by pressure; (c) addition of the self-assembled monolayer of cysteamine; and (d) PDA-His coating on the top of the membrane. (e-h) Field-emission scanning electron microscopy micrographs at the bottom: (e) gold-coated PCTE membrane with a self-assembled monolayer of cysteamine (pore size 50 nm); (f) PCTE membrane with 3-cycle coating of PDA–His on the top of chemisorbed cysteamine (control); and (g) vesicles immobilized on the PCTE membrane with 3-cycle coating of PDA–His on top. The micrograph displayed in (h) corresponds to a zoom of (g). Adapted with permission from reference ³².

reaction between the amino groups on the CA membrane surface and the carboxyl groups on the vesicle surface. Finally, a dense hydrophobic polymer layer was generated by in situ “surface imprinting” polymerization (**Figure 3.8**). This innovative membrane, which presented pores smaller than perforated PCTE,³² exhibited good and controlled selectivity together with high mechanical strength and stability during the nanofiltration.

Proteopolymersomes covalently bounded to a solid support

The last methodology reviewed in this section is the covalent attachment of proteopolymersomes onto a solid surface, which has also been previously employed for lipids.⁷³ In order to obtain nanoreactors that could carry out conversions at a precise location for the sensors development, Grzelakowski *et al.*⁶¹ applied this approach using block copolymers. For this purpose, an acid phosphatase was encapsulated and the intrusion of the substrate inside the vesicle was provided by the reconstitution of OmpF onto the polymersome membrane. The resulting proteopolymersomes were immobilized into the substrate (*i.e.* glass) by employing the receptor–ligand pair, biotin–streptavidin.⁷³ The de-phosphorylation of the fluorogenic substrate ELFTM 97 by acid phosphatase was monitored. It was observed that the reaction did not occur when OmpF

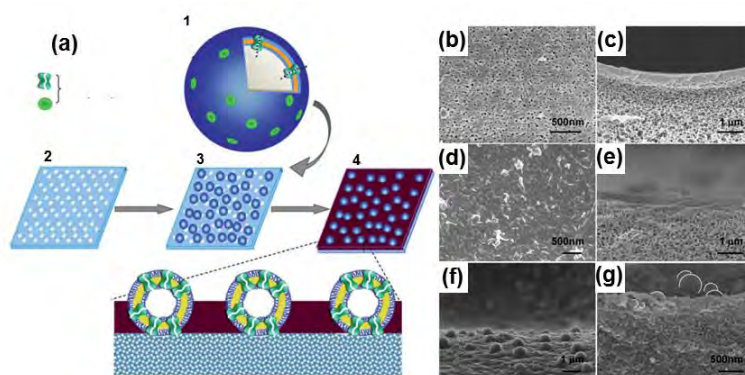


Figure 3.8 (1) Aqpz-polymer vesicles, (2) porous CA membrane substrate, (3) Aqpz vesicles immobilized on the porous membrane, (4) Aqpz-vesicle-imprinted membrane, and (5) cross-section of the Aqpz-vesicle-imprinted membrane (a). (b-g) Field-emission scanning electron microscopy micrographs displayed the membrane morphologies: (b, c) top surface and cross-section of the porous substrate CA membrane; (d, e) non-vesicle-imprinted membrane; and (f, g) Aqpz-vesicle-imprinted membrane. Adapted with permission from reference³³.

was not reconstituted, confirming the importance of the protein for the diffusion of certain molecules across the membrane.

More recently, Zhang *et al.*⁷⁵ developed “active surfaces” for selective biosensing of sugar alcohols with time and space precision (**Figure 3.9**). This bioactive platform was based on the immobilization of nanoreactors with specific MPs inserted in their membranes and sugar alcohol sensitive enzymes encapsulated in their cavities. Interestingly, the artificial surrounding within such a copolymer membrane and the high membrane thickness did not affect the functionality of the reconstituted glycerol facilitator (GlpF), which allowed the selective flux of sugar alcohols into the inner cavity of the polymer nanoreactors where the encapsulated enzymes acted as biosensing entities. An advantage of encapsulating the enzymes inside polymersomes was their protection from a potentially harmful environment, while retaining their catalytic activity. Thus, this smart approach prolonged the life-time of the enzymatic biosensor. The selective permeability of such interesting protein-polymer nanoreactors offers the opportunity of monitoring the concentration of biologically relevant sugar alcohols since GlpF is able to conduct other sugar alcohols.

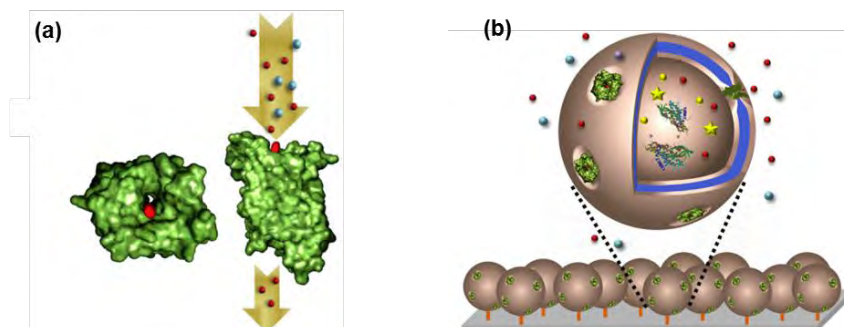


Figure 3.9 (a) GlpF molecular representation (green) together with ribitol, as a model sugar alcohol (red). Side (right) and front (left) views are represented. (b) Schematic representation of a functionalized surface serving as a sugar alcohol biosensor based on immobilized proteopolymersome nanoreactors with selective transport due to the GlpF presence and detection of sugar alcohols due to the encapsulated enzymes. Adapted with permission from reference ⁷⁵.

3.4.2 Nanostructured polymers

Researchers have focused on amphiphilic polymers for mimicking biological membranes. However, an inconvenient of amphiphilic polymer membranes is that, although the system turns out to be more stable than biological membranes, it is not strong enough to endure many practical applications.⁷⁶ In this section we discuss the use of confined biological ion channels prepared by incorporating proteins into pores of nanostructured polymers. A common methodology to control the pore size is the track-etch technique.⁷⁷ More specifically, polymer membranes are perforated when heavy ions go through the film and create damage zones on the latent track. Then, these can be converted into a pore by employing the right solution. The size and shape of the pore are regulated by varying the chemical etching conditions (*e.g.* time, temperature and solution concentration).

Balme et al.^{76,78} developed hybrid nanoporous membranes handling commercial track-etched PC films of 5 μm thickness covered with poly(vinylpyrrolidone) (PVP). The resulting nanopores, which exhibited a diameter of 15 nm, were filled with gA. Protein confinement was facilitated by the hydrophobicity of the inner parts of the membrane. Later on, the ion flux passing through the resulting hybrid membrane was evaluated by placing it between two compartments filled with a given electrolyte and pure water, respectively. Although results about the selectivity of the protein were unclear, ion diffusion was significantly higher when the protein was loaded inside the nanopores of the membrane.

The effect of the pore size was studied in a more complex system in which nanostructured polymer membranes were obtained by track etching poly(ethyleneterephthalate) (PET) films. This was followed by the deposition of a multilayer of aluminium oxide/zinc oxide to decrease the initial diameter of the pores from 36 nm to 10.6, 5.7 and 2 nm on demand (**Figure 3.10**).⁷⁹ Results evidenced that the relative contribution of the ion transport through gA increases with decreasing pore diameter. However, this effect was accompanied by a loss of specificity due to the disassembling of the head-head dimer structure.

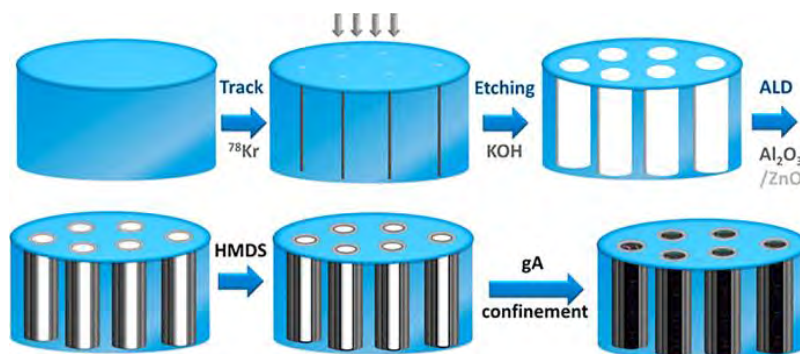


Figure 3.10 Procedure scheme for the fabrication of nanoporous membranes, the modification of nanopore size by atomic layer deposition (ALD), the creation of hydrophobic pore surfaces by vapour exposure treatment with hexamethyldisilazane (HMDS), and the immobilization of gA. Adapted with permission from reference ⁷⁹.

Within this context, an interesting OMP, named Omp2a,⁸⁰⁻⁸² was embedded in a supported poly(*N*-methylpyrrole) (PNMPy) membrane.⁸³ **Figure 3.11a** illustrates how the incorporation of the protein caused significant changes in the surface morphology of PNMPy. Thus, scanning electron microscopy (SEM) micrographs of PNMPy–Omp2a present elements of both submicrometric and micrometric dimensions with a very homogeneous and smooth texture, whereas the nodular outcrops typically found in PNMPy films (**Figure 3.11b**) are not detected. These features, which reflected the presence of the protein, were correlated with EIS measurements. It was observed that Omp2a promotes preferentially the passive transport of K^+ with respect to Na^+ in solutions with relatively high ionic concentrations. Nevertheless, such system had the inconvenience that the PNMPy membrane was electrochemically synthesized onto a solid working electrode (*i.e.* stainless steel), which represented a disadvantage for possible future applications.

More recently, instead of using conducting polymers as support for the protein, nanoporous biodegradable poly(lactic acid) (PLA) nanomembranes were used.⁸⁵ These membranes, which were self-standing, were prepared by spin-coating a mixture of poly(vinyl alcohol) (PVA) and PLA, which are immiscible polymers.⁸⁴ Nanoporous membranes with diameter of 51 ± 22 nm resulted from the combination of nanophase segregation processes and selective solvent etching (**Figure 3.11c**).⁸⁵

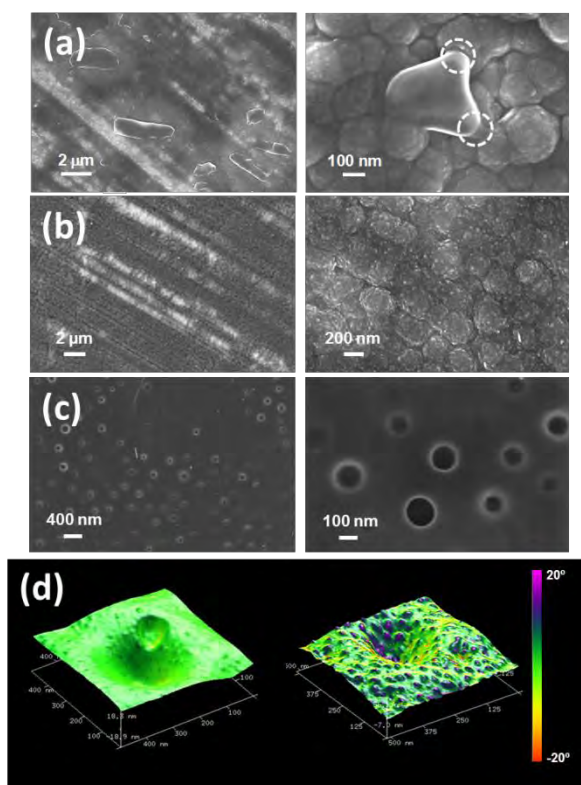


Figure 3.11 Surface morphology of (a) PNMPy–Omp2a, (b) PNMPy and (c) nanoporated PLA membranes: low- and high-magnification SEM micrographs are displayed at the left and the right, respectively. Adapted with permission from references ⁸³ and ⁸⁵. (d) 3D AFM phase images of the skin surfaces of nanoporated PLA nanomembranes before (left) and after (right) incubation with a 0.5 mg/mL Omp2a solution. Adapted with permission from reference⁸⁵.

In order to confine the protein into the nanopores, these membranes were incubated in protein solutions and, subsequently, washed many times. Contrast 3D AFM height images painted with phase skin surfaces of samples before and after incubation confirmed the presence of adsorbed oval protein aggregates around and inside the nanopores (**Figure 3.11d**). Specifically, phase channel allowed to differentiate Omp2a domains (*i.e.* dark purple aggregates with an average diameter 27 ± 5 nm) from the PLA substrate (coloured in green) where they are adsorbed onto. Moreover, EIS assays

showed an increase of conductivity and selectivity against some ions when the protein was confined onto the nanopores.⁸⁵

The thermomechanical properties of this OMP had also been characterized by immobilizing it on microcantilevers.⁸⁶ It was found that heat promotes local orientation of the immobilized biomolecules. Thus, appropriate thermal treatments could be employed to enhance the selective ion transport of the substrate since more proteins would be correctly oriented with the required thermal treatment. More interestingly, its functionality onto lipid bilayers, which represents an environment closer to the one on its biological conditions, had also been characterized.⁸⁷ The resistance of 40 w/w lipid-to-protein ratio supported lipid bilayers ($1.5 \text{ k}\Omega \text{ cm}^2$) was found to be similar to that of nanoporated Omp2a-filled PLA membranes⁸⁵ ($1.9 \text{ k}\Omega \text{ cm}^2$) and higher than that of PPy-Omp2a⁸³ ($243 \text{ }\Omega \text{ cm}^2$). As it was expected, the resistance of all systems decreased when the protein was incorporated, this effect being more pronounced for KCl electrolytic solutions. Besides, the resistance variation and the selective ion diffusion unambiguously evidenced the successful incorporation of bioactive porin.

CHAPTER 3

Table 3.1 Summary of the most important characteristics (*i.e.* preparation method, polymer, protein and activity) of biomimetic membranes made of polymers.

Type	Support	Polymer	Protein	Functionality	Permeability	Ref.
Free-standing	-	PMOXA- <i>b</i> -PDMS- <i>b</i> - PMOXA	OmpF and maltoporin	Electrophysiological studies	σ increment of 6 nS (OmpF) and 4 nS (maltoporin)	63
	-	PMOXA- <i>b</i> -PDMS- <i>b</i> - PMOXA	OmpG and Alamethicin	Electrophysiological studies	$\sigma = 0.72 \pm 0.06$ nS (OmpG) and $\sigma = 0.3, 1.1, 2.22$ and 3.34 nS (alamethicin)	64
	Air-water interface	PMOXA- <i>b</i> -PDMS- <i>b</i> - PMOXA	OmpF	Mechanical studies	Shorter copolymer chains possess enhanced biomimicry of natural lipid- based membranes	65
Solid supported	Au	PB-PEO-OH and PB- PEO-LA	Polymyxin B	Peptide effect on membrane resistance	Reduction of the resistance from 4.4 to 1.2 M Ω ·cm ²	69
	SiO ₂ wafers, glass and Au	PDMS- <i>b</i> -PMOXA with amino-linker	MloK1	Ion flow	$\sigma = 39.5 \pm 7.5$ nS	70
	Au	Functionalized PB- PEO	α HL	Ion flow	$\sigma = 31$ ns	38
Porous solid support- polymersome spanning	PCTE	PMOXA-PDMS - PMOXA	AqpZ	Water purification	Maximum water flux 16.4 \pm 1.5L m ⁻² h ⁻¹ (LMH) with a salt rejection of 98.8%	25
	Commercially available CA with pores	PMOXA- <i>b</i> -PDMS- PMOXA	AqpZ	Water purification	Maximum water flux 34.19 \pm 6.90 LMH/bar with a 200	73

BIOMIMETIC HYBRID MEMBRANES

					ppm NaCl salt rejection of 32.86 ± 9.12%	
	Porous alumina	functionalized PMOXA-PDMS- PMOXA	AqpZ	Water nanofiltration	Maximum water flux 8 LMH/bar with a salt rejection of 45.1 ± 4.2%	30
	Tefzel ethylene tetrafluoroethylene(ETFE)	PMOXA- <i>b</i> -PDMS- <i>b</i> - PMOXA	gA	Electrophysiological studies	gA is inserted and is functional	71
Porous solid support- polymersome intrusion	Au-coated PCTE	PMOXA-PDMS- PMOXA functionalized with end groups	AqpZ	Seawater desalination and water reuse	Water flux 17.6 LMH with high salt rejection 91.8%	32
	CA membrane with pore size of ~25 nm and functionalized surface	PMOXA-PDMS- PMOXA	AqpZ	Nanofiltration or forward osmosis	5.5 58 ± 0.97 LMH with a salt rejection of 50.7%	33
Immobilized polymersome	Glass surfaces chemically modified with amino groups	PMOXA- <i>b</i> -PDMS- <i>b</i> - PMOXA	GlpF	Selective detection of sugar alcohols	The lowest concentration of ribitol detected was 200 nM	75
	Glass slide with BSA-biotin- streptavidin-biotin-nanoreactor link	PMOXA- <i>b</i> -PDMS- <i>b</i> - PMOXA	OmpF	Nanoreactors for studying model enzymatic reactions	The K _m of the enzyme entrapped on the immobilized polymersome was 46mM.	61
Protein confinement in porous insulating polymer	PET film tuned by atomic layer deposition of Al ₂ O ₃ /ZnO	PET	gA	Study of protein selectivity to ions	Conductance is one order of magnitude bigger when gA is inserted. Cl ⁻ permeability is higher than Na ⁺	79
	Free-standing	PCTE covered with	gA	Study of protein	No significant ion selectivity	76

CHAPTER 3

		PVP		selectivity to ions	is observed between the mono and divalent cations	
	Free-standing	PCTE covered with PVP and treated with ethanol	gA	Study of protein selectivity to ions	Enhanced conductivity of K ⁺ vs Na ⁺	78
	Free-standing / ITO	PLA with nanoporations	Omp2a	Study of protein selectivity to ions	Enhanced conductivity of K ⁺ vs Na ⁺	85
Solid membrane conducting polymer	CP film supported onto steel	PPy	Omp2a	Study of protein selectivity to ions	Enhanced conductivity of K ⁺ vs Na ⁺	83

Table 3.2 Summary of the advantages and disadvantages encountered during the preparation and application of the different type of biomimetic membranes made of polymers

Technique	Sub-technique	Advantages	Disadvantages	Ref.
Amphiphilic polymers/Block copolymers	Free standing	No influence of the substrate. Direct measure.	Low stability. No more than 1 mm ² in area. Difficult scalability to support industrial applications	63-65
	Solid supported	Increased stability. Easy to measure the influence of the protein if the substrate is a conductive material.	Interactions with the substrate can induce the denaturation of the protein. Poor area coverage. Membrane defects. Difficult scalability to support industrial applications	38,68,70
	Porous support-polymersome spanning	The protein is not in direct contact with the substrate. There is more than enough space for the solutes to cross the membrane.	The porous substrate normally needs a pre-treatment to facilitate proteopolymersome spanning. Poor area coverage. Membrane defects. Difficult scalability to support industrial applications.	25,30,73,71
	Porous solid support-polymersome intrusion	Easier to cover all the perforations. The protein is not in direct contact with the substrate. The final material is more selective and sensible since the electrolyte needs to cross two times the membrane.	Difficult scalability to support industrial applications.	32,33
	Polymersomes covalently linked to the surface	The proteopolymersomes are covalently linked to the substrate, providing stability.	Indirect measurement. Need to encapsulate enzymes inside the proteopolymersomes.	61,75

CHAPTER 3

Nanostructured solid-state membrane	Insulating polymers	The scalability is higher. There are commercial membranes that can be used. The stability is higher and can be employed for actual applications.	Fine tune on the pore size realized on the membrane is needed. Difficult to control the correct deposition of the membrane protein on the pore.	76,78,79,85
	Conducting polymers	The polymerization can take place at the same time that the protein is embedded applying low voltages.	Influence of the polymer on the electrical measurements. High roughness and thickness which difficult the protein localization on the membrane. Difficult scalability to support industrial applications.	83

3.5 Conclusions and outlook

Biological membranes are complex systems with many molecules playing crucial interactions, which allow the communication between different compartments or directly permit cell-cell contacts. The study of these events is complicated and, therefore, artificial model membranes play an important role for unravelling the chemical and physical characteristics of the embedded proteins together with their functionality.

In early studies, phospholipid bilayers deposited onto solid substrates (so-called solid-supported membranes) were commonly used as experimental cell-surface models to gain insight into immune reactions and cell adhesion.⁸⁸⁻⁹⁵ Eventually, mimicking properties of biological elements to prepare functional hybrid materials based on polymers started to be an attractive alternative to the use of lipid bilayers. Polymer membranes in a variety of conditions (*i.e.* free standing films, solid-supported membranes, membranes spanned over porous supports, and proteopolymersomes embedded onto porous substrates) were used to insert membrane proteins not only for understanding their biofunctionality in synthetic templates but also for developing active surfaces for translational applications, such as water purification, molecules biosensing, DNA sequencing, and ion transport.

Within this context, block copolymers have been frequently used to prepare the bilayers supported on a material surface. Such block copolymer-based supramolecular assemblies exhibit many interesting properties, as for example stability, robustness and tunability. However, many of the proteins employed for basic biophysical studies or for sensor applications are known to protrude from the bilayer. These protruded parts may form strong interactions with the substrate, leading to a partial loss of functionality or even to a complete denaturation.⁹⁶ For that reason, different attempts have been done to maintain the distance between the substrate and the proteins, such as the use of nanoporations to suspended bilayers, the addition of polymer cushions, or the study of proteopolymersomes covalently linked to a solid support.

The approach based on the confinement of the protein on nanostructured polymers is particularly interesting. Polymeric membranes with nanopores and nanoporation can be prepared by track-etching and by phase segregation, the latter offering better outlook

for practical use. However, huge challenges still lie ahead both in terms of “on demand” inducing properties whilst the architecture of the membrane is preserved and of multi-functionality, which can be reached by inserting different MPs or by inserting the MPs at specific locations.

It is worth to mention that in terms of applicability, it is difficult to scale-up the production of these membranes because above all the production and folding of ion-channels is time consuming and expensive. However, over more than three decades the production of synthetic ion channels has been growing. Nowadays, there are many approaches based on chemical synthesis and supramolecular assembly to biomimick macromolecules.^{97,98} For example, chloride selective channels had been prepared via directional assembly of electron-deficient iodine atoms, which create a transmembrane pathway for facilitating anion transport,⁹⁹ potassium ion channels by means of aromatic stacking of helical oligomers,¹⁰⁰ or even artificial channels sensible to an external stimuli.¹⁰¹

Overall, the integration of biological and synthetic materials is still a promising area of research that awaits further developments. There are many different proteins with useful and accurate functions that upon incorporation on stable polymer membranes could proportionate many unique and beneficial applications.

3.6 References

1. Demarche, S.; Sugihara, K.; Zambelli, T.; Tiefenauer, L. and Vörös, J. Techniques for recording reconstituted ion channels. *Analyst*, **2011**, *136*, 1077–1089.
2. Wallin, E. and Heijne, G. Von. Genome-wide analysis of integral membrane proteins from Eubacterial, Archaean, and eukaryotic organisms. *Protein Sci.* **2008**, *7*, 1029–1038.
3. Fiori, M. C.; Jiang, Y.; Zheng, W.; Anzaldúa, M.; Borgnia, M. J.; Altenberg, G. a. and Liang, H. Polymer nanodiscs: discoidal amphiphilic block copolymer membranes as a newp for membrane proteins. *Sci. Rep.* **2017**, *7*, 15227.
4. Clarke, J.; Wu, H. C.; Jayasinghe, L.; Patel, A.; Reid, S. and Bayley, H. Continuous base identification for single-molecule nanopore DNA sequencing. *Nat. Nanotechnol.* **2009**, *4*, 265–270.
5. Mura, S.; Nicolas, J. and Couvreur, P. Stimuli-responsive nanocarriers for drug delivery. *Nat. Mater.* **2013**, *12*, 991–1003.

6. Kim, Y. R.; Jung, S.; Ryu, H.; Yoo, Y. E.; Kim, S. M. and Jeon, T. J. Synthetic Biomimetic Membranes and Their Sensor Applications. *Sensors (Switzerland)* **2012**, *12*, 9530–9550.
7. Werber, J. R.; Osuji, C. O.; Elimelech, M. Materials for next-Generation Desalination and Water Purification Membranes. *Nat. Rev. Mater.* **2016**, *1*, 1–15.
8. Fane, A. G.; Wang, R. and Hu, M. X. Synthetic membranes for water purification: status and future. *Angew. Chemie - Int. Ed.* **2015**, *54*, 3368–3386.
9. Ren, T.; Erbakan, M.; Shen, Y.; Barbieri, E.; Saboe, P.; Feroz, H.; Yan, H.; McCuskey, S.; Hall, J. F.; Schantz, a. B.; et al. Membrane protein insertion into and compatibility with biomimetic membranes. *Adv. Biosyst.* **2017**, *1*, 1700053.
10. Shen, Y. X.; Saboe, P. O.; Sines, I. T.; Erbakan, M. and Kumar, M. Biomimetic membranes: a review. *J. Memb. Sci.* **2014**, *454*, 359–381.
11. Palivan, C. G.; Goers, R.; Najer, A.; Zhang, X.; Car, A. and Meier, W. Bioinspired polymer vesicles and membranes for biological and medical applications. *Chem. Soc. Rev.* **2016**, *45*, 377–411.
12. Kowalczyk, S. W.; Blosser, T. R. and Dekker, C. Biomimetic nanopores: learning from and about nature. *Trends Biotechnol.* **2011**, *29*, 607–614.
13. Garni, M.; Thamboo, S.; Schoenenberger, C. A. and Palivan, C. G. Biopores/membrane Proteins in Synthetic Polymer Membranes. *Biochim. Biophys. Acta - Biomembr.* **2017**, *1859*, 619–638.
14. Subczynski, W. K.; Hyde, J. S. and Kusumi, A. Oxygen permeability of phosphatidylcholine--cholesterol membranes. *Proc. Natl. Acad. Sci.* **1989**, *86*, 4474–4478.
15. Gutknecht, J. Diffusion of carbon dioxide through lipid bilayer membranes. Effects of carbonic anhydrase, bicarbonate, and unstirred layers. *J. Gen. Physiol.* **1988**, *69*, 779–794.
16. Walter, A. and Gutknecht, J. Permeability of small nonelectrolytes through lipid bilayer membranes. *J. Membr. Biol.* **1986**, *90*, 207–217.
17. Orbach, E. and Finkelstein, A. The Nonelectrolyte permeability of planar lipid bilayer membranes. *J. Gen. Physiol.* **1980**, *75*, 427–436.
18. Yang, J. N. and Hinner, M. J. Getting across the cell membrane: an overview for small molecules, peptides, and proteins. *Methods Mol Biol.* **2015**, *29*–57.
19. Freigassner, M.; Pichler, H. and Glieder, A. Tuning microbial hosts for membrane protein production. *Microb. Cell Fact.* **2009**, *8*, 1–22.
20. Kistler, J. and Stroud, R. M. Crystalline arrays of membrane-bound acetylcholine receptor. *Proc. Natl. Acad. Sci. U. S. A.* **1981**, *78*, 3678–3682.
21. Junge, F.; Schneider, B.; Reckel, S.; Schwarz, D.; Dötsch, V. and Bernhard, F. Large-scale production of functional membrane proteins. *Cell. Mol. Life Sci.* **2008**, *65*, 1729–1755.
22. Gordon, E.; Horsefield, R.; Swarts, H. G. P.; de Pont, J. J. H. H. M.; Neutze, R. and Snijder, A. Effective high-throughput overproduction of membrane proteins in *Escherichia Coli*. *Protein Expr. Purif.* **2008**, *62*, 1–8.

23. Lian, J.; Ding, S.; Cai, J.; Zhang, D.; Xu, Z. and Wang, X. Improving Aquaporin Z expression in *Escherichia Coli* by fusion partners and subsequent condition optimization. *Appl. Microbiol. Biotechnol.* **2009**, 82, 463–470.
24. Verkman, A. S. Aquaporins. *Curr. Biol.* 2013, R52-R55.
25. Wang, H.; Chung, T. S.; Tong, Y. W.; Jeyaseelan, K.; Armugam, A.; Chen, Z.; Hong, M. and Meier, W. Highly permeable and selective pore-spanning biomimetic membrane embedded with Aquaporin Z. *Small* **2012**, 8, 1185–1190.
26. Wang, H.; Chung, T. S.; Tong, Y. W.; Meier, W.; Chen, Z.; Hong, M.; Jeyaseelan, K. and Armugam, A. Preparation and characterization of pore-suspending biomimetic membranes embedded with Aquaporin Z on carboxylated polyethylene glycol polymer cushion. *Soft Matter* **2011**, 7, 7274–7280.
27. Gan, H. X.; Zhou, H.; Lin, Q.; Tong, Y. W. Quantification of Aquaporin-Z Reconstituted into Vesicles for Biomimetic Membrane Fabrication. *Sci. Rep.* **2017**, 7, 1–13.
28. Li, X.; Chou, S.; Wang, R.; Shi, L.; Fang, W.; Chaitra, G.; Tang, C. Y.; Torres, J.; Hu, X. and Fane, A. G. Nature gives the best solution for desalination: aquaporin-based hollow fiber composite membrane with superior performance. *J. Memb. Sci.* **2015**, 494, 68–77.
29. Tang, C. Y.; Zhao, Y.; Wang, R.; Hélix-Nielsen, C. and Fane, A. G. Desalination by biomimetic aquaporin membranes: review of status and prospects. *Desalination* **2013**, 308, 34–40.
30. Duong, P. H. H.; Chung, T. S.; Jeyaseelan, K.; Armugam, A.; Chen, Z.; Yang, J.; Hong, M. Planar biomimetic aquaporin-incorporated triblock copolymer membranes on porous alumina supports for nanofiltration. *J. Memb. Sci.* **2012**, 409-410.
31. Sun, G.; Chung, T. S.; Jeyaseelan, K.; Armugam, A. Stabilization and immobilization of aquaporin reconstituted lipid vesicles for water purification. *Colloids surfaces B biointerfaces* **2013**, 102, 466–471.
32. Wang, H. L.; Chung, T. S.; Tong, Y. W.; Jeyaseelan, K.; Armugam, A.; Duong, H. H. P.; Fu, F.; Seah, H.; Yang, J. and Hong, M. Mechanically robust and highly permeable AquaporinZ biomimetic membranes. *J. Memb. Sci.* **2013**, 434, 130–136.
33. Xie, W.; He, F.; Wang, B.; Chung, T.-S.; Jeyaseelan, K.; Armugam, A. and Tong, Y. W. An aquaporin-based vesicle-embedded polymeric membrane for low energy water filtration. *J. Mater. Chem. A* **2013**, 1, 7592–7600.
34. Branton, D.; Deamer, D. W.; Marziali, A.; Bayley, H.; Benner, S. A.; Butler, T.; Di Ventra, M.; Garaj, S.; Hibbs, A.; Huang, X.; et al. The Potential and Challenges of Nanopore Sequencing. *Nat. Biotechnol.* **2008**, 26, 1146–1153.
35. Braha, O.; Walker, B.; Cheley, S.; Kasianowicz, J. J.; Song, L.; Gouaux, J. E.; Bayley, H. Designed protein pores as components for biosensors. *Chem. Biol.* **1997**, 4 (7), 497–505.
36. Kang, X. F.; Gu, L. Q.; Cheley, S. and Bayley, H. Single protein pores containing molecular adapters at high temperatures. *Angew. Chemie - Int. Ed.* **2005**, 44, 1495–1499.
37. Meller, A.; Nivon, L.; Brandin, E.; Golovchenko, J.; Branton, D. Rapid nanopore discrimination between single polynucleotide molecules. *PNAS* **2000**, 1997, 1079–1084.

38. Zhang, X.; Fu, W.; Palivan, C. G.; Meier, W. Natural channel protein inserts and functions in a completely artificial, solid-supported bilayer membrane. *Sci. Rep.* **2013**, *3*, 2196.
39. Urry, D. W.; Goodall, M. C.; Glickson, J. D. and Mayers, D. F. The gramicidin A transmembrane channel: characteristics of head-to-head dimerized (L,D) Helices. *PNAS* **1971**, *68*, 1907–1911.
40. Elliott, J. R.; Needham, D.; Dilger, J. P. and Haydon, D. A. The Effects of bilayer thickness and tension on gramicidin single-channel lifetime. *BBA - Biomembr.* **1983**, *735*, 95–103.
41. Kelkar, D. A. and Chattopadhyay, A. The gramicidin ion channel: a model membrane protein. *Biochim. Biophys. Acta - Biomembr.* **2007**, *1768*, 2011–2025.
42. Koebnik, R.; Locher, K. P. and Van Gelder, P. Structure and function of bacterial outer membrane proteins: barrels in a nutshell. *Mol. Microbiol.* **2000**, *37*, 239–253.
43. Discher, D. E.; Eisenberg, A. Polymer vesicles. *Science* **2002**, *297*, 967–973.
44. Hauser, H.; Phillips, M. C. and Stubbs, M. Ion permeability of phospholipid bilayers. *Nature* **1972**, *239*, 342–344.
45. Bermudez, H.; Brannan, A. K.; Hammer, D. a.; Bates, F. S.; Discher, D. E. Molecular Weight dependence of polymersome membrane structure, elasticity, and stability. *Macromolecules* **2002**, *35*, 8203–8208.
46. Nardin, C.; Winterhalter, M. and Meier, W. Giant free-standing ABA triblock copolymer membranes. *Langmuir* **2000**, *16*, 7708–7712.
47. Discher, B. M.; Won, Y. Y.; Ege, D. S.; Lee, J. C. M.; Bates, F. S.; Discher, D. E. and Hammer, D. A. Polymersomes: tough vesicles made from diblock copolymers. *Science* **1999**, *284*, 1143–1146.
48. Kowal, J.; Zhang, X.; Dinu, I. A.; Palivan, C. G. and Meier, W. Planar biomimetic membranes based on amphiphilic block copolymers. *ACS Macro Lett.* **2014**, *3*, 59–63.
49. Kaditi, E.; Mountrichas, G. and Pispas, S. Amphiphilic block copolymers by a combination of anionic polymerization and selective post-polymerization functionalization. *Eur. Polym. J.* **2011**, *47*, 415–434.
50. Gress, A.; Smarsly, B. and Schlaad, H. Formation of glycopolyamide nanofibers. *Macromol. Rapid Commun.* **2008**, *29*, 304–308.
51. Obeng, M.; Milani, A. H.; Musa, M. S.; Cui, Z.; Fielding, L. A.; Farrand, L.; Goulding, M. and Saunders, B. R. Self-assembly of poly(lauryl methacrylate)-B-poly(benzyl methacrylate) nano-objects synthesised by ATRP and their temperature-responsive dispersion properties. *Soft Matter* **2017**, *13*, 2228–2238.
52. Li, Z.-C.; Liang, Y.-Z.; Chen, G.-Q.; Li and F.-M. Synthesis of amphiphilic block copolymers with well-defined glycopolymer segment by atom transfer radical polymerization. *Macromol. Rapid Commun.* **2000**, *21*, 375–380.
53. Yu, C.-Y.; Wen, S.-H.; Yu, S.-H. and Wang, C.-C. Synthesis of phenylenevinylene and naphthylenevinylene homopolymers and block copolymers by ring-opening metathesis polymerization. *J. Polym. Sci. Part A Polym. Chem.* **2018**, *56*, 67–74.

54. Xiong, X.-B.; Binkhathlan, Z.; Molavi, O.; Lavasanifar, A. Amphiphilic block co-polymers: preparation and application in nanodrug and gene delivery. *Acta Biomater.* **2012**, *8*, 2017–2033.
55. Van Dijk, M.; Rijkers, D. T. S.; Liskamp, R. M. J.; van Nostrum, C. F.; Hennink, W. E. Synthesis and applications of biomedical and pharmaceutical polymers via click chemistry methodologies. *Bioconjug. Chem.* **2009**, *20*, 2001–2016.
56. Pawar, P. V.; Gohil, S. V.; Jain, J. P. and Kumar, N. Functionalized polymersomes for biomedical applications. *Polym. Chem.* **2013**, *4*, 3160–3176.
57. Li, M.-H. and Keller, P. Stimuli-Responsive polymer vesicles. *Soft Matter* **2009**, *5*, 927–937.
58. Schacher, F.; Ulbricht, M. and Müller, A. H. E. Self-supporting, double stimuli-responsive porous membranes from polystyrene-block-poly(N,N-dimethylaminoethyl methacrylate) Diblock Copolymers. *Adv. Funct. Mater.* **2009**, *19*, 1040–1045.
59. Li, S.; Meng, F.; Wang, Z.; Zhong, Y.; Zheng, M.; Liu, H. and Zhong, Z. Biodegradable polymersomes with an ionizable membrane: facile preparation, superior protein loading, and endosomal pH-responsive protein release. *Eur. J. Pharm. Biopharm.* **2012**, *82*, 103–111.
60. Nardin, C.; Hirt, T.; Leukel, J. and Meier, W. Polymerized ABA triblock copolymer vesicles. *Langmuir* **2000**, *16*, 1035–1041.
61. Grzelakowski, M.; Onaca, O.; Rigler, P.; Kumar, M. and Meier, W. Immobilized protein-polymer nanoreactors. *Small* **2009**, *5*, 2545–2548.
62. Winterhalter, M. Black lipid membranes. *Curr. Opin. Colloid Interface Sci.* **2000**, *5*, 250–255.
63. Nardin, C.; Winterhalter, M. and Meier, W. Reconstitution of channel proteins in polymerised-ABA triblock copolymer membranes. *Angew. Chemie.* **2000**, *39*, 4599–4602.
64. Wong, D.; Jeon, T. J. and Schmidt, J. Single molecule measurements of channel proteins incorporated into biomimetic polymer membranes. *Nanotechnology* **2006**, *17*, 3710–3717.
65. Ho, D.; Chang, S. and Montemagno, C. D. Fabrication of biofunctional nanomaterials via *Escherichia Coli* OmpF protein air/water interface insertion/integration with copolymeric amphiphiles. *Nanomedicine Nanotechnology, Biol. Med.* **2006**, *2*, 103–112.
66. Belegriou, S.; Dorn, J.; Kreiter, M.; Kita-Tokarczyk, K.; Sinner, E.-K. and Meier, W. Biomimetic supported membranes from amphiphilic block copolymers. *Soft Matter* **2010**, *6*, 179–186.
67. Edmondson, S.; Osborne, V. L. and Huck, W. T. S. Polymer brushes via surface-initiated polymerizations. *Chem. Soc. Rev.* **2004**, *33*, 14–22.
68. Dorn, J.; Belegriou, S.; Kreiter, M.; Sinner, E. K. and Meier, W. Planar block copolymer membranes by vesicle spreading. *Macromol. Biosci.* **2011**, *11*, 514–525.
69. Dixon, R. A.; Chopra, I. Polymyxin B and Polymyxin B nonapeptide alter cytoplasmic membrane permeability in *Escherichia Coli*. *J. Antimicrob. Chemother.* **1986**, *18*, 557–563.
70. Kowal, J. T.; Kowal, J. K.; Wu, D.; Stahlberg, H.; Palivan, C. G. and Meier, W. P. Functional surface engineering by nucleotide-modulated potassium channel insertion into polymer membranes attached to solid supports. *Biomaterials* **2014**, *35*, 7286–7294.

71. González-Pérez, A.; Stibius, K. B.; Vissing, T.; Nielsen, C. H. and Mouritsen, O. G. Biomimetic triblock copolymer membrane arrays: a stable template for functional membrane proteins. *Langmuir* **2009**, *25*, 10447–10450.
72. Zhong, P. S.; Chung, T. S.; Jeyaseelan, K. and Armugam, A. Aquaporin-embedded biomimetic membranes for nanofiltration. *J. Memb. Sci.* **2012**, *407-408*.
73. Vermette, P.; Meagher, L.; Gagnon, E.; Griesser, H. J. and Doillon, C. J. Immobilized liposome layers for drug delivery applications: inhibition of angiogenesis. *J. Control. Release* **2002**, *80*, 179–195.
74. Stamou, D.; Duschl, C.; Delamarche, E. and Vogel, H. Self-assembled microarrays of attoliter molecular vessels. *Angew. Chemie - Int. Ed.* **2003**, *42*, 5580–5583.
75. Zhang, X.; Lomora, M.; Einfalt, T.; Meier, W.; Klein, N.; Schneider, D. and Palivan, C. G. Active surfaces engineered by immobilizing protein-polymer nanoreactors for selectively detecting sugar alcohols. *Biomaterials* **2016**, *89*, 79–88.
76. Balme, S.; Janot, J. M.; Berardo, L.; Henn, F.; Bonhenry, D.; Kraszewski, S.; Picaud, F. and Ramseyer, C. New bioinspired membrane made of a biological ion channel confined into the cylindrical nanopore of a solid-state polymer. *Nano Lett.* **2011**, *11*, 712–716.
77. Wu, S.; Park, S. R. and Ling, X. S. Lithography-free formation of nanopores in plastic membranes using laser heating. *Nano Lett.* **2006**, *6*, 2571–2576.
78. Balme, S.; Picaud, F.; Kraszewski, S.; Déjardin, P.; Janot, J. M.; Lepoitevin, M.; Capomanes, J.; Ramseyer, C. and Henn, F. Controlling potassium selectivity and proton blocking in a hybrid biological/solid-state polymer nanoporous membrane. *Nanoscale* **2013**, *5*, 3961–3968.
79. Abou Chaaya, A.; Le Poitevin, M.; Cabello-Aguilar, S.; Balme, S.; Bechelany, M.; Kraszewski, S.; Picaud, F.; Cambedouzou, J.; Balanzat, E.; Janot, J. M.; et al. Enhanced ionic transport mechanism by gramicidin in a confined inside nanopores tuned by atomic layer deposition. *J. Phys. Chem. C* **2013**, *117*, 15306–15315.
80. Roussel, G.; Matagne, A.; De Bolle, X.; Perpète, E. A. and Michaux, C. Purification, refolding and characterization of the trimeric omp2a outer membrane porin from *Brucella Melitensis*. *Protein Expr. Purif.* **2012**, *83*, 198–204.
81. Roussel, G.; Perpète, E. A.; Matagne, A.; Tinti, E. and Michaux, C. Towards a universal method for protein refolding: the trimeric beta barrel membrane omp2a as a test case. *Biotechnol. Bioeng.* **2013**, *110*, 417–423.
82. Lopes-Rodrigues, M.; Triguero, J.; Torras, J.; Perpète, E. A.; Michaux, C.; Zanuy, D. and Alemán, C. Influence of the surrounding environment in re-naturalized β -barrel membrane proteins. *Biophys. Chem.* **2018**, *234*, 6–15.
83. Pérez-Madrigal, M. M.; del Valle, L. J.; Armelin, E.; Michaux, C.; Roussel, G.; Perpète, E. A. and Alemán, C. Polypyrrole-supported membrane proteins for bio-inspired ion channels. *ACS Appl. Mater. Interfaces* **2015**, *7*, 1632–1643.

84. Puiggali-Jou, A.; Medina, J.; Del Valle, L. J.; Alemn, C. Nanoperforations in Poly(lactic Acid) Free-Standing Nanomembranes to Promote Interactions with Cell Filopodia. *Eur. Polym. J.* **2016**, *75*, 552–564.
85. Puiggali-Jou, A.; Pérez-Madrigal, M. M.; del Valle, L. J.; Armelin, E.; Casas, M. T.; Michaux, C.; Perpète, E. A.; Estrany, F. and Alemán, C. Confinement of a β -barrel protein in nanoperforated free-standing nanomembranes for ion transport. *Nanoscale* **2016**, *8*, 16922–16935.
86. Lopes-Rodrigues, M.; Puiggali-Jou, A.; Martí-Balleste, D.; Del Valle, L. J.; Michaux, C.; Perpète, E. A. and Alemán, C. thermomechanical response of a representative porin for biomimetics. *ACS Omega* **2018**, *3*, 7856–7867.
87. Puiggali-jou, A.; Pawlowski, J.; Valle, L. J.; Perpète, E. A.; Sek, S. and Alemán, C. Properties of Omp2a-based supported lipid bilayers : comparison with polymeric bioinspired membranes. *ACS Omega* **2018**, *3*, 9003–9019.
88. Tanaka, M. and Sackmann, E. Polymer-supported membranes as models of the cell surface. *Nature*, **2005**, *437*, 656–663.
89. Brian, A. A. and McConnell, H. M. Allogeneic stimulation of cytotoxic T cells by supported planar membranes. *PNAS* **1984**, *81*, 6159–6163.
90. Erb, E. M.; Tangemann, K.; Bohrmann, B.; Muller, B. and Engel, J. Integrin α IIb β 3 reconstituted into lipid bilayers is nonclustered in its activated state but clusters after fibrinogen binding. *Biochem.* **1997**, *36*, 7395–7402.
91. Kloboucek, A.; Behrisch, A.; Faix, J. and Sackmann, E. Adhesion-induced receptor segregation and adhesion plaque formation: a model membrane study. *Biophys. J.* **1999**, *77*, 2311–2328.
92. Qi, S. Y.; Groves, J. T. and Chakraborty, A. K. synaptic pattern formation during cellular recognition. *PNAS* **2001**, *98*, 6548–6553.
93. Grakoui, A.; Bromley, S. K.; Sumen, C.; Davis, M. M.; Shaw, A. S.; Allen, P. M. and Dustin, M. L. The immunological synapse: a molecular machine controlling T cell activation. *Science* **1999**, *285*, 221–227.
94. Tamm, L. K. and McConnell, H. M. Supported phospholipid bilayers. *Biophys. J.* **1985**, *47*, 105–113.
95. Chan, P. Y.; Lawrence, M. B.; Dustin, M. L.; Ferguson, L. M.; Golan, D. E. and Springer, T. A. Influence of receptor lateral mobility on adhesion strengthening between membranes containing LFA-3 and CD2. *J. Cell Biol.* **1991**, *115*, 245–255.
96. Sinner, E. K. and Knoll, W. Functional tethered membranes. *Curr. Opin. Chem. Biol.* **2001**, *5*, 705–711.
97. Sakai, N. and Matile, S. Synthetic ion channels. *Langmuir* **2013**, *29*, 9031–9040.
98. Matile, S.; Vargas Jentsch, A.; Montenegro, J. and Fin, A. Recent synthetic transport systems. *Chem. Soc. Rev.* **2011**, *40*, 2453–2474.

99. Ren, C.; Ding, X.; Roy, A.; Shen, J.; Zhou, S.; Chen, F.; Yau Li, S. F.; Ren, H.; Yang, Y. Y. and Zeng, H. A halogen bond-mediated highly active artificial chloride channel with high anticancer activity. *Chem. Sci.* **2018**, 9, 4044–4051.
100. Lang, C.; Deng, X.; Yang, F.; Yang, B.; Wang, W.; Qi, S.; Zhang, X.; Zhang, C.; Dong, Z. and Liu, J. Highly selective artificial potassium ion channels constructed from pore-containing helical oligomers. *Angew. Chemie - Int. Ed.* **2017**, 56, 12668–12671.
101. Muraoka, T.; Umetsu, K.; Tabata, K. V.; Hamada, T.; Noji, H.; Yamashita, T. and Kinbara, K. Mechano-sensitive synthetic ion channels. *J. Am. Chem. Soc.* **2017**, 139, 18016–18023.



CHAPTER 4:

Characterization of Omp2a

SUMMARY

Omp2a β -barrel outer membrane protein has been reconstituted into supported lipid bilayers (SLBs) to compare the nanomechanical properties (elastic modulus, adhesion forces, and deformation) and functionality of the resulting bioinspired system with those of polymeric nanomembranes (NMs). Protein reconstitution into lipid bilayers has been performed using different strategies, the most successful one consisting of a detergent-mediated process into preformed liposomes. The elastic modulus obtained for the lipid bilayer and Omp2a are ~ 19 and 10.5 ± 1.7 MPa, respectively. Accordingly, the protein is softer than the lipid bilayer, whereas the latter exhibits less mechanical strength than polymeric NMs.

Besides, the thermomechanical response of Omp2a has been characterized using microcantilever technology and compared with standard proteins. For this purpose, thermally induced transitions involving the conversion of stable trimers to bigger aggregates, local reorganizations based on the strengthening or weakening of intermolecular interactions, and protein denaturation have been detected by the microcantilever resonance frequency and deflection as a function of the temperature. Measurements have been carried out on arrays of 8-microcantilevers functionalized with proteins (Omp2a, lysozyme and bovine serum albumin). Results not only demonstrate the complex behavior of porins, which exhibit multiple local thermal transitions before undergoing denaturation at temperatures higher than 105 °C, but also suggest a posttreatment to control the orientation of immobilized Omp2a molecules in functionalized biomimetic nanomembranes and, thus, increase their efficacy in ion transport.

Publications derived from this work:

Puiggalí-jou, A.; Pawlowski, J.; del Valle, L. J.; Perpète, E. A.; Sek, S. and Alemán, C. Properties of Omp2a-based supported lipid bilayers: comparison with polymeric bioinspired membranes. *ACS Omega* **2018**, 3, 9003-9019.

Lopes-Rodrigues*, M.; Puiggalí-Jou, A.*; Martí-Balleste, D.; del Valle, L. J.; Michaux, C.; Perpète, E. A. And Alemán, C. Thermomechanical response of a representative porin for biomimetics. *ACS Omega* **2018**, 3, 7856-7867.

* M.L.-R. and A.P.-J. contributed equally to this study.

4.1 Introduction

Membrane proteins (MPs) play a key role in many biological processes, such as cell recognition, signal transmission, enzymatic reactions, and transport of metabolites.¹⁻³ Their importance is proved by the fact that 50% of medical drugs currently on the market target MPs.²⁻⁴ The structure of MPs is restricted to α -helix and β -barrel due to the need to satisfy all hydrogen bonds within the water-excluded native bilayer environment. Although α -helical MPs are present in most biological membranes, β -barrel MPs are exclusively found in the outer membranes of Gram-negative bacteria⁵ and eukaryotic organelles directly derived from prokaryotic ancestors namely, mitochondria⁶ and chloroplasts.⁷

Porins are β -barrel outer membrane proteins (OMPs) that form water-filled open channels and allow the passive penetration of hydrophilic molecules. Due to their capacity in exchange of ions and small nutrients (i.e. typically < 667 Da) over the OM, porins have been used to fabricate smart biomimetic NMs that could incorporate biological functions, such as controlled ion transport.⁸

4.2 Materials and methods

Expression, purification and refolding of the Omp2a outer membrane protein from *Brucella melitensis*

Bacterial strain and growth. Cells of *E. coli* BL21 (DE3) carrying pLysS and pET2a plasmids (containing the gene Omp2a without peptide signal) were grown in Lysogeny broth (LB) medium at 37°C with constant shaking. Log cultures (OD 0.6) of 500 mL were stimulated with IPTG (0.2 mg mL⁻¹) for 3 h. Cells were then harvested by centrifugation at 4,000 g for 30 min, the resulting bacterial pellets being stored at -20°C.

Overexpression and non-native purification of Omp2a. The bacterial pellets were thawed and treated with 8 mL of TEN lysis buffer (50 mM Tris-HCl pH 8, 1 mM EDTA, 17 mM NaCl, 125 mM PMSF, 250 mg mL⁻¹ lysozyme) for 20 min at 25°C. Harvested cells were further broken by addition of 10 mg of sodium deoxycholate for 60 min at 37°C with constant shaking, and 2 mg of DNase I for 60 min at 25°C. The suspension was then

centrifuged at 14,000 g for 20 min at 4°C. The resulting pellet underwent a washing buffer (2 M urea, 20 mM Tris-HCl pH 8, 500 mM NaCl, 2% Triton X-100) and centrifuged at 14,000 g for 20 min at 4°C. The inclusion bodies were solubilized with 8 mL of TEN buffer (50 mM Tris-HCl pH 8, 1 mM EDTA, 17 mM NaCl, 8 M urea). Then, the solubilized proteins were applied onto an anion-exchange DEAE column previously equilibrated with 25 mL of buffer (50 mM Tris-HCl pH 8, 17 mM NaCl, 8 M urea). Omp2a was eluted with a 50 mL linear gradient of NaCl from 17 to 500 mM, whereas the protein profile was further analyzed using sodium dodecyl sulfate-polyacrylamide gel (SDS-PAGE). Fractions containing 39 kDa proteins were then pooled and stored at 4°C.

Omp2a refolding in SDS – 2-Methyl-2,4-pentanediol (MPD) system. To refold Omp2a, the protein solution (1 mg/mL protein, 250 mM NaCl, 50 mM Tris-HCl pH 8, and 8 M urea) was eluted onto a PD-10 column to exchange the buffer (150 mM NaCl, 50 mM Tris-HCl pH 8, and 120 mM SDS, which is 15 times the critical micellar concentration). SDS-unfolded samples were then diluted 1:1 in a refolding solution (50 mM Tris-HCl pH 8, 150 mM NaCl, 3 M MPD). The protein solution was then incubated at room temperature. The samples were stored at -20°C to stop the refolding reaction. Hereafter, Omp2a protein at this procedure stage is named as obtained Omp2a.

Accepted sequence (triple letter code) of Omp2a protein (367 amino acids):

Met - Asn - Ile - Lys - Ser - Leu - Leu - Leu - Gly - Ser - Ala - Ala - Ala - Leu - Val - Ala - Ala - Ser - Gly - Ala - Gln - Ala - Ala - Asp - Ala - Ile - Val - Ala - Pro - Glu - Pro - Glu - Ala - Val - Glu - Tyr - Val - Arg - Val - Cys - Asp - Ala - Tyr - Gly - Ala - Gly - Tyr - Phe - Tyr - Ile - Pro - Gly - Thr - Glu - Thr - Cys - Leu - Arg - Val - His - Gly - Tyr - Val - Arg - Tyr - Asp - Val - Lys - Gly - Gly - Asp - Asp - Val - Tyr - Ser - Gly - Thr - Asp - Arg - Asn - Gly - Trp - Asp - Lys - Gly - Ala - Arg - Phe - Ala - Leu - Met - Phe - Asn - Thr - Asn - Ser - Glu - Thr - Glu - Leu - Gly - Thr - Leu - Gly - Thr - Tyr - Thr - Gln - Leu - Arg - Phe - Asn - Tyr - Thr - Ser - Asn - Asn - Ser - Arg - His - Asp - Gly - Gln - Tyr - Gly - Asp - Phe - Ser - Asp - Asp - Arg - Asp - Val - Ala - Asp - Gly - Gly - Val - Ser - Thr - Gly - Thr - Asp - Leu - Gln - Phe - Ala - Tyr - Ile - Thr - Leu - Gly - Gly - Phe - Lys - Val - Gly - Ile - Asp - Glu - Ser - Glu - Phe - His - Thr - Phe - Thr - Gly - Tyr - Leu - Gly - Asp - Val - Ile - Asn - Asp - Asp - Val - Val - Ala - Ala - Gly - Ser - Tyr - Arg - Thr - Gly - Lys - Ile - Ala - Tyr - Thr - Phe - Thr - Gly - Gly - Asn - Gly - Phe - Ser - Ala - Val - Ile - Ala - Leu - Glu - Gln - Gly - Gly - Glu -

Asp - Val - Asp - Asn - Asp - Tyr - Thr - Ile - Asp - Gly - Tyr - Met - Pro - His - Val - Val - Gly - Gly - Leu - Lys - Tyr - Ala - Gly - Gly - Trp - Gly - Ser - Ile - Ala - Gly - Val - Val - Ala - Tyr - Asp - Ser - Val - Ile - Glu - Glu - Trp - Ala - Thr - Lys - Val - Arg - Gly - Asp - Val - Asn - Ile - Thr - Asp - Arg - Phe - Ser - Val - Trp - Leu - Gln - Gly - Ala - Tyr - Ser - Ser - Ala - Ala - Thr - Pro - Asn - Gln - Asn - Tyr - Gly - Gln - Trp - Gly - Gly - Asp - Trp - Ala - Val - Trp - Gly - Gly - Ala - Lys - Phe - Ile - Ala - Pro - Glu - Lys - Ala - Thr - Phe - Asn - Leu - Gln - Ala - Ala - His - Asp - Asp - Trp - Gly - Lys - Thr - Ala - Val - Thr - Ala - Asn - Val - Ala - Tyr - Gln - Leu - Val - Pro - Gly - Phe - Thr - Ile - Thr - Pro - Glu - Val - Ser - Tyr - Thr - Lys - Phe - Gly - Gly - Glu - Trp - Lys - Asp - Thr - Val - Ala - Glu - Asp - Asn - Ala - Trp - Gly - Gly - Ile - Val - Arg - Phe - Gln - Arg - Ser - Phe

4.3 Properties of Omp2a-Based Supported Lipid Bilayers

In this section we focused on the study of this protein in a more native ambient, similar to that encountered in nature. Amazingly, until now no effort has been made to study Omp2a in a SLB, which consists in a planar in vitro assembly of lipids sitting on a solid support. In such configuration, which is closer to the natural system than polymeric biomimetic NMs, the structure and properties of the protein have been probed using a variety of surface sensitive atomic force microscopy and electrochemical techniques. More specifically, mechanical mapping with PeakForce Quantitative Nanomechanical Mapping® (QNM) mode, which combines single molecule force spectroscopy with single molecule imaging, has provided information about molecular forces. Furthermore, the function of Omp2a in the SLB has been examined using electrochemical impedance spectroscopy (EIS), and the results have been compared with previous data obtained for Omp2a-based polymeric artificial membranes.

4.3.1 Methods

Liposomes production: The procedure used to prepare liposomes is depicted in **Figure 4.3.1**. Initially, liposomes were generated by dissolving and mixing lipids in 4:1 chloroform:methanol, which assured an homogeneous mixture (1). After this, the solvent was evaporated using argon stream and agitation to yield a thin lipid film (2). The film was thoroughly dried to remove residual organic solvent by placing the vial on a vacuum pump for 30 min. Then, film-rehydration was performed by adding the adequate buffer (3) and sonicated 30 min at 37° (4). Vesicles were stored at 4° C. Liposome solutions were diluted 1/5 and deposited over the mica substrate for analyses with the AFM (5).

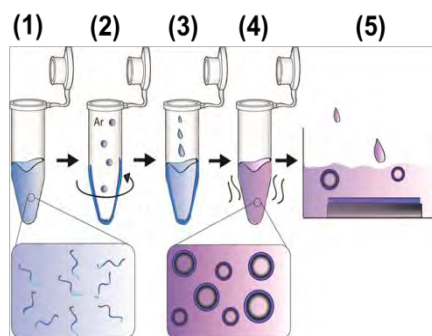


Figure 4.3.1 Scheme of the liposome fabrication.

Formation of proteoliposomes from preformed liposomes: Shortly, liposomes were detergent-destabilized by titration with Triton X-100 and, subsequently, mixed with the detergent-solubilized Omp2a transmembrane protein. After this, controlled removal of the detergent by polystyrene beads, Bio-Beads (BB), resulted in the formation of sealed proteoliposomes. Then, the proteoliposomes were incubated onto the mica substrate in order to facilitate their spreading.

Strategy of protein reconstitution by direct incorporation into SLBs: SLBs were first incubated 15 min at room temperature in the presence of the detergent (Triton X-100 at 0.01%) in order to destabilize the membrane. After this, they were further incubated at the same temperature with detergent-solubilized proteins (10 or 2 $\mu\text{g}/\text{mL}$),

allowing them to be inserted into the membrane. The excess of detergent and proteins was removed by extensive washing with mQ water.

SDS-polyacrylamide gel (SDS-PAGE): Proteoliposomes were pelleted by ultracentrifugation (15 min, 10,000 g) and the pellet was re-suspended in 25 μ L of loading buffer. The protein in the supernatant and pellet (equal volumes) were subsequently subjected to glycine SDS-PAGE using 15% acrylamide gels and visualized with Comassie Blue.

Dynamic light scattering (DLS): The size distribution of the protein in 1 \times phosphate buffer solution (PBS) pH 7.4 and in 50 mM Tris-HCl pH 8, 150 mM NaCl, 3 M MPD was determined using a NanoBrook Omni Zeta Potential Analyzer from Brookhaven Instruments Corporation. Particularly, three consecutive runs of 60 seconds each were conducted for every sample.

Atomic force microscopy (AFM) measurements: Topography imaging of the samples was performed with 5500AFM (Keysight) operating in MAC mode. In this intermittent contact mode magnetically coated cantilevers are driven by an oscillating magnetic field. This enables elimination of spurious responses generated by cantilever holding mechanism or the surrounding fluid. For imaging, we have used MAC Levers VII with nominal spring constant of 0.14 N/m, but its exact value was determined for each individual tip from thermal tuning. Nanomechanical measurements were carried out with Dimension Icon (Bruker) instrument operating in Peak Force QNM mode, which enables simultaneous imaging of the topography and mapping of the nanomechanical properties of the sample. In this mode, Z-piezo is modulated at the frequency of 2 kHz with default peak force amplitude and during each cycle the force-distance curve is recorded for every pixel of the scanned area. Based on analysis of the retract curves, it is possible to determine the adhesion force (F_{adh}) and reduced modulus of elasticity (E^*) according to Derjaguin, Muller, Toporov (DMT) contact mechanics model:

$$F_{tip} = \frac{4}{3}E^*\sqrt{Rd^3} + F_{adh} \quad (\text{Eq. 4.3.1})$$

where F_{tip} denotes force acting on AFM tip, d defines the distance between said tip and the sample surface and R is the tip radius. Modulus of elasticity (E_s) for given sample can be estimated using equation:

$$E^* = \left[\frac{1-\nu_t^2}{E_t} + \frac{1-\nu_s^2}{E_s} \right]^{-1} \quad (\text{Eq. 4.3.2})$$

where ν_t and ν_s are Poisson's ratios for the material of the tip and the sample respectively, while E_t denotes modulus of elasticity of the tip material. In order to calibrate the instrument, determination of modulus of elasticity was evaluated using poly(methylsiloxane) test sample (Bruker) with nominal value of modulus of elasticity equal 3.5 MPa. All images/maps were acquired in aqueous buffers. We have used Scan Asyst Fluid+ cantilevers (Bruker) with nominal spring constant of 0.7 N/m and the nominal tip radius of 5 nm. However, the exact value of spring constant for each cantilever was obtained from thermal tune method.

Transmission electron microscopy (TEM): The liposomes and proteoliposomes were placed on carbon-coated grids and stained with 0.5% uranyl acetate and examined by electron microscopy. Solution containing Omp2a (0.34 mg/mL) was dispersed on glow-discharged carbon coated copper grids (300 mesh) and negatively stained with uranyl acetate (2.0 % w/v). After incubation (30 s), the excess of protein was removed with filter paper, and the grids air dried for a further 1-2 s. TEM images were obtained with a Philips TECNAI 10 electron microscope operating at 100 kV.

Circular dichroism (CD): CD measurements were performed on a Chirascan-plus q CD spectrometer (Applied Photophysics, APL; UK) equipped with a temperature-controlled cell, using a cell path length 10 mm. Spectra were recorded between 180 and 260 nm. Machine settings were as follows: 1 nm bandwidth, 1 s response, 0.5 nm data pitch, 100 nm/min scan speed and cell length of 0.1 cm. All CD spectra presented in this work correspond to the average from three independent measurements.

Square-wave voltammetry (SWV): SWV experiments were carried out using glassy carbon electrodes (GCE) (2 mm diameter) as anodes. Before conducting any experiment,

the GCE was mechanically polished with powder of alumina to produce a mirror-like surface. The electrodes were subsequently sonicated to remove adhered alumina particles, rinsed with water, and left to dry. Finally, 5 μL of the corresponding sample were deposited on the top of the surface

Electrochemical characterization was carried with an Autolab PGSTAT302N. Experiments were conducted in a PBS 0.1 M (pH = 7.4) at room temperature. The initial and final potential were 0 V and + 1 V. SWV amplitude: 25 mV, frequency: 20.

EIS: EIS measurements were performed using a conventional three-electrode cell and an AUTOLAB-302N potentiostat/galvanostat operating between the frequency range of 104.5 Hz and 10^{-2} Hz and 5 mV of amplitude for the sinusoidal voltage. All experiments were performed at room temperature with lipid bilayers deposited onto ITO and using 100 mM KCl. ITO was used as working-electrode and platinum as counter-electrode, whereas Ag|AgCl saturated (KCl 3M) was employed as reference electrode. After data collection, EIS results were processed and fitted to an electrical equivalent circuit (EEC).

4.3.2 Results and discussion

Lipid formulations

The total lipid composition in *Brucella melitensis* is about 37% of phosphatidylcholine (POPC), 33% of phosphatidylethanolamine (POPE), 20% of cardiolipine (CL) and 10% of phosphatidylglycerol (POPG).⁹ Though POPE is the main phospholipid in many Gram-negative OMs, POPC is the most present in the OM of *Brucella melitensis*. This particular feature gives to this strain of bacteria high stability in the OM in comparison with other Gram-negative bacteria, whereas the content of POPE in animal cell total lipid membranes is low. For example in the blood cells, POPE and POPG constitute about 6% and 2%, respectively, of all the membrane phospholipids.¹⁰ Indeed, POPC is the major lipid component of the animal cell membranes.¹⁰

Three different lipid compositions, which consisted on mixtures of POPC, POPE, POPG and/or CL (**Figure 4.3.2**), were investigated by AFM, TEM, DLS and Z-potential: Mixt-1 composed by 4:3 POPC:POPE; Mixt-2 by 4:3:1 POPC:POPE:POPG; and Mixt-3 by 4:3:1:2 POPC:POPE:POPG:CL.

Mixt-1 showed a clear phase separation of the two lipid domains constituted by PE and PC.

Specifically, AFM images show that difference in height of the phases is ~ 0.8 nm

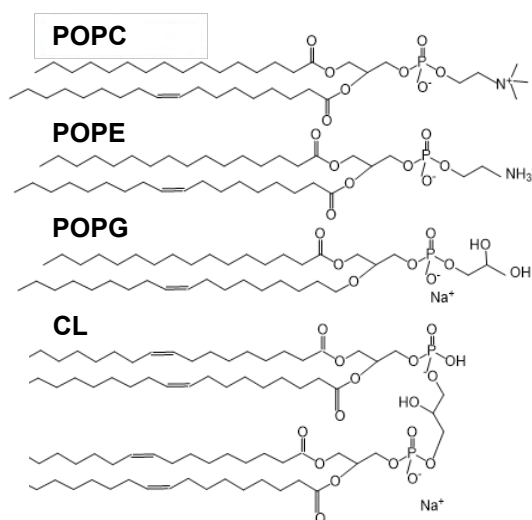


Figure 4.3.2 Scheme of the lipids chemical composition.

(**Figure 4.3.3a**) (the bilayer thickness reported for POPC and POPE is 4.33 and 4.03 nm, respectively¹¹). Instead, Mixt-2 displayed the most homogenous and flattest surface, these characteristics being expected to facilitate the rapid recognition of the protein. Consequently, Mixt-2 was selected for further studies with the porin. In this case, the thickness of the bilayer was 5.4 nm, which is significantly lower than the protein's height (around 7 nm) (**Figure 4.3.3b**). Finally, Mixt-3 showed less phase separation than Mixt-1 but still the difference between the domains was also clear, with 1.3 nm height differences (**Figure 4.3.3c**). Furthermore, as the AFM tip was prone to go through the lipid membrane, consequently disrupting the acquiring image, very low forces were needed to achieve its visualization. This feature indicates that the consistency of the lipid bilayer is lower for Mixt-3 than for Mixt-1 and Mixt-2, suggesting that CL increases the fluidity of the lipid bilayer. This hypothesis is supported by the results reported by Unsay *et al.*¹², who found that the fluidity of lipid bilayers increases and its mechanical stability decreases by enhancing the CL concentration. Thus, CL apparently decreases the packing of the lipid membrane.

It should be mentioned that results derived from TEM can be limited by the drying of the samples, which may cause deformation, or even complete destruction of the sample. The deposition of the carbon layer used to support the sample in TEM analyses could also alter the scattering of electrons. However, it has been observed that many block copolymer based assemblies and synthetic lipid bilayers tend to be rigid and, therefore, retain their shape.¹³⁻¹⁵ TEM images displayed in **Figure 4.3.3** show some small irregularities in the edges, suggesting that sizes may be slightly affected by the drying process.

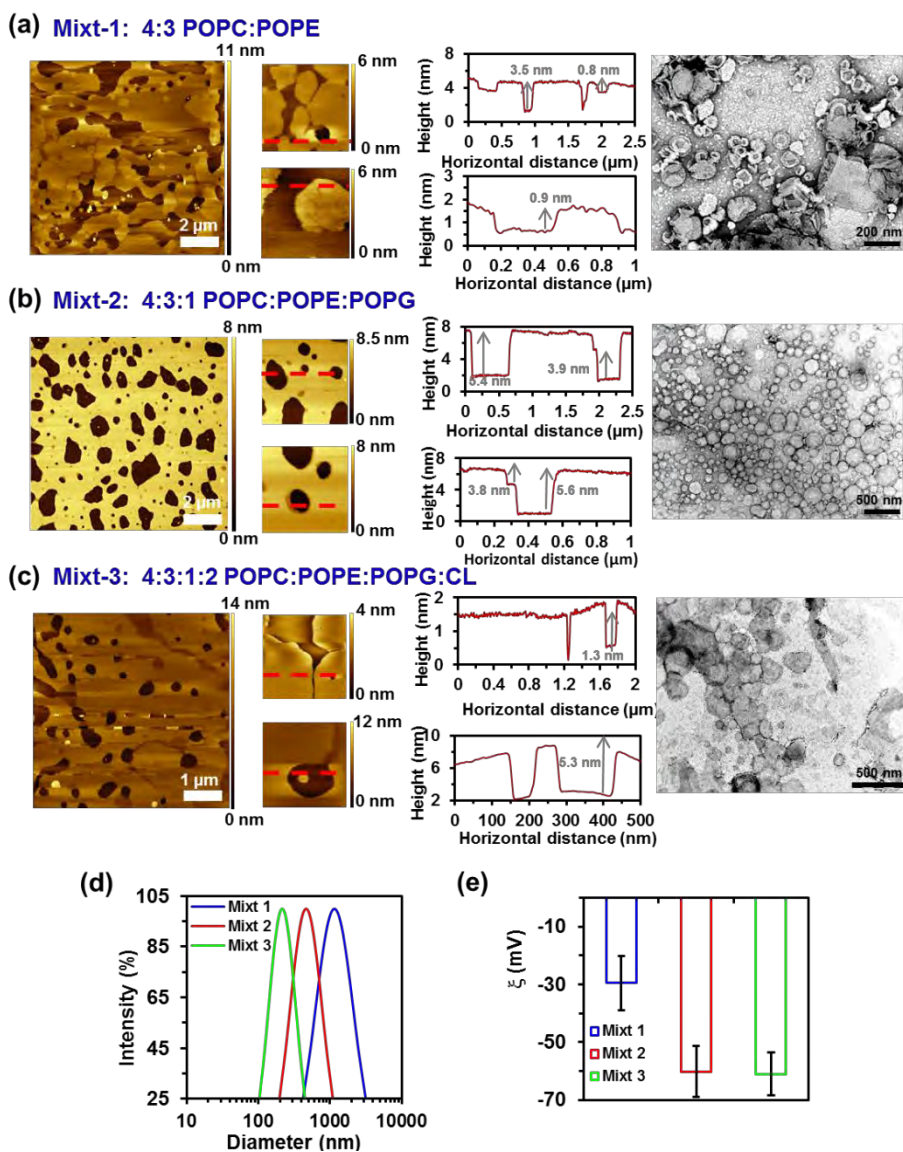


Figure 4.3.3 Topographic AFM images with the corresponding vertical profiles and TEM images of SLBs obtained from liposomes composed of: (a) 4:3 POPC:POPE (Mixt-1); (b) 4:3:1 POPC:POPE:POPG (Mixt-2); and (c) 4:3:1:2 POPC:POPE:POPG:CL (Mixt-3) diluted 1/5 in 1x PBS. (d) DLS graph expressing the intensity vs diameter and (d) the ζ -potential (e) of the mixt-1, mixt-2, and mixt-3.

DLS measurements proved that the three mixtures led to several liposome sizes (**Figure 4.3.3d**), with diameters $\phi \approx 1075$, 555 and 213 nm for Mixt-1, Mixt-2 and Mixt-3, respectively. Besides, the polydispersity in ϕ varied from sample to sample: 0.38, 0.35 and 0.19 for Mixt-1, Mixt-2 and Mixt-3, respectively. On the other hand, the Zeta-potential (ξ) reported for pure POPC, POPE, and POPG phospholipids is -2.3 ± 2.0 , -32.4 ± 3.4 , and -56.0 ± 2.2 mV, respectively.¹⁶ Interestingly, although POPC and POPE are structurally very similar zwitterionic phospholipids, they were found to exhibit dramatic differences in terms of accessible surface charge.¹⁶ The ξ values determined in neutral water for Mixt-1, Mixt-2 and Mixt-3 were -30 ± 9 , -60 ± 9 and -61 ± 8 mV, respectively (**Figure 4.3.3e**). Although POPC and POPE lipids are zwitterions (**Figure 4.3.2**), Mixt-1 was found to exhibit a moderate negative surface charge at neutral pH. The incorporation of POPG and CL, which contain anionic polar heads (**Figure 4.3.2**), markedly increased the negative- ξ of the liposomes. This behaviour has been attributed to the fact that negatively charged phosphate group is not counter-posed by any other positively charged group, as occurs in the other two tested lipids (i.e. POPC and POPE).¹⁷

Figure 4.3.4 Shows topographic AFM images of SLB obtained from 4:3:1 POPC:POPE:POPG liposomes incubated over mica overnight and diluted in $1 \times$ PBS at 1/5, 1/10 and 1/20 ratios. The highest area covered by the lipid bilayer corresponds to the 1/5 dilution, which was selected for further experiments. The breakthrough force of the lipid bilayer was ~ 0.18 nN and the apparent height 3.4 nm (**Figure 4.3.5**). Clearly, the latter value is underestimated compared with equilibrium thickness of the film. This is related to the fact that in force spectroscopy experiment AFM tip is pushed against the sample surface leading to elastic deformation of the bilayer before breakthrough event. Hence the measured thickness corresponds to elastically deformed bilayer.

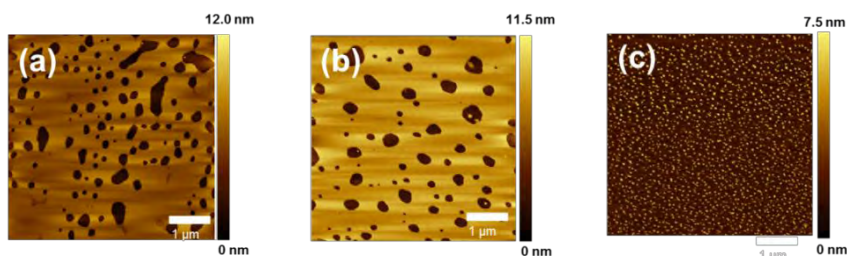


Figure 4.3.4 Topographic AFM images of SLB obtained from 4:3:1 PC:PE:PG liposomes incubated onto mica overnight and diluted in 1x PBS at (a) 1/5, (b) 1/10 and (c) 1/20 ratios.

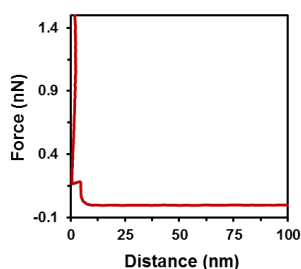


Figure 4.3.5 Force-distance curve-based AFM for SLB obtained from 4:3:1 PC:PE:PG liposomes incubated onto mica overnight and diluted in 1x PBS at 1/5 ratio.

Insertion of Omp2a into lipid bilayers

The protein was inserted into the lipid bilayer by employing two different methods: a) creation of proteoliposomes from detergent-mediated reconstitution of the protein into the preformed liposomes; and b) reconstitution directly incorporating the Omp2a protein into SLBs. The first methodology consists on the following four steps (**Figure 4.3.6**): (1) Liposomes are detergent-destabilized by titration with Triton X-100, a non-ionic surfactant; (2) Destabilized liposomes are mixed with the detergent-solubilized Omp2a; (3) Detergent is removed with BB, resulting in the formation of sealed proteoliposomes; and (4) SLB are formed by promoting the fusion of proteoliposomes onto hydrophilic mica substrate. The second approach only needed three steps (**Figure 4.3.6b**): (1) Spreading of liposomes onto mica substrate; (2) Addition of Triton X-100 to destabilize the lipid bilayer; and (3) Protein insertion onto the membrane. Results obtained from each of such two approaches are described below.

Proteoliposomes from detergent-mediated reconstitution of the protein into liposomes

In order to grasp the effect of protein reconstitution onto liposomes, the first mentioned method was studied at 40, 80 and 100 w/w lipid-to-protein ratios using earlier reported protocols.¹⁸⁻²¹ In general the diameter of the liposomes was slightly affected by protein reconstitution (**Figure 4.3.7a**), whereas ξ decreased progressively upon the incorporation of either protein or protein buffer into the liposome solution (**Figure 4.3.7b**). On the other hand, comparison of the CD spectra recorded for solutions with the free protein and the different lipid-to-proteins suggest that the protein structure undergoes some changes inside the lipid membrane (**Figure 4.3.7c**). However, in all cases the spectra contained the minimum and maximum ellipticity near 220 and -195 nm, respectively, indicating that the β -strand rich motives are maintained within the proteoliposomes.²² Incubation of Omp2a with anionic unilamellar vesicles resulted in the co-sedimentation of a major portion of protein with liposomes after centrifugation, even though some protein was lost during the proteoliposomes purification step, as shown by SDS-PAGE (**Figure 4.3.7d**). The ratio of protein in the pellet/supernatant was 3, 8 and 4.4 for samples coming from 100, 80 and 40 w/w lipid-to-protein ratios, respectively. Accordingly, the 80 w/w lipid-to-protein proportion allowed the most efficient protein retention. Interestingly, the presence of trimers and dimers is higher in proteoliposomes than in solution. Just 2% of the population presented a trimer organization in the Omp2a free solution (band at 110 KDa in **Figure 4.3.7d**), while increasing to 3.4%, 5.8% and 6.2 % in samples coming from 100, 80 and

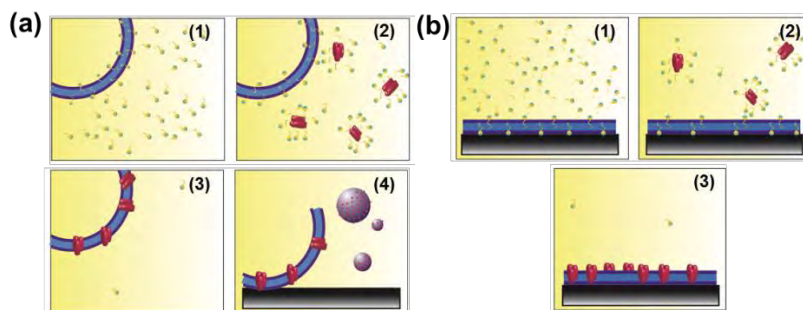


Figure 4.3.6 The protein was inserted on the lipid bilayer using two different methods: (a) Formation of proteoliposomes from preformed liposomes; and (b) Insertion of the Omp2a protein by direct incorporation the Omp2a protein into SLBs.

40 w/w lipid-to-protein ratio. This feature suggests that protein confinement into lipidic membranes enhances their reorganization, bringing them to a state closer to the natural one.

TEM images of blank liposomes (control) and proteoliposomes (**Figure 4.3.7e** and **4.3.7f**, respectively) were obtained following the protocol reported by Opaliński *et al.*²³ Micrographs denoted that the samples had some polydispersity, similar results as obtained with the DLS, the diameters of liposomes and proteoliposomes varied between 100 and 350 nm (**Figure 4.3.7e**) and between 50 and 400 nm (**Figure 4.3.7f**), respectively. The addition of Omp2a to anionic vesicles had some influence on their size and, presumably, shape, which is in full agreement with the results derived from DLS. Proteoliposomes are clearly bigger than control liposomes. In addition, the formers exhibit folds, which may be attributed to the re-organization induced by the protein reconstitution inside the lipid bilayer (*i.e.* sterically-driven re-organization). However, it should be mentioned that such folds could be also due to an artifact induced by the dry-state. Thus, the above mentioned re-organization could result in a weakening of the interactions inside the lipid bilayer and, consequently, cause deformation upon drying of the sample for TEM observation. On the other hand, the integrity of the membranes was found to be intact after conducting the four steps for protein insertion (**Figure 4.3.6a**).

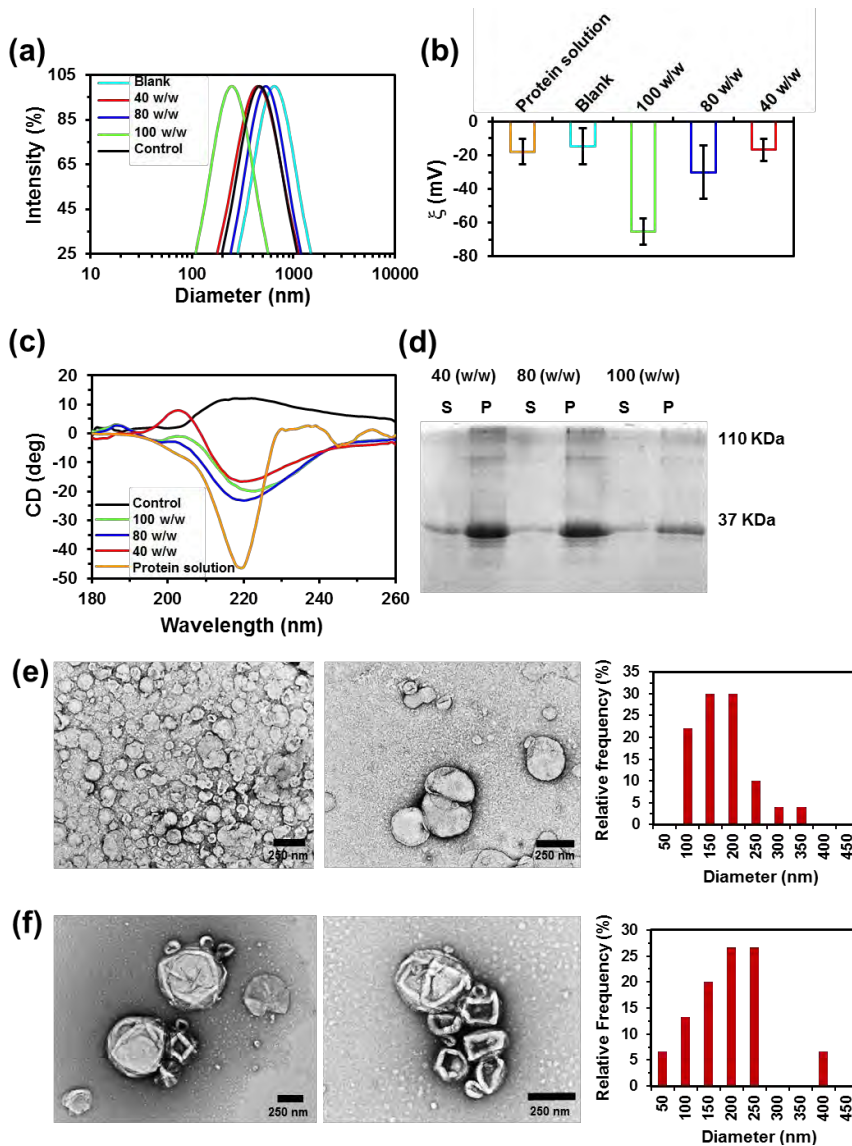


Figure 4.3.7 DLS results expressed in term of (a) intensity vs diameter, (b) ζ values and (c) CD spectra of proteoliposomes prepared from detergent-mediated reconstitution of the protein using 40, 80 and 100 w/w lipid-to-protein ratio, control liposomes (i.e. preformed liposomes), blank liposomes (i.e. preformed liposomes altered by adding the reconstitution detergent medium but without protein) and Omp2a solution. (d) SDS-PAGE gel for the proteoliposomes. TEM micrographs of (e) blank liposomes and (f) proteoliposomes prepared using 80 w/w lipid-to-protein ratio. Histograms showing the diameter distributions are also displayed.

SLBs were obtained by spreading the control liposomes and the proteoliposomes onto mica substrate. Although the most common procedure to obtain SLBs is the Langmuir-Blodgett method, this technique usually becomes far complicated when multicomponent membranes, like those including OMPs, are studied. Instead, vesicle fusion onto a planar hydrophilic solid support is perfectly suitable for such cases. Different theories have been developed to elucidate how these vesicles spread over the hydrophilic surface. One of the most accepted models assumes that the vesicles adsorb on hydrophilic surface, then undergo substrate-induced deformation which causes their rupture on a solid surface.^{24,25} However, the rupture events can be driven by several other factors including fusion between neighbouring vesicles, the high surface density of vesicles, and the presence of active edges of already formed bilayer patches. In this work the SLB formation was performed in the presence of Ca^{2+} , which favours vesicle adsorption onto mica support, especially for those containing negatively charged lipids.²⁶

Figure 4.3.8 displays AFM images of SLB onto mica substrate obtained after spreading the control liposomes and the proteoliposomes. AFM images acquired for the liposomes reflect a homogenous and flat surface (**Figure 4.3.8a**), with an average roughness of $(0.15 \pm 0.01 \text{ nm})$. Representative cross-sectional profiles indicate that the treatment for obtaining proteoliposomes does not cause protrusions in the lipid bilayer. Instead, small protuberances of $\sim 2 \text{ nm}$ in height and $\sim 25 \text{ nm}$ in width appear upon the incorporation of Omp2a (**Figures 4.3.8b-d**). Moreover, AFM images evidence that the amount of protuberances decreases with increasing lipid-to-protein ratio, while the size of the protuberances increases. More specifically, the amount of protuberances decreases $\sim 25\%$ and $\sim 35\%$ when the from the lipid-to-protein ratio increases from 40 w/w to 80 and 100 w/w, respectively. It is worth noting that large aggregates ($\sim 4 \text{ nm}$ in height and $\sim 100 \text{ nm}$ in width) appeared for the highest concentration of protein (**Figure 4.3.8d**), limiting protein nanomechanical studies.

Magnified AFM images provide improved visualization of the protein's shape (**Figures 4.3.8b-d**). More specifically, magnification of the SLB derived from proteoliposomes obtained using 80 w/w lipid-to-protein ratio reflects structures of 1.5-2 nm in height and 10 nm in width, with small cavities in the middle. This condition seems

to be the ideal in terms of protein's reconstitution efficiency and visualization. Therefore, more insights of this condition are shown in **Figure 4.3.9a**, where AFM images of different patches on this surface are displayed. Comparison with the TEM images of the free protein in solution, which are shown in **Figure 4.3.9b**, suggests that such small patches on the membrane correspond to clusters of 5 to 10 monomers laterally associated. A membrane surface screening allowed to separate large protein-detergent aggregates (> 50 nm, dark blue in **Figure 4.3.9d**) from small clusters of proteins (< 50 nm, light blue in **Figure 4.3.9d**). Analysis of the height for the population of small clusters indicates an average value of 2.3 ± 0.5 nm (**Figure 4.3.9d**), which is in accordance with the protein and lipids heights.²⁷

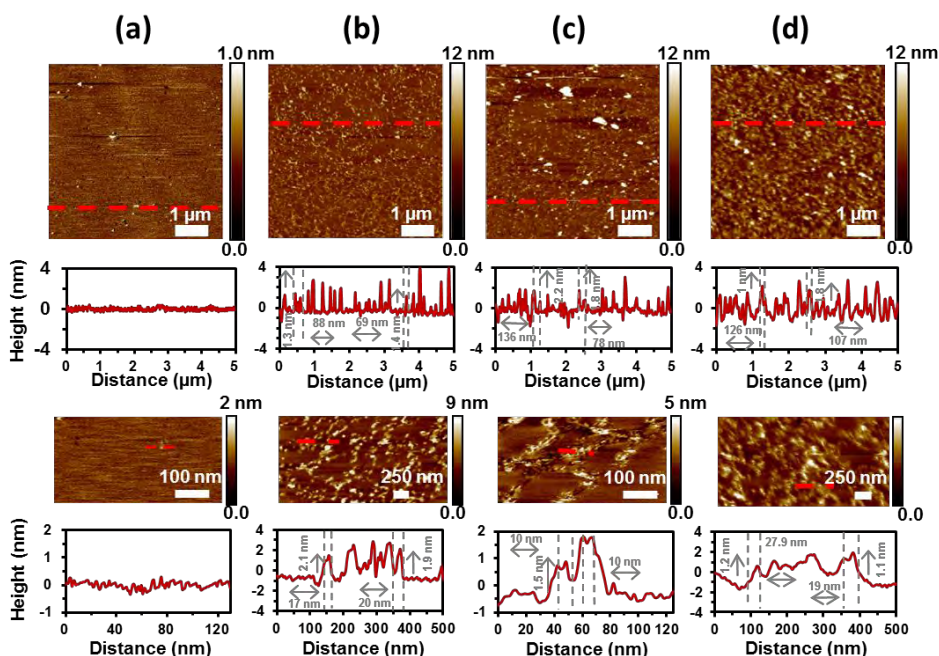


Figure 4.3.8 Topographic AFM images (first row) of SLB obtained from (a) POPC:POPE:POPG (4:3:1) liposomes or from proteoliposomes achieved using (b) 100, (c) 80 and (d) 40 w/w lipid-to-protein ratios spread over mica. Data were recorded on buffer solution (150 mM KCl, 10 mM Tris-HCl, pH 7.8). The red lines in AFM images indicate where from the vertical profile shown below (second row) each image has been extracted. Also, insets of each AFM image and profile are shown below (third and fourth rows, respectively).

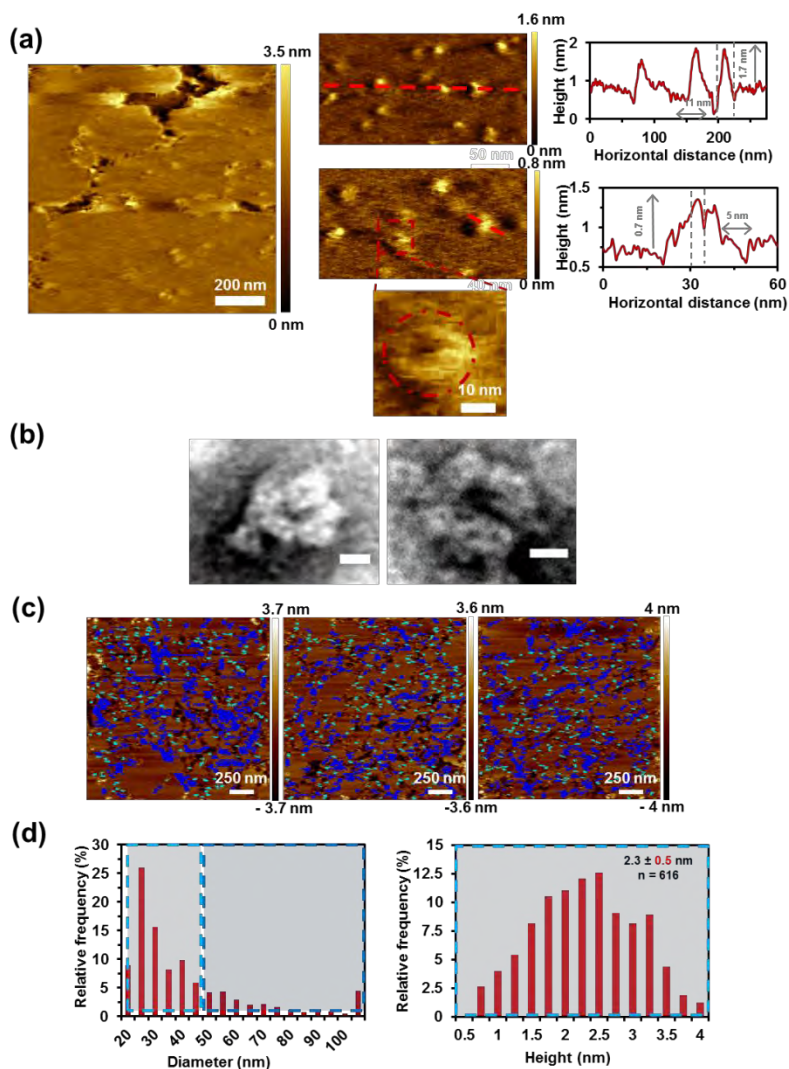


Figure 4-3.9 (a) Representative topographic AFM images of SLB obtained from POPC:POPE:POPG (4:3:1) proteoliposomes (80 w/w lipid-to-protein ratio) spread over mica. The red lines in the AFM images indicate the region used to extract vertical profile shown next to each image. (b) TEM images of Omp2a stained with uranyl acetate (scale bar: 10 nm). (c) Representative topographic AFM images of SLB obtained from POPC:POPE:POPG (4:3:1) proteoliposomes (80 w/w lipid-to-protein ratio) spread over mica. Particle analyses were performed on $2 \times 2 \mu\text{m}^2$ images. Light blue regions indicate particles below 45 nm (protein oligomers) while dark blue spots correspond to particles above 45 nm (protein aggregates). Data were recorded with a buffer solution (150 mM KCl, 10 mM Tris-HCl, pH 7.8). (d) Particle diameter distribution and height distribution of protein oligomers (< 45 nm).

Omp2a reconstitution by direct incorporation into the SLB

The alternative method of incorporation of Omp2a into SLBs, which is schematized in **Figure 4.3.6b**, was followed using AFM analysis at high resolution. The main assumption for this approach was deeply investigated by Milhiet *et al.*,²⁸ and is based on the insertion of proteins into the destabilized SLB after its deposition onto the mica substrate. In a very recent work Sumino *et al.*²⁹ directly attached transmembrane proteins, which were solubilized with an histidine-tag, to a Ni²⁺ coated mica surface. After this, detergent destabilized liposomes were added in order to fill the space between the proteins, achieving an oriented reconstitution.

In this work, SLBs were disrupted by the addition of Triton-X 100 and, afterwards, the protein was incorporated. **Figure 4.3.10** displays topographic AFM images of SLB obtained from POPC:POPE:POPG (4:3:1) liposomes at the three different steps of the reconstitution process. The spread liposomes, where two faces can be visualized, are shown in **Figure 4.3.10a**. After incubation with 0.01% Triton X-100 to destabilize the membrane, noticeable changes were observed (**Figure 4.3.10b**), that is, the surface became flatter and more homogeneous. Finally, the bilayer was further incubated in a protein refolding solution with 10 µg/mL of Omp2a. At this point, large protrusions from the lipid bilayer emerged (**Figure 4.3.10c**). The width and height of such protrusions were 93 and 2.3 nm, as is evidenced by vertical profiles extracted from the AFM images (red lines in **Figure 4.3.10c**). Nevertheless, no single units of protein were detected. Instead the bilayer was broken in many sites and agglomerates of protein were found. This was attributed to the fact that the concentration of Omp2a used in this process was too high. In addition, previous studies suggested that lipid bilayers could be destabilized by the detergent used in the refolding solution.³⁰

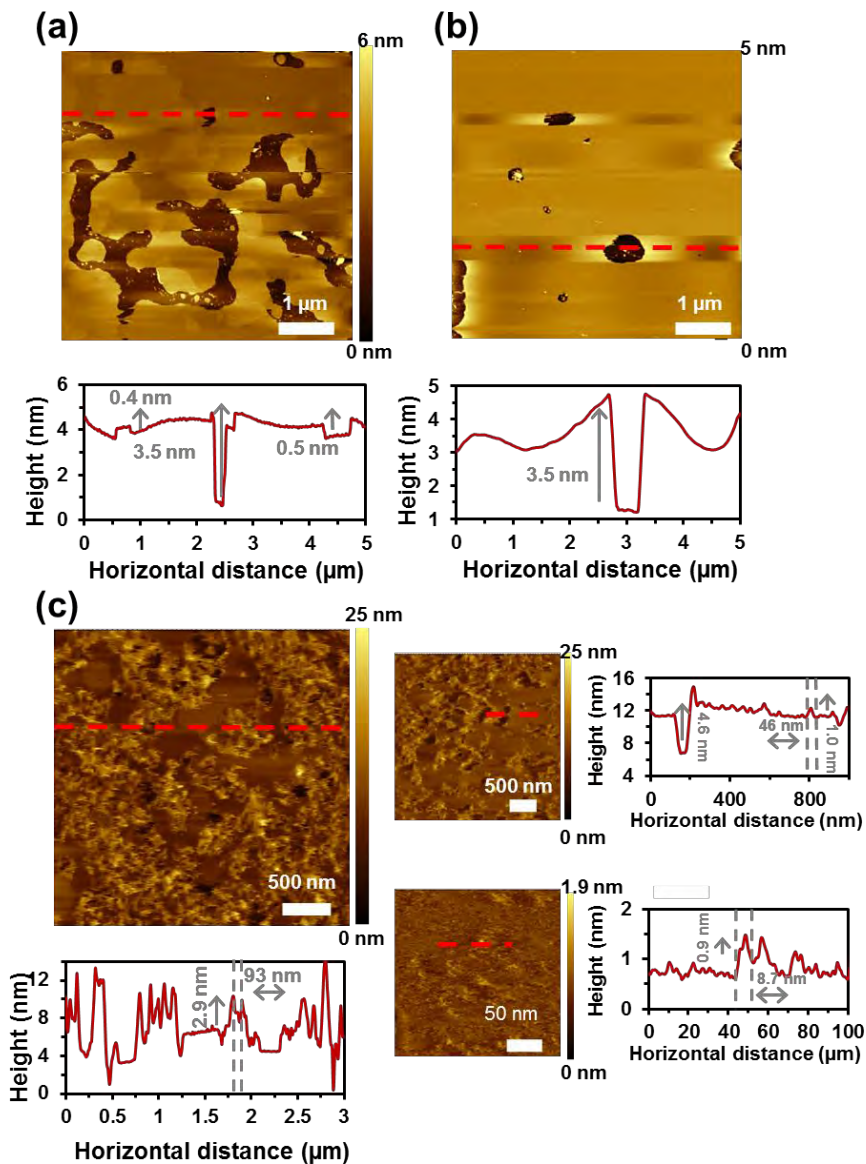


Figure 4.3.10 Topographic AFM images of: (a) SLB obtained from POPC:POPE:POPG (4:3:1) liposomes, (b) after being incubated with 0.01 %Triton X-100, and (c) further incubated in a refolding solution with 10 µg/mL of Omp2a. Data were recorded on buffer solution (150 mM KCl, 10 mM Tris-HCl, pH 7.8). The red lines in the AFM images (a-c) indicate where from the vertical profiles shown below have been extracted.

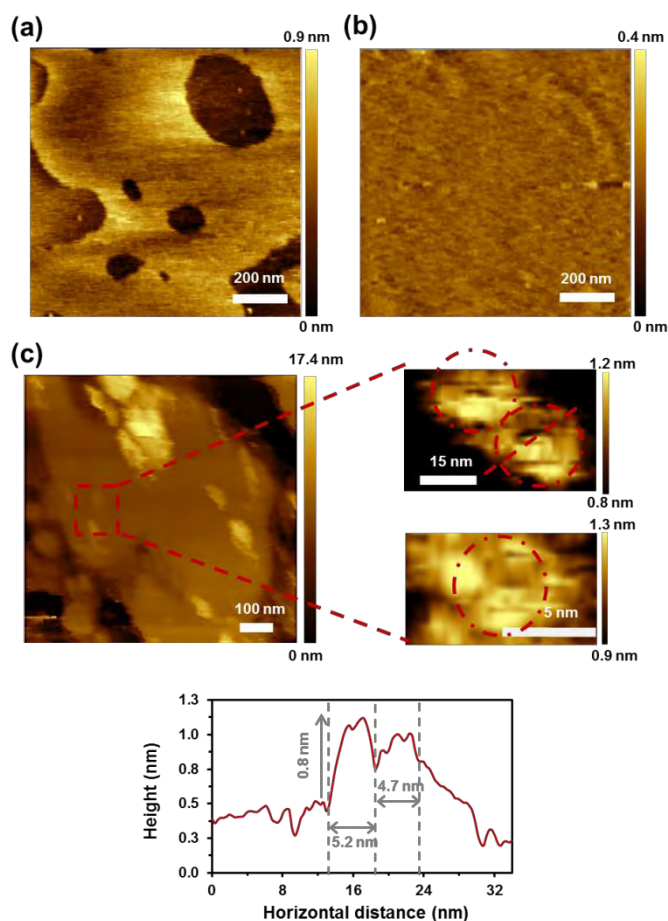


Figure 4.3.11 Topographic AFM images of: (a) SLB obtained from POPC:POPE:POPG (4:3:1) liposomes, (b) after being incubated with 0.01 %Triton X-100, and (c) further incubated in a refolding solution with 2 $\mu\text{g}/\text{mL}$ of Omp2a. Data were recorded with the buffer solution (150 mM KCl, 10 mM Tris-HCl, pH 7.8). The red square shows where the inset has been obtained from. The red line in the AFM image indicates (c) where from the vertical profile shown below has been extracted. Red circles correspond to protein agglomerates.

In order to overcome the limitation associated to the protein concentration, the latter was reduced. As occurred above, the surface of spread liposomes (**Figure 4.3.11a**) became flatter and more homogeneous after incubation with 0.01% Triton X-100 (**Figure 4.3.11b**). After incubation in a 2 $\mu\text{g}/\text{mL}$ Omp2a refolding solution, some breakages and agglomerates were also visualized (**Figure 4.3.11c**), even though at such low concentration single protein's shape could be identified when higher contrasts were

used. The recognized protein was around 10 nm wide and 1.5 nm height, showing a deeper part in the middle, as it was expected.

In summary, although high resolution images of the proteins reconstituted into the lipid bilayer were obtained, this strategy is limited by the adverse effects caused by the detergent used for the refolding procedure. Thus, the lipid bilayer is still disrupted when the protein concentration is reduced from 10 to 2 $\mu\text{g/mL}$. Due to this drawback, the strategy based on detergent-mediated reconstitution of the protein into liposomes (**Figure 4.3.6a**) was used to insert the Omp2a into the lipid bilayer for both nanomechanical and functional studies. Specifically, this methodology allows a higher control of the process, as is proved by the fact that the substrate surface is homogeneously coated by the lipid bilayer and a homogeneous protein distribution into the bilayer is observed.

Nanomechanical properties of Omp2-containing SLBs prepared using preformed liposomes

Lateral organization of lipid, carbohydrates and proteins found in biological membranes is involved in many cellular events, for example signal transduction or membrane fusion.³¹ Furthermore, structural, physical and chemical properties of biomacromolecules can control their activity at different length-scales. In particular, nanomechanical properties can affect some biological functions of proteins in processes such as cell signalling, membrane signal transduction and immune responses.³²⁻³⁴ For example, antibodies need high flexibility to bind to diversified antigens.³⁴ Accordingly, deep-end studies on how proteins modify the consistency of lipid bilayers and how soft proteins are in comparison with the hosting lipid bilayers are not only attractive but also very relevant from a biotechnological point of view. Due to recent advances in AFM technologies, it is currently possible to measure mechanical properties of single molecules in physiological conditions. Thus, force-distance (FD) curves, which are directly obtained from cantilever's deflection, can be collected at the same time as the AFM images are acquired. For each pixel of the topographic image, the AFM records FD curves with Ångstrom precision and piconewton sensitivity. More specifically, interaction forces between the AFM stylus and the biological sample surface are mapped pixel-by-

pixel, enabling quantification of the elastic modulus, adhesion forces and deformation of the sample simultaneously.³⁵ In this work, the elasticity has been extracted using the Derjaguin-Muller-Toporov (DMT) model,³⁶ whereas the adhesion force has been acquired from the vertical difference of the minimum force during retraction and the zero-force. Lipid bilayers were examined using a soft cantilever (nominal spring constant $k_s = 0.7$ N/m) with the set point adjusted to get minimum sample deformation.

Figure 4.3.12a shows a $2 \times 2 \mu\text{m}^2$ topographic image of Omp2a molecules embedded on the lipid membrane over a mica substrate, which was obtained in the peak force QNM tapping mode. The peak force set point was adjusted to a force of 544 pN. For analysis, a cross-sectional profile of $2 \mu\text{m}$ length (dashed red line) is plotted next to the AFM windows. The DMT modulus map (**Figure 4.3.12a**) reflects the presence of two domains with different constant elasticities, corresponding to the lipid bilayer surface and to the Omp2a molecules. **Figure 4.3.12b** includes the profile of elasticity fitted with the DMT modulus. The mean DMT modulus obtained for the lipid bilayer and Omp2a are 19 MPa and 10.5 ± 1.7 MPa, respectively, the latter being obtained by selecting aggregates smaller than 40 nm. These results are consistent with high resolution topographic AFM studies on OmpG reconstituted into native *E. coli* lipids that evidenced that the OMP is softer than the lipid bilayer,^{35,37} even though no quantitative estimation of the elastic modulus was provided. However, studies on other related proteins (*i.e.* bacteriorhodopsin and multiprotein complexes contained in erythrocyte membrane) using quantitative mechanical AFM mapping^{38,39} and micro-second force spectroscopy⁴⁰ probed that the stiffness of MPs depends on the environment (*e.g.* electrolyte identity and concentration, pH and substrate), ranging from a few MPa to tens of MPa. Similarly, the reported moduli of lipid bilayers ranged from ~ 10 to ~ 500 MPa depending on the chemical identity and environment.^{41,42} However, the modulus of elasticity of ~ 18 MPa was recently reported for the liquid disordered phase of mica-supported bilayer composed of lipids extracted from *E. coli*.⁴³ Moreover, the modulus of polymeric FSNMs was reported to increase from ~ 25 to ~ 35 MPa with the thickness (*i.e.* from 10-20 nm to ~ 80 nm).⁴⁴

Figure 4.3.12c displays, in one hand, the adhesion map, as obtained from the FD curves recorded in each pixel, and, in the other hand, both the profile and histogram of the difference between lipid bilayer and protein adhesion. It should be noted that the DMT model used in this work is appropriated for weak adhesive forces and tips with a small curvature radius.⁴⁵ The adhesion force of the SLB was around 200 pN, while that of Omp2a was 161.9 ± 9 pN. Lipids therefore adhered more to the AFM tip than the protein, which should be attributed to the asymmetric distributions of van der Waals forces. Consequently, the tip forms stronger interactions with the flat surface of lipids than with the curved surface of Omp2a, the latter providing less contact area.⁴⁶ It is worth noting that the adhesion forces determined for the lipid bilayer and the OMP are one order of magnitude smaller than those reported for polymeric FsNMs.¹⁷ More specifically, the adhesion force of polymeric FsNMs were found to be comprised between 5 and 7 nN.⁴⁴

Two phases are also observed in the representative deformation map displayed in **Figure 4.3.12d**. Indeed, the corresponding profile and histogram provided deformation values of ~ 1 nm and 4.6 ± 0.7 nm for the SLB and Omp2a, respectively. These results prove that mechanical properties such as the elasticity or deformation can be imaged at high resolution. Strikingly, the contour of single molecules becomes apparent when their mechanical properties are studied, even though their recognition becomes easier when height images are also considered. Similar analyses were performed for the control SLBs (*i.e.* liposomes treated like the proteoliposomes) onto mica substrate (**Figure 4.3.13**). Results corroborated that nanofeatures previously described were due to the protein reconstitution. Thus, no small protrusion was observed in **Figure 4.3.13** and, in addition, no significant changes in the DMT modulus, adhesion and deformation were detected when comparing values obtained for SLBs with and without protein.

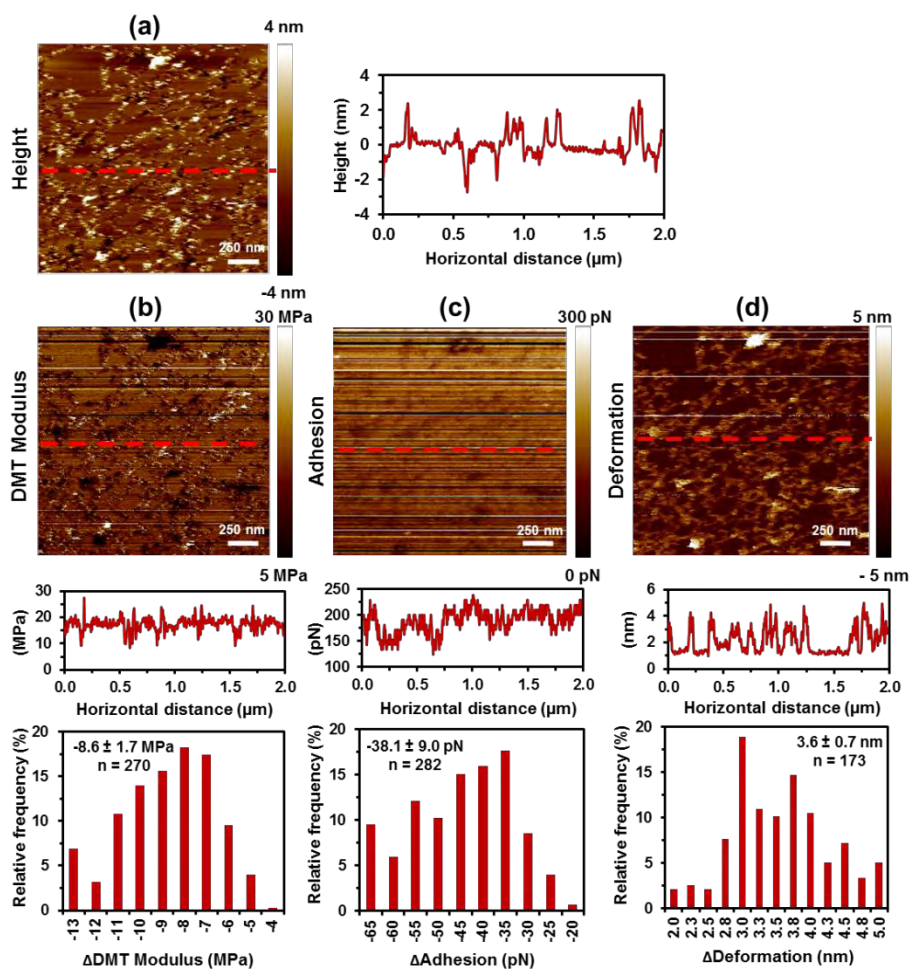


Figure 4.3.12 FD-based AFM images of POPC:POPE:POPG (4:3:1) proteoliposomes (80 w/w lipid-to-protein ratio) spread onto mica: (a) topography, (b) DMT modulus map, (c) adhesion map and (d) deformation map. Data were recorded with the buffer solution (150 mM KCl, 10 mM Tris-HCl, pH 7.8). The red lines in the AFM images (a-d) indicate where from the vertical profile shown below or next to each image has been extracted. The histograms below the profiles express the percentage of particles below 45 nm in diameter (protein oligomers) *vs* the difference in the indicated parameter with respect to lipid bilayer values.

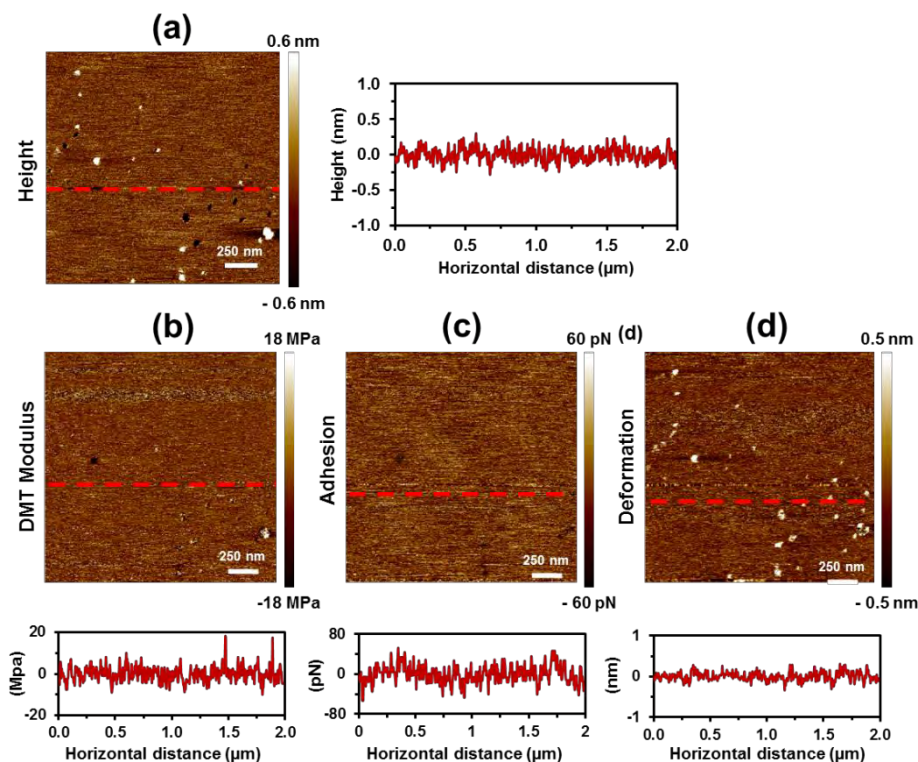


Figure 4.3.13 FD-based AFM images of PC:PE:PG (4:3:1) liposomes spread over mica: (a) topography, (b) DMT modulus map, (c) adhesion map, and (d) deformation map. Data were recorded on buffer solution (150 mM KCl, 10 mM Tris-HCl, pH 7.8). The red lines in the AFM images (a-d) indicate where the vertical profile shown below or next to each image has been extracted.

Overall, comparison of the results obtained in this section with those reported for polymeric NMs⁴⁴ indicates that immobilization of OMPs inside the nanopores of polymer-based FsNMs offers advantages over the lipid bilayer-based approaches. Indeed, although synthetic lipid bilayers, like those studied in this work, are more stable than pure biological membranes, their mechanical strength is lower than that of polymeric NMs. The fragility of lipid bilayers may be a handicap for practical applications, while the mechanical flexibility and resistance of polymeric FsNM were reported to be enough for this purpose. Thus, in many practical applications, as for example those related with molecular filtration, nanofluidics and nanodetection, stable

FsNMs are needed to sustain mechanical stress during the fabrication and operation processes.

Electrochemical detection of Omp2a in proteoliposomes

Electrochemical methods are widely accepted to detect residues with redox properties in proteins, such as tyrosine (Tyr) and tryptophan (Trp).^{47,48} Among the different electrochemical strategies (*e.g.* sweep voltammetry and cyclic voltammetry), SWV stands out since high peak resolution is obtained with very low peptide and protein concentrations after correcting with an efficient base line.⁴⁹ In addition, the usage of electrochemical method has the advantage that proteins can be easily adsorbed on many surfaces facilitating the preparation of protein-modified electrodes.⁵⁰

It is well-known that the peak potential of Tyr and Trp depend on the buffer. Thus, Vacek *et al.*⁵¹ showed that pH plays a key role on the peak potential, which shifts towards less positive values with increasing pH. Furthermore, analysis of the peak potential shifts at a given buffer conditions allows to discriminate between native and denatured forms of proteins.⁵⁷ Omp2a contains 22 Tyr and 10 Trp residues which are mainly located in the external part of the barrel on the folded protein. Therefore, in proteoliposomes are expected to be at the interface between the lipid bilayer and the medium if the protein remains stable. In order to prove the stability of the protein native form in the proteoliposomes, characterization of the Omp2a Tyr and Trp residues has been performed by applying the label-free and sensitive SWV methodology. Specifically, the response of the protein when it is alone (control of the native form) and embedded into the lipid bilayer has been compared.

Three negative controls were analysed: bare GCE, GCE covered by MPD-containing refolding buffer (GCE+MPD), and GCE covered by the spread liposomes (GCE+liposomes). As it can be seen in **Figure 4.3.14**, none of the mentioned samples gave rise to any substantial peak. Instead, when the protein was adsorbed with the refolding buffer two peaks can be visualized. These correspond to the oxidation peaks of Tyr and Trp (+0.45 V and +0.62 V, respectively). The peak current density is much higher for the first than for second, which is fully consistent with the larger quantity of Tyr than Trp in the Omp2a sequence. In contrast, a single less intense peak at +0.5 V was

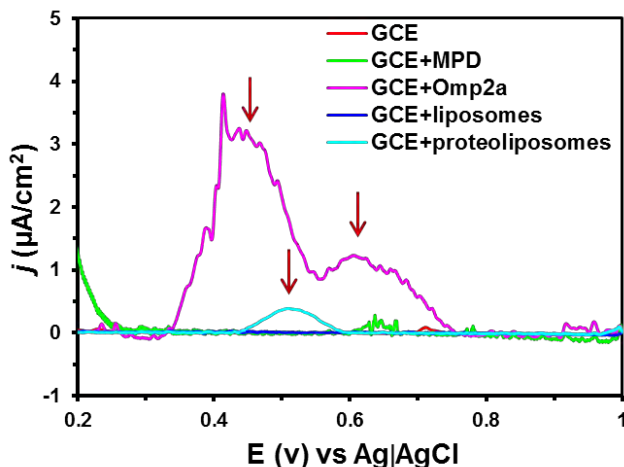


Figure 4.3.14 Voltammograms of SWV obtained for bare GCE and GCE covered by refolding buffer (GCE+MPD), spread liposomes (GCE+liposomes) and spread proteoliposomes (GCE+proteoliposomes).

found when proteoliposomes were spread onto the glassy carbon surface. This is correlated with the lower protein presence on the proteoliposomes since there is not a complete protein loading and, therefore, the monitoring of the Trp signal becomes more difficult.

Functionality of Omp2a in SLBs

The chemical environment is critical to maintain the biological functionality of OMPs. Hence, biological nanopores offer precise control over ion selectivity rectification and gating as well as outstanding permeability. Molecular recognition is the hallmark of biological interactions to enable these functions, especially the ion selectivity, so that embedded biochannels often lose their activity upon leaving the biological environment. Several strategies have been studied to transfer properties of naturally occurring nanopores to supported polymeric NMs. For example, incorporation of lipid bilayer onto supported NM⁵²⁻⁵⁴ and functionalization of the nanopores surfaces through ligands⁵⁵⁻⁵⁸ are considered as the most reliable ones. Nevertheless, the utilization of supported NMs drastically limits the practical application of the device and, unfortunately, functionalization of nanopores surfaces in polymeric FsNMs is not an easy task. In order

to engineer new strategies for the fabrication of more effective bioinspired FsNMs, this section is devoted to study the functionality of Omp2a-immobilized inside SLB, and its comparison to the results for Omp2a-based PLA FsNMs will be reported in Chapter 5.⁷

The EIS method has been employed to measure the current through electrodes covered by the systems investigated in this study. This technique exploits the fact that lipid bilayers are electrically resistant and behave as insulators, monitoring the membrane conductance related to the transport of ions. In this work, the electrode used for the functional characterization is indium tin oxide (ITO) supported on glass, which is a suitable substrate for the characterization of lipid bilayer membranes and does not induce protein denaturation.⁵⁹⁻⁶² The complex EIS signal has been related to the electrical properties of each component of the system (*i.e.* the electrode, the lipid bilayer with or without protein, and the electrolyte, KCl), representing them as electrical elements on an EEC. Each element contributes at different frequency regime enabling the separation of the effects of the components at the interface. The quality of the fitting between the experimental data and the ECC has been proved by the evaluating the percentage error associated to each circuit element, which is lower than 10% in all cases.

Consistently with previous works, the EEC (**Figure 4.3.15a**) obtained for bare ITO electrodes shows the electrolyte resistance (R_s) connected in series with the constant phase element (CPE) of the double layer semiconductor/electrolyte interface, (Q_{dl}). Here, lipid bilayer-coated electrodes behave as a circuit in which the R_s is followed by the lipid membrane CPE element (Q_M) in parallel with the membrane resistance (R_M) and the semiconductor/electrolyte interface Q_{dl} element, which arises from lipid bilayer defects (*i.e.* lipid bilayers are dynamic in nature and, therefore, the apparition of changing defects and holes is expected to be relatively frequent). Moreover, this EEC is not altered by the incorporation of Omp2a inside the bilayer (**Figure 4.3.15a**).

Figure 4.3.15b displays the Nyquist plots recorded for the bare ITO substrate and four different lipid bilayers (*i.e.* lipid bilayers using 40, 80 and 100 w/w lipid-to-protein ratio and lipid bilayer without protein) using 0.1 M KCl aqueous solution. All four bilayers display curves with one semicircle in the high frequency range, and a straight ascending line in the low frequency range. The starting point of the curve indicates R_s , while the diameter of the semicircle corresponds to the charge-transfer resistance, R_M .

Besides, the conductivity calculated for each system is represented in **Figure 4.3.15c**. The membrane conductivity (σ , in S/cm) has been determined using the following expression:

$$\sigma = \frac{L}{R_M A} \quad (\text{Eq. 4.3.3})$$

where L is the thickness of the membrane (5.5×10^{-7} cm), A is the area of the electrode (0.5 cm²), and R_M is the membrane resistance. As expected, the membrane conductivity increases as a function of the protein concentration on the lipid bilayer, being significantly higher for the 40 w/w lipid-to-protein ratio.

Figure 4.3.15d displays the Bode plots obtained for each condition, where both the difference of logarithmic impedance *vs* the logarithm of frequency ($\log f$, where f is expressed in Hz) and the change in phase angle *vs* the logarithm of frequency are represented. Bare ITO shows a steady increase of the impedance signal $\log f$ below 3, the same being observed in the difference of phase angle. Instead, when the electrode was covered by the lipid bilayer (with/without protein) a well-defined shoulder appeared at the $\log f$ regime of 1-3. This is related to the resistance and constant phase element (Q_M) induced by the presence of the lipid bilayer.

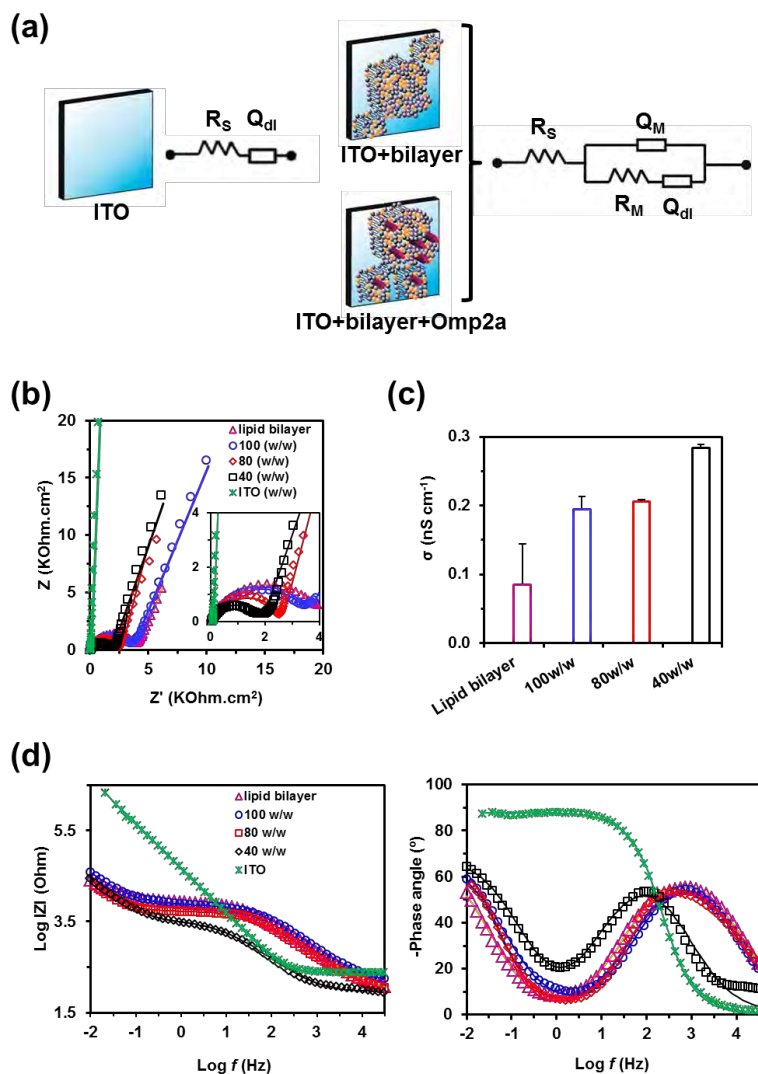


Figure 4.3.15 (a) Schemes representing the ITO, the lipid bilayer and the lipid bilayer containing Omp2a with the corresponding EEC used for fitting the experimental data from EIS measurements: R_s is the electrolyte resistance; Q_M and R_M are the membrane constant phase element and resistance, respectively; and Q_{dl} is the double layer constant phase element for the electrode surface. (b) Nyquist plots of ITO (green stars), lipid bilayer (purple triangles), lipid bilayer with the reconstituted protein at 100 (blue circles), 80 (red diamonds) and 40 w/w (black squares) lipid-to-protein ratio in 0.1 M KCl. Symbols correspond to experimental data, while lines are the fitted curves according to EEC. (c) Average conductivity measured for the lipid bilayer and those containing the protein at different lipid-to-protein ratios. (d) Bode plots of the systems described in (b).

The resistance obtained for the lipid bilayer alone ($4.2 \text{ K}\Omega\cdot\text{cm}^2$) (**Table 4.3.1**), is close to that reported for single component 1,2-dimyristoyl-sn-glycero-3-phosphocholine bilayer,⁶³ and is significantly higher than what was obtained for supported PPy membranes ($821 \text{ }\Omega\cdot\text{cm}^2$).⁶⁴ According to these results, ion diffusion decreases as follows: supported PPy > SLB. This relative order can be explained considering PPy is a conducting polymer, which facilitates the electron transfer to the electrode surface. As expected, the reduction in the resistance of each Omp2a-containing system with respect to its corresponding non-functionalized analog evidences that the incorporation of the porin channel enhances ion diffusion in all cases.

The resistance values obtained in this work for lipid bilayers are smaller than those previously reported in literature (*i.e.* $> 80 \text{ K}\Omega\cdot\text{cm}^2$).² This observation could be attributed to one of the following two reasons or to the combination of both. First, the ion concentration used in this work (*i.e.* 0.1 M KCl), which was chosen for consistency with our previous studies on Omp2a-based PPy bioinspired NMs,⁶⁴ is one order of magnitude higher than the one typically used. It is worth noting that when higher is the electrolyte concentration, lower is the membrane resistance.³ Also, the presence of defects in the bilayer and the consequent reduction in the packing density of the immobilized lipids can explain the low resistances determined in this work, in comparison with those obtained in other studies.² Thus, such imperfections could be due to the difficulty of completely covering the ITO surface with the lipid bilayer.

Table 4.3.1 R and CPE (a) for each sample, analyzed in KCl 0.1 M solution, obtained from fitting parameter with the EECs displayed in **Figure 4.3.15a**. The percentage error associated to each circuit element is included in parentheses.

	R_s ($\Omega \cdot \text{cm}^2$)	Q_M ($\text{F} \cdot \text{cm}^2 \cdot \text{s}^{n-1}$)	n	R_M ($\text{k}\Omega \cdot \text{cm}^2$)	Q_{dl} ($\text{F} \cdot \text{cm}^2 \cdot \text{s}^{n-1}$)	n
ITO	120.9 (0.6)	-	0.9 (0.5)	-	$6.9 \cdot 10^{-6}$ (0.1)	-
Lipid bilayer	44.7 (0.5)	$5.2 \cdot 10^{-6}$ (1.2)	0.7 (0.2)	4.2 (0.4)	$7.8 \cdot 10^{-4}$ (1.0)	0.8 (0.6)
Omp2a in SLB (100 w/w)	75.5 (3.3)	$4.2 \cdot 10^{-6}$ (1.2)	0.7 (1.2)	3.7 (1.9)	$4.5 \cdot 10^{-4}$ (3.4)	0.8 (1.9)
Omp2a in SLB (80 w/w)	43.8 (2.4)	$6.0 \cdot 10^{-5}$ (5.9)	0.7 (0.9)	2.7 (3.7)	$1.0 \cdot 10^{-3}$ (3.7)	0.8 (1.8)
Omp2a in SLB (40 w/w)	44.4 (2.2)	$3.2 \cdot 10^{-5}$ (8.1)	0.8 (1.6)	1.5 (3.8)	$6.3 \cdot 10^{-4}$ (3.6)	0.8 (2.2)

- a) The CPE impedances have been expressed as: $Z_{CPE} = [Q (j\omega)^n]^{-1}$. CPEs represent a capacitor and a resistor for $n=1$ and $n=0$, respectively, while it is associated with a diffusion process when $n=0.5$.

4.3.3 Conclusions

The nanomechanical properties and functionality of Omp2a reconstituted into SLBs have been evaluated and compared with those of bioinspired Omp2a-polymeric NMs. Among the three tested lipid compositions, bilayers made of 4:3:1 POPC:POPE:POPG have been found to be the most homogenous and consistent. Besides, reconstitution of the OMP into preformed liposomes using detergent as mediator has allowed obtaining homogenous and reproducible surfaces. The estimated average DMT moduli, adhesion force and deformation of Omp2a is 10.5 ± 1.7 MPa, 161.9 ± 9 pN and 4.6 ± 0.7 nm, respectively. These values are clearly distinguishable from the ones determined for the lipid bilayer, reflecting the satisfactory incorporation of the OMP. The low stiffness of Omp2a and its high deformability compared with the dimensions of the molecule (nominal height: 7 nm) reflect a high molecular flexibility. This key property, which is related to the conformational adaptability of the protein, could be responsible of an

essential aspect of Omp2a biological functionality: it allows the passage of a number of molecules with varying sizes and shapes to ensure the nutrition of the bacteria. On the other hand, the ion affinity significantly increases with the protein concentration used in the proteoliposomes reconstitution, a reduction of ~78% being observed between the control and the lowest lipid-to-protein ratio.

In summary, the reconstitution of OMPs into lipid bilayers provides platforms that fulfil both the nanometric dimensional requisite for truly mimicking biological attributes, and the conditions necessary for exploring their properties. In spite of these advantages, the properties Omp2a-based SLBs are less suitable for technological applications than those of polymeric FSNMs.

4.4 Thermomechanical response of Omp2a for biomimetics

Recently, there has been a paradigmatic shift in the experimental study of materials with applications in biomedicine: new methods have been developed to study phenomena associated to single molecules and their small supramolecular / nanostructured aggregates when embedded within complex platforms with functional interfaces for clinical applications. In particular, micro- and nano-sized mechanical techniques based on the principle that variations in electrostatic, van der Waals and steric intermolecular interactions on the surface of functionalized cantilever cause bending (deflection) of a few nanometers, are playing a fundamental role.⁶⁵ The combination of these miniaturized mechanical systems with electrical and, especially, optical displacement sensors has been applied for, among others, chemisorption measurements in air at room temperature with up to yoctogram (10^{-24} g) resolution,^{66,67} drug screening,^{68,69} characterization of the thermomechanical response and the glass transition temperatures of macromolecular ultra-thin films,^{70,71} detection of DNA strands,⁷² observation of the hydration-dehydration (swelling-deswelling) of molecular systems,⁷³⁻⁷⁵ and identification of biological species through their molecular mass and stiffness improving the capabilities of conventional mass spectrometers.^{76,77}

In this study, we investigated the organization of β -barrel OMPs in synthetic environments as a function of the temperature, thereby applying microcantilever deflection technologies to hierarchical structured Omp2a (367 residues, 39 kDa). The interpretation of these measurements has been carried out with the aid of the results obtained using other techniques, such as FTIR spectroscopy, circular dichroism (CD), dynamic light scattering (DLS), wide angle X-ray diffraction (WAXD), X-ray photoelectron spectroscopy (XPS) and atomic force microscopy (AFM). The distinctive thermal transitions identified for Omp2a, which compare with those observed for conventional proteins such as lysozyme (LYS; 129 residues, 14.4 kDa) and bovine serum albumin (BSA; 583 residues, 66.5 kDa), have been unraveled and their consequences and effects analyzed.

4.4.1 Methods

Materials: Octosensis Microcantilever-Arrays (chips with eight mono crystalline Si cantilevers, 500 μm in length) were obtained from Micromotive GmbH (Mainz, Germany). The following chemicals were purchased from Sigma-Aldrich and used as received without further purification: isopropanol, (3-glycidyloxypropyl)trimethoxysilane (98%), toluene (99.8%), $\text{N}^\alpha, \text{N}^\alpha$ -bis(carboxymethyl)-L-lysine hydrate (NTA- NH_2) (97%), 1-[(3-dimethylamino)propyl]-3-ethylcarbodiimide methiodide (EDC), N-hydroxysuccinimide (NHS), 2-(N-morpholino)ethanesulfonic acid (MES), 2-amino-2-(hydroxymethyl)-1,3-propanediol (Tris base), carbonate/bicarbonate buffer, phosphate buffered saline (PBS, pH7.4) Sodium chloride was purchased from Panreac (Spain). Bovine serum albumin (BSA, fraction V) and lysozyme (LYS) were purchased from BioLabs (England) and Fluka, respectively. The Omp2a protein was expressed, purified, and refolded using a previously reported procedure.^{78,79}

Fourier-transform infrared (FTIR) spectroscopy: FTIR spectra of BSA, LYS and Omp2a were recorded on a FTIR 4100 Jasco spectrophotometer. The samples were placed in an attenuated total reflection accessory with thermal control and a diamond crystal (Specac model MKII Golden Gate Heated Single Reflection Diamond ATR). For

each sample 46 scans were performed with a resolution of 2 cm⁻¹. Spectra were recorded at 30 °C and 100 °C.

FTIR spectroscopy was used to examine the secondary structure of the proteins. Specifically, the number and position of the peaks in the Amide I region, which were derived from the second derivative and deconvoluted spectra, provided information about the protein conformation. Fourier self-deconvolution was performed with the software PeakFit 4 (Jandel Scientific Software, AISN Software Inc.), the resulting profiles being fitted to Gaussian functions through the OriginPro 7.5 software.

Circular dichroism (CD): CD measurements of BSA and LYS were performed using a 1× commercial Dulbecco's PBS from Gibco with a protein concentration of 0.01 mg/mL, whereas a sodium dodecyl sulfate (SDS) – 2-methyl-2,4-pentanediol (MPD) buffer (60 mM SDS, 1.5 M MPD, 400 mM NaCl, 50 mM Tris-HCl pH 8) with a protein concentration of 0.005 mg/mL was used for Omp2a. It should be noted that the different buffer selection is due to the fact that the Omp2a structure is protected by amphiphilic SDS–MDP detergents.^{22,23} Spectra were recorded between 190 and 250 nm using a Chirascan-plus φ CD spectrometer (Applied Photophysics, APL; UK) equipped with a temperature-controlled cell. Spectra were obtained using heating (from 5 °C to 90 °C) and cooling (from 90 °C to 5 °C) runs stopping every 5 °C for 5 minutes with a heating rate of 5 °C/min. Machine settings were as follows: 1 nm bandwidth, 1 s response, 0.5 nm data pitch, 100 nm/min scan speed and cell length of 10 mm. All CD spectra presented in this work correspond to the average from three independent measurements. Spectra were deconvoluted using the CDSSTR method of the DichroWeb server.⁸⁰

Dynamic light scattering (DLS): The influence of the temperature in the shape and aggregation of BSA, LYS and Omp2a was studied by DLS following the variation of the particle effective diameter (D_{eff}) when the temperature increases from 20 to 60 °C. Proteins were dissolved in the buffers described above for CD measurement using the same concentrations. Measurements were performed using a NanoBrook Omni Zeta Potential Analyzer from Brookhaven Instruments Corporation. D_{eff} values correspond to

average values of the corresponding particle size distributions, which were determined in steps of 10 °C (heating/cooling rate 10 °C/min) stopping for 2 minutes before the measurement.

Wide angle X-ray diffraction (WAXD): Time resolved WAXD experiments were carried out at the NCD beamline (BL-11) of the Alba synchrotron radiation light facility of Cerdanyola del Vallès (Catalunya). The beam was monochromatized to a wavelength of 1.5406 Å. Samples were confined between Kapton films and then held in a Linkam hot stage with temperature control within ± 0.1 °C. WAXD profiles were acquired during heating and cooling runs in time frames of 7.5 s and a rate of 4 °C/min. The WAXD detector was calibrated with diffractions of a standard of a Cr₂O₃ sample. The diffraction profiles were normalized to the beam intensity and corrected considering the empty sample background. Deconvolution of WAXD peaks was performed with the PeakFit v4 program by Jandel Scientific Software using a mathematical function known as “Gaussian area”.

Functionalization of silicon microcantilever chips: The functionalization protocol, which was applied to silicon microcantilever chips previously hydroxylated at the surface with a H₂O₂:H₂SO₄ (3:1 v/v) mixture, consisted of four steps:

- (i) *Silanization.* Hydroxylated microcantilevers were silanized with 0.2 % of (3-glycidyloxypropyl)trimethoxysilane in dry toluene overnight at room temperature under nitrogen atmosphere. Afterwards, samples were washed with toluene and milli-Q water.
- (ii) *Carboxylation.* Silanized microcantilevers were incubated into 100 mM N^α,N^α-bis(carboxymethyl)-L-lysine hydrate (NTA-NH₂) solution in 50 mM carbonate buffer (pH 9.5) overnight, at room temperature, and under gentle agitation. After this, carboxylated substrates were washed with 50 mM carbonate buffer (pH 9.5) and milli-Q water.
- (iii) *Activation.* The carboxyl groups arising from NTA-NH₂ at the microcantilever surface were activated for direct reaction with primary amines via amide bond formation with a mixture of 100 mM EDC and 150 mM NHS, both dissolved in 10

mM MES (pH5.5). Samples were incubated for 30 min at 37 °C under gentle agitation and, then, extensively rinsed with 10mM MES (pH5.5).

(iv) *Protein immobilization.* A solution of 0.1 mg/mL of protein (BSA, LYS or Omp2a) was prepared in 10mM MES (pH 5.5). The cantilevers were incubated for 2 h at 37°C. After that, samples were washed with 10 mM MES (pH 5.5) and incubated for 45 minutes at 37 °C with 1×PBS with 0.3 M NaCl to desorb proteins not covalently bonded to the surface.

X-ray photoelectron spectroscopy (XPS): XPS was used to analyze the chemical composition at the surface of silicon substrates. The system (SPECS Surface Nano Analysis GmbH, Berlin, Germany) was equipped with a non-monochromatic twin anode X-ray source XR50 of Mg/Al (1253 eV/1487 eV). Specifically, the Al anode was operated at 150 W. Detector pass energy was set at 25 eV and 0.1 eV for the survey and the narrow scans (high resolution spectra), respectively, at a pressure below 7.5×10^{-9} mbar. Casa XPS software (Version 2.3.16, Casa Software Ltd., Teignmouth, UK) was used to fit and perform peak integration of spectra. The C 1s peak was used as an internal reference (284.8 eV). High resolution XPS spectra were acquired by Gaussian–Lorentzian curve fitting after S-shape background subtraction.

Wettability: Contact angle measurements were conducted using the water drop method. 0.5 μ L of milliQ water drops were deposited onto the surface of the substrate and recorded after stabilization with the equipment OCA 15EC (DataPhysics Instruments GmbH, Filderstadt). The SCA20 software was used to measure the contact angle, which is shown in this work as the average of at least 10 measures for each sample.

Atomic force microscopy (AFM): AFM was conducted to obtain topographic images of the non-functionalized and functionalized surfaces using Si TAP 150-G probes (Budget Sensors, Bulgaria) with a frequency of 150 kHz and a force constant of 5N/m. Images were obtained with an AFM VEECO Multimode under ambient conditions in tapping mode. The row scanning frequency was set between 0.6 and 0.8 Hz. The root-mean-

square roughness was determined using the statistical application of the NanoScope Analysis software (1.20, Veeco).

Resonance frequency measurements and cantilever displacement: Cantilever resonance frequency and displacement measurements were carried out by means of the SCALA equipment (Scanning Laser Analyzer, from MecWins), a recently developed technology for the optical read-out of cantilevers.^{71,81,82} The readout technique combines the optical beam deflection method and the automated two-dimensional scanning of a single layer beam by voice-coil actuators. The equipment has been implemented with a thermal chamber containing a thermoelectric cooler and a cartridge heater. These elements are capable of sweeping the chamber's temperature from $-50\text{ }^{\circ}\text{C}$ up to $220\text{ }^{\circ}\text{C}$ by flowing thermostated N_2 to the sample. A holder containing multiple thermometer probes is placed inside the chamber for a better mapping of the temperature. All measurements were performed in nitrogen environment. The temperature control was regulated by software created by the MecWins Company.

Monocrystalline Si microcantilever chips containing arrays of eight cantilevers (Micromotive GmbH) were used for the nanomechanical measurements (**Figure 4.4.8a**). Specifically, the nominal length, width, and thickness of the cantilevers were 500, 90 ± 2 and $1\text{ }\mu\text{m}$, respectively. Resonance frequency measurements were conducted in a nitrogen atmosphere at $25\text{ }^{\circ}\text{C}$. The experimental setup is based on the shift induced in the resonance frequency by the added mass onto the cantilever through functionalization. The used platform consists in the automated two-dimensional scanning with a single laser (1 mW) beam by voice-coil actuators perpendicularly located. Displacements over a range of several millimetres at speeds up to 10 mm/s and with an accuracy of 100 nm are achieved. Once the laser beam is reflected by the cantilever array, the exact position and intensity of the reflected spot is collected by a two-dimensional linear position detector. Moreover, TRACKER, which is an algorithm that recognizes reflected intensity patterns, locates cantilever sensors in a fully automated process.

4.4.2 Results and discussion

The response of Omp2a to thermal stress has been compared with those of BSA and LYS. The latter exhibits an ellipsoidal shape in which both ordered (30% α -helix, 27% β -turn and 13% β -sheet secondary structures) and unordered (30%) regions coexist,⁸³ while BSA structure is predominantly α -helical with the remaining polypeptide occurring in turns and extended or flexible regions (*i.e.* with no β -sheets).⁸⁴ Before nanomechanical measurements, the effects of the heat shift on the secondary structure and aggregation tendency of such three proteins have been examined.

Secondary structure and diameter

Temperature-induced protein denaturation is frequently detected using FTIR spectroscopy and CD in various wavelength regimes. The vibrational spectrum is selective in the absorption band frequency position, widths, and intensities in response to protein structural changes.⁸⁵ Specifically, the amide I band (1700 – 1600 cm^{-1}), which convolutes the major structural domain elements of proteins, including α -helix, β -sheet, β -turn and random coil (unstructured), has been used to visualize the response of BSA, LYS and Omp2a to heating (**Figure 4.4.1** displays the FTIR spectra recorded at 30 and 100 °C). At high temperature both BSA and LYS underwent a drastic unfolding, as is reflected by the apparition of an intense deconvoluted peak at $\sim 1640 \text{ cm}^{-1}$ that has been associated to the unstructured protein. In contrast, the resemblance between all spectra recorded for Omp2a suggests that the β -barrel structure is preserved at the highest temperature.

FTIR observations are fully consistent with the CD spectra (**Figure 4.4.2**) recorded in heating runs from 5 °C to 90 °C, which reflect an increment of the disordered motifs at temperatures higher than $\sim 55 \text{ °C}$ for both BSA and LYS while the content of ordered secondary structures, especially α -helix, decreases. The melting temperature estimated from CD results is 67 °C and 65 °C for BSA and LYS. These results are fully consistent with those early reported by different authors for LYS in aqueous solution.^{86,87} Specifically, it was concluded that the protein losses a small part of helical structures in the α -domain below 64 °C, undergoing irreversible (unless cooling start just after

reaching ~80 °C) thermal unfolding of the secondary structures at a temperature close to 75 °C. Instead, Omp2a only exhibits slight variations (*i.e.* thermal stress) in the secondary structures, the amount of unstructured protein remaining practically constant from 5 °C to 90 °C. Moreover, the thermal behavior of the three proteins is reversible, as is evidenced from the analyses of the CD spectra recorded in cooling runs (**Figure 4.4.3**). The influence of the temperature in the shape and aggregation of the proteins was assessed by DLS. Profiles displaying the variation of the particle D_{eff} with the temperature are included in **Figure 4.4.2** (both heating and cooling runs).

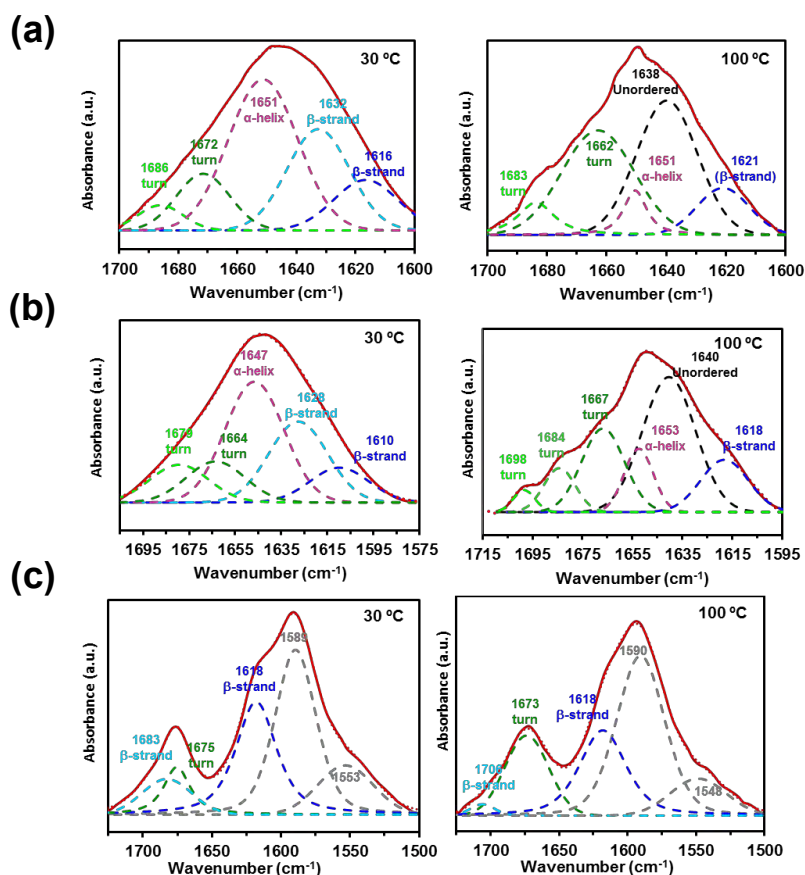


Figure 4.4.1 FTIR spectra in the region of amide I of (a) BSA, (b) LYS and (c) Omp2a at 30 °C and 100 °C (left and right, respectively). The deconvolution of the amide I absorption band is displayed in all cases.

Bimodal distributions were found for BSA at all examined temperatures and, therefore, two D_{eff} profiles are displayed in **Figure 4.4.2a**. In the first one, which corresponds to individual BSA the unfolding process is accompanied by an increment of

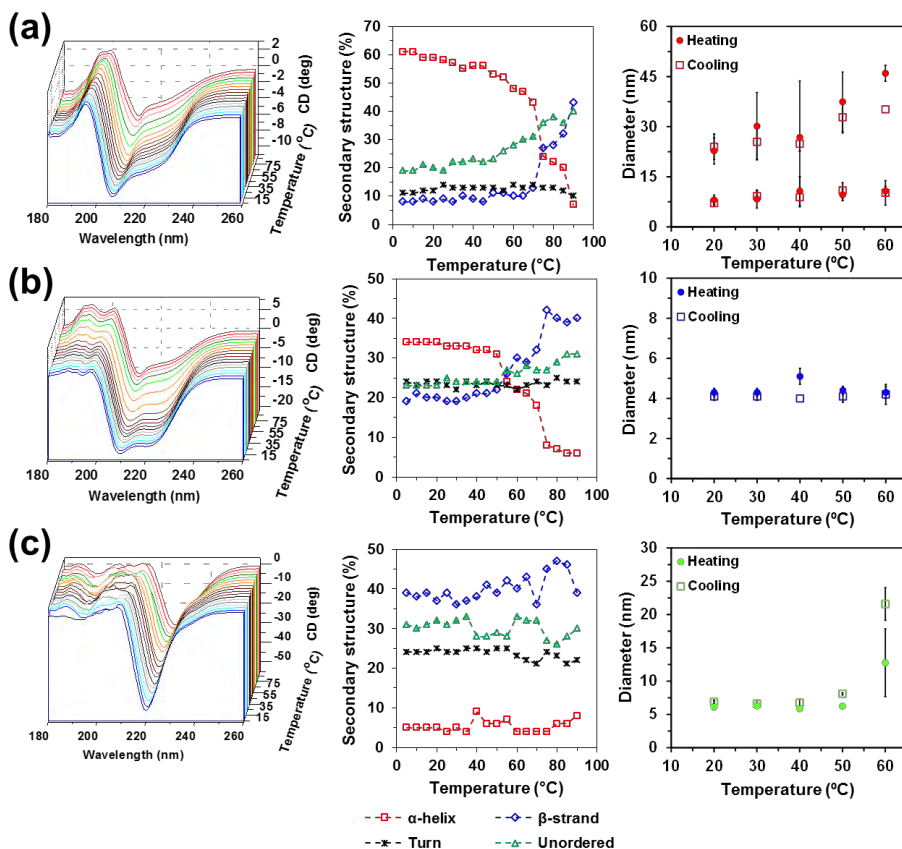


Figure 4.4.2 CD spectra (left) recorded for (a) BSA, (b) LYS and (c) Omp2a proteins at temperatures ranging from 5 °C to 90 °C (heating runs). Measurements for BSA and LYS were performed using a carbonate buffer, whereas a dodecyl sulfate (SDS) – 2-methyl-2,4-pentanediol (MPD) buffer was used for Omp2a. The variation of amount of secondary structures (in %) against the temperature is also represented (middle). Effective diameter (right) derived from DLS measurements at temperatures ranging from 20 °C to 60 °C (measures for heating and cooling runs are displayed) for (a) BSA, (b) LYS and (c) Omp2a proteins. Two profiles are displayed for BSA since a bimodal distribution was found for all examined temperatures, while a unimodal histogram was observed for both LYS and Omp2a.

the molecular dimension. The D_{eff} values of the second profile are approximately three times the values of the first one, indicating that BSA also forms trimers.. In this case, D_{eff} increases from 23 ± 4 nm at 20 °C to 46 ± 2 nm at 60 °C. In contrast, LYS presents unimodal distributions, independently of the temperature, with similar D_{eff} values (*i.e.* 4.3 ± 0.2 nm and 4.3 ± 0.5 nm at 20 and 60 °C, respectively). Although these results suggest that LYS volume is not affected by the unfolding, what actually occurs is that unfolding is accompanied by a reduction in the hydration. The latter was proved in early X-ray scattering studies at 20 °C and 80 °C,⁸⁶ which showed that the electron density of water in LYS crystals decreases with the crystallization temperature and, consequently, the radius of gyration remained practically invariant. Thus, we hypothesize that changes in protein hydration offset the thermally induced protein motion. Similar observations have been found for other proteins,⁸⁸ negative volume changes being detected in some cases.⁸⁹

Finally, Omp2a also presents a unimodal distribution, even though D_{eff} increases when the 6.1 ± 0.2 nm at 20 °C to 12.6 ± 2.4 nm at 60 °C. The former value has been associated to the trimeric state while the latter corresponds to bigger aggregates. The thermal stability observed for Omp2a combined with this significant variation, which is even higher in the cooling run (*i.e.* from 21.6 ± 5.1 nm at 60 °C to 6.9 ± 0.4 nm at 20 °C), indicates that the reversible aggregation of this OMP is notably enhanced by the temperature. Thermomechanical assays combined with these DLS results have been used to explain the aggregation phenomena of Omp2a in the Discussion section.

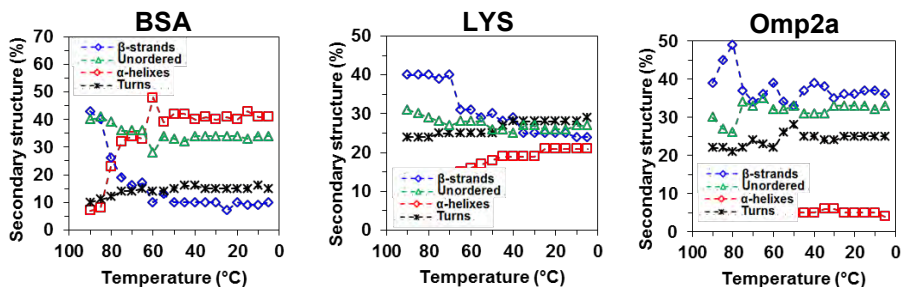


Figure 4.4.3 CD spectra recorded for BSA, LYS and Omp2a proteins at temperatures ranging from 90 °C to 5 °C (cooling runs). The figure represents the variation of amount of secondary structures (in %) against the temperature. Results obtained for the heating run are displayed in the main text.

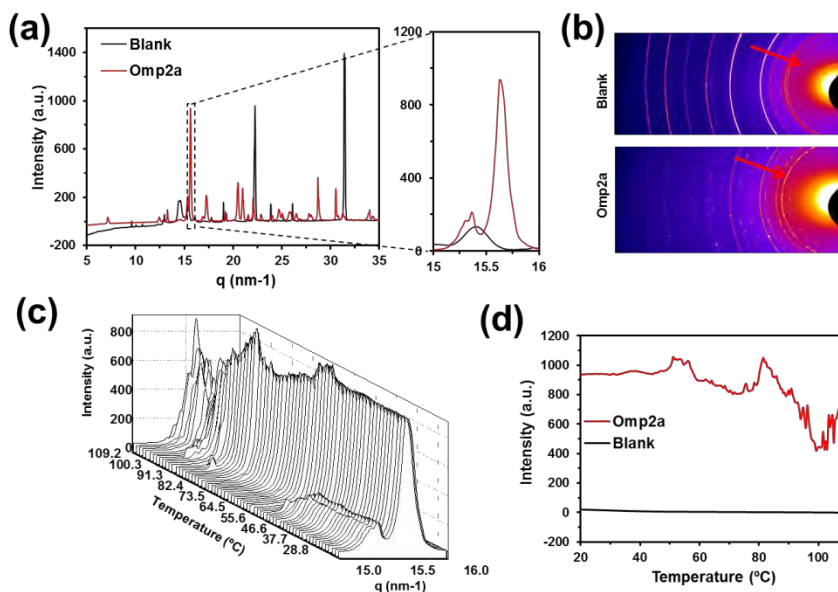


Figure 4.4.4 (a) 1D scattering patterns of blank (salts from the buffer solution) and Omp2a samples as dry powder at room temperature. (b) 2D scattering patterns of the blank and Omp2a dried samples at room temperature. (c) 1D scattering pattern of Omp2a when a temperature ramp (heating) is applied. (d) Intensity of the peak profile for the blank and the Omp2a samples at $q = 15.6$ nm⁻¹ during the temperature ramp.

Time resolved WAXD data on heating and cooling of lyophilized Omp2a

Real time WAXD experiments were performed using synchrotron radiation to examine the evolution of the β -sheets motifs in dried Omp2a during heating and cooling processes. Analyses were performed considering both Omp2a and blank samples, which were obtained by freeze drying the detergent buffer solution in presence and absence of protein, respectively. The one dimensional WAXD profile acquired for Omp2a at room temperature exhibits a sharp and intense peak at $q = 15.64$ nm⁻¹ (**Figure 4.4.4a**), which corresponds to an inter-strand spacing of $d = 4.02$ Å.^{90,91} This peak is absent in the spectra recorded for blank samples, the broad peak centered at $q = 15.40$ nm⁻¹ being attributed to the salts from the buffer (**Figure 4.4.4a**, magnification). The presence and absence of the reflection associated to the β -sheet in the Omp2a and blank samples, respectively, is clarified in the representative diffraction patterns showed in **Figure**

4.4.4b. **Figure 4.4.4c** displays a three-dimensional representation of the freeze dried Omp2a WAXD profiles in the β -sheet region ($q= 15\text{-}16\text{ nm}^{-1}$) obtained by heating at a rate of $5\text{ }^{\circ}\text{C}/\text{min}$ from $25\text{ }^{\circ}\text{C}$ to $110\text{ }^{\circ}\text{C}$, whereas **Figure 4.4.4d** represents the variation in intensity of the peak at $q= 15.6\text{ nm}^{-1}$ that occurs when heating both for Omp2a and blank samples. The variation with temperature of this narrow and intense peak has been used to monitor the effect of the different thermally-induced structural processes in inter-strand interactions. First, the intensity experiences a small increment at $50\text{-}55\text{ }^{\circ}\text{C}$, which has been attributed to the reinforcement of neighboring intermolecular connections. According to DLS observations, which evidenced the transition from the trimeric form to bigger aggregates (**Figure 4.4.2c**), this result has been interpreted as the formation of new β -sheets between neighboring protein molecules. After this, from $\sim 55\text{ }^{\circ}\text{C}$ to $\sim 75\text{ }^{\circ}\text{C}$ the intensity decreases slowly and, suddenly, grows again at $\sim 80\text{ }^{\circ}\text{C}$. These changes suggest the restructuring of the newly formed aggregates during the heating process. Finally, the peak progressively broadened and becomes less intense at higher temperatures, evidencing that temperature has some effects in the local stability of the β -sheets. In spite of this, the peak maintains 47% of its initial intensity at $100\text{ }^{\circ}\text{C}$, which is consistent with the overall stability of the β -barrel structure observed above by FTIR (**Figure 4.4.3c**).

Protein immobilization onto the surface of silicon microcantilevers

The microcantilever-based biosensing technology has been applied in this work to monitor the response of OMPs in synthetic environments against the temperature change. Analysis of the results has been carried out by comparing their thermal behavior with conventional proteins. Among other features, this nanomechanical platform is characterized by the high sensitivity, label-free detection, and small sample consumption due to the size of the microcantilevers (*ca.* $1000\text{ }\mu\text{m}^2$).⁹² For successful characterization, the first step is the functionalization of silicon microcantilevers to achieve a stable and irreversible protein–surface binding.

In this work, a recently developed procedure to covalently bind small peptides to silicon has been extrapolated and adapted to BSA, LYS and Omp2a proteins (**Figure 4.4.5a**).⁹³ This four-step protocol can be summarized as follows: (i) the microcantilever surface, previously hydroxylated with acids, is silanized with (3-glycidyloxypropyl)trimethoxysilane; (ii) epoxy groups are opened with N^{α},N^{α} -bis(carboxymethyl)-L-lysine hydrate (NTA-NH₂) at basic pH; (iii) the carboxylated surface derived from (ii) is activated with a mixture of 1-[3-(dimethylamino)propyl]-3-ethylcarbodiimide methiodide (EDC) and N-hydroxysuccinimide (NHS); and (iv) proteins are immobilized by incubating the activated surface in the corresponding protein solution. Before conducting any measurement, proteins not covalently bonded to the substrate were desorbed by washing with a PBS. Since the three proteins investigated contain a relatively large number of amine groups, corresponding to multiple lysine

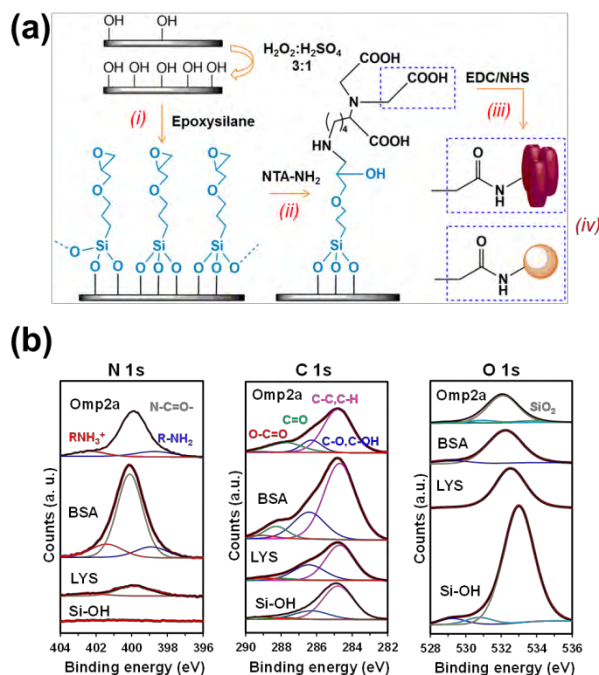


Figure 4.4.5 (a) Protein functionalization protocol for silicon substrates. (b) N 1s, C 1s and O 1s high-resolution XPS spectra for non-functionalized (hydroxylated; Si-OH) and protein functionalized (LYS, BSA or Omp2a) silicon substrates. Peaks from deconvolution are also displayed.

residues, in addition to the N-terminal amine, the study of protein-overhang interactions is limited by this immobilization procedure.

Comparison of the characteristic XPS spectra in the N 1s, C 1s and O 1s regions of hydroxylated (non-functionalized) silicon and protein-functionalized substrates (**Figure 4.4.5b**) chemically proves the success of the immobilization protocol. The presence of a peak in the C 1s region of the non-functionalized silicon spectrum has been attributed to the presence of organic contaminants from the environment. Whilst the latter makes more difficult the corroboration of the protein incorporation, the carbon content is significantly higher when silicon was functionalized with BSA, LYS and Omp2a (**Table 4.4.1**), showing a 4.5, 3.0 and 3.2 fold increase, respectively. Moreover, the apparition of the N 1s peak, which was not detected for non-functionalized substrates, is an unequivocal chemical evidence of the proteins immobilization (**Table 4.4.1**).

Table 4.4.1 Atomic percent composition (O 1s, C 1s, Si 2p and N 1s) obtained by XPS for non-functionalized (hydroxylated) and protein functionalized (*i.e.* with BSA, LYS or Omp2a covalently immobilized at the surface) silicon substrates

	O 1s	C 1s	Si 2p	N 1s
Hydroxylated silicon	47.7	13.4	38.9	-
BSA-silicon	22.5	60.0	10.8	6.7
LYS-silicon	31.6	40.2	26.7	1.5
Omp2a-silicon	30.6	43.4	20.7	5.3

Changes in surface properties, as for example the wettability (**Figure 4.4.6a**) and the surface topography (**Figure 4.4.6b**), provide indirect evidence of the binding between the substrate and the protein. Thus, contact angle (θ) measurements using deionized water showed that the hydrophilic character of silicon ($\theta = 30^\circ \pm 5^\circ$) decreased considerably upon the incorporation of protein ($\theta = 70^\circ \pm 3^\circ$, $47^\circ \pm 2$ and $49^\circ \pm 6^\circ$ for BSA, LYS and Omp2a, respectively). Similarly, 3D topographic AFM images reveal significant differences between the bare silicon substrate and the functionalized ones, which affect the root-mean-square roughness (**Figure 4.4.6c**). Moreover, inspection of the cross sectional profiles (**Figure 4.4.6d**) are consistent with the immobilization not only of

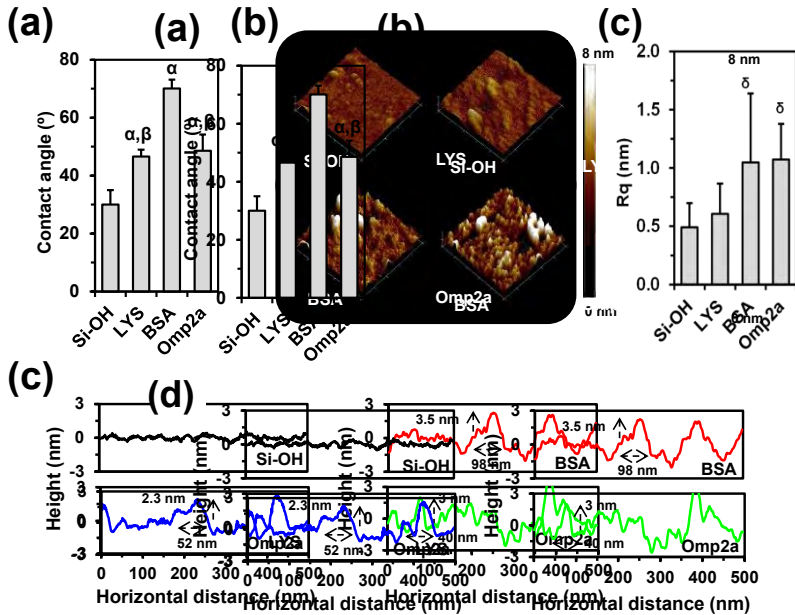


Figure 4.4.6 (a) Average contact angle of non-functionalized and functionalized silicon substrates. Greek letters on the columns refer to significant differences when 1 way ANOVA and Tukey’s multiple comparison tests are applied: α vs Si-OH ($p < 0.0001$) and β vs BSA ($p < 0.0001$). (b) Topographic AFM images of non-functionalized and functionalized substrates ($500 \times 500 \text{ nm}^2$). (c) Root-mean-square roughness (Rq) values. δ vs Si-OH ($p < 0.05$). (d) Representative cross sectional profiles for AFM images.

individual protein molecules but also of aggregates, diameter sizes ranging from 40 to 98 nm.

Thermomechanical response of protein functionalized microcantilevers

Protein-functionalized silicon chips with arrays of eight cantilevers (*i.e.* using such number of sensors in parallel) were operated in dynamic mode (**Figure 4.4.7a**). Piezoelectric excitation (*i.e.* an actuator is positioned below the chip base) and their first vibration mode were monitored by a scanning laser. After cleaning with isopropanol and hydroxylation with a $\text{H}_2\text{O}_2\text{:H}_2\text{SO}_4$ (3:1 v/v) mixture, hydroxylated chips ($100 \mu\text{m}$ wide, $500 \mu\text{m}$ long and $1 \mu\text{m}$ thick) displayed a resonance frequency of $5206 \pm 162 \text{ Hz}$ ($n = 16$) measured in a N_2 atmosphere at $25 \text{ }^\circ\text{C}$.

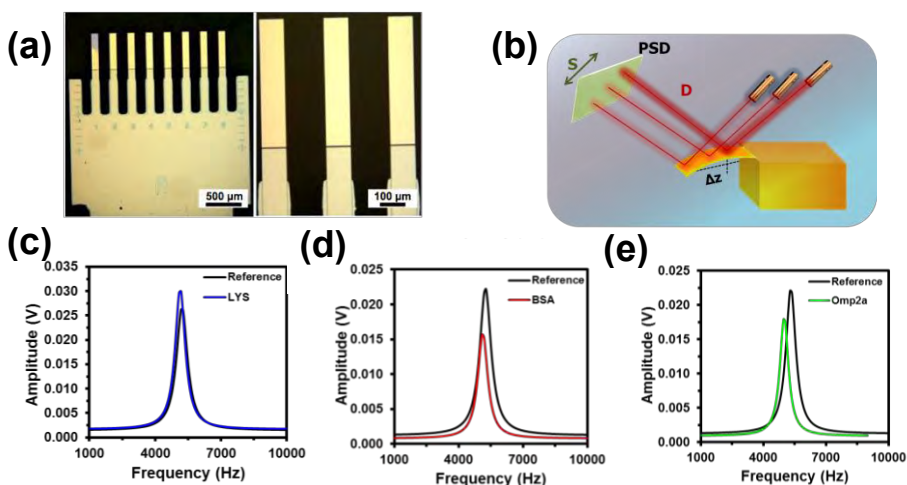


Figure 4.4.7 (a) Silicon chips with arrays of eight cantilevers used for nanomechanical measurements (Micromotive GmbH). (b) Scheme displaying the experimental setup used to evaluate the thermal response of LYS, BSA and Omp2a proteins. Nanomechanical resonance response of a silicon cantilever functionalized with (c) LYS, (d) BSA and (e) Omp2a. The shift with respect to the hydroxylated (non-functionalized) cantilever used as reference is displayed.

Figure 4.4.8a shows the resonance frequency shift of at least 16 LYS-, BSA- and Omp2a-functionalized cantilevers. As it can be seen, the frequency shift value is significantly higher for Omp2a than for BSA and LYS. Provided the molecular weight of Omp2a is supramolecular aggregates is clearly evidenced. This feature is corroborated by comparing nanomechanical first mode resonances of hydroxylated and functionalized cantilevers (**Figure 4.4.7c,d** and **e**), which provides a shift of 92, 182 and 313 Hz for LYS, BSA and Omp2a, respectively. On the other hand, the standard error of the mean calculated for Omp2a is significantly higher than for LYS and BSA. This has been attributed to the variability in the size of the Omp2a supramolecular aggregates, which induces fluctuations in the measured frequency shift values. However, it should be remarked that differences among LYS, BSA and Omp2a are large enough to be independent of such uncertainty. The thermal response of proteins have been analyzed by plotting the displacement (S) of the reflected laser spot on the position sensitive detector (PSD), which originates from the variation of the local slope at the cantilever surface with the temperature and depends on the distance (D) between the cantilever and the PSD (**Figure 4.4.7b**).

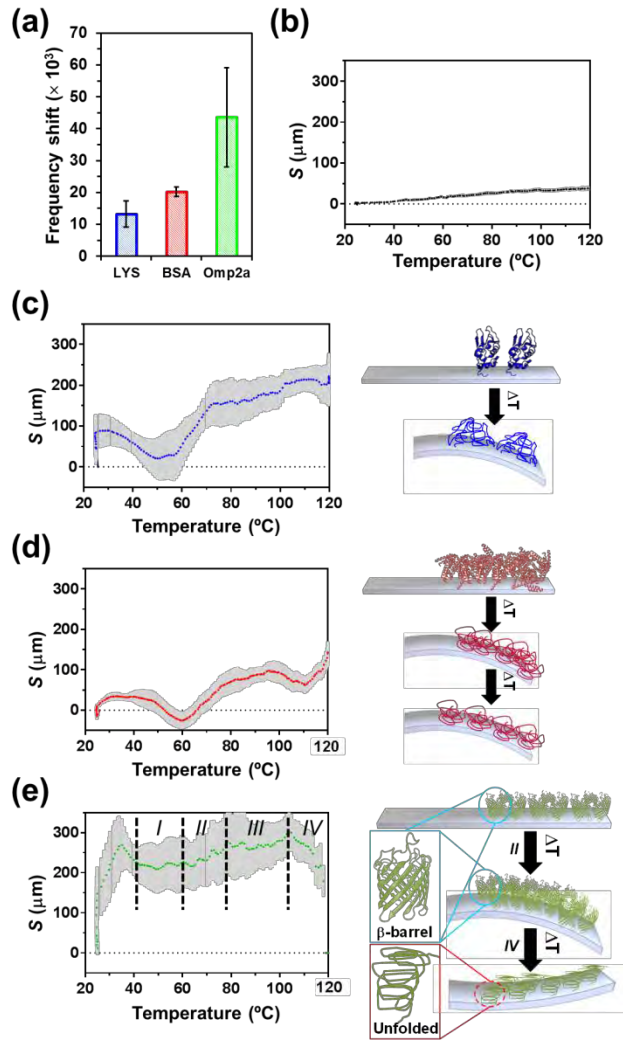


Figure 4.4.8 (a) Nanomechanical response, expressed as resonance frequency shift ($|\Delta f/f$), of functionalized cantilevers (mean values and standard error of the mean calculated with the data of at least 16 different cantilevers). (b) Relative displacement as a function of the temperature of a representative hydroxylated (non-functionalized) cantilever. Thermomechanical response of cantilevers functionalized with (c) LYS, (d) BSA and (e) Omp2a proteins. Right: mean relative displacement as a function of the temperature (blue, red and green dots in c, d and e, respectively) and the corresponding standard error of the mean (thick light-grey lines), both calculated with the data of at least 7 different cantilevers, are displayed at the right. Left: cartoons schematizing the folded \rightarrow unfolded transitions in c and d, and the trimer \rightarrow large aggregate and β -barrel \rightarrow unfolded transitions in e. The four regions described in the text are labelled in e.

It is worth noting that the variation of S with the temperature is analogous to the thermally induced cantilever deflection (Δz). As it was expected, the displacement of non-functionalized cantilevers increases slowly and progressively with the temperature (**Figure 4.4.8b**), as the deflection of rectangular bare cantilevers of length L grows linearly with the change of temperature (ΔT), that is $\Delta z \propto L^2 \Delta T$.⁹⁴

The average displacement curve obtained for LYS (**Figure 4.4.8c**), which was obtained using 16 different microcantilever sensors, reflects a behaviour very different from that obtained for non-functionalized cantilevers. The slope of the displacement curve in the region comprised from room temperature to ~ 50 °C is related to the deflection produced by the different thermal response of the two materials contained in the system (*i.e.* the silicon substrate and the attached protein). More specifically, protein-functionalized cantilevers undergo a differential stress due to the thermal expansion coefficient difference between the protein and the microcantilever itself, giving rise to the cantilever deflection. After this, at ~ 50 °C the protein starts to unfold, causing a redistribution of the molecular mass and reducing the contact between the protein and the substrate. This situation enhances the cantilever deflection, as it is reflected by the sustained increasing displacement of the profile displayed in **Figure 4.4.8c**. Thus, the melting temperature of LYS, as determined thermomechanically, is approximately 60 °C, which is consistent with the CD data (**Figure 4.4.2**). At ~ 70 °C the slope of the displacement curve changes and the curve is similar to that observed for the hydroxylated silicon cantilevers (**Figure 3.4.8b**). Thus, once LYS completes the conversion towards the unfolding state, the changes induced by the thermal dynamics of the random coil are not reflected in the deflection. At this stage the effects associated to the mass redistribution and the variation of the protein-surface interactions are negligible in average. Overall, the profile displayed in **Figure 4.4.8c** should be considered as the fingerprint to recognize the thermomechanical response of conventional proteins, in which the folded \rightarrow unfolded is the only occurring thermal transition.

Figure 4.4.8d displays the average displacement curve achieved for BSA. From a qualitative point of view, the behaviour of the curve is similar to that described above for

LYS until ~ 100 °C, even though the cantilever deflection is smaller for BSA. This has been attributed to the higher molecular weight of BSA and its tendency to aggregate, both reducing the differences in the stress distribution and the stress gradient between the protein and the substrate. Consequently, the impact of the bimetallic effects in the bending of the cantilever is relatively small before the protein denaturation at ~ 60 °C. Moreover, the effect of the redistribution of the molecular mass during the unfolding process is also smaller than for LYS. As the effect of the unfolding on the cantilever displacement is expected to be directly proportional to the amount of protein molecules, these results suggest that such amount is lower for cantilevers functionalized with BSA than with LYS. Although this could be in apparent contradiction with the nanomechanical first mode resonance shift, which is 90 Hz lower for the latter (**Figure 4.4.7c,d and e**), it is worth noting that the molecular weight of BSA is four times higher than that of LYS.

In spite of this, the dynamics of the random coil causes a change in the sense of the cantilever deflection. Thus, deflection downwards or upwards of the cantilever is mainly defined by the response of the protein within the studied temperature range and, as mentioned above, the deflection was relatively low before the unfolding. After this, the upward profile experiences an abrupt change at ~ 110 °C, which is not detected for LYS. Although this sudden drop in the displacement could be hypothesized as a disaggregation of the protein molecules, a simple thermogravimetric analysis (not shown) evidenced that it corresponds to the evaporation of water molecules that were strongly interacting with the protein. Accordingly, in addition to the molecular unfolding, thermomechanical characterization of BSA reveals sharp dehydration process that, suddenly, produces a change of sign in the stress gradient.

The displacement profile recorded for Omp2a (**Figure 4.4.8e**) exhibits unusual complexity. Although bimetallic effect initially affects the cantilever deflection, as in LYS and BSA, four regions with distinctive regimes can be distinguished above 40 °C for Omp2a. In the first one, which extends from 40 °C to 60 °C, the variation of the displacement is practically null, suggesting that the redistribution of the molecular masses and the changes in the protein...substrate interactions are minimum (*region I* in

Figure 4.4.8e). From a microscopic point of view, this region has been associated with the alteration of intermolecular interactions before the transition from trimers to bigger aggregates, which is also consistent with WAXD observations (**Figure 4.4.4**). While initially they seem to become more intense, the step prior to the conversion into bigger aggregate is characterized by a weakening of interactions among neighbouring Omp2a molecules in trimers. This phase transition is evidenced by the increasing displacement (*region II* in **Figure 4.4.8e**), which occurs in a relatively wide interval of temperatures (*i.e.* between ~ 60 °C and ~ 77 °C). After this (*region III* in **Figure 4.4.8e**), the displacement experiences small fluctuations, the average deflection increment along the whole region being very small. These fluctuations have been associated with local re-organizations in the newly formed aggregates. Above 105 °C, the displacement drops sharply (*region IV* in **Figure 4.4.8e**), suggesting that at such high temperatures the thermal stability of the β -barrel is finally lost. Therefore, the downward deflection of the cantilevers is a consequence of the folded \rightarrow unfolded transition that alters both the mass distribution and the Omp2a...substrate interactions. These observations are fully consistent with the WAXD results displayed in Figure 2d.

Discussion

Although the secondary structure of bacterial OMPs are known to be very sensitive to the polarity of the environment, they exhibit an increased thermal stability that has been typically attributed not only to the abundant β -strands barrel but also to their oligomeric architectures.⁹⁵⁻⁹⁸ However, complete understanding of the thermal response of their supramolecular oligomeric architectures in synthetic environments, which is essential for the utilization of OMPs in the fabrication of bioinspired nanodevices, is an unresolved question.⁹⁹

Our FTIR and CD results on Omp2a prove that the efficient inter-strand hydrogen bond network preserves the protein secondary structure from thermal unfolding even outside lipid environments similar to those found in nature. Besides, the heat-induced CD response of secondary structural elements in Omp2a has also been compared with that of conventional proteins. In folded proteins the α -helix is recognized by minima at ~ 220 and ~ 210 nm, while the β -sheet has a minimum at 218 nm and a maximum at ~ 195

nm.¹⁰⁰ These two structural motifs are detected in the spectra recorded for LYS and Omp2a at room temperature, whereas the spectrum of BSA mainly involves the helical motif. However, the structural signatures of BSA and LYS significantly change beyond ~55 °C, evidencing the loss of secondary structure,¹⁰¹ while the CD spectrum of Omp2a remains practically unaltered until 90 °C.

On the other hand, DLS data reflect that Omp2a self-associates into the typical trimeric state found in the outer membranes of bacteria in the detergent buffer at room temperature. Thus, the D_{eff} measured by transmission electron microscopy (TEM) for Omp2a trimers in dried samples was recently found to be 9.3±3.0 nm, which is consistent with DLS value at 20 °C (6.1±0.2 nm). However, the formation of bigger aggregates is detected by DLS when the temperature increases above 50 °C, even though they are significantly smaller (D_{eff} = 12.6±2.4 nm) than those also observed in dried samples at room temperature (D_{eff} = 25.9±4.8 nm) by TEM. Thus, the van der Waals interactions between the side groups at the external side of the β -barrel are promoted through both drying and heating. This feature points out the importance of improving the understanding of Omp2a self-association processes in non-native environments, as for example those used to fabricate bioinspired NMs for ion transport.

WAXD experiments indicate that temperature affects the β -sheet structure of Omp2a. This effect is focused in intermolecular interactions at temperatures lower than ~80 °C and in both inter- and intramolecular interactions at higher temperatures. However, the amount of β -sheets preserved at 110 °C is still high enough to preserve the β -barrel structure, which supports FTIR and CD results. Thus, WAXD results corroborate the conversion of trimers into bigger aggregates at 50-55 °C, which after equilibration through local reorganizations remain relatively stable until ~80 °C. At higher temperatures, inter- and, probably, intramolecular β -strands, are affected by the thermal stress, these interactions being roughly halved. This interpretation is consistent with the well-known increased thermal stability of bacterial porins, which exhibit temperature induced unfolding above 100 °C.^{95,102} This unusual stability is consequence of their β -barrel structural architecture composed of antiparallel β -sheets, in which strands are connected by long loops. Thus, the energy required to breakdown the secondary and

quaternary structure of bacterial porins is significantly higher than that necessary to unfold BSA and LYS. Also, yet porins aggregates are stable, a variety of transitions associated to changes in their size (*i.e.* to dimers, trimers or bigger aggregates) has been detected at temperatures significantly lower than their unfolding temperatures but comparable to the typical unfolding temperatures of conventional proteins,¹⁰²⁻¹⁰⁴ which is in agreement with the opposite behaviours of Omp2a and BSA.

The D_{eff} of LYS, which remains at 4.3 ± 0.2 nm for both 20 and 60 °C, corresponds to the monomer diameter.^{105,106} Thus, the mass contribution of aggregates, which are extremely difficult to avoid completely even with dilute samples, was null in the case of LYS. These features combined with CD and FTIR data indicate that the unfolding is the only thermally-induced transition for LYS. Finally, BSA displays an intermediate situation with two D_{eff} values originated by the bimodal distribution observed at each temperature. The lowest value, 8.1 ± 1.4 nm at 20 °C, which is consistent with the dimensions of the prolate ellipsoid shape proposed for the protein monomer (14×4 nm),¹⁰⁵ increases by 30% with the temperature, due to the unfolding. However, the highest value, 23 ± 4 nm at 20 °C, grows more than twice when the temperature reaches 60 °C. In this case, small aggregates (dimers or trimers) not only experience unfolding processes but also incorporate more protein molecules. Accordingly, BSA self-association is promoted by the temperature when already formed aggregates act as nuclei. Overall, FTIR, CD and DLS results probe that LYS and BSA are suitable controls for the present microcantilever deflection studies due to their different behavior not only with respect to Omp2a but also among them.

Proteins have been covalently linked via an epoxysilane-based protocol to silicon microcantilevers that had been efficiently activated by a hydroxylation treatment with a $H_2O_2:H_2SO_4$ mixture. The results derived from the different chemical and physical characterization techniques performed at each functionalized substrate have confirmed directly and indirectly, respectively, the suitability of the protocol to tether biomacromolecules onto the silicon surfaces. Moreover, topographic images of protein functionalized surfaces, once biomacromolecules non-covalently bonded to the surface were eliminated, evidence heights and widths of 2-4 nm and 40-100 nm, respectively,

demonstrating the immobilization of aggregates. As expected, the latter aggregates are much smaller and less abundant for LYS than for BSA and Omp2a, the former showing the flatter profile (root-mean-square roughness of non-functionalized, LYS-, BSA- and Omp2a-functionalized substrates is 4.9 ± 2.1 , 6.1 ± 2.6 , 10.5 ± 5.9 and 10.7 ± 3.0 Å, respectively).

The resonance frequency of non-functionalized cantilevers (ω), which depends on their spring rigidity (k) and effective mass (M), is obtained by the elasticity theory as:

$$\omega = \frac{1}{2\pi} \sqrt{\frac{k}{M}} \quad (\text{Eq. 4.4.1})$$

The constant k is obtained using cantilever Young modulus (E) and dimensions, length (L), width (W) and thickness (T):¹⁰⁷

$$k = \frac{EWT^3}{4L^3} \quad (\text{Eq. 4.4.2})$$

Upon protein-functionalization, the resonance frequency changes from ω to ν :

$$\nu = \omega + \Delta\omega = \frac{1}{2\pi} \sqrt{\frac{k}{M+m} + \Gamma(k, \eta)} \quad (\text{Eq. 4.4.3})$$

where $\Delta\omega$ is the resonance frequency contribution due to the tethering of the protein, m is the mass of the protein, and Γ is a function that depends on k and the surface stress (η) induced by protein-silicon surface interactions.¹⁰⁸ Particularly, the difference in frequency shift ($\Delta\omega/\omega \times 10^3$) for LYS, BSA and Omp2a was 13.2 ± 4.1 , 20.2 ± 1.4 and 43.6 ± 15.6 , respectively. These resonance frequency shifts suggest that protein-surface interactions predominate over m since the shift is two times higher for Omp2a than for BSA, whereas the molecular weight is 1.7 times higher for the latter than for the former. Accordingly, protein-surface interactions can be considered as a nanomechanical signature sensitive not only to the existence of protein aggregation phenomena but also to the distribution of the molecules in such aggregates.

In addition to the mass redistribution onto the cantilever surface, which causes changes in the resonance frequency, and to the bimetallic effect, the main mechanical effect in microcantilevers is the surface stress (σ) that induces a nanoscale bending.¹ This effect, which occurs if only one of both cantilever sides are coated or, as in this work, functionalized, is quantified using the Stoney's equation:¹⁰⁹

$$\sigma = \frac{1}{3} \left(\frac{T}{L} \right)^2 \left(\frac{E}{1-\nu} \right) \Delta z \quad (\text{Eq. 4.4.4})$$

where L is the microcantilever effective length (450 μm), T is the microcantilever thickness (1 μm), E is the Young modulus of silicon (150 GPa), ν is the Poisson ratio of silicon (0.17) and Δz is the deflection of the cantilever. The surface stress is frequently associated to intermolecular interactions between molecules anchored onto the cantilever surface, such as van der Waals forces, hydrogen bonds, electrostatic interactions, steric repulsions, etc. Ideally, protein-functionalized cantilevers should not exhibit any static surface stress if the functionalization was identical for both sides. However, in practice, the experimental set-ups used during the functionalization process do not result in two identical cantilever sides. As a consequence, the surface stress is not negligible for protein-functionalized cantilevers (*e.g.* at 120 $^{\circ}\text{C}$, $\sigma = 0.46 \pm 0.12$, 0.31 ± 0.05 and 0.30 ± 0.15 mN/m for LYS, BSA and Omp2a, respectively; **Figure 4.4.9a**), and significantly higher than that measured for hydroxylated non-functionalized ones (*e.g.* at 120 $^{\circ}\text{C}$, $\sigma = 0.08 \pm 0.012$ mN/m). Moreover, the surface stress experiences a significant increment when the temperature is higher than ~ 50 $^{\circ}\text{C}$ for all functionalized cantilevers (**Figure 4.4.9b**).

Analyses of the displacement curves obtained for protein-functionalized cantilevers allowed distinguishing folded \rightarrow unfolded conformational transitions from phase changes related with protein aggregates. Thus, the thermally-induced increment in the deflection of protein-functionalized cantilevers is not constant, as occurs for non-functionalized cantilevers. Proteins are much more sensitive than silicon to the temperature and, therefore, the general evolution of the displacement observed at relatively low temperatures (< 50 $^{\circ}\text{C}$) is mainly due to the differences in both stress distribution and stress gradient between the protein and the silicon substrate (*i.e.* the bimetallic effect). In such conditions, the bending of protein-functionalized cantilevers depends on the molecular weight and the presence of aggregates.

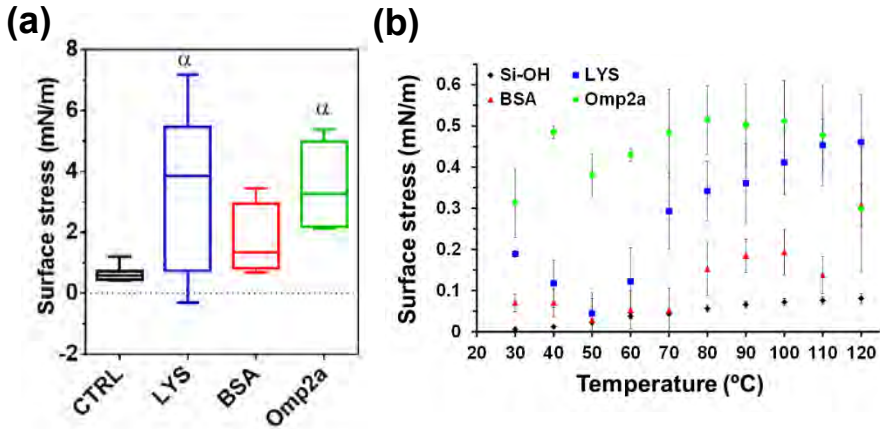


Figure 4.4.9 (a) Surface stress determined for hydroxylated (control) and protein-functionalized cantilevers at 120 °C. Significant differences are encountered on groups marked with the Greek letter α (<0.05) compared to the control group. (b) Variation of the surface stress for hydroxylated (control) and protein-functionalized cantilevers against the temperature.

After this, conventional proteins exhibit an abrupt change in the evolution of the curve, which is ascribed to their denaturalization process. This folded \rightarrow unfolded transition occurs at temperatures close to ~ 50 °C and ~ 60 °C for LYS and BSA, respectively, which are lower than those observed in water (60–70 °C). Consequently, in solution the folded structure of these soluble proteins is stabilized by intermolecular hydrogen bonds with surrounding water molecules, which are lost upon removal of the solvent. This instability induces a lower unfolding temperature.

Once the denatured protein reaches a stable random coil, the dynamics of this state should not affect the thermomechanical response of the cantilever. This is true for LYS- and BSA-functionalized substrates, which show a behavior similar to that of non-functionalized cantilevers when the temperature exceeds ~ 55 and ~ 60 °C, respectively. However, BSA-functionalized cantilevers display another transition at 110 °C that has been ascribed to the evaporation of water molecules strongly interacting with protein molecules.

The thermomechanical response of Omp2a is more complex than those of LYS and BSA because of both its intrinsic thermal stability and the tendency to form not only trimers but also larger aggregates. The thermal behavior of this porin is characterized by

local re-organizations, which affect the strength of intermolecular interactions among neighbouring Omp2a molecules, inducing the transition from trimers to larger aggregates. The formation of such larger aggregates is consistent not only with DLS results but also with previous TEM investigations, as mentioned in the Results section. The latter phase transition is poorly defined, as reflects the continuous increase of the displacement in the temperature interval comprised between ~ 60 °C and ~ 77 °C. This feature should be attributed to the fact that the size and shape of the aggregates formed at such temperatures are constrained by the functionalization of the cantilever, which defines the tethering position of the protein molecules and gives variability to the transition. Such heterogeneity explains the undefined character of the transition that, in spite of the monodisperse and precise chemical nature of Omp2a molecules, occurs within a wide interval of temperatures rather than at a precise temperature. On the other hand, the thermal unfolding of Omp2a is detected at ~ 105 °C, this temperature representing the upper threshold in relation to the manipulation of stable protein aggregates.

4.4.3 Conclusions

In summary, thermomechanical measurements at the microscopic level on functionalized cantilevers have provided molecular insights that complement the information obtained from conventional characterization techniques on ensembles formed by a very large number of molecules. A serious limitation of conventional techniques is that they provide only a sample average response and are unable to give information on specific local features on or within the sample. Within this context, the unique thermomechanical response of Omp2a-functionalized cantilevers, which exhibits four well-defined regimes above 40 °C (**Figure 4.4.8e**), suggests practical approaches to improve the efficacy of smart biomimetic NMs with porins immobilized onto the surface^{64,110-112} or confined inside synthetic pores.¹¹³⁻¹¹⁴ Specifically, although the effectiveness of NMs is regulated by the amount of porin molecules active for the ion transport, controlling their orientation once immobilized onto the surface or inside nanopores is a challenge that has not been achieved yet. However, the identification of

temperature intervals in which protein molecules experience local structural rearrangements with an enhancement of intermolecular β -sheets, suggests that soft post-thermal treatments could be very advantageous to improve the efficacy of the NMs. Thus, this could be achieved by heating the proteins from their initial assembly state to denaturalization and, subsequently, cooling under controlled conditions to maximize favourable interactions. The amount of protein molecules contributing to the selective ion transport substrate could be substantially increased by enhancing the intermolecular β -sheets, which requires local orientation of the immobilized biomolecules.

4.7 References

1. Jorest, T.; Klinger, A.; Gro, L. E.; Kawano, S.; Flinner, N.; Duchardt-Ferner, E.; Wöhnert, J.; Kalbacher, H.; Endo, T.; Schleiff, E. and Rapaport, D. Characterization of the targeting signal in mitochondrial β -barrel proteins. *Nature Commun.* **2016**, *7*, 12036.
2. Saurel, O.; Iordanov, I.; Nars, G.; Demange, P.; Le Marchand, T.; Andreas, L. B.; Pintacuda, G. and Milon, A. Local and global dynamics in klebsiella pneumoniae outer membrane protein a in lipid bilayers probed at atomic resolution. *J. Am. Chem. Soc.* **2017**, *139*, 1590–1597.
3. Hwang, P. M.; Choy, W. Y.; Lo, E. I.; Chen, L.; Forman-Kay, J. D.; Raetz, C. R. H.; Prive, G. G.; Bishop, R. E. and Kay, L. E. Solution structure and dynamics of the outer membrane enzyme PagP by NMR. *Proc. Natl. Acad. Sci.* **2002**, *99*, 13560–13565.
4. Overington, J. P.; Al-Lazikani, B. and Hopkins, A. L. How many drug targets are there? *Nat. Rev. Drug Discovery* **2006**, *5*, 993–996.
5. Koebnik, R.; Locher, K. P. and Van Gelder, P. Structure and function of bacterial outer membrane proteins: barrels in a nutshell. *Mol. Microbiol.* **2000**, *37*, 239–253.
6. Weeber, E. J.; Michael, L.; Sampson, M. J.; Anflous, K.; Armstrong, D. L.; Brown, S. E.; Sweatt, J. D. and Craigen, W. J. The role of mitochondrial porins and the permeability transition pore in learning and synaptic plasticity. *J. Biol. Chem.* **2002**, *277*, 18891–18897.
7. Fischer, K.; Weber, A.; Brink, S.; Arbinger, B.; Schünemann, D.; Borchert, S.; Heldt, H. W.; Popp, B.; Benz, R.; Link, T. A.; Eckerskorn, C. and Flügge, U.-I. Porins from plants – molecular-cloning and functional-characterization of 2 new members of the porin family. *J. Biol. Chem.* **1994**, *269*, 25754–25760.
8. Shen, Y. X.; Saboe, P.; Sines, I. T.; Erbakan, M. and Kumar, M. Biomimetic membranes: a review. *J. Membr. Sci.* **2014**, *454*, 359–381.
9. Moriyón, I. and López-Goñi, I. Structure and properties of the outer membranes of brucella abortus and *Brucella melitensis*. *Int. Microbiol.* **1998**, *1*, 19–26.
10. Uran, S.; Larsen, A.; Jacobsen, P. B. and Skotland, T. Analysis of phospholipid species in human blood using normal-phase liquid chromatography coupled with electrospray ionization

- ion-trap tandem mass spectrometry. *J. Chromatogr. B. Biomed. Sci. Appl.* **2001**, *758*, 265–275.
11. Leekumjorn, S. and Sum, A. K. Molecular characterization of gel and liquid-crystalline structures of fully hydrated POPC and POPE bilayers. *J. Phys. Chem. B* **2007**, *111*, 6026–6033.
 12. Unsay, J. D.; Cosentino, K.; Subburaj, Y. and García-Sáez, A. J. Cardiolipin effects on membrane structure and dynamics. *Langmuir* **2013**, *29*, 15878–15887.
 13. Li, Z.; Ma, J.; Lee, N. S. and Wooley, K. L. Dynamic cylindrical assembly of triblock copolymers by a hierarchical process of covalent and supramolecular interact. *J. Am. Chem. Soc.* **2011**, *133*, 1228–1231.
 14. Yan, Q.; Yuan, J.; Cai, Z.; Xin, Y.; Kang, Y. and Yin, Y. Voltage-responsive vesicles based on orthogonal assembly of two homopolymers. *J. Am. Chem. Soc.* **2010**, *132*, 9268–9270.
 15. Yan, Q.; Zhou, R.; Fu, C.; Zhang, H.; Yin, Y. and Yuan, Y. CO₂-responsive polymeric vesicles that breathe. *Angew. Chem., Int. Ed.* **2011**, *50*, 4923–4927.
 16. Willumeit, R.; Kumpugdee, M.; Funari, S. S.; Lohner, K.; Pozo-Navas, B.; Brandenburg, K.; Linsler, S. and Andrä, J. Structural rearrangement of model membranes by the peptide antibiotic NK-2. *Biochim. Biophys. Acta - Biomembr.* **2005**, *1669*, 125–134.
 17. Zeczycki, T. N.; Whelan, J.; Hayden, W. T.; Brown, D. and Shaikh, S. R. Increasing levels of cardiolipin differentially influence packing of phospholipids found in the mitochondrial inner membrane. *Biochem. Biophys. Res. Commun.* **2014**, *450*, 366–371.
 18. Rigaud, J. L.; Pitard, B. and Levy, D. Reconstitution of membrane proteins into liposomes: application to energy-transducing membrane proteins. *Biochim. Biophys. Acta - Bioenerg.* **1995**, *1231*, 223–246.
 19. Geertsma, E. R.; Nik Mahmood, N. A.; Schuurman-Wolters, G. K. and Poolman, B. Membrane reconstitution of ABC transporters and assays of translocator function. *Nat. Protoc.* **2008**, *3*, 256–266.
 20. Seddon, A. M.; Curnow, P. and Booth, P. J. membrane proteins, lipids and detergents: not just a soap opera. *Biochim. Biophys. Acta - Biomembr.* **2004**, *1666*, 105–117.
 21. Rigaud, J. and Levy, D. Reconstitution of membrane proteins into liposomes. *Methods Enzymol.* **2003**, *372*, 65–86.
 22. Santos, H. J.; Imai, K.; Makiuchi, T.; Tomii, K.; Horton, P.; Nozawa, A.; Ibrahim, M.; Tozawa, Y. and Nozaki, T. A Novel mitochondrial β -barrel outer membrane protein in entamoeba. *Sci. Rep.* **2015**, *5*, 8545.
 23. Opaliński, Ł.; Kiel, J. A. K. W.; Williams, C.; Veenhuis, M. and van der Klei, I. J. Membrane curvature during peroxisome fission requires Pex11. *EMBO J.* **2011**, *30*, 5–16. DOI: 10.1038/emboj.2010.299
 24. Leonenko, Z. V.; Carnini, A. and Cramb, D. T. Supported planar bilayer formation by vesicle fusion: the interaction of phospholipid vesicles with surfaces and the effect of gramicidin on

- bilayer properties using atomic force microscopy. *Biochim. Biophys. Acta - Biomembr.* **2000**, *1509*, 131–147.
25. Richter, R.; Mukhopadhyay, A. and Brisson, A. Pathways of lipid vesicle deposition on solid surfaces: a combined QCM-D and AFM study. *Biophys. J.* **2003**, *85*, 3035–3047.
 26. Berquand, A.; Lévy, D.; Gubellini, F.; Le Grimmeléc, C. and Milhiet, P. E. Influence of calcium on direct incorporation of membrane proteins into in-plane lipid bilayer. *Ultramicroscopy* **2007**, *107*, 928–933.
 27. Maire, M. L.; Champeil, P. and Möller, J. V. Interaction of membrane proteins and lipids with solubilizing detergents. *Biochim. Biophys. Acta* **2000**, *1508*, 86–111.
 28. Milhiet, P.-E.; Gubellini, F.; Berquand, A.; Dosset, P.; Rigaud, J. L.; Le Grimmeléc, C. and Levy, D. High-resolution AFM of membrane proteins directly incorporated at high density in planar lipid bilayer. *Biophys. J.* **2006**, *91*, 3268–3275.
 29. Sumino, A.; Uchihashi, T. and Oiki, S. oriented reconstitution of the full-length KcsA potassium channel in a lipid bilayer for AFM imaging. *J. Phys. Chem. Lett.* **2017**, *8*, 785–793.
 30. Chada, N.; Sigdel, K. P.; Reddy, R.; Gari, S.; Matin, T. R.; Randall, L. R. and King, G. M. Glass is a viable substrate for precision force microscopy of membrane proteins. *Sci. Rep.* **2015**, *5*, 12550.
 31. Lü, J.; Yang, J.; Dong, M. and Sahin, O. Nanomechanical spectroscopy of synthetic and biological membranes. *Nanoscale* **2014**, *6*, 7604–7608.
 32. Lingwood, D. and Simons, K. Lipid Rafts as a Membrane-organizing principle. *Science* **2010**, *327*, 46–50.
 33. Voss, A.; Dietz, C.; Stocker, A. and Stark, R. W. quantitative measurement of the mechanical properties of human antibodies with sub-10-nm resolution in a liquid environment. *Nano Res.* **2015**, *8*, 1987–1996.
 34. Saphire, E. O.; Stanfield, R. L.; Crispin, M. D.; Parren, P. W.; Rudd, P. M.; Dwek, R. A.; Burton, D. R. and Wilson, I. A. Contrasting IgG structures reveal extreme asymmetry and flexibility. *J. Mol. Biol.* **2002**, *319*, 9–18.
 35. Friendschuh, M.; Martinez-Martin, D.; Mulvihill, E.; Wegmann, S. and Muller, D. J. Multiparametric high-resolution imaging of native proteins by force-distance curve-based AFM. *Nat. Protoc.* **2014**, *9*, 1113–1130.
 36. Derjaguin, B. V.; Muellen, V. M. and Toporov, Y. P. Effect of contact deformations on the adhesion of particles. *J. Colloid Interface Sci.* **1975**, *53*, 314–326.
 37. Mari, S. A.; Köster, S.; Bippes, C. A.; Yildiz, Ö.; Kühlbrandt, W. and Muller, D. J. pH-Induced conformational change of the β -barrel-forming protein OMPG reconstituted into native E. coli Lipids. *J. Mol. Biol.* **2010**, *396*, 610–616.
 38. Medalsy, I. D. and Muller, D. J. Nanomechanical properties of proteins and membranes depend on loading rate and electrostatic interactions. *ACS Nano* **2013**, *7*, 2642–2650.
 39. Dong, M.; Husale, S. and Sahin, O. Determination of protein structural flexibility by microsecond force spectroscopy. *Nat. Nanotechnol.* **2009**, *4*, 514–517.

40. Picas, L.; Rico, F.; Deforet, M. and Scheuring, S. Structural and mechanical heterogeneity of the erythrocyte membrane reveals membrane stability. *ACS Nano* **2013**, *7*, 1054–1063.
41. Sullan, R. M.; Li, J. K. and Zou, S. Direct correlation of structures and nanomechanical properties of multicomponent lipid bilayers. *Langmuir* **2009**, *25*, 7471–7477.
42. Li, J. K.; Sullan, R. M. and Zou, S. Atomic force microscopy force mapping in the study of supported lipid bilayers. *Langmuir* **2011**, *27*, 1308–1313.
43. Konarzewska, D.; Juhaniewicz, J.; Guzeloglu, A. and Sek, S. Characterization of planar biomimetic lipid films composed of phosphatidylethanolamines and phosphatidylglycerols from Escherichia Coli. *Biochim. Biophys. Acta* **2017**, *1859*, 475–483.
44. Pérez-Madrugal, M.; Giannotti, M. I.; Oncins, G.; Franco, L.; Armelin, E.; Puiggalí, J.; Sanz, F.; del Valle, L. J. and Alemán, C. Bioactive nanomembranes of semiconductor polythiophene and thermoplastic polyurethane: thermal, nanostructural and nanomechanical properties. *Polym. Chem.* **2013**, *4*, 568–583.
45. Lin, D. C. and Dimitriadis, E. K. Robust strategies for automated afm force curve analysis-ii: adhesion-influenced indentation of soft, Elastic Materials. *J. Biomech. Eng.* **2007**, *129*, 904–912.
46. Medalsy, I.; Hensen, U. and Muller, D. J. Imaging and quantifying chemical and physical properties of native proteins at molecular resolution by force-volume AFM. *Angew. Chemie - Int. Ed.* **2011**, *50*, 12103–12108.
47. Ostatná, V.; Černocká, H.; Kurzatowska, K. and Paleček, E. Native and denatured forms of proteins can be discriminated at edge plane carbon electrodes. *Anal. Chim. Acta* **2012**, *735*, 31–36.
48. Brabec, V. Electrochemical oxidation of nucleic acids and proteins at graphite electrode. qualitative aspects. *J. Electroanal. Chem. Interfacial Electrochem.* **1979**, *116*, 69–82.
49. Paleček, E.; Jelen, F.; Teijeiro, V. and Fučík, T. M. Biopolymer-modified electrodes in the voltammetric determination of dna and protein at the submicrogram Level. *Anal. Chim. Acta* **1993**, *273*, 175–186.
50. Paleček, E.; Tkác, J.; Bartošík, M.; Bertók, T.; Ostatná, V. and Paleček, J. Electrochemistry of nonconjugated proteins and glycoproteins. Toward sensors for biomedicine and glycomics. *Chem. Rev.* **2015**, *115*, 2045–2108.
51. Vacek, J.; Vrba, J.; Zatloukalová, M. and Kubala, M. Electrochemical oxidation of proteins using ionic liquids as solubilizers, adsorption solvents and electrolytes. *Electrochim. Acta* **2014**, *126*, 31–36.
52. Hille, B. Ligand gated channels of fast chemical synapses. In ion channels of excitable membranes, 3rd ed.; Sinauer Associates: Sunderland, MA, **2001**; pp 169-200.
53. Fyles, T. M. Synthetic ion channels in bilayer membranes. *Chem. Soc. Rev.* **2007**, *36*, 335–347.

54. Kumar, M.; Grzelakowski, M.; Zilles, J.; Clark, M. and Meier, W. Highly permeable polymeric membranes based on the incorporation of the functional water channel protein aquaporin Z. *Proc. Natl. Acad. Sci. U. S. A.* **2007**, *104*, 20719–20724.
55. Ali, M.; Ramirez, P.; Mafe, S.; Neumann, R. and Ensinger, W. A pH-tunable nanofluidic diode with a broad range of rectifying properties. *ACS Nano* **2009**, *3*, 603–608.
56. Cao, L. X.; Guo, W.; Ma, W.; Wang, L.; Xia, F.; Wang, S. T.; Wang, Y. G.; Jiang, L. and Zhu, D. B. Towards understanding the nanofluidic reverse electro dialysis system: well matched charge selectivity and ionic composition. *Energy Environ. Sci.* **2011**, *4*, 2259–2266.
57. Vlassioug, I.; Apel, P. Y.; Dmitriev, S. N.; Healy, K. and Siwy, Z. S. Versatile ultrathin nanoporous silicon nitride membranes. *Proc. Natl. Acad. Sci. U. S. A.* **2009**, *106*, 21039–21044.
58. Kim, S.; Nham, J.; Jeong, Y. S.; Lee, C. S.; Ha, S. H.; Park, H. B. and Lee, Y. J. Biomimetic selective ion transport through graphene oxide membranes functionalized with ion recognizing peptides. *Chem. Mater.* **2015**, *27*, 1255–1261.
59. Gritsch, S.; Nollert, P.; Jähnig, F. and Sackmann, E. Impedance spectroscopy of porin and gramicidin pores reconstituted into supported lipid bilayers on indium–tin–oxide electrodes. *Langmuir*, **1998**, *14*, 3118–3125.
60. Hillebrandt, H.; Wiegand, G.; Tanaka, M. and Sackmann, E. High electric resistance polymer / lipid composite films on indium–tin–oxide electrodes. *Langmuir* **1999**, *15*, 8451–8459.
61. Lin, J.; Motylinski, J.; Krauson, A. J.; Wimley, W. C.; Searson, P. C. and Hristova, K. Interactions of membrane active peptides with planar supported bilayers: an impedance spectroscopy study. *Langmuir* **2012**, *28*, 6088–6096.
62. Wiegand, G.; Arribas-layton, N.; Hillebrandt, H.; Sackmann, E. and Wagner, P. Electrical properties of supported lipid bilayer membranes. *J. Phys. Chem. B* **2002**, *106*, 4245–4254.
63. Juhaniwicz, J. and Sek, S. Atomic force microscopy and electrochemical studies of melittin action on lipid bilayers supported on gold electrodes. *Electrochim. Acta* **2015**, *162*, 53–61.
64. Pérez-Madrigal, M. M.; del Valle, L. J.; Armelin, E.; Michaux, C.; Roussel, G.; Perpète, E. A. and Alemán, C. Polypyrrole-supported membrane proteins for bio-inspired ion channels. *ACS Appl. Mater. Interfaces* **2015**, *7*, 1632–1643.
65. Tamayo, J.; Kosaka, P. M.; Ruz, J. J.; San Paulo, A. and Calleja, M. Biosensors based on nanomechanical systems. *Chem. Soc. Rev.* **2013**, *42*, 1287–1311.
66. Li, M.; Tang, H. and Roukes, M. Ultra-sensitive NEMS-based cantilevers for sensing, scanned probe and very high-frequency applications. *Nat. Nanotechnol.* **2007**, *2*, 114–120.
67. Chaste, J.; Eichler, A.; Moser, J.; Ceballos, G.; Rurali, R. and Bachtold, A. A nanomechanical mass sensor with yoctogram resolution. *Nat. Nanotechnol.* **2012**, *7*, 301–304.
68. Ndieyira, J.; Watari, M.; Barrera, A.; Zhou, D.; Vöggtli, M.; Batchelor, M.; Cooper, M.; Strunz, T.; Horton, M. and Abell, C. Nanomechanical detection of antibiotic–mucopeptide binding in a model for superbug drug resistance. *Nat. Nanotechnol.* **2008**, *3*, 691–696.

69. Kosaka, P. M.; Tamayo, J.; Ruz, J. J.; Puertas, S.; Polo, E.; Grazu, V.; de la Fuente, J. and Calleja, M. Tackling reproducibility in microcantilever biosensors: A statistical approach for sensitive and specific end-point detection of immunoreactions. *Analyst* **2013**, 138, 863-872.
70. Soccio, M.; Luongo, G.; Esteves, C.; Salvador-Matar, A.; Ahumada, O.; Rueda, D. R.; García-Gutierrez, M.; Lotti, N.; Munari, A. and Ezquerro, T. A. Thermomechanical response of a semicrystalline polymer in the vicinity of the melting by using microcantilever technology. *Appl. Phys. Lett.* **2014**, 104, 251904.
71. Ahumada, O.; Perez-Madrigal, M. M.; Ramirez, J.; Curc6, D.; Esteves, C.; Salvador-Matar, A.; Luongo, G.; Armelin, E.; Puiggali, J. and Aleman, C. Sensitive thermal transitions of nanoscale polymer samples using the bimetallic effect: application to ultra-thin polythiophene. *Rev. Sci. Instrum.* **2013**, 84, 053904.
72. Rebollar, E.; Sanz, M.; Esteves, C.; Mart6nez, N. F.; Ahumada, O. and Castillejo, M. Gold coating of micromechanical DNA biosensors by pulsed laser deposition. *J. Appl. Phys.* **2013**, 112, 084330.
73. Bumbu, G.-G.; Wolkenhauer, M.; Kircher, G.; Gutmann, J. S. and Berger, R. Micromechanical cantilever technique: A tool for investigating the swelling of polymer brushes. *Langmuir* **2007**, 23, 2203-2207.
74. del Rey, M.; da Silva, R. A.; Meneses, D.; Petri, D. F. S.; Tamayo, J.; Calleja, M. and Kosaka, P. M. Monitoring swelling and deswelling of thin polymer films by microcantilever sensors. *Sens. Actuators B* **2014**, 204, 602-610.
75. Dominguez, C. M.; Ramos, D.; Mendieta-Moreno, J. I.; Fierro, J. L. G.; Mendieta, J.; Tamayo, J. and Calleja, M. Effect of water-DNA interactions on elastic properties of DNA self-assembled monolayers. *Sci. Rep.* **2017**, 7, 536.
76. Malvar, O.; Ruz, J. J.; Kosaka, P. M.; Dominguez, C. M.; Gil-Santos, E.; Calleja, M. and Tamayo, J. Mass and stiffness spectrometry of nanoparticles and whole intact bacteria by multimode nanomechanical resonators. *Natur. Commun.* **2016**, 7, 13452.
77. Naik, A. K.; Hanay, M. S.; Hiebert, W. K.; Feng, X. L. and Roukes, M. L. Towards single-molecule nanomechanical mass spectrometry. *Nature Nanotech.* **2009**, 4, 445-450.
78. Roussel, G.; Matagne, A.; De Bolle, X.; Perp6te, E. A. and Michaux, C. Purification, refolding and characterization of the trimeric Omp2a outer membrane porin from *Brucella Melitensis*. *Protein Expr. Purif.* **2012**, 83, 198-204.
79. Roussel, G.; Perp6te, E. A.; Matagne, A.; Tinti, E. and Michaux, C. Towards a universal method for protein refolding: The trimeric beta barrel membrane Omp2a as a test case. *Biotechnol. Bioeng.* **2013**, 110, 417-423.
80. Whitmore, L. and Wallace, B. Protein secondary structure analyses from circular dichroism spectroscopy: methods and reference databases. *Biopolymers* **2008**, 89, 392-400.
81. Lechuga G6mez, L.; 6lvarez-Sanch6z, V. and Tamayo De Miguel, F. J. Patent: US 7,646,494 B2.
82. Tamayo De Miguel, F. J.; Mertens, J. and Calleja-G6mez, M. Patent: US 7,978,344 B2.

83. Weiss, M. S.; Palm, G. J. and Hilgenfeld, R. Crystallization, structure solution and refinement of hen egg-white lysozyme at pH 8.0 in the presence of MPD. *Acta Crystallogr., Sect. D* **2000**, 56, 952-958.
84. Majorek, K. A.; Porebsky, P. J.; Dayal, A.; Zimmerman, M. D.; Jablonska, K.; Stewart, A. J.; Chruszcz, M. and Minor, W. Structural and immunologic characterization of bovine, horse, and rabbit serum albumins., *Mol. Immun.* **2012**, 52, 174-182.
85. Murayama, K. and Tomida, M. Heat-Induced secondary structure and conformation change of bovine serum albumin investigated by Fourier transform infrared spectroscopy. *Biochemistry* **2004**, 43, 11526-11532.
86. Meermans, F.; Atilgan, C.; Miles, A. J.; Bader, R.; Shang, W.; Matagne, A.; Wallace, B. A. and Koch, M. H. J. Consistent picture of the reversible thermal unfolding of hen egg-white lysozyme from experiment and molecular dynamics. *Biophys. J.* **2010**, 99, 2255-2263.
87. Knubovets, T.; Osterhout, J. J.; Connolly, P. J. and Klibanov, A. M. Structure, thermostability, and conformational flexibility of hen egg-white lysozyme dissolved in glycerol. *Proc. Natl. Acad. Sci. U.S.A.* **1999**, 96, 1262-1267.
88. Chen, C. R. and Makhatadze, G. I. Molecular determinants of temperature dependence of protein volume change upon unfolding. *J. Phys. Chem. B*, **2017**, 121, 8300-8310.
89. Chalikian, T. V. and Bresalauer, K. J. On volume changes accompanying conformational transitions of biopolymers. *Biopolymers* **1996**, 39, 619-626.
90. Maji, S. K.; Wang, L.; Greenwald, G. and Riek, R. Structure-activity relationship of amyloid fibrils. *FEBS Letters* **2009**, 583, 2610-2617.
91. Eisenberg, D. The discovery of the α -helix and β -sheet, the principal structural features of proteins. *Proc. Natl. Acad. Sci. U.S.A.* **2003**, 100, 11207-11210.
92. Martínez, N. F.; Kosaka, P. M.; Tamayo, J.; Ramírez, J.; Ahumada, O.; Mertens, J.; Hien, T. D.; Rijn, C. V. and Calleja, M. High throughput optical readout of dense arrays of nanomechanical systems for sensing applications. *Rev. Sci. Instrum.* **2010**, 81, 125109.
93. Puiggali-Jou, A.; del Valle, L. J.; Alemán, C. and Pérez-Madrigal, M. M. Weighing biointeractions between fibrin(ogen) and clot-binding peptides using microcantilever sensors. *J. Pept. Sci.* **2017**, 23, 162-171.
94. Barnes, J. R.; Stephenson, R. J.; Woodburn, C. N.; O'Shea, S. J.; Welland, M. E.; Rayment, T.; Gimzewski, J. K. and Gerber, Ch. A femtojoule calorimeter using micromechanical sensors. *Rev. Sci. Instrum.* **1994**, 65, 3793.
95. Zeth, K. and Thein, M. Porins in prokaryotes and eukaryotes: Common themes and variations. *Biochem. J.* **2010**, 431, 13-22.
96. Tamm, L. K.; Hong, H. and Liang, B. Folding and assembly of β -barrel membrane proteins. *Biochim. Biophys. Acta* **2004**, 1666, 250-263.
97. Moon, C. P.; Zaccai, N. R.; Fleming, P. J.; Gessmann, D. and Fleming, K. G. Membrane protein thermodynamic stability may serve as the energy sink for sorting in the periplasm. *Proc. Natl. Acad. Sci. U.S.A.* **2013**, 110, 4285-4290.

98. Kleinschmidt, J. H. Folding and stability of monomeric β -barrel membrane proteins. In Protein-Lipid Interactions, 1st ed.; Tamm, L. K. Ed; Wiley VCH: Weinheim, **2006**, pp 27-56..
99. Fioroni, M.; Dworeck, T. and Rodríguez-Ropero, F. β -Channels in proteins as tools in Nanotechnology. In Advances in Experimental Medicine and Biology, Vol. 794, **2014**.
100. Greenfield, N. J. Using circular dichroism collected as a function of temperature to determine the thermodynamics of protein unfolding and binding interactions. *Nat. Protoc.* **2006**, 1, 2891-2899.
101. Saha, P.; Manna, C.; Chakrabarti, J. and Ghosh, M. Reversible thermal unfolding of a yfdX protein with chaperone-like activity. *Sci. Rep.* **2016**, 6, 29541.
102. Sukumaran, S.; Hauser, K.; Maier, E.; Benz, R. and Mäntele, W. Structure-Function Correlation of Outer Membrane Protein Porin from Paracoccus Denitrificans. *Biopolymers* **2006**, 82, 344-348.
103. Sukumaran, S.; Zscherp, C. and Mantele, W. Investigation of the thermal stability of porin from paracoccus denitrificans by site-directed mutagenesis and fourier transform infrared spectroscopy. *Biopolymers* **2004**, 74, 82-86.
104. Solov'eva, T. F.; Likhatskaya, G. N.; Khomenko, V. A.; Stenkova, A. M.; Kim, N. Y.; Portnyagina, O. Y.; Novikova, O. D.; Trifonov, E. D.; Nurminski, E. A. and Isaeva, M. P. A Novel OmpY porin from yersinia pseudotuberculosis: structure, channel-forming activity and trimer thermal stability. *J. Biomol. Struct. Dyn.* **2011**, 28, 517-533.
105. Stoppel, W. L.; White, J. C.; Horava, S. D.; Bhatia, S. R. and Roberts, S. C. Transport of biological molecules in surfactant-alginate composite hydrogels. *Acta Biomater.* **2011**, 7, 3988-3998.
106. Hill, S. E.; Miti, T.; Richmon, T. and Muschol, M. Spatial extent of charge repulsion regulates assembly pathways for lysozyme amyloid fibrils. *PLoS ONE* **2011**, 6, e18171.
107. Alvarez, M. and Lechuga, L. M. Microcantilever-based platforms as biosensing tools. *Analyst* **2010**, 135, 827-836.
108. Hwang, K. S.; Eom, K.; Lee, J. H.; Chun, D. W.; Cha, B. H.; Yoon, D. S.; Kim, T. S. and Park, J. H. Dominant surface stress driven by biomolecular interactions in the dynamical response of nanomechanical microcantilever. *Appl. Phys. Lett.* **2006**, 89, 173905.
109. Thakur, G.; Jiang, K.; Lee, D.; Prashanthi, K.; Kim, S. and Thundat, T. Investigation of pH-induced protein conformation changes by nanomechanical deflection. *Langmuir* **2014**, 30, 2109-2116.
110. Ali, M.; Nasir, S.; Nguyen, Q. H.; Sahoo, J. K.; Tahir, M. N.; Tremel, W. and Ensinger, W. Metal ion affinity-based biomolecular recognition and conjugation inside synthetic polymer nanopores modified with iron-terpyridine complexes. *J. Am. Chem. Soc.* **2011**, 133, 17307-17314.
111. Hou, X.; Guo, W. and Jiang, L. Biomimetic smart nanopores and nanochannels. *Chem. Soc. Rev.* **2011**, 40, 2385-2401.

112. Zhang, X.; Fu, W.; Palivan, C. G. and Meier, W. Natural channel protein inserts and functions in a completely artificial, solid-supported bilayer membrane. *Sci. Rep.* **2013**, *3*, 2196.
113. Hall, A. R.; Scott, A.; Rotem, D.; Mehta, K. K.; Bayley, H. and Dekker, C. Hybrid pore formation by directed insertion of α -haemolysin into solid-state nanopores. *Nat. Nanotechnol.* **2010**, *5*, 874-877.
114. Balme, S.; Janot, J. M.; Berardo, L.; Henn, F.; Bonhenry, D.; Kraszewski, S.; Picaud, F. and Ramseyer, C. New bioinspired membrane made of a biological ion channel confined into the cylindrical nanopore of a solid-state polymer. *Nano Lett.* **2011**, *11*, 712-716.

CHAPTER 5:

Incorporation of Omp2a onto
nanoperforated membranes

SUMMARY

First, the production of nanoporated poly(lactic acid) (PLA) free-standing nanomembranes (FsNMs) has been prepared and optimized using a two-step process: (1) spin-coating a mixture of immiscible polymers to provoke phase segregation and formation of appropriated nanofeatures (i.e. phase separation domains with dimensions similar to the entire film thickness); and (2) selective solvent etching to transform such nanofeatures into nanoporations.

Later, bioinspired free-standing nanomembranes (FSNMs) for controlled ion transport have been tailored by immobilizing the Omp2a β -barrel membrane protein inside nanoporations created in flexible poly (lactic acid) (PLA) nanomembranes. The protein confined inside the nanopores of PLA FSNMs preserves the β -barrel structure and organizes in ovoid aggregates. The transport properties of Na^+ , K^+ , and Ca^{2+} across non-perforated PLA, nanoporated PLA, and Omp2a-filled nanoporated PLA have been monitored by measuring the nano- membrane resistance with electrochemical impedance spectroscopy (EIS). The incorporation of nanoporations enhances the transport of ions across PLA nanomembranes, whereas the functionality of immobilized Omp2a is essential to exhibit effects similar to those observed in biological nanomembranes. Indeed, Omp2a-filled nanoporated PLA nanomembranes exhibit stronger affinity towards Na^+ and Ca^{2+} ions than towards K^+ . In summary, this work provides a novel bioinspired strategy to develop mechanically stable and flexible FSNMs with channels for ion transport, which are precisely located inside artificial nanoporations, thus holding great potential for applications in biofiltration and biosensing.

Publications derived from this work:

Puiggali-Jou, A.; Medina, J.; del Valle L. J. and Alemán, C. Nanoporations in poly(lactic acid) free-standing nanomembranes to promote interactions with cell filopodia. *Eur Polym J.* **2016**, 75, 552-564.

Puiggali-Jou, A.; Pérez-Madrigal, M. M.; del Valle, L. J.; Armelin, E.; Casas, M. T.; Michaux, C.; Perpète, E. A.; Estrany, F. and Alemán, C. Confinement of a β -barrel protein in nanoporated free-standing nanomembranes for ion transport. *Nanoscale* **2016**, 8, 16922-16935.

5.1 Introduction

The term *giant nanomembrane* was coined by Kunitake *et al.*¹ to denote self-supporting membranes with thickness (L) from 1 to 100 nm and an aspect ratio of size and thickness higher than 10^6 . Besides such characteristics, these free-standing nanomembranes (FsNMs) exhibit other special properties, such as easiness of handling, low weight, high flexibility, robustness and, in some cases, transparency². In the last decade, polymeric FsNM, have emerged as versatile elements for biomedical applications as varied as overlapping therapy, burn wound infection treatment, antimicrobial platforms, scaffolds for tissue engineering, drug-loading and delivery systems, biosensors, etc., as recently reviewed Pérez-Madrigal *et. al.*³.

Among the synthetic polymers used to prepare FsNMs for biomedical applications, linear aliphatic polyesters, such as poly(lactic acid) (PLA) and poly(tetramethylene succinate) (PE44), have been extensively chosen since their biodegradation rate and mechanical properties can be easily controlled through variations in their molecular weight³⁻⁷. Within the specific case of PLA, Takeoka and co-workers⁸ developed FsNMs with $L= 23\pm 5$ nm by spin-coating polymer solutions onto poly(vinyl alcohol) (PVA) sacrificial films. The mechanical properties and adhesion strength exhibited by such PLA nanosheets, encouraged the analysis of their feasibility as a wound dressing^{8,9}. On the other hand, Pensabene *et al.*¹⁰ studied the biocompatibility, adhesion and proliferation activity of several cell types onto PLA FsNMs with an average thickness of $L= 320\pm 27$ nm, which were also prepared by spin-coating. Both, immortalized cell lines and primary cell lines cultured on those FsNMs exhibited good morphological and metabolic features and the ability to fully differentiate. Moreover, the effect of an underlying substrate on the interaction between cells and PLA FsNMs was recently investigated by collecting spin-coated nanosheets on both a stainless steel mesh and a SiO₂ substrate⁵. Although topological and mechanical properties of PLA FsNMs did not influence cell viability after 24 h of culturing, cells did geometrically sense the stiffness of the underlying material, thus affecting the adhesion geometry.

5.2 Materials and methods

Materials: PLA, a product of Natureworks (polymer 2002D), was kindly supplied by Nupik International (Polinyà, Spain). According to the manufacturer, this PLA has a D content of 4.25%, a residual monomer content of 0.3%, density of 1.24 g/cc, glass transition temperature (T_g) of 58 °C and melting point of 153 °C. The number and weight average molecular weights and polydispersity index, as determined by GPC, were $M_n=98,100$ g/mol, $M_w=181,000$ g/mol and 1.85, respectively. Polyethylene glycol (PEG) with $M_w=35,000$ g/mol was purchased from Sigma-Aldrich (Germany). PVA (87-89% hydrolysed) with $M_w=13,000 - 23,000$ g/mol was purchased from Sigma-Aldrich (USA). Dry trichloromethane stabilized with 50 ppm of amylene DS-ACS (99.9%) was purchased from Panreac Quimica S.A.U. (Spain). 1,1,1,3,3,3-Hexafluoroisopropanol (HFIP) was purchased from Apollo Scientific Limit (UK). SiO₂ cover-glasses of 14 mm of diameter were acquired to Agar Scientific (France) while the glass cover slips, 22×22 mm² were purchased at Menzel-Glässer (Germany). For cell culture experiments, Madin-Darby Canine Kidney (MDCK) and African green monkey kidney (Vero) cells were purchased from ATCC, USA. Dulbecco's phosphate buffered saline (PBS) solution without calcium chloride and magnesium chloride, Dulbecco's modified Eagle's medium (DMEM, with 4500 mg/L of glucose, 110 mg/L of sodium pyruvate and 2 mM of L-glutamine), penicillin-streptomycin, 3-(4,5-dimethylthiazol-2-yl) 2,5-diphenyltetrazolium bromide (MTT, 97.5%) and trypsin EDTA solution (0.05% trypsin, 0.02% EDTA) were all purchased from Sigma-Aldrich, (USA). Fetal bovine serum (FBS) and trypan blue stain (0.4%) were purchased from Gibco, UK.

Preparation of solutions and mixtures: For the fabrication of non-perforated PLA FSNMs, 50, 25 and 10 mg/mL polymer solutions in chloroform were prepared. Perforated FSNMs were obtained by blending PLA and PEG or PVA. PLA-PEG blends with 50:50, 60:40, 80:20 and 90:10 PLA:PEG v/v ratios were prepared by combining PLA (10 mg/mL) and PEG (10 mg/mL) chloroform solutions. On the other hand, PLA-PVA blends with 80:20 and 90:10 PLA:PVA v/v ratios were obtained by mixing PLA (10 mg/mL) and PVA (10 mg/mL) HFIP solutions.

Preparation of nanoporated free-standing nanomembranes (FSNMs):

Firstly, a PVA solution in milliQ water (100 mg/mL) was spin-coated onto a clean glass slip or ITO substrate at 2500 rpm for 60 s to obtain a sacrificial layer. Before using, substrates were cleaned by successive sonication in acetone, ethanol and water (5 min) and dried with clean dry air. After this, a PLA:PVA solution with 90:10 or 99:1 v/v ratio, which was obtained by mixing PLA (10 mg/mL) and PVA (10 mg/mL) HFIP solutions and stirring vigorously (three times at 1000 rpm for 30 s each one using a Vortex-type mixer), was spin-coated at 7000 rpm for 60 s. Finally, the substrate coated with the PLA-PVA NM was immersed into milliQ water for separation of the NM from the substrate (i.e. dissolution of the sacrificial layer) as well as for the creation of the nanoporations (i.e. dissolution of PVA phases in PLA-PVA NMs).

5.3 Nanoporations in poly(lactic acid) free-standing nanomembranes

The aim of this work is to improve the applicability of PLA FsNMs as flexible bioactive substrates for cell culture by introducing uniformly distributed nanoporations in a controllable manner. More specifically, cell adhesion and spreading have been significantly enhanced by adapting the dimensions of nanopores, which might penetrate the entire thickness of the ultra-thin film, to those of cell nanofeatures (*i.e.* promoting cell–substrate interactions). For this purpose, nanoporated FsNMs have been prepared by spin-coating mixtures of PLA and a polymer with poor affinity towards such polyester, to develop phase-segregated ultra-thin films with a thickness comparable to the dimensional scale of the phase separation domains. Application of the selective solvent etching technique, which was introduced by Walheim *et al.*¹¹ to illustrate the influence of the relative solubility of polymer blends on the structure of the films, to the biphasic nanosheets has resulted in the formation of perforated PLA FsNMs. The combination of spin-coating and selective solvent etching was recently employed by Zhang and Takeoka¹² to study the phase-separation

mechanism of immiscible polystyrene (PS): poly(methyl methacrylate) (PMMA) mixtures and to prepare nanoporated PMMA ultra-thin films.

In this work, phase-segregated ultra-thin films have been prepared by combining PLA with polyethylene glycol (PEG) and PVA. However, surface nanofeatures compatible with the fabrication of nanoporated FsNMs via selective solvent etching were only detected in PLA-PVA ultra-thin films. Cell viability assays using non-perforated and perforated PLA FsNMs have proved that the behavior of the latter as bioactive substrate is much better than that of the former, even though it drastically depends on the nanopore dimensions.

5.3.1 Methods

Preparation of free standing nanomembranes: FsNMs were prepared by applying the procedure described by Vendamme and co-workers¹³, which was successfully used in previous works^{6,7,14}. Firstly, a PVA solution in milliQ water (100 mg/mL) was spin-coated onto a glass slip, cleaned by successive sonication in acetone, ethanol, and water, at 2500 rpm for 60 s to obtain a sacrificial layer. After this, PLA, PLA:PEG and PLA:PVA solutions were spin-coated at speeds ranging from 2500 to 7000 rpm for 1 min to obtain ultra-thin films onto the sacrificial layer. Finally, samples were immersed into milliQ water for the separation of the nanomembrane from the substrate (*i.e.* dissolution of the sacrificial layer) as well as for the creation of pores (*i.e.* dissolution of PEG and PVA phases in PLA-PEG and PLA-PVA nanomembranes).

Profilometry: Film thickness measurements were carried out using a Dektak 150 stylus profilometer (Veeco, Plainview, NY). Different scratches were intentionally provoked on the nanomembranes and measured to allow statistical analysis of data. At least eighteen independent measurements were performed for two samples of each examined condition. Imaging of the films was conducted using the following optimized settings: tip radius= 65.5 μm ; stylus force= 3.0 mg; scan length= 7 mm; and speed= 100 $\mu\text{m/s}$.

Atomic force microscopy (AFM): The surface morphology and topography of nanomembranes supported onto glass slips, before and after application of selective solvent etching, were studied by AFM. Images were obtained with a Molecular Imaging PicoSPM using a NanoScope IV controller under ambient conditions. The tapping mode AFM was operated at constant deflection (*i.e.* vertical constant force with triangular shaped gold-coated silicon nitride). The row scanning frequency was set to 0.87 or 0.68 Hz, depending on the sample response, and the physical tip sample motion speed was 10 mm/s.

RMS roughness (Rq) and profile sections of the images were determined using the statistics application and tools of the NanoScope Analysis software version 1.20 (Bruker), which calculates the average considering all the values recorded in the topographic image with exception of the maximum and the minimum. The scan window sizes were 10×10 or 2×2 μm².

Scanning electron microscopy (SEM): Detailed inspection of nanomembranes before and after application of selective solvent etching was conducted by scanning electron microscopy. A Focus Ion Beam Zeiss Neon 40 instrument (Carl Zeiss, Germany) equipped with an energy dispersive X-ray (EDX) spectroscopy system and operating at 1 and 5 kV for characterization of systems without and with cells, was used. Nanomembranes supported onto glass slips were mounted on a double-sided adhesive carbon disc. FsNMs were, firstly, mounted using silver staining and, after this, were sputter-coated with an ultra-thin carbon layer (6-10 nm) to prevent sample charging problems. The diameter of the perforations was measured with the SmartTiff software from Carl Zeiss SMT Ltd.

Wettability: Static contact angle measurements with the sessile drop method were recorded and analysed at room temperature on an OCA-15EC contact angle meter from DataPhysics Instruments GmbH with SCA20 software (version 4.3.12 build 1037). The solvents, which were used as received, considered for this study were:

- MilliQ water;

- *N,N*-dimethyl formamide (DMF; Panreac, ultra-high purity);
- Ethylene glycol (EG; Merck >99.5%);

The sessile drop was gently put on the surface of non-perforated and nanoporated PLA using a micrometric syringe with a proper metallic needle (Hamilton 500 μ L). The ellipse method was used to fit a mathematical function to the measured drop contour. For each solvent and PLA system, 20 drops were examined.

Cell adhesion and cell proliferation assays: Vero and MDCK cells were cultured in DMEM supplemented with 10% FBS, 1% penicillin and 1% streptomycin at 37°C in a humidified atmosphere of 5% CO₂ in air. Culture media were changed every three days. For sub-culture, cell monolayers were rinsed with PBS and detached by incubating them with 0.25% trypsin/EDTA for 5 min at 37°C. Finally, cells were resuspended in 5 mL of fresh medium and their concentration was determined by counting at the Neubauer camera using 0.4% trypan blue as dye vital.

Perforated PLA nanomembranes were prepared by spin-coating on glass cover slips of 14 mm of diameter. Samples were placed in plates of 24 wells and sterilized using UV light for 15 min in a laminar flux cabinet. Controls were simultaneously performed by culturing cells on the surfaces of SiO₂ wafers and non-perforated PLA nanomembranes. For adhesion assays, an aliquot of 1 mL containing 6 \times 10⁴ cells was deposited on the nanomembrane of each well. After 24 h non-attached cells were washed out while attached cells were quantified. For proliferations assays, the aliquot deposited on each well contained 4 \times 10⁴ cells. Quantification of proliferated cells was performed after 7 days of culture.

The percentage of cells adhered and proliferated was calculated through the MTT [3-(4,5-dimethylthiazol-2-yl)-2,5-diphenyltetrazolium bromide] assay. This determines the cell viability⁴⁵. Results were normalized to the non-perforated PLA control and represented as relative percentages. Specifically, 50 μ L of MTT solution (5 mg/mL in PBS) were added to each well. After 2 h of incubation, samples were washed twice with PBS and stored in clean wells. In order to dissolve formazan crystals, 200 μ L of DMSO/methanol/water (70/20/10% v/v) were added. Finally, the absorbance was

measured at 570 nm through an ELISA reader (Biochrom, UK). Results were derived from the average of four replicates ($n=4$).

After culture, samples were fixed in a 2.5% formaldehyde PBS solution overnight at 4 °C. Then, they were dehydrated by washing in an alcohol battery (30°, 40°, 70°, 95° and 100°) at 4 °C for 15 min per wash. Finally, samples were air-dried and sputter-coated with carbon before SEM observation.

5.3.2 Results and discussion

Non-perforated PLA free standing nanomembranes

PLA FsNMs have been extensively studied^{3,5-10} and, therefore, the aim of this subsection is only to establish the influence of spin-coater controllable parameter in their most relevant nanofeatures. This information is relevant for the choice of the requirements subsequently employed in the preparation of perforated nanofilms.

In order to adjust the thickness, different PLA solutions in chloroform were spin-coated onto glass slides for 1 min using different conditions. **Table 5.3.1** indicates that the thickness of the films, as determined by contact profilometry, is severely affected by both the angular speed and the polymer concentration in the solution. Thus, although the variation of the thickness is inversely proportional to the speed in all cases, this phenomenon is more pronounced for the higher PLA concentrations, especially for the 50 mg/mL PLA solution. Among the tested conditions, membranes of nanometric thickness were only obtained with the lowest polymer concentration (10 mg/mL) and the highest spin-coater speed (7000 rpm). **Figure 5.3.1a** evidences that PLA nanomembranes prepared under such conditions are very homogeneous and smooth, the roughness being of only $Rq=1.1\pm0.2$ nm.

After this, PLA ultra-thin films were deposited onto a PVA sacrificial layer of $L=238\pm43$ nm and $Rq=2.6\pm0.8$ nm using the above selected condition. After coating, samples were immersed into water for the separation of the PLA membrane. Profilometry and AFM measures indicated that both the thickness ($L=238\pm43$ nm) and roughness ($Rq=2.6\pm0.8$) increased significantly with respect to the membranes

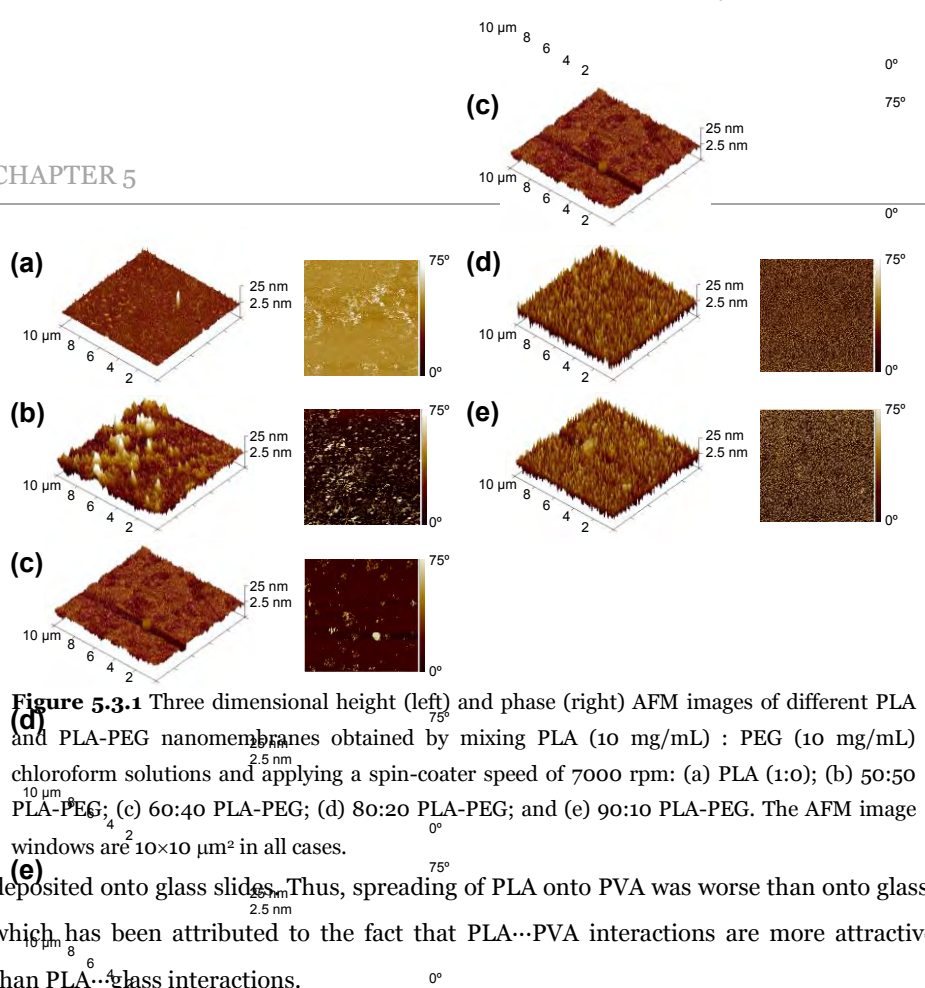


Figure 5-3.1 Three dimensional height (left) and phase (right) AFM images of different PLA and PLA-PEG nanomembranes obtained by mixing PLA (10 mg/mL) : PEG (10 mg/mL) chloroform solutions and applying a spin-coater speed of 7000 rpm: (a) PLA (1:0); (b) 50:50 PLA-PEG; (c) 60:40 PLA-PEG; (d) 80:20 PLA-PEG; and (e) 90:10 PLA-PEG. The AFM image windows are $10 \times 10 \mu\text{m}^2$ in all cases.

deposited onto glass slides. Thus, spreading of PLA onto PVA was worse than onto glass, which has been attributed to the fact that PLA...PVA interactions are more attractive than PLA...glass interactions.

PLA-PEG nanomembranes

Fabrication of nanoporous FSNMs using a technique based on the phase-segregation of two polymers and subsequent elimination of one of them via selective solvent etching requires fulfilment of the following conditions:

- The two polymers must be soluble in a common solvent to facilitate the spin-coating process.
- The two polymers must be immiscible to promote the phase separation.
- The two polymers should have similar molecular weights to facilitate the formation of nanofeatures (*i.e.* nanopores).
- The polymer used to fabricate the nanomembrane must remain unaltered by the solvent employed to dissolve the less abundant polymer.

In this work, the first attempt to obtain nanoporous FSNMs was done using PLA and PEG. Both materials are soluble in chloroform, while PLA and PEG are insoluble and

soluble in water, respectively. PLA-PEG nanomembranes were prepared by spin-coating 50:50, 60:40, 80:20 and 90:10 PLA:PEG mixtures as described in the Methods section, and applying 7000 rpm for 1 min. **Table 5.3.2** lists the thickness and roughness of the resulting nanomembranes, which are compared with those achieved for PLA under the same conditions, while the corresponding AFM images are displayed in **Figure 5.3.1**.

Although the incorporation of PEG affects significantly to both the thickness and roughness of PLA nanomembranes, these variations are apparently independent on the PEG concentration. Furthermore, no particular nanofeature is detected in the surface topography of 50:50, 80:20 and 90:10 PLA-PEG nanofilms, even though small shallow cavities are detected at the 60:40 membrane. The characteristics of PLA-PEG ultra-thin films are not consistent with a phase separation process and can be attributed to different reasons, as for example: (1) the evaporation rate of chloroform is not appropriated to produce instabilities at the polymer-polymer interface¹⁶; (2) the difference between the molecular weights of PLA and PEG is too large for the formation of PEG-like pores in the PLA matrix¹⁷; and (3) the solubility of PLA and PEG in chloroform is too different. Swaminathan *et al.*¹⁷ studied the physical properties of PLA-PEG membranes ($L= 35\pm 5 \mu\text{m}$) prepared by spin solvent-casting using PEG samples with different molecular weight.

Table 5.3.1 Physical parameters of non-perforated and perforated PLA NMs derived from 90:10 and 99:1 PLA:PVA mixtures: Average diameter of the nanopores (ϕ), root-mean-square roughness (Rq) ($5\times 5 \mu\text{m}^2$ surface area) and film thickness (L), which also corresponds to the depth of the pores.

[PLA]	2500 rpm	4000 rpm	7000 rpm
50 mg/mL	1616±148	1165±88	-
25 mg/mL	277±61	237±126	-
10 mg/mL	190±42	136±19	73±42

Membranes were found to be semi-porous, the surface pore size depending on the PEG molecular weight. These findings suggested that the PLA:PEG mixtures used in this work are not the most appropriated for the fabrication of perforated PLA nanomembranes since the dependence on PEG characteristics is too large.

PLA-PVA nanomembranes

In order to overcome the limitations detected in PLA-PEG nanomembranes, PEG was replaced by PVA in the spin-coated mixtures. Both PLA and PVA are soluble in HFIP. This solvent exhibits a low evaporation temperature (58.2 °C) and, therefore, a high evaporation rate is expected during the spin-coating process. However, it should be remarked that the sacrificial layer used to transform the supported PLA-PVA ultra-thin films into the PLA FsNM was also made of PVA. Therefore, the sacrificial layer may be significantly altered by the dropping of the HFIP solution mixture onto its surface, affecting the formation of the PLA-PVA film. In order to evaluate the impact of such effect two complementary experiments were performed.

First, a PLA solution (10 mg/mL) in HFIP was dropped onto a PVA sacrificial layer and spin-coated at 7000 rpm for 1 min. The resulting nanomembrane was characterized by AFM before and after being treated with water to eliminate the sacrificial layer (**Figures 5.3.2a and b**, respectively). It is worth noting that both the supported film and the FsNM exhibit a porous topography, even though the depth of such pores is smaller than the membrane thickness (**Figure 5.3.2c**). These results clearly indicate the HFIP affects the PVA sacrificial layer during the spin-coating process. In spite of this, the apparition of nanofeatures (*i.e.* pores) in the PLA nanomembrane should be considered as good result within the context of this work.

In the second experiment, a droplet of HFIP was deposited onto the PVA sacrificial layer ($L= 342\pm 4$ nm and $Rq= 0.3\pm 0.1$ nm) and spin-coated at 7000 rpm for 1 min. After this, the thickness was not affected by the solvent ($L= 344\pm 48$ nm) while the roughness increased considerably ($Rq= 0.5\pm 0.1$ nm). This variation, which is fully consistent with the apparition of nanofeatures in the previous experiment (**Figures 5.3.2a and b**), suggests that the instabilities created by the addition of a PLA:PVA solution in HFIP onto the PVA sacrificial layer could facilitate the fabrication of perforated PLA FsNMs. PLA-PVA nanomembranes were fabricated using 80:20 and 90:10 PLA:PVA mixtures in HFIP using the process schematically depicted in **Figure 5.3.3**. AFM topographic and phase images are displayed in **Figure 5.3.4a and b**, respectively. As it can be seen, nanofeatures obtained for both compositions are apparently compatible with the

formation of PVA nanophases crossing the thickness of the whole PLA nanomembrane (Table 5.3.2).

However, comparison between the 80:20 and 90:10 PLA-PVA films reveals important differences related with the frequency and dimensional uniformity of PVA nanophases. Thus, 80:20 nanomembranes are not uniform, the dimensions and frequency of the nanophases depending on the examined region. In contrast, 90:10 films exhibit a relatively homogeneous distribution of PVA nanophases of similar dimensions. Such differences remained in the corresponding PLA FsNMs produced by selective water etching (Figure 5.3.4b and d). A photograph displaying both a supported 90:10 PLA-PVA ultra-thin film and a nanoporated 90:10 PLA FsNM floating in water is presented in Figure 5.3.3b.

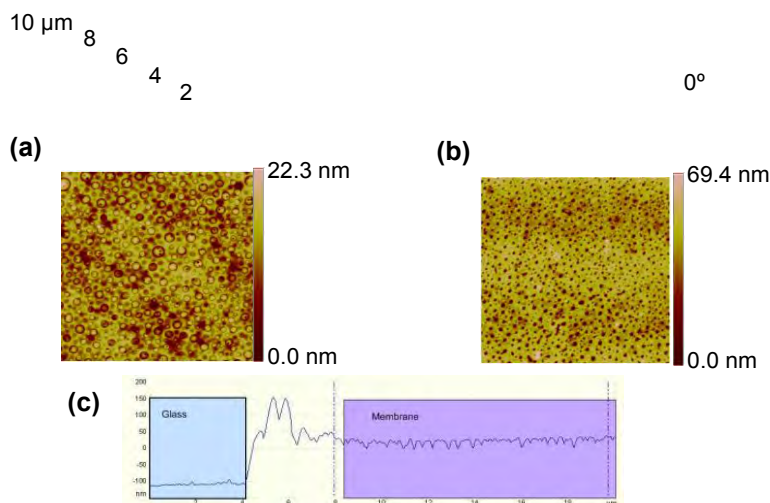


Figure 5.3.2 (a) Three dimensional height (left) and phase (right) AFM images of PLA supported nanomembrane prepared using a 10 mg/mL polymer solution in chloroform and a spin-coater speed of 7000 rpm. AFM images of PLA (b) the supported nanomembrane and (c) the corresponding FsNM prepared using a 10 mg/mL polymer solution in HFIP and a spin-coater speed of 7000 rpm. The FsNM was obtained after removing the sacrificial layer of the supported nanomembrane. The AFM image windows are $10 \times 10 \mu\text{m}^2$ in all cases. (d) Representative profilometry of supported. The blue, uncoloured and purple regions correspond to the glass support, the PVA sacrificial layer and the PLA membrane, respectively.

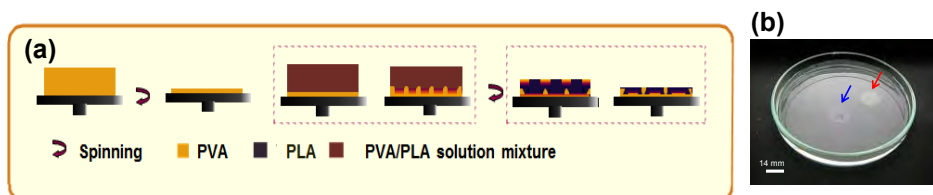


Figure 5.3.3 (a) Schematic representation of the procedure used to prepare perforated PLA nanomembranes from PLA-PVA ultra-thin films by the spin-coating technique. (b) 90:10 PLA-PVA nanomembrane supported onto a SiO₂ wafer (blue arrow) and 90:10 PLA FsNM (red arrow) floating on ultrapure water.

On the other hand, AFM images indicate that the pores obtained for the two compositions penetrate the entire thickness of the film, giving rise to perforations. Furthermore, SEM micrographs corroborate that perforations are irregular in terms of both distribution and dimensions in the FsNMs derived from the 80:20 PLA:PVA composition. Accordingly, regions with many small nanopores coexist in the same sample with regions exhibiting relatively large and infrequent pores. In contrast, the 90:10 composition results in FsNMs with regular distribution of pores.

Table 5.3.2 Thickness (L) and RMS roughness (R_q) of PLA, PLA-PEG and PLA-PVA ultra-thin films prepared in this work. Observed nanofeatures are also indicated.

	L (nm)	R_q (nm)	Nanofeatures
PLA (chloroform) ^a	238±43	1.1±0.2	-
PLA-PEG (50:50) ^b	45±2	4.0±1.0	-
PLA-PEG (60:40) ^b	48±2	1.8±0.1	Shallow surface cavities
PLA-PEG (80:20) ^b	48±2	4.6±0.3	-
PLA-PEG (90:10) ^b	50±4	6.0±1.3	-
PLA (HFIP) ^c	213±20	2.8±0.3	-
PLA-PVA (80:20) ^d	74±3	20.4±6.2	Nanophases penetrating the entire film
PLA-PVA (90:10) ^d	62±8	6.7±2.3	Nanophases penetrating the entire film
PLA-PVA (90:10) (with vigorous stirring) ^d	96±2	3.3±1.2	Nanophases penetrating the entire film

^a PLA ultra-thin film prepared by spin-coating a 10 mg/mL polymer chloroform solution. ^b PLA-PEG ultra-thin films prepared using by spin-coating PLA (10 mg/mL) : PEG (10 mg/mL) mixtures in chloroform. ^c PLA ultra-thin film prepared by spin-coating polymer (10 mg/mL) HFIP solution. ^d PLA-PVA ultra-thin films prepared using by spin-coating PLA (10 mg/mL) : PVA (10 mg/mL) mixtures in HFIP.

Characterization of perforated free-standing nanomembranes

In order to enhance control over the distribution and diameter of nanoporations obtained in FsNMs derived from 90:10 PLA-PVA nanomembranes, the mixing process of the two polymer solutions in HFIP was improved by applying vigorous stirring. More specifically, the 90:10 PLA:PVA mixture was stirred three times at 1000 rpm for 30 seconds each one using a Vortex-type mixer. Hereafter, the resulting PVA-PLA nanomembranes as well as the corresponding PLA FsNMs have been denoted PLA-PVA(stir) and PLA(stir) to differentiate them from those obtained without vigorous stirring. **Figure 5.3.5** displays illustrative AFM images of PLA-PVA(stir) ultrathin films and PLA(stir) FsNMs, respectively. The main difference between the supported 90:10 PLA-PVA and PLA-PVA(stir) nanomembranes (**Figure 5.3.4c** and **Figure 5.3.5a**, respectively) refers to the dimensions of the segregated nanophases, which are significantly smaller for the latter than for the former. After selectively solvent etching, the resulting nanoporations (**5.3.5b**) exhibit not only a diameter reduction but also higher dimensional homogeneity.

SEM micrographs provided in **Figure 5.3.6** display nanometric details on nanoporated PLA and PLA(stir) FsNMs derived from 90:10 mixtures. **Figure 5.3.6a** illustrates the nanopores typically found in perforated 90:10 PLA, while submicrometric perforations rarely found in such membranes are shown in **Figure 5.3.6b**. The distribution of homogeneous nanopores in 90:10 PLA(stir) is evidenced in **Figures 5.3.6c and d** (low and high magnification, respectively), while details of such pores are given in **Figure 5.3.6e and f**. Finally, **Figure 5.3.6g** evidences the presence of nanopores at the two sides of the same 90:10 PLA(stir) FsNM. This indirectly proves that nanopores penetrate the entire thickness of the film, transforming into nanoporations.

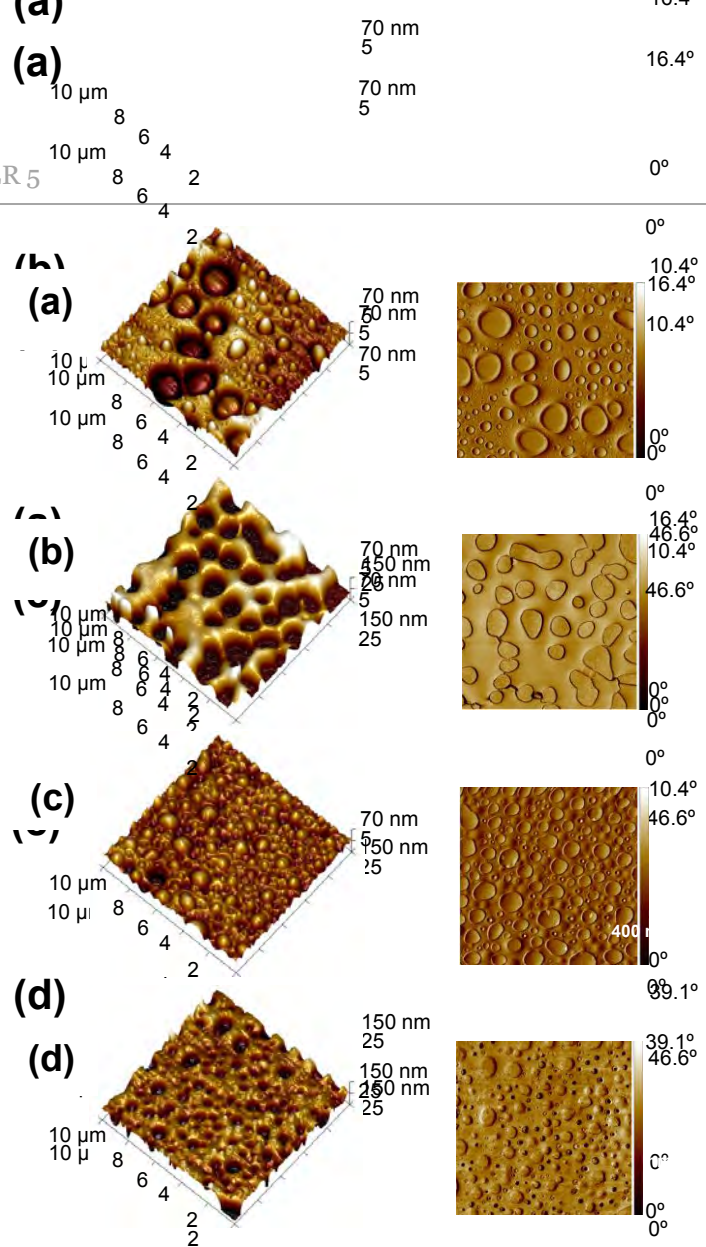


Figure 5.3.4 Three dimensional height (left) and phase (right) AFM images of PLA-PVA supported nanomembranes prepared using a (a,b) 80:20 and (c,d) 90:10 PVA:PLA mixture in HFIP. Nanoperforated PLA FSNMs obtained via selective water etching using the (b) 80:20 and (d) 90:10 PLA-PVA supported nanomembranes: The AFM image windows are 10×10 μm² in all cases.

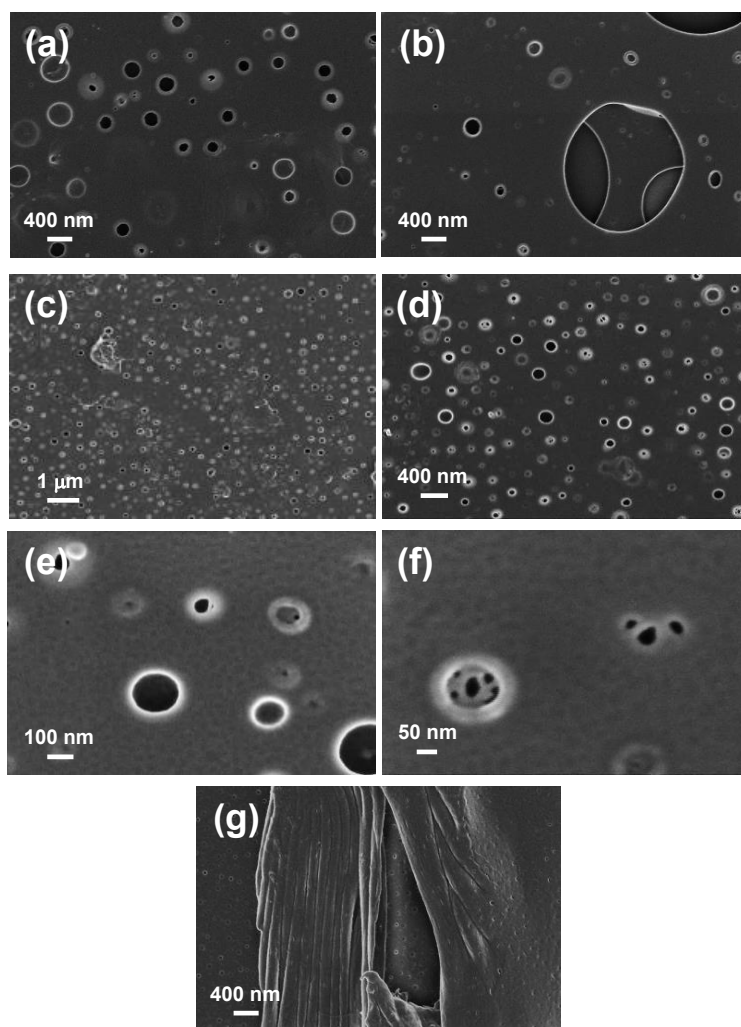


Figure 5.3.5 SEM micrographs of nanoporous (a and b) 90:10 PLA and (c-g) 90:10 PLA(stir) FsNMs prepared using 90:10 PLA:PVA mixtures in HFIP. Details on a-f are described in the text. A folded 90:10 PLA(stir) FsNM showing the presence of nanoporations at the two sides is displayed in (g). This SEM image reflects that nanoporations cross the thickness of the nanomembrane.

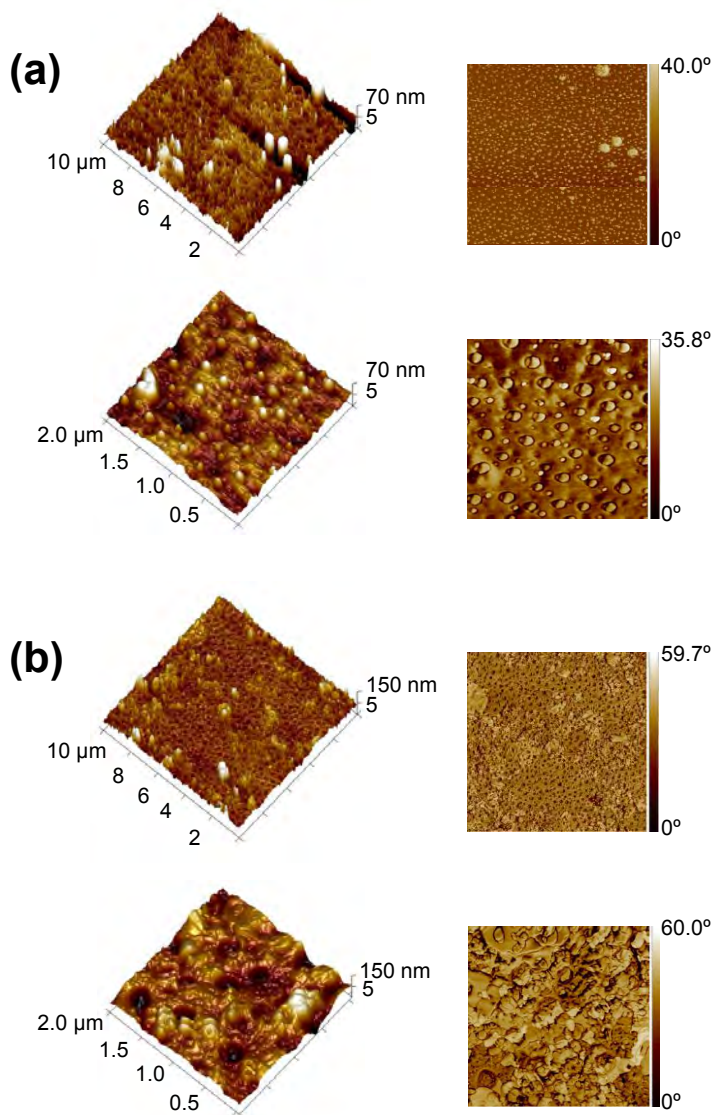


Figure 5.3.6 Three dimensional height (left) and phase (right) AFM images of (a) PLA-PVA supported nanomembranes prepared using a vigorously stirred 90:10 PVA:PLA mixture in HFIP and (b) nanoporiferated PLA FsNMs obtained via selected water etching using the supported nanomembranes displayed in (a). In all cases image windows are $10 \times 10 \mu\text{m}^2$ (top) and $10 \times 10 \mu\text{m}^2$ (bottom).

Table 5.3.3 Average diameter (ϕ) and area (A) of the pores, surface coverage by pores (SC), RMS roughness (Rq) and thickness (L) of perforated PLA FSNMs derived from 80:20 and 90:10 PLA:PVA mixtures.

FsNM	ϕ (nm)	A (nm ²)	SC (%)	Rq (nm)	L (nm)
PLA	-	-	-	1.1±0.2	116±14
80:20 PLA	841±546	555493±242886	34%	186.9±25.6	170±14
90:10 PLA	170±73	22713±4225	6%	93.2±31.2	127±10
90:10 PLA(stir)	65±32	3291±795	1%	108.9±5.7	117±16

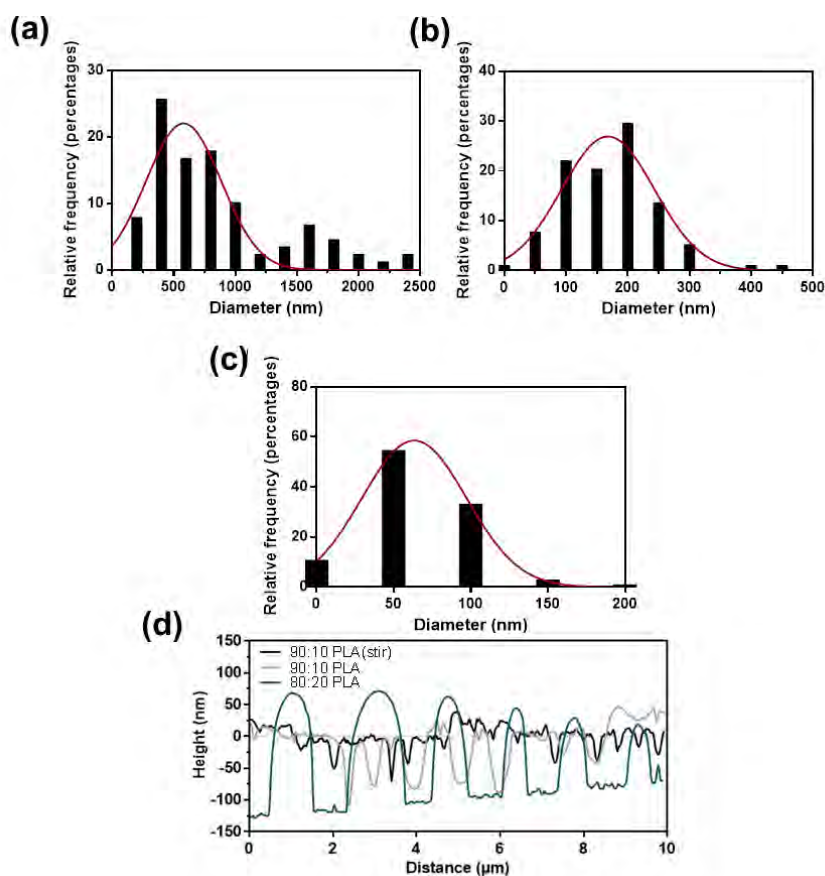


Figure 5.3.7 Pore diameter distribution for (a) 80:20 PLA, (b) 90:10 PLA and (c) 90:10 PLA(stir) nanomembranes. (d) AFM depth profiles for the 80:20 PLA, 90:10 PLA and 90:10 PLA(stir) FSNMs.

Quantitative measures of the pores, thickness and roughness were performed for perforated FsNMs derived from 80:20 and 90:10 PLA:PVA mixtures. For this purpose, five representative SEM images were considered for of each kind of nanomembrane. The average diameter and area of the pores (ϕ and A), the surface coverage by the perforations (SC), roughness and the thickness of such FsNM are listed in **Table 5.3.3**. As it was stated above, perforations in 80:20 PLA, which are the thickest ones, are submicrometric ($\phi \approx 0.8 \pm 0.5 \mu\text{m}$), representing around 34% of the nanomembrane surface. However, inspection of the results obtained for 90:10 PLA indicates that the size of the pores ($\phi = 170 \pm 73 \text{ nm}$), the area covered by them ($SC = 6\%$) and the thickness decrease with the context of PVA in the mixture. Moreover, such three parameters experiences a more drastic reduction when the 90:10 PLA:PVA mixture is submitted to vigorous stirring, this feature being particularly important for the diameter of nanopores ($\phi = 65 \pm 32 \text{ nm}$). These results are fully consistent with detailed AFM depth profiles and monomodal pore diameter distribution displayed in **Figure 5.3.7**, respectively, which provide complementary information about the shape and size of the pores.

Influence of nanoporations in the PLA wettability

Wettability, which is related with the surface topography, affects the cellular response of materials¹⁸, determination of the influence of the perforations introduced in PLA ultra-thin films being required. For this purpose, the contact angle of milliQ water, DMF and EG were determined for non-perforated PLA, 90:10 PLA and 90:10 PLA(stir) nanomembranes supported on glass slips. Results, which are displayed in **Figure 5.3.8a**, indicate that nanoporations do not provoke significant changes in the contact angle, independently of the solvent polarity. More specifically, the response of the three materials to water was very similar, indicating that the PLA hydrophilicity (*i.e.* contact angle $< 90^\circ$) remains practically unaltered after creating nanopores crossing the entire membrane thickness.

Surface energies are related with contact angle measurements through the Young's equation¹⁹. In this work, surface energies have been modelled using the Owen-Wendt-Kaelble^{20,21} (OWK) and Equation-of-State²² (EOS) relationships, results being displayed in **Figure 5.3.8b**. As it can be seen, results provided by the two models are fully consistent. Thus, although the surface energies of non-perforated and perforated films do not exhibit important difference, those of latter are slightly smaller than that of the former for both OWK and EOS models. The fact that the surface energies of nanoporated PLA are intermediate between those of non-perforated PLA and glass slip supports that nanopores cross the entire thickness of the nanomembranes. Moreover, this behaviour is consistent with the dimensions of the perforations, surface energies being slightly smaller for 90:10 PLA than for 90:10 PLA(stir).

Influence of nanoporations in cell viability

Cell adhesion and proliferation on ultra-thin films depend on different factors, as for example the material used for their fabrication (*i.e.* chemical composition) and the surface topography, which in turn may be altered through the introduction of nanofeatures. Thus, the dimensions and distribution of nanofeatures are expected to affect the behavior of nanomembranes as bioactive platforms. In this work the response

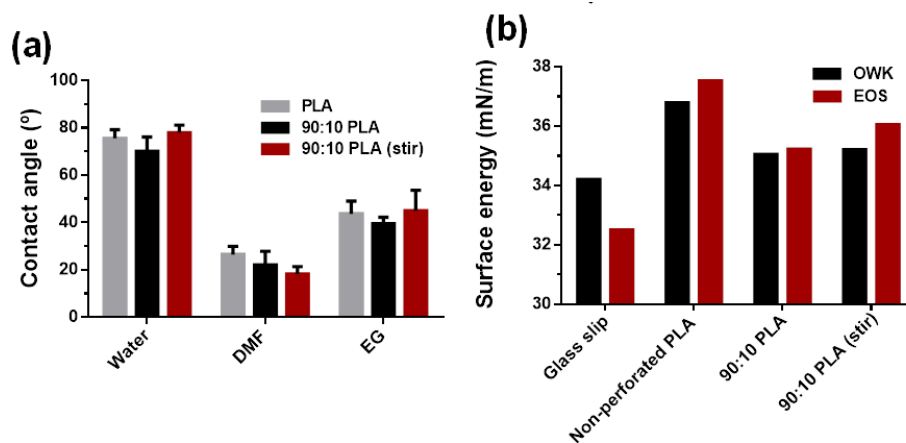


Figure 5.3.8 (a) Contact angle determined of milliQ water, DMF and EG. (b) Surface energy calculated using OWK and EOS models for non-perforated PLA, 90:10 PLA and 90:10 PLA(stir) FsNMs.

of perforated 90:10 PLA and 90:10 PLA(stir) nanomembranes to cellular adhesion and proliferation have been compared with that of non-perforated PLA considering two cellular lines: Vero and MCDK, which are epithelial-like cells. It should be emphasized that such three PLA-based systems present identical chemical composition enabling us to obtain direct evidences of the influence of both the diameter and distribution of nanopores on cell growth. Quantitative results of cellular adhesion assays are displayed in **Figure 5.3.9a**. Results indicate that nanoporations of $\phi \approx 170$ nm promote cell adhesion with respect to the absence of perforations and, specially, nanoporations of $\phi \approx 65$ nm. Thus, relative cell viability grows as follows: 90:10 PLA(stir) < non-perforated PLA < 90:10 PLA, differences being light more marked for MCDK cells than for Vero cells.

Cell proliferation assays were performed by evaluating the cellular activity on the three examined substrates after seven days of culture. Results, which are displayed in **Figure 5.3.9b**, show an appreciable increment in the cellular colonization for the two perforated nanomembranes. Evaluation of this increment with respect to the viability of adhered cells indicates that the preference of Vero and MCDK cells is higher for 90:10 PLA(stir) than for non-perforated PLA, evidencing that perforations promote the interaction between the polymeric matrix and the cells once these have been adhered. However, the most remarkable result refers to perforated 90:10 PLA FSNMs, which exhibit cell viabilities ~ 2.6 and ~ 2.2 times higher than those of non-perforated PLA and perforated 90:10 PLA(stir), respectively. This marked preference has been attributed to the similarity between the diameters of nanoporations in 90:10 PLA and the filopodia filaments in cells.

(a) OMP2A ONTO ARTIFICIAL MEMBRANES

Filopodia are thin, actin-rich structures protruding from the lamellipodial actin network^{23,24}. These elements, which are finger-like, sense the extracellular environment at their tips using cell surface receptors²⁵, playing an important role in cell migration. Thus, contact with an external target promotes the coupling of membrane-bound proteins to the backward flow of actin, which in turn produces the pushing forces needed

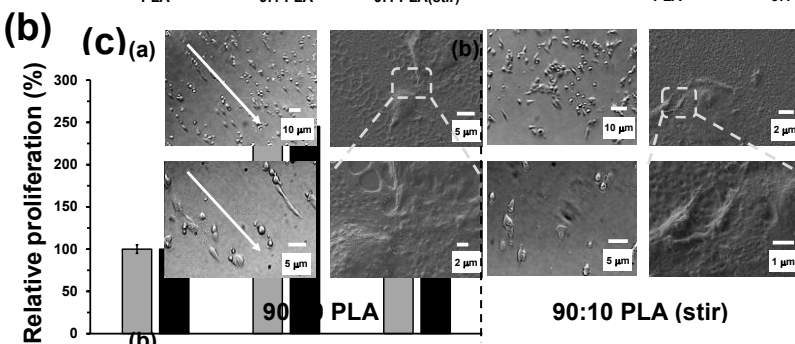
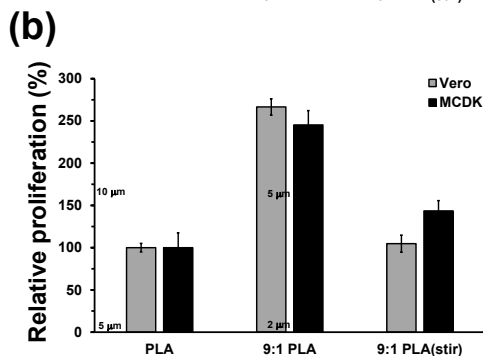
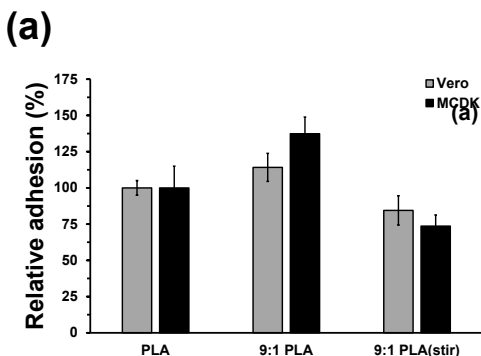
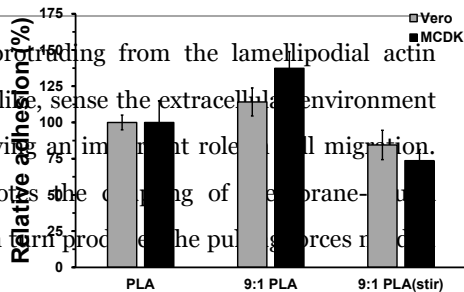


Figure 5-3-9 (a) Cellular adhesion and (b) cellular proliferation on the surface of nanoporated 90:10 PLA and PLA (stir) membranes and non-perforated PLA membranes. Vero and MCDK cells were culture during 24 h (adhesion assay) and 7 days (proliferation) (c) Optical microscopy (left) and SEM (right) images of Vero cells adhered onto perforated 90:10 PLA and 90:10 PLA(stir) nanomembranes.

for cell migration. This is essential for processes involving proliferation, as for example wound healing²⁶. Contact differences between substrates influences the response of protruding filopodia. Interestingly, filopodia are 100-200 nm in diameter²³ while the diameter of the nanoporations in 90:10 PLA is 170 ± 73 nm. Accordingly, nanoporations in 90:10 PLA FsNMs promote cell migration processes, simultaneously favouring cell proliferation.

Figure 5.3.9c displays micrographs recorded by optical microscopy and SEM of Vero cells adhered onto 90:10 PLA and 90:10 PLA(stir) perforated nanomembranes. As it can be seen, cells adhered onto 90:10 PLA exhibit a radial heterogeneous spreading with respect to the center of the film (**Figure 5.3.9c**). This particular distribution, which is supported by the elongated morphology of the cells, clearly evidences the interaction between cells and 90:10 PLA nanofeatures. In contrast, cells adhered onto 90:10 PLA(stir) presents a random distribution in which regions without cells coexist with areas having a large accumulation of cells (**Figure 5.3.9c**). Furthermore, the morphology of the cells is less elongated than that of cells adhered onto 90:10 PLA. Finally, cells adhered onto non-perforated PLA follow a distribution similar to that described for 90:10 PLA(stir), where cells present a round-like morphology (data not shown). On the other hand, observation of the micrographs displayed in **Figure 5.3.9c** evidences that ultra-thin films frequently exhibit micrometric striation flaws. These defects have been attributed to unfavorable capillary forces provoked by changes in surface tension during solvent evaporation^{12,27}. This phenomenon, which is called “Marangoni instability”, has been largely appreciated in ultra-thin films prepared by spin-coating. In this particular study, these tiny thickness undulations have very limited influence on the formation of the perforations as well as on cell adhesion and proliferation results.

The overall of these observations are fully consistent with our previous interpretation: cell elements interact intensely with nanofeatures of membranes with perforations of $\phi \approx 170$ nm while these interactions become weaker when nanoporations are too small and, especially, when they are non-existent.

5.3.3 Conclusions

In summary, nanoporated PLA FsNMs of thickness 120-130 nm have been successfully obtained using spin-coating combined with phase segregation processes in immiscible 90:10 PLA:PVA mixtures and the subsequent removal of PVA domains via selective solvent etching. The diameter of the nanopores, which cross the entire

nanomembrane thickness, has been controlled through the conditions applied to the preparation of the PLA:PVA mixture. Thus, the dimensional scale of the phase separation domain has been found to decrease when the mixing process is performed under vigorous stirring conditions. This procedure led to perforated PLA FsNM with nanopores of $\phi = 170 \pm 73$ nm (prepared without stirring) and $\phi = 65 \pm 32$ nm (prepared under vigorous stirring). The former diameter fits very well to the diameter of protruding finger-like filopodia (100-200 nm), which play an important role in cell migration processes. Cell proliferation assays considering non-perforated and perforated PLA nanomembranes as bioactive platforms indicate that ultra-thin films with nanopores of $\phi = 170 \pm 73$ nm exhibit cell viabilities that are ~ 2.2 and ~ 2.6 times higher than those with pores of $\phi = 65 \pm 32$ nm and non-perforated PLA, respectively. It is clear that this increase is enhanced by the better adhesion on such surfaces. Thus, nanopores of $\phi \approx 170$ nm promote the substrate colonization through intense interactions with cell filopodia, as clearly demonstrate changes on both cell morphology and cell spreading pattern. Hence, nanoporated FsNMs could be a great promise as novel bioactive platforms and would certainly improve the performance of current soft regenerative substrates.

5.4 Confinement of a β -barrel protein in nanoporated free-standing nanomembranes for ion transport

Biological ion channels, which smartly control the movement of ions and small molecules into and out of the cell, have inspired scientists to build materials with applications in nanofluidics,^{28,29} molecule and ion filters,^{30,31} as well as biosensors.^{32,33} Amongst the many approaches addressing selective ion transport, considerable efforts have recently been devoted to mimic the principles and functions of channels contained in biological nanomembranes (NMs).³⁴⁻³⁸

Biological membranes are made of lipid bilayers and embedded proteins sensing and subsequently controlling the exchange of substances between the cell and its environment. For instance, ion channels are self-assembled proteins that selectively transport ions through the cell membrane, while porin proteins are water-filled open channels allowing the passive penetration of hydrophilic molecules.³⁹ The latter are typically found as monomers or trimers in the outer membranes of Gram-negative bacteria, as well as in mitochondria⁴⁰ and chloroplast⁴¹ of eukaryotic cells. Gram-negative bacteria surround themselves with a second outer membrane (OM) playing the role of an effective barrier. That is, this OM is even more hydrophobic than a typical phospholipid membrane due to the presence of lipopolysaccharides, whereas the translocation of hydrophilic species across OMs is mainly governed by the presence of porins.⁴²

In this work, the attention is focused on the trimeric OM protein Omp2a from *Brucella melitensis*.⁴³ This β -barrel protein, which is formed by a sequence of 367 amino acids, allows the passive diffusion of small molecular weight hydrophilic materials (< 667 Da) across the OM (*e.g.* ions, nutrients, and drugs). It has been previously described that Omp2a first refolds under a monomeric form (39 KDa) and then self-associates into a trimeric state (115 KDa).^{44,45}

Supporting biological channels like porins, onto biological or synthetic polymeric bilayers presents limitations for practical applications due to their limited mechanical strength and stability.⁴⁶⁻⁴⁹ Synthetic solid state membranes offer several advantages over

bilayer-based approaches, such as mechanical stability, control over pore dimension and shape, and modifiable surfaces for desired functions.^{35,50} Within this context, we recently examined ion diffusion through Omp2a immobilized in a supported poly(N-methylpyrrol) (PNMPy) membrane.⁵¹ Electrical impedance spectroscopy (EIS) studies evidenced that Omp2a promotes the passive transport of K⁺ and Na⁺ in solutions with relatively high ionic concentrations, preferentially favouring the diffusion of hydrated Na⁺ with respect to that of hydrated K⁺.⁵¹ Unfortunately, some drawbacks were also identified for such system. For instance, PNMPy membranes electrochemically synthesized were not self-standing, a stainless steel support being used to electropolymerize PNMPy. Furthermore, the porin immobilization and orientation were not well-controlled. In addition, the membrane thickness (219±71 nm) was much higher than both the height of the porin (~5 nm)³⁹ and the thickness of conventional biological lipid bilayers (2-5 nm).⁵² Consequently, the passive ion transport was not only due to Omp2a, but assisted by PNMPy, which is known to be an electrochemically active polymer.^{53,54}

A few studies have reported track-etched polymeric membranes with nanopores as solid support of ion channels, despite complex chemical processes were frequently involved in the fabrication of such systems.^{35,55,56} For the selective biomolecular recognition through metal-protein specific interactions, Ali *et al.*³⁵ constructed a nanobiosensor based on the immobilization of metal terpyridine complexes inside nanopores, which were fabricated in polyethylene terephthalate membranes using asymmetric chemical etching. Guo *et al.*⁵⁵ also presented a single-pore nanofluidic energy-harvesting system that efficiently converts Gibbs free energy in the form of a salinity gradient into electricity. Experiments were conducted on ion-track-etched single nanopores embedded in polyamide membranes of 12 µm in thickness, which were irradiated with a single swift heavy ion and subsequently submitted to chemical etching. Balme *et al.*³⁴ filled nanopores (diameter= 15 nm) of commercial track-etched polycarbonate films (thickness= 5 µm) with the ion channel gramicidin A (GA). Unfortunately, such membranes did not exhibit the expected properties in terms of ion permeability and selectivity, which was attributed to the fact nanopores were not fully

filled with GA, and therefore ions diffused in the “free” electrolyte confined inside the nanopore instead of directly interacting with GA.

Here, we have prepared poly(lactic acid) (PLA) free-standing nanomembranes (FsNMs) with nanopores crossing the entire ultra-thin film thickness as solid support, then loading the Omp2a porin for selective ion transport. Nanoperforations have been obtained using spin-coating combined with phase segregation processes in immiscible PLA:poly(vinyl alcohol) (PVA) mixtures, and subsequently removing PVA domains via selective solvent etching.⁵⁶ The immobilization of Omp2a not only at the surface, but also inside the nanopores, which has been achieved by incubating nanoperforated PLA NMs in protein solutions, has led to important changes in the physical properties of nanoperforated PLA NMs, including their electrochemical impedance response towards different electrolytic media.

5.4.1 Methods

Sodium dodecyl sulfate polyacrylamide gel electrophoresis (SDS-PAGE):

Samples were loaded on 15% acrylamide SDS-PAGE gels without boiling. After electrophoresis, the gels were fixed with glacial acetic acid and methanol and stained with Coomassie blue.

Dynamic light scattering (DLS): The size distribution of the protein in 1× PBS pH 7.4 and in 50 mM Tris-HCl pH 8, 150 mM NaCl, 3 M MPD was determined using a NanoBrook Omni Zeta Potential Analyzer from Brookhaven Instruments Corporation. Particularly, three consecutive runs of 60 seconds each were conducted for every sample.

Circular dichroism (CD): CD spectra were recorded between 190 and 350 nm at room temperature using a Jasco J-815 equipment with a protein concentration of approximately 125 µg/mL and a 0.1 cm cell path. Spectra were acquired at a scan speed of 50 nm min⁻¹ with a 0.2 nm data pitch using a 2 nm bandwidth and a 4 second digital

integration time. Spectra were averaged after two accumulations and corrected by subtraction of the background spectrum.

Transmission electron microscopy (TEM): TEM images were obtained with a Philips TECNAI 10 electron microscope operating at 100 kV. Bright field micrographs were taken with an SIS MegaView II digital camera. Solution containing Omp2a (0.34 mg/mL) was dispersed on glow-discharged carbon coated copper grids (300 mesh) and negatively stained with uranyl acetate (2.0 % w/v). After incubation (30 s), the excess of protein was removed with filter paper, and the grids air dried for a further 1-2 s.

Omp2a-filled nanoporated nanomembranes: Nanoporated PLA nanomembranes supported on ITO were placed in a 24-well plate. 500 μ L of Omp2a solutions (0.5, 0.25 and 0.125 mg/mL) were deposited onto the film surface. After 48 h with slight agitation (80 rpm) at room temperature, the nanomembranes surfaces were rinsed three times with milliQ water to remove non-immobilized protein residues.

Omp2a-coated non-perforated nanomembranes: Non-perforated PLA NMs were incubated in 500 μ L of Omp2a solution (0.5 mg/mL) for 48 h with slight agitation (80 rpm) and at room temperature. After such period of time, samples were rinsed three times with milliQ water to remove non-immobilized protein residues. The resulting Omp2a-coated non-perforated NMs were used as negative control.

Detection of immobilized protein, Bradford assay: Adsorbed Omp2a was removed from the films surfaces by adding 0.2 mL of 0.1 M PBS with nonyl phenoxyethoxyethanol (NP-40) surfactant (0.5% v/v) and orbital shaking at 50 rpm during 30 min and 37°C. In order to avoid interferences between the NP40 surfactant and the Bradford reagent, the former was eliminated by precipitating the Omp2a with 20 μ L of trichloroacetic acid. Next, the precipitate-containing solution was centrifuged for 15 min at 12000 rpm. The solid (Omp2a) was washed with cold acetone and maintained at 4 °C for 1 hour. After this, the solid was centrifuged again during 15 min at 12000 rpm. The protein was dried under vacuum and, finally, dissolved in 0.1 M PBS for Bradford assay.

Standard curves were carried out using protein dilutions, which were prepared using buffer solution with concentrations of protein ranging from 0.05 to 1.00 mg/mL. Next, 5 μ L of protein standards and samples were added to a 96-well plate, blank wells being filled with 5 μ L of buffer. After this, Bradford reagent (250 μ L) was added into each well and plates were subsequently placed on a shaker for mixing (30 s). Samples were incubated at room temperature for 15 min. Finally, the absorbance was measured at 595 nm.

Profilometry: Film thickness measurements were carried out using a Dektak 150 stylus profilometer (Veeco, Plainview, NY). Different scratches were intentionally provoked on the NMs and measured to allow statistical analysis of data. At least six independent measurements were performed for two samples of each examined condition. Imaging of the films profile was conducted using the following optimized settings: tip radius= 12.5 μ m; stylus force= 3.0 mg; scan length= 3 mm; and speed= 30 μ m/s.

Atomic force microscopy (AFM): AFM was conducted to obtain topographic images of the films surface using silicon TAP 150-G probes (Budget Sensors, Bulgaria) with a frequency of 150 kHz and a force constant of 5 N/m. Images were obtained with an AFM Dimension microscope using a NanoScope IV controller under ambient conditions in tapping mode. The row scanning frequency was set between 0.6 and 0.8 Hz. The root mean square roughness (R_q), which is the average height deviation taken from the mean data plane, was determined considering 5 \times 5 μ m² surface areas and using the statistical application of the NanoScope Analysis software (1.20, Veeco). AFM measurements were performed on various parts of the films, which produced reproducible images similar to those displayed in this work.

Scanning electron microscopy (SEM): SEM micrographs were obtained using a Focussed Ion Beam Zeiss Neon 40 scanning electron microscope operating at 1 kV. Samples were mounted on a double-side adhesive carbon disc and sputter-coated with a thin layer of carbon to prevent sample charging problems.

Wettability: Contact angle (CA) measurements were conducted using the water drop method. 0.5 μL of milliQ water drops were deposited onto the surface of the films and recorded after stabilization with the equipment OCA 15EC (DataPhysics Instruments GmbH, Filderstadt). The SCA20 software was used to measure the CA, which is shown in this work as the average of at least 10 measures for each condition.

Electrochemical impedance spectroscopy (EIS): EIS measurements were performed using a conventional three-electrode cell and an AUTOLAB-302N potentiostat/galvanostat operating between the frequency range of $10^{4.5}$ Hz and 10^{-2} Hz and 5 mV of amplitude for the sinusoidal voltage. All experiments were performed at room temperature with nanomembranes deposited onto ITO and using different electrolyte solutions (NaCl, KCl and CaCl_2) at various concentrations (50, 100, 500 and 1000 mM). ITO was used as working-electrode and platinum as counter-electrode, whereas Ag|AgCl saturated (KCl 3M) was employed as reference electrode. After data collection, EIS results were then processed and fitted to an electrical equivalent circuit (EEC).

5.4.2 Results

Protein characterization

The Omp2a protein was expressed, purified, and refolded using a previously reported procedure,^{44,45} which is briefly described in **Chapter 4**. The isoelectric point of Omp2a, which contains 367 amino acids, is 4.47. The monomeric and trimeric association of refolded Omp2a was investigated by SDS-PAGE. Primary and secondary bands were observed at ~ 39 and ~ 115 kDa (**Figure 5.4.1a**), suggesting that the trimeric form was less populated than the monomeric species. The competition between monomer...monomer and monomer...SDS interactions provides a possible explanation for the low self-association of the monomers to form the trimeric units.

DLS measurements reflected that in the buffer solution used to maintain Omp2a secondary structure, SDS molecules form small micelles with an effective diameter $D_{eff}=5.7\pm 0.1$ nm (**Figure 5.4.1c**) that increases to $D_{eff}=6.4\pm 0.4$ nm upon the addition of the protein. This increment has been associated with the incorporation of the Omp2a monomer to the SDS micelles. In contrast, aggregates with $D_{eff}=228\pm 38$ nm are observed when the protein is diluted in phosphate buffered saline (PBS) solution. The formation of these aggregates has been attributed to the de-protection of the hydrophobic zones of the protein (trans-membrane), which induces the self-association process. According to these results, the SDS-containing buffer medium was not changed during protein deposition onto nanoporated membranes.

Despite the complete transformation of protein population into trimers has not been achieved, the secondary structure of the protein was well-preserved. This is evidenced by **Figure 5.4.1b**, which compares the CD spectra recorded for Omp2a in three different

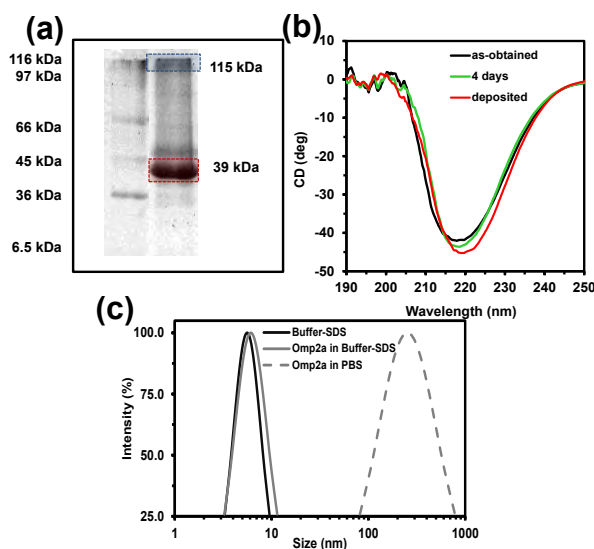


Figure 5.4.1 (a) SDS-PAGE of Omp2a. Monomers migrate at 39 kDa while trimers show an apparent molecular weight of 115 kDa. (b) CD spectra for the Omp2a protein: as-obtained, after 4 days of incubation and deposited into the nanoporations of PLA NMs. (c) DLS results showing the volume percentage of particles towards particle diameter for SDS micelles in the buffer solution used to maintain the protein, the same solution after incorporate the Omp2a protein and a PBS solution with Omp2a.

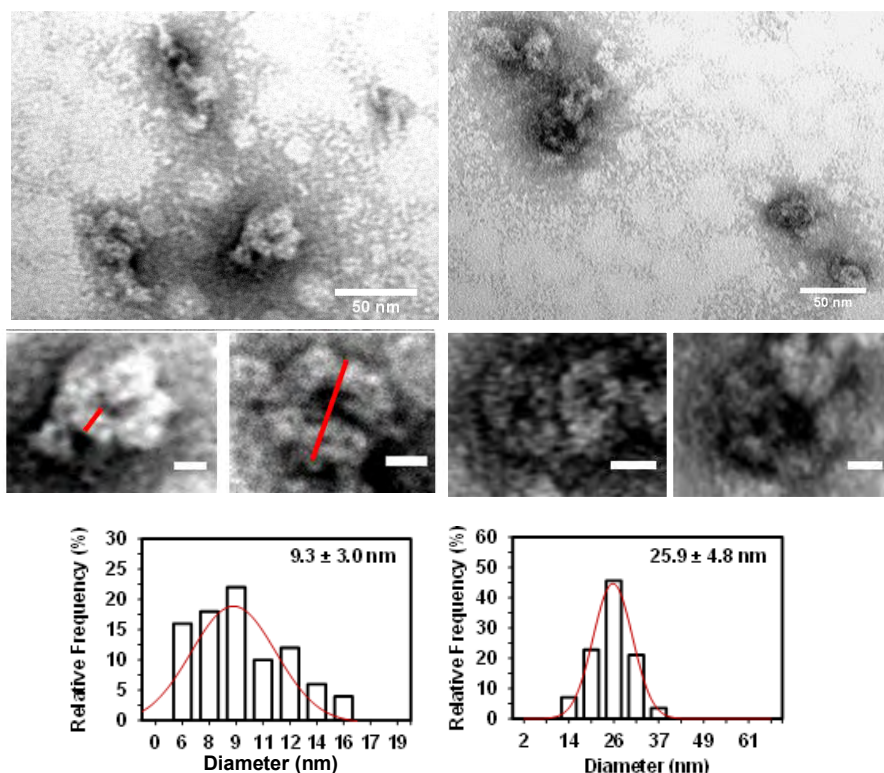


Figure 5.4.2 TEM micrographs of Omp2a trimeric units (short red line) and higher aggregates (large red line) derived from solutions stained with 2% uranyl acetate. Scale bar of the high resolution micrographs: 10 nm. The effective diameter (D_{eff} in nm) distribution for both Omp2a trimers and aggregates are also displayed (left and right, respectively).

scenarios: (i) just after being defrosted (as-obtained), (ii) after four days of incubation (4 days), and (iii) after being deposited onto the NMs (deposited). In all cases, the spectra featured a broad minimum about 217 nm that is typically associated with β -stranded proteins.⁵⁷

TEM micrographs from Omp2a solutions stained with 2% uranyl acetate enabled us to identify not only trimeric units, but also higher hierarchical structures formed by around 6-8 trimeric units due to self-association processes (**Figure 5.4.2**). All these structures have been attributed to the hydrophobic interactions promoted by the side groups at the external side of the β -barrels, consistently with the effective diameter

measured by TEM for the trimers ($D_{eff} = 9.3 \pm 3.0$ nm) and such bigger aggregates ($D_{eff} = 25.9 \pm 4.8$ nm), respectively.

Nanoperforated PLA nanomembranes

Nanoperforated PLA FSNMs were prepared using an already described two-step procedure:⁵⁶ (1) spin-coating a mixture of PLA and poly(vinyl alcohol) (PVA), which are immiscible polymers but both soluble in 1,1,1,3,3,3-hexafluoroisopropanol (HFIP), onto a PVA sacrificial layer to form the appropriated nanofeatures (*i.e.* phase separation domains with dimensions similar to the entire film thickness); and (2) selective solvent etching using milliQ water to dissolve both the PVA sacrificial layer and the PVA domains of PLA-PVA NMs, consequently transforming such nanofeatures into nanoperforations. Perforated FSNMs were initially obtained by considering 90:10 and 99:1 PLA:PVA v/v mixtures.

Table 5.4.1 Physical parameters of non-perforated and perforated PLA NMs derived from 90:10 and 99:1 PLA:PVA mixtures: Average diameter of the nanopores (ϕ), root-mean-square roughness (Rq) ($5 \times 5 \mu\text{m}^2$ surface area) and film thickness (L), which also corresponds to the depth of the pores.

NM	ϕ (nm)	Rq (nm)	L (nm)
90:10 perforated PLA	67 ± 31	106 ± 8	114 ± 11
99:1 perforated PLA	51 ± 22	21 ± 3	110 ± 7
Non-perforated PLA	-	1.7 ± 0.2	116 ± 14

Figure 5.4.3a displays 3D AFM height images coloured with phase skin of NMs obtained using 99:1 PLA:PVA mixtures. Briefly, AFM phase imaging registers phase signal shifts due to changes in the adhesion force between the tip and the surface, thus being sensitive to the surface mechanical and viscoelastic properties (*i.e.* stiffness/softness). Accordingly, AFM phase information allows for the chemical mapping of polymer composites.

Hence, **Figure 5.4.3a** illustrates how the PVA nanophases, which are clearly identified in PLA-PVA NMs as yellow domains, disappear after selective water etching while PLA phase remains (dark purple domain).

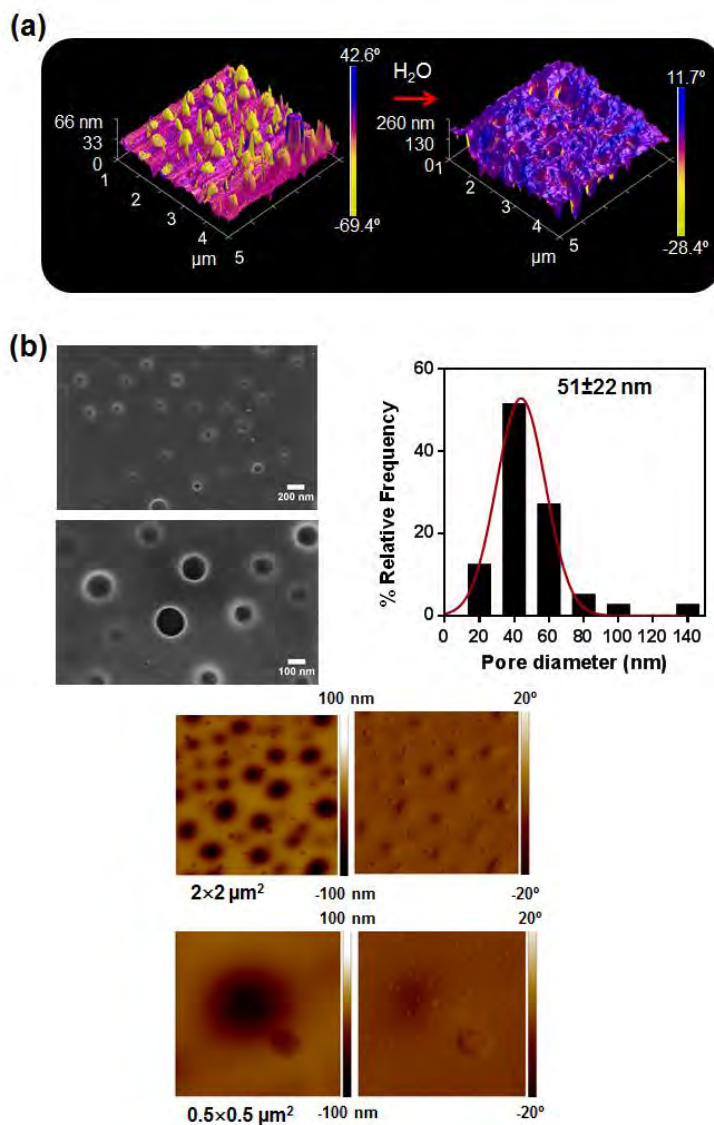


Figure 5.4.3 (a) 3D AFM height images coloured with phase skin: PLA-PVA NM obtained using a 99:1 PLA:PVA mixture (left) and nanoporous PLA NM derived from PLA-PVA *via* selective water etching (right); (b) High magnification SEM micrographs, pore diameter distribution, and AFM height images (2×2 and $0.5 \times 0.5 \mu m^2$) with their corresponding phase images for nanoporous PLA NM obtained using 99:1 PLA:PVA mixtures.

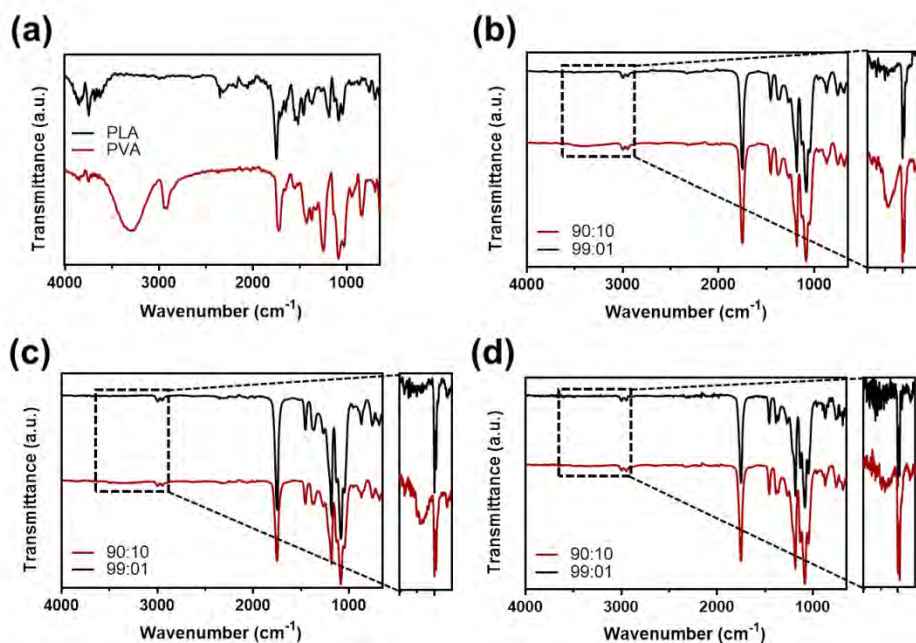


Figure 5.4.4 FTIR spectra of: (a) individual PLA and PVA membranes; (b) as prepared membranes obtained by solvent casting 99:10 and 99:1 PLA:PVA mixtures; (c) membranes of (b) after 2 h in milliQ water; and (d) membranes of (b) after one day in milliQ water.

The elimination of PVA in NMs obtained from both 90:10 and 99:1 mixtures was also followed by FTIR spectroscopy (**Figure 5.4.4**).

For perforated and non-perforated PLA NMs, **Table 5.4.1** lists the average diameter of the nanopores (ϕ), the root-mean-square roughness (Rq) values of $5 \times 5 \mu\text{m}^2$ surface areas and film thickness (L), which also corresponds to the depth of the pores. It is evidenced that Rq increases rapidly with the content of PVA in the polymer mixture. Hence, the formation of nanopores provokes drastic topographic alterations with respect to the ultra-flat non-perforated PLA NMs. In contrast, L remains almost unchanged for perforated and non-perforated NMs, the influence of PVA-induced nanofeatures being negligible in this case.

SEM and AFM micrographs provided in **Figure 5.4.3b** display nanometric details of perforated PLA FsNMs derived from 99:1 PLA:PVA mixture, while micrographs of non-perforated PLA (used as a control) are displayed in **Figure 5.4.5**. The diameter of the

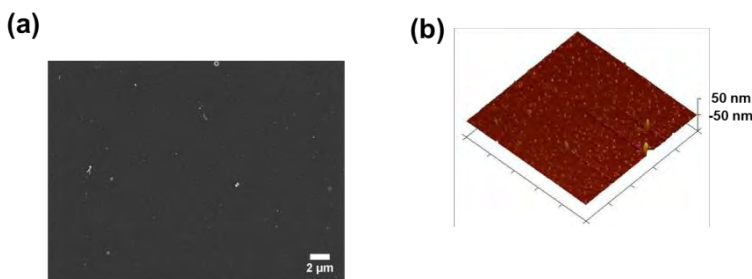


Figure 5.4.5 (a) SEM micrograph and (b) 3D AFM height image ($5 \times 5 \mu\text{m}^2$) of non-perforated PLA NMs.

nanopores as determined from SEM micrographs is 65 ± 32 nm and 51 ± 22 nm for NMs originating from 90:10 and 99:1 mixtures, respectively. As the effective diameter of Omp2a aggregates determined by TEM range from 9.3 ± 3.0 nm to 25.9 ± 4.8 nm, PLA NMs with the smallest pore diameter have been selected for immobilizing the OM protein. Moreover, AFM observations, which recorded simultaneously surface structure (height) and material composition (phase data) allow us to verify the presence of PLA region only (*i.e.* no phase contrast), thus indicating complete removal of PVA domains. These self-standing ultra-thin films are very flexible and robust, and they can be easily folded into small shapes.

Omp2a-filled nanoporated PLA nanomembranes

Nanoporated PLA NMs supported onto ITO and prepared using 99:1 PLA:PVA mixtures, were placed on a 24-well plate and incubated with 500 μL of 0.5, 0.25 or 0.125 mg/mL Omp2a solution for 48 h with slight agitation (80 rpm) at room temperature. Then, NMs samples were rinsed three times with milliQ water to remove residues. The incorporation of Omp2a preserving its β -barrel structure as proved by CD (**Figure 5.4.1b**), induces drastic changes in the physical properties of nanoporated PLA NMs (**Figure 5.4.6a**). Indeed, the wettability significantly increases upon the incorporation of the protein. CA of PLA and nanoporated PLA ($CA = 78^\circ \pm 6^\circ$ and $72^\circ \pm 7^\circ$, respectively) is just below the threshold value that separates hydrophilic and hydrophobic surfaces (*i.e.* $CA \leq 90^\circ$ and $CA > 90^\circ$, respectively), the CA of Omp2a-filled NMs is only $24^\circ \pm 14^\circ$.

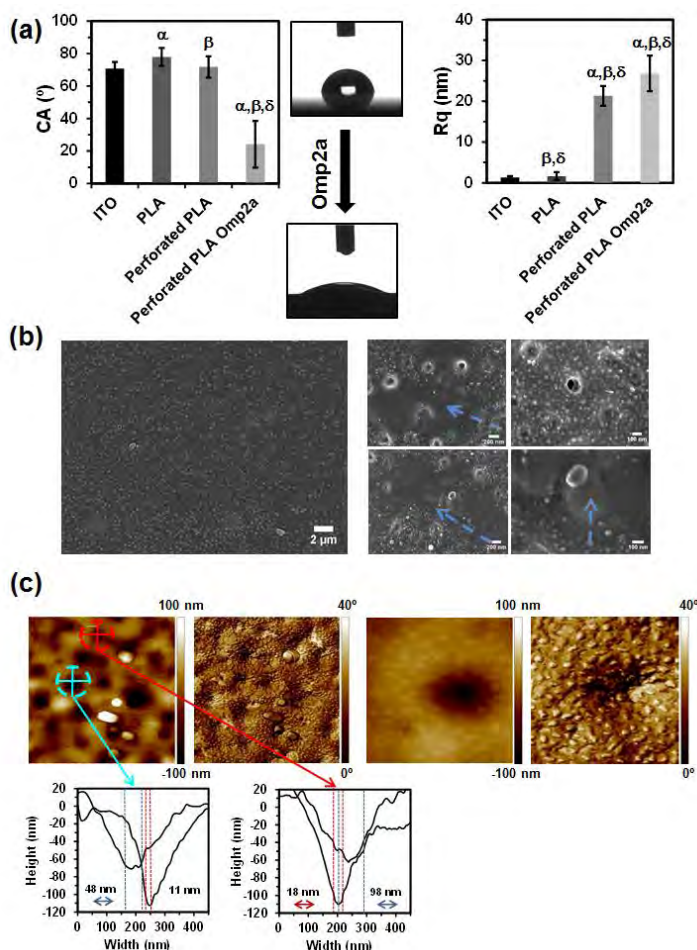


Figure 5.4.6 (a) Average CA and Rq values ($5 \times 5 \mu\text{m}^2$ surface area) determined for ITO substrate, non-perforated PLA NMs, nanoporous PLA before and after Omp2a incubation. Greek letters on the columns refer to significant differences ($p < 0.05$) when the 1 way ANOVA and Tukey's multiple comparisons test are applied: α vs ITO, β vs non-perforated PLA and δ vs nanoporous-PLA. Images of the drops onto nanoporous PLA with (bottom) and without (top) immobilized Omp2a are also displayed. (b) SEM micrographs of perforated PLA NMs after Omp2a immobilization: low and high magnifications at left and right, respectively. Dashed arrows illustrate the presence of big protein aggregates. (c) AFM height and their corresponding phase images (window: $0.5 \times 0.5 \mu\text{m}^2$) of nanoporous PLA after Omp2a incubation. Several representative cross-sectional profiles showing the topography and dimensions of the nanopores (dashed circles) are also displayed. In all samples, incubation was performed considering a 0.5 mg/mL Omp2a solution.

Similarly, the R_q ($5 \times 5 \mu\text{m}^2$ surface area) of nanoporated PLA NMs increases from 21 ± 3 nm to 27 ± 5 nm after Omp2a deposition. In order to explain these physical changes, nanoporated PLA NMs were investigated by SEM (**Figure 5.4.6b**) and AFM (**Figure 5.4.6c**).

Low and high magnification SEM micrographs, as well as AFM images reveal the presence of aggregates at the surface of PLA NMs, which has been attributed to protein agglomeration. However, these aggregates are significantly bigger than the pure Omp2a assemblies observed by TEM from stained solutions (**Figure 5.4.2**), precluding an unambiguous identification. In opposition, height and phase AFM images (**Figure 5.4.6c** and **5.4.7**) evidence the presence of aggregates both on the surface and inside the pores. Although phase contrast is not as enhanced as in **Figure 5.4.3a**, topographical and texture differences reveal the existence of different phases (**Figure 5.4.8a**). Furthermore, the dimensions of these aggregates are very varied, ranging from some hundreds to a few tenths of nanometers. Cross sectional profiles of the interior of the pores indicate that their dimensions are suitable to host protein not only as aggregates of trimers (**Figure 5.4.2**), but also as individual trimers and monomers. Furthermore, both the roughened topography of the nanopore walls and the hydrophobic character of PLA favour the physical immobilization of Omp2a, no chemical treatment being required for such purpose. On the other hand, it is worth noting that β -barrel porins typically present a significant oval shape,⁵⁸ which is preserved in the aggregates observed by both SEM and AFM (**Figure 5.4.6c**).

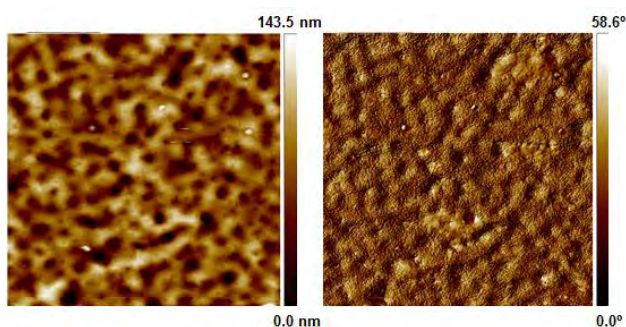


Figure 5.4.7 AFM height and their corresponding phase images (window: $5.0 \times 5.0 \mu\text{m}^2$) of nanoporated PLA after Omp2a deposition.

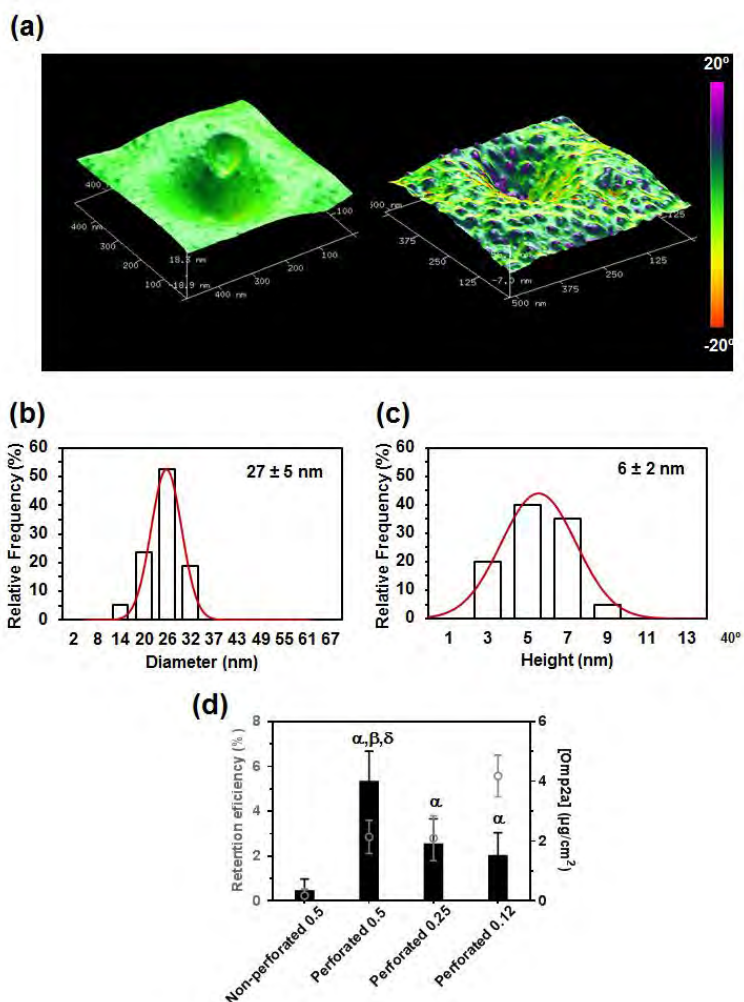


Figure 5.4.8 (a) 3D AFM phase images of the skin surfaces of perforated PLA NMs before (left) and after (right) incubation with a 0.5 mg/mL Omp2a solution. Oval protein aggregates are clearly identified at the surface and inside the nanopores. Diameter (b) and height (c) distributions of the protein aggregates observed in (a). (d) Results from Bradford assays for non-perforated (incubation with a 0.50 mg/mL Omp2a solution) and perforated (incubation with 0.5, 0.25 and 0.125 mg/mL Omp2a solutions). Grey spheres represent the retention efficiency (in %) while black bars correspond to the mass of protein entrapped per unit of area ($\mu\text{g}/\text{cm}^2$). Error bars indicate the standard deviation and greek letters on the columns refer to significant differences ($p < 0.05$) in protein entrapped per unit of area ($\mu\text{g}/\text{cm}^2$) when the 1way ANOVA and Tukey's multiple comparisons test are applied: α vs non-perforated PLA, β vs nanoporated-PLA incubated with 0.25 mg/mL and δ vs nanoporated-PLA incubated with 0.125 mg/mL.

Besides, comparison of the 3D AFM height images coloured with phase skin surfaces recorded before and after incubation with Omp2a allows confirming the presence of adsorbed oval protein aggregates around and inside the nanopores (**Figure 5.4.8a**). Specifically, phase information clearly distinguishes Omp2a domains (*i.e.* dark purple aggregates) from the PLA region they are adsorbed onto, which is coloured in green. The average diameter of such immobilized Omp2a aggregates is 27 ± 5 nm (**Figure 5.4.8b**), which is in excellent agreement with the effective diameter measured by TEM for aggregates (26 ± 5 nm in **Figure 5.4.2**). Furthermore, the average height of these aggregates is 6 ± 2 nm (**Figure 5.4.8c**), which is fully consistent with the ~ 6 nm in height identified for the majority of β -barrel porins studied so far.⁵⁸

The Omp2a retention efficiency (RE), expressed as the ratio (in %) between the mass of protein entrapped on the nanoporated PLA substrate and the mass of Omp2a in the incubation solution, was evaluated using the Bradford assay. **Figure 5.4.8d** displays the amount of immobilized protein per unit of area and the RE for both perforated and non-perforated NMs. Results indicate higher the concentration of protein in the incubation solution, the greater the amount of immobilized protein. On the contrary, the highest RE ($5.8\pm 1.0\%$) was obtained for the incubation solution with the lowest concentration of protein (0.12 mg/mL), while RE values derived after using the 0.5 and 0.25 mg/mL protein solutions were practically identical ($2.9\pm 0.7\%$ and $2.8\pm 1.3\%$, respectively). This feature indicates that the protein saturation limit is reached at 0.25 mg/mL. Interestingly, the amount of immobilized protein and RE are very low (*i.e.* 0.4 ± 0.3 $\mu\text{g}/\text{cm}^2$ and $0.3\pm 0.2\%$, respectively) for the non-perforated PLA NMs. This feature clearly indicates that, although Bradford assays do not distinguish between proteins adsorbed onto the surface of the nanofilm or confined inside the pores, the amount of protein immobilized inside the latter is significantly higher. Thus, the adsorption of protein onto the surface is difficult because of the smoothness at non-perforated regions (*i.e.* R_q is 1.7 ± 0.2 nm for non-perforated NMs), while the roughness inside the nanoporations (**Figure 5.4.6c**) is large enough to facilitate the confinement of the protein. It is well known that physical immobilization of protein aggregates on ultra-flat surfaces is a very difficult task.⁵⁹ Despite of these results, caution is required for

interpretation of the results because of the imprecision of the Bradford assays mentioned above.

Ion diffusion in Omp2a-filled nanoporated PLA nanomembranes.

EIS studies were conducted to monitor changes in the resistance and capacitance caused by the presence of nanopores filled by Omp2a aggregates. Accordingly, the impedance was measured for frequencies ranging from 10^{-2} to $10^{4.5}$ Hz for non-porated, nanoporated, and Omp2a-filled nanoporated PLA NMs using several electrolytes. For all assays, such PLA NMs were supported onto ITO semiconductor electrodes, which exhibit both a high electron density ($10^{21} e^- / \text{cm}^3$) and a good stability in aqueous solution for electrochemical applications.⁶⁰ Stability of bare ITO was essential to retain the charged protein inside the induced nanopores during EIS measurements on Omp2a-filled PLA NMs. It should be emphasized that no protein was lost during EIS measurements on Omp2a-filled PLA NMs. Thus, the concentration of Omp2a immobilized in the perforated PLA NMs, which was analysed by the Bradford assay, was maintained within the same concentration range before and after EIS studies (4.1 ± 1.0 and $5.4 \pm 1.54 \mu\text{g}\cdot\text{cm}^2$, respectively). The electrolyte concentration interval selected for this study was identical to that previously used by Balme *et al.*⁶¹ to examine the ion transport through hybrid biological/artificial solid-state nanoporous membrane as a function of salt concentration.

Figure 5.4.9 displays the Bode and Nyquist plots recorded for ITO substrate and the three PLA NMs, using 0.5 M NaCl aqueous solution. The EEC (**Figure 5.4.9e**) of the bare ITO electrode shows the electrolyte resistance (R_s) connected in series with the capacitance of the double layer semiconductor/electrolyte interface (Q_{dl}), which is consistent with the EEC reported in the literature.⁶⁰ The quality of the experimental data fitting to EECs was evaluated by the estimate percentage error associated with each circuit element, being lower than 10% in virtually all cases (**Table 5.4.2**). The R_s parameter is not affected by changes occurring on the electrode surface,⁶² whereas the Q_{dl} parameter is often modelled as a constant phase element (CPE) instead of a pure capacitance (C_{dl}) since the phase angle is lower than 90° .^{62,63}

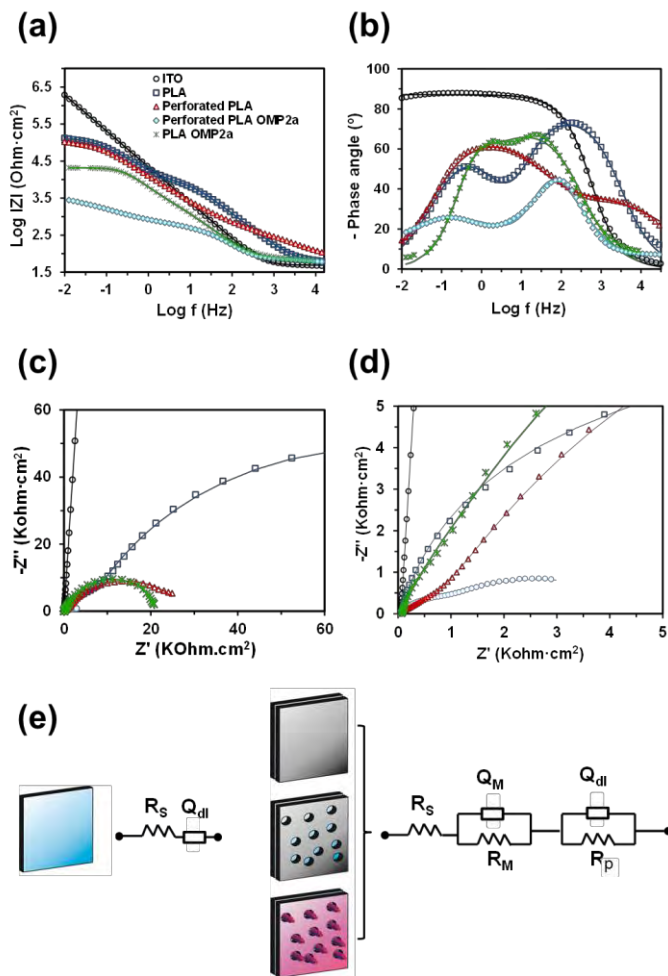


Figure 5.4.9 Bode (a, b) and Nyquist (c, d) plots of ITO (circle), non-perforated PLA (square), nanoporated PLA (triangle), Omp2a-coated non-perforated PLA (cross) and Omp2a-filled nanoporated PLA (diamond) in NaCl 0.5 M; (d) corresponds to an amplified area from (c), for better visualization of high frequency zone. Symbols correspond to experimental data, while lines are fitted curves according to EEC. (e) EEC used for fitting the experimental data from EIS measurements: R_s is the electrolyte resistance; Q_M and R_M are the membrane constant phase element and resistance, respectively; Q_{dl} and R_p are the double layer constant phase element and the pore resistance, respectively. The depicted surfaces are (left) ITO and (right) non-perforated PLA, nanoporated-PLA and Omp2a-filled nanoporated PLA NMs (from top to bottom).

Table 5.4.2 Resistances (R) and constant phase elements (CPE) for each sample, analysed in NaCl 0.5 M solution, from fitting parameters obtained with the EEC displayed in **Figure 5.4.9e**. The percentage error associated to each circuit element is included in parentheses.

	R_s ($\Omega \cdot \text{cm}^2$)	CPE_M ($\text{Fcm}^{-2} \cdot \text{s}^{-n}$))	n	R_M ($\Omega \cdot \text{cm}^2$)	CPE_{dl} ($\text{Fcm}^{-2} \cdot \text{s}^{-n}$))	n	R_p ($\Omega \cdot \text{cm}^2$)
Bare ITO	48.5 (0.75)	$7.63 \cdot 10^{-6}$ (0.57)	0.97 (0.13)				
Non-perforated PLA	56 (1.15)	$3.15 \cdot 10^{-6}$ (4.68)	0.92 (1.2)	$5.99 \cdot 10^3$ (5.37)	$1.54 \cdot 10^{-5}$ (1.22)	0.79 (1.23)	$135.5 \cdot 10^3$ (1.88)
Non-perforated PLA Omp2a-coated	64.3 (1.62)	$5.37 \cdot 10^{-5}$ (12.6)	0.76 (1.5)	$2.5 \cdot 10^3$ (20.2)	$3.11 \cdot 10^{-5}$ (6.16)	0.99 (1.23)	$18.32 \cdot 10^3$ (5.3)
Nanoperforated PLA	36.9 (1.9)	$6.41 \cdot 10^{-5}$ (5.29)	0.51 (1.17)	883 (4.78)	$6.56 \cdot 10^{-5}$ (0.83)	0.75 (0.77)	$26.8 \cdot 10^3$ (1.23)
Omp2a-filled nanoperforated PLA	56.1 (1.89)	$2.46 \cdot 10^{-5}$ (13.14)	0.96 (2.95)	317 (6.22)	$7.54 \cdot 10^{-4}$ (3.12)	0.48 (2.34)	$4.49 \cdot 10^3$ (6.44)

In addition to the heterogeneity of the electrode surface (*i.e.* roughness, porosity, reactivity), the CPE impedance (Z_{CPE}) is also related to non-uniform diffusion across the interface. That is, Z_{CPE} is defined as $[Q \cdot (j\omega)^n]^{-1}$ and is associated to a pure capacitor for $n=1$ or a pure resistor for $n=0$. For $n=0.5$, it accounts for a diffusion process. Accordingly, the impedance of ITO layer (**Figure 5.4.9a**) consists of a frequency-independent response at high frequencies (R_s), while it steadily increases for frequencies below 10^3 Hz (Q_{dl} ; $n=0.97$). Moreover, as polymer films are porous materials, two shoulders appear at $\log |Z|$ vs $\log f$ plot for systems covered by PLA membrane. **Figure 5.4.9a** exhibits a broad shoulder between 10 and 10^3 Hz, that corresponds to the parallel association of the membrane resistance (R_M) and the membrane capacitance (Q_M) (**Figure 5.4.9e**). Furthermore, a second shoulder appears at frequencies below 0 Hz, corresponding to the membrane pore resistance (R_p) in parallel with the Q_{dl} of the ITO electrolyte/interface. The electrical response is perfectly adjusted to the electrical circuit (in series) shown in **Figure 5.4.9.e**. Both shoulders represent two time constants in the Bode plot (**Figure 5.4.9b**, phase angle). Regarding the Nyquist spectra (**Figure 5.4.9c**), all three NMs display curves with two semicircles: the starting point of the curve indicates R_s , the first semicircle (at high frequencies) corresponds to R_M and Q_M , whereas the second (at low frequencies) corresponds to R_p and Q_{dl} . The offset on the high frequency impedance zone (**Figure 5.4.9d**) shows the two semi-circles from nanoporated PLA with adhered Omp2a.

Table 5.4.2 lists the contribution of each element for the several NMs tested when the electrolyte is a 0.5 M NaCl solution. As it can be seen, the R_M value of PLA membranes drastically decreases when artificial nanopores were induced across the polymer film, varying from $5.99 \text{ k}\Omega\cdot\text{cm}^2$ (non-perforated PLA) to $883 \text{ }\Omega\cdot\text{cm}^2$ (perforated PLA). The confinement of aggregates (from Omp2a protein) into PLA nanopores further reduced the membrane resistance to $317 \text{ }\Omega\cdot\text{cm}^2$, evidencing that the exchange of ions between the working electrode (bare ITO) and the electrolyte is favoured compared to nanoporated PLA without protein. However, even though Omp2a adsorbed onto non-perforated PLA nanomembranes results in a R_M value of $2.50 \text{ k}\Omega\cdot\text{cm}^2$, the confinement of aggregates (from Omp2a protein) into PLA nanopores further reduces the membrane resistance to $317 \text{ }\Omega\cdot\text{cm}^2$, evidencing that the exchange of ions between the working

electrode (bare ITO) and the electrolyte is favoured when Omp2a and nanopores are combined. Furthermore, the CPE related to the polymer membrane, which accounts for the polymer ability to store charge, increases by one order of magnitude after confining Omp2a. Moreover, we observe R_p sensible to changes occurring above the electrode, the value decreasing as follow: non-perforated PLA > nanoporated PLA > Omp2a-filled nanoporated PLA, whereas Q_{dl} varies in the opposite order, as expected. Therefore, the pore resistance has dropped down to 16.8% of its initial value (nanoporated PLA), indicating a better diffusion of ions across the pore-induced membrane. Diffusion of ions is also observed by the reduction of the n exponent in the impedance equation from 0.75 to 0.48 (**Table 5.4.2**). Whilst the diffusion of species in a polymer coating is often modelled with Warburg impedance (Z_w),⁶⁵ the diffusion processes are controlled by the pore resistance in the present study.

In order to compare the selectivity of the PLA NMs, impedance analyses were recorded using three electrolytes: NaCl, KCl, and CaCl₂ solutions with various concentrations (*i.e.* 50, 100, 500 and 1000 mM). A complete description of the results is provided in the Nyquist plots displayed in **Figure 5.4.10**, while the contribution of each element of the fitted EEC is listed in **Tables 5.3-5**. Similarly to the above-described tendency, non-perforated PLA NMs are characterized by high R_M and low Q_M values that vary with the electrolyte concentration but not with the nature of the cation (**Figure 5.4.11a**). Whilst the same trend is observed for nanoporated PLA NMs, R_M values here decrease by a factor of 8.7 ± 3.5 compared to non-perforated PLA. Thus, the presence of nanopores decreases the membrane resistance and increases the membrane capacitance, regardless the electrolyte. The R_M values for Omp2a-filled nanoporated PLA NMs, which ranged between $150.9 \Omega \cdot \text{cm}^2$ (in 1 M NaCl) and $2.2 \text{ k}\Omega \cdot \text{cm}^2$ (in 50 mM KCl), not only decrease with increasing ion concentration but they were also nature dependent.

On the other hand, the conductance ($G_m = 1/R_M$) values for Na⁺ electrolyte at 0.5 M NaCl was measured using Omp2a-coated non-perforated PLA NMs. The resulting G_m value, which is $0.30 \pm 0.1 \text{ mS}$, is in good agreement with the values obtained for uncoated non-perforated PLA nanomembranes (**Figure 5.4.11a**). This observation is consistent with the fact that the fraction of protein adsorbed onto the nanomembrane is

not contributing to the ion transport, that role being essentially attributed to the Omp2a aggregates confined in the nanopores.

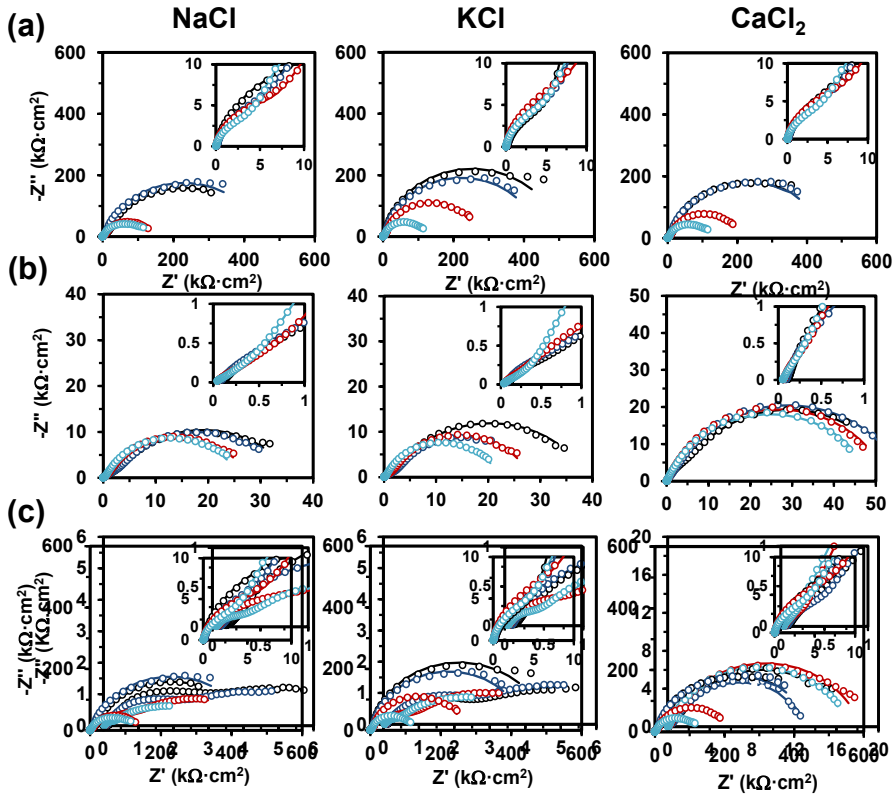


Figure 5.4.10 Nyquist plots of (a) non-perforated, (b) nanoporated and (c) Omp2a-filled nanoporated PLA NMs in NaCl, KCl and CaCl₂ aqueous solutions at 50, 100, 500 and 1000 mM concentrations (black, dark blue, red and light blue profile, respectively). Symbols correspond to experimental data, while lines are the fittings to the corresponding electrical equivalent circuit (EEC) displayed in **Figure 5.4.9e**.

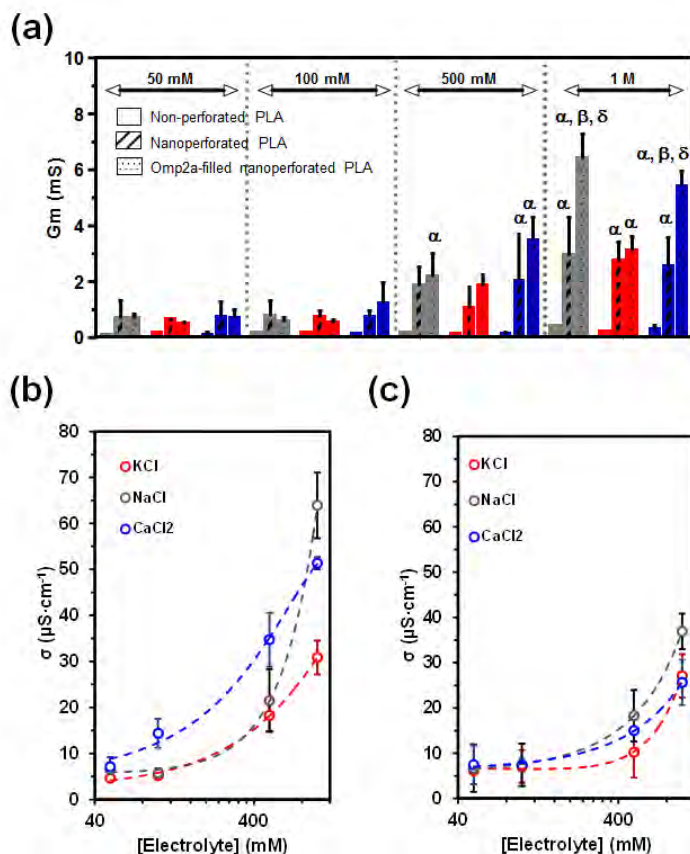


Figure 5.4.11 (a) Comparison of the NM conductance ($G_m = 1/R_M$) values for Na^+ (grey), K^+ (red), and Ca^{2+} (blue) electrolytes at different concentrations. In most of the cases, values are the mean of 3 samples and their standard deviation. Greek letters on the columns refer to significant differences ($p < 0.05$) when the 2way ANOVA and Tukey's multiple comparisons test are applied: α vs non-perforated PLA, β vs nanoperforated-PLA and δ vs Omp2a-filled nanoperforated PLA. Dependence of the conductivity (σ ; Eq. 5.4.1) as a function of the ion concentration in solution for (b) Omp2a-filled nanoperforated and (c) nanoperforated PLA NMs. Non-perforated PLA membrane conductivities are below the dotted orange line. In general the values are the mean of three samples and their standard deviation.

Figures 5.4.11b and **5.4.11c** depict the ion preferences of nanoperforated PLA NMs with and without immobilized Omp2a, respectively, in terms of membrane

conductivity (σ) against ion concentration in solution. The membrane conductivity (σ) was calculated from Eq. 5.4.1:

$$\sigma = \frac{L}{R_M A} \quad (\text{Eq. 5.4.1})$$

where σ is the proton conductivity (S/cm), L is the thickness of the membrane ($\times 10^{-5}$ cm); A is the area of the electrode (1 cm^2), and R_M is the membrane resistance of perforated and non-perforated films. As it can be seen, enhanced ion diffusion was achieved for higher ionic concentrations, especially in the case of Omp2a-containing NMs. In addition, Na^+ and Ca^{2+} ions have a stronger affinity towards the porin channel than K^+ ions, within the studied concentration range, with the best discriminative sensitivity for high concentrations of electrolyte (*i.e.* 0.5 or 1 M). Furthermore, ion selectivity between mono and divalent cations is clearly observed for electrolyte concentrations comprised between 100 and 500 mM.

Finally, changes in R_M with the concentration of electrolyte were found to be reversible. Indeed, after going from highly diluted solutions to concentrated ones and then back to low concentrated solutions, the values for R_M were maintained. This is illustrated in **Figure 5.4.12** for Omp2a-filled nanoporated PLA NMs, which displays the variation of R_M with the KCl concentration.

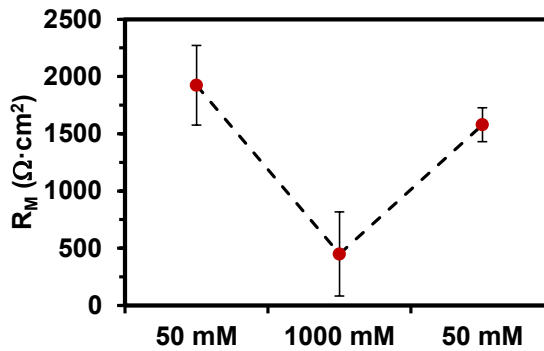


Figure 5.4.12 Variation of the Omp2a-filled nanoporated membrane resistance (R_M) with the KCl concentration. The values are the mean of three samples and their standard deviation.

Table 5.4.3 Resistances and CPEs for each sample from fitting parameters obtained with the EEC displayed in **Figure 5.4.9e**. For each system impedance parameters are displayed according to the NaCl concentrations of 50, 100, 500 and 1000 mM. The percentage errors associated to each circuit element have been included in parentheses.

	R_s ($\Omega \cdot \text{cm}^2$)	CPE_M ($F \text{cm}^{-2} \cdot \text{s}^n$))	n	R_M ($\Omega \cdot \text{cm}^2$)	CPE_{dl} ($F \text{cm}^{-2} \cdot \text{s}^n$))	n	R_p ($\Omega \cdot \text{cm}^2$)
50 mM							
Non-perforated PLA	127.8 (1.5)	$2.91 \cdot 10^{-6}$ (3.6)	0.9 (0.9)	$12.3 \cdot 10^3$ (4.7)	$1.22 \cdot 10^{-5}$ (1.2)	0.21 (1.2)	$429 \cdot 10^3$ (2.7)
Nanoperforated PLA	99.9 (1.6)	$2.95 \cdot 10^{-5}$ (4.1)	0.56 (1.0)	$2.22 \cdot 10^3$ (4.8)	$6.14 \cdot 10^{-5}$ (1.1)	0.7 (1.1)	$33.7 \cdot 10^3$ (1.6)
Omp2a-filled nanoperforated PLA	98.9 (1.9)	$1.45 \cdot 10^{-5}$ (8.5)	0.95 (2.1)	$1.06 \cdot 10^3$ (4.6)	$5.1 \cdot 10^{-4}$ (5.4)	0.49 (2.5)	$5.1 \cdot 10^3$ (5.9)
100 mM							
Non-perforated PLA	133.2 (1.6)	$4.88 \cdot 10^{-6}$ (5.6)	0.85 (1.1)	$6.88 \cdot 10^3$ (6.6)	$1.18 \cdot 10^{-5}$ (1.3)	0.85 (1.2)	$443 \cdot 10^3$ (3.2)
Nanoperforated PLA	66.2 (1.4)	$2.66 \cdot 10^{-5}$ (3.6)	0.56 (0.8)	$2.63 \cdot 10^3$ (4.9)	$6.14 \cdot 10^{-5}$ (1.3)	0.7 (1.4)	$31.6 \cdot 10^3$ (1.9)
Omp2a-filled nanoperforated PLA	93.7 (1.4)	$1.49 \cdot 10^{-5}$ (5.9)	0.94 (1.6)	$1.49 \cdot 10^3$ (3.6)	$5.77 \cdot 10^{-4}$ (5.6)	0.54 (2.8)	$4.76 \cdot 10^3$ (5.4)

OMP2A ONTO ARTIFICIAL MEMBRANES

500 mM							
Non-perforated PLA	56 (1.1)	$3.15 \cdot 10^{-6}$ (4.7)	0.92 (1.2)	$5.99 \cdot 10^3$ (5.4)	$1.54 \cdot 10^{-5}$ (1.2)	0.79 (1.2)	$135.5 \cdot 10^3$ (1.9)
Nanoperforated PLA	36.9 (1.9)	$6.41 \cdot 10^{-5}$ (5.3)	0.51 (1.2)	883 (4.8)	$6.56 \cdot 10^{-5}$ (0.8)	0.75 (0.8)	$26.8 \cdot 10^3$ (1.2)
Omp2a-filled nanoperforated PLA	56.1 (1.9)	$2.46 \cdot 10^{-5}$ (13.1)	0.96 (2.9)	317 (6.2)	$7.54 \cdot 10^{-4}$ (3.1)	0.48 (2.3)	$4.49 \cdot 10^3$ (6.4)
1000 mM							
Non-perforated PLA	45.7 (1.4)	$4.03 \cdot 10^{-6}$ (8.0)	0.95 (1.8)	$2.59 \cdot 10^3$ (7.3)	$1.59 \cdot 10^{-5}$ (1.1)	0.77 (1.0)	$124.6 \cdot 10^3$ (1.8)
Nanoperforated PLA	26.66 (2.1)	$1.52 \cdot 10^{-4}$ (4.8)	0.43 (1.2)	669 (5.1)	$6.67 \cdot 10^{-5}$ (0.54)	0.77 (0.5)	$25.25 \cdot 10^3$ (0.8)
Omp2a-filled nanoperforated PLA	45.6 (2.4)	$3.88 \cdot 10^{-5}$ (23.5)	0.97 (5.2)	150.9 (11.4)	$7.25 \cdot 10^{-3}$ (8.0)	0.49 (2.5)	$5.14 \cdot 10^3$ (8.0)

Table 5.4.4 Resistances and CPEs for each sample from fitting parameters obtained with the EEC displayed in **Figure 5.4.9e**. For each system impedance parameters are displayed according to the KCl concentrations of 50, 100, 500 and 1000 mM. The percentage errors associated to each circuit element have been included in parentheses.

	R_s ($\Omega \cdot \text{cm}^2$)	CPE_M ($F \text{cm}^{-2} \cdot \text{s}^{-n}$))	n	R_M ($\Omega \cdot \text{cm}^2$)	CPE_{dl} ($F \text{cm}^{-2} \cdot \text{s}^{-n}$))	n	R_p ($\Omega \cdot \text{cm}^2$)
50 mM							
Non-perforated PLA	184.4 (1.9)	$5.68 \cdot 10^{-6}$ (6.6)	0.8 (1.3)	$6.16 \cdot 10^3$ (6.0)	$1.04 \cdot 10^{-5}$ (1.3)	0.93 (1.0)	$492 \cdot 10^3$ (2.9)
Nanoperforated PLA	74.4 (2.6)	$3 \cdot 10^{-5}$ (8.2)	0.53 (1.8)	$1.58 \cdot 10^3$ (6.8)	$5.67 \cdot 10^{-5}$ (1.5)	0.72 (1.5)	$37.7 \cdot 10^3$ (2.6)
Omp2a-filled nanoperforated PLA	110.5 (2.6)	$1.62 \cdot 10^{-5}$ (8.4)	0.83 (2.8)	$2.2 \cdot 10^3$ (7.3)	$4.65 \cdot 10^{-4}$ (16.7)	0.51 (4.9)	$3.56 \cdot 10^3$ (8.1)
100 mM							
Non-perforated PLA	107.2 (1.5)	$4.65 \cdot 10^{-6}$ (4.6)	0.84 (0.8)	$7.41 \cdot 10^3$ (4.7)	$1.08 \cdot 10^{-5}$ (1.2)	0.92 (0.9)	$432 \cdot 10^3$ (2.4)
Nanoperforated PLA	55.5 (3.0)	$1.95 \cdot 10^{-5}$ (7.9)	0.57 (1.6)	$1.83 \cdot 10^3$ (6.6)	$6.23 \cdot 10^{-5}$ (2.0)	0.71 (2.1)	$26.25 \cdot 10^3$ (2.9)
Omp2a-filled nanoperforated PLA	79.3 (2.5)	$1.68 \cdot 10^{-5}$ (8.9)	0.84 (2.8)	$1.87 \cdot 10^3$ (7.1)	$5.21 \cdot 10^{-4}$ (13.9)	0.53 (5.4)	$3.67 \cdot 10^3$ (8.4)

OMP2A ONTO ARTIFICIAL MEMBRANES

500 mM							
Non-perforated PLA	63.7 (1.0)	$4.4 \cdot 10^{-6}$ (2.8)	0.87 (0.5)	$9.39 \cdot 10^3$ (3.8)	$1.15 \cdot 10^{-5}$ (1.0)	0.91 (0.9)	$255.6 \cdot 10^3$ (1.6)
Nanoperforated PLA	32.1 (3.8)	$6.61 \cdot 10^{-5}$ (6.1)	0.48 (1.5)	$2.1 \cdot 10^3$ (10.9)	$6.72 \cdot 10^{-5}$ (2.3)	0.78 (2.0)	$26 \cdot 10^3$ (2.7)
Omp2a-filled nanoperforated PLA	54.6 (2.2)	$3.32 \cdot 10^{-5}$ (10.4)	0.79 (3.3)	751 (9.6)	$7.07 \cdot 10^{-4}$ (9.0)	0.53 (6.5)	$3.71 \cdot 10^3$ (9.0)
1000 mM							
Non-perforated PLA	42.8 (1.3)	$5.09 \cdot 10^{-6}$ (3.9)	0.87 (0.8)	$4.92 \cdot 10^3$ (5.7)	$1.34 \cdot 10^{-5}$ (1.3)	0.87 (1.2)	$117 \cdot 10^3$ (1.7)
Nanoperforated PLA	23.73 (2.7)	$1.14 \cdot 10^{-4}$ (5.9)	0.45 (1.4)	448 (3.6)	$6.97 \cdot 10^{-5}$ (0.6)	0.78 (0.4)	$21.64 \cdot 10^3$ (0.8)
Omp2a-filled nanoperforated PLA	37.6 (2.6)	$5.41 \cdot 10^{-5}$ (18.3)	0.85 (4.7)	238.7 (10.8)	$6.53 \cdot 10^{-4}$ (3.9)	0.47 (2.3)	$4.22 \cdot 10^3$ (6.7)

Table 5.4.5 Resistances and CPEs for each sample from fitting parameters obtained with the EEC displayed in **Figure 5.4.9e**. For each system impedance parameters are displayed according to the CaCl₂ concentrations of 50, 100, 500 and 1000 mM. The percentage errors associated to each circuit element have been included in parentheses.

	R_s (Ω·cm²)	CPE_M (Fcm⁻²·sⁿ)	n	R_M (Ω·cm²)	CPE_{dl} (Fcm⁻²·sⁿ)	n	R_p (Ω·cm²)
50 mM							
Non-perforated PLA	157 (0.9)	4.3·10 ⁻⁶ (5.2)	0.85 (3.6)	9.24·10 ³ (1.4)	1.13·10 ⁻⁵ (0.9)	0.57 (3.0)	461·10 ³ (4.1)
Nanoperforated PLA	112.8 (0.6)	2.947·10 ⁻⁵ (3.6)	0.82 (1.6)	3.85·10 ³ (13.1)	4.14·10 ⁻⁵ (2.9)	0.81 (1.9)	52.6·10 ³ (2.4)
Omp2a-filled nanoperforated PLA	84.8 (1.4)	1·10 ⁻⁴ (8.4)	0.61 (2.1)	1.01·10 ³ (17.1)	8.2·10 ⁻⁵ (2.2)	0.8 (2.2)	16.31·10 ³ (3.0)
100 mM							
Non-perforated PLA	115.3 (0.7)	4.2·10 ⁻⁶ (8.3)	0.6 (4.2)	7.41·10 ³ (2.1)	1.15·10 ⁻⁵ (0.3)	0.82 (0.8)	410·10 ³ (0.8)
Nanoperforated PLA	91 (0.7)	3.67·10 ⁻⁵ (1.0)	0.81 (1.1)	1.15·10 ³ (11.2)	4.06·10 ⁻⁵ (1.0)	0.81 (1.7)	55.5·10 ³ (1.7)
Omp2a-filled nanoperforated PLA	61.4 (2.0)	8.98·10 ⁻⁵ (12.4)	0.59 (2.8)	768 (16.2)	8.52·10 ⁻⁵ (2.8)	0.83 (2.6)	12.14·10 ³ (3.4)
500 mM							

OMP2A ONTO ARTIFICIAL MEMBRANES

Non-perforated PLA	58.21 (1.0)	$3.5 \cdot 10^{-6}$ (2.0)	0.92 (0.2)	$8.21 \cdot 10^3$ (1.4)	$1.41 \cdot 10^{-5}$ (3.0)	0.87 (0.9)	$197.5 \cdot 10^3$ (1.5)
Nanoperforated PLA	60.5 (0.9)	$7.75 \cdot 10^{-5}$ (13.0)	0.77 (2.8)	326 (15.8)	$4.07 \cdot 10^{-5}$ (0.9)	0.81 (0.8)	$52.4 \cdot 10^3$ (1.5)
Omp2a-filled nanoperforated PLA	41.2 (1.2)	$7.73 \cdot 10^{-5}$ (9.7)	0.68 (1.9)	246.2 (6.2)	$8.43 \cdot 10^{-5}$ (0.9)	0.81 (0.7)	$18.02 \cdot 10^3$ (1.2)
1000 mM							
Non-perforated PLA	44.8 (3.1)	$4.55 \cdot 10^{-6}$ (1.3)	0.9 (0.9)	$3.92 \cdot 10^3$ (5.0)	$1.48 \cdot 10^{-5}$ (1.6)	0.79 (1.4)	$127 \cdot 10^3$ (4.2)
Nanoperforated PLA	53.2 (1.2)	$2.33 \cdot 10^{-4}$ (12.2)	0.61 (2.8)	411 (27.2)	$4.29 \cdot 10^{-5}$ (0.9)	0.81 (0.9)	$48.6 \cdot 10^3$ (1.4)
Omp2a-filled nanoperforated PLA	32.8 (1.1)	$1.86 \cdot 10^{-4}$ (9.3)	0.61(2.0)	196.9 (8.4)	$8.34 \cdot 10^{-5}$ (3.9)	0.81 (0.6)	$16.86 \cdot 10^3$ (1.0)

Discussion

Through the development of nanotechnology and molecular engineering, biomimetic devices based on complex biological structures are now emerging at the nanoscale. Within this context, biomimetic artificial channels and pores have been prepared using different techniques, as for example lithography⁶⁶ and ion⁶⁷ or electron⁶⁸ beam sculpting. Besides, supported OM protein-containing NMs can be prepared by spreading vesicles containing the proteins and by chemical or physical immobilization of the OM protein (*e.g.* by incorporating anchor molecules or by promoting hydrophobic protein–substrate interactions, respectively) onto the substrate.^{54,69} In spite of those important advances, supported NMs exhibit fundamental drawbacks.

The first arises from the proximity of the artificial NM and the bare solid surface it is deposited onto, which typically is metallic or ceramic. Thus, the NM–substrate distance is usually not sufficiently large to avoid direct contact between the incorporated OM protein and the solid surface, which usually induces protein denaturation. Different strategies have been proposed to reduce and even eliminate this problem. In a seminal work, Römer and Steinem,⁷⁰ inserted gramicidin D into suspended lipidic NMs. More specifically, porous alumina substrates with controlled pore diameter were prepared by anodizing electropolished aluminium foils in acidic solutions, followed by dissolution of the remaining aluminium and alumina at the backside of the pores. After coating one side of such porous material with a thin gold layer that was subsequently functionalized to achieve a hydrophobic surface, suspended 1,2-diphytanoyl-*sn*-glycero-3-phosphocholin NMs were formed, as was proved by EIS measurements.⁴³ However, direct contact between the OM protein and the solid surface can be avoided using a much simpler approach, which consists on the application of polymeric NMs to reduce the frictional coupling with the inorganic support.^{54,60} For instance, in a recent study, we preserved the β -barrel structure of the OM protein in PNMPy-Omp2a NMs, which were obtained by *in situ* anodic polymerization introducing Omp2a in the monomer-containing generation medium.⁵⁴

The second, and probably more critical, limitation of supported NMs comes from their own lack of self-supported behaviour. As a result, although supported OM protein-

containing NMs have numerous potential applications such as electrochemical biosensing, the applicability of self-supported polymeric NMs is up to now less restricted, which makes them attractive not only for biomedical applications (*e.g.* devices for controlled delivery of ions), but also to other technological fields, like nanofluidics.

In recent years, some studies have been devoted to confine porins into nanopores constructed from polymeric membranes. Jovanovic-Talisman *et al.*⁷¹ tethered porins rich in Phe-Gly domains in track-etched polycarbonate membranes with cylindrical nanopores of 30 nm in diameter and 6 μm in length. For this purpose, a thiol-modified tear porin was attached to the gold-layer previously sputtered onto one side of the NM. On the other hand, Kowalczyk *et al.*⁷² demonstrated selective transport of proteins across individual biomimetic nuclear pore complexes at the single-molecule level. This was achieved by drilling nanopores into a 20-nm thin free-standing silicon nitride (SiN) membrane with a focused transmission electron microscope beam. After this, nucleoporin-functionalization of the nanopores was performed in a complex three-step chemical process with hetero-bifunctional cross-linkers, which is similar to that employed for immobilizing DNA onto silicon surfaces.⁷³

In this work, nanoporated PLA FSNMs were fabricated using an approach based on the combination of spin-coating with phase segregation using immiscible PLA:PVA mixtures, and the subsequent removal of PVA domains via selective solvent etching.⁵⁶ The quantitative evaluation of this procedure using different conditions has shown that the diameter of the nanopores decreases from 170 ± 73 nm to 65 ± 32 nm if a 90:10 PLA:PVA mixture is prepared under vigorous stirring.⁵⁶ In order to reduce the diameter of the nanoporations (by $\sim 20\%$), the concentration of PVA in the PLA: PVA mixture was further decreased in this work. Hence, PLA FSNMs with nanopores of 51 ± 22 nm in diameter and similar depths (~ 100 nm) were obtained using 99:1 PLA:PVA mixtures.

The intrinsic conformational flexibility of OM proteins critically governs their function as elements for selective transport of ions through cell membranes. Polymeric NMs used as domains to accommodate such biomolecules through their immobilization either at the surface, inside the matrix, or inserted into nanopores as in this work, must preserve such conformational flexibility. Accordingly, the movements of NM components

(*i.e.* polymer molecules) facilitate and ultimately determine the functionality of the OM protein. These movements largely depend on the flexibility and mechanical properties of the whole NM. Within this context, it should be emphasized that PLA FSNMs are flexible and, indeed, are softer than bulk PLA. The mechanical properties of non-perforated PLA FSNMs prepared using a procedure similar to that employed in this work (*i.e.* spin-coating) were carefully examined by Okamura and co-workers⁸ using a bulging test. These authors observed that NMs with a thickness of 23 ± 5 nm and 60 ± 14 nm swelled gradually and gave almost semicircular deflection until a pressure of approximately 4 kPa and 7 kPa, respectively. The elastic moduli of these PLA FSNMs were 1.7 ± 0.1 GPa and 3.1 ± 0.5 GPa, respectively. On the other hand, the elastic modulus of ultrathin PLA-mesh systems, which consists of PLA FSNMs collected on stainless steel meshes, was found to gradually increase with the thickness.⁵ That is, the modulus grows from 3.5 ± 1.3 GPa to 5.1 ± 1.0 GPa when the thickness increases from 29 ± 1 to 213 ± 2.4 nm, respectively. Interestingly, comparison of the elastic moduli of FSNMs prepared using different polymers indicates that those coming from PLA are amongst the softer ones.³ According to these reported observations, the elastic modulus of the NMs prepared in this work, which exhibited a thickness of ~ 110 nm, are expected to be significantly lower than that reported by Eling *et al.*⁷⁴ for bulk PLA films (*i.e.* 7-10 GPa for a film thickness of 703 ± 4.4 nm).

The OM porin Omp2a was reconstituted into preformed nanoporated PLA FSNMs of moderate electrical resistivity (~ 12 k Ω). Although this value is considerably smaller than the resistance of lipid bilayers (~ 1 M Ω)^{75,76} frequently used to incorporate and study the functionality of OM proteins and ion transport,⁷⁵⁻⁷⁸ the PLA-Omp2a molecular architecture studied in this work has provided direct evidences of the enormous changes in the response of artificial nanopores when the protein is confined inside. As a consequence of their response, Omp2a-filled nanoporous PLA FSNMs should be considered hybrid biological/artificial nanosystems with very promising permeation properties for many technological, biomedical, and environmental applications.

Incubation of nanoporated PLA NMs in Omp2a solution led not only to the immobilization of oval protein aggregates onto the surface, but also to their confinement

inside the nanopores. Although the mass of protein at the nanoporated NMs progressively grew with the concentration of Omp2a in the incubation solution, the immobilized oval aggregates followed the same random distribution in all cases. This behaviour is fully consistent with both the experimental observations and the biophysical model of outer membranes growth of Gram-negative bacteria,⁷⁹ which are composed of proteins, phospholipids, lipoproteins, and lipopolysaccharides. Accordingly, patches of the new OM material, which include porins, are added in discrete bursts that evolve in time following a Stokes flow and organize randomly.

Comparison of the EIS results obtained for nanoporated PLA NMs with and without Omp2a evidences that the OM protein was properly immobilized, retaining the functionality associated to the β -barrel structure. Most importantly, the Omp2a protein was successfully retained during the overall of the EIS analyses within the membrane, and Omp2a-filled nanoporated PLA NMs exhibit selective transport of ions when the electrolyte concentrations are high. Thus, the transport of Ca^{2+} and Na^{+} was favoured with respect to the transport of K^{+} for electrolyte concentrations higher than 500 mM, this effect increasing with the concentration. This ion affinity becomes less appreciable for low electrolyte concentrations (50 mM). Interestingly, the diffusion of Na^{+} and Ca^{2+} ions are significantly lower for nanoporated PLA NMs at the highest electrolyte concentration (1 M), evidencing the crucial role played by Omp2a in the transport process. Although porins are not selective because of their pore dimensions (*i.e.* they are too large to be specific), the pore walls are known to have slight preferences for ion permeability.⁸⁰ In general, the selectivity of large pores, like those of porins, are associated with two components:⁸¹ *i)* partitioning, an equilibrium between the exclusion and accumulation of ions within the pore; and *ii)* diffusion, a non-equilibrium measure of the intrinsic ion mobility within the pore. The fact that in the present study the best discrimination was obtained for very high electrolyte concentrations (> 0.5 M) should be attributed to the low transport efficiency of the proteins confined inside the pores, which in turn is related with their relative orientations. Thus, the methodology presented in this work does not allow control the orientation of confined protein aggregates. In order to achieve the maximum transport efficiency, proteins should be oriented with the channel.

In a recent work, Balme *et al.*⁶¹ used commercial polycarbonate membranes, which were 5 μm thick and exhibited nanopores with diameter of 15 nm, to immobilize gramicidin A. The latter is a linear pentadecapeptide that presents an alternating sequence of D and L amino acids defining a right handed β -helix.⁸² The head-to-head association of gramicidin A molecules gives ion channels that are selectively permeable to monovalent cations and impermeable to anions, such as Cl^- .⁸³ Polycarbonate membranes with gramicidin A confined into the nanopores were permeable to K^+ and in a minor proportion to Na^+ and Ca^{2+} , even though the KCl/NaCl diffusion coefficient ratio was comparable to that measured through gramicidin A under biological conditions (*i.e.* lipid bilayers).⁶¹ These results were attributed to the fact the β -helical conformation was kept in the pore centre. Omp2a-filled nanoporated PLA NMs provide two important improvements with respect to polycarbonate membranes. First, the thickness of the membrane has been reduced from the micrometric to the nanometric scale preserving the free-standing behaviour. Moreover, such a reduction facilitates the movement of the polymer molecules enhancing the flexibility of the NM, which affects positively to the ion transport across the biomolecule. Second, PLA is not only biocompatible, as is polycarbonate, but is also biodegradable. Accordingly, FSNMs made of PLA and Omp2a are very promising for biomedical applications that require completely biodegradable devices for selective ion transport.

Chaaya *et al.*⁸⁴ reported the confinement of gramicidin A inside nanopores (diameter 10.6 nm, 5.7 nm and ~ 2 nm) obtained by track-etching and atomic layer deposition on flexible poly(ethyleneterephthalate) (PET) films. Amazingly, in that case confined gramicidin A exhibited a better permeability to Cl^- than to Na^+ (*i.e.* the permeability ratio $P_{\text{Na}^+}/P_{\text{Cl}^-} < 1$). This behaviour, which is contrary to the selectivity of the channel in biological membranes, was explained by the loss of gramicidin head-to-head association. In biological membranes the impermeability to Cl^- is due to changes in the hydration state near the head-to-head connection between associated gramicidin molecules and in the β -helix structure.^{85,86} However in PET membranes, the gramicidin aggregation is dismantled in the solution used for the immobilization, and is not recovered upon confinement inside the nanopore.⁸⁴ In order to preserve the operative and functional

state of the biomolecule when confined inside nanopores, the protein must retain its folded and assembled form. In this work, the β -barrel structure of the Omp2a porin (**Figure 5.4.1b**) has been saved not only because of the formation of a stable PLA–Omp2a interface, but also because of the nanometric thickness of PLA FSNMs. Thus, the confinement of biomolecules inside polymeric NMs avoids the influence of many effects typically associated with bulk polymers. For example, the formation of well-defined multiphase microdomains (*i.e.* coexisting crystalline and amorphous domains) results in different polymer–biomolecule interfaces since the properties of such domains differ. Also, with respect to NMs, the flexibility and the elastic modulus of bulk films are lower and higher. Accordingly, the formation of stable polymer–biomolecule interfaces is more difficult in bulk films because of the reduction of the polymeric molecules motion. It should be underlined that the thickness of the PET films reported by Chaaya *et al.*⁸⁴ was $\sim 5 \mu\text{m}$ and in this case, the polymer–biomolecule effects should be related to those typically found in systems involving bulk polymers.

5.4.3 Conclusions

We have examined the feasibility of FSNMs for selective ion transport by integrating an OM protein, Omp2a, into nanoporous ultra-thin films of PLA. When oval protein aggregates were immobilized inside nanoporations of diameter $51 \pm 22 \text{ nm}$, the resulting PLA NMs showed much higher ion transport activity than nanoporous films without immobilized Omp2a, especially at high electrolyte concentrations. Hence, the ion affinity of Omp2a-filled nanoporous PLA NMs increases with the concentration. In addition, ion diffusion of Ca^{2+} and Na^{+} ions through Omp2a-filled nanopores is significantly higher than for K^{+} at concentrations $\geq 500 \text{ mM}$. Overall the results suggest that the novel Omp2a–PLA platform fulfills not only the nanometric dimensional requisite for truly mimicking biological attributes, but also the conditions necessary for designing new NMs for biosensing, nanofluidics and ion-rectifying for energy conversion. This study demonstrates that the bioinspired combination of nanofeatures supported onto polymeric FSNMs with the confinement of OM proteins is a powerful approach that synergistically associates the most important advantages of each component.

5.5 References

1. Watanabe, H.; Muto, E.; Ohzono, T.; Nakao, A. and Kunitake T. Giant nanomembrane of covalently-hybridized epoxy resin and silica. *J. Mater. Chem.* **2009**, *16*, 2425-2431.
2. Sattler, K. D. Handbook of Nanophysics, Functional Nanomaterials, CRC Press, Taylor and Francis Group, BocaRaton, FL, 2011.
3. Pérez-Madrigal, M. M.; Armelin, E.; Puiggali, J. and Alemán, C. Insulating and semiconducting polymeric free-standing nanomembranes with biomedical applications. *J. Mater. Chem. B* **2015**, *3*, 5904-5962.
4. Okamura, Y.; Kabata, K.; Kinoshita, M.; Miyazaki, H.; Saito, A.; Fujie, T.; Ohtsubo, S.; Saitoh D. and Takeoka, S. Free-standing biodegradable poly(lactic acid) nanosheet for sealing operations in surger. *Adv. Mater.* **2013**, *25*, 545-551.
5. Fujie, T.; Ricotti, L.; Desii, A.; Menciassi, A.; Dario, P. and Mattoli, V. Evaluation of substrate effect on cell adhesion properties using freestanding poly(L-lactic acid) nanosheets. *Langmuir*, 2011, **27**, 13173-13182.
6. Pérez-Madrigal, M. M.; Armelin, E.; del Valle, L. J.; Estrany, F. and Alemán, C. Bioactive and electroactive response of flexible polythiophene:polyester nanomembranes for tissue engineering. *Polym. Chem.*, **2012**, *3*, 979-991.
7. Pérez-Madrigal, M. M.; Giannotti, M. I.; Oncins, G.; Franco, L.; Armelin, E.; Puiggali, J.; Sanz, F.; del Valle, L. J. and Alemán, C. Bioactive nanomembranes of semiconductor polythiophene and thermoplastic polyurethane: thermal, nanostructural and nanomechanical properties. *Polym. Chem.*, **2013**, *4*, 568-583.
8. Okamura, Y.; Kabata, K.; Kinoshita, M.; Saitoh, D. and Takeoka, S. Free-standing biodegradable poly(lactic acid) nanosheet for sealing operations in surgery. *Adv. Mater.*, **2009**, *21*, 4388-4392.
9. Miyazaki, H.; Kinoshita, M.; Saito, A.; Fujie, T.; Kabata, K.; Hara, E.; Ono, S.; Takeoka, S.; and Saitoh, D. An ultrathin poly(L-lactic acid) nanosheet as a burn wound dressing for protection against bacterial infection. *Wound Repair Regen.*, **2012**, *20*, 573-579.
10. Pensabene, V.; Taccola, S.; Ricotti, L.; Ciofani, G.; Menciassi, A.; Perut, F.; Salerno, M.; Dario P. and Baldini N., Flexible polymeric ultrathin film for mesenchymal stem cell differentiation. *Acta Biomater.*, **2011**, *7*, 2883-2891.
11. Walheim, S.; Böltau, M.; Mlynek, J.; Krausch, G. and Steiner, U. Structure formation via polymer demixing in spin-cast films. *Macromolecules*, **1997**, *30*, 4995-5003.
12. Zhang, H. and Takeoka, S. Morphological evolution within spin-cast ultrathin polymer blend films clarified by a freestanding method. *Macromolecules*, **2012**, *45*, 4315-4321.
13. Vendamme, R.; Onoue, A.; Nakao, A. and Kunitake T. Robust free-standing nanomembranes of organic/inorganic interpenetrating networks. *Nat. Mater.*, **2006**, *5*, 494-501.
14. Armelin, E.; Gomes, A. L.; Pérez-Madrigal, M. M.; Puiggali, J.; Franco, L.; del Valle, L. J.; Rodríguez-Galán, A.; Campos, J. S. C.; Ferrer-Anglada, N. and Alemán, C. Structure formation via polymer demixing in spin-cast films. *J. Mater. Chem.*, **2012**, *22*, 585-594.

15. Mosmann, T. Rapid colorimetric assay for cellular growth and survival: application to proliferation and cytotoxicity assays. *J. Immunol. Methods*, **1983**, 65, 55-63.
16. Heriot, S. Y. and Jones, R. A. L. An interfacial instability in a transient wetting layer leads to lateral phase separation in thin spin-cast polymer-blend films. *Nat. Mater.*, **2005**, 4, 782-786.
17. V. Swaminathan, R. Tchao and S. Jonnalagadda, *J. Biomater. Sci. Polym. Ed.* Physical characterization of thin semi-porous poly(lactic acid)/poly(ethylene glycol) membranes for tissue engineering, 2007, **18**, 1321-1323.
18. Pérez-Madrigal, M. M.; Giannotti, M. I.; del Valle, L. J.; Franco, L.; Armelin, E.; Puiggalí, J.; Sanz, F. and Alemán C., C. *ACS Appl. Mater. Interfaces.*, **2014**, 6, 9719-9732.
19. Molino, P. J.; Higgins, M. J.; Innis, P. C.; Kapsa, R. M. I. and Wallace, G. G. Fibronectin and bovine serum albumin adsorption and conformational dynamics on inherently conducting polymers: A QCM-D study. *Langmuir*, **2012**, 30, 8433-8445.
20. Adamson, A. W. *Physical chemistry of surfaces*, 5th ed, John Wiley: New York, **1990**.
21. Correia, N. T.; Ramos, J. M.; Saramago, B. and Calado, J. Estimation of the Surface tension of a solid: application to a liquid crystalline polymer. *J. Colloid Interface Sci.*, **1997**, 189, 361-369.
22. Owens, D. K. and Wendt, R. C. Estimation of the surface free energy of polymers. *J. Appl. Polym. Sci.*, **1969**, 13, 1741-1747.
23. Mattila, P. K. and Lappalainen, P. Filopodia: molecular architecture and cellular functions. *Nat. Rev. Mol. Cell Biol.*, **2008**, 9, 446-454.
24. Yuan, X. B.; Jin, M.; Xu, X.; Song, Y. Q.; Wu, C. P.; Poo, M. M. and Duan, S. Signalling and crosstalk of Rho GTPases in mediating axon guidance. *Nat. Cell Biol.*, **2003**, 5, 38-45.
25. Steketee, M. B. and Tosney, K. W. Three functionally distinct adhesions in filopodia: shaft adhesions control lamellar extension. *J. Neurosci.*, **2002**, 22, 8071-8083.
26. Lamoureux, P.; Buxbaum, R. E. and Heidemann, S. R. Direct evidence that growth cones pull. *Nature*, **1989**, 340, 159-162.
27. Birnie, D. P. Rational solvent selection strategies to combat striation formation during spin coating of thin films. *J. Mater. Res.* **2001**, 16, 1145-1154
28. Zeng, L.; Yang, Z.; Zhang, H.; Hou, X.; Tian, Y.; Yang, F.; Zhou, J.; Li, L. and Jiang, L. Tunable ionic transport control inside a bio-inspired constructive bi-channel nanofluidic device. *Small*, **2014**, 10, 793-801.
29. Daiguji, H. Ion transport in nanofluidic channels. *Chem. Soc. Rev.*, **2010**, 39, 901-911.
30. Ali, M.; Yameen, B.; Cervera, J.; Ramirez, P.; Neumann, R.; Ensinger, W.; Knoll, W. and Azzaroni O. Layer-by-layer assembly of polyelectrolytes into ionic current rectifying solid-state nanopores: insights from theory and experiment. *J. Am. Chem. Soc.*, **2010**, 132, 8338-8348.
31. Kumar, B. V. V. S. P.; Rao, K. V.; Sampath, S.; George, S.J. and Eswaramoorthy, M. Supramolecular gating of ion transport in nanochannels. *Angew. Chem., Int. Ed.*, **2014**, 53, 13073-13077.

32. Miles, B. N.; Ivanov, A. P.; Wilson, K. A.; Dogan, F.; Japrun, D. and Edel, J. Single molecule sensing with solid-state nanopores: novel materials, methods and applications. *Chem. Soc. Rev.*, **2013**, 42, 15–28.
33. de la Escosura-Muñiz, A. and Merkoc-i, A. Nanochannels preparation and application in biosensing. *ACS Nano*, **2012**, 6, 7556–7583.
34. Balme, S.; Janot, J. M.; Berardo, L.; Henn, F.; Bonhenry, D.; Kraszewski, S.; Picaud, F. and Ramseyer, C. New bioinspired membrane made of a biological ion channel confined into the cylindrical nanopore of a solid-state polymer. *Nano Lett.*, **2011**, 11, 712–716.
35. Ali, M.; Nasir, S.; Nguyen, Q. H.; Sahoo, J. K.; Tahir, M. N.; Tremel, W. and Ensinger, W. Metal ion affinity-based biomolecular recognition and conjugation inside synthetic polymer nanopores modified with iron-terpyridine complexes. *J. Am. Chem. Soc.*, **2011**, 133, 17307–17314.
36. Cazacu, A.; Legrand, Y. M.; Pasc, A.; Nasr, G.; Van der Lee, A.; Mahon, E. and Barboiu, M. Dynamic hybrid materials for constitutional self-instructed membranes. *Proc. Natl. Acad. Sci. U. S. A.*, **2009**, 106, 8117–8122.
37. Kim, S.; Nham, J.; Jeong, Y. S.; Lee, C. S.; Ha, S. H.; Park, H. B. and Lee, Y. J. Biomimetic selective ion transport through graphene oxide membranes functionalized with ion recognizing peptides. *Chem. Mater.*, **2015**, 27, 1255–1261
38. Kowalczyk, S. W.; Blosser, T. R. and Dekker, C. Biomimetic nanopores: learning from and about nature. *Trends Biotechnol.*, **2011**, 29, 607–614.
39. Galdiero, S.; Falanga, A.; Cantisani, M.; Tarallo, R.; Della Pepa, M. E.; D’Orlando, V. and Galdiero, M. Microbe-host interactions: structure and role of gram-negative bacterial porins. *Curr. Protein Pept. Sci.*, **2012**, 13, 843–854.
40. Weeber, E. J.; Michael, L.; Sampson, M. J.; Anflous, K.; Armstrong, D. L.; Brown, S. E.; Sweatt, J. D. and Craigen, W. J. The role of mitochondrial porins and the permeability transition pore in learning and synaptic plasticity. *J. Biol. Chem.*, **2002**, 277, 18891–18897.
41. Fischer, K.; Weber, A.; Brink, S.; Arbinger, B.; Schünemann, D.; Borchert, S.; Heldt, H. W.; Popp, B.; Benz, R.; Link, T. A.; Eckerskorn, C. and Flügge, U.-I. The role of mitochondrial porins and the permeability transition pore in learning and synaptic plasticity. *J. Biol. Chem.*, **1994**, 269, 25754–25760.
42. Cama, J.; Bajaj, H.; Pagliara, S.; Maier, T. and Braun, Y. Quantification of fluoroquinolone uptake through the outer membrane channel OmpF of *Escherichia coli*. *J. Am. Chem. Soc.*, 2015, **137**, 13836–13843.
43. Boschirolì, M.-L.; Foulongne, V. and O’Callaghan, D. A. Brucellosis: a worldwide zoonosis. *Curr. Opin. Microbiol.* **2001**, 4, 58–64.
44. Roussel, G.; Matagne, A.; De Bolle, X.; Perpète, E. A. and Michaux, C. Purification, refolding and characterization of the trimeric Omp2a outer membrane porin from *Brucella melitensis*. *Protein Expr. Purif.* **2012**, 83, 198–204.

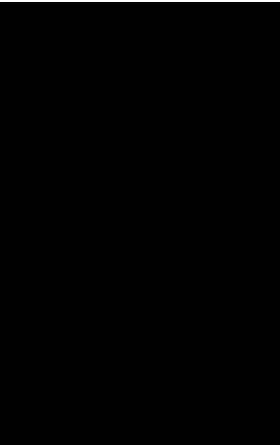
45. Roussel, G.; Perpète, E. A.; Matagne, A.; Tinti, E. and Michaux, C. Towards a universal method for protein refolding: the trimeric beta barrel membrane Omp2a as a test case. *Biotechnol. Bioeng.* **2013**, 110, 417–423.
46. Fyles, T. M. Synthetic ion channels in bilayer membranes. *Chem. Soc. Rev.*, **2007**, 36, 335–347.
47. Meier, W.; Nardin, C. and Winterhalter, M. Reconstitution of channel proteins in (polymerized) ABA triblock copolymer membranes. *Angew. Chem., Int. Ed.*, **2000**, 39, 4599–4602.
48. Kumar, M.; Grzelakowski, M.; Zilles, J.; Clark, M. and Meier, W. Highly permeable polymeric membranes based on the incorporation of the functional water channel protein Aquaporin Z. *Proc. Natl. Acad. Sci. U. S. A.*, **2007**, 104, 20719–20724.
49. Gonzalez-Perez, A.; Stibius, K. B.; Vissing, T.; Nielsen, C. H. and Mouritsen, O. G. Biomimetic triblock copolymer membrane arrays: a stable template functional membrane proteins. *Langmuir*, **2009**, 25, 10447–10450.
50. Hou, X.; Guo, W. and Jiang, L. Biomimetic smart nanopores and nanochannels. *Chem. Soc. Rev.*, **2011**, 40, 2385–2401.
51. Pérez-Madrigal, M. M.; del Valle, L. J.; Armelin, E.; Michaux, C.; Roussel, G.; Perpète, E. A. and Alemán, C. Polypyrrole-supported membrane proteins for bio-inspired ion channels. *ACS Appl. Mater. Interfaces*, **2015**, 7, 1632–1643.
52. Zhang, X.; Fu, W.; Palivan, C. G. and Meier, W. Natural channel protein inserts and functions in a completely artificial, solid-supported bilayer membrane. *Sci. Rep.*, **2013**, 3, 2196.
53. Teixeira-Dias, B.; Alemán, C.; Estrany, F.; Azambuja, D. S. and Armelin, E. Microstructures of poly(N-methylpyrrole) and their interaction with morphine. *Electrochim. Acta*, **2011**, 56, 5836–5843.
54. Aradilla, D.; Estrany, F. and Alemán, C. Symmetric supercapacitors based on multilayers of conducting polymers. *J. Phys. Chem. C*, **2011**, 115, 8430–8438.
55. Guo, W.; Cao, L.; Xia, J.; Nie, F.-Q.; Ma, W.; Xue, J.; Song, Y.; Zhu, D.; Wang, Y. and Jiang L. Energy harvesting with single-ion-selective nanopores: a concentration-gradient-driven nanofluidic power source. *Adv. Funct. Mater.* **2010**, 20, 1339–1344.
56. Puiggalí-Jou, A.; Medina, J.; del Valle, L. J. and Alemán, C. Nanoperforations in poly(lactic acid) free-standing nanomembranes to promote interactions with cell filopodia. *Eur. Polym. J.*, **2016**, 75, 552–564.
57. Paquet, J.-Y.; Diaz, M. A.; Genevrois, S.; Grayon, M.; Verger, J. M.; de Bolle, X.; Lakey, J. H.; Letesson, J.-J. and Cloeckeaert, A. Molecular, antigenic, and functional analyses of Omp2b porin size variants of *Brucella* spp. *J. Bacteriol.* **2001**, 183, 4839–4847.
58. Zeth, K. and Thein, M. Porins in prokaryotes and eukaryotes: common themes and variations. *Biochem. J.*, **2010**, 431, 13–22.

59. Rechendorff, K.; Hovgaard, M. B.; Foss, M.; Zhdanov, V. P. and Besenbacher, F. Enhancement of protein adsorption induced by surface roughness. *Langmuir*, **2006**, *22*, 10885–10888.
60. Hillebrandt, H.; Wiegand, G.; Tanaka, M. and Sackmann, E. High electric resistance polymer/lipid composite films on indium-tin-oxide. *Langmuir*, **1999**, *15*, 8451–8459.
61. Balme, S.; Picaud, F.; Kraszewski, S.; Déjardin, P.; Janot, J. M.; Lepoitevin, M.; Capomanes, J.; Ramseyer, C. and Henn, F. Controlling potassium selectivity and proton blocking in a hybrid biological/solid-state polymer nanoporous membrane. *Nanoscale*, **2013**, *5*, 3961–3968.
62. Barreiros dos Santos, M.; Azevedo, S.; Aguil, J. P.; Prieto-Simón, B.; Sporer, C.; Torrents, E.; Juárez, A.; Teixeira, V. and Samitier, J. Label-free ITO-based immunosensor for the detection of very low concentrations of pathogenic bacteria. *Bioelectrochemistry*, **2015**, *101*, 146–152.
63. Qian, X.; Gu, N.; Cheng, Z.; Yang, X. and Wang, E. Impedance study of (PEO) 10LiClO₄-Al₂O₃ composite polymer electrolyte with blocking electrodes. *Electrochim. Acta*, **2001**, *46*, 1829–1836.
64. Jorcin, J.-B.; Orazem, M. E.; Pébère, N. and Tribollet, B. CPE analysis by local electrochemical impedance spectroscopy. *Electrochim. Acta*, **2006**, *51*, 1473–1479.
65. Skale, S.; Dolecek, V. and Slemnik, M. Substitution of the constant phase element by Warburg impedance for protective coatings. *Corr. Sci.*, **2007**, *49*, 1045–1055.
66. Siwy, Z. and Fulinski, A. Fabrication of a synthetic nanopore ion pump. *Phys. Rev. Lett.*, **2002**, *89*, 198103.
67. Li, J.; Stein, D.; McMullan, C.; Branton, D.; Aziz, M. J. and Golovchenko, J. A. Ion-beam sculpting at nanometer length scales. *Nature*, **2001**, *412*, 166–169.
68. Storm, A. J.; Chen, J. H.; Ling, X. S.; Zandbergen, H. W. and Dekker, C. Fabrication of solid-state nanopores with single-nanometre precision. *Nat. Mater.*, **2003**, *2*, 537–540.
69. Tanaka, M. and Sackmann, E. Polymer-supported membranes as models of the cell surface. *Nature*, **2005**, *437*, 656–663.
70. Römer, W. and Steinem, C. Impedance analysis and single-channel recordings on nano-black lipid membranes based on porous alumina. *Biophys. J.*, **2004**, *86*, 955–965.
71. Jovanovic-Taliman, T.; Tetenbaum-Novatt, J.; McKenney, A. S.; Zilman, A.; Peters, R.; Rout, M. P. and Chait, B. T. *Nature*, **2009**, *457*, 1023–1027.
72. Kowalczyk, S. W.; Kapinos, L.; Blosser, T. R.; Magalhães, T.; van Nies, P.; Lim, R. T. H. and Dekker, C. Single-molecule transport across an individual biomimetic nuclear pore complex. *Nat. Nanotechnol.*, **2011**, *6*, 433–438.
73. Jin, L.; Horgan, A. and Levicky, R. Preparation of end-tethered DNA monolayers on siliceous surfaces using heterobifunctional cross-linkers. *Langmuir*, **2003**, *19*, 6968–6975.
74. Eling, B.; Gogolewski, S. and Pennings, A. Biodegradable materials of poly(L-lactic acid): 1. Melt-spun and solution-spun fibres. *J. Polymer*, **1982**, *23*, 1587–1593.

75. Atanasov, V.; Knorr, N.; Duran, R. S.; Ingebrandt, S.; Offenhäusser, A.; Knoll, W. and Köper, I. Membrane on a chip: A functional tethered lipid bilayer membrane on silicon oxide surfaces. *Biophys. J.*, **2005**, 89, 1780–1788.
76. Gritsch, S.; Nollert, P.; Jähnig, F. and Sackmann, E. Impedance spectroscopy of porin and gramicidin pores reconstituted into supported lipid bilayers on *Langmuir*, **1998**, 14, 3118–3125.
77. Zhu, Z.-W.; Wang, Y.; Zhang, X.; Sun, C.-F.; Li, M.-G.; Yan, J.-W. and Mao, B.W. Electrochemical impedance spectroscopy and atomic force microscopic studies of electrical and mechanical properties of nano-black lipid membranes and size dependence. *Langmuir*, **2012**, 28, 14739–14746.
78. Sugihara, K.; Vörös, J. and Zambelli, T. A. A gigaseal obtained with a self-assembled long-lifetime lipid bilayer on a single polyelectrolyte multilayer-filled nanopore. *ACS Nano*, **2010**, 4, 5047–5054.
79. Ursell, T. S.; Trepagnier, E. H.; Huang, K. C. and Therit, J. A. Analysis of surface protein expression reveals the growth pattern of the gram-negative outer membrane. *PLoS Comput. Biol.*, **2012**, 8, e1002680.
80. Aguilera, V. M.; Queralt-Martín, M.; Aguilera-Arzo, M. and Alcaraz, A. Insights on the permeability of wide protein channels: measurement and interpretation of ion selectivity. *Integr. Biol. (Camb)*, **2011**, 3, 159–172.
81. López, M. L.; Aguilera-Arzo, M.; Aguilera, V. M. and Alcaraz, A. Ion selectivity of a biological channel at high concentration ratio: insights on small ion diffusion and binding. *J. Phys. Chem. B*, **2009**, 113, 8745–8751.
82. Ketchum, R. R.; Hu, W. and Cross, T. A. High-resolution conformation of gramicidin A in a lipid bilayer by solid-state NMR. *Science*, **1993**, 261, 1457–1460.
83. Chernyshev, A.; Pomès, R. and Cukierman, S. Kinetic isotope effects of proton transfer in aqueous and methanol containing solutions, and in gramicidin A channels. *Biophys. Chem.*, **2003**, 103, 179–190.
84. Chaaya, A.A.; Le Poitevin, M.; Cabello-Aguilar, S.; Balme, S.; Bechelany, M.; Kraszewski, S.; Picaud, F.; Cambedouzou, J.; Balanzat, E.; Janot, J.-M.; Thami, T.; Miele, P. and Dejardin, P. Enhanced ionic transport mechanism by gramicidin in a confined inside nanopores tuned by atomic layer deposition. *J. Phys. Chem. C*, **2013**, 117, 15306–15315.
85. Hinton, J. F.; Fernandez, J. Q.; Shungu, D. C. and Millett, F. S. Thermodynamic parameters for the binding of divalent cations to gramicidin A incorporated into a lipid environment by TI-205 nuclear magnetic resonance. *Biophys. J.*, **1989**, 55, 327–330.
86. Allen, T. W.; Andersen, O. S. and Roux, B. Molecular dynamics-potential of mean force calculations as a tool for understanding ion permeation and selectivity in narrow channels. *Biophys. Chem.*, **2006**, 124, 251–267.

PART B

Design of intrinsically controlled
polymers for drug delivery systems



CHAPTER 6: Drug delivery
systems based on intrinsically
conducting polymers

SUMMARY

This **Chapter** tries to review the application of intrinsically conducting polymers (ICPs) for drug delivery systems (DDSs). Drugs administrated to patients do not always reach the targeted organ, which may affect other tissues leading to undesired side-effects. To overcome these associated problems with drug administration DDSs appeared. Nowadays, it is possible to target the administration and, most importantly, to achieve a controlled drug dosage upon external stimuli. In this work the attention has been focused on the drug release upon electrically stimuli employing ICPs. ICPs are well-known organic polymers with outstanding magnetic, electrical and optical properties similar to metals but also retaining some advantageous properties associated with polymers, such as mechanical stability and easiness of processing usually. Depending on the redox state, ICPs can incorporate or release anionic or cationic molecules on-demand. Besides, the releasing rate can be tuned by the type of electrical stimulation applied. Another interesting feature is that ICPs are capable to sense redox molecules such as dopamine, serotonin or ascorbic acid among others. Therefore, future prospects go towards the design of materials where the releasing rate could be self-adjusted in response to changes in the surrounding environment. This recompilation of ideas and projects provides an overview of ICP synthesis and properties relevant to their use as DDSs. Definitely, ICPs hold great potential in DDSs where the dose can be adjusted by the application of an external stimulus, hence optimizing the effect of the drug and diminishing side effects.

Publications derived from this work:

Puiggalí-Jou, A.; del Valle, L. J.; and Alemán, C. Drug delivery systems based on intrinsically conducting polymers. Draft in progress.

6.1 Introduction: drug delivery systems (DDSs)

The understanding of human and animal diseases and the ability to design and synthesize new drugs to overcome them increase year after year. Although such topics advance hand in hand, it is unforgettable that the efficiency of the delivery is a main factor for reaching the optimal therapy. Moreover, the efficacy of the drugs becomes less relevant if they are not directed to the correct target or, what is worse, if the time dosage is not appropriate for the stage of the disease or if they are left to interact with unwanted targets for a long time, leading to serious side effects.

Rapid developments are also under way in the field of biomaterials, which have a great impact on patient care.¹ Although the release and efficacy of a wide range of drugs, antibodies, enzymes and vaccines have been improved for the 60 years,^{2,3} the need of DDSs with controlled, localized and efficient drug dosage remains. The principal problems of conventional drug administration methods are poor solubility of the drugs, possible normal tissue damage, rapid degradation of the drugs, unfavourable pharmacokinetics, low biodistribution and lack of selectivity. DDSs can be used to improve the drugs solubility by incorporating amphiphilic components, such as lipids or specially designed polymers. Furthermore, DDSs provide a carrier for the drug, making difficult the accidental extravasation and increasing the protection from early stage degradation. Besides, they can slow down the renal clearance, reduce side effects and increase drug concentrations in the diseased tissue by enhancing permeability and retention (EPR) effects or by ligand-mediated targeting.

The first steps aimed at the production of DDSs were done in 1950, when drugs were incorporated into solid polymers to obtain sustained drug release for agricultural purposes. In the next decades, those approaches were extended to biomedicine.⁴ Since then, this field have not stopped burgeoning. The first patent for controlled drug release, which consisted on the utilization of coatings onto edible tablets, was deposited by Wurster in 1953.⁵ In 1968 Zaffaroni founded ALZA, the first company dedicated to the commercialization of DDSs, which started releasing low molecular weight drugs, like pilocarpine, using ethylene vinyl acetate copolymer (EVA) and poly(hydroxyethylmethacrylate) (p(HEMA)). Later on, many other polymers were used

since the principal inconvenience associated to these materials, which was the inflammation and rejection that caused to the body, was solved by introducing the proper washing steps.⁶ Besides, a few years later also high molecular weight molecules were retained on polymer pellets and released in a slow fashion manner when exposed to aqueous conditions.⁷

In the 1960s Alec Bangham studied lipids as units for bilayered structures⁸ and propelled the research of liposomes as potential drug carriers⁹. Some systems based on lipids are nowadays commercially used for cancer therapy, as for example DaunoXome (liposomal Daunorubicin), Doxil (liposomal Doxorubicin) and Ara-C liposomal (liposomal Citarabine). These systems increase the circulation half-life and tumour uptake while the toxicological profile on healthy tissues is reduced.

Later on, DDSs extended towards many other inorganic materials (*e.g.* iron oxide,^{10,11} gold,^{12,13} and silicon^{14,15}) and organic materials.¹⁶ Generally, polymeric materials outstand from the rest since they can be modelled and processed into a wide range of forms, like membranes, fibers, foams, micelles, dendrimers, nanoparticles (NPs) and hydrogels. This adjustable feature, along with ease of handling, results in materials able to be accommodated for the treatment of a huge number of medical conditions. Some of these materials have been translated to the clinical use and are being commercialized for a wide range of therapies. For instance, Lupron Depot, which is used to treat advanced prostate cancer, consists on poly(lactic-*co*-glycolic) acid (PLGA) microspheres encapsulating the hormone leuprolide.

Biodegradable polymers, as for example poly(lactic acid) (PLA) and PLGA, are suitable materials for sustained long term release *in vivo*. However, there is no control over when the drug wants to be delivered. New-born systems are those called stimuli responsive or smart biomaterials. These are designed to exert a response when there is a change in the environment (*e.g.* pressure, pH, enzymes, level of glucose or temperature) or, alternatively, they can be remotely triggered by an external stimuli (*e.g.* near infrared (NIR) light, ultrasounds, magnetic fields or electric currents). The former materials respond to localized changes on the ambient of pathological abnormalities and promote the drug release while the latter ones are stimulated on demand for pulsatile drug delivery. Overall, it has been claimed that the global advanced market for DDSs is

expected to grow from roughly \$178.8 billion in 2015 to nearly \$227.3 billion by 2020.^{17,18}

6.2 Intrinsically conducting polymers

Among all the DDSs triggerable by external stimuli, herein we focus on recent advances in intrinsically conducting polymers (ICPs). In general, ICPs are organic materials with characteristics similar to those encountered in metals (*i.e.* good electrical, magnetic and optical properties) and with the outstanding properties of conventional polymers (*i.e.* flexibility in processing, lightness of weight, and easiness in synthesis). Within the context of DDSs, ICPs are considered as electrochemically active and conducting biomaterials that allow the delivery upon electrochemical and/or electrical stimuli.

The modern era of ICPs began at the end of the 1970s when Shirakawa, Heeger and MacDiarmid discovered that the conductivity of doped polyacetylene can increase by 12 orders of magnitude upon iodine counter ions incorporation.^{19,20} The basic structural characteristic of ICPs is the conjugated π system that extends over a large number of monomer units, creating a continuous electron pathway along the polymer backbone.²¹ Thus, the conductivity essentially relies on the characteristic electronic structure of conjugated bonds consisting of alternating single and double bonds along the polymer chain. This conjugation results in an extended π -orbital system that allows charge delocalization along the polymer backbone and between adjacent chains, endowing the polymer semiconductive properties. The doping process facilitates the formation of radical cations / anions (polarons) or dications / dianions (bipolarons) in the backbone, counter-ions from the solution entering into the polymeric matrix to balance the charge.²² This ionic charge movement is reversible upon de-doping, as shown in **Figure 6.1**.

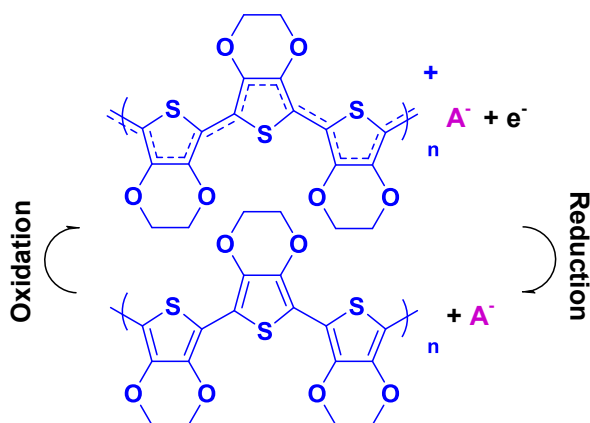


Figure 6.1 Reversible redox activity of poly(3,4-ethylenedioxythiophene) (PEDOT).

When electrons are removed from the valence band through the named p-doping process, positive charged holes are formed in the electronic structure, while negative charges are generated when electrons are injected to the conduction band through the called n-doping process. In both cases there is the necessity to counter balance the electronic charge with opposite charged ions. Obviously, the electrical conductivity of ICPs increases (**Figure 6.2a**) with the extension of the doping process (*i.e.* doping level). Nowadays, there are approximately 25 reported ICPs, which can be synthesized by oxidative chemical or electrochemical polymerization. However, polypyrrole (PPy), poly(3,4-ethylenedioxythiophene) (PEDOT) and polyaniline (PAni), which are displayed in **Figure 6.2b**, are the most employed due to their stability,²³ biocompatibility,²⁴ and good electrical and electrochemical properties.^{25–27} Nevertheless, these polymers also present some drawbacks, like brittleness, rigidity, insolubility, lack of biodegradability and poor processability. In order to overcome these limitations, many times ICPs are combined with biodegradable and / or more flexible polymers, giving place to electroactive copolymers and blends.

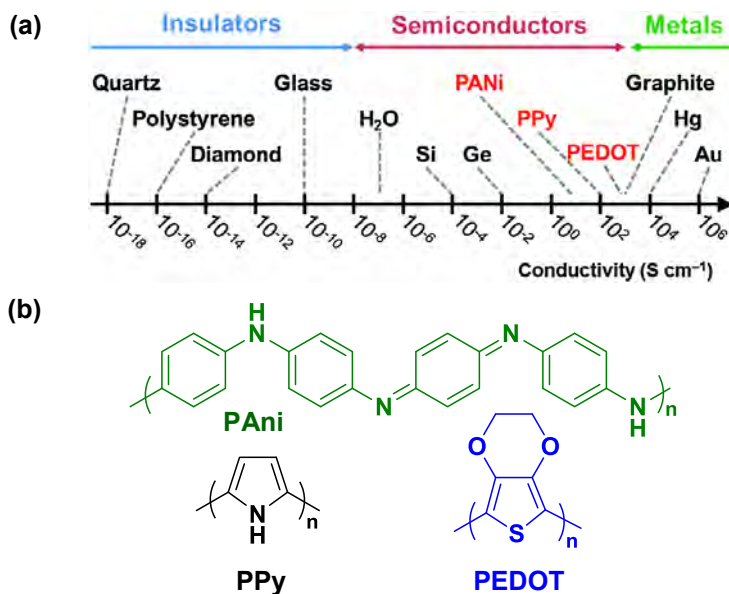


Figure 6.2 (a) Scale of material's conductivity, adapted from.²⁸ (b) Chemical structure of the most employed ICPs (PANi, PPy and PEDOT).

The biocompatibility of ICPs have been studied in a large variety of cell lines, including fibroblasts,²⁹ endothelial, bone cells,³⁰ keratinocytes,³¹ myoblast,³² neural,³³ glial,³⁴ and mesenchymal stem cells.³⁵ After the assessment that ICPs were biocompatible with biological systems, their employment in the biomedical field increased remarkably. Nonetheless, the removal of unreacted monomers, extra dopant ions or residual solvent is critical to obtain non-toxic or, at least, very little toxic ICPs.^{36,37} Moreover it has been claimed that when the materials present nanofeatures could change the toxicity values, generating adverse biological effects due to the superficial area increase.³⁸ Thus, it is vital a constant toxicity evaluation of the ICPs materials to ensure the safety of these devices when used for biomedical applications.

6.3 Architecture of ICPs for DDSs

ICPs can be prepared by chemical (by means of an oxidant agent) or electrochemical (using an oxidising potential through electrodes) synthesis. Recurrently, electrochemical methodologies are far more employed since offer a better control over the overall charge deposition and rate, which are crucial to regulate the final electrochemical and electrical properties of the material.

For their operation, simple ICP films do not provide the most efficient drug loading capacity. The use of micro- and nanostructures can offer a greater drug loading capacity since the surface area is bigger. Thus, depending on the final application, different approaches can be employed for the ICP synthesis with particular structures. Briefly, we can divide the methodologies in three strategies: use of hard templates, soft templates or template-free.^{39,40}

The use hard templates, already existing micro- or nano- structures, to direct the polymer growth is a simple and controllable approach. The biggest drawback is the later removal of the template. Sometimes, this can lead to structure collapse, film ruptures or loss of consistency. Besides, the dimension of the template limits the amount of ICP that can be produced and may restrict the scale up possibilities.⁴¹ Regarding the preparation in the case of chemical synthesis the structure is immersed in a solution containing the monomer, the dopant and the oxidant. However, when electrochemical synthesis is employed, the template needs to be conductive or situated near the electrodes.

The most common hard template include nanoporous membranes made of track-etch polycarbonate (PCTE)⁴² or porous alumina membranes (Al_2O_3).⁴³ In one of the first examples, Martin *et al.*⁴⁴ prepared nanofibers within the pores (100, 200 and 400 nm in diameter) of a PCTE membrane. Strikingly, nanowires as small as 3 nm in diameters can also be achieved following this strategy.⁴⁵ Also, already fabricated nanofibers are frequently used. For example, Feng *et al.* blended the EDOT monomer with PLGA polymer and then polymerized by exposure to an oxidative catalyst (FeCl_3)⁴⁶ or colloidal particles such as cuprous oxide (Cu_2O).⁴⁷

Soft templates are constituted of self-assembled molecules, which interact through non-covalent forces (*i.e.* van der Waals, hydrogen bonds and π - π stacking among

others).⁴⁸ This method is cheap, simple and powerful. Molecules used as soft-templates include surfactants, structure-directing molecules and oligomers. Also gas bubbles (H₂ or O₂ from H₂O electrolysis) stabilized with surfactants have been used as soft templates, which are known as soap bubbles.^{49,50} Surfactants can self-assemble into micelles, determining the polymer nanostructure. For example, core-shell nanomaterials were prepared using two different PPys, which were synthesized with different oxidants and generated by microemulsion polymerization.⁵¹ Also, a mixture of cationic surfactants (*i.e.* octyltrimethylammonium bromide, decyltrimethylammonium bromide, and dodecyltrimethylammonium bromide) were used to selectively fabricate PEDOT nanocapsules.⁵²

The template-free approach is based on the ability to control the nanostructures during the polymer formation without the use of any template. This can be done electrochemically by using high currents, which are reported to form NPs rather than films on the electrodes. Liang *et al.* achieved PANi NPs when current densities of 0.08 mA cm⁻² were used⁵³. The chemical synthesis without any template can be done on the interface between air and liquid or when the oxidant and the monomers are dissolved in two immiscible liquids.^{54,55} Nuraje *et al.*⁵⁵ reported that the oxidation of aniline and pyrrole at the aqueous/organic interface produces nanoneedles.

6.4 Drug loading

It is well-known that DDSs based on ICPs take profit of the reversible oxidation and reduction ability of these polymers to promote the uptake or expulsion of charged molecules from the polymer matrix. One of the first DDS prepared with ICPs consisted on PPy films doped with ferricyanide and glutamate.⁵⁶ A recent review of the literature on this topic²⁷ described the mechanisms for drug loading in ICPs and classified them as one step loading of anionic drugs, three- step loading of anionic drugs and loading of cationic drugs.

Obviously, the methodology employed for drug loading depends on the chemical and physical properties of the drug (*e.g.* molecular weight, charge, chemical composition...). A wide range of medicinal compounds have been explored, including anti-inflammatory,

⁵⁷⁻⁵⁹ anti-cancer,⁶⁰⁻⁶² antibiotics,^{63,64} growth factors,⁶⁵ peptides,⁶⁶ and proteins.^{67,68} Generally, small anionic drugs can be incorporated as dopants through one-step immobilization^{69,70} process during the monomer oxidation. Nevertheless, depending of the molecule, it can strongly interfere on the final properties of the ICP, for example diminishing its conductivity, increasing the brittleness and roughness of the material or leading to low loading efficiency.

As an alternative for anionic drug incorporation, a three-step methodology has been used. Firstly, the ICP is synthesized with an anionic primary dopant followed by a reduction potential to expel this primary dopant while the polymer chain is neutralized. Latter, the desired biological molecule is incorporated when the film is oxidised again and it acts as secondary dopant. This method represents a ground-breaking alternative to the one previously described since the chosen compound does not affect to the formation of the polymer structure. The limitation resides on the possible reduction of incorporated drug since when the molecule is loaded during the polymerization is more likely to be entrapped at the inner parts of the material.

Similarly, for cationic drugs the polymer is formed with a primary anionic dopant and, subsequently, the film is reduced, leading to the incorporation of the cationic molecules to counterbalance its charge.^{71,72} As expected, upon oxidation, the positive charge within the polymer backbone increases, causing the repulsion of positively charged molecules. Not so common, but some cationic drugs have been reported to be incorporated on the ICPs matrix and released under electrical stimuli, including neurotrophin growth factor-3,⁶⁸ dopamine,^{72,73} chlorpromazine,⁷¹ and N-methylphenothiazine.⁷⁴ The regulation of the oxidation state in the polymer backbone induces changes in the electrostatic forces between the drug and the polymer, enabling a controlled release. However, normally only low levels of these cations have been released because of their poor integration into the polymer matrix. The drug can be also covalently linked to the monomer of the ICP, the release depending on the hydrolysable bond rather than on the external triggerable stimuli.⁷⁵

Apparently, the entrapment of neutral medical active compounds is more complicated, even though the utilization of simple physical principal, as for example, the hydrophobic-hydrophilic effect between the drug and the anionic dopant,⁷⁴ has been

reported. Another approach is the formation of hydrogen bonds between the drug and the oxidized polymer chains. These, intermolecular interactions change during the dedoping of the ICP, making the hydrogen bonds significantly weaker than when the polymer is in the oxidized state and facilitating the drug release.⁶²

6.5 Drug release

Electrostatic forces play a prominent role when it comes to releasing the drug from ICP matrices. Moreover, the expansion and contraction (actuation) of ICPs leads to the expulsion of the drug by means of mechanical force. Since these properties occur simultaneously, it is not possible to separate them to know which is the prominent as release driving force. Drugs incorporated as dopants on an ICP matrix can be delivered by cyclic voltammetry (*i.e.* the potential of the working electrode is ramped over time at the desired scan speed and when reaches the wanted potential is reversed to return to the initial potential point), chronoamperometry (*i.e.* a fixed potential is set over a determined period of time) or chronopotentiometry (*i.e.* a fixed current is set over a determined period of time), hereafter denoted CV, CA and CP, respectively.

6.5.1 Cyclic voltammetry (CV)

CV favours the exchange of counterions between the polymeric matrix and the medium through oxidation and reduction processes, while the kinetics of such exchange depends on the scan rate. Furthermore, there is no fixed potential and, therefore, the release can be conducted without an intense optimization. Nevertheless, when many oxidation-reduction cycles are applied the films fail and crack due to polymer actuation, which supposes a limitation for devices thought to have a long life time. Besides, the machinery necessary to generate CVs is more complex than for fixed potentials. For example, electrodes covered with PPy doped with dexamethasone (Dex) were tested as micromachines for recording neural activity by modulating the inflammatory implant-host tissue reaction. The potential was swept from -0.8 to $+1.4$ V at a scan rate of 100 mV/s.⁵⁸ Nevertheless, after approximately 30 CV cycles the film experienced some physical changes due to actuation moves induced by swelling-deswelling (**Figure 6.3**).

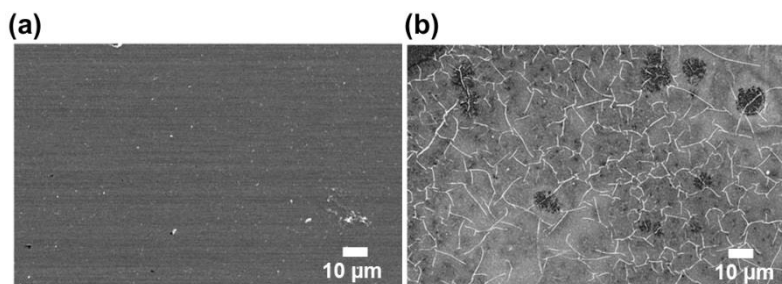


Figure 6.3 SEM images of PPy–Dex coated film: (a) as prepared and (b) after 50 CV cycles. Adapted from⁵⁸.

In another study, PPy deposited onto titanium was doped with antibiotics (penicillin/streptomycin, P/S) or an anti-inflammatory drug (Dex). Results showed that they were able to release 80% of the loaded drugs with only five CV cycles at a scan rate of 100 mV/s.⁶⁴ Interestingly, the use of CV allows detecting the oxidation/reduction peak of the desired molecule and, thus, correlating it with the quantity that remains on the film. On the other hand, controlled release of a neurotrophic factor (NT-3) from PPy was examined by pulsed potential, CV and pulsed current.⁶⁸ It was found that, independently of the film thickness (3.6 or 26 μm), CV is more effective than the other two electrochemical methods. However, after 12 min of CV the polymer started to be delaminated from the electrode surface.⁶⁸ Besides Jiang *et al.*⁷⁶ concluded that the scan rate regulates the release. More specifically, about 57, 89 and 95% of adenosine triphosphate (ATP) loaded into a PPy matrix was released applying scan rates of 50, 100, and 200 mV/s, respectively, during 10 hours.⁷⁶ Nevertheless, it should be mentioned that other molecules, as for example oligomers, monomers or salts, could be also released during the electrochemical stimuli. Other techniques to quantify the released drugs, as for example are ultraviolet absorption spectroscopy,^{58,77} electrochemical quartz crystal microbalance,^{78,79} enzyme-linked immunosorbent assays,⁸⁰ and radiometric measurements,⁸¹ may also lead to the same misinterpretation of the results. Boehler and Asplund recommended the use of high performance liquid chromatography, which allows to discriminate the signal coming from the monomer or the drug and with a detection limit below 5 ng/mL, even though this is not the most straightforward methodology.⁸² *In vivo* drug release experiments were also conducted using CV.⁸³ More specifically, Dex was released from PEDOT using three CV scans between -0.3 V and 0.45

V at a scan rate of 0.1 V/s, EDOT leakage and undesired electrochemical reactions being avoided under such electrochemical conditions.

Even though ICPs can be employed for *in vivo* implantable application they are not the optimal materials because they have low or no biodegradability. Therefore, some strategies to obtain biodegradable ICPs have been proposed. One approach is the preparation of copolymers composed of one conducting block linked to another biodegradable. For instance, Hardy *et al.*⁸⁴ obtained electroresponsive oligoaniline linked to polyethylene glycol (PEG) or polycaprolactone (PCL) via ester bonds and reported their ability to deliver an anti-inflammatory drug upon the application of electrochemical stimuli. Potential cycling was carried out between 0.7 V and -0.5 V, first sweeping in the positive direction of the potential scale at 50 mV s⁻¹. More recently, the same group prepared supramolecular polymers based on peptides (oligoalanines) combined with ICPs (oligoanilines).⁸⁵ The resulting polymers were drop-casted to obtain films (blue appearance) and doped with camphorsulfonic acid (CSA) and Dex phosphate (green appearance). These molecules were released by CV (0.7 and -0.5 V at a scan rate of 50 mV/s during 62 s).

6.5.2 Chronoamperometry and chronopotentiometry

Instead of changing the voltage over time it is possible to keep the same voltage or current during the desired time, which is the case of CA and CP, respectively. When higher voltages or longer times are used, greater is the drug release. However, the utilization of the maximum power or time is not always the best option. It is well known that, if the potential is too high, the drug can undergoes irreversible damages, losing the effectivity. Moreover, if the voltage is higher than 1.229 V hydrolysis can occur. Therefore, it is important to check at which voltage the biological molecule is oxidized or reduced prior to any use of CA and CP techniques. Generally, large currents are considered between 0.5-5 mA and large voltages between 2-25 V during the operation. However, the utilization of ICPs allows the employment of lower values since these polymers are sensible to lower electrical changes.⁸⁶ The application of positive or negative voltages will depend on the drug charge. Negative voltages will be applied to

release anionic drugs, while the opposite for cationic drugs. However, there are some exceptions. For instances, George *et al.*⁸⁷ applied 3 V during 150 s to release an anionic complex containing the nerve growth factor (NGF). Other interesting studies claimed that it is possible to employ very low voltages (*e.g.* -0.05 V) for drug release when ferric chloride is used as the oxidizing agent.⁸⁸

Although CA is the most well established methodology for drug release, there is still a clear need to test whether the delivered drugs are still bioactive. Accordingly, limitations in the utilization of prolonged times or high voltages currently restrict the general applicability of this strategy.

6.6 Nanostructure matters

Effectiveness during the design and development of the ICP DDSs is associated with drug loading capacity, system stability and biocompatibility. Micro- and nanostructures offer important advantages, such increased loading capacity and sensitivity towards the electrical stimuli. Nevertheless, there is no straightforward comparison between the different materials and structures since reported experimental setups and quantifying methods are too divergent. During the last years materials of multiple dimension scales and different shapes have been studied, ranging from polymer films, NPs, fibers and nanowires, hydrogels and other 3D organizations, incorporating the advantages of nanomaterials to enable a highly integrated and sophisticated multi-functional device (**Figure 6.4**). When these structures are made of ICPs, they exhibit unique electrical behaviours, which can lead to new frontiers in bioelectronics.

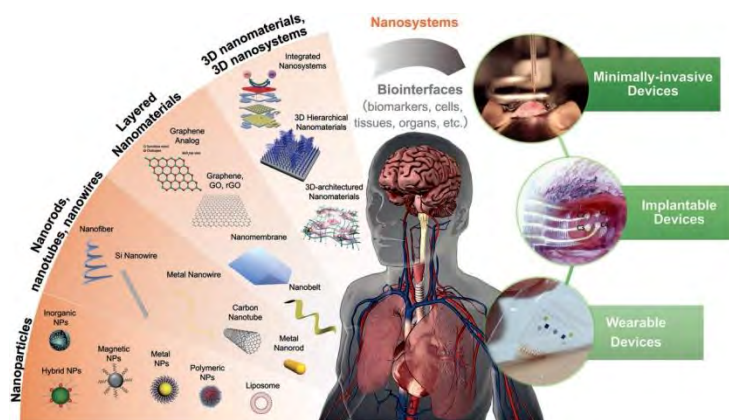


Figure 6.4 Scheme of different nanostructures. Adapted from ⁸⁹.

6.6.1 Polymer films

Electrochemically grown thin films is the most easy and common format of ICPs. The electrochemical methodology to prepare ICP films of controlled thickness and doped with biomedical active compounds is well-established. Thus, electrochemically synthesized polymer films have been largely employed to release drugs on demand.

Previous research shown that significantly different drugs such as Dex,⁵⁸ methotrexate,⁶⁰ chlorpromazine,⁷¹ sulfosalicylic acid (SSA) and ATP,⁹⁰ risperidone,⁹¹ heparine⁹² or NGF,⁸⁷ can be incorporated to ICP films and released in a controlled fashion. **Table 6.1** summarizes some remarkable examples reported in literature, which included films prepared with PPy, PEDOT, poly(N-methylpyrrole) (PNMPy), oligoaniline, oligoaniline-PCL, oligoaniline-PEG and oligoaniline-alanine.

For example, Krukiewicz *et al.*⁹³ demonstrated that PEDOT films incorporating botulin, a biological active molecule against a variety of tumours, exhibit high cytotoxicity against KB and MCF-7 cell lines. Furthermore, the cell killing increases significantly when the botulin release is facilitated by applying a potential. Therefore, these matrices hold great potential for local chemotherapy applications. In a very recent study, the neural activity was recorded by implanting electrodes in the rat hippocampus,⁸³ local inflammation being successfully avoided by a weekly drug release triggered by CV. **Figure 6.5** schematizes how such flexible electrode was implanted. The anti-inflammatory Dex was stored in the PEDOT film, which was coating an electrode, and

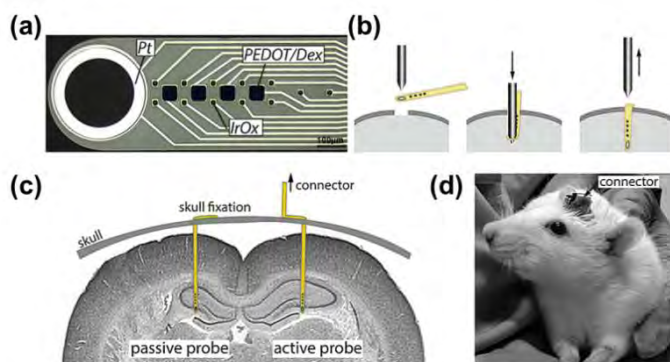


Figure 6.5 (a) Micrograph of a polyimide neural probe with 4 PEDOT/Dex coated electrode sites. Procedure for probe insertion is shown in (b) with an optical fibre as guiding tool. The final placement of the electrodes can be seen in (c). Both the passive probe (control) and the active probe (functionalized) were fixated to the skull. The connection of the active probe to the recording/stimulation equipment was achieved via a connector placed on the head of the animal (d). Reproduced with permission from reference ⁸³.

released in controlled manner. The evaluation lasted 12 weeks and the electrodes exposed to active drug release had neurons closer to the electrode sites compared to the controls.

Table 6.1 Summary of some remarkable examples of polymer films reported in literature with the most important characteristics (*i.e.* preparation method, polymer, drug, dopant and release mechanism) for DDSs made of ICP.

Polymer	Drug	Dopant	Synthesis	Release	Ref.
PPy	Dex (0.1 M)	Drug	One step, CA at 1.8 V until a charge of 25–30 mC/cm ² is reached.	CV from -0.8 to 1.4 V.	58
PPy	SA (0.005 M)	Drug	CA at 0.8 V for 900 s and, subsequently 40 CV from -0.1 to 0.8 V. Then, overoxidation in NaCl solution by CA at +1.0 V for 10 min.	-0.7 V for 30 min.	59
PPy	Methotrexate (0.01M)	Drug+cetypyridinium (0.002 M)	CA at +0.9 V for 100 s using Cl ⁻ as dopant. After this, second polymerization by CA at 0.7 V for 2400 s with the drug and cetypyridinium.	Fixed potential (0.3, -0.5, -0.7 and -0.9 V) for 2 min.	60
PPy	Dex phosphate (0.02M)	Drug	First layer: CA at 0.85 V. Second layer: Steps of potential to 0.9 V. Self-doped PANi film casted on the top.	Potential lower than -0.6 V for 40 min.	94
PPy	1-butyl-3-methylimidazolium acesulfamate (0. 1M), 1-butyl-3-methylimidazolium saccharinate (0.1 M), choline acesulfamate (0.1 M) or choline	Drug	5 CV from -1 to 1.5V or by CA at +1.5 or +1.2 V for 1 h.	Constant potential of 0.6, 1.2 or 1.5 V for 2 hours.	95

CHAPTER 6

saccharinate (0.1 M)				
PPy	SSA (0.2 M) or ATP (0.05 M)	Drug	PPy-SSA: CP with SSA at 2.5 mA/cm ² for 800 s. PPy-ATP: CA with ATP at 0.85 V until a charge of 1 mC is reached.	Constant potential (-0.5, -0.8, and -1.0 V) for 24 h (SSA) or 2 h (ATP). 90
PPy	Risperidone (0.09 M)	<i>p</i> -toluene sulfonate (0.1 M)	Two layers: CP without or with the drug at 2.5 mA/cm ² for 90 and 960 s, respectively.	Constant potential of -0.6 V or 0.6 V for 120 s followed by 500 s. Also alternating electrical stimulation at ±0.6 V (0.5 Hz). 91
PPy	Biotinylated NGF (16 µg mL ⁻¹)	Sodium dodecylbenzenesulfonate (SDBS) (0.02 M) and biotin (0.008 M)	CP at 2 mA/cm ² .	Constant potential of 3 V for a maximum of 150 s. 87
PPy	ATP (0.02 M)	Drug	CA at 0.5-1.0 V or CP at 0.1-10 mA/cm ² until achieving a relation between film thickness and charge of 3.3 µm C ⁻¹ cm ² .	Constant potential of -0.7 V for 700 s. 96
PPy	ATP (0.02 M)	Drug	First layer: PPy with ATP by CA at 0.80 V for preparing films of varied thicknesses 150, 300, 750 nm. Second layer: Poly(N-methylpyrrole) with NaCl by CA at 0.9 V for preparing films of varied thicknesses 150, 300, 450, 750 nm.	After 10 min at 0.0 V, first layer is fully reduced by stepping the potential to -0.6 V. 78

Assuming that 240 mC/cm ² yields 1 μm layer				
PPy	Risperidone (0.09 M)	<i>p</i> -toluene sulfonate (0.1 M) and drug	First layer: CP with <i>p</i> -toluene sulfonate at 2 mA/cm ² for 90 s. Second layer: CP with drug at 2mA/cm ² for 960 s.	Pulsed potential of ±0.6 V at 0.5 Hz. 97
PPy	Heparin (0.5% (w/v))	Toluene-4-sulfonic acid (0.1M)	Free-standing PPy film (thickness: 25 μm) synthesized at 8 V. Surface functionalization with poly(ethylene glycol) monomethacrylate graft copolymerization and subsequent oxidation. Covalent immobilization of poly(vinyl alcohol)-heparin hydrogel onto the functionalized surface.	Pulses of electric current ranging from 0 to 3.5 mA. 92
PEDOT	Betulin (0.005 M)	HCl (1 M)	75 CV from -0.5 to 1.4 V with NaCl. Dedoping at -0.5 V over 10 min. Immobilization of the drug at +0.5 V for 10 min.	Constant potential at -0.5 V for 10 min. 93
PEDOT	Dex (0.01 M)	Drug	CP at 800 mA/cm ² with a target charge density of 300 mC/cm ² .	<i>In vitro</i> : 45 days with 5 CV scans (from -0.3 to 0.45 V) on day 10, 14, 42 and 45. <i>In vivo</i> : 3 CV scans between -0.6 V and 0.15 V. 83
PEDOT	Anionic form of ibuprofen (0.4 M)	LiClO ₄ (0.1 M)	50 CV with LiClO ₄ from 0.0 to 1.1 V. 10 mM EDOT and 0.1 M LiClO ₄ . Reduction at -0.7 V for 10 min. Immobilization of the drug at +0.8 V for 10 min.	Constant potential at -0.5 V for 600 s. 57
PEDOT	Oleanolic acid (0.030	LiClO ₄ (1 and 0.1	One step: 50 CV with LiClO ₄ and drug from 0.0 to	Constant potential at 61

CHAPTER 6

	M)	M)	+1.1 V. Three steps: (i) 50 CV with LiClO ₄ from 0.0 to +1.1 V; (ii) reduction at -0.7 V for 10 min; (iii) Immobilization of the drug at +0.8 V for 10 min.	-0.5 V for 10min.	
PEDOT	Dex (0.01 M)	Drug	CP at 80 mA/cm ² until a charge of 100 mC/cm ² is reached.	CV from -0.6 to +0.9 V. Cathodic sweep (from -0.6 to 0.0 V) or anodic sweep (from 0.0 to -0.9 V) with 5 sweeps each time.	82
Oligoaniline-PCL and oligoaniline-PEG	Dex phosphate (doping was at mole ratio of 1 : 1 DMP : aniline pentamers) CSA (doping was at a mole ratio of 3 : 1 CSA : aniline pentamers)	Drugs	Polymers dissolved in hexafluoroisopropanol (0.1 g/mL) were casted onto insoluble substrates. Doping was carried out by adding CSA or DMP to the solution prior to the casting.	CV from 0.7 to -0.5 V: 6 cycles with 14 minutes off. Constant potential at 0.6 V: 3 cycles of 0.5 minutes on and 29.5 minutes off.	84
Oligoaniline and oligoaniline-PEG	Dex phosphate (at a mass ratio of 10:1 polymer:Dex) CSA (at a mass ratio of 1:10 CSA:MTT)	Drugs	Polymers dissolved in hexafluoroisopropanol (0.1 g/mL) were casted onto insoluble substrates. Doping was carried out by adding CSA or DMP to the solution prior to the casting.	CV from 0.7 V to -0.5 V: first sweeping in the positive direction of the potential scale (this stimulation lasted 62 s).	85
PPy	N-methylphenothiazine	Heptasulphonat	CA with heptasulphonated β- cyclodextrin by CA at	CV from -1.2 to 0.4 V at 20	74

	(0.1 M) and N-butylsulphonate phenothiazine (0.05 M)	ed cyclodextrin (0.01 M)	β -	0.4 V until a charge of 0.3 C/cm ² is reached. Incorporation of the drugs by dipping in the corresponding solutions for 90 min. Then thoroughly rinsed in CH ₃ CN, and subsequently in aqueous 0.5 M LiClO ₄ for 45 min.	mV/s for at least 7 cycles.	
PPy	Quercetin (0.006 M) Ciprofloxacin (0.007 M)	HCl (1 M)		25 CV from -0.8 to +0.8 V with NaCl. Dedoping at -0.7 V over 10 min. Immobilization of drugs at 0.6 V for 10 min.	Constant potential at -0.5 V for 12 min.	70
PPy	Neurotrophin-3 (1.35 ppm)	<i>p</i> -toluene sulfonic sodium salt (0.05 M)	acid salt	First layer: CP with <i>p</i> -toluene sulfonic acid sodium salt at 2 mA/cm ² for 90 s. Second layer: identical to the first layer but adding neurotrophin-3 to the solution.	CV from -0.8 to 1.0 V. Pulsed potential of ± 0.6 V 5 Hz. Pulsed current of ± 0.5 mA at 5 Hz. Pulsed current of ± 20 mA at 5 Hz.	68
PPy	Chlorpromazine (0.01M)	0.064 g/L melanin and HCl (0.1 M)	g/L and	CA with melanin at 0.6 V until a charge of 765.6 μ C is reached. Chlorpromazine uptake at -0.8V.	Release stepwise potential changes from -0.8 V to 0.4 V for 15 min.	71
PPy	Chlorpromazine (0.01 M)	Heparin 1 g/L or 0.2 g/L	g/L or	Pre-electropolymerization with 1 g/L heparin by CA at 0.9 V for 100 s. Subsequent polymerization with 0.2 g/L heparin by CA at 0.7 V for 900s adding chlorpromazine to the solution 0.1 M pyrrole, 0.2 g/L Hep, and 0.01 M CPZ aqueous solution, CA at 0.7 V for 900 s.	Constant potential of 0.4 V for 4 h.	88

CHAPTER 6

PPy	Brain-derived neurotrophic factor (2 µg/mL)	(2 <i>p</i> -toluene sulfonate (0.05 M)	First layer: CP with <i>p</i> -toluene sulfonate at 2 mA/cm ² for 90 s. Second layer: identical to the first layer but adding brain-derived neurotrophic factor to the solution and decreasing the polymerization time to 60 min.	Biphasic pulses at 250 Hz formed by three periods of 8 h followed by 16 h rest periods.	80
PPy	Neurotrophin-3 (2 mg/mL)	(2 <i>p</i> -toluene sulfonate (0.05 M)	First layer: CP with <i>p</i> -toluene sulfonate at 2 mA/cm ² for 90 s. Second layer: identical to the first layer but adding neurotrophin-3 to the solution and increasing the polymerization time to 60 min.	Charged-balanced biphasic current pulses at 250 Hz were applied for 1 h.	81
PEDOT	Acetylcholine chloride (0.055 M)	PSS (5 mg/mL)	CP with PSS at 0.5 mA for 1200 s reaching a charge of 0.29 mC/cm ² . Immersion in acetylcholine chloride of untreated PEDOT/PSS film.	Constant potential of +1.0 V and -1.0 V during 25 h.	99
PNMPy	Dopamine hydrobromide (0.1 M)	PSS (0.03 M)	CP with PSS at 4.4 mA/cm ² for 30 s. The film was washed and, then, placed in a dopamine hydrobromide aqueous solution. The electrode potential was stepped to -0.60 V until the cathodic current dropped to small values.	Stepping the potential to 0.5 V for 30 s.	72
PNMPy	Dopamine hydrobromide and dimethyldopamine hydrobromide (0.5 or 1 mM)	PSS	CP with PSS at 4.4 mA until 26.2 mC. Reduction of the resulting film at -0.5 or -0.6 V in a 0.5 or 1 mM drug aqueous solution with 0.01 M KCl.	Stepping the potential to 0.4, 0.5 or 0.6 V for 20 min.	73

6.6.2 Polymer nanoparticles

The development of NPs made of ICPs for electroresponsive drug delivery requires chemical synthesis and the use of surfactants to improve their colloidal stability. Compared to electrochemically synthesized films, NPs allow easier scalability (*i.e.* there is no limitation due to the substrate dimensions or electrochemical cell size), greater processability and improved drug loading (*i.e.* superficial area is bigger). It has been reported drug loadings of 51 wt%, which are much higher than those usually achieved with ICP films.⁸⁸ The main problem related to ICP NPs is how to stimulate the release. This question arises from a set up point view: is it necessary to fix the NPs on the electrode surface ?, or is it better to have them dispersed on solution ?. In order to provide an answer to this question, it is necessary to take into account that the oxidation/reduction process of NPs in solution is limited by their diffusion from the bulk to the surface of the electrode. Ge *et. al*¹⁰⁰ prepared a gel of PLGA-PEG-PLGA containing 1 wt% of PPy NPs (**Figure 6.6**), which was attached to the electrode surface. More interestingly, fluorescein was released *in vivo* upon electrical stimuli by applying an electric field of -1.5 V/cm onto the implanted gels for 40 s per each stimulus *via* two needle electrodes.

In another study, electrodes were coated with PPy NPs and drop-casted 0.05 wt%

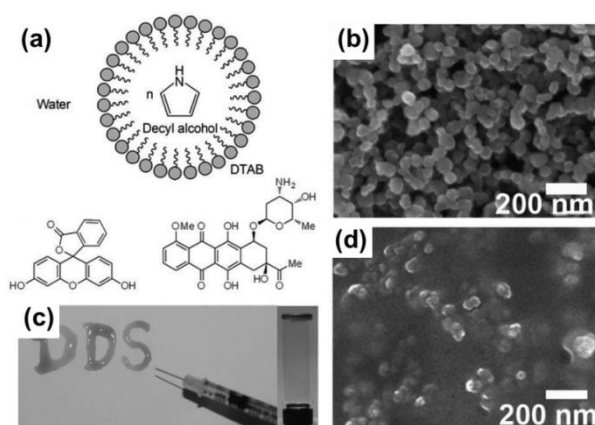


Figure 6.6 (a) Chemical synthesis of PPy NPs. (top) and chemical structures of fluorescein (bottom left) and daunorubicin (bottom right). (b) SEM image of fluorescein-encapsulated PPy NPs. (c) Photograph showing the solid-gel transition of the injectable conductive hydrogel. (d) SEM image of air-dried hydrogel containing PPy NPs. Adapted from ref¹⁰⁰.

chitosan in 0.1 M HCl to prevent the NPs detachment during the electrostimulation.⁸⁸ It has also been reported the electrostimulation of the NPs confined in dialysis bags located inside the electrochemical cell (*i.e.* the drug can diffuse across the dialysis bag but the NPs cannot).¹⁰¹ Furthermore, it was also been demonstrated the release of curcumin from PEDOT NPs attached onto a glassy carbon surface.⁶² A summary of the procedures employed for the NPs generation and electrostimulation release is presented in **Table 6.2**.

Table 6.2 Summary of some remarkable examples of polymer NPs reported in literature with the most important characteristics (*i.e.* preparation method, polymer, drug, dopant and release mechanism) for DDSs made of ICP.

Polymer	Drug	Dopant	Synthesis	Release	Ref.
PPy	Fluorescein and daunorubicin (0.6 mg/mL) or (0.002 M and 0.001 M)	Dodecyltrimethylammonium bromide (0.162 M) and decyl alcohol(decanol) (0.236 M)	Polymerization in aqueous solution using ferric chloride as oxidant agent and adding surfactant and the drugs to the reaction medium.	Fluorescein: Constant potential at -0.5 or -1.5 V for 10 s and repeated every 5 min. Daunorubicin: Constant potential at 0.5 V for 10 s, repeated every 5 min.	100
PPy	Fluorescein sodium salt and methotrexate (7.4 and 0.5 mg/mL) or (0.022 M and 0.001M)	Sodium dodecyl sulfate (SDS) (0.1 M)	PPy nanoparticles were prepared with three different oxidizing agents, hydrogen peroxide, chloroauric acid and ferric chloride. Drugs were added to the reaction medium before the particle formation.	5 stimuli at a constant potential of -0.5 V for 20 s every 3 min.	88
PPy	Insulin (5 mg/mL)	Sodium dodecyl sulfate (SDS) (0.1 M)	PPy nanoparticles using hydrogen peroxide as oxidizing agent. The encapsulation was conducted by adding the insulin to a dispersion of nanoparticles.	A thin, coiled, Pt wire was placed inside the dialysis tube as working electrode. A constant potential of -1 V was applied for 20 min.	101
PPy	Fluorescein, piroxicam and insulin (3mg/mL)	SDS (0.1 M)	Chemical polymerization in aqueous solution incorporating the drug to the reaction medium	Constant current at -50, -100, -200 and -300 μ A for 25 s.	102

CHAPTER 6

				Constant potential at -0.5 , -0.75 , -1 and -1.25 V for 3 min.
PEDOT	Curcumin (0.027 M)	SDBS (0.009 M)	Chemical polymerization in aqueous solution with ammonium persulfate as oxidizing agent and incorporating the drug to the reaction medium.	Constant potential at 0.50, 62 -0.50 , -1.00 , and -1.25 V for 3 min.

6.6.3 Polymer nanowires, fibers and nanotubes

In this section all different kinds of tubular nano- and microstructures have been grouped. Nanowires consist of elongated and intertwined nanotubes forming a mesh made of ICPs. This format has been wide investigated using PPy. Nanowires have been prepared following different approaches, such as those based on the utilization of functional molecules,^{103–105} seeding growth,¹⁰⁶ and interfacial polymerization.¹⁰⁷ Although the operation of these nanostructures in electronics such as biosensors or as energy storage have been considerably explored,¹⁰⁸ there is much less information about their use for controlled drug release. Ru *et al.*¹⁰⁹ used ATP as both morphology-directing agent and model delivery drug. Surprisingly, results showed that the ATP release efficiency increases from 53% for conventional PPy morphologies to 90% for PPy nanowires after 45 h of electrical stimulation (-0.8 V). It was also visualized by CV that PPy nanowires are much more electroactive than conventional PPy formats and by electrochemical impedance spectroscopy (EIS) it was corroborated that the material resistance was much lower. On the other hand, Lee *et al.*¹¹⁰ prepared arrays of nanowires by electrochemical deposition of a mixture of pyrrole monomers and biotin as a dopant in anodic alumina oxide membranes with pore size of $0.2\ \mu\text{m}$ as a sacrificial template (**Figure 6.7**). The length of nanowires ranged from 5 to $25\ \mu\text{m}$ depending on the polymerization time. Obviously, the number of doxorubicin (DOX) molecules conjugated with the biotin dopant (i.e. the encapsulation efficiency) increased with the nanowire length. Therefore, stimulated drug delivery assays were conducted using nanowires with an approximate length of $25\ \mu\text{m}$, which was the optimal. Positive stimulation of $+0.5$ V for 1 min did not induce as much as release as negative potential of -1 V. In fact, the amount of drug released using positive potentials was similar to that delivered from the un-stimulated controls, in which natural diffusion was the only driven force.

Drugs can also be absorbed or encapsulated into PPy nanowires without considering specific interactions with the doping agent of the ICP.⁷⁶ More specifically, Jiang *et al.* used the micro- and nanogaps generated between the nanowires as reservoirs for drug storage. These observations suggested that the charge and volume of the drug to be load

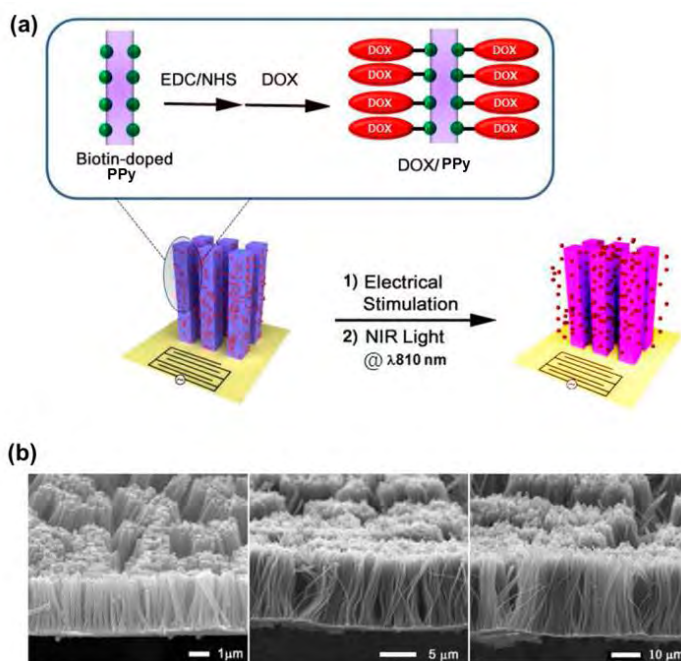


Figure 6.7 (a) Schematic illustration of DOX-attached PPy nanowires (DOX/PPy). DOX molecules were chemically conjugated to the biotin dopants of the PPy nanowires through 1-Ethyl-3-(3-dimethylaminopropyl)-carbodiimide/N-hydroxysuccinimide EDC/NHS chemistry. DOX/PPy nanowire arrays have synergistic effects in cancer therapy by direct application of an electric potential and localized NIR light. (b) SEM images of the fabricated PPy nanowire arrays. Different polymerization times were employed to achieve PPy nanowires with length of 5 (left), 15 (middle), and 25 μm (right), respectively. Adapted from¹¹⁰.

are not decisive for the loading capacity. Later on, to prevent drug leakage and to obtain a controlled release, the mesh was covered with a protective PPy film making a “sandwich”.

In their cutting edge paper, Martin and coworkers¹¹¹ produced conducting nanotubes from nanofibers of biodegradable poly(L-lactide) (PLLA) or PLGA as hard templates. First, PLLA or PLGA with dexamethasone dissolved in chloroform were electrospun onto the surface of a probe followed by electrochemical deposition of ICPs around the electrospun nanofibers. Then, the drug delivery was achieved by controlled degradation of the PLLA/PLGA or by actively acting on the ICP with an applied electrical field (1 V). Similarly, Chen *et al.*¹¹² loaded diclofenac into the microfiber core made of bacterial cellulose (BC) followed by coating it with a PEDOT shell. During electrical stimulation,

PEDOT contracted and produced a mechanical force that exerted pressure to the BC microfiber promoting the drug release. However, the fiber weight loss observed after stimulation indicated that some degradation occurred during such process, facilitating the drug release. More recently, also combining the actuation of ICPs and fiber degradation, we reported electrospun fibrous mats in which PEDOT NPs were incorporated to the curcumine-loaded PLA fibers. PEDOT NPs exerted some pressure on the PLA core when a constant potential of 1 V was applied, inducing expansion and facilitating the release of the loaded drug.¹¹³

Esrafilzade *et al.*⁶³ prepared a PEDOT:poly(styrenesulfonate) (PSS) fibres by wet-spinning, which were employed as template to electropolymerize an outer shell layer of PPy. Ciprofloxacin hydrochloride (Cipro), which was selected as model drug, was used as the dopant agent during PPy synthesis, confirming that the drug release was higher when the PPy layer was reduced.

Overall, this kind of DDSs present outstanding advantages over NPs which suffer from huge initial burst release. A summary of the procedures employed for the nanowires, nanofibers and nanotubes generation and electrostimulation release is presented in **Table 6.3**.

Table 6.3 Summary of some remarkable examples of polymer nanowires, nanofibers and nanotubes reported in literature with the most important characteristics (*i.e.* preparation method, polymer, drug, dopant and release mechanism) for DDSs made of ICP.

Polymer	Drug	Dopant	Synthesis	Release	Ref.
PPy	ATP (0.20 M)	Drug and LiClO ₄ (0.07 M)	First layer: CA with LiClO ₄ at 1.0 for 150 s. Second layer: Nanowires by CP with the drug and LiClO ₄ at 1.0 mA cm ² for 600 s.	Constant potential at -0.80 V for 45 hours. The surface was covered with a Mg layer to induce self-powered release.	109
PPy	ATP (0.01 M) and Dex (0.005 M)	<i>p</i> -toluene sulfonate (0.085 M)	Nanowire network by CP with <i>p</i> -toluene sulfonate at 0.477 mA/cm ² for 1600 s. The drug was loaded by dropping an aqueous solution onto the surface of the nanowire network. Finally, another PPy layer with <i>p</i> -toluene sulfonate was deposited.	CV from -0.9 V to 0.6 V.	76
PPy	DOX (0.0018M)	Biotin (1 mM) and PSS (0.01 M)	Nanowires with biotin and PSS at 1 V for 6, 12, and 18 min. Then, the carboxyl residue of biotin was activated and the system was incubated in a drug solution overnight at 4 °C.	Constant potential at -1 V for 1 min.	110
PEDOT	Diclofenac (not mentioned)	(not FeCl ₃ (0.154 M)	PEDOT core-shell microfiber was obtained by immersing diclofenac-loaded bacterial cellulose microfiber into a monomer ethanol solution with FeCl ₃ .	Constant potential at -0.6 V for 2 and 12h.	112
PEDOT	Dex (3.75%	PBS 1x	Polymerization by CP onto PLGA nanofibers loaded	Constant potential at 1 V	111

	dexamethasone (w/v)		with the drug at 0.9 mA/cm ² for 30 min. After electrochemical deposition, the PLGA core was dissolved in dichloromethane for 10 min.	for 10 s.	
PEDOT	Cipro (0.05 M)	Drug	PEDOT:PSS fibers were coated with PPy doped with Cipro. The latter was obtained by CP at 0.5 or 2.0 mA/cm ² for 10 or 20 min.	Constant potential at 0.3 V and reduced at -0.26 V.	63
PEDOT	Curcumin (0.5 mM)	DBSA (0.01 M)	EDOT NPs (10 mg/mL) and CUR (1.04 mg/mL) were dispersed and dissolved, respectively, in 0.5 mL of ethanol. Latter, 0.2 mL of PEDOT NPs, CUR or PEDOT NPS and CUR solutions were mixed with 1.8 mL of PCL solution and loaded in a 5 mL syringe for electrospinning.	1, 3 and 5 pulses of 1.0 V (each pulse lasts 60 s) with a time lapse of 5 s in between.	113

6.6.4 Polymer nanoporous films and sponges

In this section the increase of drug retention and the preparation of prolonged stimulative drug release profiles is based on nanoporous films and sponges. The preparation of porous surfaces is a good strategy to increase the superficial area of the desired format. Although drugs can be loaded during the ICPs polymerization into the bulk, some extra drug, not necessarily acting as dopant agent, can be loaded into the nanopores inside the polymer film. This pores can be open¹¹⁴ or sealed¹¹⁵ by a thin layer of ICP on top. The latter provides an ICP based drug release system with higher loading capacity for a wide range of drugs, which should not be limited by the charge nor the size of the molecule. In order to attain this porous morphology, hard templates can be used (*e.g.* PSS or poly(methyl methacrylate) (PMMA) beads arrangements), which can be latter dissolved with the appropriate solvent.^{114–118} For example, **Figure 6.8**, shows the procedure reported by Sharma *et. al*¹¹⁸ for the preparation of sponge like structures. First, PMMA beads were distributed as in a colloidal crystal onto a stainless steel substrate (i). Then, the electropolymerization of PPy was conducted around the PMMA hard template (ii). Afterwards, PMMA particles were dissolved using a 1:3 v/v

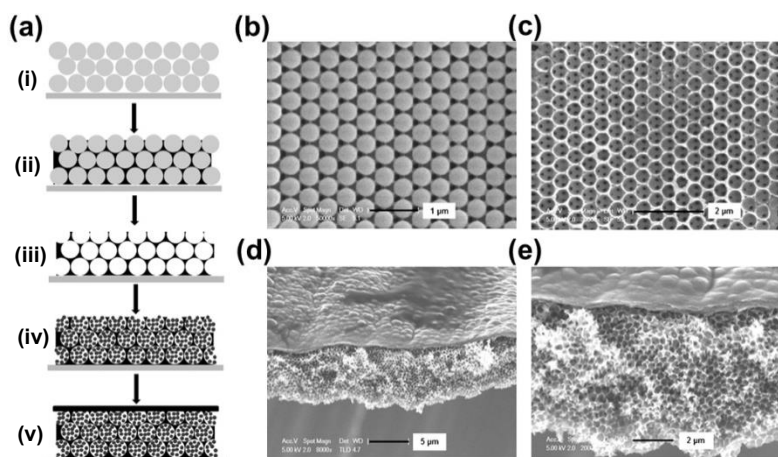


Figure 6.8 Schematic representation of PPy scaffold fabrication and drug loading (a). SEM micrographs of: (b) PMMA colloidal crystal template onto the stainless substrate; (c) the PPy film obtained by electropolymerization and subsequent PMMA template removal; (d) and (e) cross sectional views of the PPy structures following the electropolymerization of the dense PPy layer. Reproduced with permission from reference ¹¹⁸.

toluene:acetone mixture (iii). Subsequently, a drug solution was added dropwise onto the sponge-like PPy films, and then air dried at 20°C overnight (iv). Finally, a thin layer of PPy was electropolymerized above to entrap the drug (v). Corresponding SEM images are present in **Figure 6.8b-e**. The maximum drug release was observed when films were reduced with a difference in potential of -0.6 V, which was attributed to an enhancement of the drug diffusion rate due to a change in spacing between the nanopores. In another interesting work, Jeon *et. al.*¹¹⁹ used ICPs as actuators to regulate the opening and closing of artificial pores (**Figure 6.9**). They were able to promote the ion diffusion across a porous membrane when the pores were open, stopping the diffusion when pores were closed. Specifically, the pore size decreased at the reduction state while it increased at the oxidation state.

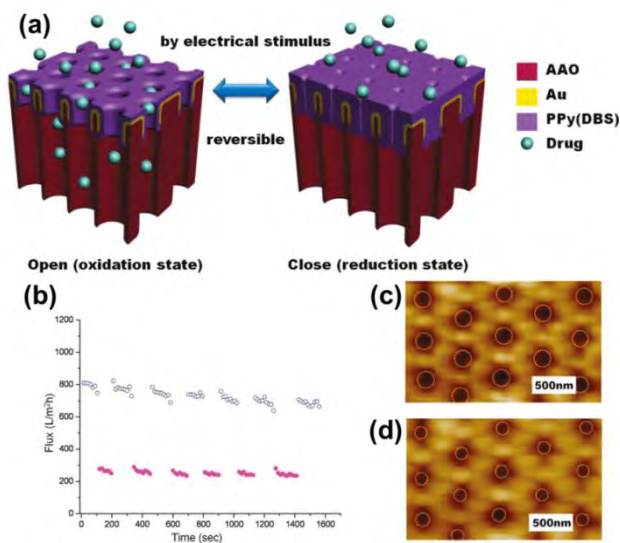


Figure 6.9 (a) Scheme of reversible changes in pore size (and the drug release rate) between oxidation and reduction states. (b) Drug flux *versus* time when the pore diameter is 110 nm (oxidation-blue open circles) and when the reduction state (magenta closed circles). A data point was collected every 10 s. (c,d) *In situ* AFM height images corresponding to the oxidation and the reduction states, respectively. Reproduced with permission from reference ¹¹⁹.

PPy doped dodecyl benzene sulfonate (DBS), hereafter PPy/DBS, was electropolymerized onto a porous aluminium oxide membrane covered with a thin layer of gold. PPy/DBS was chosen as electrically responsive material because its volume

experiences very large changes (up to 35%) with the electrochemical state. The cause that produces such changes is a complex interplay of many factors. In brief, the polymer matrix expands when solvated ions enter into it, while the matrix contracts when solvated ions escape from it. These compositional changes, which correspond to the doping process, alter the length and chemical nature of carbon-carbon bonds the angles between adjacent monomer units, affecting polymer...solvent interactions.^{121,122} Interestingly, the pulsatile release of the drug was achieved, the on demand response taking less than a few seconds.

A resume of the procedures employed for the nanoporous films and sponges generation and electrostimulation release is presented in **Table 6.4**.

Table 6.4 Summary of some remarkable examples of polymer nanoporous films and sponges reported in literature with the most important characteristics (*i.e.* preparation method, polymer, drug, dopant and release mechanism) for DDSs made of ICP.

Polymer	Drug	Dopant	Synthesis	Release	Ref.
PPy	Fluorescein (Flu) (0.01 M)	Drug	CA at a constant potential of +0.9 V for 200 s using glass carbon electrodes coated with PSS templates.	Constant potential at -2.0 V for 10 s (6 times).	114
PPy	Flu (0.01 M) and Dex (0.02 M,)	Drug	CV (one cycle) from 0.5 to 1.2 V with the drug using PSS templates.	Constant potential at 2 or 0.5 V for 5 s followed by 5 s of 0 V period.	115
PPy	Dex phosphate (0.05 M)	p-Toluene sulfonic acid (0.1 M) or Drug	CP at 2 mA/cm ² for 4 min onto PMMA colloidal crystal films. The pH was adjusted to 3 using 0.1M HCl.	Alternating potential between ±0.6 V at 0.5 Hz during 10 min for 24, 26, 28 and 30 h.	116
PPy	Biotin (0.009 M)	Drug and sodium dodecylbenzenesulfonate (0.01 M)	CA with the drug and the secondary dopant agent at 0.7 V for 24 h onto PSS colloidal crystals. The PS core was dissolved leaving hollow composites. Surfaces were further interacted with streptavidin-coated gold NPs.	Constant potential at -2 V for different time intervals (maximum 60 s).	117
PEDOT	Fluorescein	Sodium	CA with the drug and the dopant agent at 0.6 V	Alternating	119

CHAPTER 6

	isothiocyanate-labeled bovine serum albumin (0.3 mg/mL)	dodecylbenzenesulfonate (0.1 M)	for 30~240 onto porous anodic aluminum oxide.	potential at 0.1 V (oxidation) and -1.1 V (reduction).
PEDOT	Risperidone (0.1 M)	Sodium dodecylbenzenesulfonate (0.1 M) and with <i>p</i> -toluene sulfonate (0.1 M)	First layer: CA with sodium dodecylbenzenesulfonate at 2 mAcm ⁻² for 4 min onto stainless steel coated self-assembled PMMA particles. Particles were dissolved with a toluene:acetone mixture. Drug loading by dropwise using a methanol risperidone solution. Second layer: CP with <i>p</i> -toluene sulfonate at 2 mA/cm ² for 2 or 3 min.	Constant potential 120 at +0.6 V (oxidation) or -0.60 V (reduction) for 60 min.

6.6.5 Polymer hydrogels

Hydrogels, which absorb and store a huge amount of water molecules due to their hydrophilic nature, present a three-dimensional flexible polymeric network with rubbery nature.⁸⁶ These characteristics make them resemble many biological tissues, being therefore suitable as implantable DDSs. They can be used for flexible and stretchable bioelectronics. Besides, they can be modelled in a variety of shapes and with different mechanical strength, depending on the implantation zone. Hydrogels made of conventional naturally occurring biopolymers (*e.g.* hyaluronic acid chondroitin sulphate, agarose, and calcium alginate) or synthetic polymers (*e.g.* polyacrylamide, and polydimethylaminopropylacrylamide among others) require the use of relatively high power (*i.e.* from 2 to 25 V) for their operation.^{122,123} However, much lower voltages (*i.e.* from 0.1 to 3 V) can be used when ICPs are added to the polymer matrix. ICPs can be polymerized onto the hydrogels' surface, increasing both the surface area of the polymer and the amount of entrapped drug.¹²⁴

A representative example of ICP-containing hydrogel was prepared by mixing chitosan-*graft*-PAni copolymer and oxidized dextran (OD) as a cross-linker.¹²⁵ The resulting hydrogel behaved as DDS and application of a variety of voltages (*i.e.* 0, 1 and 3 V) revealed that release increases with the voltage. This system also offered a repeatable “*on-off*” pulse release. **Figures 6.10a** and **b** show the aspect of the hydrogel before and after crosslinking, respectively. **Figure 6.10c** compares the release behaviour achieved using different potential, which were repeatedly applied every 10 min. It was observed that the cumulative release percentage of amoxicillin was about 34% after 80 min at 0 V, while this value increased to 69% and 82% at of 1 V and 3 V, respectively.

Pourjavadi and Doroudian¹²⁶ prepared a hydrogel based on hydrolysed-collagen modified with PCL. Conductive fibers were incorporated by *in situ* polymerization of aniline for the controlled release of hydrocortisone. *In vitro* delivery experiments showed that the drug release profile of this material can be tailored by regulating the conductive stimuli.

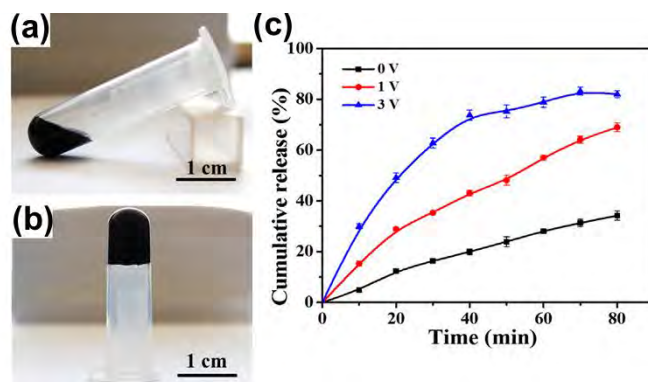


Figure 6.10 Photographs of the ICP-containing solution before crosslinking (a) and after crosslinking with OD (b). Graph showing drug release in phosphate buffered saline (PBS) solution under different electric potentials (c). Adapted from ¹²⁵.

In a different but interesting approach consisting on the assembly of an ICP film and a biohydrogel through a gelatin intermediate layer, the ICPs interface was employed for monitoring the dopamine release and the biohydrogel as drug container. Moreover, the dopamine release was regulated by electrochemical stimulation, applying potential ramps in cyclic phase to the such ICP-biohydrogel assembly.¹²⁷

More examples of DDSs based on ICP-containing hydrogels include PPy electropolymerized into poly(acrylic acid) hydrogel¹²⁸ and salicylic acid (SA) doped poly(phenylene vinylene)/polyacrylamide (PPV/PAAM) hydrogels.¹²⁹ Regarding the latter, it was noticeable that in absence of electric field the diffusion of SA was delayed in the first 3 hours due to the ionic interaction between the anionic drug and the PPV, whereas immediate release was observed upon application of an electric field.

An overview of the procedures employed for the hydrogels generation and electrostimulation release is provided in **Table 6.5**.

Table 6.5 Summary of some remarkable examples of polymer hydrogels reported in literature with the most important characteristics (*i.e.* preparation method, polymer, drug, dopant and release mechanism) for DDSs made of ICP.

Polymer	Drug	Dopant	Synthesis	Release	Ref.
PAni	Amoxicillin (0.004 M) and ibuprofen (0.007 M)	HCl (0.1 M)	Chitosan- <i>g</i> -PAni was dissolved in acetic acid aqueous solution and mixed with oxidized dextran dissolved in PBS (pH = 7.4) at 37 °C for 1h. Amoxicillin or ibuprofen was added to the mixture before gelation.	Constant potential at 0 V, 1 V and 3 V for 3 min. Repeated every 30 min or 60 min.	125
PPV	SA (0.0125 M)	Drug	A PPV solution with SA and H ₂ O ₂ was stirred for 24 h. SA-doped PPV particles were filtered and vacuum dried for 24 h. Then, a free radical polymerization of acrylamide with SA-doped PPV was conducted.	Constant potential at 0, 0.01, 0.03, 0.05, 0.07, 0.09, and 0.1 V using pH= 5.5 for 48h.	129
PPy	Safranin (0.01 M)	Sodium nitrate (1 M)	CA with sodium nitrate at +0.6 V was applied until de charge achieves a value of 10.5 C. The resulting hydrogel was immersed in a safranin solution for 5 h.	Constant potential at 0.4 and -0.4 V using pH= 6.4 or 3.8.	128
PAni	Hydrocortisone (100 mg)	HCl (1 M)	Hydrogels were swollen in a HCl solution containing aniline. After one day, the hydrogels were washed and then, placed in an ammonium persulfate solution. Finally, the dried hydrogel was immersed in a PBS solution with hydrocortisone.	Constant potential at 3 V for 3 minutes.	126

6.6.6 Polymer composites

An alternative approach to gain superficial area with respect to that of the film format is the addition of extra materials into the polymer matrix.

Nowadays, carbon nanotubes (CNTs) represent a hot topic in many research fields related with Materials Science and Engineering.^{130,131} Although this nanostructured compound is frequently used to improve the mechanical and electrical properties of the primary materials,^{132,133} CNTs have been also employed as drug nano-reservoirs for controlled release.

Luo *et al.*¹³⁴ proved that Dex-loaded CNTs can release this drug in its bioactive form under electrical stimulations. Specifically, the drug was entrapped in the inner cavity of CNTs, which were sealed at the ends with PPy films formed by electropolymerization. CNTs not only allowed the loading of high amounts of drug but also provided a linear and sustainable drug release profile. **Figure 6.11** shows a scheme of the synthetic process and SEM micrographs presenting the morphology of two types of CNTs: CNTa (outer diameter: 100-170 nm; inner diameter: 3-8 nm) and CNTb (outer diameter: 20-30 nm; inner diameter: 5-10 nm). Drug release was much higher from CNTs sealed with PPy than PPy alone. Regarding to the size of the CNTs, CNTb provided the greater release, meaning that the loading was much higher. This fact was attributed to the thinner outer diameter and wider inner diameter of the CNTb in comparison to CNTa (i.e. the drug

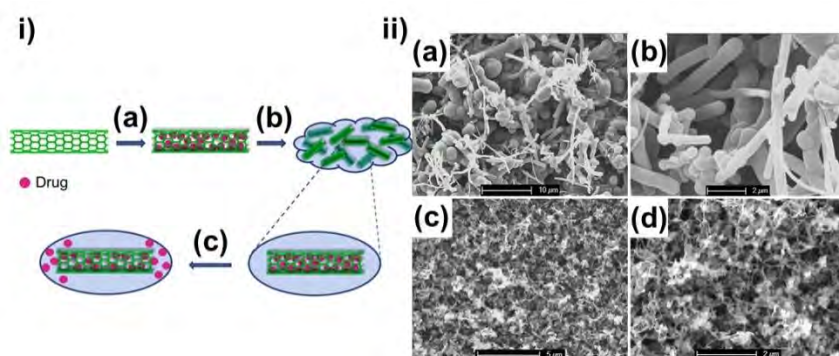


Figure 6.11 Scheme representing the loading and release process of CNT nanoreservoirs (i). SEM images of the PPy/CNTa film (a, b) and the PPy/CNTb film (c, d). CNTa: outer diameter 110-170 nm; CNTb: outer diameter 20-30 nm (ii). Reproduced with permission from reference

¹³⁴.

capacity per unit weight was higher for the former than for the latter).

Other approaches based on the addition of CNTs have been employed for electrically driven drug release^{65,78,135} and also for dual application such as the combination of controlled release and the detection of the neural network activity.¹³⁶

A related material is graphene oxide (GO), which consists of a hexagonal ring-based carbon 2D “network” (*i.e.* a sheet) having both sp²- and sp³-hybridised carbon atoms and bearing a variety of reactive oxygen functional group (*i.e.* hydroxyl, carboxyl, carbonyl and epoxide)^{137,138}. The preparation of composites containing GO is a burgeoning field since this material can improve not only the chemical stability but also the mechanical and electrical properties. Besides, the utilization of GO for DDSs has been widely explored since its oxygen-containing functional groups allow the attachment of site directed moieties or fluorophores, meanwhile the presence of localized π -electrons at the sheet surface enables the formation of intermolecular π - π interactions with facilitating the entrapment of aromatic drugs.

Weaver *et al.*¹³⁹ generated PPy matrixes by electropolymerization using GO and an anionic drug (Dex) as dopants during the oxidation process. Note that GO nanosheets are negatively charged due to carboxylic acid groups formed at their edges. As it was expected, the nanocomposite released Dex in response to electrical stimulation with a linear release profile and a dosage that can be adjusted by altering the magnitude of stimulation. Furthermore, the release persisted over 400 stimulations while there is no drug that passively diffused from the non-stimulated composite.

A different perspective is given from the fact that direct energy sources are not necessary for electrostimulated release.¹⁴⁰ From this point of view, self-powered devices could be a great promise for avoiding the reliance on power sources to operate. Besides, this could facilitate their progression from the laboratory to the biomedical marketplace. For example, Catt *et al.*¹⁴¹ covered the surface of magnesium, which is appealing for medical implant applications due to its complete *in vivo* degradation, with electropolymerized PEDOT using GO as dopant agent and Dex carrier. Magnesium substrates corrosion results in a local release of Mg²⁺, OH⁻, and H⁺, and when the surface is coated with by ICPs the corrosion rate slows down. In that work authors took profit of selective coating of the magnesium surface, therefore causing different grades of

corrosion. As it is illustrated in **Figure 6.12**, Dex release increases with the uncovered area of magnesium due to the electrical current generated from corrosion, whereas there is practically no release when PEDOT/GO/Dex is deposited onto a non-corroding gold surface. Overall, PEDOT/GO/Dex films, which delivers Dex at the corrosion site to minimize the detrimental effects of corrosion by products, can be developed into self-powered implantable drug delivery devices in which the corrosion is the driving force for drug release as well as the energy source.

A similar effect was observed when PPy· doped with ATP was added on the inner and outer part of a cellulose matrix and a thin layer of Mg^+ was deposited on one side (**Figure 6.13**).¹⁴² Herein, Mg^+ , ATP-doped PPy film, together with the electrolyte solution formed a galvanic cell. The galvanic couple of the PPy film (cathode) to the magnesium layer (anode) was the driving force for drug release. In summary, magnesium was oxidized and migrated into the solution as an ion while the PPy was reduced facilitating the ATP release.

More examples of ICPs matrices incorporating other materials, as for example gold nanoparticles,¹⁴³ montmorillonite,¹⁴⁴ and palygorskite,¹⁴⁵ are available in the literature.

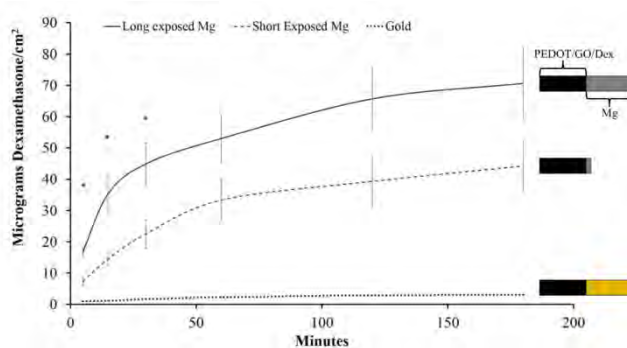


Figure 6.12 Corrosion driven drug release. Dex release from PEDOT/GO/Dex films deposited onto a magnesium surface in which the drug delivery is powered by the substrate corrosion. Magnesium samples had either long or short exposed area but the same amount of coverage by the PEDOT/GO/Dex coating. Reproduced with permission from reference ¹⁴¹.

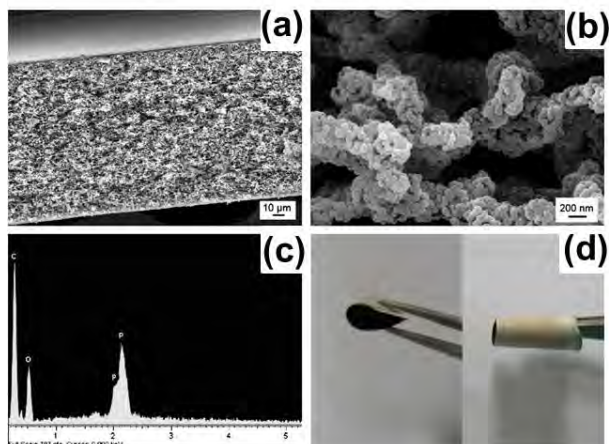


Figure 6.13 (a) Cross-section of cellulose-PPy composite film; (b) High magnification image of a. (c) Energy dispersive X-ray spectrum of cellulose-PPy composite film. (d) Digital photo of the DDS with the coating of magnesium layer on the one side of the cellulose-PPy composite film. Adapted from ¹⁴².

A summary of the different approaches for the composite generation and electrostimulation release is provided in **Table 6.6**.

Table 6.6 Summary of some remarkable examples of polymer composites reported in literature with the most important characteristics (*i.e.* preparation method, polymer, drug, dopant and release mechanism) for DDSs made of ICP.

Polymer	Drug	Dopant	Synthesis	Release	Ref.
PPy	P/S mixture (0.007 M each) or Dex (0.125 mM)	Drug	CV with drug from 0 to 1.1 V (10 cycles) of multi-walled carbon nanotubes-Ti or AuPd-Ti coated with monomer.	CV from -1 to 1 V for up to 25 cycles.	64
PPy	Aspirin (0.017 M)	Drug	CA with drug and montmorillonite at 0.8 V for 500 s.	Constant potential at -0.6 V for 230 min.	144
PPy	Dex (0.051 M)	Drug	CP with drug-loaded carbon nanotubes at +70 mA for 400 s.	A square wave electrical stimulation with 50% duty cycle; 2.0 V for 5 s followed by 0.0 V for 5 s, or -0.5 V for 5 s followed by 0.5 V for 5 s.	134
PPy	Dex (0.025 M)	Drug	CA with drug, graphene oxide nanosheets and Dex 21-phosphate disodium salt at 0.8 V until the charge density reached 400 mC/cm.	Biphasic voltage pulse at -2 V for 5 s, followed by 0 V for 5 s (1000 cycles) or -0.5 V for 5 s, followed by 0.5 V for 5 s (400 cycles).	139
PPy	Aspirin (0.017 M)	Drug	Palygorskite was dispersed in phosphate buffered saline solution with aspirin (pH 3.5) and sonicated for 1 h. The	Constant potential at -0.6 V for 160 min.	145

			monomer was added to the resulting emulsion. CA at 0.80 V for 500 s.		
PPy	ATP (0.007 M)	Ammonium persulfate (0.050 M)	A two cell compartment was separated by a cellulose nitrate-cellulose acetate film. One of the compartments contained the monomer and ATP. The other compartment was filled with ammonium persulfate. The cell was kept at 4 °C for 3.5 h. The ATP-doped PPy film was formed gradually on the outer and inner surfaces of the separating film. A thin layer of magnesium (or zinc) was magnetron sputtered on the one side of the film.	Self-powered drug delivery system driven by the oxidation of magnesium.	142
PEDOT	Dex (0.1 M)	Drug	Carbon nanotubes were tethered to Au electrodes using cysteamine was used. This electrode was coated with monomer- and Dex-containing solution. CA at 1.1 V.	CV from -0.8 V to 1.4 V.	77
PEDOT	Dex (0.008 M)	Drug	CA with previously sonicated single layer graphene oxide and Dex at 0.6 V until a total charge of 10 mC.	Pulsatile stimulation of -0.25 V for 5s followed by 0 V for 5s.	141
PEDOT	6,7-dinitroquinoxaline-2,3-dione (0.013 M) and Flu (0.017 M)	Drug	CA with drug-functionalized carbon nanotubes at 0.75-0.95 V for 15 s. to form the PEDOT/fCNT film.	Cathodic leading cosine waveform (100 ms) with an amplitude of 1, 1.5, and 2 V.	136
PPy	Insulin (100 IU/L)	LiClO ₄ (0.1	PPy nanowire: CA with 0.1 M NaClO ₄ and 0.1 M	Constant potential at -	143

CHAPTER 6

		M)		Na ₂ C ₂ O ₃ at +0.9 V vs. for 200s onto Pt. Then, Au nanoparticles were deposited onto PPy surface by CV from -1.0 V to +0.2 V (5 cycles) in a HAuCl ₄ solution. After this, thioglycolic acid was spread onto the electrode surface, incubated for 15 min and washed. Finally, the composite was immersed in 5 mL sample of aqueous insulin solution and a CA at +0.5 V was applied for 900 s.	0.6 V for 1 h using different pHs.	
PPy	NT-3	Ferric toluene sulfonate	<i>p</i> -	Aligned multi-walled carbon nanotubes were produced on a quartz plate. A thin PPy film was then deposited by a vapour-phase polymerisation method using ferric <i>p</i> -toluenesulfonate as the oxidant. Then, a thin Pt film was sputter-coated onto arrays for 10 min at 30 mA. Finally, a poly(vinylidene fluoride) layer was then cast onto the sample.	100 μs Biphasic current pulses at 250 Hz and at a current density of ± 1mA/cm ² .	135

6.6.7 Hybrid 3D-structures

Hybrid materials containing different size, shape and composition, which were engineered to obtain superior properties and multitasking capabilities, have been also recently reported. The work Feiner *et al.*,¹⁴⁶ who prepared hybrid patches for enabling the recording of cellular electrical activities and the on-demand drug release, is particularly noticeable. This hybrid patch was composed of an epoxy named SU-8 and a thin layer of gold that was also covered with rough nanoscale layer of titanium nitride. PPy was deposited on specified places and, finally, electrospinning was used to deposit PCL–gelatin fibres onto the electronics, facilitating cardiac cells attachment (**Figure 6.14**). The benefits of the fibers addition were high cell attachment, drug diffusion from the ICP and prevention of polymer delamination from the electrode surface. The final goal of this material was to collect data from its surroundings and thus ascertain when to induce electrical stimulation and/or to release drugs within the 3D microenvironment to affect the host tissue.

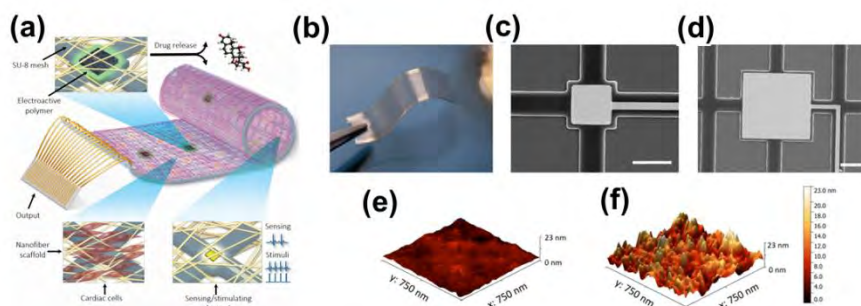


Figure 6.14 Schematics of the microelectronic cardiac patch concept (a). An image of a freestanding, flexible device consisting of 32 gold electrodes dispersed within a porous mesh of SU-8 (b). Scanning electron micrographs (SEMs) of a $50 \times 50 \mu\text{m}^2$ electrode pad designated for recording cellular electrical activities and cell and tissue stimulation (c) and a larger $150 \times 150 \mu\text{m}^2$ electrode pad, on which electroactive polymer is deposited for controlling the release of biomolecules (*i. e.* growth factors and small molecules) (d). Scale bars, $50 \mu\text{m}$. Atomic force microscopy images of a pristine gold electrode pad (e) and an electrode with a nanoscale layer of titanium nitride deposited to increase surface area (f). Adapted from ¹⁴⁶.

6.7 Conclusions and outlook

Currently, ICPs for electrical and/or electrochemical controlled drug release have reached a sufficient level of sophistication for on/off triggering and on-demand releasing profiles. The fabrication of devices combining the properties of ICPs with biodegradable polymers, metals or carbon nanostructures improve the applicability of former ones. Up to now, outstand the self-powered devices based on magnesium substrates, which would reduce the use of expensive and complicated electronic devices, and the systems able to detect real-time changes in the environment and, simultaneously, release drugs.

Future devices will benefit from features that would extend their mechanical stability achieving stretchable electronics, which will allow a proper integration in the human body. Besides, systems with additional sensing capabilities such as neuronal recording, pH, mechanical stress and heat could be used for, at the same time, deciding the optimum amount of drug to be released.

Future technology that will flourish from the use of ICPs as nano-reservoirs is expected to notify physicians of a patient's health condition followed by the possibility of remote drug triggering. Moreover, it is even possible to imagine the ability to integrate a feedback loop into the system that would self-regulate and where physician assistance may not be required. For example, the optimization of a self-regulated insulin delivery remains one of the most demanding technologies to be developed. Instead of multiple daily injections of insulin, millions of diabetes patients could take care of their glucose level for months with one injection of self-regulated insulin DDS. Therefore, we expect an increase in selectivity, sensitivity and adaptability of drug release profiles depending on the patient and allow a better understanding of the body electrophysiology during future generations.

From the material's perspective, the DDSs need further development in the following directions: (1) Better integration of the different components into one unique device; (2) More flexibility and biodegradability to improve the implantation of a foreign material into the human body; and (3) study the realization of close-looped DDSs through the integration of multiple advanced electronic devices, such as a wireless transducer or portable batteries.

6.8 References

1. Boom time for biomaterials. *Nat. Mater.* **2009**, 8, 439.
2. Yun, Y. H.; Lee, B. K. and Park, K. Controlled Drug Delivery: Historical perspective for the next generation. *J. Control. Release*, **2015**, 219, 2–7.
3. Allen, T. M. and Cullis, P. R. Drug Delivery Systems: Entering the Mainstream. *Science (80-)*. **2004**, 303, 1818–1822.
4. Langer, R. S. and Peppas, N. A. Present and future applications of biomaterials in controlled drug delivery systems. *Biomaterials* **1981**, 2, 201–214.
5. Wurster, D. E. Method of applying coatings to edible tablets or the like. US Pat. 2648609, **1953**.
6. Folkman, J. How the field of controlled-release technology began, and its central role in the development of angiogenesis research. *Biomaterials* **1990**, 11, 615–618.
7. Langer, R. and Folkman, J. Polymers for the sustained release of proteins and other macromolecules. *Nature* **1976**, 263, 797–800.
8. Bangham, A. D. and Horne, R. W. Negative staining of phospholipids and their structural modification by surface-active agents as observed in the electron microscope. *J. Mol. Biol.* **1964**, 8, IN2–IN10.
9. Torchilin, V. P. Recent advances with liposomes as pharmaceutical carriers. *Nat. Rev. Drug Discov.* **2005**, 4, 145–160.
10. Chertok, B.; Moffat, B. A.; David, A. E.; Yu, F.; Bergemann, C.; Ross, B. D. and Yang, V. C. Iron oxide nanoparticles as a drug delivery vehicle for MRI monitored magnetic targeting of brain tumors. *Biomaterials* **2008**, 28, 487–496.
11. Quan, Q.; Xie, J.; Gao, H.; Yang, M.; Zhang, F.; Liu, G.; Lin, X.; Wang, A.; Eden, H. S.; Lee, S. Zhang, G. and Chen, X. HSA coated iron oxide nanoparticles as drug delivery vehicles for cancer therapy. *Mol. Pharm.* **2011**, 8, 1669–1676.
12. Farooq, M. U.; Novosad, V.; Rozhkova, E. A.; Wali, H.; Ali, A.; Fateh, A. A.; Neogi, P. B.; Neogi, A. and Wang Z. Gold nanoparticles-enabled efficient dual delivery of anticancer therapeutics to HeLa cells. *Sci. Rep.* **2018**, 8, 1–12.
13. Dreaden, E. C.; Austin, L. A.; MacKey, M. A. and El-Sayed, M. A. Size matters: Gold nanoparticles in targeted cancer drug delivery. *Ther. Deliv.* **2012**, 3, 457–478.
14. Xia, B.; Zhang, W.; Shi, J. and Xiao, S. A novel strategy to fabricate doxorubicin / bovine serum albumin / porous silicon nanocomposites with pH-triggered drug delivery for cancer therapy. *J. Mater. Chem. B Mater. Biol. Med.* **2014**, 2, 5280–5286.
15. Anglin, E. J.; Cheng, L.; Freeman, W. R. and Sailor, M. J. Porous silicon in drug delivery devices and materials. *Adv. Drug Deliv. Rev.* **2008**, 60, 1266–1277.
16. Senapati, S.; Mahanta, A. K.; Kumar, S. and Maiti, P. Controlled drug delivery vehicles for cancer treatment and their performance. *Signal Transduct. Target. Ther.* **2018**, 3, 7.
17. Fenton, O. S., Olafson, K. N., Pillai, P. S., Mitchell, M. J. and Langer, R. Advances in biomaterials for drug delivery. *Adv. Mater.* **2018**, 30, 1–29.

18. Global Markets and Technologies for Advanced Drug Delivery Systems. **2016**. at <<https://www.bccresearch.com/market-research/pharmaceuticals/advanced-drug-delivery-systems-tech-markets-report-phm006k.html>>
19. Shirakawa, H. The discovery of polyacetylene film - The dawning of an era of conducting polymers. *Angew. Chem. Int. Ed.* **2001**, 1, 281–286.
20. Shirakawa, H., Louis, E. J., Macdiarmid, A. G., Chiang, C. K. & Heeger, A. J. Synthesis of Electrically conducting organic polymers: halogen derivatives of polyacetylene, (CH)_x. *J.C.S. Chem. Comm.* **1977**, 36, 578–580.
21. Green, R. and Abidian, M. R. Conducting polymers for neural prosthetic and neural interface applications. *Adv. Mater.* **2015**, 27, 7620–7637.
22. Bredas, J. L. and Street, G. B. Polarons, bipolarons, and solitons in conducting polymers. *Acc. Chem. Res.* **1985**, 18, 309–315.
23. Yi, N. and Abidian, M. R. Conducting polymers and their biomedical applications. *Biosynthetic Polymers for Medical Applications.* **2015**, 243-276.
24. Del Valle, L. J.; Aradilla, D.; Oliver, R.; Sepulcre, F.; Gamez, A.; Armelin, E.; Alemán, C. and Estrany, F. Cellular adhesion and proliferation on poly(3,4-ethylenedioxythiophene): Benefits in the electroactivity of the conducting polymer. *Eur. Polym. J.* **2007**, 43, 2342–2349.
25. Balint, R.; Cassidy, N. J. and Cartmell, S. H. Conductive polymers: Towards a smart biomaterial for tissue engineering. *Acta Biomater.* **2014**, 10, 2341–2353.
26. Ateh, D. D.; Navsaria, H. A. and Vadgama, P. Polypyrrole-based conducting polymers and interactions with biological tissues. *J. R. Soc. Interface* **2006**, 3, 741–752.
27. Tandon, B.; Magaz, A.; Balint, R.; Blaker, J. J. and Cartmell, S. H. Electroactive biomaterials: Vehicles for controlled delivery of therapeutic agents for drug delivery and tissue regeneration. *Adv. Drug Deliv. Rev.* **2018**, 129, 148–168.
28. Fielding, L. A.; Hillier, J. K.; Burchell, M. J. and Armes, S. P. Space Science Applications for Conducting Polymer Particles: Synthetic Mimics for Cosmic Dust and Micrometeorites. *Chem. Commun.* **2015**, 51, 16886–16899.
29. Hardy, J. G.; Li, H.; Chow, J. K.; Geissler, S. A.; McElroy, A. B.; Nguy, L.; Hernandez, D. S. and Schmidt, C. E. Conducting polymer-based multilayer films for instructive biomaterial coatings. *Futur. Sci.* **2015**, OA 1.
30. De Giglio, E.; Sabbatini, L. and Zamboni, P. G. Development and analytical characterization of cysteine-grafted polypyrrole films electrosynthesized on Pt and Ti-substrates as precursors of bioactive interfaces. *J. Biomater. Sci. Polym. Ed.* **1999**, 10, 845–858.
31. Ateh, D. D.; Vadgama, P. and Navsaria, H. A. Culture of human keratinocytes on polypyrrole-based conducting polymers. *Tissue Eng.* **2006**, 12, 645–655.
32. Li, M.; Guo, Y.; Wei, Y.; MacDiarmid, A. G. and Lelkes, P. I. Electrospinning polyaniline-contained gelatin nanofibers for tissue engineering applications. *Biomaterials* **2006**, 27, 2705–2715.

33. George, P. M.; Lyckman, A. W.; LaVan, D. A.; Hegde, A.; Leung, Y.; Avasare, R.; Testa, C.; Alexander, P. M.; Langer, R and Sur, M. Fabrication and biocompatibility of polypyrrole implants suitable for neural prosthetics. *Biomaterials* **2005**, *26*, 3511–3519.
34. Wang, X.; Gu, X.; Yuan, C.; Chen, S.; Zhang, P.; Zhang, T.; Yao, J.; Chen, F. and Chen, G. Evaluation of biocompatibility of polypyrrole in vitro and in vivo. *J. Biomed. Mater. Res. - Part A* **2004**, *68*, 411–422.
35. Jang, K.; Kim, L.; Seo, S. J. and Young Lee, J. Facile and controllable electrochemical fabrication of cell-adhesive polypyrrole electrodes using pyrrole-RGD peptides. *Biofabrication* **2017**, *9*, 0–23.
36. Humpolicek, P.; Kasparikova, V.; Saha, P. and Stejskal, J. Biocompatibility of polyaniline. *Synth. Met.* **2012**, *162*, 722–727.
37. Green, R. A.; Lovell, N. H.; Wallace, G. G. and Poole-Warren, L. A. Conducting polymers for neural interfaces: Challenges in developing an effective long-term implant. *Biomaterials* **2008**, *29*, 3393–3399.
38. Oh, W. K.; Kwon, O. S. and Jang, J. Conducting polymer nanomaterials for biomedical applications: Cellular interfacing and biosensing. *Polym. Rev.* **2013**, *53*, 407–442.
39. Uppalapati, D.; Boyd, B. J.; Garg, S.; Travas-Sejdic, J. and Svirskis, D. Conducting polymers with defined micro- or nanostructures for drug delivery. *Biomaterials* **2016**, *111*, 149–162.
40. Ghosh, S.; Maiyalagan, T. and Basu, R. N. Nanostructured conducting polymers for energy applications: Towards a sustainable platform. *Nanoscale* **2016**, *8*, 6921–6947.
41. Xia, L.; Wei, Z. and Wan, M. Conducting polymer nanostructures and their application in biosensors. *J. Colloid Interface Sci.* **2010**, *341*, 1–11.
42. Schönenberger, C.; van der Zande, B. M. I.; Fokkink, L. G. J.; Henny, M; Schmid, C.; Krüger, M.; Bachtold, A.; Huber, R.; Birk, H. and Stauffer, U. Template Synthesis of Nanowires in Porous Polycarbonate Membranes: Electrochemistry and Morphology. *J. Phys. Chem. B* **1997**, *101*, 5497–5505.
43. Han, M. G. and Foulger, S. H. 1-Dimensional structures of poly(3,4-ethylenedioxythiophene) (PEDOT): A chemical route to tubes, rods, thimbles, and belts. *Chem. Commun.* **2005**, *1*, 3092–3094.
44. Martin, C. R.; Parthasarathy, R. and Menon, V. Template synthesis of electronically conductive polymers - A new route for achieving higher electronic conductivities. *Synth. Met.* **1993**, *55*, 1165–1170.
45. Chun-Guey Wu, T. B. Conducting polyaniline filaments in a mesoporous channel hos. *Science (So-)*. **1994**, *264*, 1775–1759.
46. Wu, J.; Cho, W.; Martin, D. C.; Feng, Z. Q.; Leach, M. K.; Franz, E. W.; Naim, Y. I.; Gu, Z. Z. and Corey, J. M. Highly aligned poly(3,4-ethylene dioxythiophene) (PEDOT) nano- and microscale fibers and tubes. *Polym. (United Kingdom)* **2013**, *54*, 702–708.

47. Zhang, Z.; Sui, J.; Zhang, L.; Wan, M. Wei, Y. and Yu, L. Synthesis of polyaniline with a hollow, octahedral morphology by using a cuprous oxide template. *Adv. Mater.* **2005**, 17, 2854–2857.
48. Boal, A. K.; Ilhan, F.; DeRouchey, J. E.; Thurn-Albrecht, T.; Russell, T. P. and Rotello, V. M. Self-assembly of nanoparticles into structured spherical and network aggregates. *Nature* **2000**, 404, 746–748.
49. Qu, L.; Shi, G.; Chen, F. and Zhang, J. Electrochemical growth of polypyrrole microcontainers. *Macromolecules* **2003**, 36, 1063–1067.
50. Bajpai, V.; He, P.; Goettler, L.; Dong, J. H. and Dai, L. Controlled syntheses of conducting polymer micro- and nano-structures for potential applications. *Synth. Met.* **2006**, 156, 466–469.
51. Jang, J.; Li, X. L. and Oh, J. H. Facile fabrication of polymer and carbon nanocapsules using polypyrrole core / shell nanomaterials. *Chem. Commun.* **2004**, 794–795.
52. Jang, J.; Bae, J. and Park, E. Selective fabrication of poly(3,4-ethylenedioxythiophene) nanocapsules and mesocellular foams using surfactant-mediated interfacial polymerization. *Adv. Mater.* **2006**, 18, 354–358.
53. Liang, L.; Liu, J.; Windisch, C. F.; Exarhos, G. J. and Lin, Y. Direct assembly of large arrays of oriented conducting polymer nanowires. *Angew. Chemie - Int. Ed.* **2002**, 41, 3665–3668.
54. Dallas, P. and Georgakilas, V. Interfacial polymerization of conductive polymers: Generation of polymeric nanostructures in a 2-D space. *Adv. in Colloid and Interfac.* **2015**, 224, 46–61.
55. Nuraje, N.; Su, K.; Yang, N. I. and Matsui, H. Liquid/liquid interfacial polymerization to grow single crystalline nanoneedles of various conducting polymers. *ACS Nano* **2008**, 2, 502–506.
56. Zinger, B. and Miller, L. L. Timed Release of Chemicals from Polypyrrole Films. *J. Am. Chem. Soc.* **1984**, 106, 6861–6863.
57. Krukiewicz, K. and Zak, J. K. Conjugated polymers as robust carriers for controlled delivery of anti-inflammatory drugs. *J. Mater. Sci.* **2014**, 49, 5738–5745.
58. Wadhwa, R.; Lagenaur, C. F. and Cui, X. T. Electrochemically controlled release of dexamethasone from conducting polymer polypyrrole coated electrode. *J. Control. Release* **2006**, 110, 531–541.
59. Shamaeli, E. and Alizadeh, N. Kinetic studies of electrochemically controlled release of salicylate from nanostructure conducting molecularly imprinted polymer. *Electrochim. Acta* **2013**, 114, 409–415.
60. Alizadeh, N. and Shamaeli, E. Electrochemically controlled release of anticancer drug methotrexate using nanostructured polypyrrole modified with cetylpyridinium: Release kinetics investigation. *Electrochim. Acta* **2014**, 130, 488–496.
61. Krukiewicz, K.; Jarosz, T.; Zak, J. K.; Lapkowski, M.; Ruskowski, P.; Bobkiewicz-Kozłowska, T. and Bednarczyk-Cwynar, B. Advancing the delivery of anticancer drugs: Conjugated polymer/triterpenoid composite. *Acta Biomater.* **2015**, 19, 158–165.

62. Puiggali-Jou, A.; Micheletti, P.; Estrany, F.; del Valle, L. J. and Alemán, C. Electrostimulated Release of Neutral Drugs from Polythiophene Nanoparticles: Smart Regulation of Drug-Polymer Interactions. *Adv. Healthc. Mater.* **2017**, *6*, 1–11.
63. Esrafilzadeh, D.; Razal, J. M.; Moulton, S. E.; Stewart, E. M. and Wallace, G. G. Multifunctional conducting fibres with electrically controlled release of ciprofloxacin. *J. Control. Release* **2013**, *169*, 313–320.
64. Sirivisoot, S.; Pareta, R. and Webster, T. J. Electrically controlled drug release from nanostructured polypyrrole coated on titanium. *Nanotechnology* **2011**, *22*.
65. Green, R. A.; Lovell, N. H. and Poole-Warren, L. A. Impact of co-incorporating laminin peptide dopants and neurotrophic growth factors on conducting polymer properties. *Acta Biomater.* **2010**, *6*, 63–71.
66. Puiggali-Jou, A.; del Valle, L. J.; Armelin, E. and Alemán, C. Fibrin Association at Hybrid Biointerfaces Made of Clot-Binding Peptides and Polythiophene. *Macromol. Biosci.* **2016**, *16*, 1461–1474.
67. Bax, D. V.; Tipa, R. S.; Kondyurin, A.; Higgins, M. J.; Tsoutas, K.; Gelmi, A.; Wallace, G. G.; Mckenzie, D. R.; Weiss, A. S. and Bilek, M. M. Cell patterning via linker-free protein functionalization of an organic conducting polymer (polypyrrole) electrode. *Acta Biomater.* **2012**, *8*, 2538–2548.
68. Thompson, B. C.; Moulton, S. E.; Ding, J.; Richardson, R.; Cameron, A.; O'Leary, S.; Wallace, G. G. and Clark, G. M. Optimising the incorporation and release of a neurotrophic factor using conducting polypyrrole. *J. Control. Release* **2006**, *116*, 285–294.
69. Krukiewicz, K.; Bednarczyk-Cwynar, B.; Turczyn, R. and Zak, J. K. EQCM verification of the concept of drug immobilization and release from conducting polymer matrix. *Electrochim. Acta* **2016**, *212*, 694–700.
70. Krukiewicz, K.; Stokfisz, A. and Zak, J. K. Two approaches to the model drug immobilization into conjugated polymer matrix. *Mater. Sci. Eng. C* **2015**, *54*, 176–181.
71. Hepel, M. and Mahdavi, F. Application of the electrochemical quartz crystal microbalance for electrochemically controlled binding and release of chlorpromazine from conductive polymer matrix. *Microchem. J.* **1997**, *56*, 54–64.
72. Miller, L. L. and Zhou, Q. X. Poly(N-methylpyrrolium) Poly(styrenesulfonate): A Conductive, Electrically Switchable Cation Exchanger That Cathodically Binds and Anodically Releases Dopamine. *Macromolecules* **1987**, *20*, 1594–1597.
73. Zhou, Q. X.; Miller, L. L. and Valentine, J. R. Electrochemically controlled binding and release of protonated dimethyldopamine and other cations from poly(N-methyl-pyrrole)/polyanion composite redox polymers. *J. Electroanal. Chem.* **1989**, *261*, 147–164.
74. Bidan, G.; Lopez, C.; Mendes-Viegas, F.; Vieil, E. and Gabelle, A. Incorporation of sulphonated cyclodextrins into polypyrrole: an approach for the electro-controlled delivering of neutral drugs. *Biosens. Bioelectron.* **1995**, *10*, 219–229.

75. Carli, S. Trapella, C.; Armirotti, A.; Fantinati, A.; Ottonello, G.; Scarpellini, A.; Prato, M.; Fadiga, L. and Ricci, D. Biochemically Controlled Release of Dexamethasone Covalently Bound to PEDOT. *Chem. - A Eur. J.* **2018**, *24*, 10300–10305.
76. Jiang, S.; Sun, Y.; Cui, X.; Huang, X.; He, Y.; Ji, S.; Shi, W. and Ge, D. Enhanced drug loading capacity of polypyrrole nanowire network for controlled drug release. *Synth. Met.* **2013**, *163*, 19–23.
77. Xiao, Y.; Ye, X.; He, L. and Che, J. New carbon nanotube-conducting polymer composite electrodes for drug delivery applications. *Polym. Int.* **2012**, *61*, 190–196.
78. Pyo, M. and Reynolds, J. R. Electrochemically stimulated adenosine 5'-triphosphate (ATP) release through redox switching of conducting polypyrrole films and bilayers. *Chem. Mater.* **1996**, *8*, 128–133.
79. Syritski, V.; Öpik, A. and Forsén, O. Ion transport investigations of polypyrroles doped with different anions by EQCM and CER techniques. *Electrochim. Acta* **2003**, *48*, 1409–1417.
80. Evans, A. J.; Thompson, B. C.; Wallace, G. G.; Millard, R.; O'Leary, S. J., Clark, G. M.; Shepherd, R. K. and Richardson, R. T. Promoting neurite outgrowth from spiral ganglion neuron explants using polypyrrole/BDNF-coated electrodes. *J. Biomed. Mater. Res. - Part A* **2009**, *91*, 241–250.
81. Richardson, R. T.; Thompson, B.; Moulton, S.; Newbold, C.; Lum, M. G.; Cameron, A.; Wallace, G.; Kapsa, R.; Clark, G. and O'Leary, S. The effect of polypyrrole with incorporated neurotrophin-3 on the promotion of neurite outgrowth from auditory neurons. *Biomaterials* **2007**, *28*, 513–523.
82. Boehler, C. and Asplund, M. A detailed insight into drug delivery from PEDOT based on analytical methods: Effects and side effects. *J. Biomed. Mater. Res. - Part A* **2015**, *103*, 1200–1207.
83. Boehler, C. Kleber, C.; Martini, N.; Xie, Y.; Dryg, I.; Stieglitz, T.; Hofmann, U. G. and Asplund, M. Actively controlled release of Dexamethasone from neural microelectrodes in a chronic in vivo study. *Biomaterials* **2017**, *129*, 176–187.
84. Hardy, J. G.; Mouser, D. J.; Arroyo-Curras, N.; Geissler, S.; Chow, J. K.; Nguy, L.; Kim, J. M. and Schmidt, C. E. Biodegradable electroactive polymers for electrochemically-triggered drug delivery. *J. of Mat. Chem. B* **2014**, *39*, 6809–6822.
85. Hardy, J. G.; Amend, M. N.; Geissler, S.; Lynch, V. M. and Schmidt, C. E. Peptide-directed assembly of functional supramolecular polymers for biomedical applications: electroactive molecular tongue-twisters (oligoalanine-oligoaniline-oligoalanine) for electrochemically enhanced drug delivery. *J. Mater. Chem. B* **2015**, *3*, 5005–5009.
86. Murdan, S. E lectro-responsive drug delivery from hydrogels. *J. Control. Release* **2003**, *92*, 1–17.
87. George, P. M.; LaVan, D. A.; Burdick, J. A.; Chen, C.-Y.; Liang, E. and Langer, R. Electrically controlled drug delivery from biotin-doped conductive polypyrrole. *Adv. Mater.* **2006**, *18*, 577–581.

88. Samanta, D.; Hosseini-Nassab, N.; McCarty, A. D. and Zare, R. N. Ultra-low voltage triggered release of an anti-cancer drug from polypyrrole nanoparticles. *Nanoscale* **2018**, 10, 9773–9779.
89. Cai, P.; Leow, W. R.; Wang, X.; Wu, Y. L. and Chen, X. Programmable Nano–Bio Interfaces for Functional Biointegrated Devices. *Adv. Mater.* **2017**, 29, 1–26.
90. Ge, D. Tian, X.; Qi, R.; Huang, S.; Mu, J.; Hong, S.; Ye, S.; Zhang, X.; Li, D. and Shi, W. A polypyrrole-based microchip for controlled drug release. *Electrochim. Acta* **2009**, 55, 271–275.
91. Svirskis, D.; Wright, B. E.; Travas-Sejdic, J.; Rodgers, A. and Garg, S. Development of a controlled release system for risperidone using polypyrrole: Mechanistic studies. *Electroanalysis* **2010**, 22, 439–444.
92. Li, Y.; Neoh, K. G. and Kang, E. T. Controlled release of heparin from polypyrrole-poly(vinyl alcohol) assembly by electrical stimulation. *J. Biomed. Mater. Res. - Part A* **2005**, 73, 171–181.
93. Krukiewicz, K.; Cichy, M.; Ruskowski, P.; Turczyn, R.; Jarosz, T.; Zak, J. K.; Lapkowski, M and Bednarczyk-Cwynar, B. Betulin-loaded PEDOT films for regional chemotherapy. *Mater. Sci. Eng. C* **2017**, 73, 611–615.
94. Massoumi, B. and Entezami, A. Electrochemically controlled binding and release of dexamethasone from conducting polymer bilayer films. *J. Bioact. Compat. Polym.* **2002**, 17.
95. Carquigny, S.; Lakard, B.; Lakard, S.; Moutarlier, V.; Hihn, J.-Y. and Viau, L. Investigation of pharmaceutically active ionic liquids as electrolyte for the electrosynthesis of polypyrrole and active component in controlled drug delivery. *Electrochim. Acta* **2016**, 211, 950–961.
96. Pernaut, J.-M. and Reynolds, J. R. Use of Conducting Electroactive Polymers for Drug Delivery and Sensing of Bioactive Molecules. A Redox Chemistry Approach. *J. Phys. Chem. B* **2000**, 104, 4080–4090.
97. Svirskis, D.; Wright, B. E.; Travas-Sejdic, J.; Rodgers, A. and Garg, S. Evaluation of physical properties and performance over time of an actuating polypyrrole based drug delivery system. *Sensors Actuators, B Chem.* **2010**, 151, 97–102.
98. Shamaeli, E. and Alizadeh, N. Nanostructured biocompatible thermal/electrical stimuli-responsive biopolymer-doped polypyrrole for controlled release of chlorpromazine: Kinetics studies. *Int. J. Pharm.* **2014**, 472, 327–338.
99. Löffler, S.; Seyock, S.; Nybom, R.; Jacobson, G. B. and Richter-Dahlfors, A. Electrochemically triggered release of acetylcholine from CO₂ impregnated conductive polymer films evokes intracellular Ca²⁺ signaling in neurotypic SH-SY5Y cells. *J. Control. Release* **2016**, 243, 283–290.
100. Ge, J.; Neofytou, E.; Cahill, T. J.; Beygui, R. E. and Zare, R. N. Drug release from electric-field-responsive nanoparticles. *ACS Nano* **2012**, 6, 227–233.
101. Hosseini-Nassab, N.; Samanta, D.; Abdolazimi, Y.; Annes, J. P. and Zare, R. N. Electrically controlled release of insulin using polypyrrole nanoparticles. *Nanoscale* **2017**, 9, 143–149.

102. Samanta, D.; Hosseini-Nassab, N. and Zare, R. N. Electroresponsive nanoparticles for drug delivery on demand. *Nanoscale* **2016**, *8*, 9310–9317.
103. Tran, H. D.; Shin, K.; Hong, W. G.; D'Arcy, J. m.; Kojima, R. W.; Weiller, B. H. and Kaner, R. B. A template-free route to polypyrrole nanofibers. *Macromol. Rapid Commun.* **2007**, *28*, 2289–2293.
104. Shi, W.; Liang, P.; Ge, D.; Wang, J. and Zhang, Q. Starch-assisted synthesis of polypyrrole nanowires by a simple electrochemical approach. *Chem. Commun.* **2007**, *23*, 2414–2416.
105. Zhong, W.; Liu, S.; Chen, X.; Wang, Y. and Yang, W. High-yield synthesis of superhydrophilic polypyrrole nanowire networks. *Macromolecules* **2006**, *39*, 3224–3230.
106. Zhang, X. and Manohar, S. K. Bulk synthesis of polypyrrole nanofiber by seeding approach. *J. American Chem. Soc.* **2004**, *126*, 12714–12715.
107. Acik, M.; Baristiran, C. and Sonmez, G. Highly surfaced polypyrrole nano-networks and nanofibers. *J. Mater. Sci.* **2006**, *41*, 4678–4683.
108. Li, C.; Bai, H. and Shi, G. Conducting polymer nanomaterials: Electrosynthesis and applications. *Chem. Soc. Rev.* **2009**, *38*, 2397–2409.
109. Ru, X.; Shi, W.; Huang, X.; Cui, X.; Ren, B. and Ge, D. Synthesis of polypyrrole nanowire network with high adenosine triphosphate release efficiency. *Electrochim. Acta* **2011**, *56*, 9887–9892.
110. Lee, H.; Hong, W.; Jeon, S.; Choi, Y. and Cho, Y. Electroactive polypyrrole nanowire arrays: Synergistic effect of cancer treatment by on-demand drug release and photothermal therapy. *Langmuir* **2015**, *31*, 4264–4269.
111. Abidian, M. R.; Kim, D. H. and Martin, D. C. Conducting-polymer nanotubes for controlled drug release. *Adv. Mater.* **2006**, *18*, 405–409.
112. Chen, C.; Chen, X.; Zhang, H.; Zhang, Q.; Wang, L.; Li, C.; Dai, B.; Yang, J.; Liu, J. and Sun, D. Electrically-responsive core-shell hybrid microfibers for controlled drug release and cell culture. *Acta Biomater.* **2017**, *55*, 434–442.
113. Puiggali-Jou, A.; Cejudo, A.; del Valle, L. J. and Alemán, C. Smart drug delivery from electrospun fibers through electro-responsive polymeric nanoparticles. *ACS Appl. Bio Mater.* **2018**, *1*, 1594–1605.
114. Luo, X. and Cui, X. T. Electrochemically controlled release based on nanoporous conducting polymers. *Electrochem. commun.* **2009**, *11*, 402–404.
115. Luo, X. and Cui, X. T. Sponge-like nanostructured conducting polymers for electrically controlled drug release. *Electrochem. commun.* **2009**, *11*, 1956–1959.
116. Seyfoddin, A.; Chan, A.; Chen, W. T.; Rupenthal, I. D.; Waterhouse, G. I. and Svirskis, D. Electro-responsive macroporous polypyrrole scaffolds for triggered dexamethasone delivery. *Eur. J. Pharm. Biopharm.* **2015**, *94*, 419–426.
117. Cho, Y. and Borgens, R. B. Biotin-doped porous polypyrrole films for electrically controlled nanoparticle release. *Langmuir* **2011**, *27*, 6316–6322.

118. Sharma, M.; Waterhouse, G. I. N.; Loader, S. W. C.; Garg, S. and Svirskis, D. High surface area polypyrrole scaffolds for tunable drug delivery. *Int. J. Pharm.* **2013**, 443, 163–168.
119. Jeon, G.; Yang, S. Y.; Byun, J. and Kim, J. K. Electrically actuatable smart nanoporous membrane for pulsatile drug release. *Nano Lett.* **2011**, 11, 1284–1288.
120. Otero, T. F. Reactions drive conformations. Biomimetic properties and devices, theoretical description. *J. Mater. Chem. B* **2013**, 1, 3754–3767.
121. Smela, E. Conjugated Polymer Actuators for Biomedical Applications. *Adv. Mater.* **2003**, 15, 481–494.
122. Yuk, S. H.; Cho, S. H. and Lee, H. B. Electric Current-Sensitive Drug Delivery Systems Using Sodium Alginate/Polyacrylic Acid Composites. *Pharmaceutical Research* **1992**, 9, 955–957.
123. Kim, S. Y. and Lee, Y. M. Drug release behavior of electrical responsive poly(vinyl alcohol)/poly(acrylic acid) IPN hydrogels under an electric stimulus. *J. Appl. Polym. Sci.* **1999**, 74, 1752–1761.
124. Kim, D. H.; Abidian, M. and Martin, D. C. Conducting polymers grown in hydrogel scaffolds coated on neural prosthetic devices. *J. Biomed. Mater. Res. - Part A* **2004**, 71, 577–585.
125. Qu, J.; Zhao, X.; Ma, P. X. and Guo, B. Injectable antibacterial conductive hydrogels with dual response to an electric field and pH for localized ‘smart’ drug release. *Acta Biomater.* **2018**, 72, 55–69.
126. Pourjavadi, A. and Doroudian, M. Synthesis and characterization of semi-conductive nanocomposite based on hydrolyzed collagen and in vitro electrically controlled drug release study. *Polymer* **2015**, 76, 287–294.
127. Fabregat, G.; Giménez, A.; Díaz, A.; Puiggali, J. and Alemán, C. Dual-Functionalization Device for Therapy through Dopamine Release and Monitoring. *Macromol. Biosci.* **2018**, 18, 1800014.
128. H. Takahashi, S.; M. Lira, L. and I. Córdoba de Torresi, S. Zero-Order Release Profiles from A Multistimuli Responsive Electro-Conductive Hydrogel. *J. Biomater. Nanobiotechnol.* **2012**, 03, 262–268.
129. Niamlang, S. and Sirivat, A. Electrically controlled release of salicylic acid from poly(p-phenylene vinylene)/polyacrylamide hydrogels. *Int. J. Pharm.* **2009**, 371, 126–133.
130. Lin, H.; Li, L.; Ren, J.; Cai, Z.; Qiu, L.; Yang, Z. and Peng, H. Conducting polymer composite film incorporated with aligned carbon nanotubes for transparent, flexible and efficient supercapacitor. *Sci. Rep.* **2013**, 3, 1–6.
131. Wang, J.; Dai, J. and Yarlagadda, T. Carbon nanotube-conducting-polymer composite nanowires. *Langmuir* **2005**, 21, 9–12.
132. Gao, J.; Mikhail, E. I.; Aiping, Y.; Bekyarova, E.; Zhao, B. and Haddon, R. C. *et al.* Continuous spinning of a single-walled carbon nanotube– nylon composite fiber. *J. Am. Chem. Soc.* **2005**, 127, 3847–3854.
133. Ajayan, P. M. and Tour, J. M. Materials science: Nanotube composites. *Nature* **2007**, 447, 1066–1068.

134. Luo, X.; Matranga, C.; Tan, S.; Alba, N. and Cui, X. T. Carbon nanotube nanoreservoir for controlled release of anti-inflammatory dexamethasone. *Biomaterials* **2011**, *32*, 6316–6323.
135. Thompson, B. C.; Chen, J.; Moulton, S. E. and Wallace, G. G. Nanostructured aligned CNT platforms enhance the controlled release of a neurotrophic protein from polypyrrole. *Nanoscale* **2010**, *2*, 499–501.
136. Du, Z. J.; Bi, G.-Q. and Cui, X. T. Electrically Controlled Neurochemical Release from Dual-Layer Conducting Polymer Films for Precise Modulation of Neural Network Activity in Rat Barrel Cortex. *Adv. Funct. Mater.* **2017**, 1703988.
137. Gao, W. The chemistry of graphene oxide. *Graphene Oxide Reduct. Recipes, Spectrosc. Appl.* **2015**, 61–95.
138. Luo, X.; Weaver, C. L.; Tan, S. and Cui, X. T. Pure graphene oxide doped conducting polymer nanocomposite for bio-interfacing. *J. Mater. Chem. B* **2013**, *1*, 1340–1348.
139. Weaver, C. L.; Larosa, J. M.; Luo, X. and Cui, X. T. Electrically controlled drug delivery from graphene oxide nanocomposite films. *ACS Nano* **2014**, *8*, 1834–1843.
140. Moulton, S. E.; Imisides, M. D.; Shepherd, R. L. and Wallace, G. G. Galvanic coupling conducting polymers to biodegradable Mg initiates autonomously powered drug release. *J. Mater. Chem.* **2008**, *18*, 3608–3613.
141. Catt, K., Li, H.; Hoang, V.; Beard, R. and Cui, X. T. Self-powered therapeutic release from conducting polymer/graphene oxide films on magnesium. *Nanomedicine Nanotechnology, Biol. Med.* **2018**, *7*, 2495–2503.
142. Ge, D.; Ru, X.; Hong, S.; Jiang, S.; Tu, J.; Wang, J.; Zhang, A.; Linkov, V.; Ren, B. and Shi, W. Coating metals on cellulose-polypyrrole composites: A new route to self-powered drug delivery system. *Electrochem. commun.* **2010**, *12*, 1367–1370.
143. Shamaeli, E. and Alizadeh, N. Functionalized gold nanoparticle-polypyrrole nanobiocomposite with high effective surface area for electrochemical/pH dual stimuli-responsive smart release of insulin. *Colloids Surfaces B Biointerfaces* **2015**, *126*, 502–509.
144. Wang, R.; Peng, Y., Zhou, M. and Shou, D. Smart montmorillonite-polypyrrole scaffolds for electro-responsive drug release. *Appl. Clay Sci.* **2016**, *134*, 50–54.
145. Kong, Y.; Ge, H.; Xiong, J.; Zuo, S.; Wei, Y.; Yao, C. and Deng, Linhong. Palygorskite polypyrrole nanocomposite: A new platform for electrically tunable drug delivery. *Appl. Clay Sci.* **2014**, *99*, 119–124.
146. Feiner, R.; Engel, L.; Fleischer, S.; Malki, M.; Gal, I.; Shapira, A.; Shacham-Diamand, Y. and Dvir, T. Engineered hybrid cardiac patches with multifunctional electronics for online monitoring and regulation of tissue function. *Nat. Mater.* **2016**, *15*, 679–685.

CHAPTER 7:

Electrostimulated release

SUMMARY

In this **Chapter** two different systems for drug delivery have been developed.

Poly(3,4-ethylenedioxythiophene) (PEDOT) nanoparticles have been loaded with curcumin and piperine by *in situ* emulsion polymerization using dodecyl benzene sulfonic acid (DBSA) as both stabilizer and doping agent. The loaded drugs affect the morphology, size and colloidal stability of the nanoparticles. Furthermore, kinetics studies of non-stimulated drug release have evidenced that polymer-drug interactions are stronger for curcumin than for piperine. This observation suggests that drug delivery systems based on combination of the former drug with PEDOT are very appropriated to show an externally tailored release profile. This has been demonstrated by comparing the release profiles obtained in presence and absence of electrical stimulus. Results indicate that controlled and time-programmed release of curcumin is achieved in a physiological medium by applying a negative voltage of -1.25 V to loaded PEDOT nanoparticles.

Furthermore, electrospun poly(caprolactone) (PCL) microfibers loaded with poly(3,4-ethylenedioxythiophene) nanoparticles (PEDOT NPs) and curcumin with diameter of 3.9 ± 0.7 μm , have been prepared. PEDOT NPs, which are mainly located inside the PCL microfibers, exhibit a diameter of 99 ± 21 nm. PEDOT- and curcumin- containing PCL microfibers behave as extracellular cell matrices, facilitating cell spreading and enhancing cell proliferation because of their heterogeneity and roughness. The release of curcumin from the PCL microfibers by simple diffusion is very slow, external electric stimuli being required to boost and regulate the curcumin delivery process. PEDOT NPs behave as electro-actuators upon application of well-defined potential pulses, increasing their diameter by about 17%. This electro-mechanical actuation mechanism affects the structure of the PCL matrix, promoting the release of curcumin that increases with the number of pulses. Overall, PCL fibers loaded with electro-responsive PEDOT NPs represent a promising and valuable drug delivery system that can be regulated by using pulsatile electrical stimulation.

Publications derived from this work:

Puiggali-Jou, A.; Micheletti, P.; Estrany, F.; del Valle, L. J. and Alemán C. Electrostimulated release of neutral drugs from polythiophene nanoparticles: smart regulation of drug-polymer interactions. *Adv Healthc Mater.* **2017**, 6, 1-11.

Puiggali-Jou, A.; Cejudo, A.; del Valle, L. J. and Alemán C. Smart drug delivery from electrospun fibers through electro-responsive polymeric nanoparticles. *ACS Appl Bio Mater.* **2018**, 1, 1594-1605.

7.1 Introduction

Intrinsically conducting polymers (ICPs) allow excellent control of the electrical stimulus, possess very good electrical and optical properties, have a high conductivity/weight ratio and can be biocompatible, biodegradable and porous.¹⁻⁵ Furthermore, a great advantage of ICPs is that their properties can be tailored to the specific needs of their applications by incorporation of biopolymers, peptides, or other bio-related moieties.⁶⁻⁹

On the other hand, on-demand release of drug molecules from biomedical devices enables precise targeted dosing that can be temporally tuned to meet requirements for a variety of biomedical applications.¹⁰⁻¹² Recent advances have facilitated the use of different stimuli, such as light, magnetic and electric fields, ultrasounds and electrochemical signals, to trigger drug release from smart material formulations (*e.g.* films, micro- and nanoparticles, and implant devices).¹²⁻¹⁵ These technologies enable greater control over drug delivery compared to traditional systems that cannot be modified in response to changing therapeutic needs (*e.g.* systems based on biodegradability of polymers).

Electro-responsive drug-delivery systems are particularly attractive in this regard because electrical signals can be generated relatively easily, be accurately controlled and be remotely applied without using large, specialized and complex equipment. Moreover, it is possible to develop drug-delivery systems (DDSs) that allow repetitive dosing. In particular, recent *in vivo* assays have proved that ICPs nanoparticles (NPs) are successful electro-responsive drug delivery systems.¹⁶⁻¹⁸ Thus, the application of a small external electric field to these systems, which were subcutaneously localized by syringe injection at the place of interest, released the drug from the NPs, allowing its diffusion to the surroundings.

At present time, the existence of multiple methods to incorporate drugs into ICP matrices for their subsequent release indicates that these organic materials are potential platforms for controlled drug delivery.¹⁹ For example, molecules bound in ICPs films²⁰⁻²² through doping can be controllably expelled by applying a reducing electrical potential. Thus, the fact that they can be made porous and have delocalized charge carriers aids in

the diffusion of the bound molecules, adding a further reason why ICPs are very suitable for drug release applications.²³ Nevertheless, formulations based on ICPs thin films, which are the most frequent ones, present low drug loading as a major disadvantage.²⁴ Although more drug can be incorporated by increasing the thickness of the films, the majority of the release takes place at the surface while drug molecules at the bulk remain. Compared to films, ICP NPs have increased surface-to-volume ratio,²⁵ allowing higher drug loading. In spite of their small size, ICP NPs are electrically and electrochemically responsive, which is expected to be very advantageous for the design of controllable and programmable drug delivery systems. Considering the vast amount of possibilities, ICP NPs will undoubtedly play a decisive role in all disciplines of sciences that require programmed delivery of chemical compounds, including the biomedical field.

In some recent but still scarce studies, NPs of polypyrrole (PPy), which is probably the most studied non-toxic ICP,²⁶ has been used to trigger sensitive dosage-controlled release of drugs.^{16,27-30} More specifically, the response of PPy NPs embedded in a hydrogel against a dual stimulus (temperature and electric field) was demonstrated through *in vivo* experiments.¹⁶ Additionally, the on demand release of drugs with different polarities and molecular weights from electroresponsive PPy NPs has been evaluated.²⁷ The biocompatibility and linear response achieved with a repetitive and pulsed release evidenced that such approaches are facile and minimally invasive for potential medical applications.^{16,27} Besides, the pH-sensitive behavior of drug loaded PPy NPs has been also reported,²⁸ reflecting that the release can be controlled through the pH, the charge of the drug and/or the addition of charged amphiphiles.

Among ICPs, poly(3,4-ethylenedioxythiophene) (PEDOT) is probably the most employed for the fabrication of biomedical devices because of its outstanding capacitive performance, fast doping-undoping process, stable charge-discharge response, and high conductivity, biocompatibility and stability in continuous operation.³¹⁻⁴⁰ The structure, surface morphology and porosity of PEDOT and the above discussed PPy are completely different^{35,41,42} since the former is exclusively formed by α,α -linkages while the latter is highly crosslinked. Consequently, both the electrochemical and electrical responses of PEDOT are greatly superior to those of PPy. In spite of these advantages, the loading of

drugs into PEDOT NPs for release on demand remains practically unstudied. Paradee and Sirivat⁴³ examined the electrically-controlled release of benzoic acid loaded on PEDOT NPs blended with alginate hydrogels. More recently, Liu *et al.*⁴⁴ loaded 2-phenylethynylsulfonamide, which is a heat shock protein 70 inhibitor, into thermo-responsive poly(*N*-isopropylacrylamide) shells, incorporating PEDOT NPs as photothermal coupling agent.

7.2 Materials and methods

Materials and Cell line: 3,4-ethylenedioxythiophene (EDOT) monomer, sodium dodecylbenzene sulfonate (DBSA), ammonium persulfate (APS), curcumin (CUR), piperine (PIP), methyl thiazolyl tetrazolium (MTT), Tween-20 and Hoechst (bisBenzimide H 33258) were purchased from Sigma (USA). Cell lines PC3 (epithelial cells from human prostate adenocarcinoma) and MCF-7 (epithelial cells from human breast adenocarcinoma) were obtained from ECACC (European Collection of Cell Culture, UK). Culture media were purchased from BD Gibco: RPMI 1640 (Gibco, USA) supplemented with 10% fetal bovine serum (FBS), penicillin G (100 U/mL), and streptomycin (100 mg/mL). All cells were incubated at 37 °C with a humidified 5% CO₂ atmosphere.

Synthesis of PEDOT NPs: A 15 mL glass tube was filled with 4.5 mL of milli-Q water. After this, 0.0163 g DBSA were added and the solution was stirred for 1 hour at 750 rpm at room temperature. This was followed by the addition of 23.6 mg of EDOT monomer and, again, was allowed to stir for 1 hour at 750 rpm at room temperature. Finally, 91.2 mg of APS dissolved in 0.5 mL of milli-Q water was added to the mixture. The reaction was maintained in agitation at 40 °C overnight protected from light with aluminium foil. In this process, the colour of the reaction mixture changed from light grey to dark blue. No sedimentation was observed after the reaction, indicating a good colloidal stability. The side products and unreacted chemicals were removed by a sequence of 3 centrifugations at 11000 rpm for 40 min at 4 °C. The resulting supernatants were decanted and the pellet was re-dispersed in deionized water by using a vortex and a sonic

bath (15 min at room temperature). The last pellet was left under vacuum two days, then weighted and re-dispersed in the corresponding media at the desired concentration.

Synthesis of drug/PEDOT NPs: 0.0163 g of DBSA was added to a 15 mL tub filled with 3.99 mL of milli-Q water and the solution was stirred for 1h at 750 rpm at room temperature. After this, 23.6 mg of EDOT and 0.5 mL of drug solution (10 mg/mL in ethanol, EtOH) were added and the resulting solution was stirred at 750 rpm and room temperature during 1 h. Finally, 91.2 mg of APS dissolved in 0.5 mL of milli-Q water was added to the mixture. The reaction was protected from light (aluminium foil) and maintained in agitation at 40 °C overnight. The colour of the reaction mixture changed from light grey to dark blue. No sedimentation was observed after the reaction, indicating good colloidal stability. The side products, extra drug and unreacted chemicals were removed by a sequence of 3 centrifugations at 21000 rpm for 40 min at 4 °C. The resulting supernatants were decanted and the pellet was re-dispersed in deionized water by using a vortex and a sonic bath (15 min at room temperature). The last pellet was left under vacuum for two days, then weighted and re-dispersed in the corresponding media at the desired concentration.

Drug loading: The drug content was determined by re-suspending 5 µL of PEDOT NPs in 1 mL of ethanol (EtOH) 70%. The suspension was sonicated and vortexed for 10 min since the drug was quickly released in the alcoholic media. Then, the solution was centrifuged within a mini-centrifuge for 15 min at 2500 rpm. Finally, 200 µL of the supernatant were deposited on flat-bottomed 96 well-plates, where also a standard calibration (STC) curve was prepared with the corresponding drug in EtOH 70% and read at 425 nm for CUR and 350 nm for PIP. In order to determine the drug released during the dialysis or after the electrical stimuli the same procedure was followed, but changing the media for the STC to the adequate for each case (PBS with 0.5% Tween 20, or the same solution mixed with 10% EtOH or with 70% EtOH).

The drug loading ratio (DLR) of CUR and PIP were estimated using the following Eq.:

$$\text{DLR}(\%) = \frac{m_{drug}}{m_{drug} + m_{polymer}} \cdot 100 \quad (\text{Eq. 7.2.1})$$

where m_{drug} and $m_{polymer}$ are the mass of extracted drug and the mass of PEDOT NPs, respectively.

7.3 Electrostimulated release of neutral drugs from polythiophene nanoparticles: smart regulation of drug-polymer interactions

In this work two neutral and hydrophobic drugs have been loaded into PEDOT NPs (drug/PEDOT NPs) during their synthesis by emulsion polymerization in water. These drugs are CUR, which displays a wide spectrum of medical properties ranging from anti-bacterial, anti-viral, anti-protozoal, anti-fungal, and anti-inflammatory to anti-cancer activity,⁴⁵⁻⁴⁷ and PIP, a piperidine alkaloid with pharmacological properties as anti-inflammatory, antifertility and stimulator of serotonin synthesis in the central nervous system, among others.⁴⁹⁻⁵¹ The release of the drugs from the ICP NPs has been investigated without and with electrostimulation. Results have demonstrated that PEDOT NPs loaded with CUR serve as a drug reservoir for electric-field triggered release.

7.3.1 Methods

Scanning electron microscopy (SEM): SEM micrographs were obtained using a Focussed Ion Beam Zeiss Neon 40 scanning electron microscope operating at 10 kV. Samples were mounted on a double-side adhesive carbon disc and sputter-coated with a thin layer of carbon to prevent sample charging problems.

Atomic force microscopy (AFM): AFM was conducted to obtain topographic images of the nanoparticles surface using silicon TAP 150-G probe (Budget Sensors, Bulgaria) with a frequency of 150 kHz and a force constant of 5 N/m. Images were obtained with an Molecular Imaging PicoSPM microscope using a NanoScope IV controller under

ambient conditions in tapping mode. AFM measurements were performed on various parts of the samples, which produced reproducible images similar to those displayed in this work.

Dynamic light scattering (DLS): DLS studies were performed using NanoBrook Omni Zeta Potential Analyzer from Brookhaven Instruments. Measurement consisted of 3 runs each of 120 s duration, which were averaged to obtain the effective diameter (D_{eff}). Samples were analysed at 25 °C using a scattering angle of 90°. In order to know the Z-potential particles were re-suspended in 1 mM KCl solution and 30 consecutive measurements were taken of each sample.

Fourier transform infrared (FTIR) Spectroscopy: FTIR transmittance spectra were recorded on a FTIR Jasco 4100 spectrophotometer. Pellets were deposited on an attenuated total reflection accessory (Top-plate) with a diamond crystal (Specac model MKII Golden Gate Heated Single Reflection Diamond ATR). For each sample 64 scans were performed between 4000 and 600 cm^{-1} with a resolution of 4 cm^{-1} .

Dialysis: 1 mL of drug/PEDOT NPs (1 mg/mL) or free drug (0.1 mg/mL) were deposited into 3.5 kDa MW cut-off bags and immersed in 25 mL of PBS (pH 7.4) with 0.5 % (v/v) Tween-20 and kept in a shaker at 37 °C at 80 rpm. Each day 1 mL of the immersion solution was taken out to quantify the released drug and the whole solution was replaced by 10 mL of new media. After reaching the plateau of the drug release, the release medium was substituted by a PBS solution with 10 % EtOH and, finally, after reach again the plateau the medium was replaced by PBS with 70 % EtOH, allowing the complete drug release. All the results were normalized by the total amount of drug encapsulated within the NPs or used as a free molecule in order compare their kinetics.

Effects of voltage and time on drug release: Washed drug/PEDOT NPs were re-suspended in PBS at pH 7.4 to have a final concentration of 10 mg/mL. Then, 5 μL of the resulting solution were placed on a glassy carbon bar that acted as working electrode ($\phi=$

2 mm) and were dried under vacuum. A three electrodes configuration was used: the glassy carbon bar coated with the corresponding NPs as a working electrode (WE), a bar of glassy carbon as counter electrode (CE), and Ag|AgCl as reference electrode (RE). 1 mL of PBS with 0.5 % (v/v) Tween-20 was used as electrolytic medium. The appropriate voltage was applied for a particular period of time. After this, 100 μ L of the medium were kept to determine the drug concentration and substituted by new PBS 0.5 % (v/v) Tween-20. The absorbance was read at the maximum wavelength absorbance of each drug. To test the effect of voltage, 0.50 V, -0.50 V, -0.75 V, -1.00 V and -1.25 V were applied for 3 min. The influence of the time was evaluated by applying a voltage of -1.25 V during 30, 60, 180, 360 and 540 s. A control experiment was performed in the absence of the stimulus to compare the results. All the measures were repeated at least six times.

Cyclic voltammetry: Cyclic voltammetry (CV) studies were conducted with an Autolab PGSTAT302N galvanostat equipped with the ECD module (Ecochimie, The Netherlands). Measurements were performed on 2.5 or 5 μ L of 10 mg/mL NPs solution dried on a glassy carbon electrodes (GCE) of diameter = 2 mm or in 0.1 mg/mL of drug dissolved in PBS 1 \times (pH 7.4).

All electrochemical assays were performed using a three-electrode one compartment cell under a nitrogen atmosphere and at room temperature. The cell was filled with 10 mL of PBS 1 \times (pH 7.4) as a supporting electrolyte. Covered or bare GCE was used as the working electrode, platinum as the counter electrode, while an Ag|AgCl electrode containing KCl saturated aqueous solution was the reference electrode (offset potential versus the standard hydrogen electrode, $E^\circ = 0.222$ V at 25 $^\circ$ C). Oxidation-reduction cycles were registered within the potential range of -1.5 to +1 V at different scan rates (i.e. 10, 20, 40, 60, 80, 100, 200, 300 and 400 mV/s).

Cytotoxicity evaluation: In vitro cytotoxicity evaluation of DBSA, PEDOT NPs, free CUR and CUR/PEDOT NPs for PC3 and MCF-7 cell lines was determined by the MTT assay. Free CUR was dissolved in ethanol, the final concentration of ethanol in these samples being less than 10 %. All the other substances were prepared in PBS. Cells were

seeded at a density of 20×10^4 cells in 96-well plates and incubated overnight. Subsequently, the cells were exposed to a series of increasing DBSA, PEDOT NPs, free CUR and CUR/PEDOT NPs concentrations. Cells were incubated with the treatment for 24 h. Finally, the percentage of viable cells relative to untreated control was determined on the basis of the mitochondrial conversion of 3-(4,5-dimethylthiazol-2-yl)-2,5-diphenyltetrazolium bromide to formazan. The results were expressed as mean value \pm standard deviation (SD). All the experiments were performed in triplicate. Statistical comparison of values was based on a 2-way ANOVA using Tukey's test for pair-wise comparison with $p < 0.05$.

Cellular morphology evaluation: Cells morphology and CUR uptake were examined by epifluorescence microscopy (BA410 Model, Motic Spain S.L.). Cells were seeded at a density of 20×10^3 cells in 24-well plates coated with a round glass and incubated overnight. Later, the cells were exposed to a 50 $\mu\text{g}/\text{mL}$ of free CUR and CUR/PEDOT NPs and the equivalent of PEDOT NPs without CUR. Cells were incubated with the treatment for 24 h. Wells were cleaned three times with PBS, then fixed and permeabilized with an incubation of 5 min PBS with 70 % EtOH. Again, the wells were cleaned three times with PBS, stained with 0.5 $\mu\text{g}/\text{mL}$ for 1 h and washed three more times. The Hoechst fluorescence and the intrinsic fluorescence of CUR were detected with standard fluorescence filters sets: MF31000 filter (Exciter D350/50 \times and Emitter D460/50m) and a MF31001 filter (Exciter D480/30 \times and Emitter D535/40m), respectively.

7.3.2 Results and discussion

Although different approaches have been proposed to synthesize ICP NPs from their corresponding monomers combined with soft-templates,⁵²⁻⁵⁴ they have been criticized because of the poor control on both size and colloidal stability. Moreover, the difficulty of getting rid of the surfactant is added.⁵⁵ In a recent study, Zhou and coworkers prepared PEDOT NPs with a particle size distribution of 17.2 ± 1.6 nm applying a hydrothermal approach and using $\text{FeCl}_3 \cdot 6\text{H}_2\text{O}$ as oxidant and sodium dodecyl benzene sulfonate as

stabilizer.⁵⁶ In the present study, PEDOT NPs have been obtained in water at 40 °C using DBSA as stabilizer and doping agent simultaneously, and APS as oxidizing agent (**Figure 7.3.1a and b**). It is worth noting that the stabilizer is required to avoid the yielding of the ECP as an insoluble bulk powder with very limited processability.⁵⁷ D_{eff} of the resulting PEDOT NPs, which are displayed in **Figure 7.3.2c**, was 35 ± 6 and 84 ± 2 nm, as determined by SEM and DLS, respectively.

The two drugs, CUR and PIP (**Figure 7.3.1c**), considered in this work were loaded *in situ* during the emulsion polymerization. Due to their hydrophobicity, the drugs remained into the cores of the surfactant micelles rather than interacting with the medium. After polymerization, PEDOT NPs were formed and drugs were successfully loaded. The DLR, which was expressed as mass of encapsulated drug with respect to the total mass, was $5.9\pm 1.6\%$ and $8.0\pm 0.4\%$ for CUR and PIP, respectively, these values being similar to those achieved using other polymeric vesicles.⁵⁸ Moreover, the successful loading of the drugs within the PEDOT NPs was further confirmed by FTIR spectroscopy, discussed afterwards.

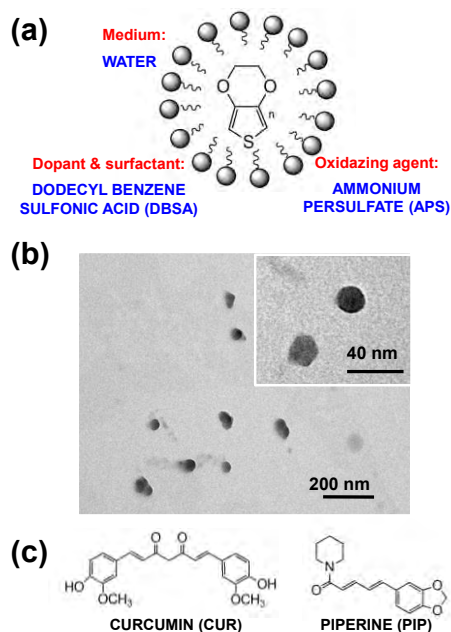


Figure 7.3.1 (a) Schematic representation of the chemical synthesis of PEDOT NPs by emulsion polymerization. (b) Transmission electron microscopy (TEM) micrographs of PEDOT NPs obtained using the procedure displayed in (a). (c) Chemical structure of CUR and PIP.

CUR- and PIP-loaded PEDOT NPs, hereafter denoted as CUR/PEDOT and PIP/PEDOT NPs, respectively, are spherical and stable in solution (**Figure 7.3.2**). Despite the CUR and PIP are neutral, hydrophobic and of similar size (*i.e.* 368.4 g/mol and 285.3 g/mol, respectively), the average D_{eff} of loaded NPs was found to be considerably affected by the drug, as observed by DLS measurements and SEM measurements. **Table 7.3.1** reflects that the CUR/PEDOT NPs are small and monodisperse (*i.e.* D_{eff} with low standard deviation), whereas PIP/PEDOT NPs are relatively large and polydisperse (*i.e.* D_{eff} with high standard deviations). The yielded NPs and their corresponding aggregates successfully remained below 4 μm , which is the smallest diameter of human blood capillaries,⁵⁹ and thus avoiding the blockage of blood vessels or the possibility of being eliminated by the body reticuloendothelial system.

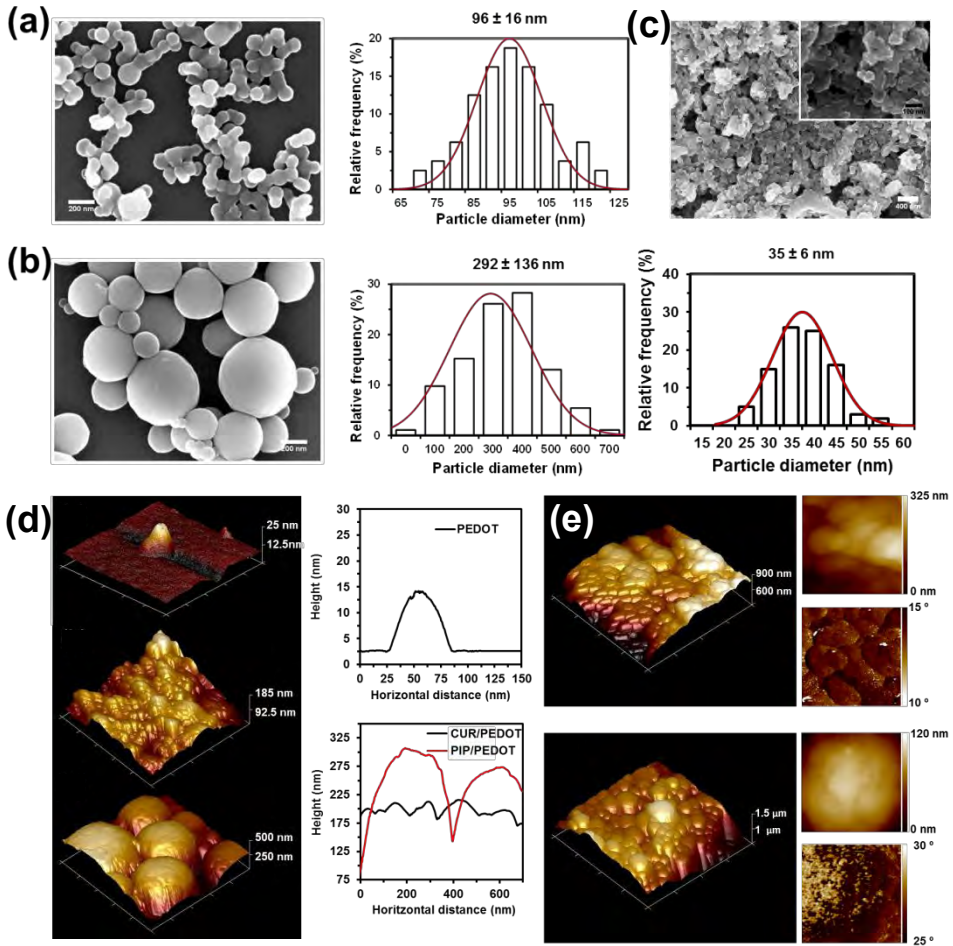


Figure 7.3.2 SEM images of (a) CUR/PEDOT NPs, (b) PIP/PEDOT NPs, (c) PEDOT NPs (Scale bar: 200 nm). Effective diameter histograms derived from SEM measurements and average values are also displayed. (d) AFM images ($1 \times 1 \mu\text{m}^2$) of (top) PEDOT, (middle) CUR/PEDOT and (bottom) PIP/PEDOT NPs. The graphs displayed in panels corresponds to the profile of the selected particles. (e) AFM images of (top) CUR/PEDOT and (bottom) PIP/PEDOT NPs: 3D height images $2 \times 2 \mu\text{m}^2$ (right column), 2D height images (left top) and 2D phase images (left bottom) $250 \times 250 \text{ nm}^2$.

SEM and DLS observations are corroborated by the AFM images displayed in **Figure 7.3.2d** and **e**, which reflect remarkable differences among PEDOT, CUR/PEDOT and PIP/PEDOT NPs. Thus, PEDOT NPs remained stable and very small while CUR/PEDOT and, especially, PIP/PEDOT exhibited higher size and tendency to aggregate.

Table 7.3.1 Effective diameter (D_{eff}) determined by SEM and DLS, drug loading ratio (DLR) and ζ -potential of unloaded-PEDOT, CUR/PEDOT and PIP/PEDOT NPs.

	D_{eff} (nm) SEM	D_{eff} (nm) DLS	DLR (%)	ζ -potential (mV)
PEDOT	35±6	84±2	-	-29.4±3.6
CUR/PEDOT	96±16	207±3	5.9±1.6	-26.5±5.1
PIP/PEDOT	292±132	304±17	8.0±0.4	-18.7±3.0

The size increment is probably due to the extremely low aqueous solubility of the two drugs, which promotes the formation of relatively large molecular cores inside PEDOT NPs. The tendency to aggregate is corroborated by the zeta- (ζ -) potential, which varies as follows: PEDOT < CUR/PEDOT < PIP/PEDOT (**Table 7.3.1**). The physical stability of an aqueous dispersion is considered to be good when the absolute value of the ζ -potential is around 30.⁶⁰⁻⁶¹ Therefore, the colloidal stability of CUR/PEDOT and PIP/PEDOT NPs (ζ -potential of -26.5±5.1 and -18.7±3.0 mV, respectively) is lower than that of PEDOT NPs (-29.4±3.6 mV).

FTIR spectroscopy has been used to determine the chemical structure of the functional groups on the surface of PEDOT NPs. **Figure 7.3.3** displays the FTIR spectra recorded for drugs, PEDOT NPs and drug/PEDOT NPs. PEDOT NPs doped with DBSA exhibit the main absorption peaks from the thiophene, ether and sulfonate groups: stretching modes of C=C in the thiophene ring at 1647 and 1557 cm^{-1} , CH_2 stretching modes at 1478, 1396 and 750 cm^{-1} , C–O–C vibrations at 1206 and 1057 cm^{-1} , and the S–O stretch at 667 cm^{-1} .

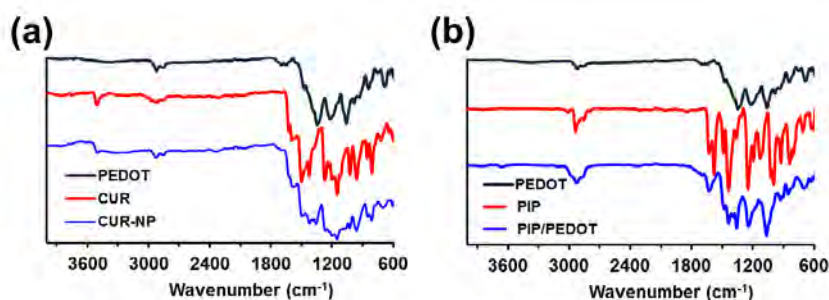


Figure 7.3.3 FTIR spectra of (a) PEDOT NPs, CUR and CUR/PEDOT NPs; and (b) PEDOT NPs, PIP and PIP/PEDOT NPs.

The addition of drugs during the polymerization process did not affect the localization of PEDOT bands; instead, the bands associated to the individual drugs were appreciated proving their incorporation. The two main characteristic C=O stretching bands at 1626 and 1535 cm^{-1} and the enol C–O peak at 1267 cm^{-1} observed for CUR alone are also detected in CUR/PEDOT NPs (**Figure 7.3.3a**). Similarly, the very broad band at 3293 cm^{-1} and the sharp peak at 3508 cm^{-1} indicate the presence of OH, whereas the peaks at 959 and 713 cm^{-1} have been attributed to the benzoate *trans*- and *cis*-CH vibrations, respectively. Finally, the FTIR spectrum of free PIP (**Figure 7.3.3b**) clearly shows the characteristic C=O stretching peaks at 1628 and 1545 cm^{-1} , which are preserved in PIP/PEDOT NPs.

Dialysis bags with a molecular weight cut-off of 3500 KDa were used to understand the kinetics of the non-stimulated drug release in different media (**Figure 7.3.4**). In order to achieve a complete CUR and PIP release, three different environments with increasing affinity for the drug were examined: PBS with 0.5% Tween 20 (which is a surfactant that helps the dissolution of the drug), and the same solution mixed with 10% EtOH and with 70% EtOH. Comparison of the released amount of drug from drug/PEDOT NPs with their respective controls (*i.e.* drugs alone) allows to visualize a different behaviour for CUR and PIP when interact with PEDOT. More specifically, the release of CUR from CUR/PEDOT NPs was much slower than that of PIP from

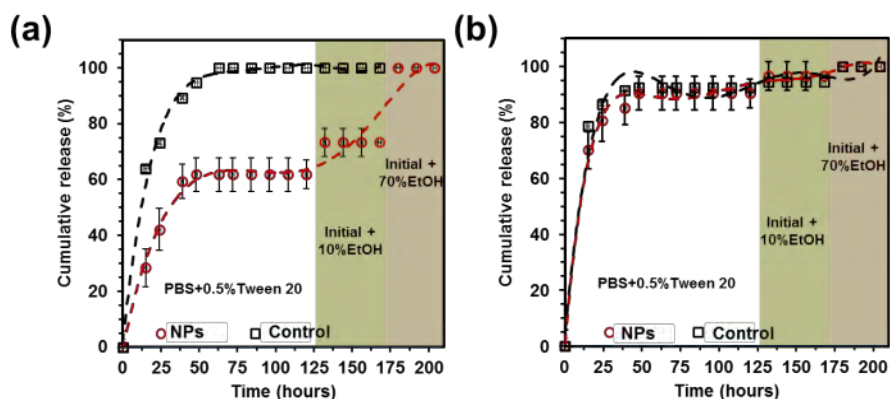


Figure 7.3.4 Cumulative drug release comparison between drug/PEDOT NPs and free drug (control) dispersed in aqueous solutions and dialysed against PBS+0.5% Tween 20, the previous PBS solution with 10% EtOH, and with 70% EtOH: (a) CUR and (b) PIP.

PIP/PEDOT NPs with respect to their corresponding controls. These results reflect a relatively strong interaction between CUR and PEDOT, making difficult the release of the

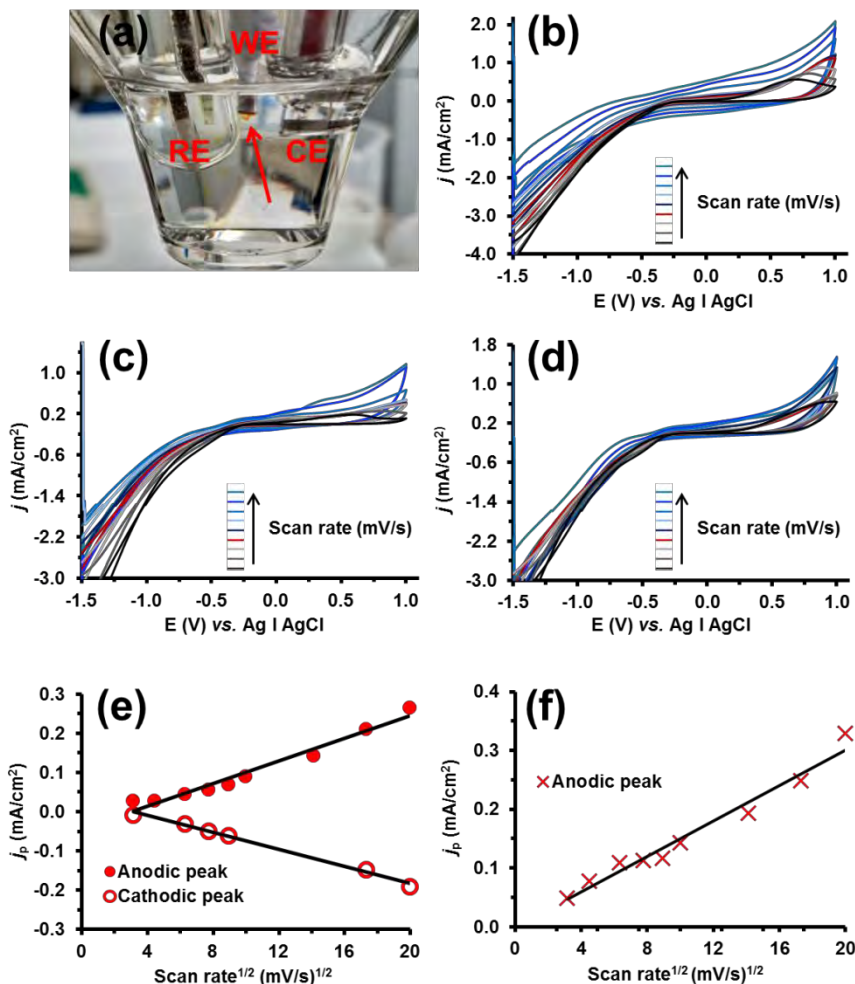


Figure 7.3.5 (a) Camera image of the three electrodes set-up for the electrochemical characterization of unloaded PEDOT and drug/PEDOT NPs. The red arrow points out released CUR in experiments with CUR/PEDOT NPs. WE, CE and RE refer to the working electrode, the counter electrode and the reference electrode, respectively. Cyclic voltammograms for (b) unloaded PEDOT NPs, (c) CUR/PEDOT NPs and (d) PIP/PEDOT NPs recorded from -1.5 to 1.0 V at different varying scan rates (10, 20, 40, 60, 80, 100, 200, 300 and 400 mV/s) using PBS $1\times$ (pH 7.4) as electrolyte medium. Variation of the current density (j_p) at the anodic and cathodic peaks (e) of CUR and at the anodic peak (f) of PIP against the square root of the scan rate.

drug from the NPs until an environment with a high alcoholic content is used (**Figure 7.3.4a**). Instead, the release of PIP from the NPs was very similar to that of the control, indicating a simple diffusion phenomenon motivated by the poor affinity between the drug and the ICP. This feature is confirmed by the almost imperceptible effect of the increment of EtOH in the release medium (**Figure 7.3.4b**). The divergent behaviour of CUR/PEDOT and PIP/PEDOT should be attributed to the different hydrogen bonding abilities of the two drugs. Thus, CUR...PEDOT hydrogen bonds are expected to be formed between the hydroxyl groups of CUR (**Figure 7.3.1c**) and the dioxane rings of PEDOT. It should be noted that this kind of specific interactions were found to play a crucial role in DNA...PEDOT interactions,⁶² which are highly dependent on the DNA sequence. In contrast, the absence of groups able to act as hydrogen bonding donors in PIP precludes the formation of PIP...PEDOT hydrogen bonding interactions. Overall, these results suggest that CUR/PEDOT NPs are promising candidates to behave as electrically responsive drug delivery systems.

Before of the electrostimulation studies, the electrochemical response of CUR, PIP, and both PEDOT and drug/PEDOT NPs was examined by cyclic voltammetry (CV), registering oxidation–reduction cycles within the potential range of -1.5 to +1 V at different scan rates. **Figure 7.3.5a** (left) displays a photograph of the three electrode configuration when cyclic voltammetry was recorded from CUR/PEDOT NPs deposited on GCE. Interestingly, it was possible to visualize the release of CUR from the NPs when low scan rates were employed.

CVs recorded for CUR and PIP are displayed in **Figure 7.3.6a** and **b**, respectively. Since CUR molecule contains two hydroxyl groups a conjugation effect can occur from the electron cloud deviation. As can be it seen CUR exhibits one well defined anodic peak at a potential of $\sim +0.4$ V and a less defined cathodic peak at ~ -0.10 V (**Figure 7.3.6a**), which are similar to that previously observed elsewhere.^{64,65} These quasi-reversible peaks have been attributed to the product of the irreversible oxidation reaction, which can be adsorbed onto the electrode surface. The intensity of the peaks increases in absolute value with the scan rate and, in addition, the peaks potential shift slightly indicating that

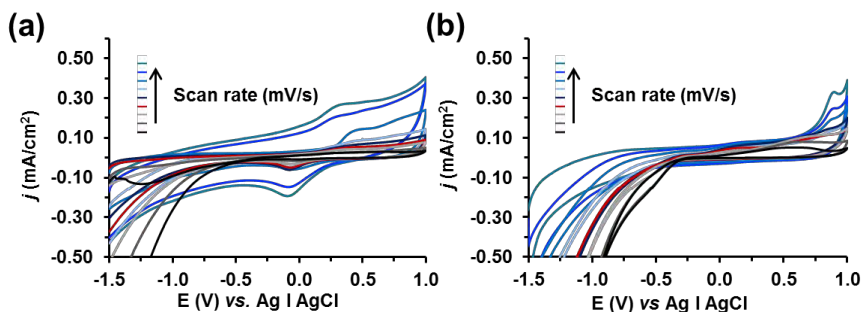


Figure 7.3.6 CV of (a) CUR and (b) PIP in PBS 1 \times (pH = 7.4). Initial and final potential: -1.5 V; reversal potential: 1.0 V. Scan rates: 10, 20, 40, 60, 80, 100, 200, 300 and 400 mV/s.

they correspond to a quasi-reversible redox process.⁶⁶ Instead, the voltammograms recorded for PIP exhibit two irreversible anodic peaks at 0.12 V and 0.92 V.

CVs of PEDOT, CUR/PEDOT and PIP/PEDOT NPs adsorbed onto glassy carbon electrodes are compared in **Figure 7.3.5b-d**. The current density increases proportionally with the scan rate suggesting that the electrochemical process depends on the diffusion.⁶⁷ Moreover, detailed inspection of the voltammograms recorded for CUR/PEDOT NPs allows identification of the CUR anodic peak at a potential between 0.4 and 0.5 V, depending on the scan rate. **Figure 7.3.5e** plots the current density at the anodic and cathodic peaks (j_p) of CUR against the square root of the scan rate, while **Figure 7.3.5f** represents the same graphic for the irreversible anodic process of PIP at 0.92 V. A linear behavior is observed in all cases. Moreover, in the case of CUR the slope was slightly higher for the anodic process than for the cathodic one. These results confirm the dependence of electrode reaction on the diffusion, which is the mass transport rate of the electroactive species to the surface of the electrode across a concentration gradient.

Experiments with electrostimulation were performed using a conventional three-electrode setup, similar to that displayed in **Figure 7.3.5a**, with glassy carbon coated with drug/PEDOT NPs as WE, bare glassy carbon as CE, and Ag|AgCl as RE. To investigate the effect of the voltage on the release of CUR and PIP from drug/PEDOT NPs, different voltages (*i.e.* 0.50 V, -0.50 V, -1.00 V and -1.25 V) were applied during 3 min. Results have been compared with control experiments, which were performed in

absence of electric voltage (hereafter denoted 0.00 V). In order to mimic a physiological medium, electrically stimulated drug release experiments were performed using PBS with 0.5 % (v/v) Tween 20 at pH 7.4 as electrolyte medium.

Results found for CUR and PIP, which are displayed in **Figures 7.3.7a** and **c**, respectively, demonstrate completely different behaviours. The percentage of released CUR with respect to the amount of encapsulated CUR was lower than 5% when the applied voltage was 0.50 V or in absence of stimulus, while increased progressively and linearly with the more negative voltage. Thus, the stimulation with -1.25 V for 3 min resulted in a CUR delivery of 38%. In the case of PIP/PEDOT NPs, the amount of released drug in absence of stimulus is 10%, increasing to 18% and 23% when the applied voltage is -0.50 and 0.50 V, respectively. No systematic behaviour was identified in the case of PIP (**Figures 7.3.7b**), indicating that the release of this drug cannot be controlled and programmed through electrostimulation.

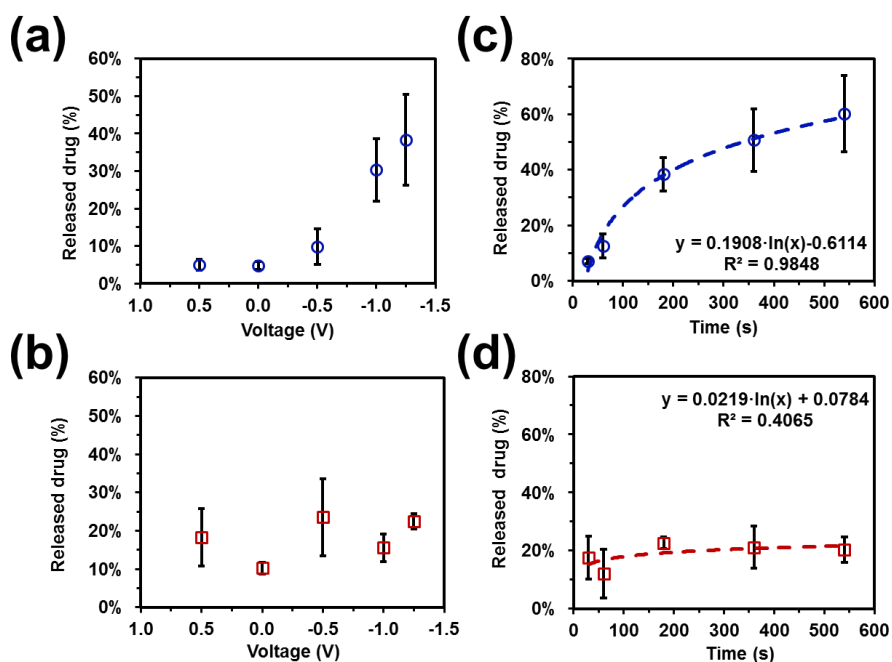


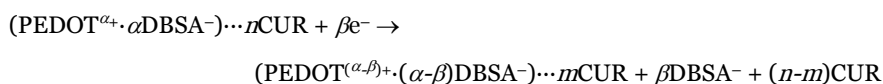
Figure 7.3.7 Effect of (a,b) voltage with time constant (3 min) and (c,d) of time with voltage constant (-1.25 V) on drug release for drug/PEDOT NPs: (a,c) CUR and (b,d) PIP ($n = 6$). The percentage of released drug is expressed with respect to the total amount of loaded drug.

Figures 7.3.7c and **d** display the release of CUR and PIP, respectively, from drug/PEDOT NPs with time. Results from these experiments, which were performed using a fixed voltage of -1.25 V, are consistent with those reported in **Figures 7.3.7a** and **b**, indicating that controlled release by electrical stimulation can be efficiently achieved only for CUR. Thus, although 7% of CUR is released after 30 s only, the amount of released drug increases logarithmically with time. In the time interval compressed between 3 and 9 min, the release grows from 38% to 60%. Also, complementary assays showed that the CUR release stops when the voltage is tuned off, proving that this is a regulated process. These results reflect that the controlled CUR release can be achieved with both time and applied potential (**Figures 7.3.7c** and **a**, respectively). Release profiles were reproducible not only with as fresh samples but also with suspensions that were stored for even one month before the release assays. The variation of PIP release with time is practically null (*i.e.* 20% after both 3 and 9 min), corroborating that the poor interactions between such drug and the ICP preclude the applicability of PIP/PEDOT NPs as dosage-controlled drug delivery vehicles.

Previous studies suggested that the take-up and rate delivery of drugs may depend on the structure, composition and oxidation state of the ICP.²⁴ In the particular case of the release of charged drugs by electrical stimulation, the main factor is the oxidation state since the driving force of this process is the apparition of repulsive drug...ICP electrostatic interactions. Thus, the oxidation and reduction of the ICP cause the release of cationic and anionic drugs, respectively.²⁴ However, CUR and PIP are neutral drugs at pH= 7 and, therefore, their electrically stimulated release is expected to be controlled by a more complex mechanism. Unfortunately, designs allowing for the controlled release of neutral drugs are very scarce. Langer and co-workers⁶⁷ used biotin-doped PPy to load biotinylated nerve growth factor (NGF) at the biotin binding sites found at the polymer surface. Reduction of the PPy film resulted in an electrically triggered NGF release, which remained biologically active. On the other hand, N-methylphenphthiazine (NMP) loaded into PPy doped with anionic β -cyclodextrins was released when oxidized, which caused the formation of positive charges on both the ICP and NMP.⁶⁹

The mechanism proposed in this work for the electrically stimulated release of CUR is based on the effect of the voltage on the oxidation state of the ICP and, therefore, on

PEDOT...CUR interactions. The release of CUR is not stimulated by the application of the positive voltage (+0.50 V), which enhances the positive oxidation state of the polymer (**Figure 7.3.6**) while the oxidation of the drug starts at around such potential (**Figure 7.3.6**). In contrast, the CUR release becomes electrostimulated upon the application of negative voltages, which induce the electrochemical de-doping (reduction) of PEDOT NPs. Thus, the fraction of reduced PEDOT sites over the number of total active sites (*i.e.* where electrons are exchanged) increases with the negative voltage, polymer chains being expected to be completely, or almost completely, reduced (*i.e.* de-doped – with neutral charge) at the voltage of -1.25 V.⁶⁷ It was observed that lower voltages caused mechanical and electrochemical degradation of the ICP NPs. The de-doping of the ICP affects the intermolecular interactions with the drug, hydrogen bonds being significantly weaker when PEDOT chains are in the neutral state than in the oxidized state.⁷⁰ Accordingly, the mechanism for the electrostimulated CUR release from CUR/PEDOT NPs can be summarized by the following Eq.:



where $n\text{CUR}$ refers to the drug molecules hydrogen bonded to the oxidized polymeric NPs, $m\text{CUR}$ corresponds to the drug molecules that remain hydrogen bonded to the polymeric NPs after pump β electrons into the system by electrical stimulation, and $\alpha+$ and $(\alpha-\beta)+$ are the oxidation states of oxidized and reduced PEDOT, respectively (*i.e.* when PEDOT is completely reduced, $\alpha=\beta$, the charge of the ICP is zero).

The release mechanism proposed in this work for neutral drugs able to form specific interactions with the ICP matrix resembles that typically reported when negatively charged drugs act as dopant ions.^{41,42} Unfortunately, this mechanism does not apply to PIP/PEDOT NPs because of the lack of hydrogen bonding donors in the drug. Accordingly, PIP molecules are rapidly released by through the walls of the polymeric NPs, such diffusion process being independent of the presence or not of external stimuli. Thus, although the application of an electric voltage affects the oxidation state of PEDOT chains, it does not improve the control in the release that is determined by the intrinsically weak dispersion interactions between PIP molecules and the aromatic rings

of the ICP. In order to overcome the limitations associated to the instability in the light, poor oral bio-availability *in vivo* and lack of solubility in aqueous solvents of CUR, the use of micro- and nanoparticles made of polymer materials, as for example poly(lactic-*co*-glycolic acid), as carriers has been extensively explored.⁴¹⁻⁷³ Although polymeric micro- and nanoparticles provided biocompatibility, in some cases also biodegradable, platforms for sustained release of CUR with improved bio-availability, several disadvantages were detected. The most important one, which is the effective control during the release, has been overcome in this work applying a controlled voltage to electrodes coated with CUR/PEDOT NPs, achieving a programmed CUR release. The biocompatibility and cytotoxicity of such system is an important characteristic to be analyzed for further biological applications. PEDOT NPs and the surfactant (DBSA) alone were tested in epithelial-like prostate and breast adenocarcinoma cells lines from human (PC3 and MCF-7, respectively) using the MTT assay measured after 24 h post-treatment (**Figure 7.3.8a**). PEDOT NPs do not exhibit any toxic effect until they are used at high concentration. Moreover, it is clearly demonstrated that, after the 3 washing steps, the quantity of dopant is lower than 6 $\mu\text{g}/\text{mL}$, when DBSA starts to be toxic. The cytotoxicity of free CUR and CUR/PEDOT NPs, which was evaluated at 24 h post-treatment using the same cell lines, reflects significant concentration dependence (**Figure 7.3.8b**). Significant differences are observed in the behaviour of the two systems, free CUR being considerably more toxic than CUR/PEDOT NPs. More specifically, for PC3 the half-maximal inhibitory concentration (IC_{50}) of the former and the latter is around 20 and 100 $\mu\text{g}/\text{mL}$, respectively, while for MCF-7 both are around 10 $\mu\text{g}/\text{mL}$. These results, combined with the fact that the drug loaded inside the NPs is only partially released in absence of external stimuli, corroborate that PEDOT nanostructures formed by emulsion polymerization is a very interesting electroactive vehicle for the controlled delivery of neutral drugs having groups able to interact with hydrogen bonds.

In order to explore the mechanisms of cytotoxicity, the cellular uptake of free CUR and CUR/PEDOT NPs on PC3 and MCF-7 cells was observed by fluorescence microscopy. **Figure 7.3.9** shows the images of non-treated cells, PEDOT NPs treated, free CUR treated and CUR/PEDOT treated for 24 h. Medium without treatment drug was regarded as control, as well as, the PEDOT NPs treated group. Both groups did not present any fluorescence at any point and there was not any diminish in cell nucleus

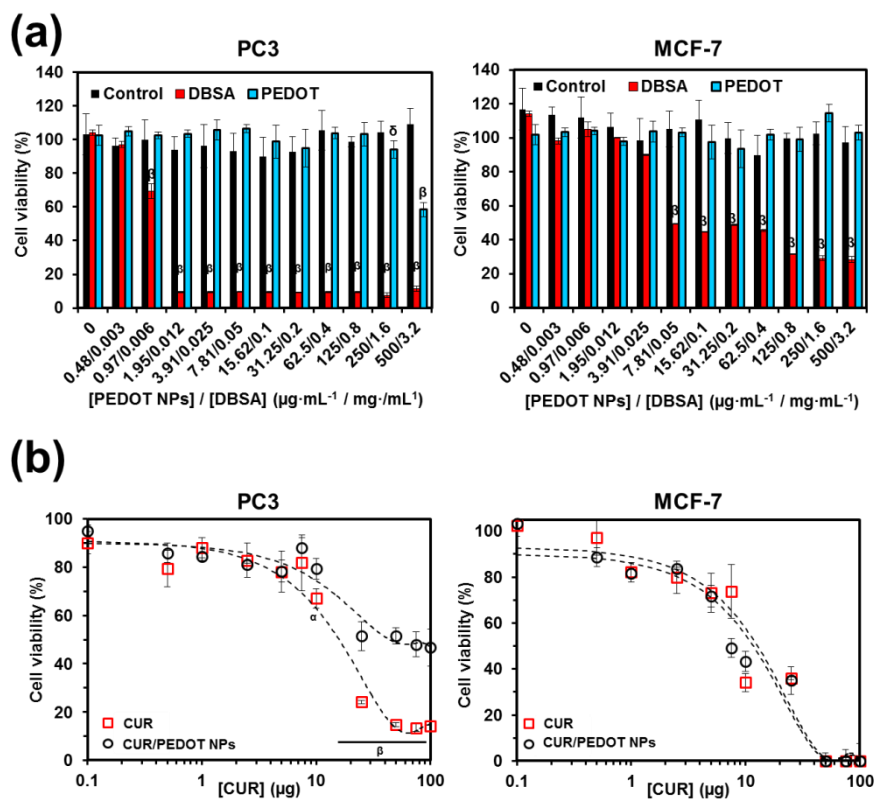


Figure 7.3.8 (a) Cytotoxicity studies of PEDOT NPs and DBSA on PC3 and MCF-7 cells for 24 h. Although they are represented in the same graphic, assays with PEDOT NPs and DBSA were performed independently. (b) Cytotoxicity evaluation of CUR and CUR/PEDOT NPs on PC3 and MCF-7 cells for 24 h. Values are the mean of 3 samples and bars indicate their standard deviation. Greek letters on the columns/points refer to significant differences when the 2-way ANOVA and Tukey's multiple comparisons test are applied: α , δ , β indicate significant differences observed within the specific concentration group with p -values lower than 0.05, 0.001 and 0.0001, respectively.

number. In contrast, an intense fluorescence was observed at the cell cytosol after 24 h for free CUR and CUR/PEDOT NPs. In addition, the two groups exhibited lower number of cell nuclei than before the treatment had been executed. Besides, different cellular morphologies were observed: cells treated with free CUR presented more rounded bodies, denoted by high circularity (**Figure 7.3.9c**), than cells treated with CUR/PEDOT. These results suggest that cells were more affected by free CUR than when

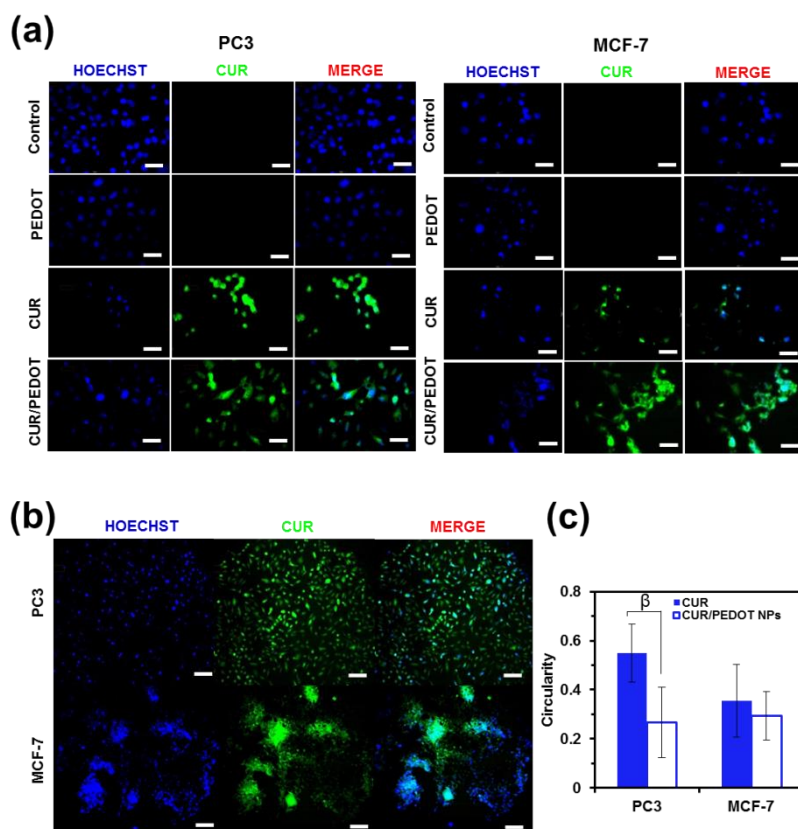


Figure 7.3.9 (a) High magnification fluorescent images of PC3 and MCF-7 cells incubated with nothing (control), PEDOT NPs, CUR and CUR/PEDOT NPs for 24 h. Scale bars represent 40 μm . (b) Low magnification cell images of PC3 and MCF-7 incubated with CUR/PEDOT NPs for 24 h. Scale bars represent 100 μm . For each panel, the images from left to right showed cell nuclei stained by Hoechst (blue), CUR fluorescence (green) and overlays of both images. (c) Cell circularity assessed by ImageJ software. β indicates significant differences with a p-value lower than 0.0001 when a t-test is performed.

it is encapsulated within the PEDOT NPs, again indicating that the complete effect of the drug would not be achieved until it is stimulated.

Overall, results obtained in this paper indicate that CUR/PEDOT NPs can be considered as potential controlled release systems for therapeutic applications based on the anti-bacterial, anti-viral, anti-protozoal, anti-inflammatory or anti-cancer activity of CUR. This system allows a given dosage at desired periodical time by applying a harmless external voltage of only -1.25 V (*i.e.* from a conventional small battery). Moreover, after its optimization to reduce a little bit more the required voltage, one could envision advanced biomedical applications of the CUR/PEDOT NPs system using the weak electric fields naturally occurring in the body for stimulation (*e.g.* the intrinsic electric fields of cardiovascular and neuronal tissues).

7.3.3 Conclusions

Encapsulation of CUR and PIP in PEDOT NPs was achieved by *in situ* emulsion polymerization using DBSA as stabilizer and doping agent. The release behaviour of these two neutral drugs, which only differ in their capacity to form hydrogen bonding interactions with the oxidized polymer chains, was very different in absence and in presence of external electrostimulation. The release of CUR is controlled through the strength of such specific drug...ICP interactions, which become weaker when polymer chains are reduced applying an external negative voltage. Therefore, CUR/PEDOT NPs are a promising combination that efficiently controls the release of the drug through external stimuli. This methodology, which can be extrapolated to other neutral drugs with similar hydrogen bonding abilities, may be a potential strategy for treatments based on the programmed dosage of CUR that, among many other medicinal properties, have demonstrated efficacy as anticancer agent for many types of malignancies, including colorectal, breast, lung, prostate, and pancreatic carcinoma.⁴⁸

7.4 Smart drug delivery from electrospun fibers through electro-responsive polymeric nanoparticles

Smart electrosensitive drug delivery systems have attracted much attention in recent years because the drug release rate can be easily controlled simply by modulating the electric field. Different approaches have been developed to confer response to electrostimulation and tune the drug release. For example, biocompatible electroconductive hydrogels have been designed to mimic the redox switching and electrical properties of intrinsically conducting polymers (ICPs), facilitating the drug release.^{4,74-76} Besides, hydrogels made of polyelectrolyte networks have been used in combination with electric fields to produce a force on counterions and immobile charged groups in the network and attract mobile ions, facilitating drug release through local swelling and shrinking of the hydrogel.^{77,78}

A very different approach is based on the use of electrosensitive nanoparticles (NPs) for drug release. Within this context, recent studies have shown that some NPs made of ICPs exhibit successful response as electrically controllable drug delivery systems. Ge *et al.*¹⁶ controlled the release of therapeutic pharmaceuticals loaded into polypyrrole (PPy) NPs through the application of a weak external direct current electric field. Willner and coworkers⁷⁹ introduced imprinted bis-aniline-cross-linked gold NPs as electro-triggered sponges for the uptake and release of π -acceptor species. In 2017, Hosseini-Nassab *et al.*¹⁷ showed that insulin can be released from PPy NPs by electrostimulation. In a very recent work⁸⁰ we used poly(3,4-ethylenedioxythiophene) (PEDOT in **Figure 7.4.1a**), which is a noncytotoxic and biocompatible ICP,^{34,81} to synthesize NPs loaded with curcumin (CUR in **Figure 7.4.1a**), a drug with antibacterial, antiviral, antifungal and anticancer activities,^{45,46,88,48} by in situ emulsion polymerization. PEDOT exhibits important advantages with respect to other ICPs, as for example PPy, because of its great environmental stability, electrical conductivity, electrochemical activity, thermoelectric behavior and high specific capacitance.^{32,83,35} Application of a selected voltage to loaded PEDOT NPs resulted in an electrically triggered CUR release, evidencing that this system is very promising for treatments based on the programmed dosage of CUR.⁸⁰

Although NPs offer important advantages (*e.g.* facilitate the loading of therapeutic agents and increase their stability),⁸⁴ some limitations that are in detriment of their use as nanocarriers are also frequently found. The most important one is related with their tendency to aggregate in physiological environment, thus causing loss of basic NP characteristics and properties.⁸⁵ Accumulation by agglomeration often makes difficult the release of the drug, even in presence of external stimulus. A strategy to prevent this undesired effect could be the dispersion of NPs into electrospun microfibers (MFs). Thus, electrospinning has been recognized as a simple and versatile method for the fabrication of polymer MF mats, which can act not only supporting the dispersed NPs but also enhancing the biocompatibility of the whole system if the appropriated polymer is chosen.⁸⁶⁻⁸⁸ Unfortunately, keeping the drug inside already loaded NPs during the electrospinning process is a very difficult task, since the operational potential is very high and the drug is easily extracted from the NPs during the processing step. Accordingly, the drug and the NPs should be loaded separately in electrospun MFs.

In this work we have designed and prepared by electrospinning a new electrosensitive bioplatfrom that combines CUR, PEDOT NPs and poly(ϵ -caprolactone) (PCL in **Figure 7.4.1a**). The latter aliphatic polyester has attracted an increasing interest in recent decades due to its biodegradability and suitability for tissue engineering applications.⁸⁹⁻⁹³ For biomedical applications, PCL has been approved for use by the USA Food and Drug Administration (FDA) since the seventies and can be found in many common sutures and suture components. PCL, like other members of this family of polymers, such as poly(L-lactide) and poly(lactide-*co*-glycolide), undergoes auto-catalyzed bulk hydrolysis, even though due to its semicrystalline nature the total loss of mass extends over two years. On the other hand, ICPs, such as PPy and polythiophene derivatives, behave as linear actuators. The actuation principle of ICP films is based on the motion of ions in and out of the film during oxidation and reduction, respectively, which cause expansion and contraction movements.^{94,95} Moreover, longitudinal expansion and contraction have been identified for ICP MFs in aqueous electrolytic solutions, proving their ability to transform electrochemical energy into linear mechanical energy.^{96,97} The electrosensitive bioplatfrom prepared and discussed in this study takes advantage of the above

mentioned principles. More specifically, the release of CUR from PCL MFs has been induced by changing the volume of PEDOT NPs, which behave as isotropic actuators upon electrostimulation.

7.4.1 Methods

Materials. 3,4-Ethylenedioxythiophene (EDOT) monomer, sodium dodecylbenzene sulfonate (DBSA), ammonium persulfate (APS) and CUR were purchased from Sigma (USA).

Electrospinning: Mixtures of [PCL, PEDOT NPs and CUR], [PCL and PEDOT] and of [PCL and CUR] were electrospun, samples being named PCL/PEDOT/CUR, PCL/PEDOT and PCL/CUR. Mixtures were prepared as follows. PCL (5.5 g) was dissolved in 32 mL of a mixture of chloroform and acetone 2:1 (v/v). The solutions were kept in 37 °C for 24 h under stirring at 100 rpm. PEDOT NPs (10 mg/mL) and CUR (1.04 mg/mL) were dispersed and dissolved, respectively, in 0.5 mL of ethanol (EtOH). Finally, 0.2 mL of PEDOT NPs, CUR or PEDOT NPs and CUR solutions were mixed with 1.8 mL of PCL solution and loaded in a 5 mL BD plastic syringe for delivery through an 18G × 1.1/2" needle at a mass-flow rate of 10 mL/h using a KDS100 infusion pump. The content of PCL, PEDOT NPs and CUR in the optimized electrospinning mixtures, unless other conditions are explicitly specified, was: (i) 15.45% (w/v) of PCL, 0.6 wt% of PEDOT NPs and 0.06 wt% CUR for PCL/PEDOT/CUR MFs; (ii) 15.45% (w/v) of PCL and 0.6 wt% of PEDOT for PCL/PEDOT MFs; (iii) and 15.45% (w/v) of PCL and 0.06 wt% of CUR for PCL/CUR MFs. As a control, fibers of pure PCL were produced using a 17.18% (w/v) concentration of polymer in 2:1 chloroform:acetone. It should be mentioned the choice of the processing conditions (i.e. distance between the syringe tip and the collector, voltage and the flow rate) were selected on the basis of preliminary experiments devoted to optimize the morphology of the MFs. Thus, appropriate selection of the processing conditions is required to avoid the formation of droplets and electrospun beads. Specifically, electrospun MFs discussed in the work were obtained by applying a voltage was 15 kV and using a needle tip-collector distance of 15 cm.

Dynamic light scattering (DLS): studies on PEDOT NPs were performed using NanoBrook Omni Zeta Potential Analyzer from Brookhaven Instruments. Measurement consisted of 3 runs each of 60 s duration, which were averaged to obtain the effective diameter. Samples were analyzed at 25 °C using a scattering angle of 90°.

Fourier-transform infrared (FTIR): transmittance spectra of PEDOT NPs were recorded on a FTIR Jasco 4100 spectrophotometer. Pellets were deposited on an attenuated total reflection accessory (Top-plate) with a diamond crystal (Specac model MKII Golden Gate Heated Single Reflection Diamond ATR). For each sample 32 scans were performed between 4000 and 600 cm^{-1} with a resolution of 4 cm^{-1} .

Micro-Raman spectroscopy: using a commercial Renishaw inVia Qontor confocal Raman microscope. The Raman setup consisted of a laser (at 785 nm with a nominal 300 mW output power) directed through a microscope (specially adapted Leica DM2700 M microscope) to the sample, after which the scattered light is collected and directed to a spectrometer with a 1200 $\text{lines}\cdot\text{mm}^{-1}$ grating. The exposure time was 10 s, the laser power was adjusted to 0.001-0.05% of its nominal output power depending on the sample, and each spectrum was collected with five accumulations.

UV-vis spectra: were carried out in a UV-vis-NIR Shimadzu 3600 spectrophotometer equipped with a tungsten halogen visible source, a deuterium arc UV source, a photomultiplier tube UV-vis detector, and an InGaAs photodiode and cooled PbS photocell NIR detectors. Spectra were recorded in the absorbance mode using the integrating sphere accessory (model ISR-3100), the range wavelength being 250-850 nm. The interior of the integrating sphere was coated with a highly diffuse BaSO_4 reflectance standard. Measurements, data collection and data evaluation were controlled by the computer software UVProbe version 2.31.

Scanning electron microscopy (SEM): micrographs were obtained using a Focused Ion Beam Zeiss Neon 40 scanning electron microscope operating at 5 kV. Samples were mounted on a double-side adhesive carbon disc and sputter-coated with a thin layer of carbon to prevent sample charging problems. The effective diameter of the electrospun

MFs and of the PEDOT NPs located at the surface of MFs was determined from the SEM images using the software SmartTIFF (v1.0.1.2.), and data was fitted to a normal curve (OriginPro 8 SR0, v8.0724).

Atomic force microscopy (AFM): studies were conducted to obtain topographic images of the nanoparticles surface using silicon TAP 150-G probe (Budget Sensors, Bulgaria) with a frequency of 150 kHz and a force constant of 5 N/m. Images were obtained with a Molecular Imaging PicoSPM microscope using a NanoScope IV controller under ambient conditions in tapping mode. AFM measurements were performed on various parts of the samples, which produced reproducible images similar to those displayed in this work.

Electrochemical response: fiber mats were evaluated by cyclic voltammetry (CV) using PGSTAT204 AUTOLAB potentiostat–galvanostat connected to a PC computer controlled through the NOVA 1.6 software using a custom made 2 ml cell. Commercial polymer-modified ITO substrates with the effective electrode area of 0.23 cm² were used as working electrodes, together with an Ag|AgCl 3 M KCl reference electrode and a Pt-wire counter electrode. Electrochemical characterizations were performed in the presence of Fe(CN) (10 mM) and KCl (100 mM). Measurements were realized at room temperature and the scan rate was set to 100 mV/s. The potential range was chosen as between -0.80 V (initial and final potential) and +1.00 V (reversal potential) vs. Ag/AgCl.

Contact angle (CA) measurements: were carried out using the sessile drop method at room temperature on an OCA 15EC with SCA20 software (Data-Physics Instruments GmbH, Filderstadt, Germany). The solvent used for these experiments was deionized water, the contact angle being determined for the first drop. For measurements, the sessile drop was gently put on the surface of samples using a micrometric syringe with a proper metallic needle (Hamilton 500 µL). The ellipse method was used to fit a mathematical function to the measured drop contour. This procedure consists on approximate the drop contour to the line of an ellipse, deviations from the true drop shape being in the range of a few percent. The ellipse method provides accurate measure

of the contact angle and holds the advantage that it is extremely fast. For each sample, no less than fifteen drops were examined.

3D cell culture: MCF-7 cells were used in all experiments. MF mats (1.2 cm in diameter and 1 mm in high) were sterilized with an UV lamp for 30 min at both sides and attached with non-toxic silicon to the flat bottom of the wells in a 24-well/plate. Cells were seeded at a density of 40000 cells/mL in Advanced DMEM (supplemented with 5% FBS, 1% penicillin/streptomycin and 4 mM L-glutamine), particularly 500 μ L per well and incubated overnight at 37 °C and 5% of CO₂. After one day, cells were washed gently with phosphate buffered saline (PBS) solution and adhesion was evaluated by MTT [3-(4,5-dimethylthiazol-2-yl)-2,5-diphe-nyltetra-zolium] which was performed according to manufacturer instructions. Cell proliferation was evaluated using same methodology but during 7 days. Assays were repeated two times independently and with n=4.

Cell morphology by confocal microscopy: Cells were fixed and stained for nucleus and F-actin on days 1 and 7. Particularly, after the desired time, cells were washed with PBS 1 \times and fixed with 2.5 % paraformaldehyde in PBS for 40 min at room temperature. After this, samples were washed 3 times 5 min each with PBS 1 \times and permeabilized with 0.05% (w/v) triton X-100 in PBS 1 \times for 20 min under agitation. Subsequently, unspecific sites were blocked with a solution containing 1% BSA, 22.52 mg/mL glycine and Tween-20 0.1 % in S 8 PBS 1 \times for 30 min. F-actin filaments were stained with phalloidin atto-488 (Stock solution 10 nmol/500 μ L methanol) used with a 1/50 dilution in PBS 1 \times for 1 hour at room temperature under agitation. Again, samples were washed 3 times 5 min each with PBS 1 \times . Finally cell nucleus was stained with bis-benzimide H33258 (stock solution 2 mM) employed at 1/100 dilution in PBS 1 \times during 30 min under soft constant agitation and mounted on the glass slides. Samples were protected from light and kept at 4°C before use. Imaging was performed using an Axio Observer Z1 fluorescence microscope (Carl Zeiss) confocal laser scanning microscope with a 10 \times and 40 \times objectives. Morphology studies were performed with ImageJ software.

Release studies: Mats of electrospun MFs (20 mg) were deposited on 40 mL tubes and, subsequently, 20 mL of the release medium, which consisted of phosphate buffer

saline (PBS, pH 7.4) supplemented with 70 v/v% of ethanol (PBS-EtOH), were added. Tubes were maintained at 37° under agitation (100 rpm). At selected time intervals, 1 mL of each tube was extracted and deposited into an Eppendorf in order to be quantified afterwards. Subsequently, each tube was supplemented with 1 mL of the liberation medium, PBSEtOH 70%, to keep the volume. At the end of the studied liberation process, matrixes were dried in an oven at 37° overnight and placed in an Eppendorf. 100 µL of CHCl₃ were added to dissolve the polymer and 1.2 mL of PBS-EtOH 70% was added to precipitate the polymer and allow the drug to be retained in the ethanol containing phase. Finally, Eppendorf were centrifuged at 10000 rpm during 3 min and the supernatant absorbance was read at 450 nm. 1V; 60 s.

Electrically stimulated drug release: Experiments were performed using steel AISI 316 sheets covered with the corresponding mats of electrospun MFs. Pulses were applied using a three-electrode compartment cell at room temperature. Steel AISI 316 sheets were used as working electrodes and platinum as counter electrode. The reference electrode was an Ag|AgCl electrode containing a KCl saturated aqueous solution. The cell was used with 10 mL of electrolyte media, which consisted in PBS (pH 7.4) supplemented with 0.05% Tween 20. After preliminary studies devoted to explore the effect of potential and duration of the pulses, the CUR-release was investigated considering 1, 3 and 5 pulses of 1.0 V (each pulse lasts 60 s) with a time lapse of 5 s in between. After the sequence of pulses, 1 mL of the electrolyte solution was withdrawn and replaced for 1mL of new electrolyte solution. After recovering the different samples the absorbance was read with a multi-well plate at 450 nm.

7.4.2 Results and discussion

Preparation and spectroscopic characterization

The synthesis of the PEDOT NPs was conducted in water mixed with EtOH (10%) at 40 °C using 3,4-ethylenedioxythiophene (EDOT) monomer, sodium dodecylbenzene sulfonate (DBSA) as stabilizer and doping agent simultaneously, and ammonium persulfate (APS) as oxidizing agent. A schematic representation of the synthetic process is provided in **Figure 7.4.1**.

Figure 7.4.2a shows a micrograph of the resulting PEDOT NPs, which exhibited an effective diameter of 99 ± 21 and 157 ± 1 nm as determined by SEM and DLS (**Figure 7.4.1c**), respectively. The FTIR spectrum of PEDOT NPs doped with DBSA is displayed in **Figure 7.4.1d**. The main absorption peaks from the thiophene, ether, and sulfonate groups corresponded to: stretching modes of C=C in the thiophene ring at 1647 and 1557

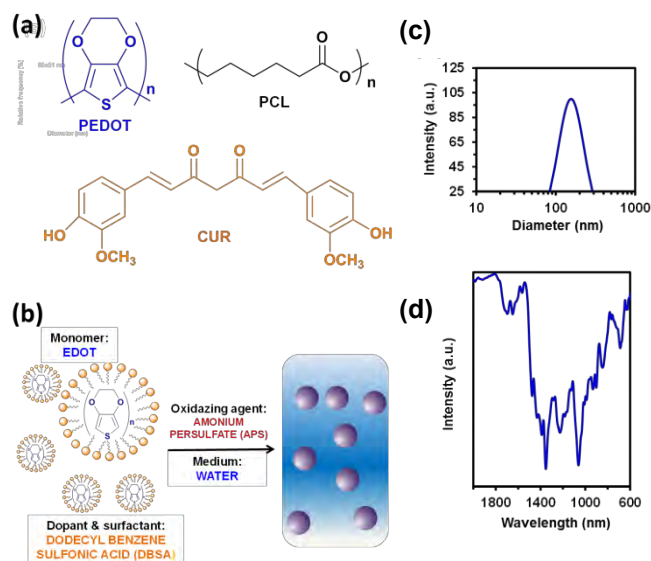


Figure 7.4.1 (a) Chemical structures of PEDOT, CUR and PCL. (b) Schematic representation of the chemical process used to prepare PEDOT NPs. (c) Effective diameter (D_{eff}) of PEDOT NPs derived from dynamic light scattering. The graph is expressed in intensity vs diameter. (d) FTIR spectra of PEDOT NPs doped with DBSA. The main absorption peaks from the thiophene, ether, and sulfonate groups correspond to: stretching modes of C=C in the thiophene ring at 1647 and 1557 cm^{-1} , CH_2 stretching modes at 1478, 1396, and 750 cm^{-1} , C–O–C vibrations at 1206 and 1057 cm^{-1} , and the S–O stretch at 667 cm^{-1} .

cm^{-1} , CH_2 stretching modes at 1478, 1396, and 750 cm^{-1} , C–O–C vibrations at 1206 and 1057 cm^{-1} , and the S–O stretch at 667 cm^{-1} .

Appropriate mixtures of PCL dissolved in 2:1 chloroform:acetone, PEDOT NPs dispersed in EtOH and/or CUR dissolved in EtOH were chosen for the electrospinning process. PCL/PEDOT/CUR, PCL/PEDOT and PCL/CUR were obtained using PCL:PEDOT NPs:CUR, PCL:PEDOT NPs and PCL:CUR mixtures as feeding solutions in the electrospinning process, while PCL MFs were directly derived from the polymer solution. Because of the characteristics of the electrospinning technique,^{86–88} the amount of CUR and/or PEDOT NPs used in the feeding solution is completely incorporated to the PCL-based system. The processing conditions and concentrations, which are

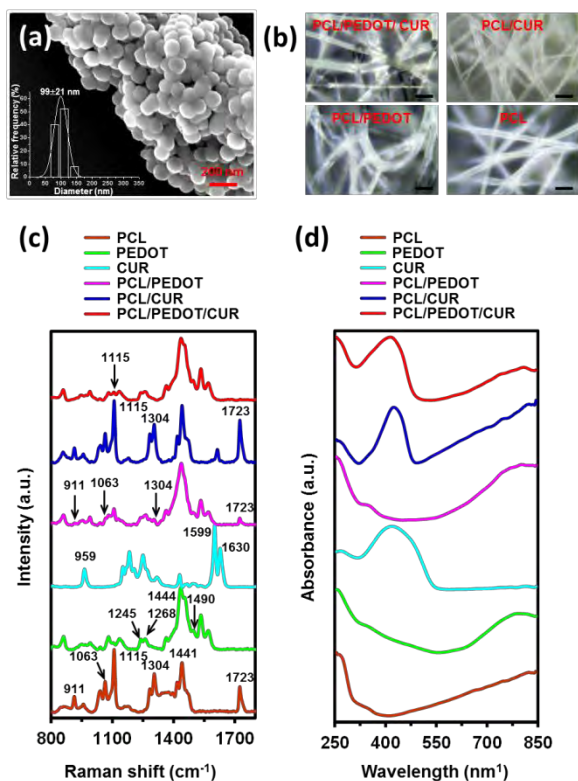


Figure 7.4.2 (a) SEM micrograph of PEDOT NPs. Inset: effective diameter histogram derived from SEM measurements. (b) Optical micrographs of electrospun MFs (scale bar: $50 \mu\text{m}$). (c) Raman and (d) UV-vis spectra of the investigated systems.

described in the materials section, were selected to avoid the formation of droplets and electrospun beads in the prepared fiber networks. After preparation, they have been initially characterized by optical microscopy in order to check the general quality of the MFs, and by micro-Raman and UV-vis spectroscopies to confirm the successful incorporation of the different components. Subsequently, fiber networks are characterized by means of SEM and AFM.

Figure 7.4.2b displays optical images taken with the Raman confocal microscope of PCL/PEDOT/CUR, PCL/PEDOT, PCL/CUR and PCL electrospun MFs obtained using optimized processing conditions. In all cases continuous well-defined fibers of homogeneous size were apparently achieved, independently of the loading of PEDOT NPs and/or CUR. Raman and UV-vis spectra of all MFs, as well as of PEDOT NPs and CUR, are compared in **Figures 7.4.2c** and **d**, respectively.

The main vibrational modes of undoped PEDOT are typically located at 1490 cm^{-1} , 1424 cm^{-1} , 1371 cm^{-1} and 1261 cm^{-1} ,⁹⁸⁻¹⁰⁰ which correspond to asymmetric $C_{\alpha}=C_{\beta}$ stretching, symmetric $C_{\alpha}=C_{\beta}$ stretching, $C_{\beta}=C_{\beta}$ stretching and $C_{\alpha}-C_{\alpha'}$ inter-ring stretching vibrations, respectively. However, the spectrum displayed in **Figure 7.4.2c** shows the appearance and disappearance of several such bands, indicating that PEDOT NPs are p-doped.¹⁰¹ Specifically, the most important changes with respect to undoped PEDOT are:

- The peak that should be centered at 1424 cm^{-1} experiences a blue shift towards 1444 cm^{-1} , indicating that the $C_{\alpha}=C_{\beta}$ stretching vibration mode is sensitive to the p-doping.
- The band that should appear at 1261 cm^{-1} splits into two peaks at 1245 and 1268 cm^{-1} due the presence of DBSA. This change, which is connected with the conversion from the benzoid to the quinoid structure, has been attributed to the variation of $C_{\alpha}-C_{\alpha'}$ and $C_{\beta}=C_{\beta'}$ to $C_{\alpha}=C_{\alpha'}$ and $C_{\beta}-C_{\beta'}$, respectively. This conversion in the electronic structure is in agreement with the interpretation of the changes in the peak at 1424 cm^{-1} .
- The intensity of the peak at 1490 cm^{-1} is very low, has been also attributed to a reduction of the double bond character in the $C_{\alpha}=C_{\beta}$ stretching due to the benzoid-to-quinoid conversion.

The Raman spectrum of CUR, which is consistent with the keto-enol tautomeric form of this drug, displays characteristic peaks at 959 , 1599 and 1630 cm^{-1} , which have been

associated with the C–OH, C=C and C=O and C=C stretching vibrations, respectively.^{102,103} According to Kotula *et al.*,¹⁰⁴ the 850 cm⁻¹ to 950 cm⁻¹ region of the PCL MFs spectrum corresponds to primarily C–COO stretches, while the one comprised between 1030 cm⁻¹ and 1110 cm⁻¹ is assigned to C–C and C–O stretching region. Other characteristic peaks of PCL are identified at 1723 cm⁻¹ for the C=O stretching, 1304 cm⁻¹ for the CH₂ twist, and 1441 cm⁻¹ for CH₂ bend. Inspection of the spectra recorded for PCL/PEDOT/CUR, PCL/PEDOT and PCL/CUR MFs confirm the presence of the different components, even though the high intensity of the p-doped PEDOT signals mask the PCL and CUR peaks in the corresponding mixtures.

UV-vis absorption spectrum of PEDOT (**Figure 7.4.2d**) shows a high dopant transition response in the region from ~550 nm to 800 nm, which is related with bipolaronic states.^{105, 106} This absorption band is preserved in the UV-vis spectra of PCL/PEDOT and PCL/PEDOT/CUR MFs, evidencing that the p-doped state of the CP is not altered by the electrospinning process. Besides, UV-vis of CUR shows the absorption maximum at wavelength 424 nm, which is clearly identified in PCL/CUR and PCL/PEDOT/CUR MFs. This maximum is due to the electronic dipole allowed $\pi - \pi^*$ type excitation of its extended conjugation system, as reported by Kim *et al.*¹⁰⁷

Surface characterization

Figure 7.4.3 shows representative low (inset) and high magnification SEM micrographs, the diameter distribution as determined by SEM, and AFM images of the prepared MFs. Unloaded PCL mats consisted of well-defined MFs with a D_{eff} of 3.7 ± 0.8 μm , even though small beads not detectable by optical microscopy were observed in some cases (marked with light blue circles in **Figure 7.4.3a**). However, the most important characteristic of PCL MFs corresponds to their relatively smooth and homogeneous surface with a root-mean-square roughness (R_q) of 73 ± 11 nm only.

The loading of CUR into PCL MFs caused the complete disappearance of defects (Figure 7.4.3b), which suggest the formation of attractive PCL...CUR interactions in the feeding solution. D_{eff} and R_q apparently increase when fibers are loaded with PEDOT NPs (Figure 7.4.3c). This has been attributed to the lack of attractive PCL...PEDOT interactions.

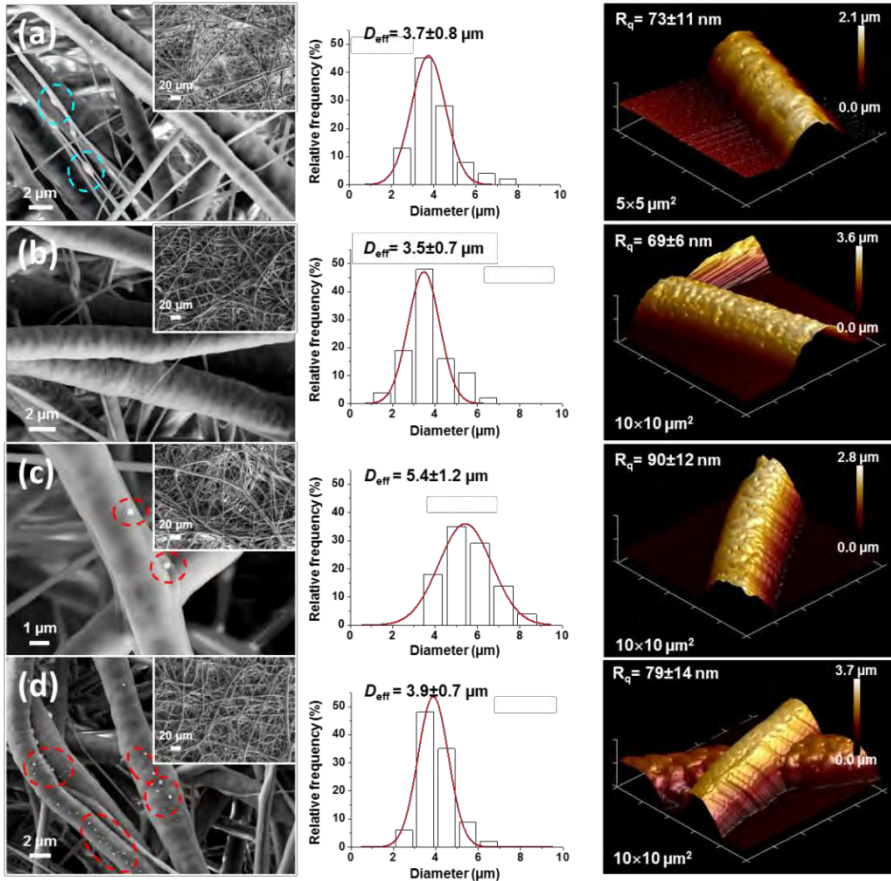


Figure 7.4.3 Low (inset) and high magnification SEM micrographs (left), effective diameter (D_{eff}) histogram derived from SEM measurements (center) and AFM image (right) of (a) PCL, (b) PCL/CUR, (c) PCL/PEDOT and (d) PCL/PEDOT/CUR electrospun MFs. The average value of D_{eff} , the root mean square roughness (R_q) and widow size of the AFM image are also displayed. The presence of small beads in (a) is highlighted with light blue circles, while PEDOT NPs at the surface of the fibers in (c) and (d) is marked with red dashed lines.

This feature is corroborated by the presence of a few spherical PEDOT NPs at the surface of the fibers (marked with red circles in **Figure 7.4.3c**), which reflects the complete separation between the PCL matrix and the PEDOT NPs. It is worth noting that these NPs cannot be attributed to fracture debris since PCL MFs are very flexible and difficult to break and, in addition, NPs are regular in shape and size.

In order to provide deeper understanding about the disconnected organization of PEDOT NPs from the whole PCL matrix, high magnification AFM images of PCL/PEDOT MFs are displayed in **Figure 7.4.4a**. Although both topographic and height images support the presence of individual PEDOT NPs distributed at the surface of PCL fibers, the colored topographic with the phase image skin confirms unequivocally such feature. AFM phase imaging registers phase signal shifts due to changes in the adhesion force between the tip and the surface, thus being sensitive to the surface mechanical and viscoelastic properties (*i.e.* stiffness-softness). Accordingly, the information provided by this technique is frequently used to examine the organization of the components in polymer composites. Hence, **Figure 7.4.4a** illustrates how the PEDOT NP, which is clearly distinguished by the dark purple domain, remains adhered to the surface of the PCL fiber. Cross sectional profile of the NPs, also included in **Figure 7.4.4a**, indicates that their diameter is around ~125 nm, which is in excellent agreement with DLS estimations. PEDOT NPs were expected to be also inside the PCL/PEDOT fibers, SEM micrographs over the cross section being performed to corroborate such assumption. Unfortunately, the cryo-fracture method was not useful for PCL-based fibers because of their high flexibility. Accordingly, the conventional mechanical fracture method, which probably caused the detachment of the PEDOT/NPs located inside the PCL matrix because of the poor affinity between both polymers, was used to cut the fibers and observe the cross sections. Due to these difficulties only a few NPs observed in PCL/PEDOT cross sections were ascribed to internal regions (**Figure 7.4.4b**). In spite of this, SEM micrographs achieved after electrostimulation of PCL/PEDOT/CUR MFs demonstrated the remarkable accumulation of PEDOT NPs inside the fibers (showed and discussed below).

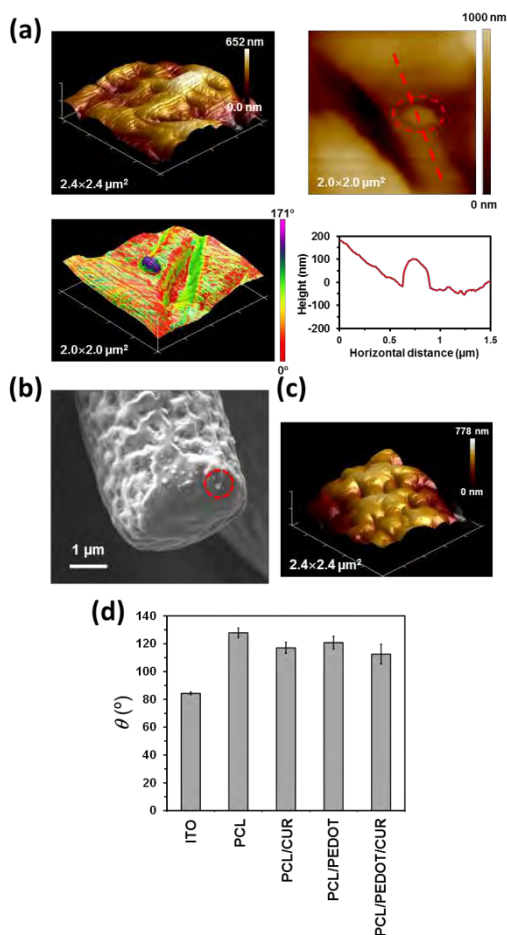


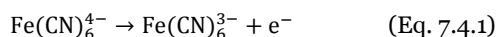
Figure 7.4.4 (a) Representative high magnification topographic (left, top), height (right, top) and colored phase (left, bottom) AFM images of PCL/PEDOT MFs, supporting the presence of individual PEDOT NPs distributed at the surface of PCL fibers. Cross sectional profile of the PEDOT NP (right, bottom) at the region marked in the height image. (b) Cross section SEM images of PCL/PEDOT. Internally located PEDOT NP is illustrated by the red circle. (c) High magnification topographic AFM image of PCL/PEDOT/CUR. Window size of the AFM images is displayed in (a) and (c). (d) CA (θ) of water for polymer-modified ITO bare and coated with PCL, PCL/CUR, PCL/PEDOT and PCL/PEDOT/CUR fiber mats. Values correspond to the mean while error bars indicate the standard deviations (*i.e.* no less than fifteen drops were examined).

PCL/PEDOT/CUR MFs exhibit structural characteristics that are intermediate between those of PCL/PEDOT and PEDOT/CUR (**Figure 7.4.3d**). Specifically, both the D_{eff} and R_q values are slightly higher (5% and 8%, respectively) than those PCL fibers, compensating the slight reduction and increase caused by the loading of CUR and PEDOT NPs, respectively. As it was expected, PCL/PEDOT/CUR MFs show PEDOT NPs individually segregated and distributed in the polyester matrix (red circles in SEM micrograph displayed in **Figure 7.4.3d**). Furthermore, representative high magnification AFM images, as that displayed in **Figure 7.4.4c**, evidence a surface topography with features that greatly resemble those obtained for PCL/PEDOT MFs (**Figure 7.4.4a**).

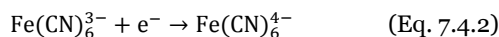
CA (θ) measurements were performed to examine the influence of the loading in the fibers wettability (**Figure 7.4.4d**). The hydrophobicity of PCL MFs decreases slightly upon loading of CUR (11°) or PEDOT NPs (7°). However, this reduction is higher when both, CUR and PEDOT NPs, are loaded simultaneously, the θ being 15° lower for PCL/CUR/PEDOT than for PCL. This effect cannot be attributed to a change in the roughness, which is similar in both cases, but to synergistic interactions between CUR and PEDOT NPs.

Electrochemical response

The electrochemical ability of the prepared fibers was examined studying by CV the oxidation and reduction of $\text{K}_4[\text{Fe}(\text{CN})_6]$. This is a redox inorganic compound that shows a reversible redox process on bare commercial polymer-modified ITO electrode (**Figure 7.4.5a**), which served as the basic material. As the potential is scanned positively, the ferricyanide experiences an oxidation process at 0.46 V:



while when the scan direction is switched the reduction is detected at -0.08 V:



Due to the insulating nature of the polyester, which is the main component of the fibers, CVs recorded using electrodes coated with PCL, PCL/CUR, PCL/PEDOT and

PCL/PEDOT/CUR MFs show a drastic reduction of the oxidation and reduction current densities (**Figure 7.4.5b**). However, the definition and intensity of the oxidation and reduction peaks increases as follows: PCL < PCL/CUR << PCL/PEDOT \approx PCL/PEDOT/CUR, evidencing that the loading with the ICP considerably improves the electrochemical response. This indicates that the conductivity and the surface PCL/PEDOT and PCL/PEDOT/CUR are suited to guarantee electrochemical response. It

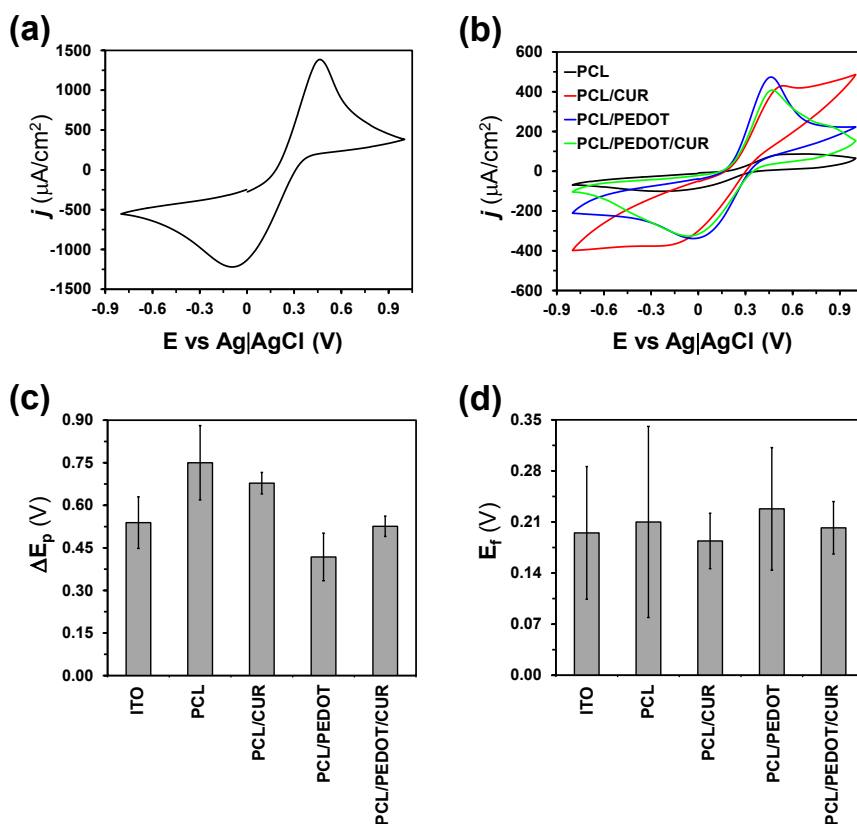


Figure 7.4.5 CVs registered within the potential range of -0.80 to $+1$ V at a scan rate of 100 mV/s using a $\text{K}_4[\text{Fe}(\text{CN})_6]$ solution for (a) commercial polymer-modified ITO electrodes and (b) commercial polymer-modified ITO electrodes coated with PCL, PCL/CUR, PCL/PEDOT and PCL/PEDOT/CUR fiber mats. (c) Peak separation (ΔE_p , in V) and (d) formal potential (E_f , in V) for commercial polymer-modified ITO bare and coated with PCL, PCL/CUR, PCL/PEDOT and PCL/PEDOT/CUR fiber mats. In (c) and (d) values correspond to the mean while error bars indicate the standard deviations (*i.e.* five independent voltammograms were recorded for each system).

should be noted that the voltammograms of PCL/CUR and PCL/PEDOT/CUR are partially masked by CUR, a phenolic compound that also experiences redox behaviour.⁶⁵ This explains the apparition of shoulders at both the oxidation and reduction scans (i.e. at a potential higher than the oxidation peak of $\text{Fe}(\text{CN})_6^{4-}$ and at a potential lower than the reduction peak of $\text{Fe}(\text{CN})_6^{3-}$, respectively) of voltammograms recorded for PCL/PEDOT/CUR.

Figure 7.4.5c represents the peak separation (i.e. the difference between the oxidation and reduction potentials) for bare and coated electrodes. The peak separation is lower for PCL/PEDOT than for the bare ITO electrode, indicating that PEDOT NPs promote faster electron transfer. In the case of PCL/PEDOT/CUR this effect is compensated by the drug (i.e. CUR has a delaying effect in electron transfer, as is reflected by the peak separation of PCL/CUR). Consequently, the peak separation is higher for PCL/PEDOT/CUR than for PCL/PEDOT, evidencing the crucial role of PEDOT NPs in the reduction of the resistance. Regarding to the formal potential, which corresponds to the average of oxidation and reduction potential (**Figure 7.4.5d**), differences are relatively small, even though PCL/PEDOT/CUR provides the closer value to bare ITO. Overall, results displayed in **Figure 7.4.5a-d** allow concluding that PCL/PEDOT/CUR networks provide a suitable interface for electrochemical response.

Cell cultures

PCL is one of the most important biomaterials for the manufacture of longer-term degradable platforms for biomedical applications (e.g. tissue regeneration, drug-delivery, and wound healing).⁸⁹ This must be attributed to its non-toxic behaviour, slow degradation rate, inexpensive production cost, easiness to be processed and manipulated, and USA FDA-approval.⁸⁹ However, an important drawback of implantable PCL-based bioplatfroms for drug-delivery is their high hydrophobicity (**Figure 7.4.4d**), which severely affects the release behavior. Thus, after the first burst of drug release, which mainly involves the drug loaded on the surface, the release rate decreases very rapidly, or even completely, making difficult to reach the therapeutic window after implantation.¹⁰⁸ Therefore, the fact of containing PEDOT NPs permits a more controlled

release like in the previous work where the drug was encapsulated within the PEDOT NPs but here is in a supported interface where the NPs are dispersed and there is no agglomeration. Clearly, the control and, consequently, the design of cell instructive materials (e.g. for smart regulation of drug dosing) are expected to attain much applicability in the future fight against cancer.

Before examining the CUR release without and with electrostimulation, in this section we examine how PEDOT NPs affect the cytotoxicity of the PCL matrix and the biological function of the drug. MCF-7, a human epithelial breast cancer cell line, was used for cell adhesion and proliferation studies, which were conducted on mats of PCL, PCL/PEDOT, PCL/CUR and PCL/PEDOT/CUR mats. For this purpose, the cell viability was evaluated by the MTT method after 24 h (cell adhesion) and 7 days (cell proliferation) of incubation. Collected MFs, which were arranged randomly, resembled the topography of the extracellular matrix. **Figure 7.4.6a** shows that MCF-7 cells adhered similarly on the different materials, including the aluminum sheets used as control. Instead, after 7 days the cell growth decreased significantly for PCL/CUR MFs (**Figure 7.4.6b**). This observation suggests not only that CUR molecules escape from PCL fibers by diffusion but also that the anticancer activity of CUR is still effective after the electrospinning process, slowing down cancer cell proliferation. In contrast, the presence of PEDOT NPs enhances the cellular proliferation (**Figure 7.4.6b**), which is consistent with the well-known biocompatibility of this ICP.^{34,81} Indeed, the highest cell proliferation was obtained for PCL/PEDOT/CUR, despite the presence of CUR. This feature is consistent with the possibility to achieve a control on drug dosage with electrical stimuli without having much CUR leaking from such MFs.

The influence of PCL, CUR and PEDOT NPs on the cell morphology (i.e. cell circularity and area) and spreading was quantitatively evaluated after 24 hours and 7 days. MCF-7 cell nucleus and F-actin were stained with Hoechst and Phalloidin Atto-488, respectively. Confocal microscopy micrographs displayed in **Figure 7.4.6c** indicate that the amount of cells visualized on the top surface of the 3D scaffolds is lower than on the 2D aluminum sheet used as control substrate. This feature was an indicator that cells penetrated inside the MFs-containing matrices, as is schematically depicted in **Figure 7.4.7a**. High magnification micrographs corroborated the presence of cell at different

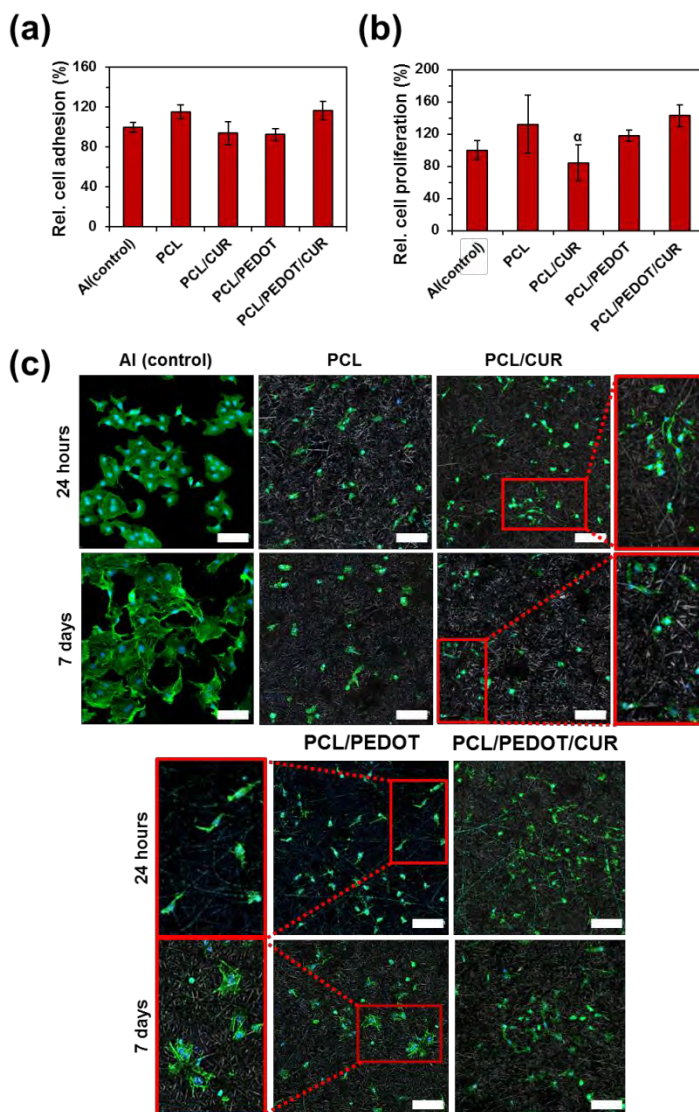


Figure 7.4.6 MTT evaluation of MCF-7 cultured on 3D MFs scaffolds for (a) 24 hours and (b) 7 days. Values are the mean and bars indicate their standard deviation (*i.e.* assays were repeated two times independently and with $n=4$). Greek letter refers to significant differences when one-way ANOVA and multiple comparison test is applied, p -value is lower than 0.05. (c) Confocal microscopy micrographs displaying the morphology of cells adhered (24 hours) and proliferated (7 days) onto 3D MFs matrices. Cells were stained for the nucleus in blue (Hoechst) and F-actin in green (Phalloidin Atto 488). Scale bar = 100 μm . Different zones magnification remarked in red. In all cases (a-c) aluminum sheets were used as control substrate.

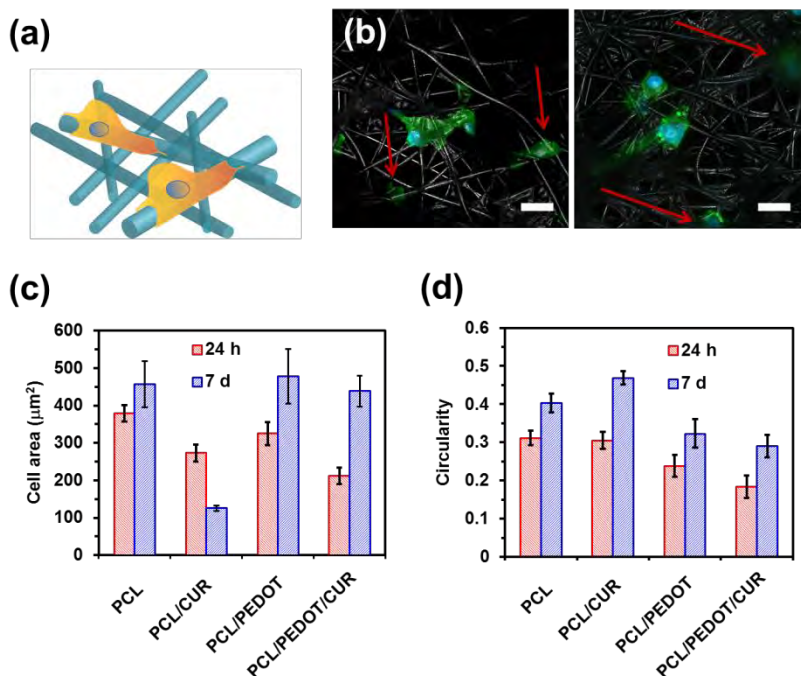


Figure 7.4.7 (a) Scheme representing cells seeded on a 3D scaffold. (b) High magnification fluorescence microscopy images of MCF-7 cells incubated on PCL MFs for 24 hours. Cells found on different planes are marked with red arrows. (c) Cell area quantification (d) and cell circularity after 24 hours and 7 days. Values correspond to the mean, while error bars indicate the standard deviations (*i.e.* no less than 20 values were considered for each case).

planes within the intertwined fibers matrices, as is illustrated in **Figure 7.4.7b** for PCL MFs. Cells seeded on PCL/CUR formed clusters after 7 days and adopted a rounded morphology. However, the cell area was approximately three times smaller for PCL/CUR than the other 3D matrices (planes within the intertwined fibers matrices, as is illustrated in **Figure 7.4.7c** for PCL MFs), while cell circularity increased by 15-38% (planes within the intertwined fibers matrices, as is illustrated in **Figure 7.4.7d** for PCL MFs). This finding reinforces the usefulness of CUR as an anticancer agent. Although after 24 hours cells seeded on all 3D-scaffolds showed an elongated appearance in the fiber direction, after 7 days mostly in the PCL/PEDOT and PCL/PEDOT/CUR MFs cells displayed a higher degree of spreading (*i.e.* non-aligned with the fiber orientation) and cell area was significantly higher. Comparison of the quantitative results displayed in planes within the intertwined fibers matrices, as is illustrated in **Figures 7.4.7c** and **d**

for PCL MFs with those shown in **Figure 7.4.3** evidences that, more heterogeneity and roughness on the fiber surface, more spreading and less circularity and, therefore, more similarity with native ECM.

Overall, these results suggest that PCL-based scaffolds containing PEDOT NPs could be of great interest for tissue implantation if electrical stimuli for regulated release are possible. Next sections are focused in this objective.

Non-stimulated release

Quantitative release assays in a simple physiological-like medium were performed with PCL/CUR and PCL/PEDOT/CUR (**Figure 7.4.8**). PBS-EtOH, which consisted in phosphate buffer saline (PBS, pH 7.4) supplemented with 70 v/v% of EtOH, was considered as release medium. It should be noted that the physical characteristics in a place of the body (e.g. pH and hydrophilicity/hydrophobicity ratio) depends on the location. The addition of EtOH to PBS is frequently used to increase the hydrophobicity of the release medium when hydrophobic drugs are delivered.^{109,110} Considering that CUR is a very hydrophobic drug, the PBS-EtOH medium employed in this work tries to mimic the hydrophobicity of lipid-and liposomes-rich environments. Furthermore, the addition of EtOH to hydrophilic PBS causes some swelling in polyester matrices,^{111,112} which is expected to accelerate the release of hydrophobic drugs, as CUR. Thus, preliminary assays using pure water and PBS as release media evidenced that the release of hydrophobic CUR is extremely low in hydrophilic media. Therefore, the PBS-EtOH medium, which mimics hydrophobic environments, was used to evaluate the release of CUR at reasonable time intervals.

Results displayed in **Figure 7.4.8a** indicate a relatively slow release for PCL/CUR: 33% ± 6% of the loaded drug was released after 24 h. This feature proves that CUR is mostly embedded into compact PCL fibers, makes difficult its diffusion for fast release to the medium. After 96 h the release is higher than 90%, even though a complete release was not achieved within such frame. Considering that drug diffusion is the only

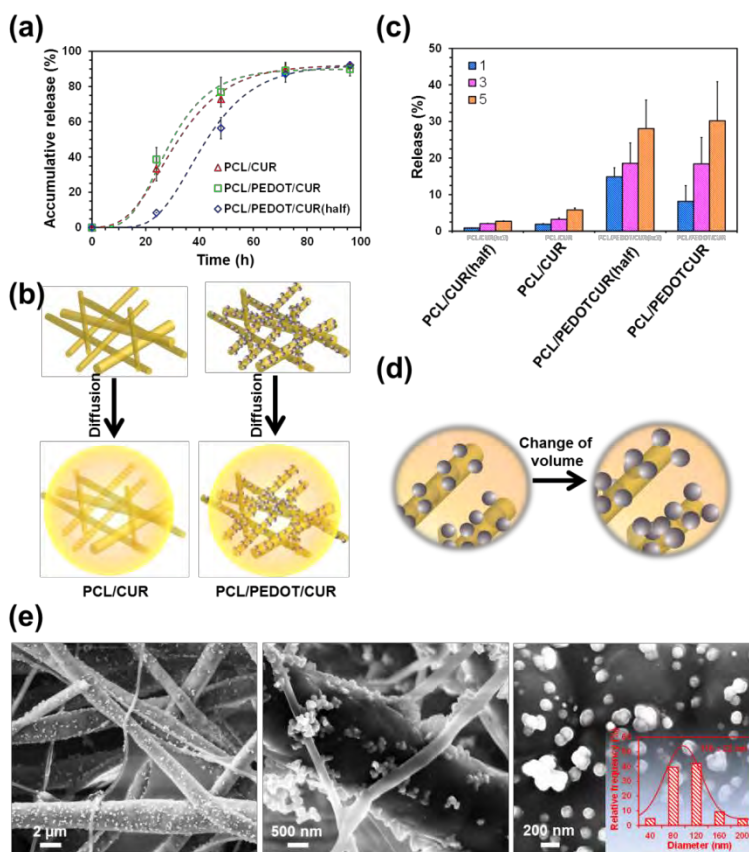


Figure 7.4.8 (a) CUR release profiles from PCL/CUR and PCL/PEDOT/CUR MFs in PBS-EtOH. The release profile obtained from PCL/PEDOT/CUR MFs prepared with half of loaded drug is displayed to illustrate the dependence with the CUR concentration. Values correspond to the mean while error bars indicate the standard deviations (*i.e.* assays were repeated four times). (b) Scheme representing the diffusion mechanism followed by PCL/CUR and PCL/PEDOT/CUR to release CUR in absence of electro-stimulation. (c) CUR release from PCL/CUR and PCL/PEDOT/CUR MFs after electro-stimulation by applying 1, 3 and 5 consecutive potential pulses (the voltage and time-length of each pulse consisted of 1.00 V and 60 s, respectively, consecutive pulses being separated by 5 s). The release obtained from PCL/CUR and PCL/PEDOT/CUR MFs prepared reducing the concentration of loaded drug by a half. (d) Scheme representing the electro-actuation mechanism followed by PCL/PEDOT/CUR MFs to release CUR upon electro-stimulation. (e) SEM micrographs of PCL/PEDOT/CUR fibers after electrostimulation. The magnification of the micrographs increases from left to right. Inset at the right micrograph: effective diameter histogram of superficial PEDOT NPs derived from SEM measurements.

mechanism expected in this case (**Figure 7.4.8b**), the uncomplete release has been attributed to the formation of either drug clusters through CUR...CUR hydrogen bonds and π - π stacking interactions or CUR...PCL hydrogen bonds. In any case, the formed specific interactions are stable enough to retain such CUR molecules entrapped into the PCL matrix.

Incorporation of the PEDOT NPs does not induce significant changes, the release profile obtained for PCL/PEDOT/CUR being very similar to that of PCL/CUR (**Figure 7.4.8a**). This feature is consistent with the wettability of both systems (**Figure 7.4.4d**) and suggests that loaded PEDOT NPs do not perturb CUR...CUR and/or CUR...PCL interactions. In order to corroborate this hypothesis, PCL/PEDOT/CUR MFs were prepared by reducing the concentration of CUR in the feeding medium by a half while the concentration of PCL and PEDOT NPs were kept constant. The obtained release profile, which has been included in **Figure 7.4.8a**, reflects a significant slowdown in the release of the drug ($8.4\% \pm 0.2\%$ of the loaded drug was released after 24 h), corroborating the importance of specific interactions involving CUR in the delivery process. In spite of this, the shape of the release profile is identical to that displayed for PCL/CUR, confirming that the diffusion of the drug is the main release mechanism (**Figure 7.4.8b**).

Electrostimulated release

Experiments with electrostimulations were performed using a conventional three-electrode setup, with steel AISI (American Iron and Steel Institute) 316 (*i.e.* a common austenitic stainless steel with a face centered cubic structure containing 1.25% Ni and 0.65-0.80% Cr) sheets coated with PCL/CUR and PCL/PEDOT/CUR fiber mats as working electrodes, bare steel as a counter electrode, and Ag|AgCl as a reference electrode. Electrically stimulated CUR release assays were conducted applying controlled potential-pulses and using PBS (pH 7.4) with 0.05% (v/v) Tween 20 as electrolyte medium, which mimics a physiological environment. It is worth noting that the non-stimulated diffusion of CUR from PCL/CUR and PCL/PEDOT/CUR MFs to such hydrophilic medium was found to be negligible. After examine the influence of different operational conditions (*i.e.* potential, time-length and number of pulses) on the release

of CUR, the voltage and time-length of each pulse were fixed at 1.00 V and 60 s, respectively. **Figure 7.4.8c** compares the results obtained after application of 1, 3 and 5 consecutive pulses, which were separated by 5 s.

Drug release from PCL/CUR was very small, independently of the number of pulses: $1.9\% \pm 0.1\%$, $3.2\% \pm 0.4\%$ and $5.8\% \pm 0.5\%$ after 1, 3 and 5 potential pulses, respectively. Moreover, release experiments performed considering PCL/CUR MFs in which the concentration of drug was reduced by half, denoted PCL/CUR(half) in **Figure 7.4.8c**, indicates that the release depends on the concentration of CUR inside the fibers (*i.e.* $0.9\% \pm 0.1\%$, $2.0\% \pm 0.1\%$ and $2.7\% \pm 0.1\%$ after 1, 3 and 5 potential pulses, respectively). This behavior indicates that the release from PCL/CUR MFs depends on small local degradations induced in the PCL matrix by the pulse potentials. Results are drastically different for PCL/PEDOT/CUR MFs. In this case, the release increases significantly with the number of pulses: reaches $8.1\% \pm 4.3\%$, $18.4\% \pm 7.2\%$ and $30.2\% \pm 10.2\%$ after 1, 3 and 5 potential pulses, respectively. This feature is independent of the CUR concentration, as is evidenced by the results obtained for PCL/PEDOT/CUR(half) MFs (**Figure 7.4.8c**), in which the CUR concentration was reduced by half in the electrospinning medium: $14.9\% \pm 2.5\%$, $18.6\% \pm 5.6\%$ and $28.1\% \pm 7.8\%$ after 1, 3 and 5 potential pulses, respectively.

The release mechanism hypothesized for PCL/PEDOT/CUR MFs is based on the voltammetric response of PEDOT NPs, which results in volume variations and structural changes. This well-known phenomenon has been extensively used to design and fabricate electro-chemo mechanical devices (*i.e.* actuators and artificial muscles), in which the dimensional changes of CP films are converted into mechanical energy through linear or angular movements.^{34,113-115} In addition to PPy and polyaniline,^{115,116} considerable volume change has been also reported for PEDOT.¹¹⁷

Figure 7.4.8d schematizes the drug release mechanism proposed for electro-stimulated PCL/PEDOT/CUR MFs. The voltage applied during each pulse causes oxidation and/or overoxidation processes in the ICP, electrons are lost from the backbone and positive charges are generated along the PEDOT chains. To keep the electroneutrality, hydrated counterions (anions) from the electrolytic release medium have to penetrate into PEDOT NPs through channels originated by conformational

changes induced by repulsive interactions among positive charges. Overall, the events produced by applied electric pulses (*i.e.* conformational movements, electrostatic repulsions and compositional variations through the entrance of hydrated anions) induce dimensional changes in PEDOT NPs (**Figure 7.4.8d**). The mechanical energy associated to such volume increment is used to alter the structure of PCL MFs, the movement of PCL molecules generating macroscopic CUR release. The significant release observed upon electro-stimulation indicates that volume changes occur not only at the surface of PCL MFs but also inside, encapsulated PEDOT NPs being also reached by the hydrated anions that penetrate through PCL chains entanglements. It is worth noting that CP-based actuators functioning with an electric potential in the range of that used in this work (1 V) are known to exert strong mechanical forces ($\sim 1\text{MPa}$) with volume changes of up to 35%.¹¹⁸

SEM micrographs of PCL/PEDOT/CUR MFs after electrostimulation with a 1.00 V potential pulse are displayed in **Figure 7.4.8e** corroborates our previous hypotheses. As it can be seen, the surface of the MFs exhibit multitude of PEDOT NPs, which are distributed individually or forming small clusters. The appearance on the surface of these NPs, which were not found before electrostimulation (**Figure 7.4.3d**), confirms that the main part of the PEDOT NPs contained in the electrospinning feeding mixture were located inside the PCL MFs. Micrographs prove that the application of potential pulses causes the migration of the embedded PEDOT NPs to the surface of the MFs. Furthermore, the D_{eff} of PEDOT NPs located onto the surface of electrostimulated fibers is 116 ± 22 nm (**Figure 7.4.8e**, inset), which represents an increment of 17% with respect to the values obtained before electrostimulation. This nanofeature is consistent with the delivery mechanism proposed in **Figure 7.4.8d**. Thus, the release of CUR should be attributed to the effect of migration of enlarged PEDOT NPs to the MFs surface, which affects the PCL structure.

7.4.3 Conclusions

In conclusion, PCL/PEDOT/CUR MFs, which have been successfully prepared by electrospinning, exhibit potential advantages to regulate the CUR release by electrical stimulation. After characterizing the influence of both PEDOT NPs and CUR on the surface properties and electrochemical response of PCL MFs, we have demonstrated that the topography of mats made of randomly collected PCL/PEDOT/CUR MFs resembles that of the extracellular matrix. Besides, *in vitro* assays have evidenced that CUR maintains the anticancer activity after the electrospinning process. Application of potential pulses causes changes at the MFs due to the migration of PEDOT NPs from inside to the surface. PEDOT NPs experience a volume change with concomitant “on-demand” CUR release. Independently of the concentration of CUR initially loaded into the MFs, the drug release dose increases with the number of potential pulses, scaling linearly. Overall, results indicate that the incorporation of isotropic actuators, as PEDOT NPs, to biodegradable electrospun MFs is a promising approach for the development of programmable drug delivery devices.

7.5 References

1. Baolin, G.; Glavas, L. and Albertsson, A.-C. Biodegradable and electrically conducting polymers for biomedical applications. *Prog. Polym. Sci.* **2013**, *38*, 1263-1286.
2. Darmanin, T. and Guittard, F. Wettability of conducting polymers: from superhydrophilicity to superoleophobicity. *Prog. Polym. Sci.* **2014**, *39*, 656-682.
3. Heinze, J.; A. Frontana-Urbe, B. and Ludwigs, S. Electrochemistry of conducting polymers persistent models and new concepts. *Chem. Rev.* **2010**, *110*, 4724-4771.
4. Guiseppi-Elie, A. Electroconductive hydrogels: synthesis, characterization and biomedical applications. *Biomaterials* **2010**, *31*, 2701-2716.
5. Otero, T. F.; Martínez, J. G. and Arias-Pardilla, J. Biomimetic electrochemistry from conducting polymers. A review: artificial muscles, Smart membranes, Smart drug delivery and computer/neuron interfaces. *J. Electrochim. Acta* **2012**, *84*, 112-128.
6. Pérez-Madrigal, M. M.; Armelin, E.; Puiggali, J. and Alemán, C. Insulating and semiconducting polymeric free-standing nanomembranes with biomedical applications. *J. Mater. Chem. B* **2015**, *3*, 5904-5932.
7. Green, R. and Abidian, M. R. Conducting polymers for neural prosthetic and neural interface applications. *Adv. Mater.* **2015**, *27*, 7620-7637.

8. Wang, Z. H.; Tammela, P.; Huo, J. X.; Zhang, P.; Stromme, M. and Nyholm, L. Solution-processed poly(3,4-ethylenedioxythiophene) nanocomposite paper electrodes for high-capacitance flexible supercapacitors. *J. Mater. Chem. A* **2016**, *4*, 1714-1722.
9. López-Pérez, D. E.; Aradilla, D.; del Valle, L. J. and Alemán, C. Capacitive composites made of conducting polymer and lysozyme: toward the biocondenser. *J. Phys. Chem. C* **2013**, *117*, 6607-6619.
10. Wan, W. K.; Yang, L. and Padavan, D. T. Use of degradable and nondegradable nanomaterials for controlled release. *Nanomedicine* **2007**, *2*, 483-509.
11. Timko, B. P. and Kohane, D. S. Materials to clinical devices: technologies for remotely triggered drug delivery. *Clin. Ther.* **2012**, *34*, S25-S35.
12. LaVan, D. A.; McGuire, T. and Langer, R. Small-scale systems for *in vivo* drug delivery. *Nat. Biotechnol.* **2003**, *21*, 1184-1191.
13. Mura, S.; Nicolas, J. and Couvreur, P. Stimuli-responsive nanocarriers for drug delivery. *Nat. Mater.* **2013**, *12*, 991-1003.
14. Timko, B. P.; Dvir, T. and Kohane, D. S. Remotely triggerable drug delivery systems. *Adv. Mater.* **2010**, *22*, 4925-4943.
15. Balmert, S. C. and Little, S. R. Biomimetic delivery with mirco- and nanoparticles. *Adv. Mater.* **2012**, *24*, 3757-3778.
16. Ge, J.; Neofytou, E.; Cahill, J.; Beygui, R. E. and Zare, R. N. Drug release from electric-field-responsive nanoparticles. *ACS Nano* **2012**, *6*, 227-233.
17. Hosseini-Nassab, N.; Samnta, D.; Abdolazimi, Y.; Annes, J. P. and Zare, R. N. Electrically controlled release of insulin using polypyrrole nanoparticles. *Nanoscale* **2017**, *9*, 143-149.
18. Yang, Y. L.; Zhang, X. J.; Yu, C. T.; Hao, X. J.; Jie, J. S.; Zhou, M. J. and Zhang, X. H. Smart nanorods for highly effective cancer theranostic applications. *Adv. Healthcare Mater.* **2014**, *3*, 906-915.
19. Svirskis, D.; Travas-Sejdic, J.; Rodgers, A. and Garg, S. Electrochemically controlled drug delivery based on intrinsically conducting polymers. *J. Controlled Release.* **2010**, *146*, 6-15.
20. Wadhwa, R.; Lagenaur, C. F. and Cui, X. T. Electrochemically controlled release of dexamethasone from conducting polymer polypyrrole coated electrode. *J. Control Release.* **2006**, *110*, 531-541.
21. Miller, L. L. and Zhou, X. U. Poly(N-methylpyrrolylium) poly(styrenesulfonate)-a conductive, electrically switchable cation exchanger that cathodically binds and anodically releases dopamine. *Macromolecules* **1987**, *20*, 1594-1597.
22. Stevenson, G.; Moulton, S. E.; Innis, P. C. and Wallace, G. G. Polyterthiophene as an electrostimulated controlled drug release material of therapeutic levels of dexamethasone. *Synth. Met.* **2010**, *160*, 1107-1114.
23. Jeon, G.; Yang, S. Y.; Byun, J. and Kim, J. K. Electrically actuatable smart nanoporous membrane for pulsatile drug release. *Nano Lett.* **2011**, *11*, 1284-1288.

24. Alshammary, B.; Walsh, F. C.; Herrasti, P. and Ponce de Leon, J. C. The importance of the film structure during self-powered ibuprofen salicylate drug release from polypyrrole electrodeposited on AZ31 Mg. *J. Solid State Electrochem.* **2016**, *20*, 3375-3382.
25. Whitesides, G. M. The “right” size in nanobiotechnology. *Nat. Biotechnol.* **2003**, *21*, 1161-1165.
26. Ateh, D. D.; Navsaria, H. A. and Vadgama, P. Polypyrrole-based conducting polymers and interactions with biological tissues. *J. R. Soc. Interface* **2006**, *3*, 741-752.
27. Samanta, D.; Hosseini-Nassab, N. and Zare, R. N. Electroresponsive nanoparticles for drug delivery on demand. *Nanoscale* **2016**, *8*, 9310-3917.
28. Samanta, D.; Meiser, J. L. and Zare, R. N. Polypyrrole nanoparticles for tunable, pH-sensitive and sustained drug release. *Nanoscale* **2015**, *7*, 9497-9504.
29. Wang, Y.; Xiao, Y. and Tang, R. Spindle-like polypyrrole hollow nanocapsules as multifunctional platforms for highly effective chemo-photothermal combination therapy of cancer cells *in vivo*. *Chem. Eur. J.* **2014**, *20*, 11826-11834.
30. Park, D.; Cho, Y.; Goh, S.-H. and Choi, Y. Hyaluronic acid-polypyrrole nanoparticles as pH-responsive theranostics. *Chem. Commun.* **2014**, *50*, 15014-15017.
31. Groenendaal, L.; Zotti, G.; Aubert, P.-H.; Waybright, S. M. and Reynolds, J. R. Electrochemistry of poly(3,4-alkylenedioxythiophene) derivatives. *Adv. Mater.* **2003**, *15*, 855-879.
32. Groenendaal, L.; Jonas, F.; Freitag, D.; Pielartzik, H. and Reynolds, J. R. Poly(3,4-ethylenedioxythiophene) and its derivatives: past, present and future. *Adv. Mater.* **2000**, *12*, 481-494.
33. Kirchmeyer, S. and Reuter, K. Scientific importance, properties and growing applications of poly(3,4-ethylenedioxythiophene). *J. Mater. Chem.* **2005**, *15*, 2077
34. del Valle, L. J.; Estrany, F.; Armelin, E.; Oliver, R. and Alemán, C. Cellular adhesion, proliferation and viability on conducting polymer substrates. *Macromol. Biosci.* **2008**, *8*, 1144-1151.
35. Aradilla, D. Estrany, F. and Alemán, C. Symmetric supercapacitors based on multilayers of conducting polymers. *J. Phys. Chem. C* **2011**, *115*, 8430-8438.
36. Shi, Y.; Peng, L. and Yu, G. Nanostructured conducting polymer hydrogels for energy storage applications. *Nanoscale* **2015**, *7*, 12796-12806.
37. Green, R. A.; Lovell, N. H.; Wallace, G. G. and Poole-Warren, L. A. Conducting polymers for neural interfaces: challenges in developing an effective long-term implant. *Biomaterials* **2008**, *29*, 3393-3399.
38. Abidian, M. R.; Corey, J. M.; Kipke, D. R. and Martin, D. C. Conducting-polymer nanotubes improve electrical properties, mechanical adhesion, neural attachment, and neurite outgrowth of neural electrodes. *Small* **2010**, *6*, 421-429.

39. Winther-Jensen, B.; Winther-Jensen, O.; Forsyth, M. and MacFarlane, D. R. High rates of oxygen reduction over a vapor phase-polymerized PEDOT electrode. *Science* **2008**, *321*, 671-674.
40. Fabregat, G.; Teixeira-Dias, B.; del Valle, L. J.; Armelin, E.; Estrany, F. and Alemán, C. Incorporation of a clot-binding peptide into polythiophene: properties of composites for biomedical applications. *ACS Appl. Mater. Interfaces* **2014**, *6*, 11940-11954.
41. Casanovas, J.; Bertran, O.; Armelin, E.; Torras, J.; Estrany, F.; Codina, M. and Alemán, C. Structural and electronic properties of poly(3-thiophen-3-yl-acrylic acid). *Polymer* **2008**, *49*, 1972-1980.
42. Aradilla, D.; Estrany, F.; Armelin, E. and Alemán, C. Morphology and growing of nanometric multi-layered films formed by alternated layers of poly(3,4-ethylenedioxythiophene) and poly(N-methylpyrrole). *Thin Solid Films* **2010**, *518*, 4203-4210.
43. Paradee, N. and Sirivat, A. Electrically controlled release of benzoic acid from poly(3,4-ethylenedioxythiophene)/alginate matrix: effect of conductive poly(3,4-ethylenedioxythiophene) morphology. *J. Phys. Chem. B* **2014**, *118*, 9263-9271.
44. Liu, D.; Ma, L.; An, Y.; Li, Y.; Liu, Y.; Wang, L.; Guo, J.; Wang, J. and Zhou, J. Thermoresponsive nanogel-encapsulated PEDOT and HSP70 inhibitor for improving the depth of the photothermal therapeutic effect. *Adv. Funct. Mater.* **2016**, *26*, 4749-4759.
45. Karunagaran, D.; Rashmi, R. and Kumar, T. R. Introduction of apoptosis by curcumin and its implications for cancer therapy. *Curr. Cancer Drug Targets.* **2005**, *5*, 117-129.
46. Hsu, C. H. and Cheng, A. L. Clinical studies with curcumin. *Adv. Exp. Med. Biol.* **2007**, *595*, 471-480.
47. Aggarwal, B. B. and Sung, B. Pharmacological basis for the role of curcumin in chronic diseases: an age-old spice with modern targets. *Trends Pharmacol. Sci.* **2009**, *30*, 85-94.
48. Anand, P.; Kunnumakkara, A. B.; Sundaram, C.; Harikumar, K.B.; Sung, B. Tharakan, S. T.; Misra, K.; Priyadarsini, I. K.; Rajasekharan, K. N. and Aggarwal, B. B. Biological activities of curcumin and its analogues (congeners) made by man and mother nature. *Biochem. Pharmacol.* **2008**, *76*, 1590-1611.
49. Daware, M. B.; Mujumdar, A. M. and Ghaskadbi, S. Reproductive toxicity of piperine in swiss albino mice. *Planta Med* **2000**, *66*, 231-236
50. Kim, S. H. and Lee, Y. C. Piperine inhibits eosinophil infiltration and airway hyperresponsiveness by suppressing T cell activity and Th2 cytokine production in the ovalbumin-induced asthma model. *J. Pharm. Pharmacol.* **2009**, *61*, 353-359.
51. Vijayakumar, R. S. and Nalini, N. Efficacy of piperine, an alkaloidal constituent from *Piper nigrum* on erythrocyte antioxidant status in high fat diet and antithyroid drug induced hyperlipidemic rats. *Cell Biochem. Funct.* **2006**, *24*, 491-498.
52. Marti, M.; Fabregat, G.; Estrany, F.; Aleman, C. and Armelin, E. Nanostructured conducting polymer for dopamine detection. *J. Mater. Chem.* **2010**, *20*, 10652-10660.

53. Han, M. G. and Foulger, S. H. Preparation of poly(3,4-ethylenedioxythiophene) (PEDOT) coated silica core-shell particles and PEDOT hollow particles. *Chem. Commun.* **2004**, *19*, 2154-2155.
54. Luo, S. C.; Yu, H. H.; Wan, A. C.; Han, Y. and Ying, J. Y. A general synthesis for PEDOT-coated nonconductive materials and PEDOT hollow particles by aqueous chemical polymerization. *Small* **2008**, *4*, 2051-2058.
55. Kelly, T. L. and Wolf, M. O. Template approaches to conjugated polymer micro- and nanoparticles. *Chem. Soc. Rev.* **2010**, *39*, 1526-1535.
56. Li, L.; Liu, Y.; Hao, P.; Wang, Z.; Fu, L.; Ma, Z. and Zhou, J. PEDOT nanocomposites mediated dual-modal photodynamic and photothermal targeted sterilization in both NIR I and II window. *Biomaterials* **2015**, *41*, 132-140.
57. Fielding, L. A.; Hillier, J. K.; Burchell, M. J. and Armes, S. P. Space science applications for conducting polymer particles: synthetic mimics for cosmic dust and micrometeorites. *Chem. Commun.* **2015**, *51*, 16886-16899.
58. Yang, X.; Li, Z.; Wang, N.; Li, L.; Song, L.; He, T.; Sun, L.; Wang, Z.; Wu, Q.; Luo, N.; Yi, C. and Gong, C. Curcumin-encapsulated polymeric micelles suppress the development of colon cancer *In Vitro* and *In Vivo*. *Sci. Rep.* **2015**, *5*, 10322.
59. Neuberger, T.; Schöpf, B.; Hofmann, H.; Hofmann, M. and Von Rechenberg, B. Superparamagnetic nanoparticles for biomedical applications: possibilities and limitations of a new drug delivery system. *J. Magn. Magn. Mater.* **2005**, *293*, 483-496.
60. Wissing, S. A.; Kayser, O. and Müller, R. H. Solid lipid nanoparticles for parenteral drug delivery. *Adv. Drug Deliver. Rev.* **2004**, *56*, 1257-1272.
61. Jacobs, C.; Kayser, O. and Müller, R. H. Nanosuspensions as a new approach for the formulation for the poorly soluble drug tarazepide. *Int. J. Pharm.* **2000**, *196*, 161-164.
62. Teixeira-Dias, B.; Zanuy, D.; Poater, J.; Solà, M.; Estrany, F.; del Valle, L. J. and Alemán, C. Binding of 6-mer single-stranded homo-nucleotides to poly(3, 4-ethylenedioxythiophene): specific hydrogen bonds with guanine. *Soft Matter* **2011**, *7*, 9922-9932.
63. Zanuy, D.; Teixeira-Dias, B.; del Valle, L. J.; Poater, J.; Solà, M. and Alemán, C. Electroactive polymers for the detection of morphine. *RSC Adv.* **2013**, *3*, 2639.
64. Zhang, D.; Ouyang, X.; Ma, J.; Li, L. and Zhang, Y. Electrochemical behaviour and voltammetric determination of curcumin at electrochemically reduced graphene oxide modified glassy carbon electrode. *Electroanalysis* **2016**, *28*, 749-756.
65. Jha, N. S.; Mishra, S.; Jha, S. K. and Surolia A. Antioxidant activity and electrochemical elucidation of the enigmatic redox behaviour of curcumin and its structurally modified analogues. *Electrochim. Acta.* **2015**, *151*, 574-583.
66. Li, K.; Li, Y.; Yang, L.; Wang, L. and Ye, B. The electrochemical characterization of curcumin and its selective detection in curcuma using a graphene-modified electrode. *Anal. Methods* **2014**, *6*, 7801-7808.

67. Marzocchi, M.; Gualandi, I.; Calieni, M.; Zironi, I.; Scavetta, E.; Castellani, G. and Fabroni, B. Physical and electrochemical properties of PEDOT:PSS as a tool for controlling cell growth. *ACS Appl. Mater. Interfaces* **2015**, *7*, 17993-18003.
68. George, P. M.; LaVan, D. A.; Burdick, J. A.; Chen, C.-Y.; Liang, E. and Langer R. Electrically controlled drug delivery from biotin-doped conductive polypyrrole. *Adv. Mater.* **2006**, *18*, 577-581.
69. Bidan, G.; Lopez, C.; Mendes-Viegas, F. and Vieil, E. Incorporation of sulphonated cyclodextrins into polypyrrole: an approach for the electro-controlled delivering of neutral drugs. *Biosens. Bioelectron.* **1994**, *9*, 219-229.
70. Teixeira-Dias, B.; Zanuy, D.; del Valle, L. J.; Estrany, F.; Armelin, E. and Alemán, C. Influence of the doping level on the interactions between poly(3,4-ethylenedioxythiophene) and plasmid DNA. *Macromol. Chem. Phys.* **2010**, *211*, 1117-1126.
71. Manaia, M. A. N.; Diculescu, V. C.; Gil, E. S. and Oliveira-Brett, A. M. Guaicolinic spices curcumin and capsaicin electrochemical oxidation behaviour at a glassy carbon electrode. *J. Electroanal. Chem.* **2012**, *682*, 83-89.
72. Chan, J. M.; Zhang, L.; Yuet, K. P.; Liao, G.; Rhee, J.-W. and Langer, R. PLGA-lecithin-PEG core-shell nanoparticles for controlled drug delivery. *Biomaterials* **2009**, *30*, 1627-1634.
73. Yuan, S.; Lei, F.; Liu, Z.; Si, T. and Xu, R. X. Coaxial electrospray of curcumin-loaded microparticles for sustained drug release. *PLOS One* **2015**, *10*, e0132609.
74. Joy, N.; Gopalan, G. P. and Eldho, J. and Francis, R. Conducting Polymers: Biomedical Applications, in *Biomedical Applications of Polymeric Materials and Composites* (eds Francis, R.; Sakthi Kumar, D.), Wiley-VCH Verlag GmbH & Co. KGaA, Weinheim, Germany, **2016**.
75. Liu, H.-W.; Hu, S.-H.; Chen, Y.-W. and Chen, S.-Y. Characterization and drug release behavior of highly responsive chip-like electrically modulated reduced graphene oxide-poly(vinyl alcohol) membranes. *J. Mater. Chem.* **2012**, *22*, 17311-17320.
76. Mac Kenna, N.; Calvert, P.; Morrin, A.; Wallace, G. G. and Moulton, S. E. Electro-stimulated release from a reduced graphene oxide composite hydrogel. *J. Mater. Chem. B* **2015**, *3*, 2530-2537.
77. Rahimi, N.; Molin, D. G.; Cleij, T. J.; van Zandvoort, M. A. and Post, M. J. Electrosensitive polyacrylic acid/fibrin hydrogel facilitates cell seeding and alignment. *Biomacromolecules* **2012**, *13*, 1448-1457.
78. Liu, K.-H.; Liu, T.-Y.; Chen, S.-Y. and Liu, D.-M. Drug release behavior of chitosan-montmorillonite nanocomposite hydrogels following electrostimulation. *Acta Biomater.* **2008**, *4*, 1038-1045.
79. Frasconi, M.; Tel-Vered, R.; Riskin, M. and Willner, I. Electrified selective "sponges" made of au nanoparticles. *J. Am. Chem. Soc.* **2010**, *132*, 9373-93829.
80. Puiggali-Jou, A.; Micheletti, P.; Estrany, F.; del Valle, L. J. and Alemán, C. Electrostimulated release of neutral drugs from polythiophene nanoparticles: smart regulation of drug-polymer interactions. *Adv. Healthcare Mater.* **2017**, *6*, 1700453.

81. del Valle, L. J.; Aradilla, D.; Oliver, R.; Sepulcre, F.; Gamez, A.; Armelin, E.; Alemán, C. and Estrany, F. Cellular Adhesion and proliferation on poly(3,4-ethylenedioxythiophene): benefits in the electroactivity of the conducting polymer. *Eur. J. Polym.* **2007**, *43*, 2342–2349.
82. Aggarwal, B. B. and Sung, B. Curcumin in clinical practice: myth or reality? *Trends Pharmacol. Sci.* **2009**, *30*, 85–94.
83. Liu, C.; Jiang, Q. and Xu, J. Effective approaches to improve the electrical conductivity of PEDOT:PSS: a review. *Adv. Electron. Mater.* **2015**, *1*, 1500017.
84. Goyal, R.; Macri, L. K.; Kaplan, H. M. and Kohn, J. Nanoparticles and nanofibers for topical drug delivery. *J. Control. Release* **2016**, *240*, 77–92.
85. Nobs, L.; Buchegger, F.; Gurny, R. and Allemann, E. Poly(lactic acid) nanoparticles labeled with biologically active neutravidin (TM) for active targeting. *Eur. J. Pharm. Biopharm.* **2004**, *58*, 483–490.
86. Sill, T. J. and von Recum, H. A. Electrospinning: applications in drug delivery and tissue engineering. *Biomaterials* **2006**, *29*, 1989–2006.
87. Hu, X.; Liu, S.; Huang, Y.; Xie, Z. and Jing, X. Electrospinning of polymeric nanofibers for drug delivery applications. *J. Control. Release* **2014**, *185*, 12–21.
88. Hasan, A.; Memic, A.; Annabi, N.; Hossain, M.; Paul, A.; Dokmeci, M. R.; Dehghani, F. and Khademhosseini, A. Electrospun scaffolds for tissue engineering of vascular grafts. *Acta Biomater.* **2014**, *10*, 11–25.
89. Woodruff, M. A. and Hutmacher, D. W. The return of a forgotten polymer-polycaprolactone in the 21st century. *Prog. Polym. Sci.* **2010**, *35*, 1217–1256.
90. Dong, R. H.; Jia, Y. X.; Qin, C. C.; Zhan, L.; Yan, X.; Cui, L.; Zhou, Y.; Jiang, X. and Long, Y. Z., *In Situ* deposition of a personalized nanofibrous dressing via a handy electrospinning device for skin wound care. *Nanoscale* **2016**, *8*, 3482–3488.
91. Ercolani, E.; Del Gaudio, C. and Bianco, A. Vascular tissue engineering of small-diameter blood vessels: reviewing the electrospinning approach. *J. Tissue Eng. Regener. Med.* **2015**, *9*, 861–888.
92. Hu, J.; Tian, L. L.; Prabhakaran, M. P.; Ding, X. and Ramakrishna, S. Fabrication of nerve growth factor encapsulated aligned poly(caprolactone) nanofibers and their assessment as a potential neural tissue engineering scaffold. *Polymers* **2016**, *8*, 54.
93. Augustine, R.; Nethi, S. K.; Kalarikkal, N.; Thomas, S. and Pata, C. R. Electrospun polycaprolactone (PCL) scaffolds embedded with europium hydroxide nanorods (EHNs) with enhanced vascularization and cell proliferation for tissue engineering applications. *J. Mater. Chem. B* **2017**, *5*, 4660–4672.
94. Otero, T. F. Reactions drive conformations. biomimetic properties and devices, theoretical description. *J. Mater. Chem. B* **2013**, *1*, 3754–3767.
95. Otero, T. F. and Martínez, J. G. Physical and chemical awareness from sensing polymeric artificial muscles. experiments and modelling. *Prog. Polym. Sci.* **2015**, *44*, 62–78.

96. Plesse, C.; Vidal, F.; Teyssie, D. and Chevrot, C. Conducting polymer artificial muscle fibres: toward an open air linear actuation. *Chem. Commun.* **2010**, 46, 2910–2912.
97. Qi, B. H.; Lu, W. and Mattes, B. R. Strain and energy efficiency of polyaniline fiber electrochemical actuators in aqueous electrolytes. *J. Phys. Chem. B* **2004**, 108, 6222–6227.
98. Garreau, S.; Duvail, J. L. and Louarn, G. Spectroelectrochemical studies of poly(3,4-ethylenedioxythiophene) in aqueous medium. *Synth. Metals* **2002**, 125, 325–329.
99. Han, Y.-K.; Chang, M.-Y.; Huang, W.-Y.; Pan, H.-Y.; Ho, K.-S.; Hsieh, T.-H. and Pan, S.-Y. Improved performance of polymer solar cells featuring one-dimensional pedot nanorods in a modified buffer layer. *J. Electrochem. Soc.* **2001**, 158, K88–K93.
100. Farah, A. A.; Rutledge, S. A.; Schaarschmidt, A.; Lai, R.; Freedman, J. P. and Helmy, A. S. Conductivity enhancement of poly(3,4-ethylenedioxythiophene)-poly(styrenesulfonate) film postspincasting. *J. Appl. Phys.* **2012**, 112, 113709.
101. Deepshikha, B. T. A review on synthesis and characterization of nanostructured conducting polymers (NSCP) and application in biosensors. *Anal. Lett.* **2011**, 44, 1126–1171.
102. López-Tobar, E.; Blanch, G. P.; Castillo, M. L. R. and Sanchez-Cortes, S. Encapsulation and isomerisation of curcumin with cyclodextrins characterized by electronic and vibrational spectroscopy. *Vib. Spectro.* **2012**, 62, 292–298.
103. Sanphui, P.; Goud, N. R.; Khandavilli, U. B. R.; Bhanoth, S. and Nangia, A. New polymorphs of curcumin. *Chem Commun.* **2011**, 47, 5013–5015.
104. Kotula, A. P.; Snyder, C. R. and Migler, K. B. Determining conformational order and crystallinity in polycaprolactone via raman spectroscopy. *Polymer* **2017**, 117, 1–10.
105. Fabregat, G.; Alemán, C.; Casas, M. T. and Armelin, E. Controlling the morphology of poly(*n*-cyanoethylpyrrole). *J. Phys. Chem. B* **2012**, 116, 5064–5070.
106. Okur, S. and Salzner, U. Theoretical modeling of the doping process in polypyrrole by calculating UV/Vis absorption spectra of neutral and charged oligomers. *J. Phys. Chem. A* **2008**, 112, 11842–11853.
107. Kim, H. J.; Kim, D. J.; Karthick, S. N.; Hemalatha, K. V.; Raj, C. J.; Ok, S. and Choe, Y. Curcumin dye extracted from *Curcuma Longa* L. used as sensitizers for efficient dye-sensitized solar cells. *Int. J. Electrochem. Sci.* **2013**, 8, 8320–8328.
108. Guo, G.; Fu, S. Z.; Zhou, L. X.; Liang, H.; Fan, M.; Luo, F.; Qian, Z. Y. and Wei, Y. Q. Preparation of curcumin loaded poly(ϵ -caprolactone)-poly(ethylene glycol)-poly(ϵ -caprolactone) nanofibers and their *in vitro* antitumor activity against glioma 9l cells. *Nanoscale* **2011**, 3, 3825–3832.
109. Han, U.; Seo, Y. and Hong, J. Effect of pH on the structure and drug release profiles of layer-by-layer assembled films containing polyelectrolyte, micelles, and graphene oxide. *Sci. Rep.* **2015**, 6, 24158.
110. Park, Y.; Choi, D. and Hong, J. Nanostructured polymer thin films fabricated with brush-based layer-by-layer self-assembly for sites elective construction and drug release. *Sci. Rep.* **2018**, 8, 3365.

111. Zurita, R.; Puiggali, J. and Rodríguez-Galan, A. Triclosan release from coated polyglycolide threads. *Macromol. Biosci.* **2006**, *6*, 58–69.
112. Maione, S.; del Valle, L. J.; Pérez-Madrigal, M. M.; Cativiela, C.; Puiggali, J. and Alemán, C. Electrospray loading and release of hydrophobic gramicidin in polyester microparticles. *RSC Adv.* **2016**, *6*, 73045–73055.
113. Otero, T. F. and Martínez, J. G. Electro-chemo-biomimetics from conducting polymers: fundamentals, materials, properties and devices. *J. Mater. Chem. B* **2016**, *4*, 2069–2085.
114. Balint, R.; Cassidy, N. J. and Cartmell, S. H. conductive polymers: towards a smart biomaterial for tissue engineering. *Acta Biomater.* **2014**, *10*, 2341–2353.
115. Otero, T. F. and Martinez, J. G. Physical and chemical awareness from sensing polymeric artificial muscles. *Experiments and Modeling. Prog. Polym. Sci.* **2015**, *44*, 62–78.
116. Kaneto, K.; Kaneko, M.; Min, Y. and MacDiarmid, A. G. “Artificial muscle”: electromechanical actuators using polyaniline films. *Synth. Met.* **1995**, *71*, 2211–2212.
117. Okuzaki, H.; Suzuki, H. and Ito, T. Electrically driven PEDOT/PSS actuators. *Synth. Met.* **2009**, *159*, 2233–2236.
118. Smela, E. and Gadegaard, N. Surprising volume change in PPy(DBS): an atomic force microscopy study. *Adv. Mater.* **1999**, *11*, 953–957.

PART C

Surface functionalization with

CREKA



CHAPTER 8:

CREKA

SUMMARY

CREKA is linear pentapeptide that recognizes clotted plasma proteins and selectively homes to tumours, while CR(NMe)EKA was engineer to improve such properties by altering peptide-fibrin interactions. The properties as biointerfaces of electroactive conducting polymer-peptide biocomposites formed by poly(3,4-ethylenedioxythiophene) (PEDOT) and CREKA or CR(NMe)EKA peptide sequences (where Glu has been replaced by *N*-methyl-Glu in the latter) have been compared. Differences between PEDOT-CREKA and PEDOT-CR(NMe)EKA reflect dissemblance in the organization of the peptides into the polymeric matrix. Both peptides affect fibrinogen thrombin-catalyzed polymerization causing the immediate formation of fibrin, whereas in absence of thrombin this phenomenon is only observed for CR(NMe)EKA. Consistently, the fibrin-adsorption capacity is higher for PEDOT-CR(NMe)EKA than for PEDOT-CREKA, even though in both cases adsorbed fibrin exhibits round-like morphologies rather than the characteristic fibrous structure. PEDOT-peptide films coated with fibrin are selective in terms of cell adhesion, promoting the attachment of metastatic cells with respect to normal cells. Within this context, the second part explores the biorecognition event between CR(NMe)EKA, and clotted-plasma proteins (fibrin and fibrinogen) by nanomechanical detection. Specifically, the tumor-homing peptide was covalently attached via epoxysilane chemistry onto silicon microcantilever chips that acted as sensors during dynamic mode experiments. The fibrin(ogen)-binding induced by CR(NMe)EKA was detected by the resonance frequency shift of the cantilevers, and a detection limit of 100 ng/mL was achieved with both proteins.

Publications derived from this work:

Puiggalí-Jou, A.; del Valle, L. J.; Armelin, E., Alemán, C. Fibrin association at hybrid biointerfaces made of clot-binding peptides and polythiophene. *Macromol Biosci.* **2016**, *16*, 1461-1474.

Puiggalí-Jou, A.; del Valle, L. J.; Alemán C. and Pérez-Madrigal, M. M. Weighing biointeractions between fibrin(ogen) and clot-binding peptides using microcantilever sensors. *J Pept Sci.* **2017**, *23*, 162-171.

8.1 Introduction

CREKA (Cys-Arg-Glu-Lys-Ala) is a linear pentapeptide that recognizes clotted plasma proteins and selectively homes to tumors.¹ Thus, this peptide, which was identified using *in vivo* screening of phage-display peptide libraries,^{2,3} recognizes the interaction of fibrin-fibronectin accumulated in walls of tumor vessels and in the interstitial spaces within tumors.¹ Tumor vessels are less robust and stable than normal vasculature, favouring the release of some molecules such as fibrinogen (Fg), which is the fibrin precursor.⁴ Leaked Fg is converted into a fibrin meshwork by the action of thrombin (THR), which cleaves and removes fibrinopeptides allowing the self-assembly of fibrin monomers into elongated fibers.⁵ CREKA linked to amino-dextran coated superparamagnetic iron oxide nanoparticles not only binds to clotted plasma proteins blood and plasma but also induces further localized tumor clotting.¹ This amplified system enhanced the homing of the nanoparticles in a mouse tumor model and the tumor imaging, without causing clotting or other obvious side effects elsewhere in the body. CREKA also homes to the surface of atherosclerotic plaques, including bivalirudin (*i.e.* a THR inhibitor that selectively and reversibly binds the active site of free and fibrin bound THR) containing micelles, and has been used to deliver and concentrate payloads onto atherosclerotic plaques in the ApoE-null mouse model.^{6,7}

The energy landscape and bioactive conformation of CREKA, which consists in a pocket-like shape with the charged groups of Arg, Glu and Lys pointing outwards to facilitate the formation of intermolecular interactions, were determined using computer assisted modelling tools.^{8,9} This information was used to engineer variants of CREKA peptide to resist proteolysis by targeted replacements.¹⁰ More specifically, peptide analogues that incorporate the synthetic α -methyl and *N*-methyl derivatives of Arg, Glu and Lys were studied. Interestingly, CREKA analogues were more effective in tumor homing than the original peptide, results being particularly good for the CREKA analogue in which the Glu was replaced by *N*-methyl-Glu, CR(*N*Me)EKA.¹¹ Additionally, in a very recent study She et al.¹² reported that CR(*N*Me)EKA retains almost completely the anticoagulant activity of the THR inhibitor bivalirudin.

8.2 Fibrin association at hybrid biointerfaces made of clot-binding peptides and polythiophene

Biocomposites derived from the conjugation of synthetic polymers with biomolecules (*e.g.* proteins and peptides) are frequently used in biomedicine because of the synergistic effects associated to combination of their individual properties.¹³⁻¹⁸ In the last few years, particular attention has been paid to biocomposites involving intrinsically conducting polymers (ICPs), which due to their excellent properties¹⁹⁻²¹ are used to fabricate electrochemically active biointerfaces. Thus, devices based on the combination of ICPs and biomolecules have been successfully used applications, as for example bioinspired channels for ion-exchange²² electromechanical actuators,²³ components of bioelectronics devices,^{24,25} aerogels for nerve regeneration,²⁶ and bioactive platforms for tissue regeneration that mimic the growth of biological tissues.^{27,28}

In a very recent work we reported the conditions required for the preparation of bioactive platforms based on the modification of an effective ICP with CREKA.¹⁸ The polymer selected for such purpose was poly(3,4-ethylenedioxythiophene) (PEDOT), which is among the most successful ICPs due to its excellent electrochemical and thermal properties, high conductivity, good environmental stability in its doped state, mechanical flexibility, relative ease of preparation, biocompatibility, and fast doping-undoping process.²⁹⁻³² PEDOT-CREKA biocomposites prepared by chronoamperometry in basic aqueous solution (pH= 10.3) and deposited onto a PEDOT internal layer (*i.e.* forming a bilayered system) were found to entrap one peptide molecule every six polymer repeat units. Although the morphology and topography of PEDOT-CREKA were completely different to those of the individual ICP, the impact of the entrapped peptide molecules in the excellent electrochemical properties of PEDOT was found to be practically negligible. Herein, we prepare and characterize a biocomposite based on the combination of PEDOT and CR(NMe)EKA, PEDOT-CR(NMe)EKA. This new material has been obtained by adapting the strategy previously used for PEDOT-CREKA¹⁸ to achieve both (*i*) a reduction of one order of magnitude in the thickness of the films, and (*ii*) an improvement of the electrochemical behavior with respect to pure PEDOT. Results indicate that the replacement of Glu by *N*-methyl-Glu affects considerably the

biocomposite-fibrin interactions, greatly influencing the properties and response of fibrin-coated biocomposites. Moreover, fibrin-coated PEDOT-CR(NMe)EKA exhibits a remarkable capacity to adhere tumour cells. Thus, such ICP-peptide-protein biocomposite is a very promising material for biomedical applications.

8.2.1 Methods

Materials: 3,4-ethylenedioxythiophene (EDOT) monomer and dodecylbenzene sulfonate (SDBS) were purchased from Aldrich and used as received without further purification. CR(NMe)EKA and CREKA peptides with > 98% of HPLC purity was purchased from Biomatik (Toronto, ON). Ultrapure milliQ water was used to prepare all the aqueous solutions. Fibrinogen from human plasma (50-70% protein; $\geq 80\%$ of protein is clottable) was purchased from Sigma (F3879). Cell lines MCF-7 (epithelial cells from human breast adenocarcinoma), PNT2 (normal prostate epithelium immortalized with SV40), and PC-3 (epithelial cells from human prostate adenocarcinoma) were obtained from ECACC (European Collection of Cell Culture, UK). Culture media were purchased from BD Gibco (Franklin Lakes, NJ, USA).

Synthesis: Anodic polymerization and electrochemical assays were performed with an Autolab PGSTAT302N equipped with the ECD module (Ecochimie, the Netherlands) using a three-electrode compartment cell under nitrogen atmosphere (99.995% pure) at room temperature. Steel AISI 316 sheets of 0.5 and 1 cm² in area were used as working and counter electrode, respectively. The reference electrode was an Ag|AgCl electrode containing a KCl saturated aqueous solution.

PEDOT-CR(NMe)EKA and PEDOT-CREKA films were prepared by chronoamperometry using an aqueous medium pH = 10.3 (adjusted with 1 M NaOH) and a constant potential of 1.10 V, which has been identified as the optimum potential for the polymerization of EDOT in water. A two-step process was used. First, steel electrode was coated with a layer of PEDOT. For this purpose, the anodic compartment of the cell was filled with 20 mL of a 20 mM EDOT aqueous solution containing 10 mM SDBS as supporting electrolyte, while the cathodic compartment was filled 10 mL of the same

electrolyte solution. The polymerization time used for the electrodeposition of this PEDOT coating layer was of $\tau = 10$ s. After this, a second layer of PEDOT-CR(NMe)EKA or PEDOT-CREKA was electrodeposited onto the surface of the PEDOT coating layer. This was achieved by filling the anodic compartment with a generation solution identical to that described above for the internal PEDOT layer but containing 1 mg/mL of CR(NMe)EKA or CREKA peptide. The applied potential and the polymerization time employed for the preparation of the second layer were 1.10 V and $\tau = 20$ s, respectively. It should be remarked that the biocomposite layer was deposited onto the internal PEDOT layer immediately after the generation of the latter. This represents an important difference with respect to our previous work,¹⁸ in which the PEDOT-CREKA layer was deposited after dry during several hours the internal PEDOT layer.

PEDOT films used as control were prepared employing the same experimental conditions that for PEDOT-CREKA and PEDOT-CR(NMe)EKA biocomposites but without the peptide addition in the second layer (i.e. two PEDOT layers prepared using polymerization times of 10 s and 20 s).

Contact profilometry: Film thickness measurements were carried out using a Dektak 150 stylus profilometer (Veeco, Plainview, NY). Scratches were intentionally provoked on the film surface and the average thickness was determined from, at least, nine measurements for each condition. Imaging of the films was conducted using the following optimized settings: tip radius= 12.5 μm ; stylus force= 3 mg; scan length= 2 μm ; speed= 2 nm/s.

Atomic force microscopy (AFM): AFM was conducted to obtain topographic images of the films surface using silicon TAP 150-G probe (Budget Sensors, Bulgaria) with a frequency of 150 kHz and a force constant of 5 N/m. Images were obtained with a AFM Dimension microscope using a NanoScope IV controller under ambient conditions in tapping mode. The row scanning frequency was set between 0.6 and 0.8 Hz. The Root Mean Square roughness (Rq), which is the average height deviation taken from the mean data plane, was determined using the statistical application of the NanoScope Analysis software (1.20, Veeco). AFM measurements were performed on various parts of the films,

which produced reproducible images similar to those displayed in this work. The scan window size was $10 \times 10 \mu\text{m}^2$.

X-ray photoelectron spectroscopy (XPS): XPS analyses were performed in a SPECS system equipped with a high-intensity twin-anode X-ray source XR50 of Mg/Al (1253 eV/1487 eV) operating at 150 W, placed perpendicular to the analyzer axis, and using a Phoibos 150 MCD-9 XP detector. The X-ray spot size was 650 mm. The pass energy was set to 25 and 0.1 eV for the survey and the narrow scans, respectively. Charge compensation was achieved with a combination of electron and argon ion flood guns. The energy and emission current of the electrons were 4 eV and 0.35 mA, respectively. For the argon gun, the energy and the emission current were 0 eV and 0.1 mA, respectively. The spectra were recorded with a pass energy of 25 eV in 0.1 eV steps at a pressure below 6×10^{-9} mbar. These standard conditions of charge compensation resulted in a negative but perfectly uniform static charge. The C 1s peak was used as an internal reference with a binding energy of 284.8 eV. High-resolution XPS spectra were acquired by Gaussian–Lorentzian curve fitting after S-shape background subtraction. The surface composition was determined using the manufacturer's sensitivity factors.

Cyclic voltammetry (CV): CV studies were run to assess the electrochemical behavior of the biocomposites. Hence, the ability to exchange charge reversibly (i.e. electroactivity) and the electrochemical stability (i.e. electrostability) were determined using a 0.1 M phosphate buffer saline solution (PBS; pH= 7.4 adjusted with NaOH). The initial and final potentials were -0.40 V, whereas a reversal potential of 0.80 V was considered. The scan rate was 50 mV/s in all cases.

The electroactivity increases with the similarity between the anodic and cathodic areas of the first control voltammogram. The electrochemical stability (i.e. loss of electroactivity, LEA), which decreases with the oxidation and reduction areas of consecutive control voltammograms, was determined using the following expression:

$$LEA = \frac{\Delta Q}{Q_i} 100 \quad (\text{Eq. 8.2.1})$$

where ΔQ is the difference of voltammetric charge between the second cycle and the last cycle and Q_i is the voltammetric charge corresponding to the second cycle. In this work all values of LEA were referred to five consecutive oxidation-reduction cycles.

Dynamic light scattering (DLS): Real-time monitoring of fibrin polymerization in presence and absence of peptide at 37 °C was conducted by DLS following the increment of the particle effective diameter. All buffers and fibrinogen (Fg) samples were filtered (0.22 μm centrifugal filter) prior to use. Final concentrations of Fg and thrombin (THR) were 0.4 mg/mL and 0.01 U/mL, respectively, in aqueous solution containing 5 mM CaCl_2 and 76 mM NaCl. Data were collected every minute. Measurements were performed using a NanoBrook Omni Zeta Potential Analyzer from Brookhaven Instruments Corporation.

Electrochemical impedance spectroscopy (EIS): Impedance spectroscopy was performed using a conventional three-electrode cell and AUTOLAB-302N potentiostat/galvanostat operating between the frequency range of 100kHz-10 mHz and 10 mV of amplitude for the sinusoidal voltage. All experiments were performed with films electrochemically deposited on stainless steel substrates (AISI 316L with 1cm² of area) and immersed in phosphate buffer saline (PBS, pH 7.4), at room temperature. Stainless steel electrodes were used as working and counter-electrodes, whereas Ag|AgCl saturated (KCl 3M) was employed as reference electrode. After data collection, EIS results were then processed and fitted to an electrical equivalent circuit (EEC).

Protein Adsorption: Analyses to examine the adsorption of proteins onto the surface of PEDOT, PEDOT-CREKA and PEDOT-CR(NMe)EKA films were performed using fibrin and bovine serum albumin (BSA, Fraction V). BSA, which is a globular plasma protein, was used as a control to study the selectivity of the examined surfaces.

PEDOT and PEDOT-peptide films were placed on a 24-well plate heated at 37 °C. Meanwhile, fibrin precursors, Fg (0.4 mg/mL) and THR (0.01 U/mL) were heated to the same temperature (solutions previously filtered). Fg and THR solutions were deposited onto the film surface using a 1:1 ratio. After 60 min with slight agitation (80 rpm) the film was rinsed in 0.1 M PBS to remove residues and non-specifically bound fibrin. The same procedure was used to adsorb BSA, the only difference being the protein concentration in the solution (0.4 mg/mL).

Detection of adsorbed proteins by Bradford assay: Adsorbed fibrin and BSA were removed from the films surfaces by adding 0.2 mL of 0.1 M PBS with nonyl phenoxypolyethoxyethanol (NP-40) surfactant (0.5% v/v) and orbital shaking at 50 rpm during 30 min and 37°C. In order to avoid interferences between the NP40 surfactant and the Bradford reagent, the former was eliminated by precipitating the fibrin with 20 µL of trichloroacetic acid. Then, the precipitate-containing solution was centrifuged for 15 min at 12000 rpm. The solid (fibrin or BSA) was washed with cold acetone and maintained at 4 °C for 1 hour. After this, the solid was centrifuged again during 15 min at 12000 rpm. The protein was dried under vacuum and, finally, dissolved in 0.1 M PBS for the Bradford assay.

Standard curves were carried out using protein dilutions, which were prepared using buffer solution with concentrations of protein ranging from 0.05 to 1.00 mg/mL. Next, 5 µL of protein standards and samples were added to a 96-well plate, blank wells were filled with 5µL of buffer. After this, Bradford reagent (250 µL) was added and, subsequently, mixed on a shaker for 30 s. Samples were incubated at room temperature for 15 min. Finally, the absorbance was measured at 595 nm.

Scanning electron microscopy (SEM): SEM micrographs were obtained using a Focussed Ion Beam Zeiss Neon 40 scanning electron microscope operating at 10 kV. Samples were mounted on a double-side adhesive carbon disc and sputter-coated with a thin layer of carbon to prevent sample charging problems. The projected area and best-fit ellipse aspect ratio of fibrin structures were calculated using ImageJ software.

Optical microscopy: To evaluate the THR-catalysed fibrin particles, samples were washed three times with milliQ water to avoid unspecific bindings. After this, fibrin particles were fixed onto the surface with 300 μL of 2.5% paraformaldehyde in PBS during 30 min at 4 $^{\circ}\text{C}$. Then, samples were progressively dehydrated using alcohols of 30 $^{\circ}$, 40 $^{\circ}$, 50 $^{\circ}$, 70 $^{\circ}$, 95 $^{\circ}$, and 100 $^{\circ}$ for 15 min each at 4 $^{\circ}\text{C}$. Samples were stained with eosin for 30 min. Eosin is a fluorescent acidic compound that binds positively charged molecules (i.e. the isoelectric point of Fg is 5.5, increases to \sim 6.3 after clipping of polar residues in the clotting response by THR). Finally, samples were washed three times again with milliQ water and left on vacuum overnight.

Wettability: Contact angle (CA) measurements were conducted using the water drop method. 0.5 μL of milliQ water drops were deposited onto the surface of the films and recorded after stabilization with the equipment OCA 15EC (DataPhysics Instruments GmbH, Filderstadt). The SCA20 software was used to measure the CA, which is shown here as the average of at least 10 measures for each condition.

Cell capture assays: Substrates were placed into a 24-well plate, and 1 mL of cell MCF-7 (breast cancer cell line), PNT2 (normal prostate epithelial cell line) or PC-3 (cancer prostate epithelial cell line) suspension (10^5 cells/mL) was loaded. After incubation for 30 min at 37 $^{\circ}\text{C}$, 5% CO_2 with slight agitation (80 rpm), the substrates were washed with PBS, located in a new 24-well plate and incubated for 24 hours. The percentage of cells adhered in the substrate with respect to the amount deposited into the well was determined using the MTT [3-(4,5-dimethylthiazol-2-yl)-2,5-diphenyltetrazolium] method. Cell capture assays were repeated two times with at least 4 replicas, showing similar results in all cases.

For the observation of the cell morphology in the SEM, all samples were previously coated with a carbon layer of 6–10 nm thickness using a K950X Turbo Evaporator to prevent sample charging problems. Before the carbon coating, samples covered with cells were fixed in a 2.5% formaldehyde PBS solution (pH = 7.2) overnight at 4 $^{\circ}\text{C}$. Then, they

were dehydrated by washing in an alcohol battery (30°; 50°; 70°; 90°; 95°; and 100°) at 4 °C for 15 min per wash. Finally, samples were air-dried and sputter-coated with carbon.

8.2.2 Results and discussion

PEDOT-peptide characterization

The synthetic approach used in this work to prepare PEDOT (control) and PEDOT-peptide bilayered films is summarized in **Figure 8.2.1**. In order to overcome the fragility of PEDOT-peptide films, an internal PEDOT layer was electrodeposited between the steel and the biocomposite. The average thickness (L) of the internal PEDOT layer was $L = 150 \pm 35$ nm. Bilayered systems containing an external PEDOT, PEDOT-CREKA or PEDOT-CR(MMe)EKA layer deposited onto the internal layer exhibited L values of 340 ± 72 , 573 ± 57 or 498 ± 35 nm, respectively. These L values, which were achieved by depositing the external layer immediately after polymerize the internal PEDOT layer, are considerably smaller than those reported in for bilayered PEDOT-CREKA ($L = 3.8 \pm 1.3$ μm).¹⁸ Thus, in the latter case the apparition of multiple, prominent, and well-localized

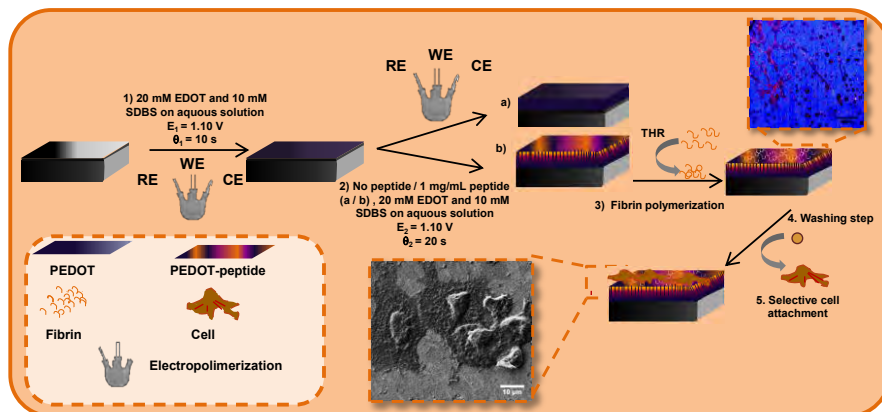


Figure 8.2.1 Scheme displaying the synthetic strategy used to prepare PEDOT (control) and PEDOT-peptide bilayered films (a and b, respectively). The strategy involved a two-step process: (1) deposition of the internal PEDOT layer onto the AISI steel electrode; and (2) deposition of PEDOT (a) or PEDOT-peptide (b) onto the layer prepared in (1). It is worth noting that a and b only differ in the absence or presence of peptide in the generation medium used for step 2. After this, subsequent surface functionalization with fibrin and application as selective bioactive surface are also displayed. RE, WE and CE refer to the reference electrode, working electrode and counter electrode, respectively.

folds homogeneously distributed was promoted by drying during several hours the internal layer before the deposition of the external layer.¹⁸ Accordingly, elimination of the drying process induces significant changes not only in L but also on the properties (see below) despite the experimental conditions used for the anodic polymerization are practically identical.

Comparison of the R_q determined by AFM for the external layer of PEDOT, PEDOT-CREKA or PEDOT-CR(NMe)EKA ($R_q = 74 \pm 9$, 133 ± 23 and 161 ± 11 nm, respectively) indicates that the peptide affects the surface topography (a) (figure 8.2.2). PEDOT's surface can be described as a very homogeneous distribution of small molecular aggregates, which has been associated with the linear growing of polymer chains. Incorporation of CR(NMe)EKA or CREKA into the polymeric matrix provokes a drastic change in the topography that exhibits high and relatively large compact blocks, explaining the enhancement of R_q . These blocks, which result from the aggregation of small clusters over the polymer surface, are essentially induced by the role of the peptide as doping agent. Thus, peptide molecules (individually or forming clusters) embedded into the PEDOT matrix alter the growing of polymer chains, which should perpendicular to the electrode surface. As PEDOT chains tend to grow forming clusters,³⁴ the tilting induced by the peptide facilitates the aggregation of neighboring clusters. These

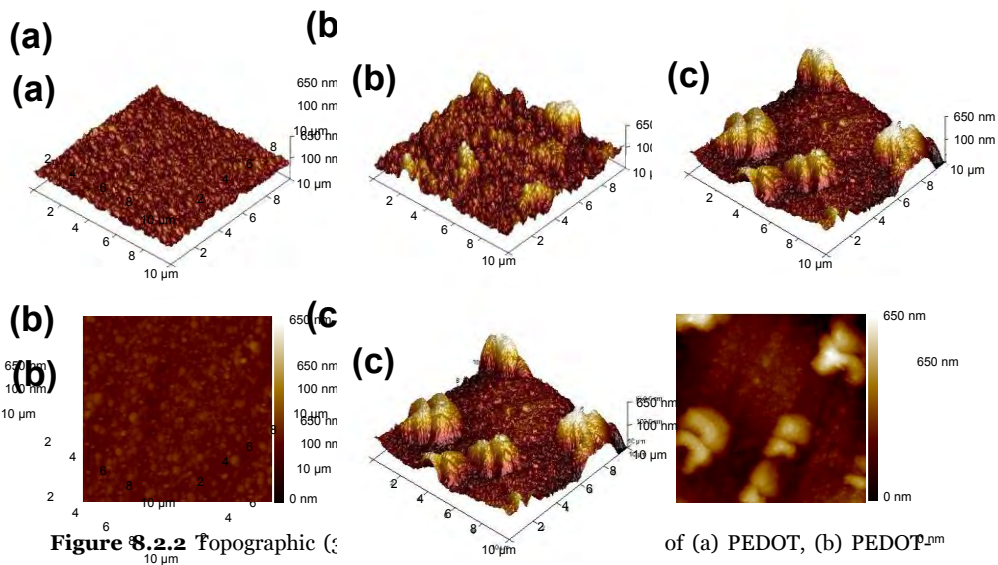


Figure 8.2.2 Topographic images of (a) PEDOT, (b) PEDOT-CREKA and (c) PEDOT-CR(NMe)EKA.

of (a) PEDOT, (b) PEDOT-CREKA and (c) PEDOT-CR(NMe)EKA.

phenomena are more pronounced for PEDOT-CR(NMe)EKA than for PEDOT-CREKA.

PEDOT and PEDOT-peptide composites were characterized by XPS. The atomic percent composition (C 1s, N 1s, O 1s and S 2p) of the three systems are compared in **Table 8.2.1**. As it can be seen, nitrogen was detected in the composition of the three systems. According to the experimental conditions used in this work, the penetration of X-ray radiation is expected to be of ~10 nm. Although the thickness of the bilayered films prepared in this work ranged from ~300 to ~600 nm, examination by SEM revealed some uncoated regions of the steel substrate. Accordingly, the presence of N 1s in PEDOT films has been attributed to the metallic substrate.^{35,36} It is worth noting that the N 1s content increases from 0.47% in PEDOT to 1.20% and 0.92% in PEDOT-CREKA and PEDOT-CR(NMe)EKA, respectively, reflecting the successful incorporation of the peptides.

Assuming that the nitrogen coming from the steel substrate is approximately the same for the three systems, the number of polymer repeat units per peptide molecule in PEDOT-CREKA and PEDOT-CR(NMe)EKA can be roughly estimated using the $S/(N_p - N_s)$ ratio (**Table 8.2.1**), where S is the total percent composition of sulfur atoms and $(N_p - N_s)$ refers to the difference between the total percent composition of nitrogen at PEDOT-peptide and PEDOT.

Table 8.2.1 Atomic percent composition (C 1s, N 1s, O 1s and S 2p) and S 2p / N 1s ratio obtained by XPS for PEDOT, PEDOT-CREKA and PEDOT-CR(NMe)EKA.

#	C 1s	N 1s	O 1s	S 2p	S / N
PEDOT	68.64	0.47	23.82	7.07	-
PEDOT-CREKA	68.57	1.20	23.06	7.17	5.97
PEDOT-CR(NMe)EKA	69.46	0.92	22.74	6.88	7.48

According to this approximation, the content of peptide in PEDOT-CREKA and PEDOT-CR(NMe)EKA is relatively high with one peptide molecule every ~10 and ~15 polymer repeat units, respectively. The smaller content of immobilized peptide molecules in PEDOT-CR(NMe)EKA is due to the increment of the molecular volume provoked by

the *N*-methylation of the Glu residue, which enhanced peptide–polymer steric interactions during the polymerization process.

Figure 8.2.3 displays the high-resolution XPS spectra in the N 1s region, which is crucial to prove the immobilization of the peptide into the ECP matrix, for PEDOT, PEDOT-CREKA and PEDOT-CR(*N*Me)EKA. The peak centered around 402 eV, which was detected in all examined samples including PEDOT ones, is consequence of impurities of the AISI 316 steel (see above).^{35,36} However, the intense peak found at 400.2 eV for both PEDOT-CREKA and PEDOT-CR(*N*Me)EKA corresponds to the peptides. Thus, this peak is typically explained as a combination of the guanidinium (400.1 eV) and the backbone amide (400.5 eV) signals.³⁷ Bhattacharyya and Gleason attributed the presence of N 1s characteristic peaks at 399.7 eV (–NH) and 400.4 eV (N–C=O) to bovine serum albumin attached to the surface of a copolymer of thiophene-3-acetic acid and EDOT.³⁸ Similarly, the XPS N–H signal of Boc-Val-Gly-Gly-Val-Gly-OEt and poly(Val-Gly-Gly-Val-Gly) were identified at 400.0 and 400.2 eV, respectively.³⁹

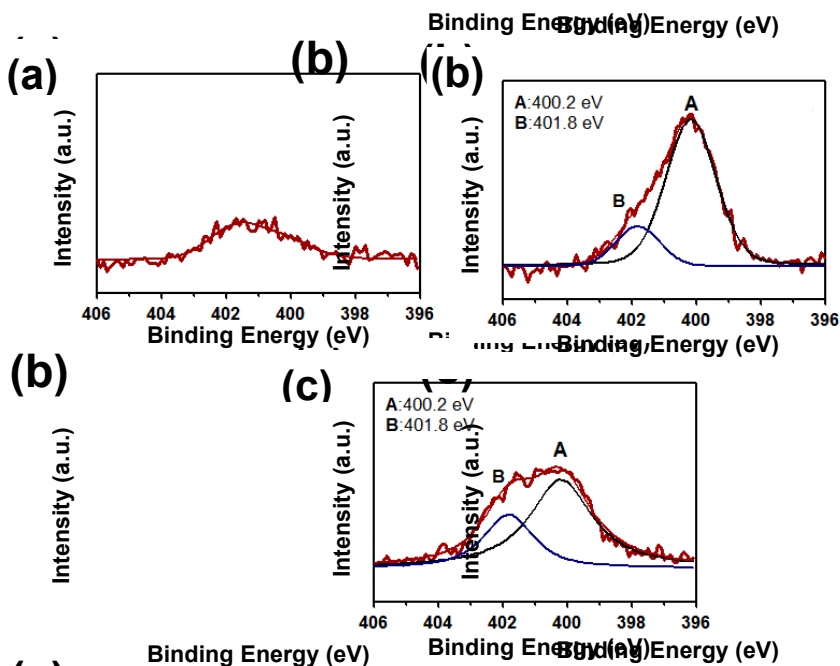


Figure 8.2.3 High-resolution XPS spectra in the N 1s region for (a) PEDOT, (b) PEDOT-CREKA, and (c) PEDOT-CR(*N*Me)EKA. Peaks from deconvolution are also displayed.

Electrochemical properties of PEDOT improve upon the incorporation of the peptide, independently of the chemical modification at the Glu residue. **Figure 8.2.4a** shows that the electroactivity of both PEDOT-peptide systems is around 15% higher than that of PEDOT. These results are consistent with the role of CREKA and CR(NMe)EKA molecules as dopant ions, participating in oxidation and reduction processes. This achievement, which is in marked contrast previous results,¹⁸ is due to the elimination of the drying step before the deposition of the external layer. The presence of the peptide also enhances the electrochemical stability of PEDOT, as is reflected by the control voltammograms recorded after five consecutive oxidation-reduction cycles in PBS (**Figure 8.2.4b**). After such amount of cycles, the electroactivity of PEDOT is lower than that of PEDOT-CREKA and PEDOT-CR(NMe)EKA by 20% and 30%, respectively. Analysis of the LEA (Eq. 8.2.1) shows a reduction of ~15% and 25% for PEDOT-peptide and PEDOT, respectively, after 5 redox cycles (**Figure 8.2.4c**).

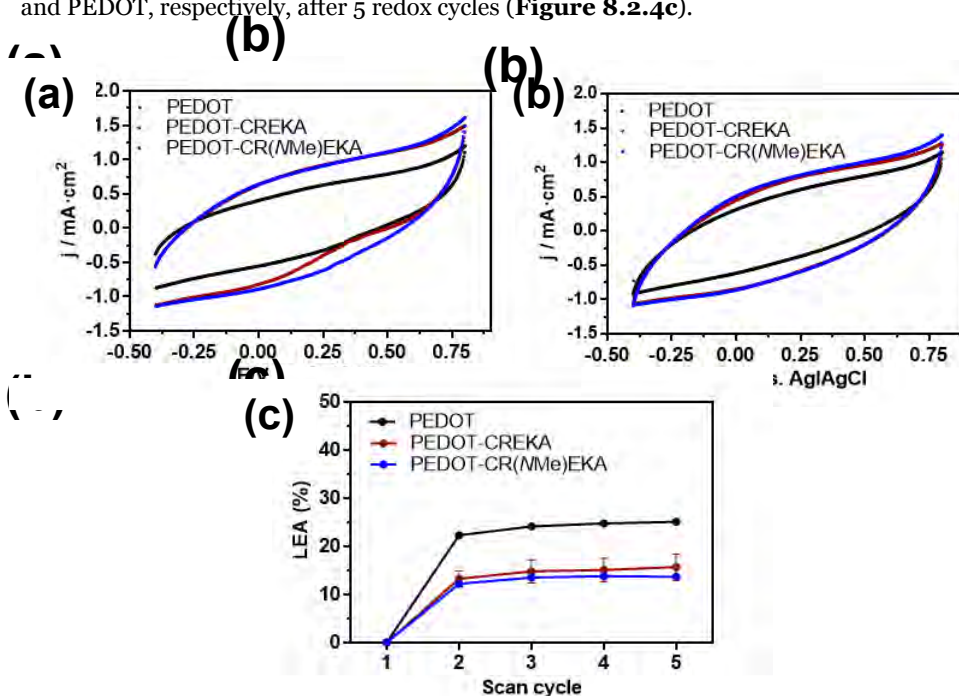


Figure 8.2.4 Initial control voltammogram (a), voltammogram after five consecutive oxidation-reduction cycles (b) and variation of the LEA (Eq. 8.2.1) against the number of redox cycles (c) in 0.1 M PBS (pH= 7.4) of PEDOT, PEDOT-CREKA and PEDOT-CR(NMe)EKA. Initial and final potentials: -0.40 V; reversal potential: 0.80 V. Scan rate: 50 mV/s.

The reduction of the electroactivity with the number of redox cycles is related with the structural degradation of the polymeric matrix that becomes less porous (*i.e.* more compact), making difficult the escape and entrance of dopant ions during the oxidation and reduction processes, respectively. In the case of PEDOT-CREKA and PEDOT-CR(NMe)EKA, the peptides impart protection to the matrix preventing its structural degradation. Although determination of such protection mechanism is not an easy task, our hypothesis is based on a steric protection due to the formation of nanometric and insoluble peptide aggregates inside the polymeric matrix. These could act as structural support avoiding the collapse of the polymeric matrix and maintaining the porosity.

Influence of the peptide in fibrinogen polymerization

The affinity of CR(NMe)EKA towards fibrin has been compared with CREKA. The formation of fibrin networks is the central event in vertebrates blood coagulation^{40,41} and is involved in several pathologies like thrombosis and cancer metastasis.^{41,42} From a physiological point of view, it represents the end of the coagulation cascade when THR activates the inactive precursor Fg.⁴¹⁻⁴⁴ Cleavage and removal of fibrinopeptides from Fg by THR promote the interaction between neighboring fibrin molecules that self-associate to form elongated fibers and fiber networks.^{5,45}

The effect of the peptides on fibrin THR-catalyzed polymerization was assessed at 37 °C by DLS. **Figure 8.2.5** represents the temporal evolution of the effective diameter (D_{eff}) of Fg particles using conditions optimized to examine the early steps in fibrin polymerization⁴⁶ (*i.e.* 0.4 mg/mL Fg aqueous solution containing 5 mM CaCl₂ and 76 mM NaCl). In absence of THR, D_{eff} stabilizes at ~32 nm (**Figure 8.2.5a**) indicating significant restrictions in association process (*i.e.* hydrodynamic radius of Fg is ~13 nm^{47,48}). Instead, D_{eff} grows rapidly and progressively over time upon the incorporation of THR (**Figure 8.2.5a**). The value of D_{eff} reaches a plateau after 55 min at approximately 2.5 μ m, which corresponds to the THR-induced fibrin polymerization.⁵

The influence of CREKA and CR(NMe)KA in fibrin polymerization was studied by adding each peptide to Fg aqueous solutions with and without THR (Figure 8.2.5b and 5c). In absence of enzyme, the increase of D_{eff} reflects that the two peptides promote the aggregation of Fg, even though quantitative differences in the aggregation mechanism are revealed. CREKA induces a sustained linear increase of D_{eff} , which grows from ~45 nm ($t=1$ min) to ~191 nm

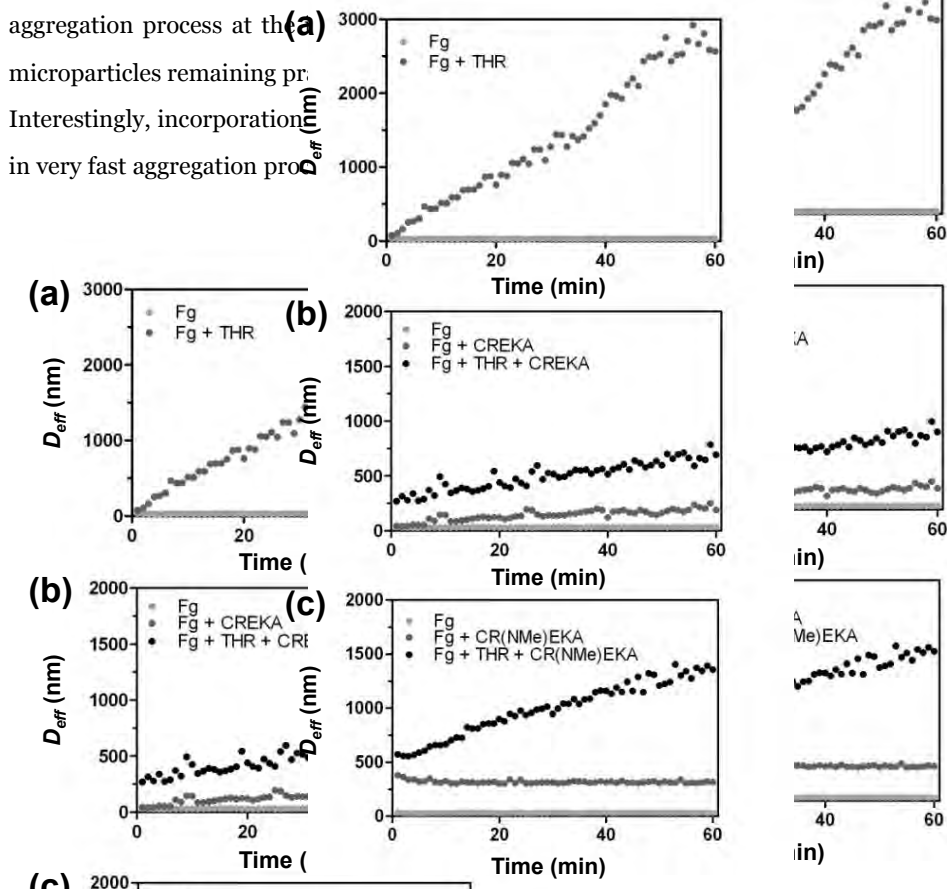


Figure 8.2.5 (a) THR-catalyzed polymerization of Fg monitored by DLS. Polymerization was initiated by adding THR (0.01 U/mL) to a Fg (0.4 mg/mL) filtered aqueous solution (5 mM CaCl₂ and 76 mM NaCl). These experimental conditions were taken from reference.⁴⁶ Polymer formation was measured through the the effective diameter (D_{eff} , in nm) as a function of time (in min). CREKA (b) and CR(NMe)KA (c) were added (0.1 mg/mL) to the same Fg solutions with and without THR to evaluate the influence of the peptide in the polymerization process. In all cases data correspond to the average of at least three independent experiments.

~271 and ~574 nm for CREKA and CR(NMe)EKA, respectively. After this initial stage, the size of particles progressively increased, even though the peptide largely influenced the growth rate. In the case of CREKA the growth rate of the particles (6.9 ± 0.3 nm/min from **Figure 8.2.5b**) decreased considerably with respect to the same solution without peptide (50.5 ± 1.8 nm/min from **Figure 8.2.5a**). After a linear growth regime, D_{eff} stabilized around ~712 nm, which represents a reduction of around 72 % with respect to the value obtained for the same solution but without CREKA. After a very fast formation stage, the growth rate of the particles formed in presence of CR(NMe)EKA progressively increases (14.1 ± 0.3 nm/min from **Figure 8.2.4c**), stabilizing at $D_{eff} \approx 1343$ nm after 55 min. Accordingly, both peptides disturb the THR-induced fibrin polymerization, even though such effect is significantly more pronounced for CREKA.

In an early work, Carr *et al.*⁴⁹ proved that positively charged poly(α -amino acid)s enhance lateral association of fibrin protofibrils during fiber bundling. This phenomenon was attributed to the charge and isoelectric point of such polypeptides. High pKa values facilitated strong interaction between the protofibrils and the poly(α -amino acid), independently of the molecular weight, promoting fibrin polymerization, as was evidenced by the increase of fibrin fibers diameter.⁴⁹ In contrast, no effect was observed for negatively charged poly(α -amino acid)s. Both CREKA and CR(NMe)EKA have an isoelectric point of 8.55 and, therefore, they are positively charged at working pH (7.4). Accordingly, such peptides could promote the lateral assembly of fibrin protofibrils, reducing the elongation capability of fibers, as suggested in **Figure 8.2.5**.

Adsorption of fibrin onto PEDOT-peptide films

The selective adsorption of fibrin by PEDOT-peptide biocomposites has been examined by comparing with the adsorption of BSA, which is a globular plasma protein. Results indicate that the affinity of PEDOT-CREKA and PEDOT-CR(NMe)EKA toward fibrin fibers was ~2.5 and ~6 times higher than that of PEDOT (**Figure 8.2.6**), respectively. Thus, ~6%, ~14% and ~37% of the fibrin from the initial solution was adsorbed onto PEDOT, PEDOT-CREKA and PEDOT-CR(NMe)EKA, respectively. In contrast, the adsorbed BSA was very scarce (*i.e.* ~8% for PEDOT-CR(NMe)EKA and

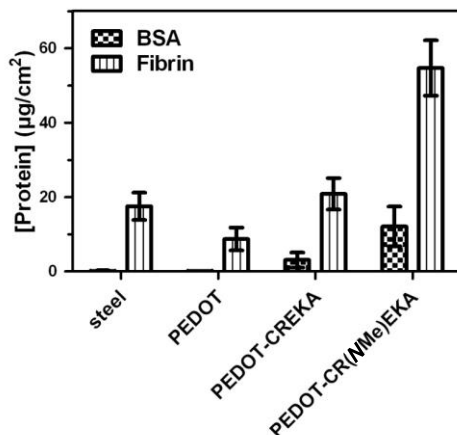


Figure 8.2.6 Adsorption of fibrin and BSA onto the surface of PEDOT and PEDOT-peptide films. Four samples were analysed for each group. Bars represent the mean \pm standard deviation.

lower than 2% for PEDOT and PEDOT-CREKA). The selectivity of PEDOT-CR(NMe)EKA towards fibrin suggests that the distribution of the charged groups in this biocomposite is appropriated for the adsorption of fibrin despite the loss of its fibrous structure (see below). However, such distribution is much less suitable for the adsorption of globular proteins, like BSA, in which polar groups are expected to be randomly distributed.

The morphology of fibrin adsorbed onto PEDOT-peptide films was studied by SEM (**Figure 8.2.7**). For this purpose, the THR-catalyzed polymerization of Fg was stopped after 60 min by the addition of formaldehyde⁴⁶ (2.5%) and, subsequently, dehydrated using 30%, 40%, 70%, 90% and 100% ethanol solutions. Amazingly, the formaldehyde-fixed fibrin onto PEDOT-peptide surfaces does not exhibit the expected mesh of fibers (see below)^{49,50} but forms agglomerates of micrometric dimensions with very varied morphologies

Thus, agglomerates of fibrin adsorbed onto PEDOT-CREKA (**Figure 8.2.7a**) were relatively small (1-4 μm) and displayed different round-like morphologies, including the spherical one. In contrast, fibrin adsorbed onto PEDOT-CR(NMe)EKA presents a larger variety of morphologies, including fiber-like, round-like and completely irregular ones

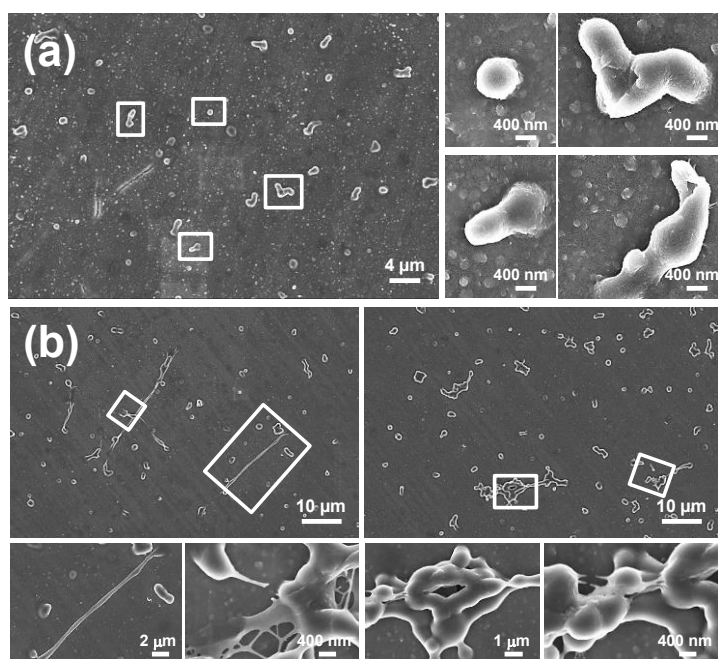


Figure 8.2.7 Low and high resolution SEM images of fibrin particles adsorbed onto (a) PEDOT-CREKA and (b) PEDOT-CR(MMe)EKA. White boxes in (a) and (b) indicate the magnified regions.

(**Figure 8.2.7b**). As the elongated fiber-like morphologies were relatively infrequent and isolated rather than immersed into a mesh, they have been related with structures formed without the participation of the peptide. Furthermore, fibrin aggregates adsorbed onto PEDOT-CR(MMe)EKA are typically bigger than those deposited onto PEDOT-CREKA. Overall, results suggest that the round-like and irregular morphologies of fibrin adsorbed onto PEDOT-peptide are controlled by the fast aggregation processes occurring at early stages of the polymerization process, which is consistent with the DLS observations (**Figure 8.2.5**). The area and aspect ratio (AR), which is defined by the ratio between length and diameter, of the morphologies observed for the 60 min formaldehyde-fixed products, were determined with the ImageJ software using SEM micrographs. Results indicate that the distribution of both areas and AR (**Figure 8.2.8**) are influenced by the peptide. Thus, 6% of structures formed onto PEDOT-CR(MMe)EKA shows an area higher than $10 \mu\text{m}^2$, such amount being imperceptible for PEDOT-CREKA.

Moreover, 8.8% and 20.3% of the structures formed onto PEDOT-CREKA and PEDOT-CR(MMe)KA, respectively, exhibit an AR > 2.0, reflecting the sporadic formation of isolated fibril-like structures in the latter (**Figure 8.2.7b**).

In order to further confirm the presence of fibrin onto PEDOT-peptide surfaces, the two biocomposites together with steel and PEDOT were stained with eosin. **Figure 8.2.9** compares optical microscopy images of red colored fibrin polymerized with THR during 60 min. Although fibrin is apparently able to bind all tested surfaces, differences in the amount of adsorbed proteins indicate a certain degree of selectivity. Thus, a typical intertwined mesh of long fibers oriented in multiple directions is observed when fibrin is deposited onto bare steel (**Figure 8.2.9a**). PEDOT affects drastically the fibrin morphology, inducing the formation of small and rounded-like agglomerates after 60 min (**Figure 8.2.9b**). The abundance of these aggregates is very scarce in comparison to those adsorbed onto steel, which is fully consistent with Bradford protein assays (**Figure 8.2.6**). Thus, the adsorption and morphology of fibrin is largely influenced by the roughness and/or chemical nature of the substrate. Dolatshahi-Pirouz *et al.*⁵⁰ showed that fibrin polymerization and, therefore, fibrillation are slower on flat than on rough surfaces. Nevertheless, steel ($R_q = 5 \pm 2$ nm) is flatter than bilayered PEDOT films ($R_q = 74 \pm 9$ nm), evidencing that the chemical nature of the surface is also regulating fibrin

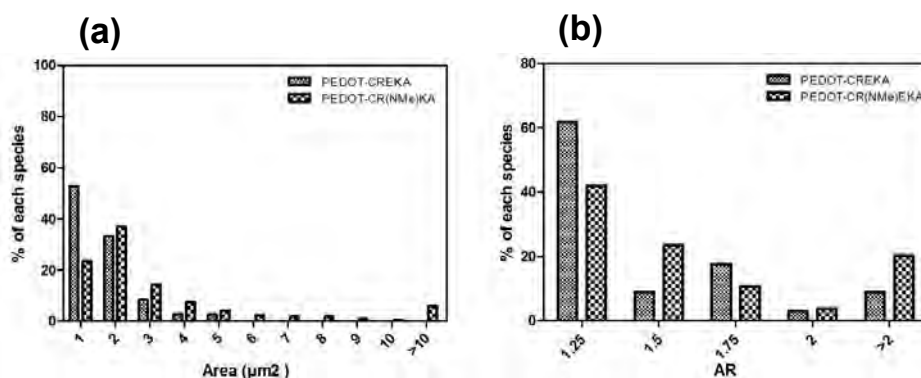


Figure 8.2.8 Quantitative assessment of the fibrin particles adsorbed onto PEDOT-CREKA and PEDOT-CR(MMe)KA surfaces. Histogram showing the percentage of (a) the area and (b) the aspect ratio (AR) of the adsorbed fibrin structures after 60 min of the addition of THR and Fig.

polymerization and morphology. The chemical nature influence is apparently reflected by the surface hydrophilicity, which is considerably higher for PEDOT and PEDOT-peptide than for steel (**Table 8.2.2**).

The hydrophilicity of PEDOT-peptide is similar to that of PEDOT (**Table 8.2.2**), even though the roughness is higher for the formers ($R_q = 133 \pm 23$ and 161 ± 11 nm for PEDOT-CREKA and PEDOT-CR(MMe)EKA, respectively) than for the latter ($R_q = 74 \pm 9$ nm). Microscopy images displayed in **Figure 8.2.9b-d** indicate that the fibrin polymerization rate onto PEDOT-containing surfaces increases with the roughness, which is in agreement with the findings of Dolatshahi-Pirouz *et al.*⁵⁰ Thus, the amount of adsorbed fibrin increases as follows: PEDOT < PEDOT-CREKA < PEDOT-CR(MMe)EKA.

Comparison between the CAs for the different surfaces without and with adsorbed fibrin reveals differences in the wettability (**Table 8.2.2**), especially for PEDOT and PEDOT-peptide systems. Thus, the highly hydrophilic character of such CP and its two biocomposites ($CA < 20^\circ$) transforms into hydrophobic ($CA > 90^\circ$) upon the adsorption of fibrin particles. This effect is much less pronounced for steel. The transformation of Fg into fibrin was reported to be accompanied by a change in the wettability from very

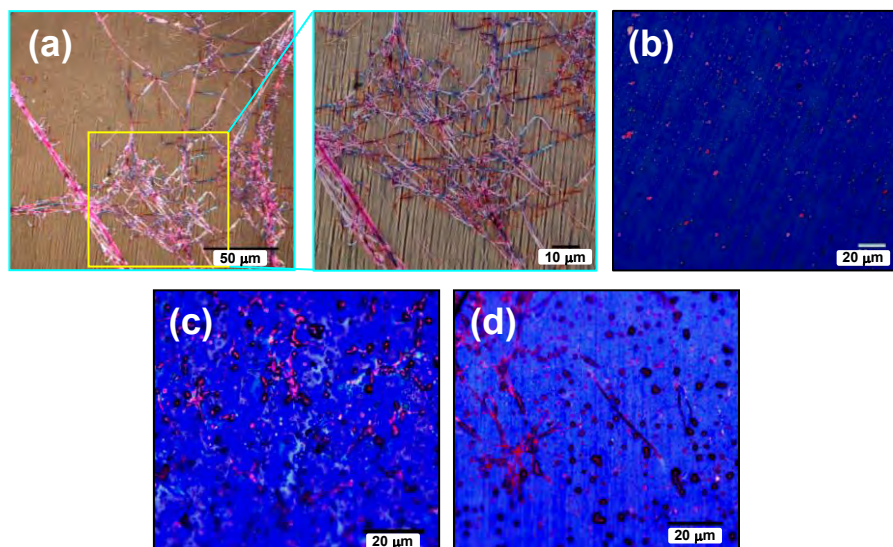


Figure 8.2.9 Optical images of eosin stained fibrin adsorbed on (a) steel, (b) PEDOT, (c) PEDOT-CREKA and (d) PEDOT-CR(MMe)EKA.

hydrophilic (Fg) to moderately but definitely hydrophobic (fibrin).⁵¹

Table 8.2.2 Contact angle (CA) determined for the surfaces examined in this work before and after adsorption of fibrin.

Surface	CA
Steel	68°±5°
PEDOT	< 20°
PEDOT-CREKA	< 20°
PEDOT-CR(NMe)EKA	< 20°
Steel / fibrin	94°±4°
PEDOT / fibrin	112°±1°
PEDOT-CREKA / fibrin	114°±2°
PEDOT-CR(NMe)EKA / fibrin	107°±4°

Influence of fibrin in PEDOT-peptide electrochemical and electrical properties

CVs of PEDOT and PEDOT-peptide films coated with fibrin are displayed in **Figure 8.2.10**. Comparison with those reported in **Figure 8.2.4a** indicates that the adsorbed protein affects negatively the electrochemical response of both the ICP and the biocomposites. More specifically, the adsorption of fibrin reduces the electroactivity of PEDOT, PEDOT-CREKA and PEDOT-CR(NMe)EKA by 35%, 50% and 51%, respectively. The adsorbed protein also affects negatively to the electrochemical stability of the two biocomposites.

Thus, after only 5 consecutive redox cycles, the LEA is 18%, 22% and 25% for PEDOT, PEDOT-CREKA and PEDOT-CR(NMe)EKA, respectively. Accordingly, the behavior of the biocomposites relative to the ICP is in terms of electrostability the opposite that the one displayed in absence of fibrin (**Figure 8.2.4b**). These results should be attributed to the combination of two related effects: (i) the amount of protein at the surface of the biocomposites is considerably higher than at the surface of PEDOT; and (ii) protein aggregates are more compact than polymeric and biocomposite matrices. Accordingly, the exchange of ions between the matrix and the PBS electrolytic medium during redox processes is more difficult at regions covered by the protein, which are more abundant at the biocomposites than at PEDOT.

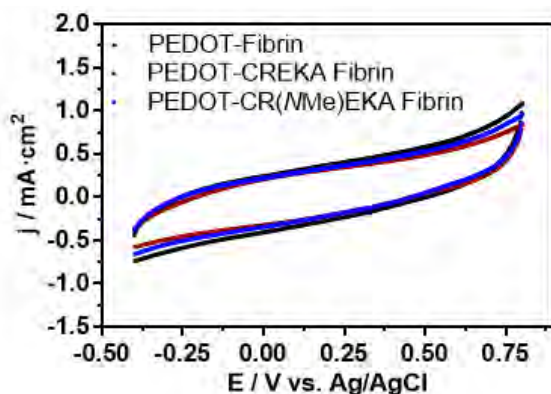


Figure 8.2.10 Control voltammograms in 0.1 M PBS (pH= 7.4) of fibrin-coated PEDOT, PEDOT-CREKA and PEDOT-CR(NMe)EKA films. Initial and final potentials: -0.40 V; reversal potential: 0.80 V. Scan rate: 50 mV/s.

A similar behaviour was observed by EIS analyses. The electrode impedance is related to the interfacial surface area between the electrode and electrolyte.

The bare metal only exhibits a low double layer capacitance (CPE_{dl}) and a high polarization resistance coming from the interaction between the ions of the electrolytic medium (PBS) and the heterogeneous steel surface (R_p) (**Figure 8.2.11a**). On the other hand, the impedance of the electrodes covered with a semiconducting material is more complex and other time constants can appear due to several interfaces. More specifically, the impedance of PEDOT-coated electrodes decreases three orders of magnitude with respect to the bare metal across frequencies between 0.01–10 Hz, which correspond to the zone of the coating resistance. This must be attributed, at least partially, to an increase in the effective surface area, which is provided by the porous PEDOT electrode. The coating resistance (R_c), which is identified from the first diameter of the semicircle in the Nyquist plots (**Figure 8.2.12**), describes the resistance for transferring the electrons from the PBS ions to the conducting polymer film. The diffusion of ions across the films is enhanced upon the incorporation of peptide to PEDOT, leading to lower R_c values (**Table 8.2.3**). The R_c of fibrin-coated PEDOT-peptide films is higher than that of biocomposites without fibrin (**Table 8.2.3**) since the protein aggregates block the pores (*i.e.* barrier effect). This behaviour is more pronounced for PEDOT-CR(NMe)KA, supporting that fibrin interacts more favourably with CR(NMe)KA than with CREKA.

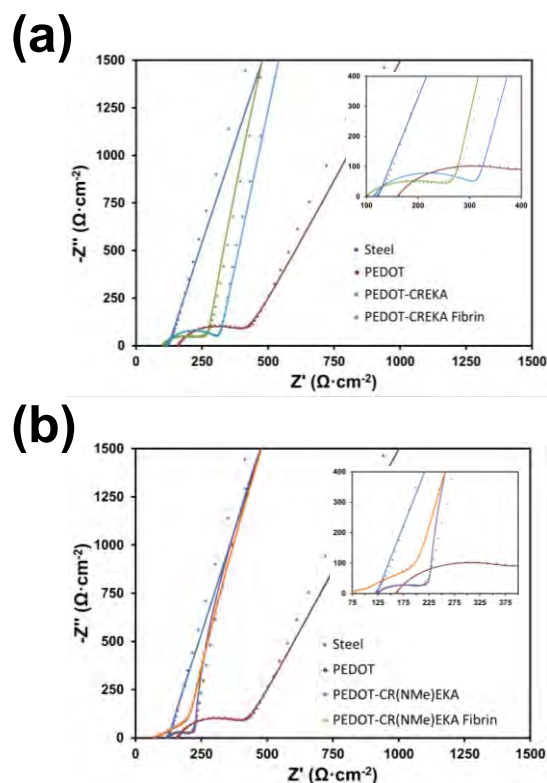


Figure 8.2.12 Nyquist plots for all stainless steel electrodes coated with (a) PEDOT-CREKA and (b) PEDOT-CR(NMe)EKA without and with fibrin adsorbed at the surface.

Furthermore, another constant phase element (CPE_{diff} , with $n=0.90$) is required to model the response of PEDOT-CR(NMe)EKA with fibrin (**Figure 8.2.12b**). This is probably due to favourable fibrin-peptide interactions, which cause a slow diffusion of ions at very low frequency range. The best-fit values for the adjusted resistances and capacitances are listed in **Table 8.2.3**

Table 8.2.3 Resistances and constant phase for each sample analysed with EIS technique and after adjusting the parameters using the EEC shown in **Figure 8.2.11b**.

Sample	R_s ^{a)}	R_c ^{b)}	CPE_c ^{c)}	n	R_p ^{d)}	CPE_{dl} ^{e)}	n	CPE_{dif} ^{f)}	n
	($\Omega \cdot \text{cm}^2$)	($\Omega \cdot \text{cm}^2$)	($\text{F cm}^{-2} \text{s}^{n-1}$)		($\Omega \cdot \text{cm}^2$)	($\text{F cm}^{-2} \text{s}^{n-1}$)		($\text{F cm}^{-2} \text{s}^{n-1}$)	
Stainless steel (bare)	123	-	-	-	594k ^{g)}	3.85×10^{-5}	0.85	-	-
PEDOT	162	267	4.03×10^{-5}	0.83	-	1.08×10^{-3}	0.76	-	-
PEDOT-CREKA	100	188	1.00×10^{-4}	0.74	-	1.12×10^{-3}	0.93	-	-
PEDOT-CREKA with fibrin	155	209	3.49×10^{-5}	0.73	-	1.23×10^{-3}	0.91	-	-
PEDOT-CR(NMe)EKA	119	128	2.29×10^{-4}	0.54	-	0.82×10^{-3}	1.00	-	-
PEDOT-CR(NMe)EKA with fibrin	97	294	6.30×10^{-4}	0.63	138 ^{h)}	0.87×10^{-3}	1.00	2.25×10^{-4}	0.90

^{a)} R_s = solution resistance, ^{b)} R_c = Coating resistance, ^{c)} CPE_c = coating capacitance, ^{d)} R_p = polarization resistance, ^{e)} CPE_{dl} = double layer capacitance ^{f)} CPE_{dif} = diffusion capacitance, ^{g)} Value of resistance for the stainless steel bare (without conducting polymer) is attributed to the polarization resistance (R_p) in the electrode/electrolyte interface at low frequency. ^{h)} This parameter is better related to the R_{dif} = ion diffusion resistance across the film (see the last EEC in **Figure 8.2.11b**).

Cell capture selectivity: tumor versus normal cells

PEDOT and PEDOT-peptide samples have been used to investigate the effect of fibrin adsorption on cell capturing with MCF-7 cells (breast cancer cell line). Results, which are displayed in **Figure 8.2.13a**, clearly indicate that MCF-7 cells are captured more efficiently by the biocomposites than by PEDOT. Moreover, the highest cell viability was obtained for PEDOT-CR(NMe)EKA coated with fibrin evidencing that such ECP-peptide-protein biocomposite is a very promising material for biomedical applications. Representative SEM micrographs of cells adhered to PEDOT-CR(NMe)EKA without and with fibrin are displayed in **Figures 8.2.13b-c**, respectively.

On the other hand, the ability of PEDOT-peptide biocomposites to differentiate between tumor and normal cells was examined by conducting cell attachment assays using normal (PNT2) and metastatic (PC-3) prostate epithelial cell lines. Results displayed in **Figure 8.2.13d** indicate that the amount of normal and tumor attached cells is practically the same for the two uncoated biocomposites, no clear preference being exhibited. Moreover, the influence of the peptide is practically negligible since the cell attachment was practically the same for PEDOT and PEDOT-peptide films. However, assays considering biocomposite films coated with fibrin reveal not only an enhancement of cell attachment but also of cell identification (**Figure 8.2.13d**), *i.e.* normal cells *vs* tumor cells. Thus, both PEDOT-CREKA and PEDOT-CR(NMe)EKA films with adsorbed fibrin promoted the adhesion of tumor cells with respect to normal cells by around 12%. Moreover, the capture of PNT2 cells is slightly less efficient for biocomposites with adsorbed fibrin than without such protein. Overall results suggest that cell capture selectivity depends on a balance between different factors, which include surface roughness and morphology in addition to chemical structure.

SEM micrographs of PC3 cells adhered onto non-coated PEDOT films and fibrin-coated PEDOT-CR(NMe)EKA are displayed in **Figures 8.2.13e** and **8.2.13f**, respectively. The former ICP-peptide-protein composite promotes cell attachment, as is clearly reflected by both the formation of multiple inter-cell connections and a very homogeneous spreading of the adhered cells. These features are less evident in **Figure 8.2.13e**, which exhibits not only a lower number of cells but also much less connections.

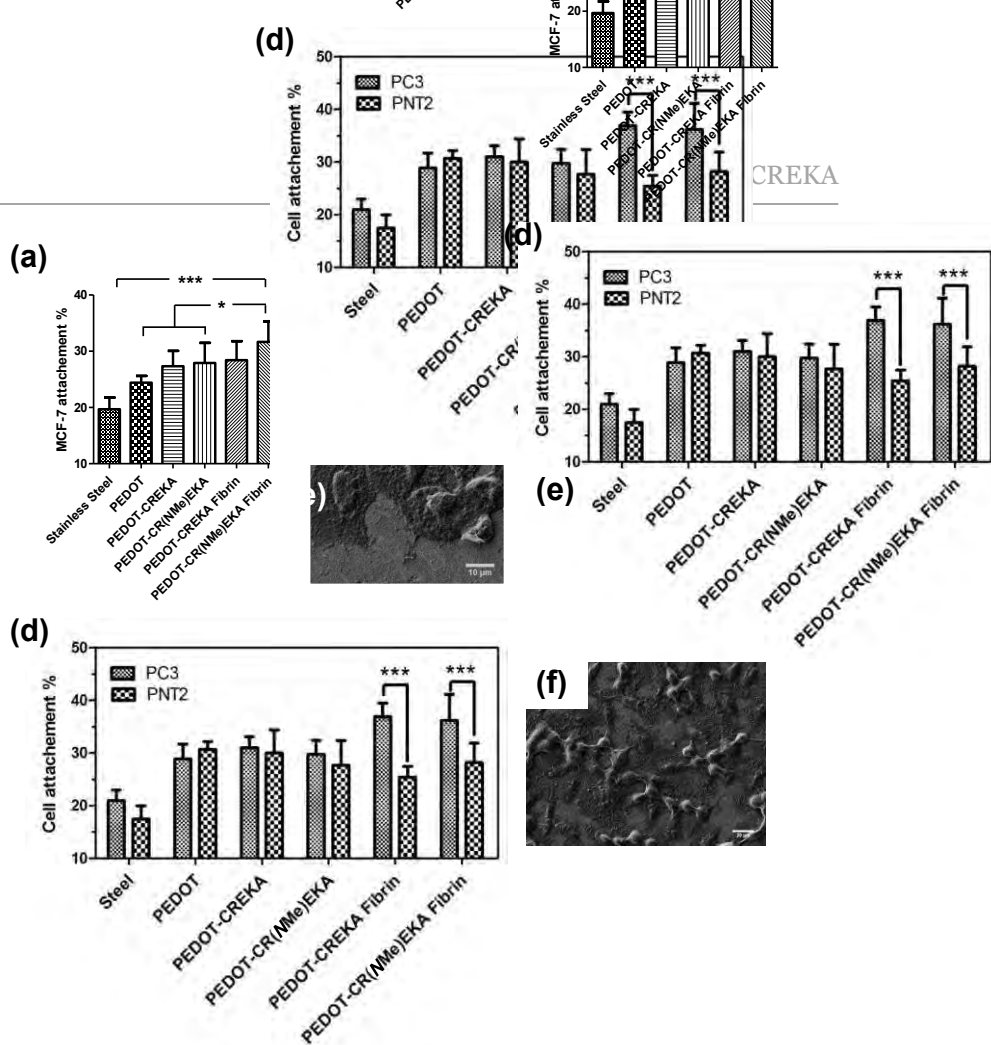


Figure 8.2.13 (a) Percentage of MCF-7 cells attached to different surfaces: bare steel, PEDOT, biocomposites, and biocomposites coated with fibrin. In all cases data correspond to the average of five independent assays \pm the standard deviation. Asterisk marks (*) and (***) represent significant difference among the samples at $p < 0.05$ and $p < 0.001$, respectively. SEM micrographs of MCF-7 cells onto PEDOT-CR(NMe)EKA films (b) without and (c) with adsorbed fibrin at the surface. (d) Comparison of the percentage of normal (PNT2) and metastatic (PC3) prostate epithelial cells attached to different surfaces. The description of both the surfaces and the marks is identical to that given for (a). SEM micrographs of PC-3 cells onto (e) PEDOT films and (f) PEDOT-CR(NMe)EKA. Scale bar: 20 μm .

8.2.3 Conclusions

PEDOT-peptide biocomposites have been prepared by chronoamperometry in basic aqueous solution. The electrochemical and electrical response of the resulting biocomposites is significantly better than that of the ECP in terms of electroactivity, electrostability and electrical conductivity. Such improvement suggests that peptide molecules play simultaneously two roles acting, on one side, as dopant agents that participate actively in oxidation and reduction processes and, on the other side, as structural supports that preclude the degradation of the ECP during redox processes. The replacement of Glu by *N*Me-Glu in the peptide alters the surface topology of the biocomposite, entrapped CR(*N*Me)EKA forming bigger aggregates than CREKA.

Both CREKA and CR(*N*Me)EKA affect the fibrin THR-catalyzed polymerization inducing a very fast aggregation process. However, in absence of catalytic enzyme such fast aggregation phenomenon is only promoted by CR(*N*Me)KA, whereas CREKA induces a stepwise linear grow of fibrin particles. This behavior is fully consistent with the ability of the different materials to adsorb fibrin at the surface, which grows in the following way: PEDOT < PEDOT-CREKA < PEDOT-CR(*N*Me)EKA. The two PEDOT-peptide biocomposites, which adsorb selectively fibrin, transform the shape of the adsorbed protein from the typical mesh of fibers to agglomerates with different round-like morphologies. This remarkable change has been attributed to the fact that the morphology of fibrin adsorbed onto the biocomposites is kinetically controlled through the very rapid aggregation process detected at the early stages of the Fg polymerization.

Cell adhesion assays have evidenced that PEDOT-peptide-fibrin films promote the attachment of metastatic cells with respect to that of normal cells. However, this clearly manifested selectivity towards tumor cells is lost in absence of the fibrin coating. The overall of the results obtained in this work for PEDOT-CR(*N*Me)EKA films are currently used to develop new biomedical applications based on hollow nano- and microspheres of such biocomposite.

8.3 Weighing biointeractions between fibrin(ogen) and clot-binding peptides using microcantilever sensors

Cancer, which represents the leading cause of morbidity and mortality worldwide (*i.e.* 14 million new cases and 8.2 million cancer related deaths in 2012, the latter year in which information is available,⁵² requires detection at an early stage to increase the percentage of success of the oncological treatment. Within this context, molecular imaging, which is based on tumor-specific molecular ligands with high binding affinity, plays a central role in cancer detection in conjugation with conventional anatomic clinical imaging techniques (*e.g.* computed x-ray tomography, magnetic resonance imaging, or ultrasound).⁵³ Hence, molecular imaging not only provides molecular and physiological information that reveals the presence of cancer in a curable stage, but also it is expected to allow for individualized treatment in real time and drug development.⁵³

As reviewed by Li and Cho,⁵⁴ tumor-homing peptides are promising agents to deliver drugs and imaging contrast to tumor sites due to their features⁵⁵: improved tissue penetrating ability (*i.e.* they have a smaller molecular weight - less than 50 amino acids in average - than traditional molecular targeting agents, which include antibodies or their fragments), low immunogenicity, high affinity to targets, as well as stability *in vivo* and easy of handling during synthetic preparation.⁵⁶⁻⁵⁸ For instance, Arg-Gly-Asp (RGD) and Asn-Gly-Arg (NGR), which are two of the most widely used peptides targeting tumor vascularity (*i.e.* formation of new blood vessels - tumor angiogenesis - during tumor growth and progression), have also been applied to deliver anticancer drugs (*e.g.* chemotherapeutic drugs, cytokines, toxins, nucleic acids, radioactive isotopes, *etc.*).⁵⁹⁻⁶² Recently, other novel peptides targeting tumor neovasculature have been reported and tested, such as SVSVGMPKSPRP (SP5-52; several tumor types tested),⁶³ CGKRK and CDTRL (HPV16-induced skin carcinoma and breast carcinoma),³ CKAAKNK (KAA) and CKGAKAR (KAR) (pancreatic tumors),⁶⁴ or IFLLWQR (IF7; melanoma and colorectal cancer).¹⁵

Among those, Cys-Arg-Glu-Lys-Ala (CREKA), which is a linear pentapeptide recognizing clotted plasma proteins in the blood vessels and stroma of tumors,¹ was identified using *in vivo* screening of phage-display peptide libraries^{1-3,64,65} and has been

the focus of recent studies.^{6,7} Although the exact site of binding remains unknown, evidences strongly suggest that CREKA interacts with fibrin-fibronectin complexes present in tumor vessels.⁶ CREKA has targeted different tumor types (*i.e.* prostate cancer, gliomas, and lung cancer),^{11,66,67} and it has also induced tumor clotting, thus creating further binding sites in a self-amplifying effect.¹¹ However, as stated by Stefanelli and Baker,⁶⁸ CREKA's specific binding affinity has not been reported yet.

The excellent electrochemical properties displayed by PEDOT were retained when combined with CREKA and even improved when using the *N*-methyl variant. Moreover, the presence of *N*-methyl-Glu was found to modify the biocomposite-fibrin interactions, being fibrin-coated PEDOT-CR(*N*Me)EKA able to promote the adhesion of tumor cells.⁶⁹

During the last years, the application of nanomechanical sensing for biological purposes⁷⁰ has increased considerably, as the review by Calleja *et al.* clearly evidences⁷¹. Briefly, this technology is based on the microcantilever mechanical response after interacting with a biological analyte, either as a deformation-bending (static mode) or a resonance frequency shift (dynamic mode)⁷². However, despite the fact that this biodetection tool is still far from being a practical alternative to other well established bioanalytical techniques (*e.g.* ELISA, microarrays and electrophoresis methods), nanomechanical sensors display other advantages (*e.g.* manageability, easy of synthesis and functionalization, and high intrinsic sensitivity)⁷³, that make them suitable for specific biomedical purposes: drug detection,⁷⁴ quantification of biological agents,^{75,76} as well as understanding biological interactions,⁷⁷ and detecting bacterial resistance to antibiotics.⁷⁸ Additionally, nanomechanical sensors achieve lower limits of detection than those obtained with other commonly used non-labeled techniques, such as surface plasmon resonance or quartz crystal microbalance.⁷⁹ For example, Kosaka *et al.* detected ultralow concentrations (*i.e.* ranging from 10 ag/mL to 1 pg/mL in undiluted serum) of two low-abundant cancer biomarkers using microcantilevers as nanomechanical transducers in sandwich bioassays labelled with gold nanoparticles (NPs).⁷⁵ Similarly, highly crystalline TiO₂ shells on magnetic cores were applied onto microcantilever sensors to detect very low concentrations (0.1 pg/mL) of multiple protein biomarkers in human serum.⁷⁶ Some recent reviews highlight the mechanical phenomena that occur in

suspended mechanical structures when either biological adsorption or interactions take place on their surface.^{80,81}

Within this context, and considering that CREKA-based biocomposites behave as excellent candidates to be applied for biomedical purposes, it seems of major importance to make an effort in understanding the biological interactions that the tumor-homing peptide CR(NMe)EKA establishes. Accordingly, this work aims on detecting biomolecular recognition events between CR(NMe)EKA-functionalized microcantilever arrays and fibrin (Fb), fibrinogen (Fg), or bovine serum albumin (BSA) by means of nanomechanical sensing and, if possibly, quantitatively determine the detection limit. The modified pentapeptide has been covalently attached to Si surfaces *via* epoxysilane chemistry. Thus, to ensure an efficient surface immobilization, each step of the functionalization process has been characterized by a wide range of techniques. Finally, dynamic mode tests have evidenced changes in the resonance frequency of the cantilevers according to the adsorbed mass.

8.3.1 Methods

Materials: single side polished Si wafers (3 in. diam. × 0.5 mm thickness, <100>, N-type, crystalline with a cubic lattice of $a = 5.4037 \text{ \AA}$) were purchased from Sigma-Aldrich, while Octosensis Microcantilever-Arrays (chips with 8 mono crystalline Si cantilevers, 500 μm in length) were obtained from Micromotive GmbH (Mainz, Germany). CREKA and CR(NMe)EKA peptides with > 98% of HPLC purity were purchased from Biomatik (Toronto, ON). The following chemicals were purchased from Sigma-Aldrich and used as received without further purification: isopropanol, (3-glycidyloxypropyl)trimethoxysilane (98%, SigmaAldrich), toluene (99.8%), N^{α},N^{α} -bis(carboxymethyl)-L-lysine hydrate (NTA-NH₂) (97%), 1-[(3-dimethylamino)propyl]-3-ethylcarbodiimide methiodide (EDC), *N*-hydroxysuccinimide (NHS), 2-(*N*-morpholino)ethanesulfonic acid (MES), 2-amino-2-(hydroxymethyl)-1,3-propanediol (Tris base), 3,3',5,5'-tetramethylbenzidine (TMB) ($\geq 99\%$), carbonate/bicarbonate buffer, phosphate buffered saline (PBS, pH 7.4), BSA (lyophilized powder, crystallized, $\geq 98.0\%$), Tween® 20, and Fg and Fb from human plasma. Sodium chloride was

purchased from Panreac (Spain). Finally, the primary (anti-Fib/Fg, mouse monoclonal IgM, MFB-HB) and the conjugate antibodies (anti-Mouse IgM secondary ab, HRP conjugated, Goat IgG polyclonal) used in ELISA tests were purchased from ThermoFisher Scientific.

Silicon functionalization: the functionalization protocol, which was applied to Si substrates (either Si pieces or microcantilever chips) was composed of different steps:

- 1) *Cleaning.* Si disks were cut into 0.5×0.5 cm² pieces. Before being functionalized, Si pieces and microcantilevers were activated by UV/ozone treatment. Specifically, samples were washed 3 times (5 min each) with isopropanol and placed in a UVO-Cleaner (model 42-220, Jelight Company, Inc., Irvine, CA, USA) for 30 min. Samples were stored under vacuum.
- 2) *Silanization.* Activated samples were silanized with 0.2% solution of (3-glycidyloxypropyl)trimethoxysilane in dry toluene overnight at room temperature under nitrogen atmosphere. Afterwards, samples were washed with toluene and milli-Q water. Then, they were incubated into 100 mM NTA-NH₂ solution in 50 mM carbonate buffer (pH 9.5) overnight at room temperature under gentle agitation. Later, Si substrates were washed with 50 mM carbonate buffer pH 9.5 and milli-Q water.
- 3) *Activation.* In this step, the carboxyl groups of NTA-NH₂ at the Si surface were activated for direct reaction with primary amines via amide bond formation with a mixture of 100 mM EDC and 150 mM NHS, both dissolved in 10 mM MES (pH 5.5). Samples were incubated for 30 minutes at 37 °C under gentle agitation and then extensively rinsed with 10 mM MES (pH 5.5). Specifically, EDC couples NHS to carboxyls, thus forming a stable NHS ester which allows for an efficient conjugation to primary amines.
- 4) *Immobilization of the pentapeptide.* A solution of 100 µg/mL of CREKA or CR(NMe)EKA were prepared in 10 mM MES (pH 5.5). The cantilevers/Si pieces were incubated for 2 hours at 37 °C. After that, the samples were washed with 10 mM MES (pH 5.5) and incubated for 45 minutes at 37 °C with PBS (300 mM NaCl,

2.7 mM KCl, 10 mM Na₂HPO₄, and 1.8 mM KH₂PO₄) to desorb those peptide fragments not covalently bonded to the surface. The surface of the cantilever/Si pieces was subsequently blocked to prevent nonspecific interactions by dipping the substrates into a 1 mg/mL BSA solution in 10 mM MES with 0.05% Tween® 20 (pH 5.5) for 1 hour at room temperature with gentle agitation. Thereafter, samples were washed using MES pH 5.5 with 0.05% Tween 20 (pH 5.5).

- 5) *Protein recognition.* The blocked surfaces were incubated in Fg or Fb solutions (PBS with 0.05% Tween® 20 at pH 7.4) with varying protein concentration (0, 50, 100, 500, and 10000 ng/mL). Fibrin, which is an insoluble powder, was firstly dissolved in 1 N NaOH at 1 mg/mL. Subsequently, this solution was further diluted with PBS (0.05% Tween® 20 at pH 7.4) to obtain all the aliquots. After the incubation time (1 hour, 37 °C), samples were washed with PBS + 0.05% Tween® 20, PBS, and water, and were finally dried at room temperature.

Wettability: Contact angle (CA) measurements were conducted using the water drop method. 0.5 µL of milliQ water drops were deposited onto the Si surface and recorded after stabilization with the equipment OCA 15EC (DataPhysics Instruments GmbH, Filderstadt). The SCA20 software was used to measure the CA, which is shown here as the average of at least 30 measures for each condition.

X-ray photoelectron spectroscopy (XPS): XPS was used to analyze the chemical composition of Si surfaces. The system (SPECS Surface Nano Analysis GmbH, Berlin, Germany) was equipped with a non-monochromatic twin anode X-ray source XR50 of Mg/Al (1253 eV/1487 eV). Specifically, the Al anode was operated at 150 W. Detector pass energy was set at 25 eV and 0.1 eV for the survey and the narrow scans (high resolution spectra), respectively, at a pressure below 7.5×10^{-9} mbar. Casa XPS software (Version 2.3.16, Casa Software Ltd., Teignmouth, UK) was used to fit and perform peak integration of spectra. The C 1s peak was used as an internal reference (284.8 eV). High resolution XPS spectra were acquired by Gaussian–Lorentzian curve fitting after S-shape background subtraction.

Interferometry: Green light interferometry in vertical scanning interferometry mode (Wyko NT9300 Optical Profiler, Veeco Instruments, New York, NY, USA) was used to evaluate the roughness of Si pieces after each functionalization step. The mean root square roughness (Rq), which is the average height deviation taken from the mean data plane, was measured in five randomly chosen areas ($25 \times 25 \mu\text{m}^2$) of three replicates for each step.

Atomic force microscopy (AFM): AFM was conducted to obtain topographic images of the functionalized surfaces using Si TAP 150-G probes (Budget Sensors, Bulgaria) with a frequency of 150 kHz and a force constant of 5 N/m. Images were obtained with an AFM Dimension microscope using a NanoScope IV controller under ambient conditions in tapping mode. The row scanning frequency was set between 0.6 and 0.8 Hz. The Rq was determined using the statistical application of the NanoScope Analysis software (1.20, Veeco).

Protein binding affinity (ELISA): Si wafers ($0.5 \times 0.5 \text{ cm}^2$) were deposited into a standard 96 well-plate. The coating protein (BSA, Fg, or Fb) was diluted to a concentration of 1 $\mu\text{g}/\text{mL}$ within the coating buffer (0.2 M bicarbonate buffer pH 9.4) and added (100 μL per well) on the plate. The 96-well plate was incubated overnight at 4 $^\circ\text{C}$ for 1 hour at 37 $^\circ\text{C}$. Later, the plate was washed 3 times (5 minutes each) with 200 μL of the washing buffer (25 mM Tris, 0.15 M NaCl, 0.05% Tween 20 pH 7.2). Then, 300 μL of the blocking buffer (2 % BSA in washing buffer) were added to each well. The plate was covered and incubated at room temperature for 1 hour or overnight at 4 $^\circ\text{C}$. The blocker was removed, and 200 μL of the primary antibody (Anti-Fib/Fg, mouse monoclonal IgM, MFB-HB) (1:1000) were added to each well. The plate was covered and incubated at room temperature for 1 hour. Afterwards, the plate was washed 3 times (5 minutes each) with the washing buffer (200 μL). The conjugated antibody (Anti-Mouse IgM secondary ab, HRP conjugated, Goat IgG polyclonal) (1:50000) was added to each well (200 μL). Again, the plate was covered and incubated at room temperature for 1 hour. The plate was washed 6 times (5 minutes each) with the washing buffer (200 μL).

The substrate, TMB, was allowed to equilibrate at room temperature before use and was protected from light. Finally, after removing the washing buffer, 100 μL of TMB were added. The color of the solution slowly developed to 650 nm; after 15 min at 37 $^{\circ}\text{C}$ the plate was read.

Statistical analysis: All the experiments were performed in triplicate. Statistical comparison of values was based on a 2-way ANOVA using Tukey's test for pair-wise comparison with $p < 0.05$.

Nanomechanical biosensing, resonance frequency measurements:

Monocrystalline Si microcantilever chips containing arrays of 8 cantilevers (Micromotive GmbH) were used for the nanomechanical biosensing measurements. Specifically, the nominal length, width, and thickness of the cantilevers were 500, 90 ± 2 and 1 μm , respectively. The fundamental resonance frequency is 5205.6 ± 161.7 kHz, obtained after averaging the response of 65 cantilevers. Resonance frequency measurements were conducted less than 24 hours after the protein (BSA, Fg, or Fb) recognition event took place onto the cantilever surface in a nitrogen atmosphere at 25 $^{\circ}\text{C}$. **Figure 8.3.1** illustrates the experimental setup. Hence, added mass onto the cantilever induces a shift in the resonance frequency that can be quantitatively measured by either an optomechanical or an electromechanical transduction scheme. In this case, SCALA (Scanning Laser Analyzer) is the optical read-out technology used during testing (Mecwins S.L., Spain).^{82,83} This platform is based on the automated two-dimensional scanning of a single laser (1 mW) beam by voice-coil actuators perpendicularly located. Displacements over a range of several millimeters at speeds up to 10 mm/s and with an accuracy of 100 nm are achieved. Once the laser beam is reflected by the cantilever array, the exact position and intensity of the reflected spot is collected by a two-dimensional linear position detector (PSD). Moreover, TRACKER, which is an algorithm that recognizes reflected intensity patterns, locates cantilever sensors in a fully automated process.

8.3.2 Results and discussion

CREKA and CR(MMe)EKA, which are the tumor-homing pentapeptides used in this work, are displayed in **Figure 8.3.2**. Both biomolecules bind to clotted plasma proteins overexpressed in cancerous tissue (tumor stroma and the walls of vessels).⁸⁴ Briefly, plasma proteins, such as Fg, which is the Fb precursor, and fibronectin, another protein crosslinked to Fb during blood clotting, leak from tumor vessels (*i.e.* they are more fragile and irregular than normal vasculature), thus being converted to Fb by procoagulant factors, which are commonly found in tumor environments.⁸⁴ Hence, the Fb meshwork localized in the interstitial spaces of tumors acts as CREKA's binding sites for effective tumor imaging or drug delivery.

The tumor-homing response of CREKA was enhanced by protecting the pentapeptide against proteolytic degradation.¹¹ Specifically, several *N*- and *C*^α-methylated amino acids were replaced without inducing changes in the peptide conformational profile. Among them, CR(MMe)EKA (Glu residue modified, **Figure 8.3.2**) was reported to be significantly more active than CREKA while displaying greater stability. Although both pentapeptides accumulate in areas rich in Fb and Fg, CR(MMe)EKA is chosen as the tumor-specific molecular ligand in this work for nanomechanical biosensing experiments. However, during the optimization and characterization of the functionalization protocol, CREKA is used as control to verify any variation provoked by the presence of the MMe-Glu residue.

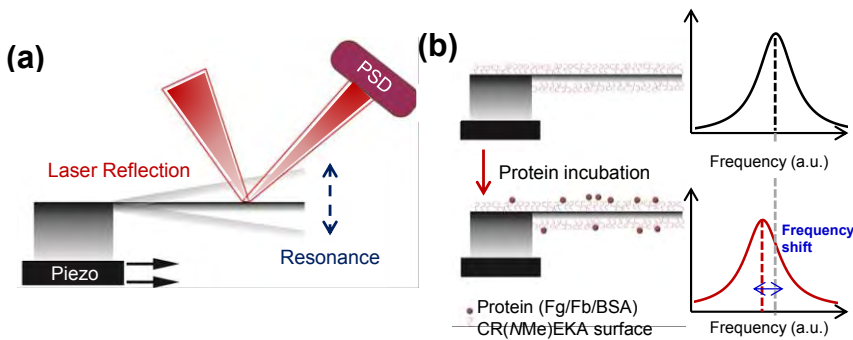


Figure 8.3.1 Experimental set-up for the nanomechanical biosensing tests.

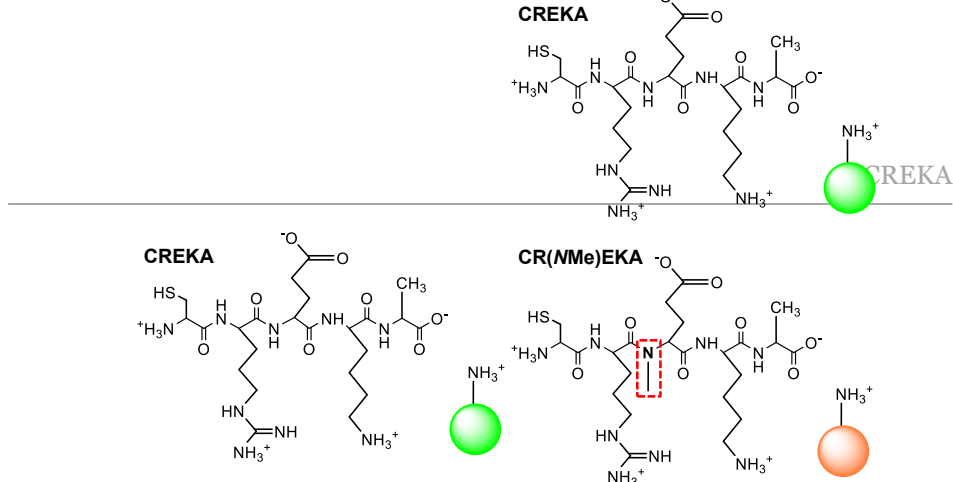


Figure 8.3.2 Tumor-homing peptides used in this work: CREKA and CR(NMe)EKA.

CREKA/CR(NMe)EKA silicon surface functionalization

Before immobilizing CR(NMe)EKA onto the surface of chips used for nanomechanical biosensing, the reliability and efficiency of the functionalization protocol was confirmed by using bare Si substrates ($0.5 \times 0.5 \text{ cm}^2$) as control test surface. **Figure 8.3.3** depicts the functionalization protocol followed to bind CR(NMe)EKA onto Si surfaces. The pentapeptide was covalently bonded to the surface by following a previously reported silanization process.⁸⁵ Although this approach requires more steps than other procedures (*i.e.* physical adsorption of the biomolecule onto the surface), it results in an irreversible and more stable binding.

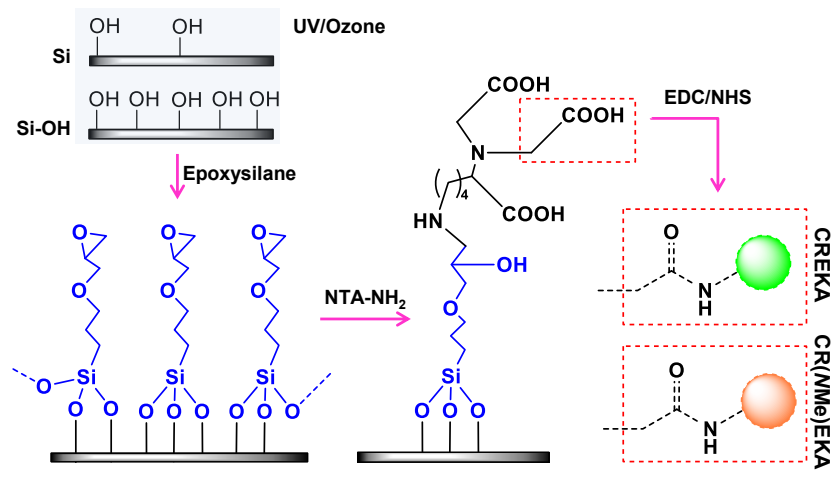


Figure 8.3.3 Functionalization protocol of silicon surfaces with CREKA or CR(NMe)EKA pentapeptides.

As it can be observed in **Figure 8.3.3**, after generating hydroxyl groups by UV/ozone exposure (all physisorbed contamination is removed prior modification), silanization was conducted with (3-glycidyoxypropyl)trimethoxysilane. In the next step, the epoxy groups were opened by the amino group of NTA-NH₂ (basic pH), and thus NTA-NH₂ enriched the surface with carboxyl groups that were subsequently activated by EDC/NHS. Finally, CR(NMe)EKA was covalently attached to the surface by the amide bonds created between activated carboxylates and the amino groups from the pentapeptide. It should be noted that, as the sulfhydryl group of the single Cys residue is not required for binding, this strategy allows for coupling the pentapeptide to other moieties, such as anticancer drugs or fluorescent dyes. Accordingly, this procedure can add multifunctionality to CREKA-tethered systems if required in a biomedical context.

As an initial indicator of the satisfactory evolution of the functionalization process, **Figure 8.3.4a** displays the variation in the wettability of the Si surface according to each step of the protocol previously described. Hence, -OH groups generated due to the UV/ozone treatment notably decrease the CA value of bare Si from $92.7^\circ \pm 5.0^\circ$ to $30.0^\circ \pm 5.0^\circ$, indicating the formation of a highly hydrophilic surface. This observation can be ascribed to both the removing of hydrophobic substances from the Si surface, as well as the newly formed hydroxyl groups. In contrast, hydrophobic epoxysilane-coated surfaces

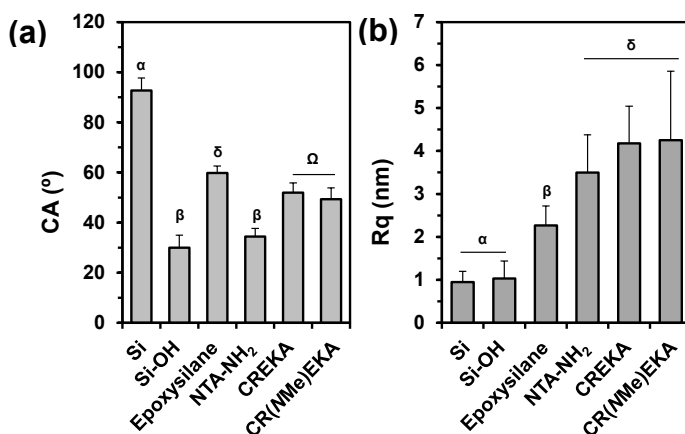


Figure 8.3.4 (a) CA values of water and (b) Rq of the silicon square surface in each different step of the functionalization process. Greek letters are assigned to statistically significant different groups (p -value < 0.05).

show a CA value of $59.8^\circ \pm 2.8^\circ$, which decreases to $34.4^\circ \pm 3.3^\circ$ in the next step because of $-\text{COOH}$ groups provided by NTA-NH_2 .

The final step of the functionalization process induces a slight increase in the surface hydrophobicity regardless the pentapeptide used, CREKA ($51.9^\circ \pm 3.9^\circ$) or CR(NMe)EKA ($49.4^\circ \pm 4.5^\circ$).

Table 8.3.1 Functionalization protocol of silicon surfaces with CREKA or CR(NMe)EKA pentapeptides.

	O 1s	C 1s	Si 2p	N 1s	N/C	O/C	N/Si
Si-OH	47.7	13.4	38.9	-	-	3.56	-
Epoxy silane	40.1	23.5	36.4	-	-	1.71	-
NTA-NH₂	36.2	24.8	39.1	-	-	1.46	-
CREKA	32.1	34.8	31.1	2.0	0.06	0.92	0.06
CR(NMe)EKA	36.7	29.6	31.4	2.3	0.08	1.24	0.07

Although CA results are in good agreement with the expected chemical composition of each functionalization step, the functionalization protocol was corroborated by XPS. **Table 8.3.1** summarizes the atomic percentage composition and N/C, N/O, and N/Si atomic ratio values of the surfaces throughout each step of the functionalization process.

As expected, the composition of control Si-OH surfaces accounts for O 1s (47.7%) and Si 2p (38.9%), with the percentage of C 1s (13.4%) ascribed to atmospheric contamination. In good agreement with CA values, the UV/ozone treatment is responsible for the high percentage of O 1s signal ($\text{O/Si} = 1.19$ and $\text{O/C} = 3.56$). In the next two functionalization steps, epoxy silane and NTA-NH_2 are bonded to Si-OH surfaces. Consequently, the O/C ratio decreases to 1.71 and 1.46, respectively. However, although the content of N 1s is not altered by the incorporation of NTA-NH_2 , the CA value of the surface ($34.4^\circ \pm 3.3^\circ$) confirms the presence of NTA-NH_2 .

Table 8.3.2 Atomic percentage composition and N/C, N/O and N/Si atomic ratio for CR(NMe)EKA-functionalized surfaces before and after sonication in PBS 1x at 37 °C for 1 hour.

	O 1s	C 1s	Si 2p	N 1s	N/C	O/C	N/Si
CR(NMe)EKA	38.2	32.0	26.0	3.8	0.12	1.19	0.15
CR(NMe)EKA after sonication	29.6	45.0	23.7	1.7	0.04	0.66	0.07

Finally, the adequate covalent binding of the two pentapeptides onto the Si substrates is detected not only by the increase in the N 1s content to 2% and 2.3% for CREKA and CR(NMe)EKA, respectively, but also by the reduction in the atomic percentage of Si 2p as well as the increase in C 1s content. The high resolution spectra of N 1s (**Figure 8.3.5**) confirm the peptide attachment since the deconvolution of the signal led to three well-defined peaks. The central peak, which is located at 400 eV, corresponds to the amide bonds of the peptide backbone (N-C=O) as well as uncharged, hydrogen-bonded amines (C-NH₂), whereas the other two peaks at ~398 eV and ~401 eV are attributed to C=N- and free protonated amino groups (NH₃⁺), respectively, present in the side chain groups of CREKA and CR(NMe)EKA.^{86,87}

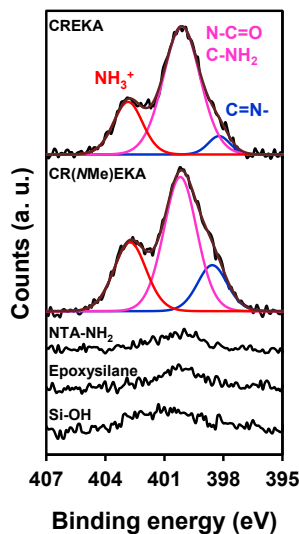


Figure 8.3.5 N 1s high-resolution XPS spectra for each silicon surface throughout the functionalization protocol. Peaks from deconvolution are also displayed.

In order to determine the stability of the peptide binding, CR(NMe)EKA functionalized silicon wafers were sonicated at 37 °C in PBS (1x) for 1 hour. Then, both the wettability and chemical composition of the samples were examined again by CA and XPS measurements, respectively. CA values for CR(NMe)EKA-functionalized surfaces were $49.6^\circ \pm 2.96^\circ$ and $57.6^\circ \pm 1.3^\circ$ before and after sonication, respectively, while the atomic percentage composition and N/C, N/O, and N/Si atomic ratio values of CR(NMe)EKA-surfaces decreased upon sonication but were not completely reduced (**Table 8.3.2**), which confirms the stability of the peptide binding to Si substrates.

Moreover, the topography of the modified surfaces (scanned areas of $5 \times 5 \mu\text{m}^2$) was observed by AFM to monitor each step of the functionalization process. **Figure 8.3.6** displays height and phase images of Si–OH and CR(NMe)EKA-functionalized surfaces, whereas the results for the intermediate steps (*i.e.* epoxysilane and NTA-NH₂) and CREKA-functionalized surfaces are included in **Figure 8.3.7**. Upon coating with the pentapeptide (**Figure 8.3.4b**), the smooth and homogenous features of Si–OH ($R_q = 0.4 \text{ nm}$) evolves towards a rougher surface, even though the R_q values of the modified interfaces are still small (in the range between 0.4 nm and 1 nm). Moreover, AFM phase images, which register phase signal shifts due to changes in the adhesion force between the tip and the surface (*i.e.* stiffness/softness), allow for the chemical mapping of the surface. Specifically, no phase contrast is observed for any step of the functionalization process, thus verifying the complete coverage of the Si substrate, which is in good agreement with the XPS results.

Aware that R_q values depend on the analyzed area, interferometric measurements were also conducted to determine such parameter but considering bigger scanned areas ($25 \times 25 \mu\text{m}^2$). As it is depicted in **Figure 8.3.4b**, the UV/ozone treatment did not alter the topography of the Si surface (*i.e.* R_q values for Si and Si–OH surfaces are $0.9 \pm 0.3 \text{ nm}$ and $1.0 \pm 0.4 \text{ nm}$, respectively). As described previously, R_q increases after each step of the functionalization process. Thus, with respect to Si–OH, there is an increment in roughness of 120%, 239%, 305%, and 312% for epoxysilane ($2.3 \pm 0.5 \text{ nm}$), NTA-NH₂ ($3.5 \pm 0.9 \text{ nm}$), CREKA ($4.2 \pm 0.3 \text{ nm}$), and CR(NMe)EKA ($4.3 \pm 1.6 \text{ nm}$), respectively.

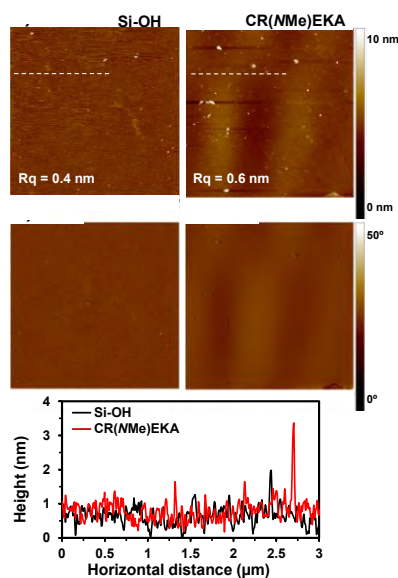


Figure 8.3.6 Topographical characterization (areas of $5 \times 5 \mu\text{m}^2$): (top) 2D AFM height and (middle) phase micrographs of Si–OH (left) and CR(NMe)EKA (right) surfaces. (bottom) Height profile of a horizontal line drawn as depicted.

Overall, the findings derived from CA measurements, topographical characterization, and, most importantly, chemical composition analyses, confirm the proper covalent attachment of CREKA and CR(NMe)EKA onto Si surfaces. Hence, the suitability of the described functionalization protocol, which is based on a silanization process, has been proven, and thus can be applied to microcantilever Si chips for the following nanomechanical experiments.

CREKA and CR(NMe)EKA binding affinity

Before analyzing the interactions between CR(NMe)EKA pentapeptide and Fb or Fg by means of nanomechanical characterization, ELISA binding assays were conducted to verify such biorecognition event. In this case, we approached the experiment qualitatively, our focus being whether CREKA- and CR(NMe)EKA-functionalized Si surfaces still recognize clotted plasma.

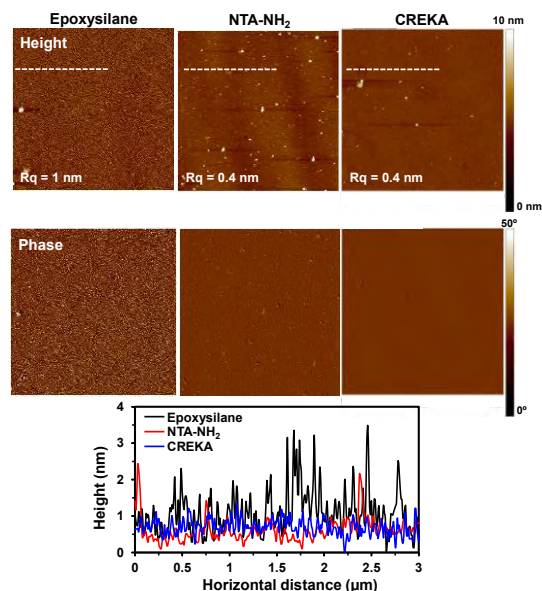


Figure 8.3.7 Topographical characterization (areas of $5 \times 5 \mu\text{m}^2$): 2D AFM height (top) and phase micrographs (bottom) of Epoxy silane (left), NTA-NH₂ (middle) and CREKA (right) surfaces. Height profile of a horizontal line drawn as depicted in height images.

Figure 8.3.8 depicts the binding affinity of CREKA and CR(MMe)EKA-functionalized Si surfaces towards Fb, Fg, or BSA as the absorbance at 650 nm in PBS media. Tissue culture polystyrene (TCP) and Si-OH surfaces were used as control substrates. As it can be seen, in PBS, the Fb- and Fg-binding capability of CR(MMe)EKA-functionalized Si surfaces is 118% and 174% higher, respectively, than that displayed by CREKA-functionalized substrates. Besides, no BSA interaction occurred, thus further confirming the biorecognition of this tumor-homing peptide for Fb and Fg complexes. The overall of these results corroborate the role played by MMe-Glu in Fb/Fg interaction.¹⁴ More specifically, such residue is crucial to promote the protein binding mechanism, either by enhancing the activity of the tumor-homing peptide or improving its stability. In addition, the binding site of CR(MMe)EKA is not altered by the functionalization protocol. Accordingly, on the light of these results and considering our previous works,^{18,69} we selected CR(MMe)EKA as the molecular ligand for nanomechanical biosensing tests.

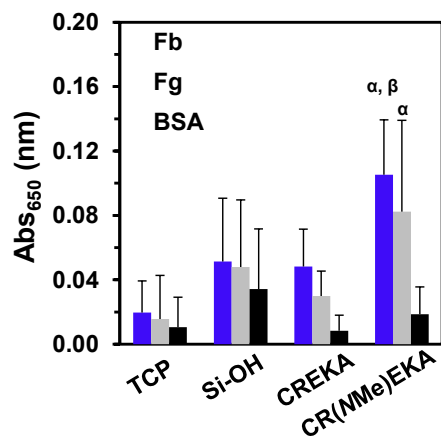


Figure 8.3.8 Protein adhesion assay carried out in PBS. Absorbance values were obtained from ab-HRP activity. Greek letters on the columns refer to significant differences (p -value < 0.05) when the 2-way ANOVA and Tukey's multiple comparisons test are applied: α vs Si-CR(NMe)EKA BSA absorbance, β vs Fb absorbance on TCP.

Nanomechanical biosensing: Resonance frequency measurements

The microcantilever-based biosensing emerging technology has been applied in this work to observe and analyze the binding affinity of CR(NMe)EKA towards Fb and Fg proteins. Among other features, this platform is characterized by high sensitivity, label-free detection, and small sample consumption due to the size of the microcantilevers (*ca.* 1000 μm^2).⁸⁸

Specifically, CR(NMe)EKA-functionalized Si chips containing arrays of 8 cantilevers, thus using various sensors in parallel, were operated in the dynamic mode combining a scanning laser, the beam deflection method, piezoelectrical excitation (an actuator is located beneath the chip base) and analysis of the first vibration mode.⁸⁹ After being cleaned (*i.e.* isopropanol + 30' UV/ozone exposure), these commercial chips - 500 μm long, ~100 μm wide, and 1 μm thick - exhibited a fundamental resonance frequency of 5205.6 ± 161.7 kHz ($n = 65$) measured in a N_2 atmosphere at 25 °C. The eigenmode shape obtained during frequency excitation is plotted for a representative cleaned chip in **Figure 8.3.9**.

In general, the results take into consideration the response of at least 10 cantilevers at each concentration. Besides, data for the Fb-binding event was collected in two independent experiments. **Figure 8.3.10a** plots the resonance frequency shift of

microcantilevers incubated in the presence of Fb, Fg, or BSA at a concentration of 10 $\mu\text{g}/\text{mL}$ (*i.e.* BSA was used as a negative control since no binding is expected for this protein). As it is shown, CR(NMe)EKA biointeracts towards the two clotted plasma proteins, being the frequency shift values higher for Fb/Fg recognition than for BSA.

Moreover, provided the molecular weight of Fg and Fb is similar and *ca.* 340 kDa (Fb, which is an insoluble protein, was first dissolved in 1 N NaOH at 1 mg/mL, and then highly diluted in PBS), a slightly higher number of binding events occurred for Fg than Fb. As a representative example, **Figure 8.3.10b** depicts the nanomechanical 1st mode resonance response of a CR(NMe)EKA-functionalized Si cantilever before and after Fb incubation. The same trend was observed when Fg was used (**Figure 8.3.11a**), whereas BSA incubation did not lead to any significant change in the cantilever resonance frequency (**Figure 8.3.11b**).

Additionally, in an effort to determine the detection limit for CR(NMe)EKA, lower protein concentrations were tested in the interval between 50 ng/mL and 10 $\mu\text{g}/\text{mL}$. **Figure 8.3.10c** and **d** shows the relation between the resonance frequency shift and Fg or Fb concentration, respectively. As it can be observed, regardless the protein, the resonance frequency shift exhibits a linear dependence with the protein concentration: the higher the concentration, the more mass is being recognized by the pentapeptide, which induces greater changes in the mechanical vibration of the cantilever. Control experiments, which consisted on incubating CR(NMe)EKA-functionalized Si chips in solutions with no protein, allow us to establish a noise level produced by non-specific interactions (grey shadowed areas in **Figure 8.3.10c** and **d**). Hence, the detection limit

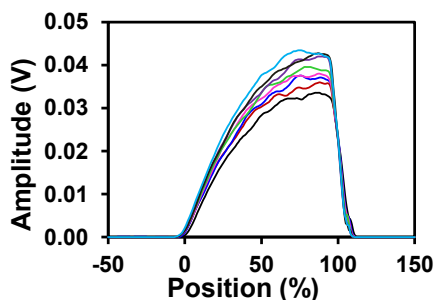


Figure 8.3.9 Eigenmode shape response of the 8 cantilevers of a cleaned chip (1st resonance mode).

is set at 100 ng/mL for both Fb and Fg. Despite the fact that the detection limit obtained in these measurements is above the detection range of the technique generally used to determine the concentration of Fb and Fg (*i.e.* ELISA, 0.5 - 6.25 ng/mL and 1.25 - 80 ng/mL, respectively), this label-free nanomechanical sensing offers simplicity and affordability. Furthermore, it has been proven to reach values in the order of magnitude of fg/mL by using a different configuration.^{75,76} Consequently, to improve the detection limit of the measurement, different strategies can be applied: (*i*) use of smaller cantilevers; (*ii*) amplify the signal by means of CREKA-functionalized nanoparticles, such as those previously described;^{1,11} or (*iii*) optimize the receptor biolayer (*i.e.* polyethylene glycol (PEG), an antifouling agent, has been used as an alternative to BSA to

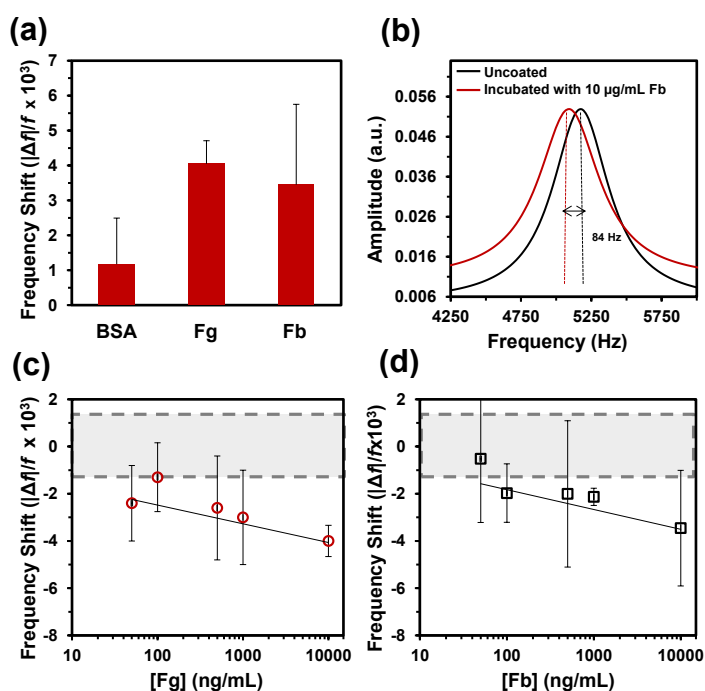


Figure 8.3.10 Nanomechanical response: (a) absolute frequency shift of cantilevers after being incubated with 10 $\mu\text{g/mL}$ of BSA, Fg and Fb; (b) mechanical resonance frequency of a Si cantilever before and after the Fb recognition event (10 $\mu\text{g/mL}$ in PBS); (c and d) relative resonance-frequency shift vs protein concentration of (c) Fg and (d) Fb in PBS. Mean values and standard deviations are calculated with the data of a minimum of 10 different cantilevers. Lines are a guide for the eye.

prevent nonspecific interactions).⁹⁰

Finally, it is important to note that the comprehension of protein biorecognition is complex and time-demanding. Although the proteins chosen in this work play a major role in coagulation events, the study of CR(NMe)EKA binding events towards other proteins, such as fibronectin and Fb/fibronectin mixtures, is required to further explore the underlying binding mechanism of CREKA-based tumor-homing peptides. Our results confirm the promising application of nanomechanical sensing for such purpose.

Bearing all these considerations, this study establishes a challenging line of research focused on CREKA and CR(NMe)EKA tumor-homing peptides and their bioapplication

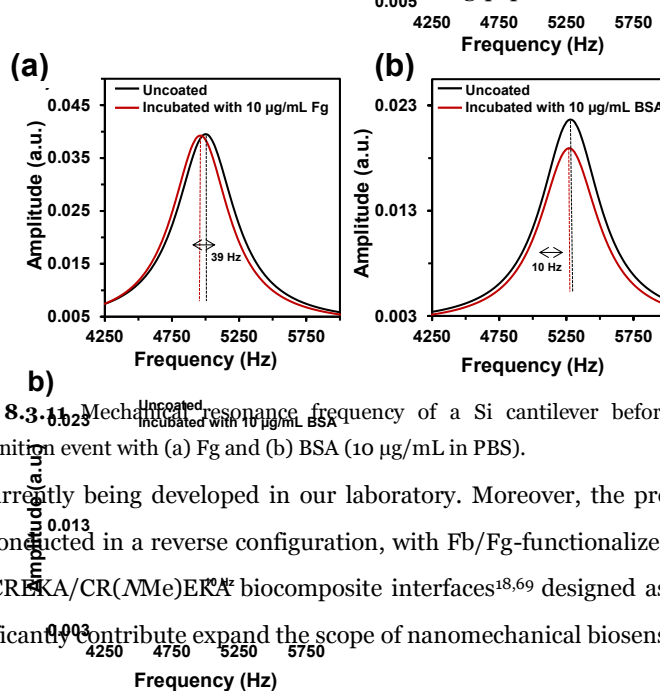


Figure 8.3.11 Mechanical resonance frequency of a Si cantilever before and after the biorecognition event with (a) Fg and (b) BSA (10 µg/mL in PBS).

that is currently being developed in our laboratory. Moreover, the protein recognition event if conducted in a reverse configuration, with Fb/Fg-functionalized cantilevers and PEDOT-CREKA/CR(NMe)EKA biocomposite interfaces^{18,69} designed as nanoparticles⁹¹, can significantly contribute to expand the scope of nanomechanical biosensing.

8.3.3 Conclusions

In this chapter, we have examined the biorecognition event between clotted plasma proteins and a tumor-homing pentapeptide, CR(NMe)EKA, by applying a label-free sensing technology based on microcantilevers. For such purpose, CREKA and CR(NMe)EKA were covalently linked *via* an epoxysilane-based protocol to Si substrates that had efficiently been activated by UV/ozone treatment. The results derived from the

different characterization techniques performed at each one of the functionalization steps confirmed the suitability of the protocol to tether these linear, small pentapeptides onto Si surfaces. Moreover, although the presence of the *N*Me-Glu residue had no impact regarding the functionalization result, CR(*N*Me)EKA-functionalized silicon substrates yield the highest Fb adsorption in PBS in comparison to CREKA-functionalized surfaces. Hence, after the covalent binding of CR(*N*Me)EKA onto Si surfaces, *N*Me-Glu residue still promotes Fb-binding. Finally, dynamic mode nanomechanical tests were carried out using CR(*N*Me)EKA-functionalized microcantilever sensors. This simple and manageable label-free detection technique provided information regarding the interaction between Fb/Fg and the clot-binding peptide, thus establishing a detection limit of 100 ng/mL. However, although further improvement is required to lower the detection limit and determine the specific binding affinity of CREKA and its analogues, the overall of these results reflect the importance of developing emerging technologies suitable for specific biomedical purposes. With that goal in mind, extensive investigation is being performed in our laboratory to comprehend CREKA and CR(*N*Me)EKA-mediated clot-binding and expand their applications in the biotechnological field.

8.3 References

1. Simberg, D.; Duza, T.; Park, J. H.; Essler, M.; Pilch, J.; Zhang, L.; Derfus, A. M.; Yang, M.; Hoffman, R. M.; Bathia, S.; Sailor, M. J. and Ruoslahti, E. Biomimetic amplification of nanoparticle homing to tumors. *Proc. Natl. Acad. Sci. U.S.A.* **2007**, *104*, 932-936.
2. Pasqualini, R. and Ruoslahti, E. Organ targeting *in vivo* using phage display peptide libraries. *Nature* **1996**, *380*, 364
3. Hoffman, J. A.; Giraudo, E.; Singh, M.; Zhang, L.; Inoue, M.; Porkka, K.; Hanahan, D. and Ruoslahti, E. Progressive vascular changes in a transgenic mouse model of squamous cell carcinoma. *Cancer Cell* **2003**, *4*, 383-391.
4. Yuan, F.; Dellian, M.; Fukumura, D. and Leunig, M. Vascular permeability in a human tumor xenograft: molecular size dependence and cutoff size. *Cancer Res.* **1995**, *55*, 3752-3756.
5. O'Brien III, E. T.; Falvo, M. R.; Millard, D.; Eastwood, B.; Taylor II, R. M. and Superfine, R. Ultrathin self-assembled fibrin sheets. *Proc. Natl. Acad. Sci.* **2008**, *105*, 19438-19442.

6. Peters, D.; Kastantin, M.; Kotamraju, V. R.; Karmali, P. P.; Gujraty, K.; Tirrell, M. and Ruoslahti, E. Targeting atherosclerosis by using modular, multifunctional micelles. *Proc. Natl. Acad. Sci. U.S.A.* **2009**, *106*, 9815-9819.
7. Hamzah, J.; Kotamraju, V. R.; Seo, J. W.; Agemy, L.; Fogal, V.; Mahakian, L. M.; Peters, D.; Roth, L.; Gagnon, M. K.; Ferrara, K. W. and Ruoslahti, E. Specific penetration and accumulation of a homing peptide within atherosclerotic plaques of apolipoprotein E-deficient mice. *Proc. Natl. Acad. Sci. U.S.A.* **2011**, *108*, 7154-7159.
8. Zanuy, D.; Flores-Ortega, A.; Casanovas, J.; Curco, D.; Nussinov, R. and Alemán C. The energy landscape of a selective tumor-homing pentapeptide. *J Phys Chem B* **2008**, *112*, 8692-8700.
9. Zanuy, D.; Curc6, D.; Nussinov, R. and Alemán, C. Influence of the dye presence on the conformational preferences of CREKA, a tumor homing linear pentapeptide. *Biopolymers (Pept Sci)* **2009**, *92*, 83-93.
10. Zanuy, D.; Sayago, F. J.; Revilla-L6pez, G.; Ballano, G.; Agemy, L.; Kotamraju, V. R.; Jim6nez, A. I.; Cativiela, C.; Nussinov, R.; Sawvel, A. M.; Stucky, G.; Ruoslahti, E. and Alemán, C. Engineering strategy to improve peptide analogs: from structure-based computational design to tumor homing. *J. Comput. Aided. Mol. Des.* **2013**, *27*, 31-42.
11. Agemy, L.; Sugahara, K. N.; Kotamraju, V. R.; Gujraty, K.; Girard, O. M.; Kono, Y.; Mattrey, R. F.; Park, J.-H.; Sailor, M. J.; Jimenez, A. I.; Cativiela, C.; Zanuy, D.; Sayago, F. J.; Alemán, C.; Nussinov, R. and Ruoslahti, E. Nanoparticle-induced vascular blockade in human prostate cancer. *Blood* **2010**, *116*, 2847-2856.
12. She, Z. G.; Liu, X.; Kotamraju, V. R. and Ruslahti, E. Clot-targeted micellar formulation improves anticoagulation efficacy of bivalirudin. *ACS Nano* **2014**, *8*, 10139-10149.
13. Han, F.; Qi, X.; Li, L.; Bu, L.; Fu, Y.; Xie, Q.; Guo, M.; Li, Y.; Ying, Y. and Yao, S. Bio-Inspired Preparation of Fibrin-Boned Bionanocomposites of Biomacromolecules and Nanomaterials for Biosensing. *Adv. Funct. Mater.* **2014**, *24*, 5011-5018.
14. Wong, C. K.; Laos, A. J.; Sorivadi, A. H.; Wiedenmann, J.; Curmi, P. M. G.; Gooding, J. J.; Marquis, C. P.; Stenzel, M. H. and Thordarson, P. Polymersomes prepared from thermoresponsive fluorescent protein-polymer bioconjugates: capture of and report on drug and protein payloads. *Angew. Chem. Int. Ed.* **2015**, *54*, 5317-5322.
15. Wu, Y. Z.; Ng, D. Y. W.; Kuan, S. L. and Weil, T. *Biomater. Sci.* **2015**, *3*, 214.
16. Gunawan, S. T.; Kempe, K.; Such, G. K.; Cui, J. W.; Liang, K.; Richardson, J. J. and Johnston, A. P. R. Tuning particle biodegradation through polymer-peptide blend composition. *Biomacromolecules* **2014**, *15*, 4429-4438.

17. Guo, B.; Glavas, L. and Albertsson, C. A. Biodegradable and electrically conducting polymers for biomedical applications. *Prog Polym Sci.* **2013**, *38*,1263-1286.
18. Fabregat, G.; Teixeira-Dias, B.; del Valle, L. J.; Armelin, E.; Estrany F. and Alemán, C. Incorporation of a clot-binding peptide into polythiophene: properties of composites for biomedical applications. *Appl. Mater. Interfaces* **2014**, *6*, 11940-11954.
19. Li, C.; Bai, H. and Shi, G. Conducting polymer nanomaterials: electrosynthesis and applications. *Chem. Soc. Rev.* **2009**, *38*, 2397-2409.
20. Coelho, E. C. S.; Nascimento, V. B.; Ribeiro, A. S. and Navarro, M. Electrochemical and optical properties of new electrochromic and fluorescent nitrobenzoyl polypyrrole derivatives. *Electrochim. Acta* **2014**, *123*, 441-449.
21. Long, Y.-Z.; Li, M.-M.; Gu, C.; Wan, M.; Duvail, J.-L.; Liu, Z. and Fan, Z. Recent advances in synthesis, physical properties and applications of conducting polymer nanotubes and nanofibers. *Prog. Polym. Sci.* **2011**, *36*, 1415-1442.
22. Pérez-Madrugal, M. M.; del Valle, L. J.; Armelin, E.; Michaux, C.; Roussel, G.; Perpetè, E. A. and Alemán, C. Polypyrrole-supported membrane proteins for bio-inspired ion channels. *ACS Appl. Mater. Interfaces* **2015**, *7*, 1632-1643.
23. Romero, I. S.; Bradshaw, N. P.; Larson, J. D.; Severt, S. Y.; Roberts, S. J.; Schiller, M. L.; Leger, J. M. and Murphy, A. R. Biocompatible electromechanical actuators composed of silk-conducting polymer composites. *Adv. Funct. Mater.* **2014**, *24*, 3866-3878.
24. Hamed, M.; Wiggenius, J.; Tai, F.-I.; Björk, P. and Aili D. Polypeptide-guided assembly of conducting polymer nanocomposites. *Nanoscale*, **2010**, *2*, 2058-2061.
25. López-Pérez, D. E.; Aradilla, D.; del Valle, L. J. and Alemán, C. Capacitive composites made of conducting polymer and lysozyme: toward the biocondenser. *J. Phys. Chem. C* **2013**, *117*, 6607-6619.
26. Shi, Z. Q.; Gao, H. C.; Feng, J.; Ding, B. B.; Cao, X. D.; Kuga, S.; Wang, Y. J.; Zhang, L. N. and Caj, J. *In situ* synthesis of robust conductive cellulose/polypyrrole composite aerogels and their potential application in nerve regeneration. *Angew. Chem. Int. Ed.* **2014**, *53*, 5380-5384.
27. Soto-Delgado, J.; Torras, J.; del Valle, L. J.; Estrany, F. and Alemán C. Examining the compatibility of collagen and a polythiophene derivative for the preparation of bioactive platforms. *RSC Adv.*, **2015**, *5*, 9189-9203.
28. Pérez-Madrugal, M. M.; Giannotti, M. I.; del Valle, L. J.; Franco, L.; Armelin, E.; Puiggalí, J.; Sanz, F. and Alemán, C. Thermoplastic polyurethane: polythiophene nanomembranes for

- biomedical and biotechnological applications. *ACS Appl. Mater. Interfaces*, **2014**, *6*, 9719-9732.
29. Groenendaal, L.; Zotti, G.; Aubert, P.-H.; Waybright, S. M. and Reynolds J. R. Electrochemistry of poly(3, 4-alkylenedioxythiophene) derivatives. *Adv. Mater.* **2003**, *15*, 855-879.
 30. Groenendaal, L.; Jonas, F.; Freitag, D.; Pielartzik, H. and Reynolds, J. R. Poly(3,4-ethylenedioxythiophene) and its derivatives: past, present, and future. *Adv. Mater.* **2000**, *12*, 481-494.
 31. Kirchmeyer, S. and Reuter, K. Scientific importance, properties and growing applications of poly(3,4-ethylenedioxythiophene). *J. Mater. Chem*, **2005**, *15*, 2077-2088.
 32. del Valle, L. J.; Estrany, F.; Armelin, E.; Oliver, R. and Alemán, C. Cellular adhesion, proliferation and viability on conducting polymer substrates. *Macromol. Biosci.* **2008**, *8*, 1144-1151.
 33. Aradilla, D.; Azambuja, D. S.; Estrany, F.; Casas, M. T.; Ferreira, C. A. and Alemán, C. Hybrid polythiophene-clay exfoliated nanocomposites for ultracapacitor devices. *J. Mater. Chem.* **2012**, *22*, 13110-13122.
 34. Zanuy, D. and Alemán, C. Resolving the subnanometric structure of ultrathin films of poly(3,4-ethylenedioxythiophene) on steel surfaces: a molecular modeling approach. *Soft Matter* **2014**, *9*, 11634-11644.
 35. Fabregat, G.; Ballano, G.; Armelin, E.; del Valle, L. J.; Cativiela, C. and Alemán, C. An electroactive and biologically responsive hybrid conjugate based on chemical similarity. *Polym. Chem.* **2012**, *4*, 1412-1424.
 36. Maione, S.; Gil, A. M.; Fabregat, G.; del Valle, L. J.; Triguero, J.; Laurent, A.; Jacquemin, D.; Estrany, F.; Jiménez, A. I.; Zanuy, D.; Cativiela, C. and Alemán, C. Electroactive polymer-peptide conjugates for adhesive biointerfaces. *Biomater. Sci.* **2015**, *3*, 1395-1405.
 37. Stevens, J. S.; de Luca, A. C.; Pelendritis, M.; Terenghi, G.; Downes, S. and Schroeder, S. L. M. Quantitative analysis of complex amino acids and RGD peptides by X-ray photoelectron spectroscopy (XPS). *Surf. Interface Anal.* **2013**, *45*, 1238-1246.
 38. Bhattacharyya, D. and Gleason, K. K. Single-step oxidative chemical vapor deposition of-COOH functional conducting copolymer and immobilization of biomolecule for sensor application. *Chem. Mater.* **2011**, *23*, 2600-2605.
 39. Flamia, R.; Lanza, G.; Salvi, A. M.; Castle, J. E. and Tamburro, A. M. Conformational study and hydrogen bonds detection on elastin-related polypeptides using X-ray photoelectron spectroscopy. *Biomacromolecules* **2005**, *6*, 1299-1309.

40. Doolittle, R. F. *The molecular biology of fibrin*, in *The Molecular Basis of Blood Diseases* (Eds: G. Stamatoyannopoulos, P. W. Majerus, R. M. Perlmutter and H. Varmus), Saunders, Philadelphia **2000**, pp 719-739.
41. Blombäck, B. Fibrinogen and fibrin-proteins with complex roles in hemostasis and thrombosis. *Thromb. Res.* **1996**, *83*, 1-75.
42. Boccaccio, C. and Medico, E. Cancer and blood coagulation. *Cell. Mol. Life Sci.* **2006**, *63*, 1024-1027.
43. Doolittle, R. F. Fibrinogen and fibrin. *Annu. Rev. Biochem.* **1984**, *53*, 195-229.
44. Weisel, J. W. Fibrinogen and fibrin. *Adv. Protein Chem.* **2005**, *70*, 247-299.
45. Weisel, J. W. Structure of fibrin: impact on clot stability. *J Thromb Haemost* **2007**, *5*, 116-124.
46. Huang, L.; Hsiao, J. P.-L.; Powierza, C.; Taylor II, R. M. and Lord, S. T. Does topology drive fiber polymerization? *Biochemistry* **2014**, *53*, 7824-7834.
47. Wasilewska, M.; Adamczyk, Z. and Jachimska, B. Structure of fibrinogen in electrolyte solutions derived from dynamic light scattering (DLS) and viscosity measurements. *Langmuir* **2009**, *25*, 3698-3704.
48. Zavyalova, E. G.; Protopopova, A. D.; Kopylov, A. M. and Yaminsky, I. V. Investigation of early stages of fibrin association. *Langmuir* **2011**, *27*, 4922-4927.
49. Carr Jr., M. E.; Cromartie, R. and Gabriel, D. A. Effect of homo poly(L-amino acids) on fibrin assembly: role of charge and molecular weight. *Biochemistry* **1989**, *28*, 1384-1388.
50. Dolatshahi-Pirouz, A.; Foss, M. and Besenbacher, F. Interfacial fibrin polymerization and fibrillation kinetics is influenced by nanoscale roughness and fibrinogen-fibrin cleavage in solution. *J. Phys. Chem. C* **2011**, *115*, 13617-13623.
51. van Oss, C. J. Surface properties of fibrinogen and fibrin. *J Protein Chem.* **1990**, *9*, 487-491.
52. Stewart B.W., Wild C. P. "World Cancer Report 2014," Lyon, **2014**.
53. Weissleder, R. Molecular imaging in cancer. *Science* **2006**, *312*, 1168-1171.
54. Li, Z.J. and Cho, C.H. Peptides as targeting probes against tumor vasculature for diagnosis and drug delivery. *J. Transl. Med.* **2012**, *10*(Suppl 1): S1.
55. Hajitou, A.; Pasqualini, R. and Arap, W. Vascular targeting: recent advances and therapeutic perspectives. *Trends Cardiovasc. Med.* **2006**, *16*, 80-88.
56. Deutscher, S.L. Phage Display in Molecular Imaging and Diagnosis of Cancer. *Chem. Rev.* **2010**, *110*, 3196-3211.
57. Li, Z.J. and Cho, C.H. Development of Peptides as Potential Drugs for Cancer Therapy. *Curr. Pharm. Des.* **2010**, *16*, 1180-1189.
58. Lee, S.; Xie, J. and Chen, X. Peptide-Based Probes for Targeted Molecular Imaging.

- Biochemistry* **2010**, 49: 1364–1376.
59. Arap, W.; Pasqualini, R. and Ruoslahti E. Cancer treatment by targeted drug delivery to tumor vasculature in a mouse model. *Science* **1998**, 279, 377–380.
 60. Ellerby, H.M.; Arap, W.; Ellerby, L.M.; Kain, R.; Andrusiak, R.; Rio, G.D.; Krajewski, S.; Lombardo, C.R.; Rao, R.; Ruoslahti, E.; Bredesen, D.E. and Pasqualini, R. Anti-cancer activity of targeted pro-apoptotic peptides. *Nat. Med.* **1999**, 5, 1032–1038.
 61. Hood, J.D.; Bednarski, M.; Frausto, R.; Guccione, S.; Reisfeld R.A.; Xiang R. and Cheresch, D.A. Tumor regression by targeted gene delivery to the neovasculature. *Science* **2002**, 296, 2404–2407.
 62. Sacchi, A.; Gasparri, A.; Gallo-Stampino, C.; Toma, S.; Curnis, F. and Corti, A. Synergistic antitumor activity of cisplatin, paclitaxel, and gemcitabine with tumor vasculature-targeted tumor necrosis factor- α . *Clin. Cancer Res.* **2006**, 12, 175–182.
 63. Lee, T.-Y.; Lin, C.-T.; Kuo, S.-Y.; Chang, D.-K. and Wu, H.-C. Peptide-mediated targeting to tumor blood vessels of lung cancer for drug delivery. *Cancer Res.* **2007**, 67, 10958–10965.
 64. Joyce, J.A.; Laakkonen, P.; Bernasconi, M.; Bergers, G.; Ruoslahti, E. and Hanahan, D. Stage-specific vascular markers revealed by phage display in a mouse model of pancreatic islet tumorigenesis. *Cancer Cell* **2003**, 4, 393–403.
 65. Hatakeyama, S.; Sugihara, K.; Shibata, T.K.; Nakayama, J.; Akama, T.O.; Tamura, N.; Wong, S.-M.; Bobkov, A.A.; Takano, Y.; Ohyama, C.; Fukuda, M. and Fukuda, M. N. Targeted drug delivery to tumor vasculature by a carbohydrate mimetic peptide. *Proc. Natl. Acad. Sci. U. S. A.* **2011**, 108, 19587–19592.
 66. Kruse, A.M.; Meenach, S.A.; Anderson, K.W. and Hilt, J.Z. Synthesis and characterization of CREKA-conjugated iron oxide nanoparticles for hyperthermia applications. *Acta Biomater.* **2014**, 10, 2622–2629.
 67. Chung, E.J.; Cheng, Y.; Morshed, R.; Nord, K.; Han, Y.; Wegscheid, M.L.; Auffinger, B.; Wainwright, D.A.; Lesniak, M.S. and Tirrell, M.V. Fibrin-binding, peptide amphiphile micelles for targeting glioblastoma. *Biomaterials* **2014**, 35, 1249–1256.
 68. Stefanelli, V.L. and Barker, T.H. The evolution of fibrin-specific targeting strategies. *J. Mater. Chem. B* **2015**, 3, 1177–1186.
 69. Puiggalí-Jou, A.; del Valle, L.J.; Armelin, E. and Alemán, C. Fibrin Association at Hybrid Bointerfaces Made of Clot-Binding Peptides and Polythiophene. *Macromol. Biosci.* **2016**, 16, 1461–1474.
 70. Shekhawat, G.S. and Dravid, V.P. Biosensors: Microcantilevers to lift biomolecules. *Nat. Nanotechnol.* **2015**, 10, 830–831.
 71. Calleja, M.; Kosaka, P.M.; San Paulo, Á. and Tamayo, J. Challenges for nanomechanical sensors in biological detection. *Nanoscale* **2012**, 4, 4925–4938.
 72. Waggoner, P.S. and Craighead, H.G. Micro- and nanomechanical sensors for environmental, chemical, and biological detection. *Lab Chip* **2007**, 7, 1238–1255.
 73. Arlett, J.L.; Myers, E.B. and Roukes, M.L. Comparative advantages of mechanical biosensors.

- Nat. Nanotechnol.* **2011**, 6, 203–215.
74. Ndieyira, J.W.; Kappeler, N.; Logan, S.; Cooper, M.A.; Abell C.; Mckendry, R.A. and Aeppli, G. Surface-stress sensors for rapid and ultrasensitive detection of active free drugs in human serum. *Nat. Nanotechnol.* **2014**, 9, 225–232.
 75. Kosaka, P.M.; Pini, V.; Ruz, J.J.; Silva, R. a da; González, M.U.; Ramos, D.; Calleja, M. and Tamayo, J. Detection of cancer biomarkers in serum using a hybrid mechanical and optoplasmonic nanosensor. *Nat. Nanotechnol.* **2014**, 9, 1047–53.
 76. Joo, J.; Kwon, D.; Yim, C. and Jeon, S. Highly sensitive diagnostic assay for the detection of protein biomarkers using microresonators and multifunctional nanoparticles. *ACS Nano* **2012**, 6, 4375–4381.
 77. Huber, F.; Lang, H.P.; Backmann, N.; Rimoldi, D. and Gerber, C. Direct detection of a BRAF mutation in total RNA from melanoma cells using cantilever arrays. *Nat. Nanotechnol.* **2013**, 8, 125–129.
 78. Wafula Ndieyira, J.; Watari, M.; Donoso Barrera, A.; Zhou, D.; Gtli, M.V.; Batchelor, M.; Cooper, M.A.; Strunz, T.; Horton, M.A.; Abell, C.; Rayment, T.; Aeppli, G. and Mckendry, R.A. Nanomechanical detection of antibiotic– mucopeptide binding in a model for superbug drug resistance. *Nat. Nanotechnol.* **2008**, 3, 691–696.
 79. Alvarez, M. and Lechuga, L.M. Microcantilever-based platforms as biosensing tools. *Analyst* **2010**, 135, 827–836.
 80. Tamayo, J.; Kosaka, P.M.; Ruz, J.J.; San Pauloa, A. and Call M. Biosensors based on nanomechanical systems. *Chem. Soc. Rev.* **2013**, 42, 1287–1311.
 81. Zhang, W.-M.; Hu, K.-Mi.; Peng, Z.-K. and Meng, G. Tunable Micro- and Nanomechanical Resonators. *Sensors* **2015**, 15, 26478–26566.
 82. Lechuga Gómez, L.; Álvarez-Sánchez, V. and Tamayo de Miguel, F. J. “U.S. patent 7,646,494 B2,” **2007**.
 83. Tamayo De Miguel, F. J.; Mertens, J. and Calleja-Gómez, M. “U.S. patent 7,978,344 B2,” **2011**.
 84. Ruoslahti, E.; Bhatia, S.N. and Sailor, M.J. Targeting of drugs and nanoparticles to tumors. *J. Cell Biol.* **2010**, 188, 759–768.
 85. Chevalier, S.; Cuestas-Ayllon, C.; Grazu, V.; Luna, M.; Feracci, H. and De La Fuente, J.M. Creating biomimetic surfaces through covalent and oriented binding of proteins. *Langmuir* **2010**, 26, 14707–14715.
 86. Eby, D.M.; Artyushkova, K.; Paravastu, A.K. and Johnson, G.R. Probing the molecular structure of antimicrobial peptide-mediated silica condensation using X-ray photoelectron spectroscopy. *J. Mater. Chem.* **2012**, 22, 9875–9883.
 87. Park, S.S.; Chu, S.-W.; Xue, C.; Zhaob, D. and Ha, C.-S. Facile synthesis of mesoporous carbon nitrides using the incipient wetness method and the application as hydrogen adsorbent. *J. Mater. Chem.* **2011**, 21, .
 88. Martínez, N.F.; Kosaka, P.M.; Tamayo, J.; Ramírez, J.; Ahumada, O.; Mertens, J.; Hien, T.D.;

-
- Rijn, C.V. and Calleja, M. High throughput optical readout of dense arrays of nanomechanical systems for sensing applications. *Rev. Sci. Instrum.* **2010**, 81, 125109.
89. Tamayo, J.; Pini, V.; Kosaka, P.; Martinez, N.F.; Ahumada, O. and Calleja, M. Imaging the surface stress and vibration modes of a microcantilever by laser beam deflection microscopy. *Nanotechnology* **2012**, 23, 315501.
90. Kosaka, P.M.; Tamayo, J.; Ruz, J.J.; Puertas, S.; Polo, E.; Grazu, V.; de la Fuente, J.M. and Calleja, M. Tackling reproducibility in microcantilever biosensors: a statistical approach for sensitive and specific end-point detection of immunoreactions. *Analyst* **2013**, 138, 863-872.
91. Han, M.G. and Foulger, S.H. Crystalline Colloidal Arrays Composed of Poly(3,4-ethylenedioxythiophene)-Coated Polystyrene Particles with a Stop Band in the Visible Regime. *Adv. Mater.* **2004**, 16, 231-234.



CHAPTER 9:

Conclusions

This chapter summarizes the main conclusions drawn from this Thesis.

9.1 General conclusions

Part A: Biomimetic membranes based on Omp2a transmembrane protein

First, an ambient resembling to the one encountered in nature is provided to study the Omp2a mechanical and morphological properties.

- The reconstitution of Omp2a into lipid bilayers provides platforms that fulfil both the nanometric dimensional requisite for truly mimicking biological attributes, and the conditions necessary for exploring their properties. Thus, a strategy able to collect the potential individual benefits of lipid bilayers and polymer-based nanomembranes into a single platform is expected to provide important advantages from a biotechnological point of view. For example, the immobilization of Omp2a-based lipid bilayers into the pores of nanoporated polymeric membranes would probably improve the ion affinity detection capability since the protein environment would be very close to native conditions and, therefore, the negative influence of the polymer in the protein structure would be eliminated.

Subsequently, physicochemical and structural properties of the protein organization upon thermal treatment are studied.

- Thermomechanical measurements at the microscopic level on functionalized cantilevers have provided molecular insights that complement the information obtained from conventional characterization techniques on ensembles formed by a very large number of molecules. A serious limitation of conventional techniques is that they provide only a sample average response and are unable to give information on specific local features on or within the sample.
- Soft post-thermal treatments could be very advantageous to improve the efficacy of polymeric NMs with porins immobilized onto the surface or confined inside synthetic pores. These treatments could regulate the amount of porin molecules active for the ion transport, controlling their orientation.

Finally, artificial interfaces for accommodating the protein are generated.

- Nanoperforated PLA FSNMs have been prepared using a two-step process: (1) spin-coating a mixture of immiscible polymers to cause phase segregation and formation of appropriated nanostructures (*i.e.* phase separation domains with dimensions similar to the entire film thickness); and (2) selective solvent etching to transform such nanostructures into nanoporations. For this purpose, PLA has been mixed with PVA and the diameter of the nanopores has been controlled through both the PLA:PVA ratio and the processing conditions of the mixture.
- Bioinspired FSNMs for selective ion transport have been tailored by immobilizing the Omp2a β -barrel membrane protein inside nanoporations created in flexible PLA nanomembranes. The bioinspired combination of nanostructures supported onto polymeric FSNMs with the confinement of OM proteins is a powerful approach that synergistically associates the most important advantages of each component. Thus, the incorporation of nanoporations enhances the transport of ions across PLA nanomembranes, whereas the functionality of immobilized Omp2a is essential to exhibit effects similar to those observed in biological nanomembranes.

Part B: Design of intrinsically controlled polymers for drug delivery systems

This part is devoted to the preparation of materials made of conducting polymers with nano- or microstructures for drug loading and delivery upon electrical stimuli.

- Hydrophobic drugs have been loaded into PEDOT by *in situ* emulsion polymerization. Polymer-drug interactions have been used to tailor the drug release profile by applying an externally electrical stimulus. More specifically, controlled and time-programmed release of CUR has been achieved in a physiological medium by applying a negative voltage of -1.25 V to loaded PEDOT nanoparticles.
- Electrospun PCL microfibers loaded with PEDOT NPs and CUR have been prepared and characterized. The smart release of CUR from the PCL microfibers has been achieved by applying well-defined potential pulses, which induce the

electro-mechanical response of PEDOT NPs, affecting the structure of the PCL matrix and promoting the release of drug.

Part C: Surface functionalization with CREKA

This section is thought to optimize platforms for protein recognition based on conducting films or silicon microcantilevers functionalized with pentapeptides.

- Comparison of PEDOT-CREKA and PEDOT-CR(MMe)EKA as biointerfaces reflects dissemblance in the organization of the peptides into the polymeric matrix. Both peptides affect fibrinogen thrombin-catalyzed polymerization causing the immediate formation of fibrin, whereas in absence of thrombin this phenomenon is only observed for CR(MMe)EKA. Consistently, the fibrin-adsorption capacity is higher for PEDOT-CR(MMe)EKA than for PEDOT-CREKA, even though both PEDOT-peptide films coated with fibrin are selective in terms of cell adhesion, promoting the attachment of metastatic cells with respect to normal cells.
- Tumor-homing peptides CREKA and CR(MMe)EKA have been covalently attached via epoxysilane chemistry onto silicon microcantilever chips that acted as sensors during dynamic nanomechanical experiments. The fibrin(ogen)-binding induced by CR(MMe)EKA has been detected by the resonance frequency shift of the cantilevers, and a detection limit of 100 ng/mL has been achieved. Our nanomechanical studies reflect the promising application of emerging technologies capable of assisting in the fully comprehension of biological interactions and their implications in the biotechnological field.

9.1 Specific conclusions

Part A: Biomimetic membranes based on Omp2a transmembrane protein

- The nanomechanical properties of Omp2a reconstituted into bilayers made of 4:3:1 POPC:POPE:POPG, which have been found to be the most homogenous and consistent among those studied in this Thesis, can be summarized as follows: average DMT moduli= 10.5 ± 1.7 MPa; adhesion force= 161.9 ± 9 pN; and protein deformation= 4.6 ± 0.7 nm, respectively.

- Nanomechanical properties of reconstituted Omp2a are clearly distinguishable from the ones determined for the lipid bilayer and reflect not only the satisfactory incorporation of the protein but also its low stiffness and high molecular flexibility. This key role played by Omp2a in the nutrition of bacteria.
- Electrochemical impedance spectroscopy measures of bilayers with different lipid-to-protein ratios indicate that the ion affinity increases with the protein concentration used in the proteoliposomes reconstitution. More specifically, a reduction of ~78% being observed between the control and the lowest lipid-to-protein ratio.
- The properties Omp2a-based SLBs are less suitable for technological applications than those of polymeric FSNMs with Omp2a immobilized in nanoporations.
- The unique thermomechanical response of Omp2a-functionalized cantilevers, which exhibits four well-defined regimes above 40 °C, suggests practical approaches to improve the efficacy of smart biomimetic NMs with porins immobilized onto the surface or confined inside synthetic pores.
- Maximization of favourable interactions among porin molecules has been achieved by heating the proteins from their initial assembly state to denaturalization and, subsequently, cooling under controlled conditions. This thermal treatment enhances the intermolecular β -sheets, which requires local orientation of the immobilized biomolecules.
- Nanoperforated PLA FSNMs of thickness 120-130 nm have been successfully obtained using spin-coating combined with phase segregation processes in immiscible 90:10 PLA:PVA mixtures and the subsequent removal of PVA domains via selective solvent etching.
- The diameter of the nanopores has been controlled through the conditions applied to the preparation of the PLA:PVA mixture, the dimensional scale of the phase separation domain decreasing when the mixing process is performed under vigorous stirring conditions. This procedure led to perforated PLA FSNM

with nanopores of $\phi = 170 \pm 73$ nm (prepared without stirring) and $\phi = 65 \pm 32$ nm (prepared under vigorous stirring).

- Cell proliferation assays showed that PLA nanomembranes with nanopores of $\phi = 170 \pm 73$ nm interact intensely with cell filopodia, which are protruding finger-like structures of $\phi = 100$ - 200 nm. Consequently, these nanomembranes exhibited cell viabilities significantly higher than those of nanofilms with pores of $\phi = 65 \pm 32$ nm and without perforations.
- The Omp2a porin has been integrated into nanoporated ultra-thin films of PLA by confining oval protein aggregates inside nanoporations of $\phi = 51 \pm 22$ nm. The resulting device, in which the protein preserves the β -barrel structure, fulfils the nanometric dimensional requisite for truly mimicking biological attributes.
- Omp2a-containing PLA NMs showed much higher ion transport activity than nanoporated films without immobilized Omp2a, especially at high electrolyte concentrations. Hence, the ion affinity of Omp2a-filled nanoporated PLA NMs increases with the concentration.
- The diffusion of Ca^{2+} and Na^{+} ions through Omp2a-filled nanopores is significantly higher than for K^{+} at concentrations ≥ 500 mM, suggesting that the novel Omp2a-PLA platform fulfils the conditions necessary for designing new NMs for biosensing, nanofluidics and ion-rectifying for energy conversion.

Part B: Design of intrinsically controlled polymers for drug delivery systems

- Encapsulation of CUR and PIP in PEDOT NPs was achieved by *in situ* emulsion polymerization using DBSA as stabilizer and doping agent. These two neutral drugs differ in their capacity to form hydrogen bonding interactions with the oxidized polymer chains, regulation of these interactions being used to tailor the release profile.
- The release of CUR is controlled through the strength of drug...PEDOT specific interactions, which become weaker when polymer chains are reduced applying an external negative voltage.

- CUR/PEDOT NPs are a promising combination that efficiently controls the release of the drug through external stimuli. This methodology, which can be extrapolated to other neutral drugs with similar hydrogen bonding abilities, may be a potential strategy for treatments based on the programmed dosage of CUR.
- PCL/PEDOT/CUR MFs have been successfully prepared by electrospinning. PEDOT NPs exhibit a diameter of 99 ± 21 nm and are mainly located inside the PCL MFs with diameter of 3.9 ± 0.7 μm .
- The topography of mats made of randomly collected PCL/PEDOT/CUR MFs resembles that of the extracellular matrix, facilitating cell spreading and enhancing cell proliferation because of their heterogeneity and roughness. Furthermore, *in vitro* assays have evidenced that CUR maintains the biological activity after the electrospinning process.
- PCL/PEDOT/CUR MFs exhibit potential advantages to regulate the CUR release by electrical stimulation. Thus, application of potential pulses causes changes at the MFs due to the migration of PEDOT NPs from inside to the surface. PEDOT NPs experience a volume change with concomitant “on-demand” CUR release.
- Independently of the concentration of CUR initially loaded into PCL/PEDOT/CUR MFs, the drug release dose increases with the number of potential pulses, scaling linearly. This feature proves that the incorporation of isotropic actuators, as PEDOT NPs, to biodegradable electrospun MFs is a successful approach for the development of programmable drug delivery devices.

Part C: Surface functionalization with CREKA

- PEDOT-peptide biocomposites have been prepared by chronoamperometry in basic aqueous solution. The electrochemical and electrical response of the resulting biocomposites is significantly better than that of PEDOT in terms of electroactivity, electrostability and electrical conductivity. Such improvement suggests that peptide molecules play simultaneously two roles acting, on one

side, as dopant agents that participate actively in oxidation and reduction processes and, on the other side, as structural supports that preclude the degradation of the polymer matrix during redox processes.

- Both CREKA and CR(NMe)EKA affect the fibrin THR-catalyzed polymerization inducing a very fast aggregation process. However, in absence of catalytic enzyme such fast aggregation phenomenon is only promoted by CR(NMe)KA, whereas CREKA induces a stepwise linear grow of fibrin particles. This behaviour is fully consistent with the ability of the different materials to adsorb fibrin at the surface, which grows in the following way: PEDOT < PEDOT-CREKA < PEDOT-CR(NMe)EKA.
- The two PEDOT-peptide biocomposites, which adsorb selectively fibrin, transform the shape of the adsorbed protein from the typical mesh of fibres to agglomerates with different round-like morphologies. This remarkable change has been attributed to the fact that the morphology of fibrin adsorbed onto the biocomposites is kinetically controlled through the very rapid aggregation process detected at the early stages of the Fg polymerization.
- Cell adhesion assays indicated that PEDOT-peptide-fibrin films promote the attachment of metastatic cells with respect to that of normal cells. However, this clearly manifested selectivity towards tumor cells is lost in absence of the fibrin coating.
- The biorecognition event between clotted plasma proteins and a tumor-homing pentapeptide, CR(NMe)EKA has been examined by applying a sensing technology based on microcantilevers. For such purpose, CREKA and CR(NMe)EKA were covalently linked via an epoxysilane-based protocol to Si substrates that efficiently activated by UV/ozone treatment. The results derived from the different characterization techniques performed at each one of the functionalization steps confirmed the suitability of the protocol to tether these linear, small peptides onto Si surfaces.
- CR(NMe)EKA-functionalized silicon substrates yield the highest Fb adsorption in PBS in comparison to CREKA-functionalized surfaces. Hence, after the

covalent binding of CR(NMe)EKA onto Si surfaces, NMe-Glu residue still promotes Fb-binding. Dynamic mode nanomechanical tests using CR(NMe)EKA-functionalized microcantilever sensors provided information regarding the interaction between Fb/Fg and the clot-binding peptide, thus establishing a detection limit of 100 ng/mL.

- Although further improvement is required to lower the detection limit and determine the specific binding affinity of CREKA and its analogues, the overall of nanomechanical results reflect the importance of developing emerging technologies suitable for specific biomedical purposes. With that goal in mind, extensive investigation is currently being performed in our laboratory to comprehend CREKA and CR(NMe)EKA-mediated clot-binding and expand their applications in the biotechnological field.

ANNEX

List of publications

1. Puiggali-Jou, A.; Medina, J.; del Valle L. J. and Alemán, C. Nanoperforations in poly(lactic acid) free-standing nanomembranes to promote interactions with cell filopodia. *Eur Polym J.* **2016**, 75, 552-564.
2. Puiggali-Jou, A.; del Valle, L. J.; Armelin, E., Alemán, C. Fibrin association at hybrid biointerfaces made of clot-binding peptides and polythiophene. *Macromol Biosci.* **2016**, 16, 1461-1474.
3. Puiggali-Jou, A.; Pérez-Madrugal, M. M.; del Valle, L. J.; Armelin, E.; Casas, M. T.; Michaux, C.; Perpète, E. A.; Estrany, F. and Alemán, C. Confinement of a β -barrel protein in nanoperforated free-standing nanomembranes for ion transport. *Nanoscale* **2016**, 8, 16922-16935.
4. Puiggali-Jou, A.; del Valle, L. J.; Alemán C. and Pérez-Madrugal, M. M. Weighing biointeractions between fibrin(ogen) and clot-binding peptides using microcantilever sensors. *J Pept Sci.* **2017**, 23, 162-171.
5. Puiggali-Jou, A.; Micheletti, P.; Estrany, F.; del Valle, L. J. and Alemán C. Electrostimulated release of neutral drugs from polythiophene nanoparticles: smart regulation of drug-polymer interactions. *Adv Healthc Mater.* **2017**, 6, 1-11.
6. Lopes-Rodrigues, M.; Puiggali-Jou, A.; Martí-Balleste, D.; del Valle, L. J.; Michaux, C.; Perpète, E. A. And Alemán, C. Thermomechanical response of a representative porin for biomimetics. *ACS Omega* **2018**, 3, 7856-7867.
7. Puiggali-Jou, A.; Pawlowski, J.; del Valle, L. J.; Perpète, E. A.; Sek, S. and Alemán, C. Properties of Omp2a-based supported lipid bilayers: comparison with polymeric bioinspired membranes. *ACS Omega* **2018**, 3, 9003-9019.
8. Puiggali-Jou, A.; Cejudo, A.; del Valle, L. J. and Alemán C. Smart drug delivery from electrospun fibers through electro-responsive polymeric nanoparticles. *ACS Appl Bio Mater.* **2018**, 1, 1594-1605.
9. Puiggali-Jou, A.; del Valle, L. J.; and Alemán, C. Biomimicking biological membranes incorporating transport proteins onto polymeric supports. Submitted to *Soft Matter*.
10. Puiggali-Jou, A.; del Valle, L. J.; and Alemán, C. Drug delivery systems based on intrinsically conducting polymers. Draft in progress.
11. Molina, B. G.; Cuesta, S.; Puiggali-Jou, A. and Alemán, C.; Electroactive, robust and flexible free-standing films by in situ anodic electropolymerization of PEDOT onto nanoperforated poly(lactic acid). Draft in progress.

Conference contributions

16th Iberian Peptide Meeting (16EPI) / 4th Chemical Biology Group Meeting (4GEQB)

Microcantilevers for weighting, sensing and thermal transitions characterization of proteins.

Puiggali-Jou, A.; Lopes-Rodrigues, M.; Martí-Balleste, D.; Pérez-Madrigal, M. M.; del Valle, L. J.;

Michaux, C.; Perpète, E. and Alemán, C.

Poster

Barcelona, Spain

05.02.2018-07.02.2018

II Peptide Materials for Biomedicine and Nanotechnology 2016 (II Pepmat 2016)

Fibrin association at hybrid biointerfaces made of clot-binding peptides and polythiophene.

Puiggali-Jou, A.; del Valle, L. J.; Armelin, E. and Alemán, C.

Poster

Barcelona, Spain

14.05.2016-16.05.2016

European Polymer Congress 2015 (EPC 15)

Self-supporting ultrathin membranes with tunable por size by means of lateral phase separation.

Puiggali-Jou, A.; Medina, J.; Estrany, F.; del Valle, L. J. and Alemán, C.

Poster

Dresden, Germany

21.06.2015-26.06.2015

Internships

April 2017-May 2017

University of Namur

Supervisors: Prof. Eric A. Perpète and Dr. Catherine Michaux

October 2016-December 2016

University of Warsaw, biological and chemical research centre

Supervisor: Prof. S. Sek.

April 2018-July 2018

Free University of Berlin

Supervisor: Prof. M. Calderon

